

# Theoretical Mechanistic Insight into Ground- and Excited-State Approaches to Modifying Reactivity

Nicholas Simon Hill

January, 2020



Australian  
National  
University

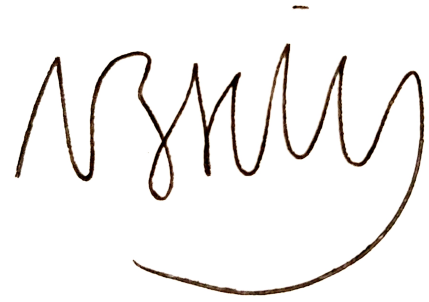
A thesis submitted for the degree of Doctor of Philosophy of  
The Australian National University.

©Copyright by Nicholas Simon Hill 2020

All Rights Reserved

## Declaration

This thesis presents my own original work and, to the best of my knowledge, contains no material written or published by any other person, except where due reference has been made. This work has not been previously submitted for any other degree or diploma at any university or institution.

A handwritten signature in brown ink, appearing to read 'N. Simon Hill', with a large, sweeping flourish underneath.

Nicholas Simon Hill

January 2020

## Acknowledgements

First and foremost, I'd like to thank my supervisor Professor Michelle Coote. Without Michelle, I would not have been involved with so many projects and different collaborators and through those been able to visit all corners of Australia for conferences and research visits. Michelle, thank you for answering my email in mid-2016 and inviting me to apply to the ANU and I look forward to following your continuing academic career successes.

I'd also like to thank the wider Coote research group, who over the past few years have been a fantastic group of scientists to work alongside and I will miss our conference group adventures to various Australian cities. In particular, I'd like to single out Dr. Benjamin Noble, who unknowingly taught me so much about computational chemistry and how to actually use it. Thank you for the conversations and the tips and tricks about Gaussian that has enabled me to make the progress evident in this thesis. Thank you again and good luck Ben.

It is also important to acknowledge the research bodies that allowed me to perform my research at all. Thank you to the ARC Centre of Excellence for Electromaterials Science for providing me with the funding; to the National Computational Infrastructure for their generous allocation of computing time; and to the Research School of Chemistry and the ANU for providing me with the opportunity to study in their world-class facilities.

Finally, many thanks to all of my friends and family who have supported me over the course of my PhD. Being on the other side of the world it can often feel like we're a long way apart. All of the trips and adventures we've had regardless have made the past few years all the more enjoyable.

## Abstract

In this thesis, theoretical chemistry methods have been employed to study different photochemical reactions, organocatalysts, and how this chemistry can be employed in the rational design of more efficient compounds. As necessary, computational methods and procedures were assessed and benchmarked for appropriateness and, when possible, calculated results and conclusions were set in context against experimental data. The main findings of this work are as follows.

Multi-component anthraquinone-based systems were studied for their visible light photoinitiating ability. Experimental and theoretical approaches were used to elucidate the photoinitiation mechanisms and rationalize the difference in reactivity between substitution patterns. Excited state redox processes were found to take place, and the substitution patterns and functional groups affect the radical cation and anion stabilities, relative to their excited states. These “electron shuttles” can initiate both cationic and radical polymerizations, as necessary.

Electric fields were applied to Norrish Type I photoinitiators, and compared with more established methods of altering photochemical behaviour. It was found that electric fields, introduced with charged functional groups, were a flexible approach (de)stabilizing different excited states, and tuning photochemical pathways.

Nitroxide-mediated photopolymerization agents were studied. Mesolytic cleavage, akin to what is observed upon electrochemical oxidation of alkoxyamines, is identified as being able to compete with the homolytic cleavage required for nitroxide-mediated polymerization. A strategy for designing agents that can undergo either cleavage pathways is developed, based on anthraquinone functionalization and electric fields.

Finally, Lewis acid and enzyme-inspired catalysis of two different reactions were investigated, demonstrating their respective effectiveness and rationalizing the source of the catalytic action.

# Contents

Declaration . . . . .	ii
Acknowledgments . . . . .	iii
Abstract . . . . .	iv
1 General Introduction . . . . .	1
1.1 Overview . . . . .	1
1.2 Outline of Thesis . . . . .	4
1.3 List of Publications . . . . .	5
1.4 References . . . . .	7
2 Review of Theoretical Methods and Their Application to Ground and Ex- cited States . . . . .	8
2.1 Introduction and Key Findings . . . . .	8
2.2 Publication 1 . . . . .	11
2.3 Publication 2 . . . . .	96
2.4 Summary and Outlook . . . . .	144
2.5 References . . . . .	145
3 Multi-functionalized Anthraquinone-based Photoinitiating Systems . . .	146
3.1 Introduction and Key Findings . . . . .	146
3.2 Publication 3 . . . . .	149
3.3 Publication 4 . . . . .	157
3.4 Publication 5 . . . . .	168
3.5 Publication 6 . . . . .	179
3.6 Publication 7 . . . . .	189

3.7	Implications and Applications . . . . .	196
3.8	References . . . . .	196
4	Strategies for the Rational Modification of Photochemical Properties . .	197
4.1	Introduction and Key Findings . . . . .	197
4.2	Publication 8 . . . . .	201
4.3	Publication 9 . . . . .	208
4.4	Implications and Applications . . . . .	217
4.5	References . . . . .	218
5	Theoretical Exploration and Rational Design of Nitroxide Mediated Pho- topolymerization and Photoalkylation Reactions . . . . .	219
5.1	Introduction and Key Findings . . . . .	219
5.2	Publication 10 . . . . .	222
5.3	Publication 11 . . . . .	230
5.4	Implications and Applications . . . . .	239
5.5	References . . . . .	241
6	Mechanistic Insights into Organo- and Lewis Acid Catalysis . . . . .	242
6.1	Introduction and Key Findings . . . . .	242
6.2	Publication 12 . . . . .	246
6.3	Publication 13 . . . . .	269
6.4	Implications and Applications . . . . .	284
6.5	References . . . . .	285
7	General Conclusions . . . . .	286
7.1	Summary of Key Findings . . . . .	286
7.2	Future Work . . . . .	288
7.3	References . . . . .	290
A	Appendices . . . . .	A1
A.1	Quantum Chemistry and Theoretical Procedures . . . . .	A1

A.2	Supporting Information: Rational Design of Photo-cleavable Alkoxyamines for Polymerization and Synthesis: Promotion and Deactivation of Cleavage Pathways . . . . .	A20
-----	---	-----

# 1 General Introduction

## 1.1 Overview

Polymerization reactions are an important class of organic reaction, as they provide chemists with access to macromolecular structures (polymers) that exhibit physical properties that can be tuned as necessary. As a result, polymeric materials are used in all commodity plastics, as well as in increasingly complex environments, for example *in vivo* as drug delivery systems<sup>1</sup> or in 3D-printed tissue repair,<sup>2</sup> as well as in smart polymer materials.<sup>3,4</sup> As polymer applications advance, so too must our scientific understanding of these systems and new ways of forming these materials must be formulated as current approaches to their synthesis may not be appropriate. To that end, this thesis details the studies performed that improve visible light photoinitiation efficiency for a class of functionalized anthraquinones, apply electric fields to Norrish Type I photoinitiation, and examine how the introduction of extra components for initiation may also result in favourable catalysis of subsequent chemical steps.

There are several key concepts that are dealt with throughout this thesis: free radical polymerization reactions, photochemistry, and organocatalysis. These are introduced below.

A chain polymerization reaction occurs via three steps:

1. Initiation: The first step, in which there is a net increase in the amount of radicals present.

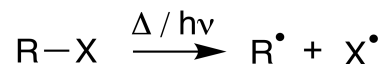


Figure 1.1: Dissociation of initiating species to form radical species

2. Propagation: The second step, in which there is no net change in the amount of radicals present, and the bulk of the polymer chain is formed.



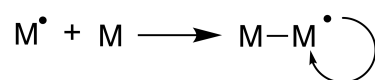


Figure 1.2: Propagation of monomer radical to form a polymer chain

3. Termination: The final step, in which there is a net decrease in the amount of radicals present, and the polymer chain growth stops.

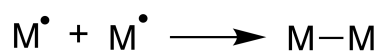


Figure 1.3: Radical-radical coupling step that terminates propagation

These steps are the same for cationic and anionic polymerization reactions, except with the free-radicals replaced with the relevant reactive species. Free-radical polymerizations are robust reactions, and are tolerant towards monomer functionality and reaction impurities. Precise temporal control of free-radical polymerizations can also be achieved by so-called “pseudo-living” polymerizations.<sup>5-7</sup>

Many polymerization reactions can be carried out under mild conditions, however the initiation step often requires more extreme conditions, either in the form of elevated temperatures or the absorption of ultraviolet (UV) light. These more extreme conditions may lead to issues in certain applications, however. For example, when 3D-printing tissue material, achieved by UV-curing gelatin methacrylate (GelMA),<sup>8</sup> the initiating photon of light can cause mutagenesis in printed cells due to UV damage to DNA.<sup>9</sup> Elevated temperatures are also not an option in this situation, as cellular proteins will begin to denature. There is therefore a clear motivation for the continuing development of efficient, mild initiating agents.

UV curing is an example of a photochemical reaction. Photochemistry a broad term relating to reactions that take place upon the absorption of a photon (or multiple photons) of light. These reactions can be, for example, excited state energy transfer,<sup>10</sup> electron transfer (redox) processes,<sup>11</sup> proton transfers,<sup>12</sup> photoisomerization reactions,<sup>13</sup> or decomposition reactions.<sup>14</sup> Due to their complicated and short-lived nature, excited state reactions are often difficult to study using experimental methods, and designing more efficient photochemical reactions is therefore difficult. As a result, theoretical

chemistry is a useful tool as the excited state energies and properties of a particular system can be calculated and studied, without the constraints arising from using spectroscopic methods. However, the accuracy of these methods cannot be taken for granted, and they must be assessed and benchmarked for suitability prior to drawing conclusions from their results.

The final key concept explored in this thesis is catalysis, the process by which a substance increases the rate of a reaction without undergoing a net chemical change.<sup>15</sup> Two different organic reactions are examined using theoretical methods, both of which are related to polymerization reactions. Computational modelling and design of catalysts is an active and expanding area of research,<sup>16-19</sup> as the thermodynamic and kinetic properties of both the uncatalysed and catalysed reactions can be calculated and compared. This is relevant to the rest of the work performed in this thesis as the introduction of functionality to a photo-reaction will also alter the ground state reactivity of the system. These effects need to be investigated as they may, like upon the introduction of Lewis acids, impart useful catalytic effects on subsequent reaction steps.

From the three fundamental concepts described above, the aims of this thesis are:

1. Review recent literature to establish both the “state-of-the-art” with respect to modelling excited states, and best practice with respect to modelling open-shell systems in general
2. In conjunction with experimental collaborators, provide computational insight into photoinitiation and catalytic mechanisms of reactions using organic molecules, from which design improvements can be identified
3. Using this knowledge and refined approach to modelling these complex reactions, design new photoinitiating molecules that offer clear advantages over the existing class of molecules

Throughout this thesis, free energy calculations were performed and the results of which form the basis of many different arguments, conclusions, and predictions. It is therefore worth noting that although IUPAC now recommends using the term “Gibbs energy”, this

thesis, in line with journal conventions, uses the term “Gibbs free energy”.

## 1.2 Outline of Thesis

This thesis is presented as a series of peer-reviewed articles that have been published or accepted for publication, organized into the following chapters:

**Chapter 2** includes an extensive review of literature published in the last five years that utilizes, in some manner, theoretical chemistry to study excited states, and helps to identify reliable methodology for the calculations used in this thesis [*Publication 1*]. Building on this work, the second publication is a methodological guide to studying nitroxide molecules. Nitroxide molecules are an excellent class of molecules against which to establish computational modelling best practice, as they exhibit a full range of calculable properties that are a challenge for current theoretical methods [*Publication 2*]. This chapter provides a base of knowledge, upon which subsequent chapters and studies are built.

**Chapter 3** describes the extensive studies performed investigating functionalized anthraquinone molecules for visible-light photoinitiation. These are collaborative projects, using both experimental and theoretical results to assess their performance and initiation mechanisms [*Publications 3-7*].

**Chapter 4** details how static electric fields, introduced by functionalization with acid and base groups, can be applied to acetophenone, a Norrish Type I photoinitiator, in a manner that is controlled, predictable, and useful [*Publication 8*]. The effect of the electric fields is then applied to a molecule more likely to benefit from their introduction, and the effect is compared and contrasted to other approaches to manipulating photochemistry [*Publication 9*].

**Chapter 5** studies the performance of nitroxide mediated photopolymerization reactions, and highlights how different cleavage reactions can be used to explain the observed chromophore and monomer dependent polymerization behaviour [*Publication 10*]. Building on this study, and those in Chapters 3 and 4, a computational study into how different substitution patterns of anthraquinone-functionalized can be used to en-

hance or deactivate different cleavage pathways is performed, and how these molecules can be used for either free radical or alkylation reactions [Publication 11].

**Chapter 6** is the final chapter describing experimental and theoretical studies performed, and details the studies into Lewis acid catalysis [Publication 12] and the performance of a novel, artificial catalytic triad [Publication 13].

**Chapter 7.** A summary of the key findings within this thesis, an overall conclusion to the work performed, and ideas for future work, are all described in this chapter.

**Appendices.** Appendix A.1 gives a thorough introduction and overview of theoretical chemistry and the methods used throughout this thesis to perform computational studies. Appendix A.2 contains the supporting information for Publication 11 which wasn't available online as of submission of this thesis.

### 1.3 List of Publications

This thesis is presented as a series of peer reviewed articles. In each publication in which I am not listed as first author, I am the first named computational chemist author.

**Publication 1.** Hill, N. S.; Coote, M. L.; “A Comparison of Methods for Theoretical Photochemistry: Applications, Successes and Challenges” in *Annual Reports in Computational Chemistry*, Chapter 7, Volume 15, **2019**, Pages 203-285

**Publication 2.** Hill, N. S.; Noble, B. N.; Rogers, F. J. M.; Fung A. K. K.; Coote, M. L.; “Computational Tools for Nitroxide Design” in *Nitroxides: Synthesis, Properties and Applications*, **2020**

**Publication 3.** Zhang, J.; Hill, N. S.; Lalevée, J.; Fouassier, J.-P.; Zhao, J.; Graff, B.; Schmidt, T. W.; Kable, S.H.; Stenzel, M. H.; Coote, M. L.; Xiao, P., “Multihydroxy-Anthraquinone Derivatives as Free Radical and Cationic Photoinitiators of Various Photopolymerizations under Green LED”, *Macromol. Rapid Commun.*, **2018**, 1800172

**Publication 4.** Zhang, J.; Lalevée, J.; Hill, N. S.; Launay, K.; Morlet-Savary, F.; Graff, B.; Stenzel, M. H.; Coote, M. L.; Xiao, P., “Disubstituted Aminoanthraquinone-based Multicolor Photoinitiators: Photoinitiation Mechanism and Ability of Cationic Polymerization under Blue, Green, Yellow and Red LEDs”, *Macromolecules*, **2018**, 51,

**Publication 5.** Zhang, J.; Launay, K.; Hill, N. S.; Zhu, D.; Cox, N.; Langley, J.; Lalevée, J.; Stenzel, M. H.; Coote, M. L.; Xiao, P., “Disubstituted Aminoanthraquinone-based Photoinitiators for Free Radical Polymerization and Fast 3D Printing under Visible Light”, *Macromolecules*, **2018**, 51, 10104–10112.

**Publication 6.** Wang, G.; Hill, N. S.; Zhu, D.; Xiao, P., Coote, M. L.; Stenzel, M. H., “An Efficient Photoinitiating System Based on Diaminoanthraquinone for 3D Printing of Polymer/Carbon Nanotube Nanocomposites Under Visible Light”, *ACS Appl. Polym. Mat.*, **2019**, 1, 1129–1135.

**Publication 7.** Zhang, J.; Lalevée, J.; Hill, N. S.; Peng, X.; Zhu, D.; Kiehl, J.; Morlet-Savary, F.; Stenzel, M. H.; Coote, M. L.; Xiao, P., “Photoinitiation Mechanism and Ability of Monoamino-Substituted Anthraquinone Derivatives as Cationic Photoinitiators of Polymerization under LEDs”, *Macromol. Rapid Commun.*, **2019**, 40, 1900234

**Publication 8.** Hill, N. S.; Coote, M. L., “Internal Oriented Electric Fields as a Strategy for Selectively Modifying Photochemical Reactivity”, *J. Am. Chem. Soc.*, **2018**, 140, 17800–17804

**Publication 9.** Hill, N. S.; Coote, M. L., “Strategies for Red-Shifting Type I Photoinitiators: Internal Electric Fields vs Lewis Acids vs Increasing Conjugation”, *Aust. J. Chem.*, **2019**, 72, 627–632

**Publication 10.** Hill, N. S.; Fule, M. J., Morris, J., Clement, J. L., Guillaneuf, Y., Gigmes, D., Coote, M. L., “Mesolytic versus Homolytic Cleavage in Photochemical Nitroxide Mediated Polymerization”, *Macromolecules*, **2020**, 53, 1567–1572.

**Publication 11.** Hill, N. S.; Coote, M. L., “Rational Design of Photo-cleavable Alkoxyamines for Polymerization and Synthesis: Promotion and Deactivation of Cleavage Pathways”, *Physical Chemistry Chemical Physics*, **2020** Submitted

**Publication 12.** Hill, N. S.; Noble, B. N.; Coote, M. L., “Mechanistic Insights into Lewis Acid Mediated Sequence- and Stereo-control in Radical Copolymerization” in *Reversible Deactivation Radical Polymerization: From Mechanisms to Materials and Applications*, Eds. Tsarevsky, N.; Gao, G.; Matyjaszewski, K.; Sumerlin, B., American Chemical

Society 2018

**Publication 13.** Nothling M. D.; Xiao Z.; Hill, N. S.; Blyth M. T.; Bhaskaran A.; Sani MA.; Espinosa-Gomez A.; Ngov K.; White J.; Buscher T.; Separovic F.; O'Mara M.; Coote M. L.; Connal L. A.; "A Multi-Functional Surfactant Catalyst Inspired by Hydrolyases" *Science Advances* **2020**, 6, eaaz0404

## 1.4 References

- (1) Liechty, W. B.; Kryscio, D. R.; Slaughter, B. V.; Peppas, N. A. *Annual Review of Chemical and Biomolecular Engineering* **2010**, 149–173.
- (2) Klotz, B. J.; Gawlitta, D.; Rosenberg, A. J. W. P.; Malda, J.; Melchels, F. P. W. *Trends in Biotechnology* **2016**, 34, 394–407.
- (3) Roy, I.; Gupta, M. N. *Chemistry & Biology* **2003**, 10, 1161–1171.
- (4) Aguilar, M. R.; San Román, J. In *Smart Polymers and their Applications*; Woodhead Publishing: 2014, pp 1–11.
- (5) Wang, J.-S.; Matyjaszewski, K. *Journal of the American Chemical Society* **1995**, 117, 5614–5615.
- (6) Georges, M. K.; Veregin, R. P. N.; Kazmaier, P. M.; Hamer, G. K. *Macromolecules* **1993**, 26, 2987–2988.
- (7) Chiefari, J.; Chong, Y. K. (; Ercole, F.; Krstina, J.; Jeffery, J.; Le, T. P. T.; Mayadunne, R. T. A.; Meijs, G. F.; Moad, C. L.; Moad, G.; Rizzardo, E.; Thang, S. H. *Macromolecules* **1998**, 31, 5559–5562.
- (8) Yue, K.; Trujillo-de Santiago, G.; Alvarez, M. M.; Tamayol, A.; Annabi, N.; Khademhosseini, A. *Biomaterials* **2015**, 73, 254–271.
- (9) Dahle, J.; Kvam, E.; Stokke, T. *Journal of Carcinogenesis* **2005**, 4, 11.
- (10) Sun Cho, H.; Jeong, D. H.; Yoon, M. C.; Kim, Y. H.; Kim, Y. R.; Kim, D.; Jeoung, S. C.; Kim, S. K.; Aratani, N.; Shinmori, H.; Osuka, A. *Journal of Physical Chemistry A* **2001**, 105, 4200–4210.
- (11) Corrigan, N.; Shanmugam, S.; Boyer, C. *Chemical Society Reviews* **2016**, 36, 385–394.
- (12) Ma, H.; Huang, J.-D. *RSC Advances* **2016**, 6, 96147–96153.
- (13) Diau, E. W. G. *Journal of Physical Chemistry A* **2004**, 108, 950–956.
- (14) Frick, E.; Ernst, H. a.; Voll, D.; Wolf, T. J. a.; Unterreiner, A.-N.; Barner-Kowollik, C. *Polymer Chemistry* **2014**, 5, 5053.
- (15) Atkins, P.; De Paula, J., *Atkins' Physical Chemistry*, Ninth Edit; Oxford University Press: Oxford, 2010.
- (16) Hammes-Schiffer, S. *Accounts of Chemical Research* **2017**, 50, 561–566.
- (17) Poree, C.; Schoenebeck, F. *Accounts of Chemical Research* **2017**, 50, 605–608.

- (18) Lam, Y. H.; Grayson, M. N.; Holland, M. C.; Simon, A.; Houk, K. N. *Accounts of Chemical Research* **2016**, *49*, 750–762.
- (19) Cheong, P. H. Y.; Legault, C. Y.; Um, J. M.; Çelebi-Ölçüm, N.; Houk, K. N. *Chemical Reviews* **2011**, *111*, 5042–5137.

## 2 Review of Theoretical Methods and Their Application to Ground and Excited States

### 2.1 Introduction and Key Findings

Before beginning research into photochemical reactions with computational chemistry, it is important to first conduct a comprehensive review of the recent literature on the topic. Doing so will allow for the relative merits of the excited state methods available in modern electronic structure software packages, as well as their successes and failings, to be identified and assessed. It is also necessary to determine the best scientific approach to modelling molecular properties and reactions, as with the increasing popularity of computational chemistry in contemporary scientific literature it is important to make sure any conclusions drawn are valid and of publishable quality.

Publication 1 is the literature review itself, focusing on studies published in the five years prior to its publication, i.e. 2013-2018. Instead of studying all possible methods, the review highlights research performed using HF-based methods,<sup>1</sup> multireference methods,<sup>2</sup> and time-dependent density functional theory (TD-DFT) methods.<sup>3</sup> Each of these three methods hold advantages and disadvantages over each other, and these are highlighted within the publication. A thorough introduction to quantum chemistry, the different available theories, and basis sets is in Appendix A.1.

To summarise the review, uncorrelated wavefunction methods (HF-based) are the cheapest methods to run computationally, and can therefore be applied to systems that are too large for other methods. Due to the lack of electron correlation, HF methods are generally inaccurate and therefore not often used. Multireference calculations, in particular those employing the complete-active space perturbation theory (CASPT $n$ ) method, continue to be regarded as the gold-standard in excited state modelling, at the expense of low computational cost and so-called “black box” behaviour.<sup>4</sup> A black box method is one that will systematically compute the energies of  $n$  excited states with no explicit intervention from a user being required. Most multireference methods are



not black box because an “active space” has to be defined. An active space contains the chemically relevant orbitals which are to be correlated in the overall wavefunction. Often this orbital selection is non-systematic, and different active spaces applied to the same molecule can give different excited state energies and properties. As well as this, the computational cost of increasing the size of an active space is factorial, restricting calculations to those that involve correlating no more than approximately 18 orbitals.

Finally, TD-DFT studies are reviewed. TD-DFT is the most widely used of all the excited state methods, and is used extensively throughout this thesis. TD-DFT generally suffers from the same drawbacks as DFT; energies and structures are exchange correlation functional-dependent, and errors are non-systematic difficult to predict.<sup>5</sup> Despite this, TD-DFT offers the best compromise between computational cost and accuracy. Where quantitative information or a complete description of an excited state potential energy surface is required, TD-DFT is not the best method available. However, where a qualitative description of a molecule’s photochemistry is desired, TD-DFT performs well and is able to capture trends in photoreactivity. There also exists a large number of published benchmarking studies comparing TD-DFT performance against that of high-level, *ab initio* excited state methods for a range of different molecules, allowing for the appropriate selection of an exchange correlation functional.<sup>6</sup>

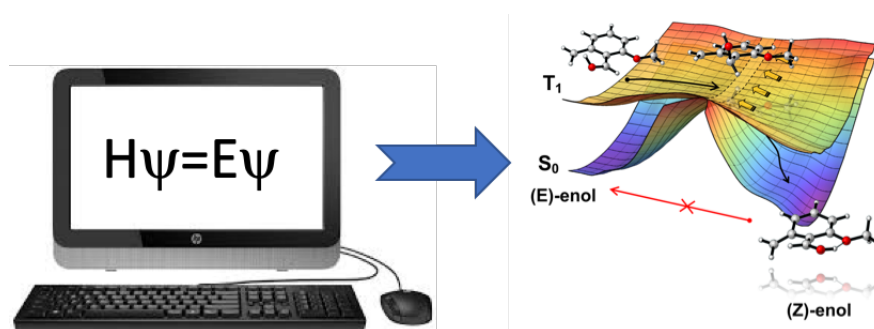
Building on Publication 1, Publication 2 is a methodological guide to studying and computing the properties of nitroxide molecules. Nitroxide molecules are a challenge for theoretical chemists as they exhibit a wide range of properties that can be computed, including oxidation and reduction potentials,<sup>7</sup> photoreactivity,<sup>8</sup> and electron paramagnetic spin resonance.<sup>9</sup> Not all of these properties can be calculated in every electronic software package, nor with every level of theory, and there are many practical considerations including the choice of basis set, and the accuracy required from the proper treatment of electron correlation. The guide provides overviews of theoretical concepts and considerations, case studies, and method recommendations for computational chemists, rather than in-depth studies into nitroxide chemistry. The lessons and practical considerations are applicable to a wide-range of organic molecules and their reactions.

## 2.2 Publication 1

### A Comparison of Methods for Theoretical Photochemistry: Applications, Successes and Challenges

Nicholas S. Hill, Michelle L. Coote

*Annual Reports in Computational Chemistry* 2019



This publication is a peer-reviewed manuscript published as a book chapter in *Annual Reports in Computational Chemistry*. The literature review, and subsequent insight and discussion of are my own work. Prof. Michelle Coote assisted with the direction of the review and corrected my drafts.

### Statement of Contribution

This thesis is submitted as a Thesis by Compilation in accordance with [https://policies.anu.edu.au/ppi/document/ANUP\\_003405](https://policies.anu.edu.au/ppi/document/ANUP_003405)

I declare that the research presented in this Thesis represents original work that I carried out during my candidature at the Australian National University, except for contributions to multi-author papers incorporated in the Thesis where my contributions are specified in this Statement of Contribution.

Title: A Comparison of Methods for Theoretical Photochemistry: Applications, Successes and Challenges

Authors: Nicholas S. Hill, Michelle L. Coote

Publication outlet: Annual Reports in Computational Chemistry

Current status of paper: Published

Contribution to paper: I reviewed the literature and wrote the draft manuscripts

Senior author or collaborating authors endorsement: Michelle Coote

Nicholas Hill



20/01/2020

Candidate - Print Name

Signature

Date

### Endorsed

Michelle Coote



20/01/2020

Primary Supervisor – Print Name

Signature

Date

Luke Connal



20/01/2020

Delegated Authority – Print Name

Signature

Date



# A comparison of methods for theoretical photochemistry: Applications, successes and challenges

Nicholas S. Hill, Michelle L. Coote\*

ARC Centre of Excellence for Electromaterials Science, Research School of Chemistry, Australian National University, Canberra, ACT, Australia

\*Corresponding author: e-mail address: michelle.coote@anu.edu.au

## Contents

1. Introduction	204
2. Photochemical phenomena	205
2.1 Excited state potential energy surfaces (PESs)	205
2.2 Simulation of spectra	207
2.3 Other important phenomena	207
3. Time-dependent Hartree-Fock (TD-HF)	208
3.1 Nonlinear optical properties	208
3.2 Electron dynamics	209
3.3 Supplementing TD-HF with TD-DFT	210
3.4 Assessment	211
4. Configuration interaction	211
4.1 Absorption and emission spectra	212
4.2 Assessment	214
5. Multireference studies	215
5.1 Mechanistic studies	216
5.2 Restricted active spaces (RAS)	221
5.3 Quantum Monte-Carlo (QMC)	223
5.4 Benchmarking studies	224
5.5 Assessment	227
6. Time-dependent density functional theory	228
6.1 Methodological developments	228
6.2 Dye chemistry	232
6.3 Excited state intramolecular proton transfer	238
6.4 Photoinitiation	241
6.5 Other photochemical reactions	243
6.6 UV-Vis spectra and excitation energies	245
6.7 Thermally activated delayed fluorescence (TADF)	249

6.8	Fluorescence and quenching	252
6.9	Other properties	255
6.10	Assessment	257
7.	Solvent and environmental effects	258
7.1	Continuum versus explicit solvent	258
7.2	Equilibrium versus nonequilibrium solvation	262
7.3	Other environmental effects	263
8.	Conclusion	264
	Conflicts of interest	265
	Acknowledgments	265
	References	265
	Further reading	284

## Abstract

Herein we highlight recent studies and active areas of interest in the ongoing challenge to model photochemical processes in a wide variety of molecules. We also discuss recent significant methodological improvements and developments that may aid future investigations. Studies using the wide range of techniques available in modern electronic structure software packages have been included, with their successes and shortcomings forming part of the discussion. This study should therefore aid in the design of future computational studies.



---

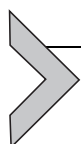
## 1. Introduction

Photochemical processes cover a wide-range of physical phenomena that molecules can undergo upon the absorption of radiation, and to this day remain a challenge to model using computational methods. While ground state chemistry is dominated by the relative energies of reactants, products, and the resulting possible transition states, and can be subjected to traditional thermodynamic and kinetic arguments, often in photochemistry these central tenets no longer hold. The interplay of competing processes, generally described as radiative and nonradiative, can result in observed behavior arising due to degeneracies in electronic states, symmetry arguments, the nature of the excited state, often while a molecule is populating a nonequilibrium geometry.

The difficulty in modeling the excited states of molecules initially arises from the failings of the traditional self-consistent field (SCF) approach to variationally solving the time-independent Schrodinger equation. Simply taking, for example, a ground state Hartree-Fock (HF) reference wavefunction and

promoting an electron into a virtual orbital to form a new, excited state Slater determinant may make physical sense in the description of the state of interest, however, a standard SCF procedure will then simply drive the determinant back to its ground state form, leaving the excited state inaccessible. This variational collapse, while avoidable in some rare, favorable cases, is ubiquitous.

A wide range of theories have therefore been developed that guard against such issues, including theories based on HF wavefunctions, post-HF wavefunctions, e.g., coupled-cluster (CC), Møller-Plesset (MP $n$ ) perturbation theory, multireference wavefunctions, and Density Functional Theory (DFT).<sup>1</sup> Dynamic simulations can also be performed using a variety of theories. Each method has its own associated shortcomings and scaling issues, and suitability to modelling different types of photochemical phenomena. This review will therefore aim to determine which methods are favored in recent literature, to assess if progress toward addressing shortcomings has been made, and to highlight continuing challenges. This review builds on previous significant reviews focused on photochemistry by Santoro,<sup>2,3</sup> Laurent,<sup>4</sup> Garavelli,<sup>5</sup> and Serrano-Andres<sup>6</sup> by focusing on recent studies, namely, those published within the last 5 years. Moreover, our focus is on comparing a range of different theoretical methods and where they were applied, rather than on applications of a single method or advances made within the formalism of the method itself.



## 2. Photochemical phenomena

There are many photochemical effects that can be modeled using the wide-range of computational methods available (Fig. 1); the most important types of phenomena are outlined below.

### 2.1 Excited state potential energy surfaces (PESs)

Invariably, excitation energies along reaction coordinates are essential for gaining mechanistic insight into photochemical reactions. Accurate energies can, for example, show how transition state energies for a reaction can decrease upon excitation, or how a reaction coordinate can become dissociative upon excitation, leading to homolysis. They are also necessary for simulation of radiative decay processes, e.g., emission energies, as these are dependent on the relaxed geometry of the molecule of interest. PESs are also important as observed photochemical behavior is often not defined by a single excited state, instead, population of a certain state can take place followed by crossing to a different state on which the reaction takes place,

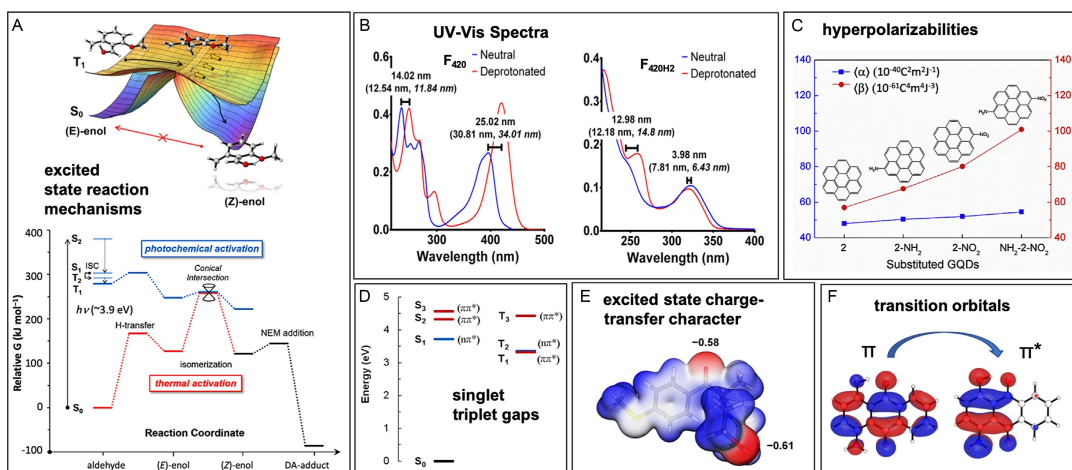


**Fig. 1** Typical examples of the types of photochemical phenomena that can be modelled using theoretical chemistry: (A) the excited reaction mechanism for keto-enol tautomerization of an *o*-methyl benzaldehyde derivative (methyl 4-((2-formyl-3-methylphenoxy)methyl)benzoate) that is subsequently trapped in a Diels-Alder reaction<sup>7</sup>; experimental and simulated UV-Vis spectra for the deaflavin dependent nitroreductase enzyme bound cofactor F<sub>420</sub> and its reduced form F<sub>420H2</sub> in their respective neutral and deprotonated forms<sup>8</sup>; (C) electronic polarizability and second hyperpolarizability of graphene quantum dots as a function of substituent<sup>9</sup>; the (D) vertical singlet-triplet excitation energies and (E) electrostatic potential surface of the T<sub>1</sub> ππ\* excited state of 2-Methyl-4'-(methylthio)-2-morpholinopropiophenone<sup>10</sup>; (F) the orbitals involved in the S<sub>1</sub> ππ\* transition of 1-amino-4-hydroxyanthraquinone.<sup>11</sup> *Figures adapted with permission from the original references.*

known as nonradiative processes.<sup>12</sup> The proper capture of the nature of electronic (near) degeneracies, either at conical intersections or avoided crossings, can be required when quantitative insight into the photochemical mechanism(s) is sought. As shown below, not all methods can produce such accuracy; however, qualitative insight may only be necessary, and approximate PES can often be obtained from cheaper methods.

## 2.2 Simulation of spectra

Many implemented excited state codes, where  $n$  excited states are obtained variationally, can compute oscillator strengths and transition dipole moments between the  $S_0$  and the  $n$ th excited state; this information can be coupled with the corresponding excitation energy to simulate different types of spectra. Simulation of spectra can provide invaluable insight into the initial photochemical processes taking place upon excitation; UV–vis spectra are often experimentally available and the similarity between the computed and experimental spectra can suggest the excitation features are being correctly modelled. Modern implementations also include the orbitals involved in the transition, from which it is possible to determine the nature of the excited state; for example, is the lowest energy transition to a bright  $\pi\pi^*$  state, as can be observed in both computed and experimental spectra, or is it a dark  $n\pi^*$  state, which won't be visible but could be photochemically relevant? Emission spectra can also be computed using the relaxed excited state geometry, from which Stokes' shifts can be estimated. Often, absolute accuracy of the computed spectra is not necessary; instead, the capture of trends may be more important. For example, one may be attempting to tune a certain property of a molecule (e.g., HOMO-LUMO gap), for which a range of substituents may be tested. Proper capture of the substituent effects (e.g., red-shift vs blue-shift) on the property therefore provides insight for targeted design.

## 2.3 Other important phenomena

Excited state PESs and simulated spectra are two popular uses for excited state methods; other phenomena that can be modeled include the following.

*Singlet-triplet energy gaps ( $\Delta E_{ST}$ ).* Accurate values of  $\Delta E_{ST}$  can provide insight into the likelihood of singlet-triplet crossing upon excitation.

*Charge-transfer (CT) vs local excitation (LE).* An excited state with CT character involves a significant shift in electron density to different region of a molecule. These states can have profound effects on a molecule's optical



properties, yet can be challenging to model due to self-interaction error<sup>13</sup> (in DFT), and significant orbital relaxation being required.

*Nonlinear optical effects.* Not all photochemistry necessarily arises from the absorption/emission of a single photon. It is therefore sometimes necessary to compute two-photon cross-sections, for when two-photon absorption is observed. It is also sometimes necessary to compute high-order hyperpolarizabilities, which can give rise to, for example, high-order harmonic generation effects.



### 3. Time-dependent Hartree-Fock (TD-HF)

HF theory is the theoretical cornerstone for all ab initio quantum chemistry theories, and therefore provides a natural starting point for extension to excited state. The main excited state HF-based methods are configuration interaction with single and double substitutions (CIS and CISD, respectively), and time-dependent HF (TD-HF). However, HF theory infamously neglects dynamic electron correlation. In certain situations, for example when modeling isodesmic reactions, HF can provide quantitative accuracy due to favorable error cancellation; however, in excited states where orbital occupancies are different to the ground state, and where the excited state electron density will be necessarily more diffuse, there is no reasonable expectation for the electron correlation energy of the two states to cancel. CIS(D) and TD-HF do, however, benefit from favorable scaling with respect to system size, so can be employed where high-level, high-accuracy ab initio calculations are simply not feasible.

#### 3.1 Nonlinear optical properties

Recent studies<sup>14–17</sup> employing TD-HF have focused on investigating nonlinear optical (NLO) properties, predominantly due to the implementation of the relevant calculations required to compute these properties. Karakas et al.<sup>16</sup> investigated the two-photon absorption (TPA) cross-sections, electric dipole moment, and the second-order hyperpolarizability of tetrathiafulvalene derivatives, with and without Pt(II) and Pd(II). The authors claim good agreement with previous experimental data, despite the theoretical values for isotropic second hyperpolarizabilities being overestimated, compared to experimental data, by between 1 and 2 orders of magnitude. Guezguez et al.<sup>17</sup> performed a similar study on Au(III) dithiolene complexes, in which electric dipole moments, dispersion-free and frequency-dependent dipole polarizability, and second hyperpolarizability

tensor components were calculated. The calculations show much closer agreement with experimental values of third order susceptibility ( $X^3$ ) than from similar calculations presented in Karakas<sup>14,16</sup> and Zawadzka<sup>15</sup> (2015) employ similar calculations but this time to styrylquinolinium dyes and metallophthalocyanine chlorides, respectively. In these four studies, TD-HF is successful as the calculation of second- and third-order nonlinear properties is relatively trivial, and the inaccuracy of TD-HF is largely irrelevant; instead, the studies utilize the results for qualitative trends, rather than for mechanistic arguments.

In a similar vein, Wu et al.<sup>18</sup> used TD-HF to calculate second-order hyperpolarizabilities on a variety of increasingly substituted triarylamine chromophores, finding that addition of several methoxy groups resulted in a large increase in hyperpolarizability, compared to the unsubstituted molecule. This is likely due to the increased electron density in the  $\pi$ -system of the molecule, and this conclusion is supported by that of Alparone,<sup>19</sup> who showed that increasing fluoro-substitution of benzene, and hence decreasing electron density in the  $\pi$ -framework, results in a decrease in calculated second-order hyperpolarizability. Alparone used MP2 to calculate the second-order hyperpolarizabilities as well as TD-HF, and both sets of results are in good agreement. The TD-HF results are systematically underestimated for all 13 molecules investigated compared to the MP2 results, however, trends are identical.

NLO studies have also been performed using TD-HF on a dithienylethene-indolinooxazolidine-benzazoolooxazolidine system,<sup>20</sup> on merocyanine dyes,<sup>21</sup> on an explicitly benzene-solvated nitrobenzene system,<sup>22</sup> on triarylamine (TAA) chromophores,<sup>18</sup> on fluorobenzenes,<sup>19</sup> on 2-aminobenzimidazole complexes,<sup>23</sup> and on 3-(4-methoxyphenyl)-1-(4-nitrophenyl)prop-2-en-1-one (MNC).<sup>24</sup> All of these studies involve relatively large molecules (>20 heavy atoms) and therefore benefit from the relative inexpensive HF calculations.

### 3.2 Electron dynamics

Studies by Lötstedt et al.<sup>25</sup> and Hu et al.<sup>26</sup> use TD-HF to study the electron dynamics of acetylene upon exposure to an intense laser field; here using time-dependent in the literal, rather than theoretical, sense. Luzanov<sup>27</sup> and Nguyen and Parkhill<sup>28</sup> also apply TD-HF to nonstationary photochemical behavior. Nguyen and Parkhill use real-time TD-HF as a comparison for their newly developed time-dependent open self-consistent field at

second order (OCSF2) propagation method on 4-((4-(dimethylamino)-phenyl)buta-1,3-diyne-1-yl)benzotrile, demonstrating that their method can cope with nonadiabatic dynamic behavior. Sato and Ishikawa<sup>29</sup> also applied TD-HF to laser-field ionization dynamics, using a one-dimensional helium atom as the test case, as a full numerical solution to the dynamic ionization process in this system is possible. However, they found that the closed shell TD-HF model is insufficient to model the relatively extreme dynamics produced upon exposure to strong lasers.

### 3.3 Supplementing TD-HF with TD-DFT

Bondu et al. (2015), Bruckner et al. (2015), and Maidur et al. (2017) use a combined TD-HF and DFT approach, with the increase in electron correlation included in DFT benefitting the thermodynamic and equilibrium properties of the molecules of interest. The main focus of the work by Bruckner et al. (2015), however, was to study the excited state reorganization energies. Bondu et al. (2015) also used TD-DFT for comparison with TD-HF results for linear (i.e., one-photon absorption) properties of different isomers of dithienylethene-indolinooxazolidine-benzazoloaxazolidine, finding in general that while TD-HF overestimated vertical excitation energies, it was able to provide qualitative trends for each of the four types of molecule investigated, in agreement with TD-DFT results. Bruckner et al. also initially employed TD-DFT, but quote “charge-transfer contamination” in their TD-DFT calculations as the reason for instead using TD-HF. It is unclear if usage of a long-range corrected DFT functional, for example, CAM-B3LYP rather than B3LYP, could have improved TD-DFT results.

Like Bondu et al. (2015), Maidur et al. (2017) also found that their TD-HF absorption spectrum is blue-shifted compared with TD-DFT calculations. There is also significant deviation in the computed oscillator intensities among the DFT functionals used (B3LYP, CAM-B3LYP, and  $\omega$ B97X-D), and also between TD-DFT and TD-HF calculations. The main transitions of interest involve the HOMO  $\rightarrow$  LUMO and (HOMO-1)  $\rightarrow$  (LUMO+1) orbitals, which appear to be  $\pi\pi^*$  and  $n\pi^*$  transitions, respectively, and it is unclear whether TD-HF and TD-DFT correctly capture this ordering. TD-HF vertical excitation energies and oscillator strengths also show significant deviation from TD-DFT results when applied to 1-[N-(2-pyridyl) aminomethylidene]-2(1H)-naphthalenone.<sup>30</sup> For each of these studies, when necessary, TD-HF was exclusively used to calculate

the higher order polarizabilities of the molecules of interest; predominantly, these results were used for internal comparisons, rather than being compared to experimental values.

### 3.4 Assessment

It is clear from the relatively small number of studies over the past 5 years, that TD-HF is not a favored technique for providing chemical insight into the behavior of photo-excited molecules. However, the favorable scaling allows its application to large systems, and the wide range of nonlinear properties that can be calculated do allow for the study of less common photochemical phenomena (Table 1). Mechanistic arguments have not generally been drawn from TD-HF results, however, TD-HF has been shown to be able to qualitatively reproduce observed trends and can be used for comparison against higher level calculations.



## 4. Configuration interaction

A more popular HF-based theory is configuration interaction singles, and its variants with and without double excitations (CIS, CISD, CID, CIS(D)), and in recent years, this theory has been applied to a much wider range of molecules than TD-HF. CISD benefits compared to TD-HF due to inclusion of double excitations in its formalism, and can lead to improvements in the description of ground state dissociation processes; however this increase in accuracy comes at increased computational cost. CIS is essentially TD-HF within the Tamm-Dancoff approximation,<sup>31</sup> generally overestimates excitation energies, and has been found to systematically overestimate charge-transfer states.<sup>32</sup> However, given the lightweight HF wavefunction

**Table 1** TD-HF summary.

Property	Trends	Quantitative
Nonlinear optical properties	Yes	Rarely <sup>a</sup>
Absorption Spectra	No	No
Fluorescence Spectra	No	No
Photochemical mechanisms	No	No
Quantitative photochemical kinetics	No	No

<sup>a</sup>Depends on the system and whether it is a first, second, third order hyperpolarizability, with higher order polarizabilities modelled better than lower order ones.

and lack of post-HF corrections, it remains the fastest excited state method, and can therefore be applied to large systems. Moreover, CIS can also give significantly improved estimations of triplet excitation energies compared to TD-HF.<sup>33</sup>

#### 4.1 Absorption and emission spectra

Nithya et al.<sup>34</sup> utilized a combined CIS and TD-DFT approach to investigate the structural and electronic properties of cyclopentadithiophene derivatives, using the good agreement of TD-DFT calculated vertical excitation energies to simulate absorption and emission spectra, but using optimized excited state geometries as calculated by CIS. Cebrián et al.<sup>35</sup> employed a similar approach in their study of the photophysical properties of several alkenyl-1H-,1,2,4-triazole compounds. Here, the PBE0 functional was used for ground state geometries and absorption/emission simulations, with the emission calculations being performed on CIS excited state geometries. It is found that utilizing TD-PBE0 excited state geometries resulted in emission errors an order of magnitude larger than those calculated from CIS. Tathe et al.<sup>36</sup> studied the excited state intramolecular proton transfer of 2-(2',6'-dihydroxyphenyl)benzoxazole, again using CIS and TD-DFT to calculate absorption and emission spectra. It is found that the TD-DFT results were in much better agreement for both types of spectra than those calculated by CIS, which provided absorption and emission maxima that varied by  $\sim 25\%$ . As a result, TD-DFT was favored for modelling the full excited state intramolecular proton transfer.

Laurent et al.<sup>37</sup> examined the basis set dependence of CIS(D), TD-DFT, second-order polarization propagator approximation (SOPPA), ADC(2), CC2, and EOM-CCSD, as well as some spin-scaled variants, on the vertical excitation energies of nine different molecules. It was found that spin-opposite scaled CIS(D) (SOS-CIS(D)) displayed the largest basis set dependence and generally the largest errors in vertical excitation energies, and ordinary CIS(D) did not fare much better. The study generally shows that, for calculations of vertical excitation energies, CIS(D) is not an accurate method, compared with DFT and higher-level ab initio methods. It also demonstrates that spin-scaling for CIS(D) does not constitute a systematic fix for the shortcomings of CIS(D). CIS was also used as a starting point for the further, higher-level calculations of the excited states of hypobromous acid<sup>38</sup>; no comment is made however on the accuracy of the CIS calculations. Another benchmarking study was performed by Shinde,<sup>39</sup> in which CIS,

EOM-CCSD, random-phase approximation (RPA), and various DFT functionals are applied to the linear absorption properties of boron wheels. EOM-CCSD excitation energies are taken as reference value, and CIS shows a significant overestimation of these energies. However, the true extent of the CIS overestimation is unclear as EOM-CCSD can also suffer from significant errors, and no calculations utilizing the generally accepted “gold standard” ab initio methods, e.g. CC3 or CASPT2, were performed.

Shayan and Nowroozi<sup>40</sup> also used a combined approach of different single-determinant excited state methods, again using CIS and TD-DFT to study the formation of an intramolecular hydrogen bond in the first excited states of malonaldehyde derivatives. Annaraj et al.<sup>41</sup> used CIS and TD-DFT to support the experimental observations that the fluorescence of 2-(1-methyl-1H-imidazole-2-carboxamido)-3-phenyl propanoic acid (PAIC) is selectively turned on in the presence of  $\text{Ni}^{2+}$ . CIS is used to optimize the excited state of the PAIC- $\text{Ni}^{2+}$  complex, upon which TD-DFT calculations are run. These calculations demonstrate a significant decrease in the HOMO-LUMO gap of PAIC upon complexation, from 5.56 eV to 2.97 eV, which is used as justification for the increase in favorability for fluorescence.

Kocherzhenko et al.<sup>42</sup> used CIS calculated excitation energies, along with TD-DFT energies, to parametrize an exciton model that can be applied to extremely large chromophore assemblies; here they tackle single, dimer, and hexamer aggregates of the 2-[4-[(E,3E)-3-[3-[(E)-2-[4-[bis[2-[tert-butyl-(dimethyl)silyl]oxyethyl]amino]phenyl]ethenyl]-5,5-dimethylcyclohex-2-en-1-ylidene]prop-1-enyl]-3-cyano-5-phenyl-5-(trifluoromethyl)furan-2-ylidene]propanedinitrile (YLD124) chromophore. The aim of the study was to parametrize an exciton model for further study of much larger chromophore aggregates, and it was found that CIS, TD-DFT, and the exciton model calculated spectra are all in reasonable agreement.

CIS based methods have also been applied to the absorption behavior of He clusters. Farrokhpur et al.<sup>43</sup> used CIS and TD-DFT to simulate the absorption of  $\text{He}_n$  clusters, where  $n$  ranges from 2 to 29. The authors note that the standard 6-311 + G(2d,p) basis set coupled with CIS is insufficient to reliably reproduce the absorption characteristics; instead, it needs to be augmented with further diffuse functions, resulting in a decrease in the CIS error to below 0.5 eV. Ge et al.<sup>44</sup> use a modified version of CIS, i.e. CIS based on absolutely localized molecular orbitals (ALMO), with a spatially localized charge transfer (CT) included in the modified ALMO-CIS formalism. The study predominantly focuses on derivation and implementation of ALMO-CIS + CT, and general qualitative agreement with experimental absorption

spectra of He clusters, however, it is noted that fine-detail remains elusive. The main advantage for CIS, and its modified variants, in these He cluster situations is that experimental clusters are generally of the size of 1000's of He atoms, for which higher-level calculations are unfeasible.

Finally, studies have been performed using spin-flip CIS (SF-CIS)<sup>45</sup> and scaled-opposite-spin CIS(D) (SOS-CIS(D)).<sup>46</sup> Tsuchimochi (2015) extended the SF-CIS approach by including exact spin-projection (giving SFPCIS) and included a benchmark of the method against the excited states of some small molecules; namely, HF, H<sub>3</sub>, N<sub>2</sub>, and H<sub>4</sub>. It was found that SFPCIS is capable of qualitatively reproducing conical intersections and general potential energy surface characteristics, as computed using full configuration-interaction (FCI). Chibani et al.<sup>47,48</sup> and Ponce-Vargas et al.<sup>49</sup> have applied SOS-CIS(D) to large, highly  $\pi$ -conjugated boron containing dyes. In these three studies, SOS-CIS(D) energies are used to correct overestimated TD-DFT excitation energies, while keeping several key features that are better captured by TD-DFT; e.g. band shaped of dyes presenting vibronic coupling, solvatochromic effects, CT transfer characteristics, and the impact of auxochromes on the meeting point between absorption and fluorescence curves (AFCP). This hybrid approach is found to decrease the errors in the calculated adiabatic transition energies for the M06-2X functional, however results obtained with the M06 functional are poorer. From this work it was concluded that the M06-2X functional is systematically overestimating the energies, and this systematic error can therefore be reduced; as for the M06 functional, it is unclear as to the origin of the poor agreement.

## 4.2 Assessment

Summing up, the inaccuracies CIS methods are well documented, and compared with multireference and TD-DFT calculations, they have somewhat fallen out of favor (Table 2). Along with TD-HF, they do remain, however, the cheapest possible excited state methods available today, and for extremely large systems, they remain the only viable methods. The simplicity of the methods and their wide-spread implementation means that they are also often included in benchmarking studies, particularly for absorption/emission spectra simulation. Generally, it is found that their accuracy is highly basis set dependent, and the need for large basis sets counteracts their cost advantage. As a result, TD-DFT is generally preferred, although CIS is sometimes more attractive for excited state geometry optimizations for subsequent TD-DFT single points.

**Table 2** Configuration interaction summary.

Property	Trends	Quantitative
Nonlinear optical properties	TD-HF	TD-HF <sup>a</sup>
Absorption spectra	Sometimes <sup>b</sup>	Rarely <sup>b</sup>
Fluorescence spectra	No <sup>c</sup>	No <sup>c</sup>
Photochemical mechanisms	No	No
Quantitative photochemical Kinetics	No	No

<sup>a</sup>Depends on the system and whether it is a first, second, third order hyperpolarizability, with higher order polarizabilities modelled better than lower order ones.

<sup>b</sup>Depends on the exact method and basis set, with these requiring very large basis sets for accuracy (which in turn defeats its cost advantage).

<sup>c</sup>Due to its low cost, CIS is sometimes used for geometry optimizations in the excited state with TD-DFT improved energies.



## 5. Multireference studies

While HF-based singlet determinant methods, i.e., TD-HF and CIS, have somewhat fallen out of favor due to the general improvement in qualitative studies found when using TD-DFT, the same cannot be said for multireference studies. Multireference methods benefit from being able to fully model regions of electronic degeneracies and can therefore provide accurate information about the shape of excited state potential energy surfaces. As such, they provide mechanistic insights into the photochemical process of choice. In particular, complete active space second order perturbation theory (CASPT2), is often used as the ab initio benchmark, against which the performance of all other computational excited state methods is compared. However, multireference calculations suffer from the exponential scaling of the number of wavefunction configurations that have to be considered with respect to the number of orbitals included in the calculation, limiting these highly accurate methods to systems in which no more than  $\sim 20$  orbitals are required to be correlated.<sup>50</sup> These methods also suffer from non-“black box” behavior; in general, there is no systematic approach to choosing which orbitals are to be included in a multireference calculation. The resulting calculations are therefore dependent on the quality of the nonsystematic starting guess, and therefore the results can suffer.



## 5.1 Mechanistic studies

The most important use of multireference methods is in clarifying and quantifying photochemical reaction mechanisms, which is often not possible using lower-cost procedures. Below, a number of recent such studies are highlighted.

Sumita and Morihashi<sup>51</sup> studied the generation of singlet oxygen from an excited thiophene/oxygen exciplex, employing MRMP2-corrected CAS-SCF geometries. It is found the thiophene undergoes intersystem crossing to a low-lying triplet state after initial excitation, before forming an exciplex with  $^3\text{O}_2$ . Further decay, either radiative or non-radiative, takes place to the singlet state, after which either a [2 + 4] cycloaddition takes place, or  $^1\text{O}_2$  is generated.

Excited state proton transfer of pyruvic acid was studied by Chang et al.<sup>52</sup> with TD-DFT and CASPT2//CASSCF. The TD-DFT vertical excitation energies are in reasonable agreement with those calculated with CASSCF, and the CASPT2 energy is found to be in excellent agreement with the experimental value. Four nonadiabatic pathways are suggested, and movement along the excited state intramolecular proton transfer coordinate results in a three-way intersection between the  $S_1/T_1/S_0$  states. Excited state intramolecular proton transfer of 1-cyclopropyldiazo-2-naphthol was studied by Cui et al.<sup>53</sup> by CASPT2//CASSCF. Their calculations suggest that initial excitation takes place to the  $\pi\pi^*$  state, from which barrierless radiationless decay can take place to the  $S_0$  keto structures, or crossing to the  $n\pi^*$  state can take place, after which the molecule undergoes decay to the  $S_0$  enol structures via a  $S_1/S_0$  conical intersection.

Casellas and Reguero<sup>54</sup> applied a CASPT2//CASSCF approach to study the competition between photosensitization and photocyclization in 9-phenylphenalenone (9-PhPn). It had been found previously that the closely related phenalenone molecule, upon excitation to a low-lying  $^1\pi\pi^*$ , undergoes internal conversion followed by efficient intersystem crossing, via a conical intersection, to a  $^3\pi\pi^*$  state.<sup>55</sup> This triplet state is then available for an efficient energy transfer to form a singlet oxygen species with a quantum yield of 0.95. In contrast, 9-PhPn exhibits a quantum yield of merely 0.08.<sup>56</sup> The authors employed CASSCF optimised geometries upon which improved CASPT2 single-point energies were calculated. It was shown that the decrease in quantum yield is due to the photocyclization reaction that can take place between the neighboring phenyl and ketone groups. As with the original study, the CASPT2-corrected CASSCF geometries are

generally found to be sufficiently accurate to provide insight into the observed processes. However, the critical minimum energy geometries of the  $^1\pi\pi^*$  state, as calculated individually at the CASSCF and CASPT2 levels of theory, have drastically different structures. The equilibrium structure from CASSCF has a phenyl group almost perpendicular to the rest of the phenalenone structure, but the CASPT2 structure has these two groups almost planar to each other. This has important consequences in the ensuing cyclization reaction, in which the close vicinity of the two reacting groups is necessary; in this respect, it is a failure of the CASSCF method.

Casellas et al.<sup>57,58</sup> have also applied the CASPT2/CASSCF approach to studying the photoisomerization reactions of azobenzene and phenylazopyridine. Given the planar structure of the N=N double bond, it is possible for the isomerization to take place via either a rotational or non-rotational pathway; for both azobenzene and phenylazopyridine, the rotational pathway is favored thermally. On the excited states, however, the potential energy surface shows that both pathways become competitive.

Dai et al.<sup>59</sup> have employed CASPT2 corrected CASSCF potential energy surfaces to explore the photolysis of the carbon–iodine bond found in iodouracil, finding intersystem crossing and conical intersections are involved in converting the bright  $\pi\pi^*$  to dissociative  $\pi\sigma^*$  and  $n\sigma^*$  states. The calculated vertical excitation energies for the first 5 electronic states of iodouracil are found to be in good agreement with the experimental UV–vis absorption, with the calculations showing the lowest excited state is in fact a dark  $\pi\sigma^*$  transition, followed by the bright  $\pi\pi^*$  transition.

Another recent study by Menzel et al.<sup>7</sup> utilizes CASSCF calculations to explore the photoreactivity of two ligation reactions; i.e., photoactivation of *o*-methylbenzaldehyde to form a reactive *o*-quinodimethane, via a conical intersection, and the photolysis of 2,5-diphenyltetrazole, in which conical intersections also play a profound role. In both systems, CASSCF potential energy surfaces (PES) were found to be sufficient to describe the geometries at which electronic degeneracies were found. As well, the study also employed TD-DFT to provide qualitative insight into the nature of the first few low-lying excited states. While TD-DFT is incapable of fully describing the conical intersections involved, it is sufficient in describing the symmetry forbidden, and therefore spectroscopically dark,  $n\pi^*$  transition. It is this transition that is responsible for the observed peak in per-photon reactivity taking place at a lower wavelength than the absorption maxima.

From an experimental perspective, it is interesting to compare this wavelength dependence to the study by Dai et al., as in the latter study the

reactivity is directly reconciled by the experimentally observed absorption spectrum of iodouracil; i.e., the higher energy, bright  $\pi\pi^*$  state is initially populated and is the origin of the resulting photochemistry. However, Menzel et al. demonstrate that absorption efficiency does not necessarily correspond to photochemical efficiency, and that from a per-photon perspective, it can be much more useful to directly aim for the dark states. Certainly, from the PES shown by Dai et al., directly hitting the lower energy  $\pi\sigma^*$  state should directly result in the C—I bond photolysis and could be more efficient as competition from higher energy pathways may no longer be relevant.

Yuan and Bernstein et al. have also performed several number of multireference studies in the past few years, applying CASSCF calculations to the excited state decomposition reactions of 3,3'-diamino-4,4'-bisfuroxan and 4,4'-diamino-3,3'-bisfuroxan,<sup>60</sup> bis(ammonium)5,5'-bistetrazolate and bis(triaminoguanidinium) 5,5'-azotetrazolate,<sup>61</sup> dihydroxylammonium 5,5'-bistetrazole-1,1'-diolate and dihydroxylammonium 3,3'-dinitro-5,5'-bis-1,2,4-triazole-1,1'-diol,<sup>62</sup> nitrophenyl derivatives,<sup>63</sup> and 1,1-diamino-2,2-dinitroethylene,<sup>64</sup> as well as the fragmentation of excited state ammonia-based clusters.<sup>65</sup> In the five decomposition studies, the products are a ring-opened tetra/triazoles, NO and/or N<sub>2</sub>. In particular, emphasis is placed on the role of conical intersections in the ring opening/decomposition reactions; generally, neither the ground state nor excited state PES are dissociative, however, the conical intersections found between the two states are accessible and result in a vibrationally hot molecule with sufficient energy to undergo homolysis. In the case of the bisfuroxan derivatives, it is found that MP2-corrected CASSCF calculations are required to produce a PES capable of reconciling experimental observations.

A CASPT2//CASSCF study by Datar and Hazras<sup>66</sup> examined the two possible nonradiative decay pathways of 5,6-dihydroxyindole. Upon excitation and internal conversion, it is found that there are two conical intersections between the low-lying  $\pi\sigma^*$  and S<sub>0</sub> states, along both an OH and the NH bond stretching coordinates. The barrier to the conical intersection located along the OH coordinate is lower than the corresponding barrier along the NH coordinate. Once over the barriers, it is possible not only to decay to the ground state, but also to continue to dissociation to form a dihydroxyindole radical and free hydrogen atom. However, it is noted that nonadiabatic dynamics simulations are required to fully determine the extent of the competition between the two pathways. Kobayashi et al.<sup>67</sup> employed extended multistate (XMS-) CASPT2 and ultrafast visible and infrared

spectroscopy to probe the dynamics of the delocalized biradical excited form of pentaarylbiimidazole. The ultrafast spectroscopy revealed the existence of two transient isomers, each with a differing amount of biradical character. XMS-CASPT2 calculations demonstrate the metastable isomers are likely stabilized by the  $\pi$ -stacking present between the imidazole rings present.

Kim et al.<sup>68</sup> employed CASSCF, DFT, and CC methods to study the photoisomerization of 1,2-dihydro-1,2-azaborine, in which the planar, six-membered ring can isomerize to a Dewar product by two possible pathways. The study finds that one of the transition states is greatly reduced on the  $S_1$  state, and the molecule can decay to the  $S_0$  state by a conical intersection to form a stable intermediate product. This product is then able to further isomerize either to the Dewar product or back to the planar, six-membered ring. Gao et al.<sup>69</sup> studied the photoisomerization of 1,1'-dimethyl-2,2'-pyridocyanine, using CASPT2//CASSCF energies. The isomerization takes place on the  $\pi\pi^*$ , on which it is barrierless, before decaying to the  $S_0$  state via a conical intersection. Lei et al.<sup>70</sup> studied the photoisomerization of stilbene with CASSCF, finding four left-hand and four right-hand conical intersections between the  $S_0$  and  $S_1$  states.

Suaud et al.<sup>71</sup> used CASSCF to fully correlate the  $\pi$ -electrons of some conjugated, mono- and di-radical hydrocarbons, against which the delocalization of the radicals as calculated with ROHF is compared. It is found that the SOMO as calculated with ROHF are generally much more localized than as calculated with CASSCF, and that increasing the size of the active space also results in an increase in delocalization. Zhang et al.<sup>72</sup> used CASSCF to gain insight into the electronic spectra of linear carbene chains  $H_2C_n$ , where  $n = 3-10$ . The study shows that chains with even values of  $n$  are more stable than those where  $n = \text{odd}$ , and that there is a nonlinear relationship between chain length and vertical excitation energy. Hlavacek et al.<sup>73</sup> studied the  $\pi$ -conjugated acrolein molecule with CASPT2 and CCSD(T), in order to determine structural properties of the its  $T_1$  state. The methods are used to simulate cavity ringdown (CRD)<sup>74</sup> spectra, finding good agreement between the experimentally obtained and simulated spectra. No comparison with other, lower levels of theory is included, however.

Li et al.<sup>75,76</sup> compared CASSCF/CASPT2 with CASPT2-corrected SF-TD-DFT for the photoisomerization of 9-(2,4,7-trimethyl-2,3-dihydro-1H-inden-1-ylidene)-9H-fluorene, an example of a 2nd generation rotary molecular motor. The results show the importance of the conical intersections that lead the cis-stable to the trans-unstable isomer upon excitation and find the TD-DFT-based methods can capture this behavior.

However, the TD-DFT based geometries are generally lower in energy than the multireference energies, but the structural parameters of the conical intersection geometries are in close agreement. Amatatsu has also performed CASSCF calculations on 9-(5-methyl-2-phenyl-2-cyclopenten-1-ylidene)-9H-fluorene (MPCPF) and various derivatives,<sup>77–81</sup> showing initially that the design of molecular rotary motors should include groups with internal vibrations that are strongly coupled with the bridging carbon-carbon double bond. The later investigations more fully characterize the conical intersections along the isomerization pathway.

The excitation energy transfer mechanism in a peridinin-chlorophyll *a* complex has been studied by Bricker and Lo.<sup>82,83</sup> Here, the low-lying excited states of the complex are calculated using CASSCF, and the corresponding transition dipole moments were used to determine the Coulombic couplings between the two species within the complex. It was found that there is significant coupling between not only the  $S_1$  and  $Q_y$  states of the peridinin and chlorophyll *a*, respectively, but also between the  $S_2$  and  $Q_{x/y}$  states. It is this extra coupling, that explains the experimentally observed, highly-efficient energy transfer.

Further multireference investigations into photomechanisms of organic molecules include a study by Guan et al.<sup>84</sup> who used CASPT2//CASSCF and TD-DFT energies to study the photochemistry of Sudan I and Orange II dyes, employing an azobenzene parent structure that is present in both sets of molecules as the computational model. It was found that initial excitation of the azobenzene structure is to the  $S_2$ ,  $\pi\pi^*$  state, from which barrierless decay can take place along either the  $\pi\pi^*$  state to the keto  $S_0$  state, via a  $S_2/S_0$  conical intersection, or crossing to the  $n\pi^*$  state can take place to either the cis- or trans-enol structures. Another study employed CASSCF/CASPT2 to assess the two possible elimination reactions of 6,7-dihydro-5<sup>4</sup>-benzo[*d*]pyrido [2,1-*f*]azaborininr; the two eliminations either produce  $H_2$ , or  $BH_3$  and a corresponding ring contraction. On the ground state, the ring contraction mechanism is found to be thermally favorable; the reaction barrier for  $H_2$  production is  $\sim 43 \text{ kJ mol}^{-1}$  higher in energy. However, on the excited state it is found the PES for  $H_2$  production is essentially barrierless, with a reaction barrier for ring contraction increasing from  $+233.5 \text{ kJ mol}^{-1}$  on the  $S_0$  state to  $+252.8 \text{ kJ mol}^{-1}$  (from the Franck-Condon point) on the first excited state. There are also several conical intersection geometries found, between the  $S_0$  and  $S_1$  states, with the two intersections on the  $H_2$  pathway either taking the molecule to the original equilibrium geometry, or to the  $H_2$  product on the ground state.

## 5.2 Restricted active spaces (RAS)

Although multireference methods suffer from exponential scaling issues with respect to the number of orbitals included in the calculations, they can still be applied to large systems with some success. Ben Amor et al.<sup>77</sup> employed CASPT2 to study the valence excitations of an iron-porphyrin complex. In this complex, if all possible  $\pi/\pi^*$  and metallic 3d orbitals were included, an active space of 36 electrons in 36 orbitals would be required, far beyond current computational capabilities. Instead, a truncated active space is used employing the  $3d_n$  orbitals of the iron and 6  $\sigma^*$  and  $\pi^*$  orbitals that exhibit significant changes in occupancy upon excitation. Also, only the excited states up to approximately 3 eV are investigated, above this point (the so-called Soret Band), excitations are dominated by  $\pi\pi^*$  transitions and would require their inclusion in the active space. The difficulties in determining an appropriate active space and the expense of the resulting calculations may warrant the usage of a cheaper method, for example TD-DFT. However, CASPT2 results reveal the presence of not only singly excited states, generally dominated by  $d_n\pi^*$  transitions, but also low-lying doubly excited states; states that are necessarily not included in TD-DFT calculations.

Venturinelli et al.<sup>78</sup> used CAS- and RAS- procedures to study the spin states of manganese-porphyrin complexes. Like Ben Amor et al., the Mn-Por complexes also require an extremely large active space to fully accommodate the relevant d,  $\sigma$ , and  $\pi$  orbitals; however, partitioning of the active space in order to fully and partially correlate different orbitals, as is the case with RASSCF and RASPT2, allows for a larger number of orbitals and electrons to be included than would otherwise be possible. In their study, Venturinelli et al. were able to correlate 28 electrons in 28–30 orbitals using a RAS-procedure, significantly more than the 14 electrons in 16–18 orbitals that were able to be correlated in the accompanying CAS calculations. The calculations demonstrate the existence of low-lying, high-spin configurations of the Mn-porphyrin complexes, which have significant implications for the catalytic activity of such species. Bai et al.<sup>79</sup> employed CASSCF, along with a number of other excited state methods, to study a ruffled porphyrin species. The active space used was, however, reasonably small (6 electrons, 6 orbitals), with little emphasis placed on the CASSCF results. Crossing points were located, however, between the  $T_1$  and  $S_0$  states, and presented as a possible route for excited state energetic decay.

The excited states of nucleobases have been studied by Segarra-Martí et al.,<sup>80,81,85–87</sup> with CASSCF and RASSCF, and their corresponding perturbation theory CASPT2 and RASPT2 counterparts. In the study of

adenine alone,<sup>80</sup> its high energy electronic states are investigated by RAS-calculations, as this allows a larger active space, and therefore higher energy virtual- and lower energy occupied-orbitals, to be considered. Interestingly, the nonlinear optical properties of adenine were investigated, as this allows the modelling of pump-probe experiments to be performed accurately. The third-order nonlinear properties of cytosine, thymine, and uracil were then studied,<sup>86</sup> finding that the resulting two-dimensional spectra are highly sensitive to small structural changes, especially important when trying to differentiate between the similar thymine and uracil nucleobases.

CASPT2//CASSCF studies were then performed on thymine to study the possible photodeactivation pathways that are available upon excitation to the low-lying, bright  $\pi\pi^*$  state. It was found that the CASSCF and CASPT2 relaxed geometries for this state are similar, however CASPT2 points to a twisted geometry, compared with a planar structure predicted by CASSCF, and that radiationless decay takes places via a  $\pi\pi^*/S_0$  conical intersection. As well as this, the CASSCF PES was found to be overly steep compared with that of CASPT2, and this difference would likely lead to inaccurate dynamic simulations, as needed for quantitative analysis of the excited state lifetimes. Finally, the dissociative electron detachment (DEA) reactions of the four DNA nucleobases was studied, again with CASPT2//CASSCF energies. For each of the four nucleobases, each possible N-H homolysis reaction was modelled. For each N-H coordinate, the PES of the anionic  $\pi\pi^*$ - and dissociative  $\pi\sigma^*$ -, and neutral  $S_0$  are calculated, and generally intersections are found between the bright  $\pi\pi^*$ - and dark  $\pi\sigma^*$ -, that will result in hydrogen ejection. The relative energies of these intersections are used to determine the contributions of the respective dissociation channels.

Santolini et al.<sup>88</sup> used CASSCF and RASSCF to study the photochemical reactions of cis-butadiene and cyclopentadiene. It was found that small CASSCF active spaces result in a poor balance of covalent and ionic valence bond (VB) structures, and an extended active space is therefore required for accurate potential energy surfaces. To that end, RASSCF is a natural choice for this active space extension. Calculations of vertical excitation energies demonstrate the failing of CASSCF to correctly predict the ordering of the first two excited states for both cis-butadiene and cyclopentadiene, whereas the larger RAS calculations correctly predict the ordering and are closer to experimental values of excitation energy. Xia et al.<sup>89</sup> studied the ring-opening of cyclopropanone, cyclobutanone, cyclopentanone, and cyclohexanone. The authors use CASPT2-corrected CASSCF

structures to compute the PES, finding that the excited state pathway to the  $S_0$  ring-opened isomers is via a  $S_1/S_0$  conical intersection in all four molecules. Increasing ring strain is also found to decrease the barrier to the conical intersection geometry. Bera et al.<sup>90–92</sup> studied the excited state decomposition reactions of dimethylnitramine and corresponding clusters with Fe, Zn, and Al with CASSCF and RASSCF calculations. The calculations were able to find a variety of conical intersections between the relevant electronic excited states and determine which are dissociative and result in decomposition.

### 5.3 Quantum Monte-Carlo (QMC)

Manni et al.<sup>93</sup> employed (metallo-) porphyrins as a difficult test case for multireference calculations, to test the performance of their newly developed full configuration interaction quantum Monte Carlo (FCIQMC) code for solving the CASSCF equations. Here, instead of a deterministic approach to fully correlating a subset of orbitals, a QMC approach is employed in which the configuration state functions are sampled stochastically. The authors find good agreement with experimentally obtained data for the absorption and ground state properties of the porphyrins studied. Further investigations are required, however, to determine the impact of including dynamic correlation corrections to the obtained wavefunctions.

Asturiol and Barbatti<sup>94</sup> studied the formation of  $^1O_2$  upon encountering excited porphyrin. It is found that efficient intersystem crossing will predominantly yield triplet porphyrin, which leads to inefficient generation of singlet oxygen. However, formation of  $^1O_2$  is efficient if singlet excited porphyrin is encountered. Kornobis et al.<sup>95</sup> used TD-DFT with a range of functionals, EOM-CCSD, and MC-XQDPT2-corrected CAS-SCF energies, to study the  $S_1$  state of  $Co^{3+}$ -corrinoids. Previous literature had described the  $S_1$  state as either a  $\pi\pi^*$  transition<sup>96,97</sup> or a metal to ligand charge transfer transition,<sup>98–100</sup> and this study aimed to unambiguously determine the dominant character of the  $S_1$  state, finding with the MC-XQDPT2 calculations that it is, in fact, dominated by MLCT character. It is found that the B3LYP, mPW1PW91, and TPSS-h functionals incorrectly predict a  $\pi\pi^*$  state, whereas EOM-CCSD, and the BP86, BLYP, MPWPW91, and LC-BLYP functionals correctly predict metal to ligand charge transfer dominant character.

Rotllant et al.<sup>101</sup> studied the photochemistry of acetophenone using CASSCF and XMCQDPT2. The equilibrium geometries of the low-lying, singlet and triplet  $\pi\pi^*$  and  $n\pi$  states are optimised at both levels of theory,



and the carbon–oxygen bond stretch is found to be a convenient reaction coordinate. The efficient crossing from the  $^1n\pi^*$  is thought to take place via a three-state crossing point between the  $^1n\pi^*$ ,  $^3n\pi^*$ , and  $^1\pi\pi^*$  states. It is also found that CASSCF generally underestimates the length of the carbon–oxygen bond for each of the equilibrium structures, highlighting the importance of including dynamic correlation in the calculations.

In other studies, Xu et al.<sup>102</sup> proposed a diabaticization scheme, and applied it to the dissociation of phenol. Energies were calculated using MC-QDPT2 and coupling modes at the conical intersections between the  $\pi\pi^*/\pi\sigma^*$  and  $\pi\pi/\pi\sigma^*$  states were calculated. As the algorithm was shown to give good, smooth results, it was proposed that it can therefore be used in dynamic simulations. Kletsii et al.<sup>103</sup> studied the competition between Norrish-type reactions in butanal, pentanal, penta-2-one, buten-2-al, butanimine-1, and nitrosopropane with CASSCF and XMCQDPT2. For each molecule, the possible dissociation and H-transfer pathways were studied in order to determine their relative competition, finding that increasing alkyl chain length had limited effect on the Norrish-I reaction pathway, but decreased the energy of the H-transfer reactions.

## 5.4 Benchmarking studies

In addition to studying photochemical reactivity, multireference methods of various flavors are also commonly used to test the accuracy of lower-cost methods such as TD-DFT, or indeed lower-cost multireference methods. Retinal, and various derivatives and truncated models of it, have been employed in recent years as a system against which a wide-range of methods can be tested and benchmarked. Andruniów et al.<sup>104–106</sup> have employed CASPT2, CASPT3, CASSCF, CASPT2/CASSCF, DFT, MP2, (L)CC2, and CCSD(T) to test the accuracy of optimised geometries, and vertical and adiabatic excitation energies; CASPT2 energies/geometries are taken as the benchmark. For the study including 9 retinal derivatives,<sup>105</sup> it was generally found that methods that include dynamic correlation (i.e., not CASSCF), gave ground state geometries in good agreement with those of CASPT2, with CASSCF giving significant differences in bond lengths, and in two retinal models, significantly twisted structures that are planar by the other methods. CASSCF was also found to consistently overestimate vertical excitation energies, however, the CASPT2 vertical excitation energies on CASSCF geometries were found to be accurate, provided the CASSCF geometry resembles the equivalent CASPT2 geometry.

A smaller retinal model was used to test the CASPT3 method,<sup>104</sup> finding that it performed exceptionally well for ground state geometries, was insensitive to IPEA shifts, but more sensitive to basis set size than CASPT2. A further three retinal models were employed to test CASPT2/CASSCF, CASPT2, and CC2.<sup>106</sup> It was found that CASSCF is incapable of locating the planar  $S_1$  minimum geometry structures for four out of the five studied retinol models. CC2, on the other hand, was as successful as CASPT2 in locating these minimum energy geometries. However, when CASSCF finds the correct structure, the one-electron properties, emission, and adiabatic energies are in excellent agreement with those of CASPT2. When extended to the  $S_2$  states, which are found to have significant multireference/double excitation character, CC2 is found to give transition energy errors of  $>1$  eV. Notably there does not seem to be any clear indicators of when CASSCF geometries will fail, in which case CASPT2 corrections will not result in any improvements in mechanistic accuracy. This is, thus, especially troublesome in larger molecules, when running CASPT2 geometry optimizations may not be feasible due to their computational expense.

Further benchmarking studies with retinal models have been performed by Olivucci et al.<sup>107–114</sup> The original study<sup>107</sup> employed CASSCF and multireference methods that capture dynamic electron correlation (MRCISD, CASPT2, NEVPT2, and XMCQDPT2) to explore the ground state PES of a retinal model. As with the studies by Andruniów et al., it is found that the CASSCF geometries, and resulting PES, are liable to failure, and the additional inclusion of dynamic correlation results in a significant reshaping of the PES. Subsequent studies employed TD-DFT,<sup>108,109</sup> coupled-cluster based methods,<sup>110–112</sup> quantum Monte Carlo,<sup>113</sup> and ADC(2) and ADC(3) methods,<sup>114</sup> which were generally compared with the high-level MRCISD(+Q) PES. Generally, most methods were capable of qualitatively reproducing the PES from high-level calculations, with the EOM-CC methods seemingly capable of reproducing key photochemical pathways, with EOM-SF-CCSD(dT) shown to be capable of quantitatively describing some photoisomerization pathways.

TD-DFT and CASSCF/CASPT2 calculations were applied to the pyrene and its 3 possible protonated forms by Chin and Lin,<sup>115</sup> from which absorption and fluorescence spectra were calculated. The calculated vertical excitation energies calculated by TD-B3LYP and CASPT2 are in close agreement for the four pyrene species, however, the size of the basis set, i.e., cc-pVDZ, is reasonably small. Cacelli et al.<sup>116</sup> employed TD-DFT and multireference calculations to study the absorption behavior of anthocyanidins,

again finding reasonable agreement between DFT and MRPT2 vertical excitation energies, with B3LYP finding the closest agreement. However, the vertical excitation energies were calculated for DFT equilibrium geometries, with no comparison made between DFT and MRPT2 structural parameters. Were these to be included, the vertical excitation energies may be significantly different.

The competition between photoisomerization and photodegradation mechanisms in the first excited state of tetrazoline oxime ether has been studied with TD-DFT and CASSCF by Fréneau et al.<sup>117,118</sup> The calculations show that the photodegradation pathway is favored in the *E*-isomer, whereas photoisomerization is favored in the *Z*-isomer; this is due to the hydrogen-bond present in the *Z*-isomer that prevents that photolysis pathway from being favored. López-de-Luzuriaga et al.<sup>119</sup> used TD-DFT and CASSCF/CASPT2 to study the dual-fluorescence of 4-(dimethylamino)-pyridine in different solvent environments, finding good agreement between the two methods and experimental data. Li et al.<sup>120</sup> used TD-B3LYP and CASPT2/CASSCF energies to study the low-lying excited states of coumarin, finding good agreement between both methods and experimental data.

Olsen<sup>121</sup> employed CASSCF to study the competition between the charge-transfer (CT) and locally excited (LE) states of green fluorescent protein (GFP) derivatives, finding that strongly electron donating groups enhance CT character in the  $S_1$  state, compared with weakly donating/electron withdrawing groups. Ai et al.<sup>122</sup> used TD-DFT and CASSCF to study the one- and two-photon absorption of GFP. CASSCF is found to give results in good agreement with experimental data, whereas CAM-B3LYP is found to be in poor agreement. The blue-shift observed was found to be due to the vibronic coupling present through a carbon-carbon single, double bond moiety.

In other studies, Zhang et al.<sup>123</sup> applied TD-B3LYP and CASPT2 to study substituent effects on the absorption properties of phenol radicals, finding good agreement between the TD-DFT, CASPT2, experimental absorption spectra. Palmer et al. have recently performed a number of multireference studies on several organo-halide molecules; namely, iodopentafluorobenzene,<sup>124,125</sup> difluoromethane,<sup>126</sup> pyridine-N-oxide,<sup>127</sup> iodobenzene,<sup>128</sup> and chlorobenzene.<sup>129</sup> Each study used both single- and multireference calculations, and generally finds good agreement between both types of calculations and experimental data, for both adiabatic and vertical excitation energies.

## 5.5 Assessment

To summarize, multireference methods have been applied to a wide range of molecules, from some as large as porphyrin to those as small as hydrogen. Applied properly, they offer high degrees of accuracy but at the high computational expense (Fig. 2). In particular, multireference calculations provide accurate insight into the photochemical processes being investigated, against which less accurate, but cheaper, methods are compared; most notably, TD-DFT. Multireference calculations continue to be successfully applied to systems in which nonadiabatic behavior plays an important role in the photochemical process of interest. A particularly popular approach involves using CASSCF calculated geometries, upon which potential energies are improved by performing MRPT2 single-point calculations. However, it has been shown that the neglect of dynamic correlation in CASSCF can result in incorrect geometry minima, which can have a profound effect when attempting to reconcile observed photochemical behavior. These spurious geometries can be unpredictable, and so it can be difficult to ensure that truly correct behavior is being simulated if CASPT2 calculations are not feasible. The methods also suffer from active orbital choice, also has a profound impact on the success or failure of these methods, though the careful use of restricted active space methods and quantum Monte-Carlo methods can effectively address that problem.

Multi-reference methods	
Advantages	Disadvantages
<p><b>Highly Accurate</b></p> <ul style="list-style-type: none"> <li>• sometimes the only accurate approach available e.g. for non-adiabatic surfaces, many other photochemical reactions</li> </ul> <p><b>Main Applications</b></p> <ul style="list-style-type: none"> <li>• photochemical reaction mechanisms</li> <li>• excited state optimizations</li> <li>• benchmarking lower-cost levels of theory</li> </ul>	<p><b>High computational cost made worse by need for</b></p> <ul style="list-style-type: none"> <li>• <b>large active spaces</b> RAS- or QMC methods can be used to expand active space at lower cost</li> <li>• <b>dynamic correlation</b> CASPT2//CASSCF often used to improve efficiency but some CASSCF geometries are inaccurate and these are hard to anticipate</li> </ul>

Fig. 2 Main advantages and disadvantages of multireference studies.



## 6. Time-dependent density functional theory

TD-DFT and its counterpart that employs the Tamm-Dancoff approximation (TDA-TD-DFT)<sup>130</sup> are hugely popular excited state methods that are largely analogous to TD-HF and CIS, respectively, but with the inherent advantage of the included dynamic correlation present in DFT. The methods benefit from the cost-effectiveness of DFT and can therefore be applied to a huge range of molecules that are simply not feasible for ab-initio methods, providing qualitative and, sometimes, quantitative insight into photochemical processes. However, as with ground state DFT studies, the accuracy of the calculations is dependent on the functional of choice, which can provide wildly different values for identical calculations. TD-DFT will suffer when excitations include charge-transfer, Rydberg character, or when the excited state wavefunction requires anything other than a single-determinant description (regions of degeneracy, double-excitations). Due to the large volume of literature that include TD-DFT calculations of some description, this section will concentrate on some of the most highly cited studies in the 2013–2018 period.

### 6.1 Methodological developments

#### 6.1.1 Long-range corrected functionals

One of the key decisions in choosing a functional is whether or not it is long range corrected (LC). LC functionals treat electron–electron exchange using HF at large separation and using a generalized gradient exchange (GGA) at short range and have been shown to have improved accuracy for states with significant charge transfer character.<sup>131–133</sup> The performance of LC functionals depends on the choice of the range separation parameter ( $\omega$ ) that determines the balance of GGA and HF exchange at intermediate inter-electronic distance.<sup>134–139</sup> While the parameter can be used ad hoc to fit predictions to experimental data, a more “a priori” approach has been advocated by Baer in which the parameter is tuned to make the negative of the highest occupied molecular orbital (HOMO) equal to its ionization potential in accordance with Kohn-Sham theory.<sup>140–143</sup>

Gąsiorowski et al.<sup>144,145</sup> employed a modified form of the B3LYP, CAM-B3LYP, and LRC-BLYP functionals, for which the exchange screening parameter,  $\omega$ , was varied, in order to study the absorption and fluorescence properties of 1,3-diphenyl-1H-pyrazolo[3,4-*b*]quinoxalines. The study finds that the long-range corrected functionals give absorption/emission

in closer agreement than the uncorrected B3LYP functional. However, this good agreement could be the result of fitting  $\omega$  to the data. No comment is made on the nature of the excited state, and whether this seems to be functional dependent.

Arulmozhiraja and Coote<sup>146</sup> used four long-range corrected functionals (CAM-B3LYP,  $\omega$ -B97X-D, LC-BLYP, and LC- $\omega$  PBE), along with standard hybrid and double hybrid functionals, in an attempt to describe the excited states of indole and azaindole. The long-range corrections were determined a priori using Baer's method. It was found that while some excited properties were improved, others were not and no one functional predicted the correct order of all of the excited states for both species.

In a similar vein, Eriksen et al.<sup>147</sup> discuss in detail the failure of CAM-B3LYP to correctly describe the charge-transfer character of the  $S_1$ ,  $\pi\pi^*$  transition of para-nitroaniline. In particular, compared to CCSD and SOPPA calculations, CAM-B3LYP is found to not only be unable to reproduce experimental gas-phase absorption spectra, but also fails in describing the bathochromic shift that is also observed experimentally; this is a worrying failure as, the authors note, the CAM-B3LYP functional is designed to correct for the failings of B3LYP when modeling charge transfer in molecules. The study also includes other hybrid functionals, for example, BHLYP, as well as CIS/RPA, finding that the errors are even more pronounced. The incorrect energies are found to arise from an overestimation of charge-transfer character in the ground state, apparent through a calculated dipole moment that is larger with CAM-B3LYP than with CCSD, and a resulting underestimation of CT in the  $S_1$  state. This effect is found to become more pronounced in the solvent calculations; the authors also examine the contribution of the solvent field to the excitation energies, finding similar contributions for both TD-DFT and CCSD calculations, suggesting the solvent model is not to blame. Finally, the authors find that the difference in TD-DFT and TDA-TD-DFT energies can be used as a measure for the extent of CT.

Körzdörfer and Brédas<sup>148</sup> also note that the failings of semilocal and global hybrid functionals can be attributed to the error associated with electron delocalization inherent in such functionals. However, the authors show that tuning the  $\omega$  value of the LC- $\omega$ PBE against the ionization potential of the molecules of interest can reduce ensuing error in ensuing TD-DFT calculations. Similarly, Sun et al.<sup>149</sup> employ a set of organic emitters that undergo thermally activated delayed fluorescence (TADF), which represent a challenge for TD-DFT with traditional functionals. In particular, the authors

note that the organic emitters exhibit donor-acceptor behavior and therefore they tune the  $\omega$  value against both ionisation potential and electron affinity. The studies show that the mean absolute deviation and maximum absolute error for the tuned functional are greatly reduced, particularly for the adiabatic singlet-triplet energy gaps. Sun et al also, however, continue to find good performance of the B3LYP and M06-2  $\times$  functionals for the properties investigated, however, this is attributed to favorable error cancellation rather than proper treatment of physical phenomena.

Penfold<sup>150</sup> also tunes the range-separated parameter associated with the LC-BLYP functional against both ionization potential and electron affinity of TADF emitters. Although Penfold employs a slightly different formalism in terms of optimization procedure, like Sun et al., Penfold finds that such an a priori tuning reduces errors associated with vertical ionization energy and the singlet-triplet energy gaps that are important when considering TADF candidates. Penfold also notes that the spin orbit coupling between the singlet and triplet states are not considered in his work, which are also important properties to consider as they determine the efficiency of any possible state-crossing processes.

Moore and Autschbach<sup>151</sup> evaluated the performance of TD-DFT (BP, PBE, PBE0, LC-PBE\*, LC-PBE0\*) in describing the excited states of linear cyanines. The study finds that, unlike with charge transfer states, minimizing the delocalization error ( $\Delta E$ ), for example, by tuning the range-separated functionals, does not lead to a concomitant increase in accuracy in absorption maxima. It is also found that local pure functionals overestimate vertical excitation energy, and a  $\Delta$ SCF approach significantly underestimates the vertical excitation energy. TD-DFT in general is also found to overestimate singlet-triplet energy gaps.

### 6.1.2 Relaxed versus unrelaxed densities

Maschietto et al.<sup>152</sup> have compared the effect of using relaxed or unrelaxed excited state density when attempting to describe the nature and properties of excited states. Excited state charge-transfer characteristics of extended phenyl chains are examined by computing  $D_{CT}$  values for each molecule, using either relaxed ( ${}^R D_{CT}$ ) or unrelaxed ( ${}^U D_{CT}$ ) excited state densities. These values correspond to the spatial extent of the charge transfer upon excitation and the charge transfer distances, respectively. In total, 52 exchange correlation functionals were employed in order to determine their performances. Generally, it was found that the description of the CT state was qualitatively described by both  ${}^R D_{CT}$  and  ${}^U D_{CT}$  values, and that as charge-transfer increased in distance, the use of  ${}^U D_{CT}$  becomes more

appropriate. The performance of the CT description was found to be relatively functional independent, and much more dependent on the extent of the CT instead.

### 6.1.3 Dual-functional Tamm-Dancoff approximation

Shu, Parker, and Truhlar<sup>153</sup> report a new implementation of TD-DFT, i.e., Dual-Functional Tamm-Dancoff Approximation (DF-TDA), that should correctly reproduce the  $3N-8$ , where  $N$  is the number of atoms, dimensionality that describes conical intersections. The proposed implementation uses two DFT functionals; the first functional is used to optimize the orbitals of the system, and the second functional is used to construct the TD-DFT/TDA Hamiltonian; the method is implemented in GAMESS. In order to assess the performance of the method, combinations of the M06, M11, and MN15 functionals were combined and applied to the dissociation of  $\text{NH}_3$ , which exhibits a conical intersection between the  $S_1$  and  $S_0$  states, and to the pyramidalization and twisting of ethylene. The DFT results show very close agreement with the PES calculated with CASPT2 and could provide a new approach to tackling difficult intersection points.

### 6.1.4 Simplified Tamm-Dancoff approximation

Grimme et al. have performed a wide-range of studies focusing on both implementation and development of TD-DFT methods as well as their subsequent application to organic systems. The derivations for simplified TDA<sup>154</sup> and full TD-DFT<sup>155</sup> are presented, which allow for the computation of excited states for large molecules, i.e. up to  $\sim 1000$  atoms; systems that still today present a significant challenge. The sTDA and sTD-DFT methods yield significant speed-ups compared to the full calculations, and the sTD-DFT provides the benefit of more reliable oscillator intensities, crucial for simulation of various spectra, compared to sTDA, and exhibits similar calculation errors to that of the full calculations. A subsequent study<sup>156</sup> extends sTDA from just global hybrid exchange-correlation functionals (XCFs) to several range-separated hybrids, namely, the  $\omega$ B97 family of functionals, PBE0, B3LYP, CAM-B3LYP, and LC-BLYP. The study finds that CAM-B3LYP and  $\omega$ B97X-D3 perform best for most excitations, and that in general the RSH functionals perform better than global hybrids. As well as this, a study<sup>157</sup> applying the  $\omega$ B97X and BHHLYP in conjunction with sTD-DFT to simulate the electronic circular dichroism (ECD) spectra of [16] helicene, finds good agreement with experiment; ECD spectra represent a challenge for TD-DFT as the spectra are sensitive to oscillator intensities.



A further extension of sTDA is tight-binding based (sTDA-xTB),<sup>158</sup> which is a semi-empirical approach to speeding up the generation of ground-state Kohn-Sham orbitals and eigenvalues, upon which the sTDA method can be applied for generation of excited states. The method is found to perform well for both low-energy valence and Rydberg states and outperforms other semi-empirical methods. The sTDA-xTB method was then applied to several biomolecular systems (thousands of atoms present) in order to simulate their UV-vis and CD spectra, finding excellent agreement between experimental and calculated spectra.<sup>159</sup> sTD-DFT and sTDA has also been applied to the ECD spectra of several large, highly  $\pi$ -conjugated systems<sup>160</sup>; namely, C<sub>76</sub> fullerene, [11]helicene, part of a chiral (11,7) carbon nanotube, and a section of a long,  $\alpha$ -helical polypeptide chain. The study notes the differences between TDA-TD-DFT and full TD-DFT in terms of computing excited state properties, notably the difference that can arise when calculating the rotary strengths, a signed property on which simulation of ECD spectra depends. The study shows that, for C<sub>76</sub> fullerene and [11]helicene, TDA (and sTDA) TD-DFT produce rotary strengths opposite in sign to that of a full TD-DFT (and sTD-DFT), resulting in incorrect spectra that would affect any attempt of assignment. In the case of [11]-helicene, the ECD spectrum is reasonably well simulated, however, a band of opposite sign to experiment is observed in the 250–280 nm, demonstrating that the incorrect signs of rotary strengths from (s)TDA is not systematic and cannot simply be multiplied by  $-1$ . (s)TD-DFT is found to give spectra in excellent agreement with experiment when combined with the  $\omega$ B97X-D3 functional.

Full TD-DFT has also been applied to the examination of 20 different 3,4,5-triaryl-1-R-1,2-diphosphole derivatives, in order to determine their applicability as optoelectronic materials.<sup>161</sup> The study found that structural changes, for example, introduction of substituents to the *para*-positions of the aryl groups, or changing the substitution of the phosphorus atoms, can be used to tune the HOMO-LUMO gap of the molecules. TD-DFT and TDA-TD-DFT were also applied to the study of some fluorescent benzimidazolylquinoxaline derivatives,<sup>162</sup> finding good agreement between experiment and calculations using the PBE0 and B3LYP functionals.

## 6.2 Dye chemistry

### 6.2.1 Overview

One of the most popular applications of TD-DFT is the study of dyes, particularly in the context of dye-sensitized solar cells. Jacquemin has applied

TD-DFT to a large range of systems from both a benchmarking and exploratory perspective.<sup>2,47,163–183</sup> Among other things, the performance of TD-DFT with respect to reproducing several excited state phenomena exhibited by several types of dye (i.e., anthraquinones, cyanines, coumarins, naphthalimides, BODIPY and similar dyes, photoacids and biodyes, and photoswitches) has been examined.<sup>179</sup> The properties modelled included absorption and emission spectra and understanding their band shapes, charge-transfer characteristics for optimization in solar cells, and excited state proton transfers/photoacidity. TD-DFT was found to accurately reproduce vertical excitation energies using hybrid functionals, e.g., B3LYP and PBE0, with MAE of 0.10 eV. Multiple linear regression, with parameterized components from both PBE0 and B3LYP, was found to reduce the MAE to 0.08 eV, and reduced the number of erroneously large deviations. However, TD-DFT was found to severely overestimate the transition energies of cyanine and its derivatives; for example, B3LYP exhibits MAE of 0.31 eV when applied to cyanine, and B3P86 exhibits a MAE of 0.25 eV when applied to anthocyanine. With respect to exploring dye-sensitized solar cells, the same authors<sup>179</sup> note the importance for including the surface in the time-dependent calculation, as the surface has a polarizing effect on the molecular electronic structure which will affect absorption behavior. Finally, the authors find that TD-DFT can also be applied to photoreactivity, i.e., excited state intermolecular proton transfer and photoswitching, which moves TD-DFT away from simply calculating intrinsic properties on equilibrium geometries.

A review focused on the application of quantum chemistry to cyanine excited states<sup>172</sup> finds that TD-DFT can be used to find a specific cyanine transition; the transition will be functional independent and upshifted in energy when the Tamm–Dancoff approximation<sup>130</sup> is employed, and the respective excited state geometries are well modelled. Single reference methods with included dynamic correlation are required for acceptable reproduction of the absolute transition energies, however. A review into the photodeactivation dynamics of phosphors<sup>178</sup> highlights the non-systematic errors exhibited by TD-DFT when applied to systems with transition metals present. 0–0 energies and vibrationally resolved spectra are also reviewed,<sup>2</sup> generally finding that M06-2x, B3LYP, M06, and  $\omega$ B97X-D give small maximum absolute errors for absorption spectra, which increase for emission spectra. LC-PBE was found to perform poorly for both sets of spectra.

Jacquemin et al. have also employed TD-DFT for a range of systems. The second-order NLO behavior of a Pt(II) complex<sup>171</sup> was reported

and investigated experimentally and with TD-DFT; using PBE0 to model the absorption behavior and  $\omega$ B97X-D to compute the first hyperpolarizabilities. The computed absorption spectra are in good energetic agreement with the experimental spectra. Benelhadj and Jacquemin et al.<sup>176,184–186</sup> have published studies into excited state intramolecular proton transfer processes in benzazole<sup>184</sup> and benzoxazole<sup>176</sup> derivatives, and the luminescent properties of borate complexes.<sup>185,186</sup> The benzoxazole derivatives were found to exhibit fluorescence of white light, arising from dual fluorescence from enol and keto phototautomers. TD-DFT was employed to explore the excited state PES for excited state intramolecular proton transfer.<sup>165,174</sup> This study was subsequently expanded to over 110 potential excited state intramolecular proton transfer dyes with a TD-DFT/ADC(2) hybrid approach.<sup>175</sup> TD-DFT was used for vibrational and structural parameters, and ADC(2) was used for absolute and transition energies. This hybrid approach was found to give good agreement with experimental fluorescence spectra and, more importantly, consistently predicted whether fluorescence would arise from the keto or enol forms, or if dual fluorescence would dominate. Diketopyrrolopyrrole molecules<sup>170</sup> were investigated for their solar cell sensitizing properties; specifically 4 different dyes were investigated. Experimentally, each of the dyes exhibit absorption at similar wavelengths, which is captured by TD-DFT. However, changing terminal thiophene groups for trisarylamine groups was found to enhance CT character in the excited states, a property beneficial for sensitizing dyes. The CT character was found to be well modelled by the CAM-B3LYP functional.

### 6.2.2 Dye-sensitized solar cell applications

Le Bahers et al.<sup>187</sup> have discussed the proper practice for examining dye-sensitized solar cells with quantum chemistry; summarizing the procedure as: (a) compute the structural and electronic properties of the dye-sensitized solar cell; (b) employ diagnostic tools to determine the accuracy and reliability of the calculations; (c) assess impact of dye adsorption; and (d) evaluate electron injection efficiency, incident photon-to-charge carrier efficiency (IPCE), and  $J_{SC}$ . Coupled with the PBE0 functional, three similar pyridinium derivatives were examined, finding good agreement with experimentally obtained results.

Mathew et al.<sup>188</sup> report the success of two bis(2',4'-bis(hexyloxy)-[1,1'-biphenyl]-4-yl)amine-functionalised porphyrin-based dyes for solar cell sensitization, which exhibit power conversion efficiencies of up to 13%.

The two dyes are similar in that their donor groups (porphyrin core + amine groups) are identical but differ in that their acceptor groups are either a benzoic acid group (dye SM371), or a benzothiazole group (dye SM315); SM315 is found to be the more efficient of the two dyes. The M06 functional was employed in order to rationalize the observed differences in absorption behavior, finding that SM315 exhibited a greater amount of donor  $\rightarrow$  acceptor CT character in the  $S_1$  state than SM371, as well as a series of bright absorption peaks extending to  $\sim 400$  nm, which are used to explain the observed panchromatic absorbance of the dye and the resulting efficiency.

Liu et al.<sup>189</sup> employed B3LYP and CAM-B3LYP to study the linear and non-linear optical properties of 6 derivatives of triphenylamine ( $\pi$ -indandione) chromophores. Here, CAM-B3LYP was employed to optimize the ground state structures of the molecules as B3LYP is said to be less capable of reproducing the correct geometries or modelling the charge transfer taking place to give rise to the non-linear optical properties. However, it appears that B3LYP was nonetheless employed to simulate the absorption and emission spectra of the molecules, rather than CAM-B3LYP. The authors do, however, find good agreement between the simulated and experimental spectra, and find that asymmetric modification of indandione groups results in a profound effect on the calculated first-order hyperpolarizabilities.

Linares-Flores et al.<sup>190</sup> also used (CAM-)B3LYP to study the effect of different electron-donating substituents and anchors on the optical properties of porphyrin-based zinc phthalocyanine dyes. The ground state geometries were obtained using both functionals, with B3LYP giving a band gap in good agreement with experimental values, 3.2 eV vs 3.4 eV, respectively; however, CAM-B3LYP gave an estimated band gap of approximately 6 eV, a somewhat spectacular failure. However, reasonable agreement is obtained for each functional between the calculated vertical excitation energy and oscillator strengths and experimental values obtained from similar compounds. The work was motivated by applications in dye-sensitized solar cells, and the study demonstrates that it is possible to use theory to optimize structural parameters so as to increase the efficiency of the electron injection process critical to photovoltaic action.

An earlier study by Zarate et al.<sup>191</sup> also studied dye-sensitized solar cell models, employing both B3LYP with added dispersion corrections and CAM-B3LYP. Here, CAM-B3LYP was employed to calculate the vertical excitation energy, and a comparison to values as calculated by the

$\omega$ B97X-D, BHHLYP, M06-2 $\times$ , M11, HISSbPBE, HSE06, M06, PBE, and TPSSh functionals was performed. It was found that a smaller number of bridging units between the chromophore and the dye-sensitized surface gave rise to a larger absorption. Zarate et al.<sup>192</sup> also studied the electron photoinjection mechanism and photovoltaic properties of TiO<sub>2</sub>-adsorbed donor-acceptor bridges with the B3LYP, CAM-B3LYP, PW91, PBE, and M06-L functionals. In total, 11 different donor motifs were compared to alizarin and naphthalenediol, which can undergo both Type I and Type II photoinjection mechanism mechanisms, and it was found that different donor systems were capable of driving favorability for a photoinjection mechanism.

Li et al.<sup>193</sup> used B3LYP (ground state geometries), CAM-B3LYP (absorption/emission), and M06-2 $\times$  (dye regeneration mechanism) to study various properties of three organic dyes, to determine their potential for application to dye-sensitized solar cells. The simulated absorption spectra are in good agreement with experiment, and charge density plots of the S<sub>0</sub> and S<sub>1</sub> states show clear charge transfer from the donor to the acceptor regions of the molecule, suggesting CAM-B3LYP can reproduce these effects. In general, the study shows that CAM-B3LYP was capable of reproducing experimental observations, including which species had the higher molar absorption characteristics, and that substitution along the  $\pi$ -bridge had a significant impact on the absorption properties of the molecule.

Nachimuthu et al.<sup>194</sup> studied the effects of anchoring groups on the optical and aggregation properties of a 4-methoxy- N-(4-methoxyphenyl)-N-phenylbenzeneamine donor moiety coupled with several different acceptor and anchoring units. In particular, the role of the anchoring groups in dye aggregation was examined as extensive aggregation can result in a decrease in electron transport through a solar cell, and hence a decrease in its efficiency. The B3LYP,  $\omega$ B97XD, BHHLYP, M06-2 $\times$ , and CAM-B3LYP functionals were used in the excited state calculations, with the  $\omega$ B97XD proving to be the most accurate. The study finds that dyes with a dithioic (CSSH) anchoring group exhibit the lowest energy transitions, and that the inclusion of a CN group into the anchoring moiety can also enhance absorption. Compared to the COOH anchoring group, molecular dynamics (MD) calculations found that dyes with CSSH favored aggregation to a greater extent, demonstrating that optimal choice of the anchoring group can be used to enhance favorable, and limit unfavorable, physical characteristics.

Baheti et al.<sup>195,196</sup> used B3LYP to study the effect of functionalizing fluorene-based sensitizers for dye-sensitized solar cells. In their first study,

one or two fluorenylidene moieties were incorporated into triarylamine donor units, coupled with cyanoacrylic acceptor units and (bi)thiophene conjugated bridges. All of the fluoro-containing dyes studied exhibit significant charge-transfer character arising from the HOMO-LUMO transition, and they also have red-shifted absorbance compared to the reference and dicyanovinyl containing dyes. As well as this, the fluoro-containing dyes exhibited higher molar extinction coefficients and HOMO-LUMO energy levels close to that of  $\text{TiO}_2$  that resulted in a higher photocurrent density than that arising from the dicyanovinyl species. In their second study the authors studied the effect of functionalizing rod-like and T-shaped dyes. They found that the rod-shaped dyes exhibit lower-energy  $S_0 \rightarrow S_1$  transitions compared to that of T-shaped dyes, and this arises from the extended delocalization found in the rod-like dyes. As well as this, it is found that (bi)thiophene linkers result in a red-shift in absorbance. Finally, while the rod-like have a lower-energy absorbance compared to the T-shaped dyes, the latter are in fact the more efficient sensitizers if they were to be used in a dye-sensitized solar cells.

Venkateswararao<sup>197</sup> used B3LYP and MPW1K to characterize the behavior of carbazole donor units with  $\pi$ -linkers. The calculations demonstrate significant charge-transfer character from the HOMO-LUMO transition at energies appropriate for electron injection to  $\text{TiO}_2$ . Feng et al.<sup>198</sup> use B3LYP and CAM-B3LYP in order to simulate the spectra of several molecules functionalized with an ullazine donor group, finding that the spectra demonstrate the applicability of ullazine to dye-sensitized solar cells.

Kulinich et al.<sup>199</sup> used the B97D3, B3LYP, B3PW91, and  $\omega$ B97X-D functionals to study the excited states of merocyanine. The study finds good agreement for all functionals between the calculated and experimental spectra, with the B97D3 functional performing best. The B97D3 functional suggests that the low energy,  $S_0$  to  $S_1$  transition is a  $\pi\pi^*$  transition at 2.81 eV, in very close agreement with the experimental band centered at 2.8 eV. The  $S_0$  to  $S_2/S_3$  excitations are found to be symmetry forbidden and therefore unresolvable in either experimental or simulated spectra. The B3LYP, B3PW91, and  $\omega$ B97X-D functionals consistently overestimate the vertical excitation energy, with the  $\omega$ B97X-D energies being the least accurate.

Kowalska-Baron et al.<sup>200</sup> used the B3LYP and CAM-B3LYP functionals, as well as the  $\omega$ B97X-D functional, to study the distyrylnaphthalene chromophore. However, only the B3LYP functional was employed to study the excited state. Again, no description of the character of the  $S_1$  state is included. The experimental absorption and fluorescence spectra are also

broad and ill-defined, meaning it is unclear if the excited states are being correctly modelled. The chromophore also has an extensive  $\pi$ -system and the paper also mentions that charge transfer takes place in the  $S_1$  state, for which TD-DFT, and B3LYP in particular, is known to fail.<sup>131–133</sup> It is unclear, then, if the TD-DFT calculations are properly describing either the ground or excited state structures and energies of the chromophore.

In other studies, Lee et al.<sup>201</sup> employed B3LYP to study the excited states of several fluorene containing iridium complexes. The complexes exhibit “deep-blue” phosphorescence, and significant metal-to-ligand charge-transfer character is found for the triplet excited states, suggesting significant spin orbit coupling between the excited states. Estrada et al.<sup>202</sup> provide insight into the change in electronic structure of isoindigo upon functionalization. Different functionalization patterns are found to change not only the broadness of the absorption spectra but also the oscillator intensities. Thienyl groups were found to planarize the molecules. Lourenço Neto et al.<sup>203</sup> employed B3LYP to simulate the absorption spectra of eight different phenolic acids, which were then be compared to the experimentally obtained spectra of four Brazilian fruits. From the calculations, the B3LYP spectra are in good agreement with the experimentally obtained absorption spectra, and the acidic makeup of the fruits can be elucidated.

### 6.3 Excited state intramolecular proton transfer

Excited state intramolecular proton transfer studies have also found TD-DFT a useful and often accurate method. Huang et al.<sup>204,205</sup> employed TD-DFT to study the excited state intramolecular proton transfer mechanisms of 3-hydroxy-2-(thiophen-2-yl)chromen-4-one (3-HTC) and 2,5-bis(benzoxazol-2-yl)thiophene-3,4-diol with B3LYP. In their earlier study, 3-HTC is found to undergo excited state intramolecular proton transfer due to the strengthening of an internal OH hydrogen bond upon excitation. The  $S_0$  and  $S_1$  H-transfer PES were calculated and the favorability for excited state intramolecular proton transfer is clear. The simulated absorption and fluorescence spectra are in good agreement with the experimental spectra. Similarly, upon excitation an internal NH hydrogen present in 2,5-bis(benzoxazol-2-yl) thiophene-3,4-diol is strengthened, and the calculated PES show clear favorability for the excited state intramolecular proton transfer. However, with 2,5-bis(benzoxazol-2-yl) thiophene-3,4-diol, a double excited state intramolecular proton transfer process is in fact favored.

As with 3-HTC, good agreement between simulated absorption/emission spectra is obtained. Zhu et al.<sup>206</sup> studied the excited state intramolecular proton transfer of five molecules containing the 10-aminobenzo[h] quinoline chromophore group.

Liu et al.<sup>207</sup> studied the excited state double proton transfer mechanism of 8-hydroxyquinoline (8HQ) using the B3LYP and CAM-B3LYP functionals. The 8HQ molecules were micro-solvated with either NH<sub>3</sub>, H<sub>2</sub>O, or AcOH. The HOMO-LUMO transitions for each species is of  $\pi\pi^*$  character, and the strength of the H-bond between the 8HQ and solvating species results in slightly different H-transfer mechanisms. With NH<sub>3</sub>, the OH(8HQ) H-bond is found to be strongest and is therefore the first proton transfer to take place, followed by an H-transfer from the NH<sub>4</sub><sup>+</sup> species back to the 8HQ. The opposite is found to be true for the 8HQ-AcOH species, and with H<sub>2</sub>O, each of the two H-bonds are found to be similar in strength, which leads to a concerted double proton transfer. Ground state analysis of the proton transfer for the 8HQ-NH<sub>3</sub> species shows a significant activation barrier, whereas TD-DFT results suggest a near-barrierless PES in the S<sub>1</sub> state.

Pina et al.<sup>208</sup> studied the excited state intramolecular proton transfer of Indigo and a monohexyl-substituted derivative with the CAM-B3LYP functional. The study aims to provide evidence for whether the transfer is either a single or double excited state intramolecular proton transfer, and if the transfer involves rotation about the central carbon-carbon bond. It is found that only a singlet excited state intramolecular proton transfer takes place, and rotation is feasible but according to experimental ultrafast spectroscopy it is a non-competitive pathway.

The excited state intramolecular proton transfer of 1,5-dihydroxyquinone was studied by Zhou et al.<sup>209</sup> with B3LYP. The simulated absorption and fluorescence spectra are found to agree well with experimental spectra, and the intermolecular H-bonds are found to be strengthened upon excitation to the S<sub>1</sub> state. It is also found that a single excited state intramolecular proton transfer takes place on the T<sub>1</sub> surface. The S<sub>0</sub> to S<sub>1</sub>/S<sub>2</sub> transitions are likely to be  $\pi\pi^*/n\pi^*$  transitions, respectively, based on the relative oscillator intensities of the two transitions (0.2866 vs 0, respectively). The population of the T<sub>1</sub> state is attributed to internal conversion to the S<sub>1</sub> state followed by ISC to the T<sub>1</sub> state; however, no description of the character of the T<sub>1</sub> state is included, on which the efficiency of the ISC is dependent. It may be found that the higher  $n\pi^*$  state may be involved in populating the triplet states, however this possibility is not explored.



Li et al.<sup>210,211</sup> used TD-B3LYP to explore excited state intramolecular proton transfer in 6-amino-2-(2'-hydroxyphenyl)-benzoxazole (6A-HBO) with and without an explicit methanol molecule present. The role of the methanol hydrogen bond does not appear to be significant; the uncomplexed 6A-HBO exhibits a H-transfer transition state energy that lies 9.6 kcal mol<sup>-1</sup> above the ground state and a shallow H-transferred minimum, and upon excitation the transition state decreases in energy to 8.7 kcal mol<sup>-1</sup> and a slightly deeper H-transferred minimum. Complexation to the MeOH molecule serves to stabilize the transition states for both the S<sub>0</sub> and S<sub>1</sub> state, to 6.4 kcal mol<sup>-1</sup> and 5.2 kcal mol<sup>-1</sup>, respectively. Questions remain about the accuracy of B3LYP for predicting transition state energies, it would be interesting, therefore, to assess if other DFT functionals give similar potential surfaces. The authors also studied 6A-HBO and 5-amino-2-(2'-hydroxyphenyl)benzoxazole (5-HBO) excited state intramolecular proton transfer in the context of the role of the amino group, finding again that the OH→N hydrogen bond is significantly increased in strength in the S<sub>1</sub>, hence promoting excited state intramolecular proton transfer.

Zhang and Liu<sup>212</sup> used TD-DFT to study the absorption behavior of 2,4,6-trisbenzothiazolylphenol, which can undergo excited state intramolecular proton transfer upon excitation the S<sub>1</sub> state. The authors note that design of molecules that undergo excited state intramolecular proton transfer can be difficult and here, TD-B3LYP calculations were used to show that the HOMO-LUMO gap can be red-shifted by increasing the extent of conjugation in the molecule. The calculated absorption (384 nm) and emission (619 nm) maxima were also found to be in good agreement with experimental values, at 376 and 570 nm, respectively.

Zhao et al. studied the excited state intramolecular proton transfer mechanisms of 3-hydroxyisoquinoline (3HIQ),<sup>213</sup> bis-2,5-(2-benzoxazolyl)-hydroquinone (BBHQ) and its derivatives,<sup>214</sup> and 1,8-dihydroxybenzo [*a,h*]phenazine (DHBP)<sup>215</sup>; each study used TD-B3LYP. In the case of 3HIQ, three model proton transfers were considered; the first involved a single 3HIQ molecule along which the enol-keto tautomerization proceeds via a high barrier of approximately 37 kcal mol<sup>-1</sup>. The second and third transfer reactions involved (a) 3HIQ self-association in cyclohexane with a step-wise double proton transfer via a 3HIQ + H<sup>+</sup>/3HIQ<sup>-</sup> charge-separated intermediate, and (b) 3HIQ H-bonding to an acetic acid molecule that involves a simultaneous 3HIQ → ACID/ACID → 3HIQ double proton transfer to form the keto species. Mechanism (b) is found to be essentially barrierless. The studies of BBHQ and DHBP also employed a TD-DFT

PES and demonstrated the feasibility for either single- or double-proton transfer mechanisms, as the respective hydrogen-bonds of interest are strengthened in the  $S_1$  states. However, no work is done to definitively determine which mechanism actually takes place.

Liu et al.<sup>216</sup> performed a similar study focusing on quinoline-pyrazole isomerization, which involves excited state intramolecular proton transfer. Two isomeric systems were considered, labelled QP-I and QP-II, as it is found experimentally that, upon photoexcitation, QP-I undergoes emission at a wavelength corresponding to the proton-transferred (PT) isomer; however, no such emission is observed for QP-II. The authors find that the PES for H-transfer in QP-II exhibits a lower barrier than that of QP-I on the  $S_1$  state, suggesting QP-II excited state intramolecular proton transfer is in fact more favorable than that of QP-I. The lack of emission is therefore attributed to the small energy gap ( $\sim 0.29$  eV) between the  $S_1/T_2$  states found in PT-QP-II, which could result in ISC and therefore no fluorescence. The equivalent energy gap in PT-QP-I is found to be  $\sim 0.77$  eV, which results in the observed fluorescence.

## 6.4 Photoinitiation

Photoinitiation is the process by which involves a molecule that undergoes  $\alpha$ -decomposition (Type I) or a hydrogen atom abstraction (Type II) to generate either free radicals or ions upon irradiation with (usually UV) light.<sup>217</sup> Fig. 3 shows the both types of photoinitiation, adapted from ref.<sup>217</sup>

Huix-Rotllant et al.<sup>108,218,219</sup> have applied TD-DFT to retinal, acetophenone, and photoinitiation of nitroxide mediated polymerization (NMP). In the case of retinal, TD-DFT and TDA-TD-DFT with the B3LYP, CAM-B3LYP, BHHLYP, M06-2 $\times$ , and mPW2PLYP functionals was compared to MRCISD+Q, SF-EOMCCSD(dT), and SA-CAS. The study explores the ground and excited state PES, finding generally that the single-reference TD-DFT was unsuitable, and was incapable of describing the diradical and CT intersection geometries. As well as this, TD-DFT was found to produce “kinks” in the PES, artefacts that were not present in higher-level calculations. Out of all the functionals tested, the double hybrid mPW2PLYP functional performed the best. mPW2PLYP was also found to perform the best in describing the three-state crossing between the  $^1(n\pi^*)$ ,  $^3(n\pi^*)$ , and  $^3(\pi\pi^*)$  states, in particular when combined with TDA-TD-DFT. The double hybrid functional was the only functional to predict a three-state crossing and produced energies and geometric

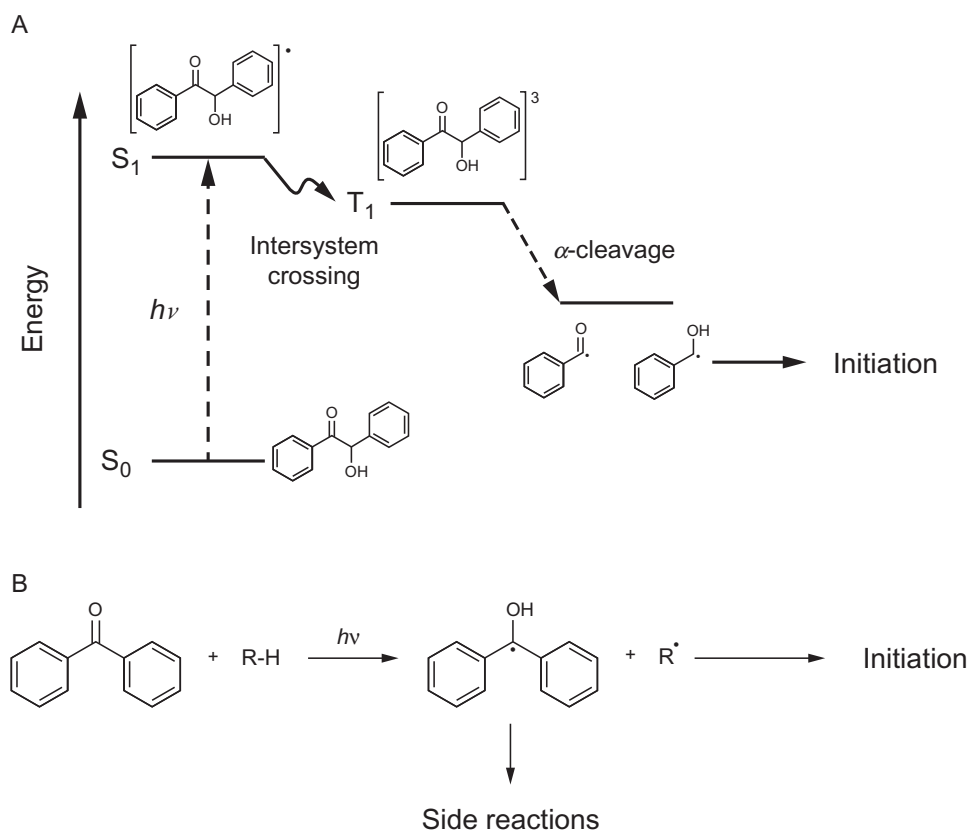


**Fig. 3** Example mechanism for Type I (A) and Type II (B) photoinitiation.

parameters in closest agreement with multireference calculations. The increase in accuracy of mPW2PLYP is attributed to the larger inclusion of double-excitations in the excited states arising from the MP2 component of the calculation. Full TD-DFT, and CAM-B3LYP in particular, was found to perform badly when describing the triplet surfaces, and TDA-TD-DFT is found to correct these issues.

For the NMP study, several different isomers of an NMP iniferter (An iniferter is an initiator for radical polymerizations.), which combine a chromophoric acetophenone moiety with an alkoxyamine group that will undergo cleavage to initiate the reaction, were studied using TD-B3LYP. The calculations suggest that the photochemical processes of the iniferters are defined by singlet-triplet crossing, followed by excitation delocalization across the alkoxyamine moiety, which results in bond homolysis. It was also found that C—N and O—C dissociations can compete, which could account for low initiation efficiencies. However, in their acetophenone study Huix-Rottlant et al.<sup>218</sup> recommend the use of mPW2PLYP/TDA for exploring the excited states of acetophenone-based chromophores,

not B3LYP/TD-DFT which is found to perform poorly. As well as this, B3LYP is known to fail for describing radical bond dissociations,<sup>220</sup> so the competition between the different  $\sigma$ -cleavage pathways remains unclear.

Frick et al.<sup>221</sup> explored the relationship between the structure and reactivity of benzoin-based radical photoinitiators, using a combination of pulsed-laser polymerization with subsequent electrospray-ionization mass spectrometry (PLP-ESI-MS), femtosecond transient absorption (fs-TA) spectroscopy, and ab initio calculations. TD-B3LYP was employed to compute the excited state properties, finding generally that there was no significant relationship existed between the brightness of an excited state and the subsequent dissociation reaction. In fact, dark  $n\pi^*$  states generally dominate the  $S_1$  state, and it is the population of these states that most efficiently leads to dissociation. The study also finds that if too many singlet/triplet states lie below the likely most reactive states, photoinitiation becomes less favorable due to increased competition with internal conversion decay pathways.

Xiao et al.<sup>11,222,223</sup> employed TD-DFT to study the absorption characteristics and photoinitiation mechanism of anthraquinone derivatives. The studies highlight the impact of different substitution patterns can have on altering the ordering of  $n\pi^*$  and  $\pi\pi^*$  transitions, also finding that the anthraquinone molecules undergo excited state redox processes when co-initiating molecules are present.

## 6.5 Other photochemical reactions

A range of other photochemical triggered reactions are possible, and below is just a few of the processes studied via TD-DFT. Luo et al.<sup>224</sup> employed ultrafast spectroscopic techniques and TD-M06-2 $\times$  to investigate the efficacy of sinapoyl malate and sinapic acid for natural UV-protection. In this case, TD-DFT is found to be able to qualitatively reproduce the  $S_{0/1}$  PES, finding that the cis-trans isomerization is barrierless for both systems on the  $S_1$  state, and leads back to the ground state. However, it is observed that the cis-isomer of sinapic acid is less able to absorb UV light than its trans-counterpart; in contrast, sinapoyl malate exhibits no significant difference in the absorption characteristics of either cis/trans isomer and continues to absorb UV light efficiently. This is used to reconcile why sinapoyl malate is prevalent in nature rather than sinapic acid.

Mazzone et al.<sup>225</sup> used several functionals, M06-2 $\times$ , M06, PBE0, and B3LYP, to examine the electronic properties and spin-orbit couplings of two thienopyrrole BODIPY (BODIPY = a boron-dipyrromethene).

All four functionals gave consistent structural parameters and  $S_1/T_1$  energy gaps, and M06 and B3LYP gave  $S_0$  to  $S_1$  transition energies closest to the experimental values. The spin orbit coupling between the  $S_1$  and  $T_1$  states was found to be higher than Foscan<sup>®</sup> (Temoporfin photosensitizer) taken as a reference molecule, and the BODIPY derivatives are therefore feasible photosensitizers for singlet oxygen generation.

Liu et al.<sup>226</sup> designed a cross-coupling reaction between thiol and aryl halides that is promoted by visible light, and results in a highly synthetically useful carbon-sulfur bond. TD-DFT was applied in order to gain insight into the process taking place upon excitation, using the CAM-B3LYP functional. The calculations suggest that, upon excitation, a preformed negatively charged electron donor-acceptor (EDA) complex undergoes CT to form a negatively charged species now on the acceptor molecule, and a biradical across the complex. These biradicals are localized on the carbon and sulfur atoms that then undergo coupling to form the product.

Kozłowski et al.<sup>227</sup> give a perspective on the photochemistry of cobalamins; in particular, methylcobalamin (MeCbl), adenocobalamin (AdoCbl), cyanocobalamin (CNCbl) a.k.a. vitamin-B<sub>12</sub>, and hydroxocobalamin (HOcbl). These molecules have significant biological relevance, for example, some enzymes are found to be dependent on AdoCbl in radical-mediated rearrangement reactions; the cobalamins also possess a “unique  $\sigma$  Co—C bond”. The rich chemistry of the cobalamins also involves complex excited state properties that are found to be dependent not only on the relative substitutions of various chemical groups, but also the local environment. In particular, cobalamins are found to undergo bond photolysis, resulting in a Co(III)→Co(II) oxidation and production of alkyl radicals, and detailed understanding of the photolysis mechanism is therefore sought. Due to the size of the systems, TD-DFT was employed rather than ab initio methods, along with a significantly truncated model that captures the cobalamin Co core and leaves out any functional groups extending beyond the pyrrolic halo. B3LYP, and dispersion corrected B97-D and BP86 functionals were used, finding that, for MeCbl, B3LYP incorrectly predicted a  $S_1$  state dominated by  $\pi\pi^*$  character, whereas BP86 correctly (according to ab initio and spectroscopic results) predicts predominantly metal to ligand charge transfer character. The results concentrate on the singlet excited states of the four cobalamin complexes, finding that cobalamin low-lying excited states can be dominated by  $\pi\pi^*$ ,  $\sigma\pi^*$ ,  $\pi d$ , and  $d\pi^*$  characters, which give rise to complicated dissociation pathways from which reactivity can be difficult to elucidate. As well as this, the authors find that TD-DFT is insufficient to

explain the experimentally observed wavelength independence of AdoCbl with respect to photolysis, as the calculations draw similarities between AdoCbl and MeCbl that do not translate to experimental similarities. The involvement of triplet excited states is also fielded as a potential avenue for further study and could provide further insight into currently unexplained phenomena.

Ding and Liu<sup>228</sup> used TD-DFT and SF-TD-DFT to study the bioluminescence mechanism of luciferin in *Watasenia scintillans*. The bioluminescence of this structure is important it is a derivative of a core skeleton structure that is found in wide range of bioluminescent organisms. CAM-B3LYP was applied to TD-DFT calculations, from which a range of ground- and excited-state PES were calculated, to either support or refute the proposed bioluminescence mechanism.<sup>229</sup> As well as this, BHLYP was used in conjunction with SF-TD-DFT to perform non-adiabatic dynamics simulations with on-the-fly trajectory surface hopping (THP) to model the chemiluminescent decomposition reaction. SF-TD-DFT was chosen as it is more capable of coping with regions of electronic degeneracy. These two methods were found produce qualitatively correct surfaces and results, from which the previously proposed mechanism is strongly supported.

## 6.6 UV-Vis spectra and excitation energies

Ashwood et al.<sup>230</sup> studied the excited state dynamics of 6-thioguanine (6tGua) and its N9-glycosylated derivative (6tGuo) with ultrafast spectroscopy, and TD-DFT was used to provide theoretical insight; the PBE0 functional was used. The calculations find low-lying triplet states that are close in energy to the  $S_1$  and  $S_2$  states. The calculations and dynamics experiments appear to disagree, as the difference in the vertical excitation energy of 6tGua and 6tGuo are small, however, upon the excitation, the triplet states of the 6tGuo are populated nearly twice as quickly as the 6tGua molecule. This is attributed to an increase in vibronic coupling between various singlet and triplet states due to the 6tGuo molecule being significantly larger.

Simone et al.<sup>231</sup> studied the effect of substituting hydrogen atoms for either bromine or iodine atoms at various positions of aza-BODIPY. Aza-BODIPY has potential for therapeutic use as a photosensitizer for generation of singlet oxygen, which is cytotoxic and can be used to kill targeted cells. For a photosensitizer to be efficient, the triplet states of the molecule need to be effectively and rapidly populated after excitation. The M06 functional was used to calculate the ground state and absorption properties of the

substituted derivatives, finding that neither bromine nor iodine had a significant impact on the absorption properties. TD-DFT also predicted that for all compounds investigated, the lowest energy transition is the  $\pi\pi^*$  transition, and that the low-lying triplet states are of  $n\pi^*$  character, and therefore populating these states, according to the El-Sayed rules,<sup>232</sup> should be reasonably favorable.

Boron dipyritylmethene (DIPYR) dyes, which are pyridine based BOPDIY derivatives, were studied by Golden et al.<sup>233</sup> TD-DFT and XMCQDPT2 calculations were performed on boron dipyritylmethene, boron diquinolymethene, and boron diisoquinolymethene. B3LYP was employed, and the calculated vertical excitation energies were found to be systematically overestimated and were subsequently scaled by subtracting 0.44 eV from all calculated values; doing so resulted in good agreement with experimental values for the three molecules. The lack of fluorescence exhibited by DIPYR is attributed to the near degeneracy between the  $S_1$  and  $T_2$  states which leads to efficient ISC between the two. The authors note that manipulation of the relative energies of these two states, e.g. by benzannulation, can lead to an increase in fluorescence behavior.

Lorenz et al.<sup>234</sup> studied the electronic structure of poly(*p*-phenylene iminoborane) with TD-B3LYP. This was done to determine the extent of the  $\pi$ -conjugation across the polymer backbone; the TD-DFT calculations were performed to find the HOMO-LUMO transition, which was found to be a  $\pi\pi^*$  transition, providing evidence that there is such a  $\pi$ -system. Three different chain lengths were studied, and it was found that conjugation extends with chain length.

Margar et al.<sup>235</sup> studied difluoroboron-curcumin complexes, another highly  $\pi$ -conjugated system, in which the hydroxy-groups were replaced with methoxy and tosylate groups. Absorption and emission properties were calculated with B3LYP and are in good agreement with experimental values, and the first-order hyperpolarizability was calculated, suggesting that the molecules could exhibit significant non-linear optical properties. Kamada et al.<sup>177</sup> also studied difluoroboron curcuminoid molecules with TD-B3LYP, using it to calculate the one- and two-photon absorption properties. In agreement with Margar et al., the fluorophores are shown to exhibit significant non-linear optical properties, and B3LYP calculations are in good agreement with the experimental absorption spectra, if somewhat blue-shifted.

Cabrera-González et al.<sup>236</sup> studied a set of carborane clusters for their photophysical properties, finding experimentally that ortho- vs meta- bonding to the stilbene groups does not affect the absorption profile of the

different molecules. TD-B3LYP found that for all systems the  $S_1$  state was dominated by a HOMO-LUMO transition localized to the stilbene moieties, leading to absorption behavior independent to the bonding patterns of the stilbene units. This is found to be in direct contrast to previously reported carborane diads,<sup>237,238</sup> which find that the  $S_1$  states are dominated by CT character and are therefore significantly affected by structural parameters.

Momeni and Brown<sup>239</sup> note that BODIPY and aza-BODIPY are challenging systems for TD-DFT to model accurately, and therefore benchmark the performance of a range of functionals (B3LYP, PBE, BLYP, PBE0, LC-BLYP, LC-PBE, CAM-B3LYP,  $\omega$ B97X-D, and LC- $\omega$ PBE) against ab initio methods (TD-HF, CIS, CIS(D), EOM-CCSD, SAC-CI, LCC2, CCS, CC2, LR-CCSD, CCSDR(T), CCSDR(3), CASSCF, and CASPT2), all with the cc-pVTZ basis set. The correlated methods provide the authors with the means to analyze the different contributions to the excited state wavefunctions, for example dynamic correlation arising from the coupled-cluster methods, or double excitations that can appear in CASSCF calculations. The study finds that TD-DFT generally overestimates the vertical excitation energy by  $>0.3$  eV, and that within the test-set of functionals used, the range-separated functionals generally performed the best. Although the ab initio methods are computationally expensive, the authors find that SAC-CI and LCC2 with reasonably sized basis sets (cc-pVDZ/cc-pVTZ) provide greater accuracy than TD-DFT, while still being applicable to medium-sized systems.

Fujikawa et al.<sup>240</sup> were able to rationalise the UV-vis absorption behavior of two isomers, twisted- and meso-, of their synthesized double helicene molecule. The meso-isomer was found to exhibit a similar spectrum to that of the twisted-isomer, albeit shifted to higher energies. This was found, via TD-B3LYP, to arise from an increase in contribution from the HOMO-2 orbital to the  $S_1$  state for the meso-isomer, resulting in a higher energy excitation compared to that of the twisted-isomer. This is a neat example of how TD-DFT can be used to separate the behavior of two isomers.

Maier et al. report the seminumerical implementation<sup>241</sup> and performance<sup>242</sup> of TD-DFT for global and local hybrid XCF functionals. The semi-numerical implementation is found to scale favourably compared to analytical implementations available for global hybrids. The performance of several popular XCFs namely SVWN, BLYP, PBE, TPSS, TPSSh, PBE0, B3LYP, BMK, BLYP, M06-2X, CAM-B3LYP, LC- $\omega$ PBE, and  $\omega$ B97X-D, is compared to that of the following local hybrid (*Lh*) functionals; *Lh*-SVWN, *Lh*-SsifPW92, and *Lh*-SsirPW92. The local hybrid functionals are found to perform well when calculating the singlet and triplet



excitation energies of the Thiel benchmark set of molecules,<sup>243,244</sup> and provide a good balance between accurate energies for valence, core, and Rydberg states. However, the local hybrids were found to perform poorly for charge-transfer excitations.

Zhekova et al.<sup>245</sup> benchmark the performance of adiabatic TD-DFT (ATD-DFT) with and without the Tamm-Dancoff approximation. The performance of ATD-DFT is compared to that of CC2 and a  $\Delta$ SCF procedure for energies corresponding to the first  $\pi\pi^*$  transition in a number of cyanine molecules. The ATD-DFT excitation energies were found to be reasonably functional independent, however, this still corresponded to significant singlet and triplet energy over- and underestimation, respectively. The  $\Delta$ SCF procedure was found to exhibit significant functional dependence, with the authors finding that the BHLYP functional with the proportion of exact HF exchange set at 50% gave the excitation energies closest to ab initio results.

Cao et al.<sup>246</sup> studied the effect of antiaromatic bispentalene derivatives fused attached to either a benzene or naphthalene core. The focus of the paper is generally toward the experimental work carried out, showing with NMR that, although the molecules of interest fit the classical rule of aromaticity (i.e.,  $[4n + 1]$   $\pi$  electrons), the pentalene protons experience a significant upfield shift like that of antiaromatic compounds. As well as this, ring currents around the rings were measured using nucleus-independent chemical shift (NICS)-XY-scans, which demonstrated a global paratropic ring current (consistent with antiaromaticity) and a local diatropic current around the benzene core. The result of these opposing ring currents is present in the UV-vis spectra which show, for all of the systems studied, broad, low-energy absorption characteristics. Here, TD-CAM-B3LYP was used to characterize these broad peaks finding, compared to fully aromatic molecules with the same number of fused rings, significantly lower HOMO-LUMO energy gaps. Particularly impressive is the significant absorption taking place at  $>650$  nm.

Etienne et al.<sup>247</sup> developed a method of quantifying the extent of charge-transfer that takes place upon excitation, essentially by determining the extent of the overlap between the ground- and excited-state electron densities. The index,  $\phi_S$ , is found to be relatively insensitive to the type of orbital employed, e.g. natural transition orbitals (NTO) vs. Kohn-Sham, is computationally cheap to calculate. The index can also be employed to assess the failing of XCF functionals that are not range-corrected, so as to determine the extent of any potential XCF failing.

Ji et al.<sup>248</sup> synthesized several boron-containing oligothiophene chromophores, and employed TD-B3LYP in order to examine both the one- and two-photon absorption behavior of the molecules. The simulated one-photon absorption spectra are in good agreement with the experimental data, and the calculated TPA spectra are found to be systematically overestimated by B3LYP. However, the calculated TPA trends between each of the molecules studied were found to be reproduced qualitatively. In another interesting study Arulmozhiraja et al.<sup>249</sup> used TD-DFT and SAC-CI to explain the strong UV-absorbance of Arsenicin A, a compound with no formal  $\pi$  bonds. It was shown that the chromophore facilitated by through-space and through-bond interactions between the lone pairs on the arsenic and oxygen atoms and the  $\sigma$ -bonding framework of the molecule. These destabilize occupied and stabilize unoccupied molecular orbitals thus favoring the transitions.

## 6.7 Thermally activated delayed fluorescence (TADF)

Samanta et al.<sup>250</sup> applied TD-DFT to the up-conversion intersystem crossing (UISC) of 11 different organic emitting molecules that undergo thermally activated delayed fluorescence (TADF). B3LYP was used to optimize the ground state structures, and CAM-B3LYP was used to optimize the excited state geometries.  $S_1$  and  $T_2$  states were optimized with TD-DFT, and the  $T_1$  state was optimized with unrestricted DFT; the excitation energies, however, were calculated with a tuned LC- $\omega$ PBE functional. The spin-orbit couplings (SOC) between the singlet and triplet states of interest were also calculated, and it is well established that the smaller the energy difference between singlet and triplet states ( $\Delta E_{TS}$ ), the larger the SOC, and ultimately the faster the rate of UISC. The study finds that  $\Delta E_{TS}$  cannot be reduced by simply extending the spatial separation between the donor-acceptor regions within the molecule; instead, it is found that increasing the CT character of the  $T_1$  results in a concomitant decrease in  $\Delta E_{TS}$ . It is also found that, if possible, the symmetry of the singlet and triplet states needs to be different, which according to El Sayed's rules results in an increase in SOC.

Cai et al.<sup>251</sup> employed TD-DFT with the BMK functional to tune TADF of organic light emitting diodes (OLEDs). Four rate parameters are identified as important for determining the crucial excited state lifetime of TADF ( $\tau_{TADF}$ ); the rate of fluorescence ( $k_F$ ), the rate of intersystem crossing (ISC,  $k_{ISC}$ ), the rate of reverse ISC (RISC,  $k_{RISC}$ ), and the rate of

internal conversion (IC,  $k_{IC}$ ).  $\tau_{TADF}$  is required to be short for OLEDs to be at their most efficient, and it is found that increasing  $k_{RISC}$  has the most profound effect in shortening  $\tau_{TADF}$ , even when large values of  $k_{ISC}$  and small values of  $k_F$  are observed. It was also found that tuning the dihedral angles of the molecule can decrease  $\Delta E_{ST}$ ; these factors are to be considered when designing OLED candidate systems.

Gómez-Bombarelli et al.<sup>252</sup> applied a high-throughput screening approach to target novel TADF OLED candidates. Ultimately TD-B3LYP was employed to quantify the excited state properties of the molecules of interest, finding that it performed well for calculating vertical absorption. Improvement in the calculated values were not obtained through usage of M06-2x, BHHLYP, LC- $\omega$ PBE0, CAM-B3LYP, or  $\omega$ B97X-D functionals, nor through employing the PCM implicit solvent model. It was found that TD-B3LYP was incapable of accurately reproducing  $S_1$  PES as it overestimated the extent of the CT character of the excited state, and UDFT was therefore employed to optimize the  $T_1$  state. It is unclear if basis set choice was also considered for the calculations, as the 6-31G(d) basis set used is lacking the diffuse functions generally required to model the more diffuse excited state electron densities.

Valchanov et al.<sup>253</sup> also examined TADF of a series of donor-bridge-acceptor organic chromophores using the B3LYP and PBE0 functionals. The absorption and emission spectra were simulated, and singlet-singlet and singlet-triplet energy gaps were evaluated in order to determine the likelihood of (R)ISC processes. The authors find that the optical properties can be significantly altered by varying any one of the following physical parameters; the spacer fragment used, the binding positions to it, and the structure/elemental makeup of the donor and acceptor units. Chen et al.<sup>254</sup> examined TADF from a more fundamental perspective; that is, exploring the role of nonadiabaticity in the observed RISC mechanisms. TD-BMK is employed to explore some of the potential energy surfaces of some donor-acceptor molecules.

Zhang et al.<sup>255</sup> applied TD-DFT as a means to design anthraquinone-based TADF emitters, based on the requirement for a system that exhibits large fluorescence rates ( $k_F$ ) and small singlet-triplet energy gaps ( $\Delta E_{S-T}$ ). In order to achieve these desirable qualities, the authors paired anthraquinone acceptor units with diphenylamine (DPA), bis(4-biphenyl)amine (BBPA), 3,6-di-tert-butylcarbazole (DTC), and 9,9-dimethyl-9,10-dihydroacridine (DMAC) as the donor units, using phenyl rings as the bridging units. The authors found that increasing the distance between the

acceptor/donors increased the rate of fluorescence without increasing the  $\Delta E_{S-T}$ , as is desirable. However, geometry optimizations of the molecules on the  $S_1$  excited state found significant out-of-plane relaxation resulting in a decrease in  $\Delta E_{S-T}$  with a lower  $k_F$  and an increase in radiationless internal processes. Predictions made with TD-DFT with respect to emission peaks and photoluminescence quantum yield ( $\Phi$ ) were found to be in good agreement with experimental observations, despite the fact the B3LYP functional was employed for systems that exhibit significant charge-transfer.

Walter et al.<sup>256</sup> investigated the performance of TD-DFT and the semi-empirical OM2<sup>257</sup> method against spin-component scaled (SCS-) CC2 and SCS-ADC(2) by application to perylene and perylene bisimide (PBI) dimer aggregates. The functionals used were CAM-B3LYP,  $\omega$ B97X-D,  $\omega$ B97X, LC- $\omega$ PBE, and LC-BLYP. The dimer aggregates are  $\pi$ -electron rich systems, and a significant component of the stabilizing energy holding the systems together is likely to arise from dispersion forces, however, no dispersion correction to any of the functionals was introduced so this effect has not been studied. The study finds that the CAM-B3LYP and  $\omega$ B97X-D functionals give the best results for the perylene dimer, and for PBI the predicted ordering of the excited states is found to be incorrect when calculated with CAM-B3LYP. The  $\omega$ B97X-D functional results were found to be extremely sensitive to the monomer geometries of PBI, and this was attributed to near-degeneracies in the low-lying excited states. The long-range corrected functionals were found to give qualitatively correct results but overestimated the CT state energies. A combination of  $\omega$ B97X-D monomer geometry and  $\omega$ B97X transition energies was found to provide an accurate approach, and it was also found that tuning the  $\omega$  parameter of  $\omega$ B97X-D to  $\omega = 0.25$  yielded results similar to the ab initio methods. However, the authors note that this approach needs to be further investigated. The OM2 method was found to give poor results.

Huang et al.<sup>258</sup> examine the HF exact-exchange dependence with respect to the calculation of charge-transfer states in organic fluorophores that could be employed in TADF. The authors highlight the importance for the accurate prediction of singlet- and triplet-charge-transfer adiabatic energies for assessment of a molecules potential and employ a range of XCFs that incorporate different percentages of HF exchange, the most extreme examples being BLYP (0% HF) to M06-HF (100% HF). All the calculations point to a significant %HF dependency when describing CT character.

## 6.8 Fluorescence and quenching

Qian et al.<sup>259</sup> used TD-DFT to gain insight into the suppression of Kasha's rule found in the fluorescent behavior of 8 derivatives of the BODIHY chromophore. The PBE functional was chosen, and its suitability was determined by comparison of calculated low energy bands against experimental absorption spectra, finding the predicted absorption maxima are within approximately 5 nm of the experimental values, and the predicted intensities are within approximately 10%. The PBE functional also correctly predicts the observed blue-shift in absorption upon addition of ortho-methyl groups and the observed red-shift upon addition of para-electron withdrawing groups. TD-DFT calculations also find that the  $S_1$  state is not the first observable transition in the experimental spectra, instead the absorption maxima correspond to the  $S_0$  to  $S_2$  transition. It is also found that for the highly fluorescent molecules, the  $S_2$  state is significantly higher in energy than the  $S_1$  state, and the less fluorescent molecules have a smaller  $S_1/S_2$  energy gap. The difference in the energy gaps is inversely correlated to the efficiency of the  $S_2/S_1$  internal conversion, the smaller the gap, the greater the extent of internal conversion. As the  $S_1$  state is dark, this increase in population will result in less fluorescence, as observed.

Escudero<sup>260</sup> reviewed the oft-quoted mechanism for fluorescence quenching in donor-acceptor molecules, photoinduced electron transfer (PET). Escudero argues that PET is overused as a mechanism for fluorescence quenching in fluorescent sensors/switches and employs TD-DFT and multireference calculations to provide evidence for this. Instead of PET, Escudero finds that enhancement of "dark" excited states, e.g.  $n\pi^*$  states, are the most likely explanation, as they provide nonradiative pathways not previously accessible in the "ON" state of the sensor/switch. TD-PBE0 was found to be capable of reproducing adiabatic PES of the lowest-lying excited states and finds that multireference (CASPT2//CASSCF) calculations are required for proper treatment of any higher states that may be relevant.

Shepard et al.<sup>261</sup> used increasing halogen substitution to form high-spin iron(II)-polypyridines complexes, in order to extend the excited-state lifetime of the metal-to-ligand charge-transfer (MLCT) excited states. The study employs the APFD hybrid density functional, and the TD-DFT calculations show that the low-lying states remain predominantly metal-to-ligand, i.e. metal d-orbitals to ligand  $\pi^*$ -orbitals, in nature. It is also found that the increased number of chlorine atoms does indeed increase the MLCT lifetime, however, this evidence is obtained experimentally rather than from the TD-DFT calculations.

Nobusue et al.<sup>262</sup> report the synthesis and physical properties of tetracyclopenta[def,jkl,pqr,vwx]tetraphenylene (TCPTP), which is found to potentially exhibit tetraradicaloid nature. Here, a combination of CASSCF and TD-DFT, using either BHLYP or LC-BLYP, were used to study the structure and occupation of the LUMO and LUMO+1 of the species. Imposing  $D_{2h}$  symmetry on the structures results in the lowest energy geometry with a relatively small diradical nature, whereas  $D_{4h}$  symmetry resulted in a higher energy structure with a LUMO and LUMO+1 population (1.000 and 0.166, respectively) indicative of tetraradicaloid character. TD-B3LYP was also employed, showing that it was possible to decrease the energy of the HOMO-LUMO transition of TCPTP by substituting extended conjugation onto the ring. Hu et al.<sup>263</sup> studied the tetraradicaloid nature of p-quinodimethane (p-QDM) units fused to either a naphthalene or a benzene ring. DFT and TD-DFT calculations were used to study the UV-vis absorption of the molecules as well as study the orbital occupancies that would suggest polyradicaloid character of the species; in this case, the tetraradicaloid character of the molecules was found to be very small. However, different fusion modes of the p-QDM to the benzene/naphthalene moieties had a pronounced effect on diradical characteristics.

Lou et al.<sup>264</sup> note the advantages of using TD-DFT when exploring the photochemistry of redox-responsive fluorescent probes for use in biological systems. In particular, these complicated systems can give rise to experimental data that can be difficult to rationalize; however, such experimental results can be used in conjunction with TD-DFT calculations to determine the photophysical processes taking place, and therefore can well describe the biological system of interest. As well as this, the biological probes are generally very large, and can incorporate heavy metals, for example, selenium, and can therefore only feasibly be tackled with TD-DFT.

Daday et al.<sup>265</sup> used a range of excited state methods, namely, TD-DFT (CAM-B3LYP, LC-BLYP), CASPT2, NEVPT2, and QMC, with lower level theories, i.e. static point charges (QM/MM), DFT embedding (QM/DFT), and classical polarizable embedding through induced dipoles (QM/MMpol), in order to determine which combinations of theory were able to fully capture the complex photophysical behavior of the green fluorescent protein (GFP), which is known to be dependent on its environment. The authors study the GFP in both its neutral and anionic form, finding better agreement for the anionic form of the GFP compared to the neutral species, which is found to exhibit greater sensitivity to the structure of the environment. This sensitivity is demonstrated by the spread of

excitation energies found for several different “frames” in the MD simulations. It is also found that the QM/MM approach to the environment results in a systematic blue-shift in excitation energies, and the QM/DFT approach is also unable to provide results in good agreement with experiment. The QM/MMpol approach, specifically the linear-response (polLR) approach, results in a chromophore-protein resonance that leads to a red-shift in excitation energy and subsequently more accurate excitation energies. The TD-DFT energies were found to be blue-shifted relative to that of CASPT2, although both sets of energies followed a similar trend with respect to the lower-level approach to environment.

Wu *et al.*<sup>266</sup> study the effect of aggregation on the absorption/emission characteristics of three highly conjugated systems; 9,10-distyrylanthracene (DSA), 2,3-dicyano-5,6-diphenylpyrazine (DCDPP), and *cis,cis*-1,2,3,4-tetraphenyl-1,3-butadiene (TPBD). Generally, it is found that upon aggregation optical emission spectra will be red-shifted relative to the solvent-phase species; however, the emission spectra of the three molecules investigated in this study are found to undergo a blue-shift upon aggregation. The authors employ a PCM model for solvent calculations and a QM/MM approach in order to model the aggregate systems, using the PBE0-D3 functional. The calculations find that the absorption behavior of the molecules in both phases is largely the same; only the emission is affected. This is found to arise from the fact that the molecules are unable to fully relax in the aggregate phase compared to the solution phase, resulting in a smaller Stokes' shift and blue-shifted emission.

Adamska *et al.*<sup>265</sup> study a set of intriguing cycloparaphenylenes (CPP), highly conjugated ring systems that exhibit a ring-size independency with respect to absorbance maxima, and exhibit a ring-size dependency with respect to extinction coefficient. Fluorescence of these molecules is also found to be ring-size dependent, with a strong red-shift with respect to ring-size. CAM-B3LYP was used in order to study the absorbance of 8 different sized CPP hoops, finding across all of the molecules studied that the lowest energy transition results in a nodeless  $S_1$  state that is delocalized across the entire structure which, due to the circular nature of the systems, results in no net transition dipole. The  $S_2$  and  $S_3$  states are found to be degenerate in even-numbered ring systems and quasi-degenerate in odd-numbered ring systems; both states have nodes and therefore exhibit significant transition dipole moments and therefore high spectroscopic absorbance. The increasing absorbance with respect to ring size is attributed to the increase in conjugation found in such systems. The ring-size independency with respect to

absorbance maxima is found to arise from the near-exact cancellation of two competing effects. Increasing the ring size would result in a red-shift arising from increased conjugation as well as a decrease in the splitting between the  $S_1$  and  $S_2/S_3$  states; however, increasing the ring size would also serve to blue-shift the absorbance due to a decrease in favorable through-space  $\pi$ -interactions (pseudo  $\pi$ -stacking) between neighbouring phenyl groups. The authors also employ non-adiabatic dynamics simulations in order to study the behavior of the molecules upon excitation, using PES generated on-the-fly by TD-DFT. These calculations demonstrate that the fluorescence observed for the larger CPP systems is due to strong vibronic coupling that results in a spatial localization of an exciton.

## 6.9 Other properties

Johnson et al.<sup>267</sup> tackle the ability of DFT methods to accurately compute both first-order hyperpolarizabilities ( $\beta$ ) and absorption values, as large  $\beta$  values give rise to efficient, high-bandwidth electro-optical devices and therefore accurate modelling of these systems will allow for their optimization. The authors focus on hybrid DFT functionals, i.e. those that incorporate some amount of HF exchange, finding that those with <50% HF exchange were unable to accurately reproduce  $\beta$  values, whereas those with >50% HF exchange provided better estimates of  $\beta$  with, however, significantly blue-shifted absorbance energies. The authors suggest MP2 for  $\beta$  calculations, and find that CAM-B3LYP and M06-2X were the most successful of the functionals tested in terms of accuracy.

Pescitelli and Bruhn<sup>268</sup> give a review on good practice toward the computation of electronic circular dichroism spectra in molecules, and is also reviewed by Longhi et al.<sup>269</sup> Ferrer et al.<sup>270</sup> discuss the approach to first-principle simulation of vibrationally resolved absorption and emission spectra that include temperature and solvent effects.

Rozzi et al.<sup>271</sup> combined femtosecond spectroscopy and TD-DFT to study the dynamics of a carotene-porphyrin-fullerene triad, in order to examine quantum coherence effects that could be exploited in artificial photosynthesis. The Perdew-Zunger functional<sup>272</sup> (PZ81) was employed which uses the local density approximation (LDA), and should be suitable given the lack of charge-transfer character exhibited by the excited states of interest. The study finds that PZ81 was able to reproduce the Soret band and to some extent the Q-band of the porphyrin, once the calculated spectrum was red-shifted by 180 meV. The semi-classical dynamic simulations, where



the nuclei are modelled as classical particles, find that almost complete charge-flow from the porphyrin to the fullerene takes place in approximately 70 fs, in good agreement with the experimentally observed timescale. In other studies, Santhanamoorthi et al.<sup>273</sup> and Karthikeyan et al.<sup>274</sup> used B3LYP with the 6-31G(d) basis set in order to investigate the effects of different sensitizers on the absorption behavior of porphyrin-based dyes.

Guido et al.<sup>275</sup> benchmarked the performance of the B3LYP, CAM-B3LYP, and PBE0 functionals in determining relaxed gas- and solvent-phase excited state geometries, compared to RI-CC2. The chromophores chosen in the test set exhibit both  $n\pi^*$  and  $\pi\pi^*$  transitions, and PCM-acetonitrile solvation is used. Adiabatic energies are not considered. The B3LYP and PBE0 functionals are found to perform best for vertical excitation energy and ground-state structure; however, CAM-B3LYP is found to perform best for excited state geometries.

Sousa et al.<sup>276</sup> coupled TD-DFT and CASSCF/CASPT2 to study the ultrafast deactivation mechanism of  $[\text{Fe}(2,2\text{-bipyridine})_3]^{2+}$ . The TD-DFT calculations with the PBE0 functional were used to calculate the geometries and frequencies of the ground and excited states of the different spin states of the complex, and CASPT2 calculations were used for the ultimate energy comparisons and SOC computations. This combined approach suggests a 5-step deactivation process that involves singlet  $\rightarrow$  triplet intersystem crossing, triplet  $\rightarrow$  triplet internal conversion, with a final triplet  $\rightarrow$  quintuplet intersystem crossing.

Cerezo et al.<sup>277</sup> studied the issue of coordinate choice when modelling vibrationally resolved absorption spectra. The excited state PES were constructed using the adiabatic (AH) and vertical Hessian (VH) models, with internal coordinates and Cartesian coordinates used with AH. The study finds that, when the  $S_0 \rightarrow S_1$  transition results in significant geometric displacement, Cartesian coordinates perform poorly for absorption spectra due to being unable to cope with curvilinear displacements; using internal coordinates alleviates this issue. The VH approach is found to generally give good agreement between experimental and computed spectra independent of the extent of relaxation in the excited state.

Long et al.<sup>278</sup> designed a coumarin-based fluorescent probe capable of detecting biological thiols. The initial compound is found to exhibit almost no fluorescence in solution, and upon reaction with a thiol fluorescence is switched on. B3LYP is used to determine the extent of the CT for the different forms of the probe, finding that CT, and therefore fluorescence, is inhibited in the non-thiol-reacted form. However, as B3LYP fails with CT states it's unclear to what extent this is true.

Baiardi et al.<sup>279</sup> present the implementation of a time-independent model that can include Franck-Condon, Herzberg-Teller, and Duchinsky effects<sup>280</sup> in the simulation of vibrationally resolved absorption spectra. The authors note the importance of simulating electronic transitions when attempting to assign experimental spectra, but also highlight how, generally, the simulation of spectra is limited to the simple fitting of a symmetric Gaussian function to the absorption maximum. This in turn limits the amount of information that can be extracted from the calculations and can prevent them from truly complementing experimental results. The authors therefore developed this vibronic model in order to enhance excited state calculations. The BLYP functional was employed against a test set of molecules that included anthracene, furan, phenyl radical, *R,R*-dimethyloxirane, and coumarin 339. The resulting spectra exhibit significant vibrational fine structure in good agreement with experimentally obtained photoionization and absorption spectra.

Mitri et al.<sup>281</sup> employed a QM/MD approach to simulating the absorption and emission spectrum of 4-naphthoxyloxy-1-methoxy-2,2,6,6-tetramethyl-piperidine (NfO-TEMPO-Me) in toluene; the MD calculations were run for 3 ns, frames of which were used to build an average UV-vis spectrum as calculated with CAM-B3LYP and PBE0. The MD approach was employed due to the flexibility of the NfO-TEMPO system, which can occupy a range of spectroscopically relevant equilibrium structures at the temperature of 300 K. The calculations find good agreement with experimental data, when comparing vertical excitation energies, Stoke's shift, and solvatochromic shifts.

Li et al. have applied TD-DFT to open-shell systems<sup>282-285</sup> and to the effect of solvent on the excited states of triphenylamine-thiadiazole (TPA-NZP).<sup>286</sup> In particular, for the open-shell systems, which often suffer from spin-contamination issues, the spin-adapted (X-) TD-DFT method was found to cope well and offer an increase in accuracy for doublet-doublet and doublet-quartet transitions. In the case of TPA-NZP, the  $S_0$  geometries were found to be solvent independent, and the  $S_1$  geometry was found to be solvent dependent. The study also finds that increasing the solvent polarity increases the amount of CT in the  $S_1$  state. However, as the excited states were computed with B3LYP, it is unclear to what extent the CT really dominates.

## 6.10 Assessment

TD-DFT methods are certainly the most widely used in photochemical studies as they offer the best compromise between accuracy and

**Table 3** TD-DFT summary.

Property	Trends	Quantitative
Nonlinear optical properties	TD-HF	TD-HF <sup>a</sup>
Absorption spectra	Yes <sup>b</sup>	Yes <sup>b</sup>
Fluorescence spectra	Yes <sup>b</sup>	Yes <sup>b</sup>
Photochemical mechanisms	Sometimes <sup>b</sup>	No
Quantitative photochemical Kinetics	No	No

<sup>a</sup>Depends on the system and whether it is a first, second, third order hyperpolarizability, with higher order polarizabilities modelled better than lower order ones.

<sup>b</sup>Depends on system and choice of functional. In particular, states involving charge transfer character need to be treated with a long-range corrected functional, relaxed densities are needed for emission spectra and modern functional with improved correlation/dispersion treatment tend to perform better.

computational cost. They are also much simpler to use than the more accurate multireference methods, which in turn require careful selection of active space orbitals. The main applications of TD-DFT are in the prediction of absorption and emission spectra, and their accuracy depends upon the system and choice of functional (Table 3). As a general rule, systems involving significant charge-transfer character require long-range corrected functionals, but even these are not always sufficiently accurate. Owing to its low cost, TD-DFT is also frequently used to study photochemical reaction mechanisms such as excited state intermolecular proton transfer, photo-initiation, and photoisomerization. Often it is able to qualitatively explain experimental results, but does have failures and is rarely used for quantitative studies. However, new developments such as Truhlar's Dual-Functional Tamm-Dancoff Approximation<sup>153</sup> show enormous promise in raising the accuracy of TD-DFT to that of equivalent multireference methods, but at a fraction of the cost. At the other extreme, Grimme's Simplified Tamm-Dancoff Approximation has recently been shown to reproduce standard TD-DFT at a fraction of the cost, allowing systems with 1000s of atoms to be studied.<sup>154</sup>



## 7. Solvent and environmental effects

### 7.1 Continuum versus explicit solvent

Solvent effects can have profound influences on the excited state behavior, which can be difficult to fully capture. Implicit solvent effects remain popular; however, they will fail, when explicit solvent-solute bonding is

taking place. For example, hydrogen bonding of water to a carbonyl oxygen will result in the blue-shift in the corresponding  $n\pi^*$  transition, due to stabilisation of the nonbonding oxygen electrons, and implicit solvent models will therefore be inherently inaccurate when considering such an effect.

Including explicit solvent molecules can add to the cost of already expensive calculations. To address this, Zhang et al.<sup>287</sup> have implemented a local excitation approximation (LEA) for CIS, TD-HF, and TD-DFT, in which an optically active region (containing the chromophore) is defined in a QM/MM, chromophore/solvent system. Using local excitation serves to truncate excited state calculations as most of the explicit solvent molecules are not considered. However, the method benefits relative to simply using the polarizable continuum models (PCM), as important solvent-chromophore interactions are still included. The LEA-TD-DFT implementation results in a speedup of 6–10 times for calculations, compared with a standard TD-DFT calculation for the same system. The LEA schemes for all three of the tested methods also show significant blue-shifting of the  $n\pi^*$  transition observed for aqueous acetone, compared with gas-phase acetone, suggesting the LEA scheme is correctly capturing explicit solvent-chromophore interactions. However, no comparison to experimental data is provided, so it is unclear if the LEA-TD approach is outperforming traditional PCM-TD approaches.

Milanese et al.<sup>288</sup> studied the convergence of excited state calculations with respect to increasing the number of explicit water molecules solvating four 1,4-diphenylbuta-1,3-diene derivatives in a full QM approach, from 0 to 400 water molecules, citing concerns with defining the QM/MM regions as to why such a system was not used. TD-DFT and CIS methods are compared with several basis sets (3-21G, 6-31G, 6-31G\*, 6-31+G\*), and the emphasis is on the TD-(LC-) $\omega$ PBE results. The addition of polarization functions, from 6-31G to 6-31G\*, was found to have an insignificant effect on the absorption spectra, however, increasing the size of the basis set, from 3-21G to 6-31G, then to the 6-31+G\* results in a concomitant decrease in the HOMO-LUMO transition energy. The biggest change in transition energy, for all basis sets with CIS and TD-DFT approaches, arises in approximately the 0–100 water molecule regime. The authors note that CIS convergence with respect to explicit solvation is faster than that of TD-DFT, and that increasing the size of the basis set also results in faster convergence. Clearly, however, there is a balance, between increasing the number of solvating molecules and increasing the basis set size, with respect to computational expense.

Like that of Zhang,<sup>287</sup> neither experimental nor PCM-TD absorption spectra are included for comparison, so convergence with respect to physical relevance/computational expense is not quantified. Such a comparison would also allow for better estimation of the required size of a QM region of solvated chromophore, and therefore whether a full QM, rather than a QM/MM, treatment is required.

The contrast between implicit and explicit solvation is illustrated in studies by Martínez-Fernández et al.<sup>289</sup> and Szabla et al.<sup>290</sup> of the absorption properties of methylated cytosine derivatives. Martínez-Fernández et al. used TD-CAM-B3LYP and CASPT2/MM to describe how the low-lying  $\pi\pi_1^*$ ,  $\pi\pi_2^*$ ,  $n_N\pi^*$ , and  $n_O\pi^*$  are vibronically coupled, and therefore population of the dark states is possible. These states are then able to decay to the ground state, and the excited state lifetimes are estimated using the CASPT2/MM approach. However, Szabla et al. argued that the approach by Martínez-Fernández et al. is insufficient to properly describe the experimentally observed behavior of the cytosine/cytidine derivatives, as the CASPT2/MM calculations do not include any explicit solvent molecules in the QM region, and the TD-DFT calculations utilize the nonexplicit PCM solvent model. In their study, Szabla et al. find that microsolvation of the N1-methylcytosine by two H<sub>2</sub>O molecules results in a dark, low-lying water-to-chromophore charge transfer state, denoted  $n_N\pi_{CT}^*$ , and significant destabilization of the  $n_O\pi^*$  state to approximately 3 eV above the CT state. Exploring the PES of the  $n_N\pi_{CT}^*$  state demonstrates the possibility for an electron-driven proton transfer (EDPT), along the coordinate of which there is a conical intersection between the S<sub>1</sub> and S<sub>0</sub> state, which forms a reactive hydroxyl anion that could further react to form uracil derivatives.

Li et al.<sup>291</sup> also studied the effect of explicit solvent molecules on the absorption spectrum of cytosine, using a QM/MM approach. The structure of the solute is determined using CASSCF, upon which CASPT2 vertical excitation energies are calculated. The approach is found to blue-shift the  $n\pi^*$  transitions, relative to values calculated with PCM, a result that is to be expected as the inclusion of explicit solvent-solute hydrogen-bonds stabilises the  $n$ -orbitals. There is also, however, significant deviation observed for some of the  $\pi\pi^*$  transitions; this is likely due to the CASSCF calculated geometries not being accurate enough. Spata and Matsika<sup>292</sup> studied a conical intersection in a 9-methyladenine homodimer, finding that, upon excitation to a low-lying  $\pi\pi^*$  state significant charge-transfer takes place between the two adenine species. Radiationless decay can also take place between the S<sub>0</sub> and S<sub>1</sub> states, and higher energy excitations result in the population of the dissociative part of the S<sub>0</sub> PES.

Fang and Kim<sup>293</sup> used (MRPT2-)CASSCF to study the excited state tautomerization of 7-azaindole complexed with a methanol molecule; the tautomerization involves transfer of a hydrogen atom to the methanol molecule, before a subsequent H-transfer from the methanol to a neighboring nitrogen atom. The rates of transfer were calculated with variational transition state theory, and it is also found that the integral equation formalism PCM (IEFPCM) solvent model was not capable of reproducing the correct energetics of the reaction.

Zuehlsdorff et al.<sup>294,295</sup> have studied the effect of including explicit solvent molecules on the simulated absorption properties of Nile Red and alizarin. The study of alizarin used a QM/MM model (TD-PBE and TD-CAM-B3LYP for the QM region) and found a relatively slow convergence of absorption accuracy vs number of explicit solvent molecules, with up to 380 water molecules being required for accurate results. The slow convergence was attributed to charge transfer to solvent molecules in the immediate vicinity of the alizarin molecule, and long-range electrostatic effects of the water molecules. The study of Nile Red found that the failure of implicit solvent models to describe  $\pi$ -stacking and H-bonding interactions led to significant deviations in calculated absorption peaks. The study also found that the PBE functional systematically underestimated excitation energies, and that CAM-B3LYP could be used to improve the results.

Chang et al.<sup>296</sup> studied the photoprotection mechanism of p-methoxy methylcinnamate, which was found to display increased radiationless decay to the  $S_0$  state upon addition of water. CASPT2-corrected CASSCF calculations demonstrate that initial excitation is to a  $^1\pi\pi^*$ , which can undergo either internal conversion to a  $^1n\pi$  state, or deactivation to the  $S_0$  state via a conical intersection along the photoisomerization pathway. The  $H_2O$  explicit solvent molecule is found to stabilize the  $\pi\pi^*$  state and destabilise the  $n\pi^*$  state, compared with the unsolvated species, resulting in an increase in favorability for the photoisomerization deactivation pathway to take place.

Charlton et al.<sup>297</sup> used several flavors of the PBE functional including the LC- $\omega$ PBE functional, the optimally tuned (OT-) LC- $\omega$ PBE, and the PBE functional itself, to study the effect of including explicit, near-neighbour, nitrogen-doped pentacene molecules around a single pentacene molecule. The use of the long-range corrected functionals was to negate some of the error associated with charge-transfer excited states, which were being modeled. The study found that the explicit inclusion of the surrounding molecules resulted in a red-shift in the  $S_1$  state, compared to values calculated with a PCM solvent model.

Marazzi et al.<sup>298</sup> used TD-DFT and CASPT2 to calculate the electronic properties of Nile red and Nile blue chromophores. The authors also employed two types of geometry upon which vertical excitation energies were calculated; that is, QM optimized  $S_0$  equilibrium structures, and dynamic, explicitly solvated structures as calculated with MD. The dynamic structures were found to give red-shifted energies compared with the static structures and are in closer agreement with experimental data.

Mewes et al.<sup>299</sup> reported the implementation and performance of a correction scheme for vertical excitation energies calculated with ADC(n) and TD-DFT (LRC- $\omega$ PBE) in a PCM solvent environment, using a test set of molecules mainly made up of nitroaromatic compounds. The correction is possible with both linear-response (LR-PCM) and state-specific (SS-PCM) PCM schemes. At best, the study finds that the correction scheme is able to reproduce experimental solvent shifts, when the shifts arise from bulk electrostatic interactions, with maximum absolute errors and mean absolute deviations of 50 meV and 20–30 meV, respectively. The authors also find that the success of LR-PCM vs SS-PCM is dependent on the extent of orbital relaxation included in the excited-state calculation; methods that do not include orbital relaxation, i.e., TD-DFT/ADC(1), performed best with LR-PCM (essentially unrelaxed PCM), whereas higher-order ADC(n) calculations performed best with SS-PCM.

Isborn et al.<sup>300</sup> studied the issues when using TD-DFT with chromophores explicitly solvated by water molecules to explore QM/MM calculations that often result in the spurious, low-energy solvent  $\rightarrow$  chromophore (or vice versa) charge-transfer states. These charge-transfer artefact states are found to arise from so-called “edge” water molecules, molecules that are hydrogen-bond unsaturated and therefore have high-lying HOMOs. The effects of the edge waters are exacerbated by small basis sets, unoptimized geometries, and when using functionals that do not contain any exact HF exchange. However, the LC- $\omega$ PBEh functional, which is both long-range corrected and incorporates 20% HF exchange, is found to reduce the impact of the edge water molecules and gives low-energy excitations corresponding to the optically relevant chromophore valence states.

## 7.2 Equilibrium versus nonequilibrium solvation

Molecules in their excited states are dynamic systems, exhibiting different phenomena that take place over a range of timescales,<sup>301</sup> and different components of the model system exhibit different response timescales to each other.

This gives rise to “nonequilibrium” solvation effects, in which the redistribution of electron density upon photon absorption is assumed to be faster than solvent nuclei redistribution. Vertical excitation energies, i.e., the instantaneous redistributions of electron density, are therefore calculated using nonequilibrium solvation, whereas relaxed properties, for example, excited state geometry optimizations, are calculated using equilibrium solvation. In calculations including explicit solvent effects, nonequilibrium vertical excitation energies are achieved simply by taking single-point energies. In continuum solvent models this is generally achieved by separating the solvent response into a dynamic component, which is relaxed alongside the new solute electron density, and an inertial component, which is kept frozen in equilibrium with the initial state of the molecule.<sup>302</sup>

Li<sup>303</sup> provides a comprehensive overview of continuum models for nonequilibrium solvation. Generally, however, studies explicitly dealing with nonequilibrium versus equilibrium solvation effects do so with respect to comparing state-specific and linear-response formalisms for excited state calculations.<sup>302,304–306</sup>

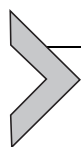
### 7.3 Other environmental effects

Chromophores involving lone pairs (e.g., on oxygen or nitrogen) undergo  $n\pi^*$  transitions. These can be disrupted by protonating the lone pair through pH changes. Likewise, if conjugated with a  $\pi$  system, the stability of the  $\pi$  and  $\pi^*$  orbitals can also change dramatically the protonation state of acidic or basic functional groups. These pH effects can be studied conveniently *in silico* by considering the charged and neutral forms. This approach can be used in conjunction with experimental spectroscopic data to help ascertain the protonation state of a species, particularly in environments (such as enzymes) where direct titration is difficult.<sup>8</sup> In a similar vein, complexation with Lewis acids has been shown to dramatically alter the photochemical behavior of photoinitiators, blue shifting the  $n\pi^*$  excitations of type I photoinitiators, methyl-4'-(methylthio)-2-morpholinopropiophenone (MMMP) and 2,2-dimethoxy-2-phenylacetophenone (DMPA), while concurrently red shifting the  $\pi\pi^*$  transitions.<sup>10</sup>

Even when direct conjugation is not possible, the electrostatic effect of charged functional groups can also influence the relative energies of excited states due to their different polarities. Recently Hill and Coote showed used TD-DFT that by including these charged functional groups as nonconjugated substituents, simple pH changes can be used to



selectively modify the relative energies (and even ordering) of the  $n\pi^*$  and  $\pi\pi^*$  states of an acetophenone derivative.<sup>307</sup> This proof-of-concept study suggests significant opportunities to selectively tune photochemical reactivity.



## 8. Conclusion

While photochemical processes are challenging to model using computational methods, much progress has been made in this field over recent years. Expensive multireference calculations remain the gold standard for studying photochemical reactions, particularly on nonadiabatic surfaces (Fig. 4). However, improvements to TD-DFT, such as long range corrections, dispersion corrections and, most recently, the Dual-Functional Tamm-Dancoff Approximation,<sup>153</sup> has meant that they are starting to rival multireference in accuracy even for excited state potential energy surfaces. More generally, TD-DFT has become routine for the prediction of absorption and emission spectra, and in most cases provides qualitatively if not quantitatively useful results. For large systems, the wavefunction based TD-HF and CIS methods have traditionally been the only option, providing useful predictions of nonlinear optical properties but generally failing for other photochemical phenomena. However, the use of methods based on localized orbitals (for correlated wavefunctions), and the Simplified Tamm-Dancoff Approximation<sup>154</sup> and TD-DFT<sup>155</sup> has made it possible to apply more accurate methods to increasingly larger systems. At the same time the use of QM/MM methods have also made it possible to provide increasingly accurate treatments of solvent effects on photochemical processes without the prohibitive cost of including explicit solvent molecules in the excited state QM treatment.

The value of these methodological improvements is evident in the wide range of applications highlighted herein. Theory has proven extremely useful in clarifying photochemical reaction mechanisms and, for example, showing that targeting dark states sometimes provides more efficient reactivity. Theoretical studies have helped to provide an insight into structure-reactivity trends in a range of photochemical phenomena, in turn providing guidelines for optimizing nonlinear optical properties, dye-sensitized solar cells, redox-responsive fluorescent probes and visible light photoinitiators, among other applications. Moreover, the recent demonstration of electrostatic tuning of photochemical reactivity may open up yet further avenues for computational design in this field.

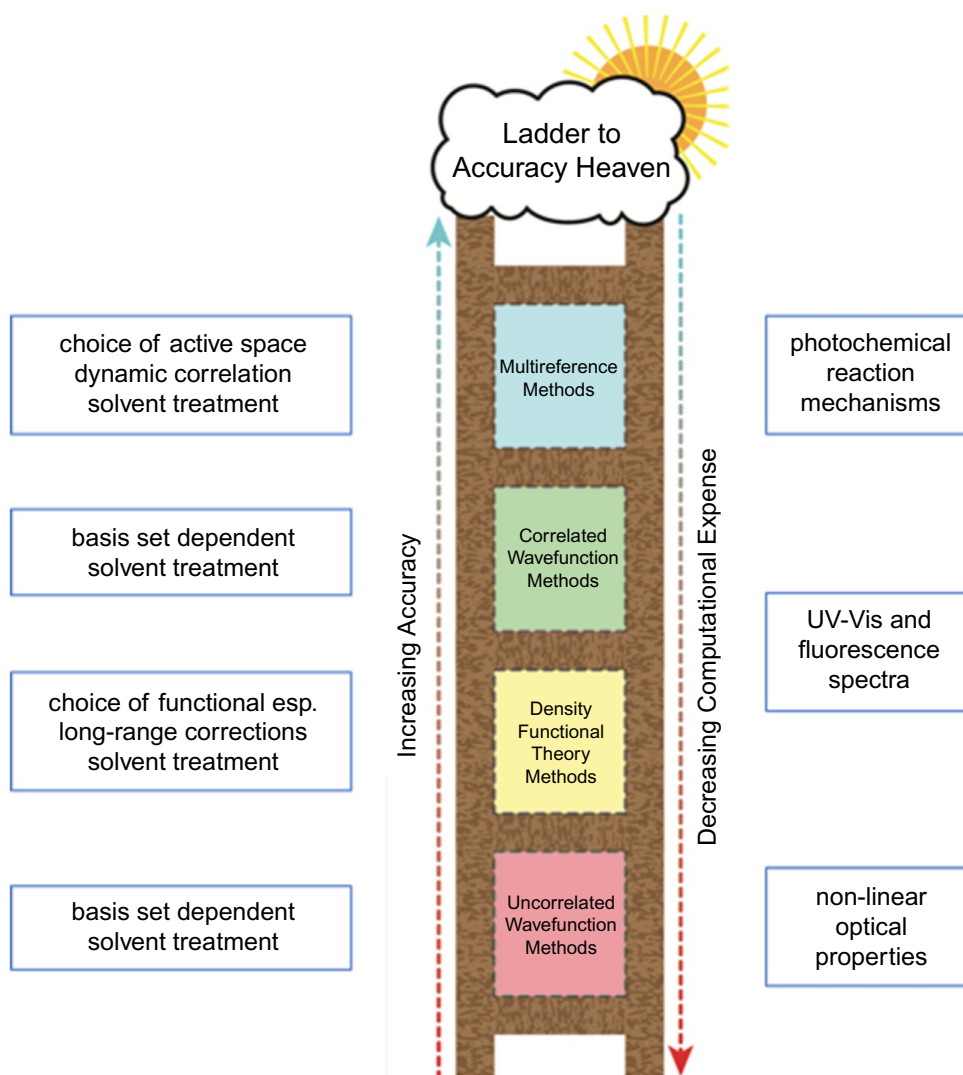


Fig. 4 Guidelines for selecting theoretical methods.

## Conflicts of interest

There are no conflicts to declare.

## Acknowledgments

The authors acknowledge financial support from the Australian Research Council (ARC: CE140100012, FL170100041) Centre of Excellence for Electromaterials Science, and an ARC Laureate Fellowship (to M.L.C.).

## References

1. Raghavachari, K.; Anderson, J. B. Electron Correlation Effects in Molecules. *J. Phys. Chem.* **1996**, *100*(31), 12960–12973.
2. Santoro, F.; Jacquemin, D. Going Beyond the Vertical Approximation With Time-Dependent Density Functional Theory. *Wiley Interdiscip. Rev. Comput. Mol. Sci.* **2016**, *6*(5), 460–486.

3. Improta, R.; Santoro, F.; Blancafort, L. Quantum Mechanical Studies on the Photo-physics and the Photochemistry of Nucleic Acids and Nucleobases. *Chem. Rev.* **2016**, *116*(6), 3540–3593.
4. Laurent, A. D.; Jacquemin, D. TD-DFT Benchmarks: A Review. *Int. J. Quantum Chem.* **2013**, *113*(17), 2019–2039.
5. Garavelli, M. Computational Organic Photochemistry: Strategy, Achievements and Perspectives. *Theor. Chem. Acc.* **2006**, *116*(1–3), 87–105.
6. Serrano-Andrés, L.; Merchán, M. Quantum Chemistry of the Excited State: 2005 Overview. *J. Mol. Struct. Theochem* **2005**, *729*, 99–108.
7. Menzel, J. P.; Noble, B. B.; Lauer, A.; Coote, M. L.; Blinco, J. P.; Barner-Kowollik, C. Wavelength Dependence of Light-Induced Cycloadditions. *J. Am. Chem. Soc.* **2017**, *139*(44), 15812–15820.
8. Mohamed, A. E.; Ahmed, F. H.; Arulmozhiraja, S.; Lin, C. Y.; Taylor, M. C.; Krausz, E. R.; Jackson, C. J.; Coote, M. L. Protonation State of F420H2 in the Prodrug-Activating Deazaflavin Dependent Nitroreductase (Ddn) From Mycobacterium Tuberculosis. *Mol. Biosyst.* **2016**, *12*(4), 1110–1113.
9. Li, H. P.; Bi, Z. T.; Xu, R. F.; Han, K.; Li, M. X.; Shen, X. P.; Wu, Y. X. Theoretical Study on Electronic Polarizability and Second Hyperpolarizability of Hexagonal Graphene Quantum Dots: Effects of Size, Substituent, and Frequency. *Carbon N. Y.* **2017**, *122*, 756–760.
10. Noble, B. B.; Mater, A. C.; Smith, L. M.; Coote, M. L. The Effects of Lewis Acid Complexation on Type I Radical Photoinitiators and Implications for Pulsed Laser Polymerization. *Polym. Chem.* **2016**, *7*, 6400.
11. Zhang, J.; Lalevée, J.; Hill, N. S.; Launay, K.; Morlet-Savary, F.; Graff, B.; Stenzel, M. H.; Coote, M. L.; Xiao, P. Disubstituted Aminoanthraquinone-Based Multicolor Photoinitiators: Photoinitiation Mechanism and Ability of Cationic Polymerization under Blue, Green, Yellow, and Red LEDs. *Macromolecules* **2018**, *51*, 8165–8173.
12. Blancafort, L. Photochemistry and Photophysics at Extended Seams of Conical Intersection. *ChemPhysChem* **2014**, *15*(15), 3166–3181.
13. Polo, V.; Kraka, E.; Cremer, D. Electron Correlation and the Self-Interaction Error of Density Functional Theory. *Mol. Phys.* **2002**, *100*(11), 1771–1790.
14. Karakas, A.; Karakaya, M.; Taser, M.; Ceylan, Y.; Gozutok, A.; Arof, A. K.; El Kouari, Y.; Sahraoui, B. Computational Studies on Linear, Second and Third-Order Nonlinear Optical Properties of Novel Styrylquinolinium Dyes. *Chem. Phys. Lett.* **2016**, *648*, 47–52.
15. Zawadzka, A.; Karakas, A.; Płóciennik, P.; Szatkowski, J.; Łukasiak, Z.; Kapceoglu, A.; Ceylan, Y.; Sahraoui, B. Optical and Structural Characterization of Thin Films Containing Metallophthalocyanine Chlorides. *Dye. Pigment.* **2015**, *112*, 116–126.
16. Karakas, A.; Dag, T.; El Ouazzani, H.; Sebiaai, K.; Boughaleb, Y. Two-Photon Absorption and Third-Order Nonlinear Optical Characterization of Pyrrolo-Tetrathiafulvalene Derivatives. *Opt. Quantum Electron.* **2014**, *46*(1), 165–170.
17. Guezguez, I.; Karakas, A.; Iliopoulos, K.; Derkowska-Zielinska, B.; El-Ghayoury, A.; Ranganathan, A.; Batail, P.; Migalska-Zalas, A.; Sahraoui, B.; Karakaya, M. Theoretical and Experimental Investigations on the Nonlinear Optical Properties of Gold(III) Dithiolene Complexes. *Opt. Mater. (Amst).* **2014**, *36*(1), 106–111.
18. Wu, J.; Wilson, B. A.; Smith, D. W., Jr.; Nielsen, S. O. Towards an Understanding of Structure-Nonlinearity Relationships in Triarylamine-Based Push-Pull Electro-Optic Chromophores: The Influence of Substituent and Molecular Conformation on Molecular Hyperpolarizabilities. *J. Mater. Chem. C* **2014**, *2*(14), 2591.
19. Alparone, A. Nonlinear Optical Properties of Fluorobenzenes: A Time-Dependent Hartree-Fock Study. *Comput. Theor. Chem.* **2013**, *1013*, 23–24.

20. Bondu, F.; Quertinmont, J.; Rodriguez, V.; Pozzo, J.-L.; Plaquet, A.; Champagne, B.; Castet, F. Second-Order Nonlinear Optical Properties of a Dithienylethene-Indolinoxazolidine Hybrid: A Joint Experimental and Theoretical Investigation. *Chem. A Eur. J.* **2015**, *21*(51), 18749–18757.
21. Brückner, C.; Walter, C.; Stolte, M.; Bräida, B.; Meerholz, K.; Würthner, F.; Engels, B. Structure-Property Relationships for Exciton and Charge Reorganization Energies of Dipolar Organic Semiconductors: A Combined Valence Bond Self-Consistent Field and Time-Dependent Hartree-Fock and DFT Study of Merocyanine Dyes. *J. Phys. Chem. C* **2015**, *119*(31), 17602–17611.
22. Hidalgo Cardenuto, M.; Champagne, B. QM/MM Investigation of the Concentration Effects on the Second-Order Nonlinear Optical Responses of Solutions. *J. Chem. Phys.* **2014**, *141*(23), 234104.
23. Tamer, Ö.; Gözüaçık, F.; Avci, D.; Atalay, Y. Theoretical Analysis on Structural, Spectroscopic, and Electronic Properties of Some 2-Aminobenzimidazole Complexes by Using PBE1PBE, B3LYP, and HF Methods. *Opt. Spectrosc.* **2014**, *116*(1), 12–32.
24. Maidur, S. R.; Patil, P. S.; Rao, S. V.; Shkir, M.; Dharmaprasanth, S. M. Experimental and Computational Studies on Second- and Third-Order Nonlinear Optical Properties of a Novel D- $\pi$ -A Type Chalcone Derivative: 3-(4-Methoxyphenyl)-1-(4-Nitrophenyl) Prop-2-En-1-One. *Opt. Laser Technol.* **2017**, *97*, 219–228.
25. Lötstedt, E.; Kato, T.; Yamanouchi, K. Intramolecular Electron Dynamics in the Ionization of Acetylene by an Intense Laser Pulse. *J. Chem. Phys.* **2013**, *138*(10), 104304.
26. Hu, S.-L.; Zhao, Z.-X.; Chen, J.; Shi, T.-Y. Ionization Dynamics of C<sub>2</sub>H<sub>2</sub> in Intense Laser Fields: Time-Dependent Hartree-Fock Approach. *Phys. Rev. A* **2015**, *92*(5) 053409.
27. Luzanov, A. V. Nonstationarity and Related Measures for Time-Dependent Hartree-Fock and Multiconfigurational Models. *Int. J. Quantum Chem.* **2013**, *113*(23), 2489–2505.
28. Nguyen, T. S.; Parkhill, J. Nonadiabatic Dynamics for Electrons at Second-Order: Real-Time TDDFT and OSKF2. *J. Chem. Theory Comput.* **2015**, *11*(7), 2918–2924.
29. Sato, T.; Ishikawa, K. L. The Structure of Approximate Two Electron Wavefunctions in Intense Laser Driven Ionization Dynamics. *J. Phys. B At. Mol. Opt. Phys.* **2014**, *47*(20), 204031.
30. Tanak, H.; Toy, M. Molecular Structure and Vibrational Assignment of 1-[N-(2-Pyridyl) Aminomethylidene]-2(1H)-Naphthalenone by Density Functional Theory (DFT) and Ab Initio Hartree-Fock (HF) Calculations. *Spectrochim. Acta A Mol. Biomol. Spectrosc.* **2016**, *152*, 525–529.
31. Dreuw, A.; Head-Gordon, M. Single-Reference Ab Initio Methods for the Calculation of Excited States of Large Molecules. *Chem. Rev.* **2005**, *105*(11), 4009–4037.
32. Subotnik, J. E. Communication: Configuration Interaction Singles Has a Large Systematic Bias against Charge-Transfer States. *J. Chem. Phys.* **2011**, *135*(7), 071104.
33. Cheng, C. Y.; Ryley, M. S.; Peach, M. J. G.; Tozer, D. J.; Helgaker, T.; Teale, A. M. Molecular Properties in the Tamm-Dancoff Approximation: Indirect Nuclear Spin-Spin Coupling Constants. *Mol. Phys.* **2015**, *113*(13–14), 1937–1951.
34. Nithya, R.; Sowmiya, M.; Kollandaivel, P.; Senthilkumar, K. Structural, Optical, and Charge Transport Properties of Cyclopentadithiophene Derivatives: A Theoretical Study. *Struct. Chem.* **2014**, *25*(3), 715–731.
35. Cebrián, C.; De Mata Muñoz, J.; Strassert, C. A.; Prieto, P.; Díaz-Ortiz, Á.; De Cola, L.; De La Hoz, A. Synthesis of Bright Alkenyl-1H-1,2,4-Triazoles: A Theoretical and Photophysical Study. *Chempluschem* **2014**, *79*(10), 1489–1497.
36. Tathe, A. B.; Gupta, V. D.; Shreykar, M. R.; Ramasami, P.; Sekar, N. Excited State Intramolecular Proton Transfer of 2-(2',6'-Dihydroxyphenyl)Benzoxazole: Insights Using Computational Methods. *J. Lumin.* **2014**, *154*, 267–273.

37. Laurent, A. D.; Blondel, A.; Jacquemin, D. Choosing an Atomic Basis Set for TD-DFT, SOPPA, ADC(2), CIS(D), CC2 and EOM-CCSD Calculations of Low-Lying Excited States of Organic Dyes. *Theor. Chem. Acc.* **2015**, *134*(6), 1–11.
38. Aziz, S. G.; Alyoubi, A. O.; Elroby, S. A.; Hilal, R. H. Photochemical Dissociation of HOBr. A Nonadiabatic Dynamics Study. *J. Photochem. Photobiol. A Chem.* **2016**, *324*, 8–13.
39. Shinde, R. Benchmarking Quantum Chemical Methods for Optical Absorption in Boron Wheels. *ACS Omega* **2016**, *1*(4), 578–585.
40. Shayan, K.; Nowroozi, A. The First Singlet Excited State (S1) Intramolecular Hydrogen Bond of Malonaldehyde Derivatives: A TD-DFT and CIS Study. *Struct. Chem.* **2016**, *27*(6), 1769–1780.
41. Annaraj, B.; Mitu, L.; Neelakantan, M. A. Synthesis and Crystal Structure of Imidazole Containing Amide as a Turn on Fluorescent Probe for Nickel Ion in Aqueous Media. An Experimental and Theoretical Investigation. *J. Mol. Struct.* **2016**, *1104*, 1–6.
42. Kocherzhenko, A. A.; Sosa Vazquez, X. A.; Milanese, J. M.; Isborn, C. M. Absorption Spectra for Disordered Aggregates of Chromophores Using the Exciton Model. *J. Chem. Theory Comput.* **2017**, *13*(8), 3787–3801.
43. Farrokhpour, H.; Dehdashti Jahromi, M. Absorption Spectra of Small Helium Nano Clusters (4Hen; n = 2–029) and Characterization of Their Low-Lying Excited States. *J. Mol. Liq.* **2017**, *230*, 190–199.
44. Ge, Q.; Mao, Y.; White, A. F.; Epifanovsky, E.; Closser, K. D.; Head-Gordon, M. Simulating the Absorption Spectra of Helium Clusters (N = 70, 150, 231, 300) Using a Charge Transfer Correction to Superposition of Fragment Single Excitations. *J. Chem. Phys.* **2017**, *146*(4), 044111.
45. Krylov, A. I. Spin-Flip Configuration Interaction: An Electronic Structure Model That Is Both Variational and Size-Consistent. *Chem. Phys. Lett.* **2001**, *350*(5–6), 522–530.
46. Rhee, Y. M.; Head-Gordon, M. Scaled Second-Order Perturbation Corrections to Configuration Interaction Singles: Efficient and Reliable Excitation Energy Methods. *J. Phys. Chem. A* **2007**, *111*(24), 5314–5326.
47. Chibani, S.; Laurent, A. D.; Le Guennic, B.; Jacquemin, D. Improving the Accuracy of Excited-State Simulations of BODIPY and Aza-BODIPY Dyes with a Joint SOS-CIS(D) and TD-DFT Approach. *J. Chem. Theory Comput.* **2014**, *10*(10), 4574–4582.
48. Chibani, S.; Laurent, A. D.; Le Guennic, B.; Jacquemin, D. Excited States of Ladder-Type  $\pi$ -Conjugated Dyes With a Joint SOS-CIS(D) and PCM-TD-DFT Approach. *J. Phys. Chem. A* **2015**, *119*(21), 5417–5425.
49. Ponce-Vargas, M.; Azarias, C.; Jacquemin, D.; Le Guennic, B. Combined TD-DFT-SOS-CIS(D) Study of BOPHY Derivatives with Potential Application in Biosensing. *J. Phys. Chem. B* **2017**, *121*(48), 10850–10858.
50. Pulay, P. A Perspective on the CASPT2 Method. *Int. J. Quantum Chem.* **2011**, *111*, 3273–3279.
51. Sumita, M.; Morihashi, K. Theoretical Study of Singlet Oxygen Molecule Generation via an Exciplex with Valence-Excited Thiophene. *J. Phys. Chem. A* **2015**, *119*(5), 876–883.
52. Chang, X. P.; Fang, Q.; Cui, G. Mechanistic Photodecarboxylation of Pyruvic Acid: Excited-State Proton Transfer and Three-State Intersection. *J. Chem. Phys.* **2014**, *141*(15), 2–10.
53. Cui, G.; Guan, P. J.; Fang, W. H. Photoinduced Proton Transfer and Isomerization in a Hydrogen-Bonded Aromatic Azo Compound: A CASPT2//CASSCF Study. *J. Phys. Chem. A* **2014**, *118*(26), 4732–4739.
54. Casellas, J.; Reguero, M. Photosensitization Versus Photocyclization: Competitive Reactions of Phenylphenalenone in Its Role as Phytoanticipins in Plant Defense Strategies. *J. Phys. Chem. A* **2018**, *122*(3), 811–821.

55. Segado, M.; Reguero, M. Mechanism of the Photochemical Process of Singlet Oxygen Production by Phenalenone. *Phys. Chem. Chem. Phys.* **2011**, *13*(9), 4138.
56. Flors, C.; Ogilby, P. R.; Luis, J. G.; Grillo, T. A.; Izquierdo, L. R.; Gentili, P.-L.; Bussotti, L.; Nonell, S. Phototoxic Phytoalexins. Processes That Compete with the Photosensitized Production of Singlet Oxygen by 9-Phenylphenalenes. *Photochem. Photobiol.* **2006**, *82*(1), 95–103.
57. Casellas, J.; Alcover-Fortuny, G.; de Graaf, C.; Reguero, M. Phenylazopyridine as Switch in Photochemical Reactions. A Detailed Computational Description of the Mechanism of Its Photoisomerization. *Mater. (Basel, Switzerland)* **2017**, *10*(12), 1342.
58. Casellas, J.; Bearpark, M. J.; Reguero, M. Excited-State Decay in the Photoisomerisation of Azobenzene: A New Balance between Mechanisms. *ChemPhysChem* **2016**, *17*(19), 3068–3079.
59. Dai, X.; Song, D.; Liu, K.; Su, H. Photoinduced C—I Bond Homolysis of 5-Iodouracil: A Singlet Predissociation Pathway. *J. Chem. Phys.* **2017**, *146*(2) 025103.
60. Yuan, B.; Bernstein, E. R. Initial Mechanisms for the Unimolecular Decomposition of Electronically Excited Bisfuroxan Based Energetic Materials. *J. Chem. Phys.* **2017**, *146*(1), 014301.
61. Yuan, B.; Bernstein, E. R. Initial Mechanisms for the Unimolecular Decomposition of Electronically Excited Nitrogen-Rich Energetic Salts with Tetrazole Rings: (NH<sub>4</sub>)<sub>2</sub>BT and TAGzT. *J. Chem. Phys.* **2016**, *145*(6) 064306.
62. Yuan, B.; Yu, Z.; Bernstein, E. R. Initial Mechanisms for the Decomposition of Electronically Excited Energetic Salts: TKX-50 and MAD-X1. *J. Phys. Chem. A* **2015**, *119*(12), 2965–2981.
63. Yuan, B.; Yu, Z.; Bernstein, E. R. Azole Energetic Materials: Initial Mechanisms for the Energy Release from Electronical Excited Nitroprazoles. *J. Chem. Phys.* **2014**, *140*(3) 034320.
64. Yuan, B.; Yu, Z.; Bernstein, E. R. Initial Decomposition Mechanism for the Energy Release from Electronically Excited Energetic Materials: FOX-7 (1,1-Diamino-2,2-Dinitroethene, C<sub>2</sub>H<sub>4</sub>N<sub>4</sub>O<sub>4</sub>). *J. Chem. Phys.* **2014**, *140*(7), 074708.
65. Yuan, B.; Shin, J.-W.; Bernstein, E. R. Dynamics and Fragmentation of van Der Waals and Hydrogen Bonded Cluster Cations: (NH<sub>3</sub>)<sub>n</sub> and (NH<sub>3</sub>BH<sub>3</sub>)<sub>n</sub> Ionized at 10.51 eV. *J. Chem. Phys.* **2016**, *144*(14), 144315.
66. Datar, A.; Hazra, A. Pathways for Excited-State Nonradiative Decay of 5,6-Dihydroxyindole, a Building Block of Eumelanin. *J. Phys. Chem. A* **2017**, *121*(14), 2790–2797.
67. Kobayashi, Y.; Okajima, H.; Sotome, H.; Yanai, T.; Mutoh, K.; Yoneda, Y.; Shigeta, Y.; Sakamoto, A.; Miyasaka, H.; Abe, J. Direct Observation of the Ultrafast Evolution of Open-Shell Biradical in Photochromic Radical Dimer. *J. Am. Chem. Soc.* **2017**, *139*(18), 6382–6389.
68. Kim, J.; Moon, J.; Sik Lim, J. Theoretical Investigation of the Reaction Mechanism of the Photoisomerization of 1,2-Dihydro-1,2-Azaborine. *ChemPhysChem* **2015**, *16*, 1670–1675.
69. Gao, A.; Zhang, P.; Zhao, M.; Liu, J. Photoisomerization Mechanism of 1,1'-Dimethyl-2,2'-Pyridocyanine in the Gas Phase and in Solution. *Spectrochim. Acta A Mol. Biomol. Spectrosc.* **2015**, *136*(PB), 1157–1166.
70. Lei, Y.; Yu, L.; Zhou, B.; Zhu, C.; Wen, Z.; Lin, S. H. Landscapes of Four-Enantiomer Conical Intersections for Photoisomerization of Stilbene: CASSCF Calculation. *J. Phys. Chem. A* **2014**, *118*(39), 9021–9031.
71. Suaud, N.; Ruamps, R.; Malrieu, J. P.; Guihery, N. Singly Occupied MOs in Mono- and Diradical Conjugated Hydrocarbons: Comparison between Variational Single-Reference, Pi-Fully Correlated and Huckel Descriptions. *J. Phys. Chem. A* **2014**, *118*(31), 5876–5884.

72. Zhang, Y.; Wang, L.; Li, Y.; Zhang, J. Theoretical Insight into Electronic Spectra of Carbon Chain Carbenes  $H_2C_n$  ( $n = 3-10$ ). *J. Chem. Phys.* **2013**, *138*(2013), 204303.
73. Hlavacek, N. C.; McAnally, M. O.; Drucker, S. Lowest Triplet ( $n, \pi^*$ ) Electronic State of Acrolein: Determination of Structural Parameters by Cavity Ringdown Spectroscopy and Quantum-Chemical Methods. *J. Chem. Phys.* **2013**, *138*(6), 064303.
74. Wheeler, M. D.; Newman, S. M.; Orr-Ewing, A. J.; Ashfold, M. N. R. Cavity Ring-down Spectroscopy. *J. Chem. Soc. Faraday Trans.* **1998**, *94*(3), 337–351.
75. Liu, F.; Morokuma, K. Computational Study on the Working Mechanism of a Stilbene Light-Driven Molecular Rotary Motor: Sloped Minimal Energy Path and Unidirectional Nonadiabatic Photoisomerization. *J. Am. Chem. Soc.* **2012**, *134*(10), 4864–4876.
76. Li, Y.; Liu, F.; Wang, B.; Su, Q.; Wang, W.; Morokuma, K. Different Conical Intersections Control Nonadiabatic Photochemistry of Fluorene Light-Driven Molecular Rotary Motor: A CASSCF and Spin-Flip DFT Study. *J. Chem. Phys.* **2016**, *145*(24), 244311.
77. Ben Amor, N.; Soupart, A.; Heitz, M. C. Methodological CASPT2 Study of the Valence Excited States of an Iron-Porphyrin Complex. *J. Mol. Model.* **2017**, *23*(2), 53.
78. Venturinelli Jannuzzi, S. A.; Phung, Q. M.; Domingo, A.; Formiga, A. L. B.; Pierloot, K. Spin State Energetics and Oxy Character of Mn-Oxo Porphyrins by Multiconfigurational Ab Initio Calculations: Implications on Reactivity. *Inorg. Chem.* **2016**, *55*(11), 5168–5179.
79. Bai, F. Q.; Nakatani, N.; Nakayama, A.; Hasegawa, J. Y. Excited States of a Significantly Ruffled Porphyrin: Computational Study on Structure-Induced Rapid Decay Mechanism via Intersystem Crossing. *J. Phys. Chem. A* **2014**, *118*(23), 4184–4194.
80. Nenov, A.; Giussani, A.; Segarra-Martí, J.; Jaiswal, V. K.; Rivalta, I.; Cerullo, G.; Mukamel, S.; Garavelli, M. Modeling the High-Energy Electronic State Manifold of Adenine: Calibration for Nonlinear Electronic Spectroscopy. *J. Chem. Phys.* **2015**, *142*(21), 0–17.
81. Segarra-Martí, J.; Garavelli, M.; Aquilante, F. Multiconfigurational Second-Order Perturbation Theory with Frozen Natural Orbitals Extended to the Treatment of Photochemical Problems. *J. Chem. Theory Comput.* **2015**, *11*(8), 3772–3784.
82. Bricker, W. P.; Lo, C. S. Efficient Pathways of Excitation Energy Transfer from Delocalized  $S_2$  Excitons in the Peridinin-Chlorophyll *a*-Protein Complex. *J. Phys. Chem. B* **2015**, *119*(18), 5755–5764.
83. Bricker, W. P.; Lo, C. S. Excitation Energy Transfer in the Peridinin-Chlorophyll *a*-Protein Complex Modeled Using Configuration Interaction. *J. Phys. Chem. B* **2014**, *118*(31), 9141–9154.
84. Guan, P. J.; Cui, G.; Fang, Q. Computational Photochemistry of the Azobenzene Scaffold of Sudan I and Orange II Dyes: Excited-State Proton Transfer and Deactivation via Conical Intersections. *ChemPhysChem* **2015**, *16*(4), 805–811.
85. Francés-Monerris, A.; Segarra-Martí, J.; Merchán, M.; Roca-Sanjuán, D. Complete-Active-Space Second-Order Perturbation Theory (CASPT2//CASSCF) Study of the Dissociative Electron Attachment in Canonical DNA Nucleobases Caused by Low-Energy Electrons (0–3 eV). *J. Chem. Phys.* **2015**, *143*(21), 0–14.
86. Giussani, A.; Segarra-Martí, J.; Nenov, A.; Rivalta, I.; Tolomelli, A.; Mukamel, S.; Garavelli, M. Spectroscopic Fingerprints of DNA/RNA Pyrimidine Nucleobases in Third-Order Nonlinear Electronic Spectra. *Theor. Chem. Acc.* **2016**, *135*(5), 1–18.
87. Segarra-Martí, J.; Francés-Monerris, A.; Roca-Sanjuán, D.; Merchán, M. Assessment of the Potential Energy Hypersurfaces in Thymine within Multiconfigurational Theory: CASSCF vs. CASPT2. *Molecules* **2016**, *21*(12), 1–18.
88. Santolini, V.; Malhado, J. P.; Robb, M. A.; Garavelli, M.; Bearpark, M. J. Photochemical Reaction Paths of Cis-Dienes Studied with RASSCF: The Changing Balance Between Ionic and Covalent Excited States. *Mol. Phys.* **2015**, *113*(13–14), 1978–1990.

89. Xia, S. H.; Liu, X. Y.; Fang, Q.; Cui, G. Excited-State Ring-Opening Mechanism of Cyclic Ketones: A MS-CASPT2//CASSCF Study. *J. Phys. Chem. A* **2015**, *119*(15), 3569–3576.
90. Bera, A.; Bhattacharya, A. Excited Electronic State Decomposition Mechanisms of Clusters of Dimethylnitramine and Aluminum. *J. Chem. Sci.* **2015**, *127*(1), 71–82.
91. Bera, A.; Maroo, S.; Bhattacharya, A. Electronically Nonadiabatic Decomposition Mechanisms of Clusters of Zinc and Dimethylnitramine. *Chem. Phys.* **2015**, *446*, 47–56.
92. Bera, A.; Ghosh, J.; Bhattacharya, A. Ab Initio Multiple Spawning Dynamics Study of Dimethylnitramine and Dimethylnitramine-Fe Complex to Model Their Ultrafast Nonadiabatic Chemistry. *J. Chem. Phys.* **2017**, *147*(4), 044308.
93. Manni, G. L.; Smart, S. D.; Alavi, A. Combining the Complete Active Space Self-Consistent Field Method and the Full Configuration Interaction Quantum Monte Carlo within a Super-CI Framework, With Application to Challenging Metal-Porphyrins. *J. Chem. Theory Comput.* **2016**, *12*(3), 1245–1258.
94. Asturiol, D.; Barbatti, M. Electronic States of Porphycene-O<sub>2</sub> Complex and Photoinduced Singlet O<sub>2</sub> Production. *J. Chem. Phys.* **2013**, *139*(7), 074307.
95. Kornobis, K.; Kumar, N.; Lodowski, P.; Jaworska, M.; Piecuch, P.; Lutz, J. J.; Wong, B. M.; Kozłowski, P. M. Electronic Structure of the S1 State in Methylcobalamin: Insight from CASSCF/MC-XQDPT2, EOM-CCSD, and TD-DFT Calculations. *J. Comput. Chem.* **2013**, *34*(12), 987–1004.
96. Stich, T. A.; Brooks, A. J.; Buan, N. R.; Brunold, T. C. Spectroscopic and Computational Studies of Co<sup>3+</sup>-Corrinoids: Spectral and Electronic Properties of the B12 Cofactors and Biologically Relevant Precursors. *J. Am. Chem. Soc.* **2003**, *125*(19), 5897–5914.
97. Brunold, T. C.; Conrad, K. S.; Liptak, M. D.; Park, K. Spectroscopically Validated Density Functional Theory Studies of the B12 Cofactors and Their Interactions With Enzyme Active Sites. *Coord. Chem. Rev.* **2009**, *253*(5–6), 779–794.
98. Walker, L. A.; Jarrett, J. T.; Anderson, N. A.; Pullen, S. H.; Matthews, R. G.; Sension, R. J. Time-Resolved Spectroscopic Studies of B12 Coenzymes: The Identification of a Metastable Cob(III)Alamin Photoproduct in the Photolysis of Methylcobalamin. *J. Am. Chem. Soc.* **1998**, *120*(15), 3597–3603.
99. Shiang, J. J.; Walker, L. A.; Anderson, N. A.; Cole, A. G.; Sension, R. J. Time-Resolved Spectroscopic Studies of B 12 Coenzymes: The Photolysis of Methylcobalamin Is Wavelength Dependent. *J. Phys. Chem. B* **1999**, *103*(47), 10532–10539.
100. Harris, D. A.; Stickrath, A. B.; Carroll, E. C.; Sension, R. J. Influence of Environment on the Electronic Structure of Cob(III)Alamins: Time-Resolved Absorption Studies of the S1 State Spectrum and Dynamics. *J. Am. Chem. Soc.* **2007**, *129*(24), 7578–7585.
101. Huix-Rotllant, M.; Siri, D.; Ferré, N. Theoretical Study of the Photochemical Generation of Triplet Acetophenone. *Phys. Chem. Chem. Phys.* **2013**, *15*(44), 19293–19300.
102. Xu, X.; Yang, K. R.; Truhlar, D. G. Diabatic Molecular Orbitals, Potential Energies, and Potential Energy Surface Couplings by the 4-Fold Way for Photodissociation of Phenol. *J. Chem. Theory Comput.* **2013**, *9*(8), 3612–3625.
103. Kletskii, M. E.; Lisovin, A. V.; Burov, O. N.; Kurbatov, S. V. Competing Mechanisms of Norrish and Norrish-like Reactions in a Wide Range of Systems—From Carbonyl Compounds to Nitrogen Oxide Donators. *Comput. Theor. Chem.* **2014**, *1047*(1), 55–66.
104. Grabarek, D.; Walczak, E.; Andruniow, T. Assessing the Accuracy of Various Ab Initio Methods for Geometries and Excitation Energies of Retinal Chromophore Minimal Model by Comparison with CASPT3 Results. *J. Chem. Theory Comput.* **2016**, *12*(5), 2346–2356.



105. Walczak, E.; Szeftczyk, B.; Andruniów, T. Geometries and Vertical Excitation Energies in Retinal Analogues Resolved at the CASPT2 Level of Theory: Critical Assessment of the Performance of CASSCF, CC2, and DFT Methods. *J. Chem. Theory Comput.* **2013**, *9*(11), 4915–4927.
106. Szeftczyk, B.; Grabarek, D.; Walczak, E.; Andruniów, T. Excited-State Minima and Emission Energies of Retinal Chromophore Analogues: Performance of CASSCF and CC2 Methods as Compared With CASPT2. *J. Comput. Chem.* **2017**, *38*(20), 1799–1810.
107. Gozem, S.; Huntress, M.; Schapiro, I.; Lindh, R.; Granovsky, A. A.; Angeli, C.; Olivucci, M. Dynamic Electron Correlation Effects on the Ground State Potential Energy Surface of a Retinal Chromophore Model. *J. Chem. Theory Comput.* **2012**, *8*(11), 4069–4080.
108. Huix-Rotllant, M.; Filatov, M.; Gozem, S.; Schapiro, I.; Olivucci, M.; Ferré, N. Assessment of Density Functional Theory for Describing the Correlation Effects on the Ground and Excited State Potential Energy Surfaces of a Retinal Chromophore Model. *J. Chem. Theory Comput.* **2013**, *9*(9), 3917–3932.
109. Xu, X.; Gozem, S.; Olivucci, M.; Truhlar, D. G. Combined Self-Consistent-Field and Spin-Flip Tamm-Dancoff Density Functional Approach to Potential Energy Surfaces for Photochemistry. *J. Phys. Chem. Lett.* **2013**, *4*(2), 253–258.
110. Gozem, S.; Krylov, A. I.; Olivucci, M. Conical Intersection and Potential Energy Surface Features of a Model Retinal Chromophore: Comparison of EOM-CC and Multireference Methods. *J. Chem. Theory Comput.* **2013**, *9*(1), 284–292.
111. Gozem, S.; Melaccio, F.; Lindh, R.; Krylov, A. I.; Granovsky, A. A.; Angeli, C.; Olivucci, M. Mapping the Excited State Potential Energy Surface of a Retinal Chromophore Model with Multireference and Equation-of-Motion Coupled-Cluster Methods. *J. Chem. Theory Comput.* **2013**, *9*(10), 4495–4506.
112. Gozem, S.; Melaccio, F.; Valentini, A.; Filatov, M.; Huix-Rotllant, M.; Ferre, N.; Frutos, L. M.; Angeli, C.; Krylov, A. I.; Granovsky, A. A.; et al. Shape of Multireference, Equation-of-Motion Coupled-Cluster, and Density Functional Theory Potential Energy Surfaces at a Conical Intersection. *J. Chem. Theory Comput.* **2014**, *10*(8), 3074–3084.
113. Zen, A.; Coccia, E.; Gozem, S.; Olivucci, M.; Guidoni, L. Quantum Monte Carlo Treatment of the Charge Transfer and Diradical Electronic Character in a Retinal Chromophore Minimal Model. *J. Chem. Theory Comput.* **2015**, *11*(3), 992–1005.
114. Tuna, D.; Lefrancois, D.; Wolanski, L.; Gozem, S.; Schapiro, I.; Andruniow, T.; Dreuw, A.; Olivucci, M. Assessment of Approximate Coupled-Cluster and Algebraic-Diagrammatic-Construction Methods for Ground- and Excited-State Reaction Paths and the Conical-Intersection Seam of a Retinal-Chromophore Model. *J. Chem. Theory Comput.* **2015**, *11*(12), 5758–5781.
115. Chin, C.-H.; Lin, S. H. Theoretical Investigations of Absorption and Fluorescence Spectra of Protonated Pyrene. *Phys. Chem. Chem. Phys.* **2016**, *18*(21), 14569–14579.
116. Cacelli, I.; Ferretti, A.; Prampolini, G. Predicting Light Absorption Properties of Anthocyanidins in Solution: A Multi-Level Computational Approach. *Theor. Chem. Acc.* **2016**, *135*(6), 1–17.
117. Fréneau, M.; de Sainte Claire, P.; Hoffmann, N.; Vors, J.-P.; Geist, J.; Euvrard, M.; Richard, C. Phototransformation of Tetrazoline Oxime Ethers: Photoisomerization vs Photodegradation. *RSC Adv.* **2016**, *6*(7), 5512–5522.
118. Fréneau, M.; Hoffmann, N.; Vors, J.-P.; Genix, P.; Richard, C.; De Sainte Claire, P. Phototransformation of Tetrazoline Oxime Ethers—Part 2: Theoretical Investigation. *RSC Adv.* **2016**, *6*(68), 63965–63972.

119. López-de-Luzuriaga, J. M.; Manso, E.; Monge, M.; Sampedro, D. Dual Fluorescence of 4-(Dimethylamino)-Pyridine: A Comparative Linear Response TDDFT versus State-Specific CASSCF Study Including Solvent With the PCM Model. *Theor. Chem. Acc.* **2015**, *134*(5), 55.
120. Li, J.; Rinkevicius, Z.; Cao, Z. A Time-Dependent Density-Functional Theory and Complete Active Space Self-Consistent Field Method Study of Vibronic Absorption and Emission Spectra of Coumarin. *J. Chem. Phys.* **2014**, *141*(1), 014306.
121. Olsen, S. Locally-Excited (LE) versus Charge-Transfer (CT) Excited State Competition in a Series of Para-Substituted Neutral Green Fluorescent Protein (GFP) Chromophore Models. *J. Phys. Chem. B* **2015**, *119*(6), 2566–2575.
122. Ai, Y.; Tian, G.; Luo, Y. Role of Non-Condon Vibronic Coupling and Conformation Change on Two-Photon Absorption Spectra of Green Fluorescent Protein. *Mol. Phys.* **2013**, *111*(9–11), 1316–1321.
123. Zhang, L.; Muchall, H. M.; Peslherbe, G. H. Substituent Effects in the Absorption Spectra of Phenol Radical Species: Origin of the Redshift Caused by 3,5-Dimethoxyl Substitution. *Photochem. Photobiol.* **2013**, *89*(3), 536–544.
124. Palmer, M. H.; Hoffmann, S. V.; Jones, N. C.; Coreno, M.; de Simone, M.; Grazioli, C.; Peterson, K. A.; Baiardi, A.; Zhang, T.; Biczysko, M. A Combined Theoretical and Experimental Study of the Valence and Rydberg States of Iodopentafluorobenzene. *J. Chem. Phys.* **2017**, *146*(17), 174301.
125. Palmer, M. H.; Coreno, M.; de Simone, M.; Hoffmann, S. V.; Jones, N. C.; Grazioli, C.; Peterson, K. A.; Baiardi, A.; Zhang, T.; Biczysko, M. A Combined Theoretical and Experimental Study of the Ionic States of Iodopentafluorobenzene. *J. Chem. Phys.* **2017**, *146*(8) 084302.
126. Palmer, M. H.; Biczysko, M.; Baiardi, A.; Coreno, M.; De Simone, M.; Grazioli, C.; Hoffmann, S. V.; Jones, N. C.; Peterson, K. A. The Ionic States of Difluoromethane: A Reappraisal of the Low Energy Photoelectron Spectrum Including Ab Initio Configuration Interaction Computations. *J. Chem. Phys.* **2017**, *147*(7), 074305.
127. Palmer, M. H.; Hoffmann, S. V.; Jones, N. C.; Smith, E. R.; Lichtenberger, D. L. The Electronic States of Pyridine-N-Oxide Studied by VUV Photoabsorption and Ab Initio Configuration Interaction Computations. *J. Chem. Phys.* **2013**, *138*(21), 214317.
128. Palmer, M. H.; Ridley, T.; Hoffmann, S. V.; Jones, N. C.; Coreno, M.; De Simone, M.; Grazioli, C.; Biczysko, M.; Baiardi, A.; Limão-Vieira, P. Interpretation of the Vacuum Ultraviolet Photoabsorption Spectrum of Iodobenzene by Ab Initio Computations. *J. Chem. Phys.* **2015**, *142*(13), 134302.
129. Palmer, M. H.; Ridley, T.; Vronning Hoffmann, S.; Jones, N. C.; Coreno, M.; De Simone, M.; Grazioli, C.; Zhang, T.; Biczysko, M.; Baiardi, A.; et al. Combined Theoretical and Experimental Study of the Valence, Rydberg, and Ionic States of Chlorobenzene. *J. Chem. Phys.* **2016**, *144*(12), 124302.
130. Besley, N. A. Calculation of the Electronic Spectra of Molecules in Solution and on Surfaces. *Chem. Phys. Lett.* **2004**, *390*(1–3), 124–129.
131. Jacquemin, D.; Perpe, E. A.; Scuseria, G. E.; Ciofini, I.; Adamo, C. TD-DFT Performance for the Visible Absorption Spectra of Organic Dyes: Conventional versus Long-Range Hybrids. *J. Chem. Theory Comput.* **2008**, *4*, 123–135.
132. Jacquemin, D.; Perpète, E. A.; Ciofini, I.; Adamo, C. Assessment of the  $\Omega$ B97 Family for Excited-State Calculations. *Theor. Chem. Acc.* **2011**, *128*(1), 127–136.
133. Goerigk, L.; Grimme, S. Assessment of TD-DFT Methods and of Various Spin Scaled CIS(D) and CC2 Versions for the Treatment of Low-Lying Valence Excitations of Large Organic Dyes. *J. Chem. Phys.* **2010**, *132*(18) 184103.

134. Rohrdanz, M. A.; Martins, K. M.; Herbert, J. M. A Long-Range-Corrected Density Functional That Performs Well for Both Ground-State Properties and Time-Dependent Density Functional Theory Excitation Energies, Including Charge-Transfer Excited States. *J. Chem. Phys.* **2009**, *130*(5), 054112.
135. Vydrov, O. A.; Heyd, J.; Krukau, A. V.; Scuseria, G. E. Importance of Short-Range versus Long-Range Hartree-Fock Exchange for the Performance of Hybrid Density Functionals. *J. Chem. Phys.* **2006**, *125*(7), 0–9.
136. Peach, M. J. G.; Helgaker, T.; Sałek, P.; Keal, T. W.; Lutnæs, O. B.; Tozer, D. J.; Handy, N. C. Assessment of a Coulomb-Attenuated Exchange-Correlation Energy Functional. *Phys. Chem. Chem. Phys.* **2006**, *8*(5), 558–562.
137. Peach, M. J. G.; Cohen, A. J.; Tozer, D. J. Influence of Coulomb-Attenuation on Exchange-Correlation Functional Quality. *Phys. Chem. Chem. Phys.* **2006**, *8*(39), 4543–4549.
138. Rohrdanz, M. A.; Herbert, J. M. Simultaneous Benchmarking of Ground- and Excited-State Properties with Long-Range-Corrected Density Functional Theory. *J. Chem. Phys.* **2008**, *129*(3), 034107.
139. Shcherbin, D.; Ruud, K. The Use of Coulomb-Attenuated Methods for the Calculation of Electronic Circular Dichroism Spectra. *Chem. Phys.* **2008**, *349*(1–3), 234–243.
140. Kuritz, N.; Stein, T.; Baer, R.; Kronik, L. Charge-Transfer-like  $\Pi \rightarrow \pi^*$  Excitations in Time-Dependent Density Functional Theory: A Conundrum and Its Solution. *J. Chem. Theory Comput.* **2011**, *7*(8), 2408–2415.
141. Stein, T.; Kronik, L.; Baer, R. Reliable Prediction of Charge Transfer Excitations in Molecular Complexes using Time-Dependent Density Functional Theory. *J. Am. Chem. Soc.* **2009**, *131*(8), 2818–2820.
142. Stein, T.; Eisenberg, H.; Kronik, L.; Baer, R. Fundamental Gaps in Finite Systems from Eigenvalues of a Generalized Kohn-Sham Method. *Phys. Rev. Lett.* **2010**, *105*(26), 1–4.
143. Stein, T.; Kronik, L.; Baer, R. Prediction of Charge-Transfer Excitations in Coumarin-Based Dyes Using a Range-Separated Functional Tuned From First Principles. *J. Chem. Phys.* **2009**, *131*(24), 244119.
144. Gąsiorowski, P.; Matusiewicz, M.; Gondek, E.; Uchacz, T.; Wojtasik, K.; Danel, A.; Shchur, Y.; Kityk, A. V. On the Spectral Properties of Methyl and Methoxy Derivatives of 1,3-Diphenyl-1H-Pyrazolo[3,4-b]Quinoxalines: Experiment and DFT/TDDFT Calculations. *Spectrochim. Acta A Mol. Biomol. Spectrosc.* **2017**, *186*, 89–98.
145. Gąsiorowski, P.; Matusiewicz, M.; Gondek, E.; Pokladko-Kowar, M.; Armatys, P.; Wojtasik, K.; Danel, A.; Uchacz, T.; Kityk, A. V. Efficient Green Electroluminescence from 1,3-Diphenyl-1H-Pyrazolo[3,4-b]Quinoxaline Dyes in Dye-Doped Polymer Based Electroluminescent Devices. *Dye. Pigment.* **2018**, *151*(January), 380–384.
146. Arulmozhiraja, S.; Coote, M. L. 1La and 1Lb States of Indole and Azaindole: Is Density Functional Theory Inadequate? *J. Chem. Theory Comput.* **2012**, *8*(2), 575–584.
147. Eriksen, J. J.; Sauer, S. P. A.; Mikkelsen, K. V.; Christiansen, O.; Jensen, H. J. A.; Kongsted, J. Failures of TDDFT in Describing the Lowest Intramolecular Charge-Transfer Excitation in Para-Nitroaniline. *Mol. Phys.* **2013**, *111*(9–11), 1235–1248.
148. Körzdörfer, T.; Brédas, J. L. Organic Electronic Materials: Recent Advances in the DFT Description of the Ground and Excited States Using Tuned Range-Separated Hybrid Functionals. *Acc. Chem. Res.* **2014**, *47*(11), 3284–3291.
149. Sun, H.; Zhong, C.; Brédas, J. L. Reliable Prediction With Tuned Range-Separated Functionals of the Singlet-Triplet Gap in Organic Emitters for Thermally Activated Delayed Fluorescence. *J. Chem. Theory Comput.* **2015**, *11*(8), 3851–3858.
150. Penfold, T. J. On Predicting the Excited-State Properties of Thermally Activated Delayed Fluorescence Emitters. *J. Phys. Chem. C* **2015**, *119*(24), 13535–13544.

151. Moore, B.; Autschbach, J. Longest-Wavelength Electronic Excitations of Linear Cyanines: The Role of Electron Delocalization and of Approximations in Time-Dependent Density Functional Theory. *J. Chem. Theory Comput.* **2013**, *9*(11), 4991–5003.
152. Maschietto, F.; Campetella, M.; Frisch, M. J.; Scalmani, G.; Adamo, C.; Ciofini, I. How Are the Charge Transfer Descriptors Affected by the Quality of the Underpinning Electronic Density? *J. Comput. Chem.* **2018**, 735–742.
153. Shu, Y.; Parker, K. A.; Truhlar, D. G. Dual-Functional Tamm-Dancoff Approximation: A Convenient Density Functional Method That Correctly Describes S1/S0-Conical Intersections. *J. Phys. Chem. Lett.* **2017**, *8*(10), 2107–2112.
154. Grimme, S. A Simplified Tamm-Dancoff Density Functional Approach for the Electronic Excitation Spectra of Very Large Molecules. *J. Chem. Phys.* **2013**, *138*(24), 0–14.
155. Bannwarth, C.; Grimme, S. A Simplified Time-Dependent Density Functional Theory Approach for Electronic Ultraviolet and Circular Dichroism Spectra of Very Large Molecules. *Comput. Theor. Chem.* **2014**, *1040–1041*, 45–53.
156. Risthaus, T.; Hansen, A.; Grimme, S. Excited States Using the Simplified Tamm-Dancoff-Approach for Range-Separated Hybrid Density Functionals: Development and Application. *Phys. Chem. Chem. Phys.* **2014**, *16*(28), 14408–14419.
157. Bannwarth, C.; Seibert, J.; Grimme, S. Electronic Circular Dichroism of [16]Helicene With Simplified TD-DFT: Beyond the Single Structure Approach. *Chirality* **2016**, *28*, 365–369.
158. Grimme, S.; Bannwarth, C. Ultra-Fast Computation of Electronic Spectra for Large Systems by Tight-Binding Based Simplified Tamm-Dancoff Approximation (STDA-XTB). *J. Chem. Phys.* **2016**, *145*(5), 054103.
159. Seibert, J.; Bannwarth, C.; Grimme, S. Biomolecular Structure Information from High-Speed Quantum Mechanical Electronic Spectra Calculation. *J. Am. Chem. Soc.* **2017**, *139*(34), 11682–11685.
160. Bannwarth, C.; Grimme, S. Electronic Circular Dichroism of Highly Conjugated  $\pi$ -Systems: Breakdown of the Tamm-Dancoff/Configuration Interaction Singles Approximation. *J. Phys. Chem. A* **2015**, *119*(15), 3653–3662.
161. Zvereva, E. E.; Grimme, S.; Katsyuba, S. A.; Burganov, T. I.; Zagidullin, A. A.; Milyukov, V. A.; Sinyashin, O. G. Application of Time-Dependent Density Functional Theory and Optical Spectroscopy toward the Rational Design of Novel 3,4,5-Triaryl-1-R-1,2-Diphospholes. *J. Phys. Chem. A* **2013**, *117*(31), 6827–6834.
162. Burganov, T. I.; Zhukova, N. A.; Mamedov, V. A.; Bannwarth, C.; Grimme, S.; Katsyuba, S. A. Benzimidazolylquinoxalines: Novel Fluorophores with Tuneable Sensitivity to Solvent Effects. *Phys. Chem. Chem. Phys.* **2017**, *19*(8), 6095–6104.
163. Jacquemin, D.; Duchemin, I.; Blase, X. 0–0 Energies Using Hybrid Schemes: Benchmarks of TD-DFT, CIS(D), ADC(2), CC2, and BSE/GW Formalisms for 80 Real-Life Compounds. *J. Chem. Theory Comput.* **2015**, *11*(11), 5340–5359.
164. Ameline, D.; Diring, S.; Farre, Y.; Pellegrin, Y.; Naponiello, G.; Blart, E.; Charrier, B.; Dini, D.; Jacquemin, D.; Odobel, F. Isoindigo Derivatives for Application in P-Type Dye Sensitized Solar Cells. *RSC Adv.* **2015**, *5*(104), 85530–85539.
165. Houari, Y.; Charaf-Eddin, A.; Laurent, A. D.; Massue, J.; Ziessel, R.; Ulrich, G.; Jacquemin, D. Modeling Optical Signatures and Excited-State Reactivities of Substituted Hydroxyphenylbenzoxazole (HBO) ESIPT Dyes. *Phys. Chem. Chem. Phys.* **2014**, *16*(4), 1319–1321.
166. Ji, S.; Ge, J.; Escudero, D.; Wang, Z.; Zhao, J.; Jacquemin, D. Molecular Structure-Intersystem Crossing Relationship of Heavy-Atom-Free Bodipy Triplet Photosensitizers. *J. Org. Chem.* **2015**, *80*(11), 5958–5963.

167. Fihey, A.; Perrier, A.; Browne, W. R.; Jacquemin, D. Multiphotochromic Molecular Systems. *Chem. Soc. Rev.* **2015**, 3719–3759.
168. Chibani, S.; Charaf-Eddin, A.; Mennucci, B.; Le Guennic, B.; Jacquemin, D. Optical Signatures of OBO Fluorophores: A Theoretical Analysis. *J. Chem. Theory Comput.* **2014**, *10*(2), 805–815.
169. Jacquemin, D.; Moore, B.; Adamo, C.; Autschbach, J. Performance of an Optimally Tuned Range-Separated Hybrid Functional for 0–0 Electronic Excitation Energies. *J. Chem. Theory Comput.* **2014**, *10*, 1677–1685.
170. Farré, Y.; Zhang, L.; Pellegrin, Y.; Planchat, A.; Blart, E.; Boujita, M.; Hammarström, L.; Jacquemin, D.; Odobel, F. Second Generation of Diketopyrrolopyrrole Dyes for NiO-Based Dye-Sensitized Solar Cells. *J. Phys. Chem. C* **2016**, *120*(15), 7923–7940.
171. Boixel, J.; Guerschais, V.; Le Bozec, H.; Jacquemin, D.; Amar, A.; Boucekkine, A.; Colombo, A.; Dragonetti, C.; Marinotto, D.; Roberto, D.; et al. Second-Order NLO Switches from Molecules to Polymer Films Based on Photochromic Cyclometalated Platinum(II) Complexes. *J. Am. Chem. Soc.* **2014**, *136*(14), 5367–5375.
172. Le Guennic, B.; Jacquemin, D. Taking Up the Cyanine Challenge with Quantum Tools. *Acc. Chem. Res.* **2015**, *48*(3), 530–537.
173. Jacquemin, D.; Duchemin, I.; Blase, X. Benchmarking the Bethe–Salpeter Formalism on a Standard Organic Molecular Set. *J. Chem. Theory Comput.* **2015**, *11*(7), 3290–3304.
174. Houari, Y.; Chibani, S.; Jacquemin, D.; Laurent, A. D. TD-DFT Assessment of the Excited State Intramolecular Proton Transfer in Hydroxyphenylbenzimidazole (HBI) Dyes. *J. Phys. Chem. B* **2015**, *119*, 2180–2192.
175. Azarias, C.; Budzák, Š.; Laurent, A. D.; Ulrich, G.; Jacquemin, D. Tuning ESIPT Fluorophores into Dual Emitters. *Chem. Sci.* **2016**, *7*(6), 3763–3774.
176. Benelhadj, K.; Muzuzu, W.; Massue, J.; Retailleau, P.; Charaf-Eddin, A.; Laurent, A. D.; Jacquemin, D.; Ulrich, G.; Ziessel, R. White Emitters by Tuning the Excited-State Intramolecular Proton-Transfer Fluorescence Emission in 2-(2-Hydroxybenzofuran)Benzoxazole Dyes. *Chem. A Eur. J.* **2014**, *20*(40), 12843–12857.
177. Kamada, K.; Namikawa, T.; Senatore, S.; Matthews, C.; Lenne, P. F.; Maury, O.; Andraud, C.; Ponce-Vargas, M.; Le Guennic, B.; Jacquemin, D.; et al. Boron Difluoride Curcuminoid Fluorophores With Enhanced Two-Photon Excited Fluorescence Emission and Versatile Living-Cell Imaging Properties. *Chem. A Eur. J.* **2016**, *22*(15), 5219–5232.
178. Escudero, D.; Jacquemin, D. Computational Insights Into the Photodeactivation Dynamics of Phosphors for OLEDs: A Perspective. *Dalton Trans.* **2015**, *44*(18), 8346–8355.
179. Laurent, A. D.; Adamo, C.; Jacquemin, D. Dye Chemistry With Time-Dependent Density Functional Theory. *Phys. Chem. Chem. Phys.* **2014**, *16*(28), 14334–14356.
180. Guido, C. A.; Jacquemin, D.; Adamo, C.; Mennucci, B. Electronic Excitations in Solution: The Interplay between State Specific Approaches and a Time-Dependent Density Functional Theory Description. *J. Chem. Theory Comput.* **2015**, *11*(12), 5782–5790.
181. Charaf-Eddin, A.; Le Guennic, B.; Jacquemin, D. Excited-States of BODIPY-Cyanines: Ultimate TD-DFT Challenges? *RSC Adv.* **2014**, *4*(90), 49449–49456.
182. Pascal, S.; Haeferle, A.; Monnereau, C.; Charaf-Eddin, A.; Jacquemin, D.; Le Guennic, B.; Andraud, C.; Maury, O. Expanding the Polymethine Paradigm: Evidence for the Contribution of a Bis-Dipolar Electronic Structure. *J. Phys. Chem. A* **2014**, *118*(23), 4038–4047.

183. Boulanger, P.; Jacquemin, D.; Duchemin, I.; Blase, X. Fast and Accurate Electronic Excitations in Cyanines with the Many-Body Bethe-Salpeter Approach. *J. Chem. Theory Comput.* **2014**, *10*(3), 1212–1218.
184. Heyer, E.; Benelhadj, K.; Budzák, S.; Jacquemin, D.; Massue, J.; Ulrich, G. On the Fine-Tuning of the Excited-State Intramolecular Proton Transfer (ESIPT) Process in 2-(2'-Hydroxybenzofuran)Benzazole (HBBX) Dyes. *Chem. A Eur. J.* **2017**, *23*(30), 7324–7336.
185. Benelhadj, K.; Massue, J.; Retailleau, P.; Chibani, S.; Le Guennic, B.; Jacquemin, D.; Ziessel, R.; Ulrich, G. Solution- and Solid-State Luminescent Borate Complexes Based on a Substituted  $\pi$ -Conjugated 2-(6 J-Hydroxy-5 J-Benzofuryl) Scaffold. *Eur. J. Org. Chem.* **2014**, *2014*(32), 7156–7164.
186. Massue, J.; Benelhadj, K.; Chibani, S.; Le Guennic, B.; Jacquemin, D.; Retailleau, P.; Ulrich, G.; Ziessel, R. Fluorescent 2-(2'-Hydroxybenzofuran)Benzoxazole (HBBO) Borate Complexes: Synthesis, Optical Properties, and Theoretical Calculations. *Tetrahedron Lett.* **2014**, *55*(30), 4136–4140.
187. Le Bahers, T.; Pauporté, T.; Lainé, P. P.; Labat, F.; Adamo, C.; Ciofini, I. Modeling Dye-Sensitized Solar Cells: From Theory to Experiment. *J. Phys. Chem. Lett.* **2013**, *4*(6), 1044–1050.
188. Mathew, S.; Yella, A.; Gao, P.; Humphry-Baker, R.; Curchod, B. F. E.; Ashari-Astani, N.; Tavernelli, I.; Rothlisberger, U.; Nazeeruddin, M. K.; Grätzel, M. Dye-Sensitized Solar Cells With 13% Efficiency Achieved Through the Molecular Engineering of Porphyrin Sensitizers. *Nat. Chem.* **2014**, *6*(3), 242–247.
189. Liu, Z.; Hua, S.; Yan, X. Linear and Nonlinear Optical Properties of Triphenylamine-Indandione Chromophores: Theoretical Study of the Structure-Function Relationship Under the Combined Action of Substituent and Symmetry Change. *J. Phys. Chem. A* **2018**, *122*(9), 2344–2352.
190. Linares-Flores, C.; Schott, E.; Claveria-Cadiz, F.; Zarate, X. Energy Conversion Process of Substituted Phthalocyanines With Potential Application to DSSC: A Theoretical Study. *Theor. Chem. Acc.* **2018**, *137*(4), 52.
191. Zarate, X.; Saavedra-Torres, M.; Rodriguez-Serrano, A.; Gomez, T.; Schott, E. Exploring the Relevance of Thiophene Rings as Bridge Unit in Acceptor-Bridge-Donor Dyes on Self-Aggregation and Performance in DSSCs. *J. Comput. Chem.* **2017**, 685–698.
192. Zarate, X.; Schott-Verdugo, S.; Rodriguez-Serrano, A.; Schott, E. The Nature of the Donor Motif in Acceptor-Bridge-Donor Dyes as an Influence in the Electron Photo-Injection Mechanism in DSSCs. *J. Phys. Chem. A* **2016**, *120*(9), 1613–1624.
193. Li, Y.; Xu, B.; Song, P.; Ma, F.; Sun, M. D-A- $\pi$ -A System: Light Harvesting, Charge Transfer, and Molecular Designing. *J. Phys. Chem. C* **2017**, *121*(23), 12546–12561.
194. Nachimuthu, S.; Chen, W.-C.; Leggesse, E. G.; Jiang, J.-C. First Principles Study of Organic Sensitizers for Dye Sensitized Solar Cells: Effects of Anchoring Groups on Optoelectronic Properties and Dye Aggregation. *Phys. Chem. Chem. Phys.* **2016**, *18*(2), 1071–1081.
195. Baheti, A.; Justin Thomas, K. R.; Lee, C.-P.; Li, C.-T.; Ho, K.-C. Organic Dyes Containing Fluoren-9-Ylidene Chromophores for Efficient Dye-Sensitized Solar Cells. *J. Mater. Chem. A* **2014**, *2*(16), 5766.
196. Baheti, A.; Justin Thomas, K. R.; Li, C. T.; Lee, C. P.; Ho, K. C. Fluorene-Based Sensitizers with a Phenothiazine Donor: Effect of Mode of Donor Tethering on the Performance of Dye-Sensitized Solar Cells. *ACS Appl. Mater. Interfaces* **2015**, *7*(4), 2249–2262.

197. Venkateswararao, A.; Thomas, K. R. J.; Lee, C. P.; Li, C. T.; Ho, K. C. Organic Dyes Containing Carbazole as Donor and  $\pi$ -Linker: Optical, Electrochemical, and Photo-voltaic Properties. *ACS Appl. Mater. Interfaces* **2014**, *6*(4), 2528–2539.
198. Feng, J.; Jiao, Y.; Ma, W.; Nazeeruddin, M. K.; Grätzel, M.; Meng, S. First Principles Design of Dye Molecules With Ullazine Donor for Dye Sensitized Solar Cells. *J. Phys. Chem. C* **2013**, *117*(8), 3772–3778.
199. Kulinich, A. V.; Ishchenko, A. A.; Kukhta, I. N.; Mitryukhin, L. K.; Kazakov, S. M.; Kukhta, A. V. Electron Impact Excitation of the Merocyanine Molecule in the Gas Phase. *Chem. Phys.* **2018**, *503*, 20–24.
200. Kowalska-Baron, A.; Zurawinski, R.; Lukasik, B.; Chworos, A.; Wysocki, S. Theoretical and Experimental Study on the Electronic Structure of Distyrylnaphthalene-Based Conjugated Oligoelectrolytes. *J. Lumin.* **2018**, *196*(December 2017), 81–89.
201. Lee, S.; Kim, S. O.; Shin, H.; Yun, H. J.; Yang, K.; Kwon, S. K.; Kim, J. J.; Kim, Y. H. Deep-Blue Phosphorescence from Perfluoro Carbonyl-Substituted Iridium Complexes. *J. Am. Chem. Soc.* **2013**, *135*(38), 14321–14328.
202. Estrada, L. A.; Stalder, R.; Abboud, K. A.; Risko, C.; Brédas, J. L.; Reynolds, J. R. Understanding the Electronic Structure of Isoindigo in Conjugated Systems: A Combined Theoretical and Experimental Approach. *Macromolecules* **2013**, *46*(22), 8832–8844.
203. Lourenço Neto, M.; Agra, K. L.; Suassuna Filho, J.; Jorge, F. E. TDDFT Calculations and Photoacoustic Spectroscopy Experiments Used to Identify Phenolic Acid Functional Biomolecules in Brazilian Tropical Fruits in Natura. *Spectrochim. Acta A Mol. Biomol. Spectrosc.* **2018**, *193*, 249–257.
204. Ma, H.; Huang, J.-D. Ab Initio Study of the Excited-State Proton Transfer Mechanisms for 3-Hydroxy-2-(Thiophen-2-Yl)Chromen-4-One. *RSC Adv.* **2016**, *6*(98), 96147–96153.
205. Huang, J. D.; Yu, K.; Ma, H.; Chai, S.; Dong, B. Theoretical Investigation of Excited-State Single and Double Proton Transfer Mechanisms for 2,5-Bis(Benzoxazol-2-Yl)Thiophene-3,4-Diol. *Dye. Pigment.* **2017**, *141*, 441–447.
206. Zhu, Q.; Wen, K.; Feng, S.; Wu, W.; An, B.; Yuan, H.; Guo, X.; Zhang, J. Theoretical Insights into the Excited-State Intramolecular Proton Transfer (ESIPT) Mechanism in a Series of Amino-Type Hydrogen-Bonding Dye Molecules Bearing the 10-Aminobenzo[h]Quinoline Chromophore. *Dye. Pigment.* **2017**, *141*, 195–201.
207. Liu, Y.-H.; Wang, S.-M.; Zhu, C.; Lin, S. H. A TDDFT Study on the Excited-State Double Proton Transfer Reaction of 8-Hydroxyquinoline Along a Hydrogen-Bonded Bridge. *New J. Chem.* **2017**, *41*(16), 8437–8442.
208. Pina, J.; Sarmiento, D.; Accoto, M.; Gentili, P. L.; Vaccaro, L.; Galvão, A.; Seixas de Melo, J. S. Excited-State Proton Transfer in Indigo. *J. Phys. Chem. B* **2017**, *121*(10), 2308–2318.
209. Zhou, Q.; Du, C.; Yang, L.; Zhao, M.; Dai, Y.; Song, P. Mechanism for the Excited-State Multiple Proton Transfer Process of Dihydroxyanthraquinone Chromophores. *J. Phys. Chem. A* **2017**, *121*(24), 4645–4651.
210. Li, C.; Ma, C.; Li, D.; Liu, Y. Excited State Intramolecular Proton Transfer (ESIPT) of 6-Amino-2-(2'-Hydroxyphenyl)Benzoxazole in Dichloromethane and Methanol: A TD-DFT Quantum Chemical Study. *J. Lumin.* **2016**, *172*, 29–33.
211. Li, C.; Yang, Y.; Ma, C.; Liu, Y. Effect of Amino Group on the Excited-State Intramolecular Proton Transfer (ESIPT) Mechanisms of 2-(2'-Hydroxyphenyl)Benzoxazole and Its Amino Derivatives. *RSC Adv.* **2016**, *6*(6), 5134–5140.
212. Zhang, X.; Liu, J. Y. Solvent Dependent Photophysical Properties and Near-Infrared Solid-State Excited State Intramolecular Proton Transfer (ESIPT) Fluorescence of 2,4,6-Trisbenzothiazolyphenol. *Dye. Pigment.* **2016**, *125*, 80–88.

213. Zhao, J.; Chen, J.; Cui, Y.; Wang, J.; Xia, L.; Dai, Y.; Song, P.; Ma, F. A Questionable Excited-State Double-Proton Transfer Mechanism for 3-Hydroxyisoquinoline. *Phys. Chem. Chem. Phys.* **2015**, *17*(2), 1142–1150.
214. Zhao, J.; Chen, J.; Liu, J.; Hoffmann, M. R. Competitive Excited-State Single or Double Proton Transfer Mechanisms for Bis-2,5-(2-Benzoxazolyl)-Hydroquinone and Its Derivatives. *Phys. Chem. Chem. Phys.* **2015**, *17*(18), 11990–11999.
215. Zhao, J.; Yao, H.; Liu, J.; Hoffmann, M. R. New Excited-State Proton Transfer Mechanisms for 1,8-Dihydroxydibenzo[a,h]Phenazine. *J. Phys. Chem. A* **2015**, *119*(4), 681–688.
216. Liu, Y.-H.; Lan, S.-C.; Zhu, C.; Lin, S.-H. Intersystem Crossing Pathway in Quinoline–Pyrazole Isomerism: A Time-Dependent Density Functional Theory Study on Excited-State Intramolecular Proton Transfer. *J. Phys. Chem. A* **2015**, *119*(24), 6269–6274.
217. Yuan, H.; Cao, C. A Substructure-Based Topological Quantum Chemistry Approach for the Estimation of the Ultraviolet Absorption Energy of Some Substituted Linear Conjugated Compounds. *Comput. Theor. Chem.* **2016**, *1096*, 66–73.
218. Huix-Rotllant, M.; Ferre, N. Triplet State Photochemistry and the Three-State Crossing of Acetophenone within Time-Dependent Density-Functional Theory. *J. Chem. Phys.* **2014**, *140*(13), 134305.
219. Huix-Rotllant, M.; Ferre, N. Theoretical Study of the Photochemical Initiation in Nitroxide-Mediated Photopolymerization. *J. Phys. Chem. A* **2014**, *118*(25), 4464–4470.
220. Izgorodina, E. I.; Coote, M. L.; Radom, L. Trends in R–X Bond Dissociation Energies (R = Me, Et, i-Pr, t-Bu; X = H, CH<sub>3</sub>, OCH<sub>3</sub>, OH, F): A Surprising Shortcoming of Density Functional Theory. *J. Phys. Chem. A* **2005**, *109*(33), 7558–7566.
221. Frick, E.; Schweigert, C.; Noble, B. B.; Ernst, H. A.; Lauer, A.; Liang, Y.; Voll, D.; Coote, M. L.; Unterreiner, A. N.; Barner-Kowollik, C. Toward a Quantitative Description of Radical Photoinitiator Structure–Reactivity Correlations. *Macromolecules* **2016**, *49*(1), 80–89.
222. Xiao, P.; Dumur, F.; Graff, B.; Fouassier, J. P.; Gigmès, D.; Lalevée, J. Cationic and Thiol–Ene Photopolymerization upon Red Lights Using Anthraquinone Derivatives as Photoinitiators. *Macromolecules* **2013**, *46*, 6744–6750.
223. Zhang, J.; Hill, N. S.; Lalevée, J.; Fouassier, J.; Zhao, J.; Graff, B.; Schmidt, T. W.; Kable, S. H.; Stenzel, M. H.; Coote, M. L.; et al. Multihydroxy-Anthraquinone Derivatives as Free Radical and Cationic Photoinitiators of Various Photopolymerizations under Green LED. *Macromol. Rapid Commun.* **2018**, *39*(9) 1800172.
224. Luo, J.; Liu, Y.; Yang, S.; Flourat, A. L.; Allais, F.; Han, K. Ultrafast Barrierless Photoisomerization and Strong Ultraviolet Absorption of Photoproducts in Plant Sunscreens. *J. Phys. Chem. Lett.* **2017**, *8*(5), 1025–1030.
225. Mazzone, G.; Quartarolo, A. D.; Russo, N. PDT-Correlated Photophysical Properties of Thienopyrrole BODIPY Derivatives. Theoretical Insights. *Dye. Pigment.* **2016**, *130*, 9–15.
226. Liu, B.; Lim, C. H.; Miyake, G. M. Visible-Light-Promoted C–S Cross-Coupling via Intermolecular Charge Transfer. *J. Am. Chem. Soc.* **2017**, *139*(39), 13616–13619.
227. Kozłowski, P. M.; Garabato, B. D.; Lodowski, P.; Jaworska, M. Photolytic Properties of Cobalamins: A Theoretical Perspective. *Dalt. Trans.* **2016**, *45*(11), 4457–4470.
228. Ding, B. W.; Liu, Y. J. Bioluminescence of Firefly Squid via Mechanism of Single Electron-Transfer Oxygenation and Charge-Transfer-Induced Luminescence. *J. Am. Chem. Soc.* **2017**, *139*(3), 1106–1119.
229. Tsuji, F. I. Bioluminescence Reaction Catalyzed by Membrane-Bound Luciferase in the “Firefly Squid,” *Watasenia Scintillans*. *Biochim. Biophys. Acta Biomembr.* **2002**, *1564*(1), 189–197.



230. Ashwood, B.; Jockusch, S.; Crespo-Hernández, C. E. Excited-State Dynamics of the Thiopurine Prodrug 6-Thioguanine: Can N9-Glycosylation Affect Its Phototoxic Activity? *Molecules* **2017**, *22*(3), 379.
231. De Simone, B. C.; Mazzone, G.; Pirillo, J.; Russo, N.; Sicilia, E. Halogen Atom Effect on the Photophysical Properties of Substituted Aza-BODIPY Derivatives. *Phys. Chem. Chem. Phys.* **2017**, *19*(3), 2530–2536.
232. McNaught, A. D.; Wilkinson, A. *IUPAC. Compendium of Chemical Terminology*, 2nd ed.; Blackwell Scientific Publications, 1997.
233. Golden, J. H.; Facendola, J. W.; Sylvinson, D. M. R.; Baez, C. Q.; Djurovich, P. I.; Thompson, M. E. Boron Dipyrldylmethene (DIPYR) Dyes: Shedding Light on Pyridine-Based Chromophores. *J. Org. Chem.* **2017**, *82*(14), 7215–7222.
234. Lorenz, T.; Crumbach, M.; Eckert, T.; Lik, A.; Helten, H. Poly(p-Phenylene Iminoborane): A Boron–Nitrogen Analogue of Poly(p-Phenylene Vinylene). *Angew. Chemie Int. Ed.* **2017**, *56*(10), 2780–2784.
235. Margar, S. N.; Rhyman, L.; Ramasami, P.; Sekar, N. Fluorescent Difluoroboron-Curcumin Analogs: An Investigation of the Electronic Structures and Photophysical Properties. *Spectrochim. Acta A Mol. Biomol. Spectrosc.* **2016**, *152*, 241–251.
236. Cabrera-González, J.; Viñas, C.; Haukka, M.; Bhattacharyya, S.; Gierschner, J.; Núñez, R. Photoluminescence in Carborane–Stilbene Triads: A Structural, Spectroscopic, and Computational Study. *Chem. A Eur. J.* **2016**, *22*(38), 13588–13598.
237. Ferrer-Ugalde, A.; Juárez-Pérez, E. J.; Teixidor, F.; Viñas, C.; Sillanpää, R.; Pérez-Inestrosa, E.; Núñez, R. Synthesis and Characterization of New Fluorescent Styrene-Containing Carborane Derivatives: The Singular Quenching Role of a Phenyl Substituent. *Chem. A Eur. J.* **2012**, *18*(2), 544–553.
238. Weber, L.; Kahlert, J.; Brockhinke, R.; Böhling, L.; Brockhinke, A.; Stammler, H. G.; Neumann, B.; Harder, R. A.; Fox, M. A. Luminescence Properties of C-Diazaborolyl-Ortho-Carboranes as Donor-Acceptor Systems. *Chem. A Eur. J.* **2012**, *18*(27), 8347–8357.
239. Momeni, M. R.; Brown, A. Why Do TD-DFT Excitation Energies of BODIPY/Aza-BODIPY Families Largely Deviate From Experiment? Answers From Electron Correlated and Multireference Methods. *J. Chem. Theory Comput.* **2015**, *11*(6), 2619–2632.
240. Fujikawa, T.; Segawa, Y.; Itami, K. Synthesis, Structures, and Properties of  $\pi$ -Extended Double Helicene: A Combination of Planar and Nonplanar  $\pi$ -Systems. *J. Am. Chem. Soc.* **2015**, *137*(24), 7763–7768.
241. Maier, T. M.; Bahmann, H.; Kaupp, M. Efficient Semi-Numerical Implementation of Global and Local Hybrid Functionals for Time-Dependent Density Functional Theory. *J. Chem. Theory Comput.* **2015**, *11*(9), 4226–4237.
242. Maier, T. M.; Bahmann, H.; Arbuznikov, A. V.; Kaupp, M. Validation of Local Hybrid Functionals for TDDFT Calculations of Electronic Excitation Energies. *J. Chem. Phys.* **2016**, *144*(7), 0–14.
243. Schreiber, M.; Silva-Junior, M. R.; Sauer, S. P. A.; Thiel, W. Benchmarks for Electronically Excited States: CASPT2, CC2, CCSD, and CC3. *J. Chem. Phys.* **2008**, *128*(13), 134110.
244. Silva-Junior, M. R.; Schreiber, M.; Sauer, S. P. A.; Thiel, W. Benchmarks for Electronically Excited States: Time-Dependent Density Functional Theory and Density Functional Theory Based Multireference Configuration Interaction. *J. Chem. Phys.* **2008**, *129*(10), 104103.
245. Zhekova, H.; Krykunov, M.; Autschbach, J.; Ziegler, T. Applications of Time Dependent and Time Independent Density Functional Theory to the First  $\pi$  to  $\Pi^*$  Transition in Cyanine Dyes. *J. Chem. Theory Comput.* **2014**, *10*(8), 3299–3307.

246. Cao, J.; London, G.; Dumele, O.; Von Wantoch Rekowski, M.; Trapp, N.; Ruhlmann, L.; Boudon, C.; Stanger, A.; Diederich, F. The Impact of Antiaromatic Subunits in  $[4n+2]$   $\pi$ -Systems: Bispentalenes with  $[4n+2]$   $\pi$ -Electron Perimeters and Antiaromatic Character. *J. Am. Chem. Soc.* **2015**, *137*(22), 7178–7188.
247. Etienne, T.; Assfeld, X.; Monari, A. Toward a Quantitative Assessment of Electronic Transitions' Charge-Transfer Character. *J. Chem. Theory Comput.* **2014**, *10*(9), 3896–3905.
248. Ji, L.; Edkins, R. M.; Sewell, L. J.; Beeby, A.; Batsanov, A. S.; Fucke, K.; Drafz, M.; Howard, J. A. K.; Moutounet, O.; Ibersiene, F.; et al. Experimental and Theoretical Studies of Quadrupolar Oligothiophene-Cored Chromophores Containing Dimesitylboryl Moieties as  $\pi$ -Accepting End-Groups: Syntheses, Structures, Fluorescence, and One- and Two-Photon Absorption. *Chem. A Eur. J.* **2014**, *20*(42), 13618–13635.
249. Arulmozhiraja, S.; Coote, M. L.; Lu, D.; Salem, G.; Wild, S. B. Origin of the Unusual Ultraviolet Absorption of Arsenicin A. *J. Phys. Chem. A* **2011**, *115*(17), 4530–4534.
250. Samanta, P. K.; Kim, D.; Coropceanu, V.; Brédas, J. L. Up-Conversion Intersystem Crossing Rates in Organic Emitters for Thermally Activated Delayed Fluorescence: Impact of the Nature of Singlet vs Triplet Excited States. *J. Am. Chem. Soc.* **2017**, *139*(11), 4042–4051.
251. Cai, X.; Li, X.; Xie, G.; He, Z.; Gao, K.; Liu, K.; Chen, D.; Cao, Y.; Su, S.-J. “Rate-Limited Effect” of Reverse Intersystem Crossing Process: The Key for Tuning Thermally Activated Delayed Fluorescence Lifetime and Efficiency Roll-off of Organic Light Emitting Diodes. *Chem. Sci.* **2016**, *7*(7), 4264–4275.
252. Gómez-Bombarelli, R.; Aguilera-Iparraguirre, J.; Hirzel, T. D.; Duvenaud, D.; Maclaurin, D.; Blood-Forsythe, M. A.; Chae, H. S.; Einzinger, M.; Ha, D. G.; Wu, T.; et al. Design of Efficient Molecular Organic Light-Emitting Diodes by a High-Throughput Virtual Screening and Experimental Approach. *Nat. Mater.* **2016**, *15*(10), 1120–1127.
253. Valchanov, G.; Ivanova, A.; Tadjer, A.; Chercka, D.; Baumgarten, M. Understanding the Fluorescence of TADF Light-Emitting Dyes. *J. Phys. Chem. A* **2016**, *120*(35), 6944–6955.
254. Chen, X. K.; Zhang, S. F.; Fan, J. X.; Ren, A. M. Nature of Highly Efficient Thermally Activated Delayed Fluorescence in Organic Light-Emitting Diode Emitters: Nonadiabatic Effect Between Excited States. *J. Phys. Chem. C* **2015**, *119*(18), 9728–9733.
255. Zhang, Q.; Kuwabara, H.; Potscavage, W. J.; Huang, S.; Hatae, Y.; Shibata, T.; Adachi, C. Anthraquinone-Based Intramolecular Charge-Transfer Compounds: Computational Molecular Design, Thermally Activated Delayed Fluorescence, and Highly Efficient Red Electroluminescence. *J. Am. Chem. Soc.* **2014**, *136*(52), 18070–18081.
256. Walter, C.; Krämer, V.; Engels, B. On the Applicability of Time-Dependent Density Functional Theory (TDDFT) and Semiempirical Methods to the Computation of Excited-State Potential Energy Surfaces of Perylene-Based Dye-Aggregates. *Int. J. Quantum Chem.* **2017**, *117*(6), 1–14.
257. Weber, W.; Thiel, W. Orthogonalization Corrections for Semiempirical Methods. *Theor. Chem. Ac.* **2000**, *103*(6), 495–506.
258. Huang, S.; Zhang, Q.; Shiota, Y.; Nakagawa, T.; Kuwabara, K.; Yoshizawa, K.; Adachi, C. Computational Prediction for Singlet- and Triplet-Transition Energies of Charge-Transfer Compounds. *J. Chem. Theory Comput.* **2013**, *9*(9), 3872–3877.
259. Qian, H.; Cousins, M. E.; Horak, E. H.; Wakefield, A.; Liptak, M. D.; Aprahamian, I. Suppression of Kasha's Rule as a Mechanism for Fluorescent Molecular Rotors and Aggregation-Induced Emission. *Nat. Chem.* **2017**, *9*(1), 83–87.

260. Escudero, D. Revising Intramolecular Photoinduced Electron Transfer (PET) From First-Principles. *Acc. Chem. Res.* **2016**, *49*(9), 1816–1824.
261. Shepard, S. G.; Fatur, S. M.; Rappé, A. K.; Damrauer, N. H. Highly Strained Iron(II) Polypyridines: Exploiting the Quintet Manifold to Extend the Lifetime of MLCT Excited States. *J. Am. Chem. Soc.* **2016**, *138*(9), 2949–2952.
262. Nobusue, S.; Miyoshi, H.; Shimizu, A.; Hisaki, I.; Fukuda, K.; Nakano, M.; Tobe, Y. Tetracyclopenta[Def]Jkl,Pqr,Vwx]Tetraphenylene: A Potential Tetraradicaloid Hydrocarbon. *Angew. Chem. Int. Ed.* **2015**, *54*(7), 2090–2094.
263. Hu, P.; Lee, S.; Herng, T. S.; Aratani, N.; Gonçalves, T. P.; Qi, Q.; Shi, X.; Yamada, H.; Huang, K. W.; Ding, J.; et al. Toward Tetraradicaloid: The Effect of Fusion Mode on Radical Character and Chemical Reactivity. *J. Am. Chem. Soc.* **2016**, *138*(3), 1065–1077.
264. Lou, Z.; Li, P.; Han, K. Redox-Responsive Fluorescent Probes With Different Design Strategies. *Acc. Chem. Res.* **2015**, *48*(5), 1358–1368.
265. Daday, C.; Curutchet, C.; Sinicropi, A.; Mennucci, B.; Filippi, C. Chromophore-Protein Coupling beyond Nonpolarizable Models: Understanding Absorption in Green Fluorescent Protein. *J. Chem. Theory Comput.* **2015**, *11*(10), 4825–4839.
266. Wu, Q.; Zhang, T.; Peng, Q.; Wang, D.; Shuai, Z. Aggregation Induced Blue-Shifted Emission—The Molecular Picture From a QM/MM Study. *Phys. Chem. Chem. Phys.* **2014**, *16*(12), 5545–5552.
267. Johnson, L. E.; Dalton, L. R.; Robinson, B. H. Optimizing Calculations of Electronic Excitations and Relative Hyperpolarizabilities of Electrooptic Chromophores. *Acc. Chem. Res.* **2014**, *47*(11), 3258–3265.
268. Pescitelli, G.; Bruhn, T. Good Computational Practice in the Assignment of Absolute Configurations by TDDFT Calculations of ECD Spectra. *Chirality* **2016**, *28*, 466–474.
269. Longhi, G.; Castiglioni, E.; Koshoubu, J.; Mazzeo, G.; Abbate, S. Circularly Polarized Luminescence: A Review of Experimental and Theoretical Aspects. *Chirality* **2016**, *28*, 696–707.
270. Avila Ferrer, F. J.; Cerezo, J.; Soto, J.; Improta, R.; Santoro, F. First-Principle Computation of Absorption and Fluorescence Spectra in Solution Accounting for Vibronic Structure, Temperature Effects and Solvent Inhomogenous Broadening. *Comput. Theor. Chem.* **2014**, *1040–1041*, 328–337.
271. Rozzi, C. A.; Falke, S. M.; Spallanzani, N.; Rubio, A.; Molinari, E.; Brida, D.; Maiuri, M.; Cerullo, G.; Schramm, H.; Christoffers, J.; et al. Quantum Coherence Controls the Charge Separation in a Prototypical Artificial Light Harvesting System. *Nat. Commun.* **2013**, *4*, 1602–1607.
272. Perdew, J. P.; Zunger, A. Self-Interaction Correction to Density-Functional Approximations for Many-Electron Systems. *Phys. Rev. B* **1981**, *23*(10), 5048–5079.
273. Santhanamoorthi, N.; Lo, C. M.; Jiang, J. C. Molecular Design of Porphyrins for Dye-Sensitized Solar Cells: A DFT/TDDFT Study. *J. Phys. Chem. Lett.* **2013**, *4*(3), 524–530.
274. Karthikeyan, S.; Lee, J. Y. Zinc-Porphyrin Based Dyes for Dye-Sensitized Solar Cells. *J. Phys. Chem. A* **2013**, *117*(42), 10973–10979.
275. Guido, C. A.; Knecht, S.; Kongsted, J.; Mennucci, B. Benchmarking Time-Dependent Density Functional Theory for Excited State Geometries of Organic Molecules in Gas-Phase and in Solution. *J. Chem. Theory Comput.* **2013**, *9*(5), 2209–2220.
276. Sousa, C.; De Graaf, C.; Rudavskiy, A.; Broer, R.; Tatchen, J.; Etinski, M.; Marian, C. M. Ultrafast Deactivation Mechanism of the Excited Singlet in the Light-Induced Spin Crossover of [Fe(2,2-Bipyridine)<sub>3</sub>]<sup>2+</sup>. *Chem. A Eur. J.* **2013**, *19*(51), 17541–17551.

277. Cerezo, J.; Zúñiga, J.; Requena, A.; Ávila Ferrer, F. J.; Santoro, F. Harmonic Models in Cartesian and Internal Coordinates to Simulate the Absorption Spectra of Carotenoids at Finite Temperatures. *J. Chem. Theory Comput.* **2013**, *9*(11), 4947–4958.
278. Long, L.; Zhou, L.; Wang, L.; Meng, S.; Gong, A.; Du, F.; Zhang, C. A Coumarin-Based Fluorescent Probe for Biological Thiols and Its Application for Living Cell Imaging. *Org. Biomol. Chem.* **2013**, *11*(47), 8214.
279. Baiardi, A.; Bloino, J.; Barone, V. General Time Dependent Approach to Vibronic Spectroscopy Including Franck–Condon, Herzberg–Teller, and Duschinsky Effect. *J. Chem. Theory Comput.* **2013**, *9*(9), 4097–4115.
280. Small, G. J. Herzberg–Teller Vibronic Coupling and the Duschinsky Effect. *J. Chem. Phys.* **1971**, *54*(8), 3300–3306.
281. De Mitri, N.; Monti, S.; Prampolini, G.; Barone, V. Absorption and Emission Spectra of a Flexible Dye in Solution : A Computational Time-Dependent Approach. *J. Chem. Theory Comput.* **2013**, *9*, 4507–4516.
282. Li, Z.; Suo, B.; Zhang, Y.; Xiao, Y.; Liu, W. Combining Spin-Adapted Open-Shell TD-DFT With Spin–Orbit Coupling. *Mol. Phys.* **2013**, *111*(24), 3741–3755.
283. Li, Z.; Liu, W. Critical Assessment of TD-DFT for Excited States of Open-Shell Systems: I. Doublet-Doublet Transitions. *J. Chem. Theory Comput.* **2016**, *12*(1), 238–260.
284. Li, Z.; Liu, W. Critical Assessment of Time-Dependent Density Functional Theory for Excited States of Open-Shell Systems: II. Doublet-Quartet Transitions. *J. Chem. Theory Comput.* **2016**, *12*, 2517–2527.
285. Suo, B.; Shen, K.; Li, Z.; Liu, W. Performance of TD-DFT for Excited States of Open-Shell Transition Metal Compounds. *J. Phys. Chem. A* **2017**, *121*, 3929–3942.
286. Fan, D.; Yi, Y.; Li, Z.; Liu, W.; Peng, Q.; Shuai, Z. Solvent Effects on the Optical Spectra and Excited-State Decay of Triphenylamine-Thiadiazole With Hybridized Local Excitation and Intramolecular Charge Transfer. *J. Phys. Chem. A* **2015**, *119*, 5233–5240.
287. Zhang, C.; Yuan, D.; Guo, Y.; Li, S. Efficient Implementation of Local Excitation Approximation for Treating Excited States of Molecules in Condensed Phase. *J. Chem. Theory Comput.* **2014**, *10*(12), 5308–5317.
288. Milanese, J. M.; Provorse, M. R.; Alameda, E.; Isborn, C. M. Convergence of Computed Aqueous Absorption Spectra With Explicit Quantum Mechanical Solvent. *J. Chem. Theory Comput.* **2017**, *13*(5), 2159–2171.
289. Martínez-Fernández, L.; Pepino, A. J.; Segarra-Martí, J.; Jovaišaitė, J.; Vaya, I.; Nenov, A.; Markovitsi, D.; Gustavsson, T.; Banyasz, A.; Garavelli, M.; et al. Photo-physics of Deoxycytidine and 5-Methyldeoxycytidine in Solution: A Comprehensive Picture by Quantum Mechanical Calculations and Femtosecond Fluorescence Spectroscopy. *J. Am. Chem. Soc.* **2017**, *139*(23), 7780–7791.
290. Szabla, R.; Kruse, H.; Šponer, J.; Góra, R. W. Water–Chromophore Electron Transfer Determines the Photochemistry of Cytosine and Cytidine. *Phys. Chem. Chem. Phys.* **2017**, *19*(27), 17531–17537.
291. Li, Q.; Mennucci, B.; Robb, M. A.; Blancafort, L.; Curutchet, C. Polarizable QM/MM Multiconfiguration Self-Consistent Field Approach With State-Specific Corrections: Environment Effects on Cytosine Absorption Spectrum. *J. Chem. Theory Comput.* **2015**, *11*(4), 1674–1682.
292. Spata, V. A.; Matsika, S. Bonded Excimer Formation in  $\pi$ -Stacked 9-Methyladenine Dimers. *J. Phys. Chem. A* **2013**, *117*(36), 8718–8728.
293. Fang, H.; Kim, Y. Excited-State Tautomerization of 7-Azaindole in Nonpolar Solution: A Theoretical Study Based on Liquid-Phase Potential Surfaces of Mean Force. *J. Chem. Theory Comput.* **2013**, *9*(8), 3557–3566.

294. Zuehlsdorff, T. J.; Haynes, P. D.; Payne, M. C.; Hine, N. D. M. Predicting Solvatochromic Shifts and Colours of a Solvated Organic Dye: The Example of Nile Red. *J. Chem. Phys.* **2017**, *146*(12), 124504.
295. Zuehlsdorff, T. J.; Haynes, P. D.; Hanke, F.; Payne, M. C.; Hine, N. D. M. Solvent Effects on Electronic Excitations of an Organic Chromophore. *J. Chem. Theory Comput.* **2016**, *12*(4), 1853–1861.
296. Chang, X. P.; Li, C. X.; Xie, B. B.; Cui, G. Photoprotection Mechanism of P-Methoxy Methylcinnamate: A CASPT2 Study. *J. Phys. Chem. A* **2015**, *119*(47), 11488–11497.
297. Charlton, R. J.; Fogarty, R.; Bogatko, S.; Horsfield, A. P.; Haynes, P. D.; Hine, N. D. M. Implicit and Explicit p-Terphenyl Host Effects on Excitons in Pentacene Derivatives. *J. Chem. Phys.* **2018**, *148*, 104108.
298. Marazzi, M.; Gattuso, H.; Monari, A. Nile Blue and Nile Red Optical Properties Predicted by TD-DFT and CASPT2 Methods: Static and Dynamic Solvent Effects. *Theor. Chem. Acc.* **2016**, *135*(3), 1–11.
299. Mewes, J. M.; You, Z. Q.; Wormit, M.; Kriesche, T.; Herbert, J. M.; Dreuw, A. Experimental Benchmark Data and Systematic Evaluation of Two a Posteriori, Polarizable-Continuum Corrections for Vertical Excitation Energies in Solution. *J. Phys. Chem. A* **2015**, *119*(21), 5446–5464.
300. Isborn, C. M.; Mar, B. D.; Curchod, B. F. E.; Tavernelli, I.; Martínez, T. J. The Charge Transfer Problem in Density Functional Theory Calculations of Aqueously Solvated Molecules. *J. Phys. Chem. B* **2013**, *117*(40), 12189–12201.
301. Tomasi, J.; Mennucci, B.; Cammi, R. Quantum Mechanical Continuum Solvation Models. *Chem. Rev.* **2005**, *105*(8), 2999–3093.
302. Caricato, M. A Comparison Between State-Specific and Linear-Response Formalisms for the Calculation of Vertical Electronic Transition Energy in Solution With the CCSD-PCM Method. *J. Chem. Phys.* **2013**, *139*(4), 044116.
303. Li, X. Y. An Overview of Continuum Models for Nonequilibrium Solvation: Popular Theories and New Challenge. *Int. J. Quantum Chem.* **2015**, *115*(11), 700–721.
304. Fukuda, R.; Ehara, M. Electronic Excitation of Molecules in Solution Calculated Using the Symmetry-Adapted Cluster-Configuration Interaction Method in the Polarizable Continuum Model. *AIP Conf. Proc.* **2015**, 1702.
305. Caricato, M. A Corrected-Linear Response Formalism for the Calculation of Electronic Excitation Energies of Solvated Molecules With the CCSD-PCM Method. *Comput. Theor. Chem.* **2014**, *1040–1041*, 99–105.
306. Mewes, J. M.; Herbert, J. M.; Dreuw, A. On the Accuracy of the General, State-Specific Polarizable-Continuum Model for the Description of Correlated Ground- and Excited States in Solution. *Phys. Chem. Chem. Phys.* **2017**, *19*(2), 1644–1654.
307. Hill, N. S.; Coote, M. L. Internal Oriented Electric Fields as a Strategy for Selectively Modifying Photochemical Reactivity. *J. Am. Chem. Soc.* **2018**, *140*, 17800–17804.

## Further reading

308. Amatatsu, Y. Theoretical Design of a Light-Driven Molecular Rotary Motor with Low Energy Helical Inversion: 9-(5-Methyl-2-Phenyl-2-Cyclopenten-1-Ylidene)-9H-Fluorene. *J. Phys. Chem. A* **2011**, *115*(46), 13611–13618.
309. Amatatsu, Y. Theoretical Study of Topographical Features Around the Conical Intersections of Fluorene-Based Light-Driven Molecular Rotary Motor. *J. Phys. Chem. A* **2013**, *117*(17), 3689–3696.
310. Amatatsu, Y. Theoretical Study of Topographical Features around the Conical Intersections of 9-(2-Cyclopenten-1-Ylidene)-9H-Fluorene. *J. Phys. Chem. A* **2013**, *117*(47), 12529–12539.

311. Amatatsu, Y. Theoretical Study on Conformational-Dependent Photochemical Behaviors of a Fluorene-Based Light-Driven Molecular Rotary Motor. *Bull. Chem. Soc. Jpn.* **2015**, *88*(10), 1417–1430.
312. Amatatsu, Y. Theoretical Study on the Torsional Direction of Simple Ethylenoids after Electronic Relaxation at the Conical Intersection in the Cis-Trans Photoisomerization. *Chem. Phys. Lett.* **2015**, *631–632*, 47–53.
313. Adamska, L.; Nayyar, I.; Chen, H.; Swan, A. K.; Oldani, N.; Fernandez-Alberti, S.; Golder, M. R.; Jasti, R.; Doorn, S. K.; Tretiak, S. Self-Trapping of Excitons, Violation of Condon Approximation, and Efficient Fluorescence in Conjugated Cycloparaphenylenes. *Nano Lett.* **2014**, *14*(11), 6539–6546.

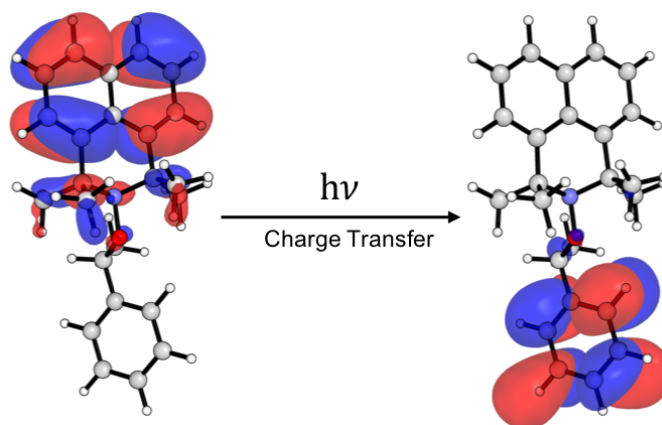
## 2.3 Publication 2

### Computational Tools for Nitroxide Design

Nicholas S. Hill, Benjamin B. Noble, Fergus J. M. Rogers, Alfred K. K. Fung, Michelle L. Coote

Editors: Olivier Ouari and Didier Gigmes

in *Nitroxides: Synthesis, Properties and Applications* 2020



This publication is a peer-reviewed manuscript published as a book chapter in *Nitroxides: Synthesis, Properties and Applications*. This chapter was a collaborative effort with several other group members, and my contribution is the section on how to model photochemically-active nitroxides and their electron paramagnetic resonance properties. Prof. Michelle Coote assisted with the direction of the review and corrected my drafts.

### Statement of Contribution

This thesis is submitted as a Thesis by Compilation in accordance with [https://policies.anu.edu.au/pp/document/ANUP\\_003405](https://policies.anu.edu.au/pp/document/ANUP_003405)

I declare that the research presented in this Thesis represents original work that I carried out during my candidature at the Australian National University, except for contributions to multi-author papers incorporated in the Thesis where my contributions are specified in this Statement of Contribution.

Title: Computational Tools for Nitroxide Design

Authors: Nicholas S. Hill, Benjamin B. Noble, Fergus J. M. Rogers, Alfred K. K. Fung, Michelle L. Coote


Publication outlet: Nitroxides: Synthesis, Properties and Applications

Current status of paper: Accepted

Contribution to paper: This chapter was a collaborative effort with several other group members, and my contribution is the section on how to model photochemically-active nitroxides and their electron paramagnetic resonance properties. I also compiled the sections written by co-authors into a single manuscript for submission

Senior author or collaborating authors endorsement: Michelle Coote

Nicholas Hill



20/01/2020

Candidate - Print Name

Signature

Date

#### Endorsed

Michelle Coote



20/01/2020

Primary Supervisor – Print Name

Signature

Date



Delegated Authority – Print Name



Signature

20/01/2020

Date



# Chapter 6

## Computational Tools for Nitroxide Design

**Nicholas S. Hill, Benjamin B. Noble, Fergus J. M. Rogers, Alfred K. K. Fung and Michelle L. Coote\***

*\*ARC Centre of Excellence for Electromaterials Science, Research School of Chemistry, Australian National University, Canberra ACT 2601, Australia*

\*Corresponding author: michelle.coote@anu.edu.au

### Table of Contents

ABSTRACT.....	2
6.1 INTRODUCTION.....	3
6.2 MODELLING COMPLEX SPIN SYSTEMS.....	3
6.2.2 Multireference Methods.....	6
6.2.3 Single-Reference Methods for Strongly Correlated Systems.....	7
6.2.4 Selected Applications.....	8
6.2.5 Concluding remarks.....	10
6.3 COMPUTATION OF ELECTRON PARAMAGNETIC RESONANCE SPECTRA.....	11
6.3.2 Simulating EPR Spectra.....	14
6.3.3 Selected Applications.....	15
6.4 PREDICTING OXIDATION POTENTIALS.....	16
6.4.1 Definitions and Key Equations.....	18
6.4.2 Electronic Structure Methods and Gas-Phase IEs and EAs.....	20
6.4.3 Solvent Effects and Redox Potentials.....	22
6.4.4 Selected Applications.....	24
6.5 MODELLING NITROXIDE MEDIATED POLYMERISATIONS.....	29
6.5.1 Methodology.....	30
6.5.2 Selected Applications.....	30
6.5 STUDYING PHOTOACTIVE NITROXIDES.....	33
6.6.1 Methodological Aspects.....	34
6.6.2 Selected Applications.....	36
6.6.3 Concluding remarks.....	37
6.7 FURTHER APPLICATIONS.....	37
ACKNOWLEDGMENTS.....	38
REFERENCES AND NOTES.....	38

## **Abstract**

Computational tools for modelling nitroxide radical chemistry are outlined and illustrated through a series of case studies. Different types of application raise different problems. Herein we outline and assess the computational methods available for modelling high spin systems, predicting EPR hyperfine coupling constants, redox potentials, alkoxyamine dissociation equilibria and photochemical processes. While high spin systems and excited states are best modelled with complex multi-reference methods incorporating static and dynamic correlation, there is a growing family of more economical approaches that can often achieve an acceptable level of accuracy. Redox potentials and alkoxyamine dissociation equilibria require only single reference methods, albeit at a high level of theory, but the accurate treatment of solvation remains an ongoing challenge. Modelling EPR requires a range specialist techniques and basis sets to accurately capture core correlation. Through the case studies presented here we not only show that accurate and useful quantitative predictions are possible, but introduce a wide range of complementary tools for enhancing our qualitative understanding of structure-reactivity trends.

## 6.1 Introduction

Nitroxides are a class of molecules that exhibit a wide range of chemical properties, the most significant and useful of which is their stability as radical species. This radical stability has been utilised for a wide range of chemical applications, including nitroxide-mediated polymerisations, as fluorescent probes, and in electron paramagnetic resonance spectroscopy. They are also able to undergo reversible oxidation and reduction, which has been harnessed in batteries, solar cells, synthesis and even as medicinal antioxidants. The many and various properties of nitroxides and their applications have been explored throughout this book; this chapter will focus primarily on the methods and considerations for simulating their properties and reactivity.

Computational chemistry is becoming an increasingly powerful tool for modern chemists, as require theoretical insights are often invaluable when rationalising experimental results. Throughout the chapter, emphasis has been placed on utilising modern methods, software packages, and literature references to provide an up-to-date overview of how a new computational chemist may begin to tackle the challenges of nitroxide chemistry. Many of the computational lessons taught in this chapter are generally applicable to other areas of organic chemistry; the challenge often with nitroxides is that many of their properties that may be otherwise calculated in isolation are often coupled, for example combining nitroxide-mediated polymerisations (NMP), with their dependence on accurate kinetic parameters, with photochemistry, and the difficulties when modelling excited states, is necessary to study photo-NMP.

To that end, for type of model chemistry, different theoretical considerations are explored, such as single- vs multi-reference and combinations thereof, and the impact of different basis sets. Quantitative and qualitative results are also discussed throughout, as are the ability for different approaches to achieve them, and wherever possible recommendations are made. We start with a discussion of the methods needed to model complex spin systems, for which the challenge is the accurate treatment of static correlation without incurring the massive costs of extensive multi-reference calculations. We then examine the methods needed to simulate EPR spectra, which among other things requires specialised basis sets for the correct treatment of core correlation. We then turn to redox chemistry, where the focus shifts to the high-level single reference methods needed for treating dynamic correlation. For redox chemistry in particular, the treatment of solvent effects also becomes a major potential source of error, due to the participation of charged species. We then examine alkoxyamine dissociation in the context of nitroxide mediated polymerization, which uses similar methods to redox chemistry but quite different strategies in structure-reactivity analysis. Finally, we examine methods for the treatment of excited states, particularly in the context of photo-NMP.

## 6.2 Modelling Complex Spin Systems

Many problems of interest are not adequately handled by conventional methods. Important examples involving nitroxides can be found in transition metal complexes, polyradicals, many excited-states, as well as the intermediate structures encountered in bond-dissociation events.<sup>1-5</sup> These cases are said to be “strongly correlated”, meaning that methods based on a *single reference* wavefunction are a poor approximation of the exact solution. Numerous

strategies for dealing with these problems are nonetheless available to the modern chemist, but the functionality is often peculiar and system dependent. We discuss the general theory supported by some recent applications here.

### 6.2.1 Dynamic versus Static Correlation Energy

Quantum-chemical methods differ in their accuracy and complexity primarily through their approaches to modelling the correlation energy ( $E_c$ ). In the crudest sense, correlation is the error arising from the Hartree-Fock (HF) approximation to the exact, non-relativistic, time-independent Schrodinger equation within the Born-Oppenheimer approximation:<sup>6,7</sup>

$$E_c = E - E_0 \quad (1)$$

where  $E$  is the exact energy of the system, and  $E_0$  is the energy of the corresponding (HF) wavefunction. Correlation has a somewhat different definition in density functional theory (DFT), however the implications are similar.<sup>8</sup>

In the HF regime, the many-body wavefunction is reduced to a Slater determinant  $|\Psi\rangle$  of one-electron molecular spin-orbitals (MO). Each MO is “independent”, experiencing only the average field generated by all the electrons in the system, such that the explicit many-body nature of the problem is substituted for a coupled set of soluble one-body problems. Indeed, it is from this model that we derive the familiar MO conception of molecular electronic structure.

The ground-state solution to the resultant set of HF equations provides an upper-bound to the exact ground-state energy such that the error,  $E_c$ , is always negative; although this is not necessarily true of the excited states. In general, the complex MOs cannot not be determined analytically, so a finite basis set of  $N$  basis functions or atomic orbitals (AO) is introduced, and the MOs are expanded in terms of these. Since the HF equations are nonlinear, the AOs are iteratively mixed together to construct the lowest energy set of  $N$  MOs (the self-consistent field method) such that, for an  $M$  electron HF system,  $M$  MOs are completely occupied and  $N - M$  are empty or virtual. In this sense HF is a single-reference approximation, as a Slater determinant is evidently based on only one “configuration” of occupied MOs.

Correlation energy can be systematically recovered by expanding the total ground-state wavefunction  $|\Phi\rangle$ , as a linear combination of the HF reference  $|\Psi\rangle$ , and its “excited” configurations (configuration interaction or CI):

$$|\Phi_0\rangle = c_0|\Psi_0\rangle + \sum_{i>a}^m c_a^i|\Psi_a^i\rangle + \sum_{i,j>a,b}^m c_{a,b}^{i,j}|\Psi_{a,b}^{i,j}\rangle + \dots \quad (2)$$

where and  $|\Psi_i^a\rangle$ ,  $|\Psi_{i,j}^{a,b}\rangle$  are the singly and doubly excited determinants formed by elevating electrons from occupied ( $i, j$  etc.) to virtual HF MOs ( $a, b$  etc.). The expansion coefficients  $c_n$ , are determined from the CI matrix– an eigenvalue problem – whose solutions correspond to the ground- and excited-states of the system. In the full CI (FCI) limit, where all possible excitations are considered,

the exact correlation energy is recovered completely within the bounds of the basis set. Such a calculation is virtually unfeasible however, as the number of determinants in the CI expansion has factorial dependence on the number of AOs. In practical applications,  $E$  is instead approximated by truncating the expansion or more commonly, by applying perturbation, coupled pair or Green's function theory. For the interested reader, archetypal methods are discussed in Chapter 4 onwards of Ref [6].

Single-reference post-HF and DFT methods deal directly with so-called dynamical correlation, i.e. the error relating to electronic motion. Static correlation, the focus of this section, arises from errors due to the use of a single reference wavefunction, and occurs when there is more than one dominant resonance contributor.<sup>9</sup> A simple but illustrative example is the  $\sigma$ -bond dissociation problem. At the equilibrium geometry, the HF reference consisting of the  $\sigma^2$  configuration, is physically sensible. As the bond is stretched however, the  $(\sigma^*)^2$  configuration becomes increasingly important such that at the dissociation limit, both configurations have equal weight in the ground-state wavefunction. In this case, at least two MO configurations are necessary for a valid description of  $\sigma$ -bond dissociation.

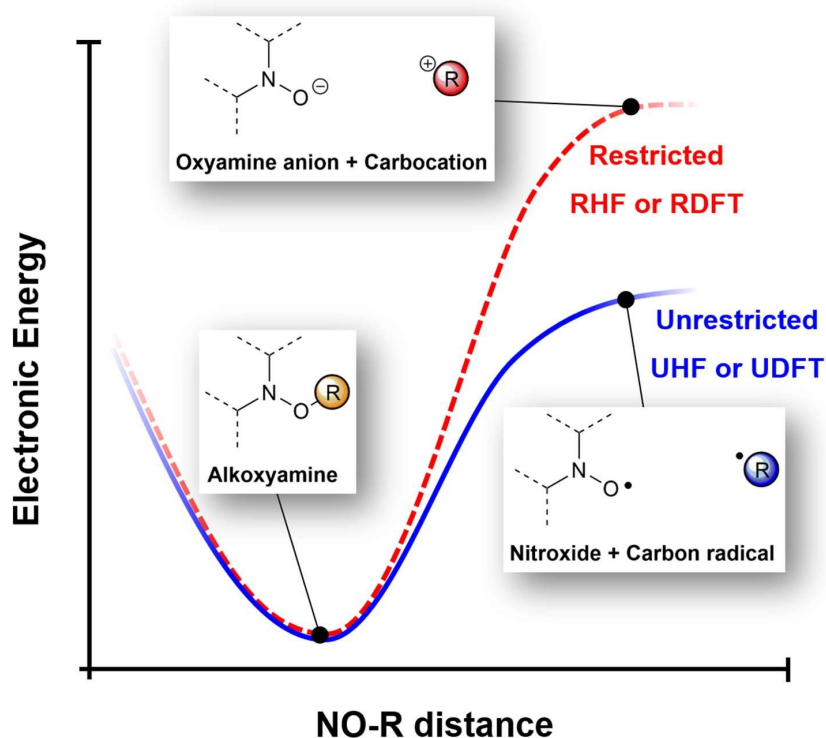


**Figure 6.1.** Idealised potential energy surfaces for NO-R bond dissociation. Restricted theory (RHF and correlated variants, RDFT) uses the same spatial components for both alpha and beta spin orbitals and consequently it cannot describe bond homolysis. In Unrestricted theory (UHF and correlated variants, UDFT) these spatial components are allowed to vary, which provides a better description of homolytic processes (albeit with the introduction spin contamination, see text).

Unlike dynamical correlation, static correlation is recovered only slowly by expansions of the type in equation (2). Efficient treatment of statically correlated

problems therefore requires instead a more general reference than the single-reference wavefunction. Such a wavefunction can be found in the multireference framework, i.e. where the reference is a superposition of two or more MO configurations. In the multi-configurational self-consistent field (MCSCF) method, the multireference generalisation of SCF, MOs and CI coefficients are varied simultaneously in solving for a particular state. In this way, MCSCF could be thought of as the union of HF, where only MOs of a single determinant are varied, and CI, where the expansion coefficients are varied within a basis set of frozen MOs.<sup>10</sup>

### 6.2.2 Multireference Methods.

MCSCF is most commonly encountered in two related formalisms, namely the complete active space self-consistent field (CASSCF) method, and its reduced analogue, restricted active space self-consistent field (RASSCF). In both schemes, the determinants defined for MCSCF are generated by a full CI treatment of an active space, a selection of orbitals generated by an initial HF calculation.<sup>11</sup> CASSCF considers every configuration of the expansion, whilst RASSCF invokes a set of selection criterion to reduce the number of configurations to only the most pursuant contributors. These specifications are denoted  $[n, m]$ -RAS/CASSCF or RAS/CAS( $n, m$ ), where  $n$  and  $m$  are the number of active space electrons and orbitals respectively.

The resultant set of configurations grows aggressively with the size of the active space, so the practical challenge occurs in selecting a computable specification which best represents the chemistry of the problem. As a minimum, this must include all MOs that are expected to change significantly during some transformation, as well as those which are partially occupied.<sup>12</sup> Orbital point group symmetry should also be considered especially in the calculation of spectroscopic properties where selection rules are important; occasionally Rydberg orbitals might also be necessary.<sup>13</sup> All these considerations mean CAS/RASSCF is rather esoteric for the uninitiated, but we stress that orbital selection, which we do not flesh out here, is extremely important.<sup>14, 15</sup> Introductory guides can be found in chapter 4.6 of Ref 7 or chapter 14 of Ref 10.

Like HF, the multireference family is populated by a very large variety of dynamically correlated methods. Common examples include variations on multireference configuration interaction (MRCI) such as difference dedicated configuration interaction (DDCI),<sup>16-21</sup> multireference Moller-Plesset (MRMP $n$ ) and restricted/complete active space perturbation theory (RAS/CASPT $n$ ),<sup>22, 23</sup> as well as multireference coupled cluster theory (MRCC) among others.<sup>24-26</sup> CASPT2, being the most affordable option, is of course most often encountered in the literature, although it should be noted that perturbation theory in general is susceptible to spurious issues, such as intruder states, which are not always foreseeable in the reference wavefunction.<sup>27-30</sup> Other methods have more limited application, but may be the only options capable of satisfactory outcomes for especially difficult problems.

RASSCF and many dynamical correlation methods are not size-consistent, i.e. the energy of a non-interacting dimer is the higher than the sum of each monomer considered in isolation. For large problems where this is a concern – typically more than 100 electrons – specialized methods such as second-order

N-Electron Valence State Perturbation Theory (NEVPT2) and variations of MRCC ought to be considered.<sup>31-33</sup> This said, CASPT2 and MRCI are nearly size-consistent, and so are nonetheless popular options for investigations of multireference nitroxides of moderate size, such as the biradicals studied by Angeli et al.<sup>32</sup> and the many polyradicals modelled by Barone et al.<sup>34-42</sup>

### 6.2.3 Single-Reference Methods for Strongly Correlated Systems

For predicting ground state multiplicities and estimating useful properties such as singlet-triplet (S-T) energy gaps, one may appeal to one of several single reference methods which are considerably cheaper.<sup>43</sup> These tend to operate under a similar *modus operandi*, i.e. a strongly correlated low-spin state, such as an open-shell singlet, is estimated by projection or spin excitation from a much less correlated high-spin reference, typically a triplet, quintet etc. for which the single reference approximation is valid.

The simplest approach can be found in broken-symmetry density functional theory (BS-DFT),<sup>44-47</sup> a method which works within the unrestricted Kohn-Sham formalism (UDFT), where the spatial components of MOs are allowed to differ. Owing to its computational efficiency, UDFT is often a first approximation for modelling open-shell systems. However, unrestricted wavefunctions suffer from a serious issue known as the spin contamination error, the artificial mixing of higher spin states into the wavefunction in such a way that the total spin is greater than its formal value.<sup>48</sup> Strongly correlated problems tend to be highly spin-contaminated, so a direct UDFT calculation on for instance, an open-shell singlet, will certainly be erroneous.<sup>49</sup> The BS-DFT method resolves this issue via spin projection.<sup>44-47</sup> In the simplest case, a contaminated BS singlet is referenced to the negligibly contaminated triplet state which results in the following expression for the vertical S-T gap,<sup>50</sup>

$$\Delta_{S-T}^{vert} = \frac{2(E_{BS} - E_T)}{\langle S_T^2 \rangle - \langle S_{BS}^2 \rangle} \quad (3)$$

such that the true singlet energy can be approximated as,

$$E_S = \Delta_{S-T}^{vert} + E_T \quad (4)$$

where  $E$  is the electronic energy of the contaminated BS singlet,  $E$  is the energy of the triplet, at the BS singlet geometry, and  $\langle S \rangle$  and  $\langle S \rangle$  are the total spin eigenvalues of the BS singlet and triplet states respectively. Numerical values for these quantities are printed in the output of most quantum chemistry codes. The adiabatic S-T gap may be written as,

$$\Delta_{S-T}^{adia} = \frac{2(E_{BS^i} - E_{T^i})}{\langle S_{T^i}^2 \rangle - \langle S_{BS^i}^2 \rangle} + E_{T^i} - E_{T^j} \quad (5)$$

or in its approximate form,

$$\Delta_{S-T}^{adia,approx} = \frac{2(E_{BS^i} - E_{T^j})}{\langle S_{T^j}^2 \rangle - \langle S_{BS^i}^2 \rangle} \quad (6)$$

where  $i$  and  $j$  indicate the optimised geometries of the BS singlet and triplet states respectively. A suitable guess for the BS singlet can be accomplished by mixing the HOMO and LUMO orbitals of a closed-shell UDFT singlet (e.g., by invoking the Guess=Mix keyword in Gaussian) thus breaking the spin symmetry of the singlet wavefunction. This method is not limited to singlet-triplet couples and a generalisation can be made for any low-spin, high-spin dimer.<sup>51-56</sup> The quality of the projection is quite sensitive to one's level of theory.

Global hybrid functionals such as B3LYP, BMK and M06-2X are recommended,<sup>57,58</sup> although we tend to advise use of the latter for more reliable treatment of organic radicals. Adiabatic gaps are typically improved through the inclusion of zero-point corrections to the energy terms.

A more robust strategy for ground-state calculations is the spin-flip (SF) ansatz of Krylov et al.<sup>59</sup> These methods involve an excitation operator whose action is to perform a spin-flip type excitation of an electron from the reference wavefunction thus changing its multiplicity.<sup>59</sup> In simple terms, a set of low-spin configurations, constituting the strongly correlated problem, are spawned by flipping unpaired electrons in the frozen basis of MOs constituting a high-spin reference. The quality of the resultant wavefunction hinges on the quality of the reference, which in the single reference framework can be systematically improved forming a familiar hierarchy, i.e. SF-SCF/SF-DFT through to SF-MP2 and high-order SF-EOM-CC etc.<sup>60-64</sup> The SF operator is perfectly compatible with a UHF, although a restricted open-shell (ROHF) reference, where each electron pair is confined to a pair of degenerate MOs, has been shown to benefit predictive power.<sup>65</sup> Several "spin-correct" techniques, that attempt to rectify the spin-contamination problem, have been proposed in recent literature.<sup>66-68</sup>

Another popular addition to the single reference family is the RAS-SF approach of Casanova et al.<sup>69</sup> In this method, the active space is defined under the usual RAS specifications for a ROHF high-spin reference. A larger and more general set of determinants is subsequently generated, describing a wavefunction that is spin-complete and size-consistent.<sup>70</sup> One particular advantage of RAS partitioning is in its regular treatment of polyradicals of arbitrary degree, as these ordinarily pose something of a challenge to single reference methods. Like RASSCF however, active space specification has great influence on the quality of the wavefunction, not neglecting the exponential scaling in the number of determinants generated (although scaling with molecular size with a fixed active space is manageable). Recent implementations of RAS-SF also permit a degree of orbital relaxation, admitting this scheme to the multireference family of methods.

#### 6.2.4 Selected Applications

**Case Study 1: The role of the multiconfigurational character of nitronyl-nitroxide in the singlet-triplet energy gap of its diradicals.**<sup>41</sup> This recent publication by the Barone group illustrates some of the caveats that must be considered when applying a multi-reference solution to a typical problem. In this case, the effect of the active space on the quality of calculated singlet-triplet (S-T) energy gaps for three nitronyl-nitroxide (NN) based diradicals (Figure 6.1) were assessed for the multireference, dynamically correlated DDCI method and its simplified variant, DDCI2. ROHF/6-311G(d) calculations of the triplet states for each species were initially performed on their X-ray crystal structures in the



software package GAMESS. For each diradical, an Ad hoc fragmentation was then undertaken, and the dimensionality of the problem for the multi-reference component was reduced to the most pertinent features (shown as blue in Figure 6.2), after which the active space was defined. DDCI calculations were then performed in the BALOO code, an inhouse program developed independently by Barone for these problems.

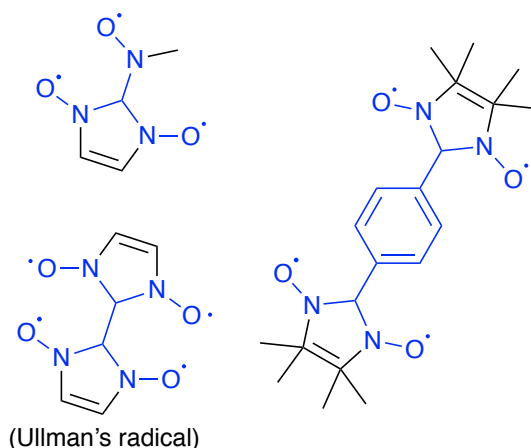


**Figure 6.2.** Test set in Ref <sup>41</sup>. Blue indicates the fragments, whose MOs are considered in the construction of the DDCI space.

Several interesting observations can be made from this work. For reliable treatment of polyradicals involving an NN radical, it was speculated that the CAS reference must include at least three orbitals and electrons for satisfactory agreement with experiment, i.e. one for each N-O fragment and a third for the central carbon. Thus, S-T gaps for Ullmann's diradical (see Figure 6.2), was only accurately approximated (i.e. with transition frequencies between 90 - 110% of experimental values) with a CAS(6,6) reference involving the LUMO+2 to HOMO-3 MOs, as these encapsulate both features as well as the linker. The minimal CAS(2,2) reference involving only the magnetic HOMO and HOMO1 orbitals was woefully inadequate in every example, resulting in transition frequencies of 10-30% of experiment. Unsurprisingly, DDCI2 was found to be less reliable than DDCI with the low-quality CAS(2,2) reference. However, the performance became comparable when the (6,6) active space was included. This highlights one of the many subtleties of multi-reference calculations, namely, the balance between a more complete (read larger) active space, and a more rigorous (read reliable) method for a given allocation of computational resources.

**Case Study 2: Spin coupling interactions in C=C or B-B-cored porphyrin-mimetic graphene patch nitroxide diradicals.**<sup>71</sup> A useful example of both single and multireference methodologies can be found in this recent article on the S-T energy gaps for an isomeric family of C=C, and B-B coupled porphyrin bridged nitroxide diradicals (Figure 6.3). These larger systems are practically out of reach for most multi-reference methods, but typical of the problems quantified with single-reference approximations in the literature. In this case, gas phase BS singlet and triplet structures were first optimized in Gaussian with UB3LYP/6-311G(d,p). BS-DFT predictions of the adiabatic S-T gap were then estimated using Yamaguchi's approximate expression, with subsequent calculations of the SF-DFT energies obtained from single point SF-

PBE50/6311G(d,p) and SF-5050/6-311G(d,p) calculations performed in Q-Chem.

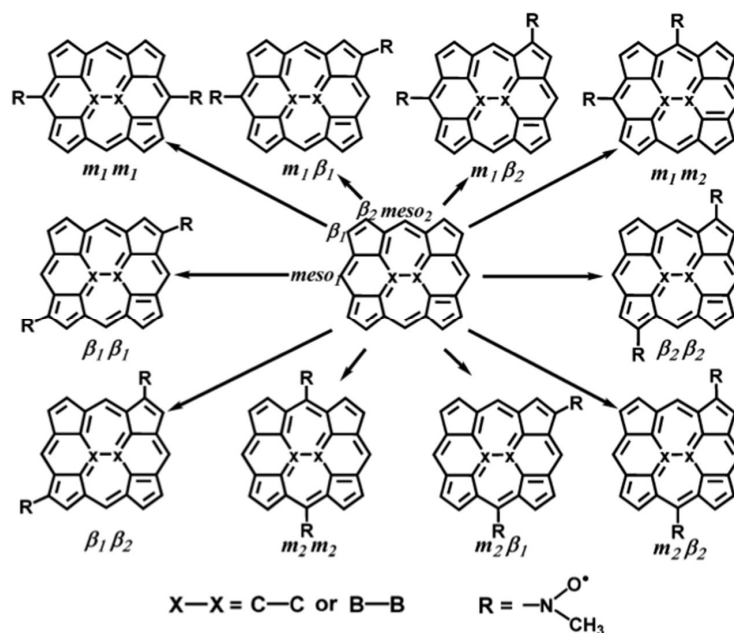


**Figure 6.3.** Test set of porphyrin bridged nitroxide diradicals in Ref <sup>71</sup>. Figure reproduced directly from this reference.

The results of this comparison are useful, as they highlight the deficiencies one is likely to encounter when compromising with a single-reference method. Interestingly, both BS- and SF-DFT are in complete agreement as far predicting the ground-state multiplicities is concerned, (i.e. the sign of the S-T gap) however the disagreement in the energy itself is quite dramatic (with BS-B3LYP predicting  $\sim 30\%$  of the SF-DFT average). The authors complete the remainder of their calculations with BS-B3LYP. However, it is very difficult to comment on which approach is most reliable given the absence of an experimental reference (which is often the case), or a high-level computational reference.

### 6.2.5 Concluding remarks

Correct application of multireference methodology is something of an acquired art. The approach used and its accuracy will vary depending of the nature of the problem and / or the resources available to handle it. CAS and RASSCF are available in most quantum chemistry software packages and are useful as a first approximation. However, neglect of the dynamical component will not lead quantitative agreement with experiment in most cases. For this, methods such as MRCI or high-level perturbation theory, up to CASPT3, are required and for these we recommend the licensed packages MOLPRO or MOLCAS. As for MRCC, the powerful implementation of Kallay et al.<sup>72</sup> is promising but limited to a stand-alone package of the same name. Fortunately, the code is free for academic use and may be interfaced through the MOLPRO environment. These packages possess somewhat complex input formats that can be unfriendly to the less-experienced user. More agreeable platforms can be found in ORCA or DALTON, the latter of which is also open-source. Any package supporting DFT

is suitable for BS calculations, although the SF methods are mostly limited to Q-Chem. In all cases, we advise readers to consult the relevant manual entries before setting any unfamiliar calculations.

### 6.3 Computation of Electron Paramagnetic Resonance Spectra

Given the range of applications in which nitroxide radicals are formed and take part in chemical reactions, monitoring the formation and presence of the nitroxide radical species can be desirable. To that end, electron paramagnetic resonance (EPR) spectroscopy is an extremely useful technique and a one that can be complemented with quantum chemistry simulation to help assign complex spectra and relate that to the underlying structural properties of the radical. Fundamentally, EPR involves measuring the energy at which the magnetic moment of an unpaired electron is flipped in the presence of an external magnetic field (Figure 6.4). To simulate the resulting spectra, one first needs parameters (the  $g$ -factor and hyperfine splitting constants, defined below) describing the response of the electron to the magnetic field, and one then needs to take into account the experimental environment and aspects as the tumbling regime and whether the magnetic field is continuous or pulsed. Quantum chemistry can help with the former, and the methodology developed for this purpose is outlined below (section 6.3.1), while the methodology for the latter is briefly outlined in section 6.3.2.

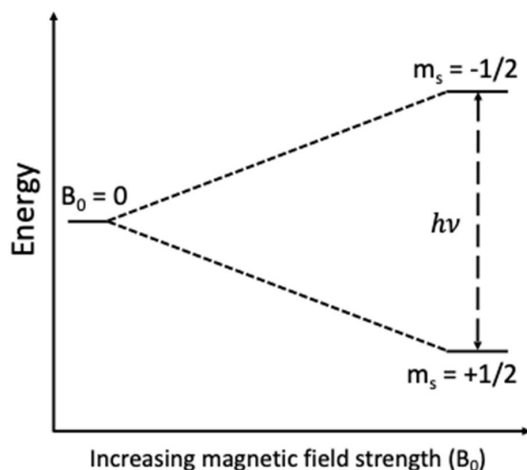


**Figure 6.4.** Splitting in electron spin states observed upon introduction of a magnetic field

#### 6.3.1 Computing $g$ -Tensors and Hyperfine Coupling Constants with Quantum Chemistry.

The main working equation of EPR is given by:

$$\Delta E = h\nu = g_e \mu_B B_0 \quad (7)$$

where:  $g_e$  is the electronic  $g$ -factor (approximately 2.0 for a free electron),  $\mu_B$  is the Bohr magneton, and  $B_0$  is the external magnetic field strength. Electrons are not, however, “free” in a molecule, as they will interact with both the external

magnetic field and internal magnetic fields generated by the nuclei. This generates an effective magnetic field,  $B$  :

$$B_{eff} = B_0(1 - \sigma) \quad (8)$$

where  $\sigma$  includes local magnetic effects. Eq. (8) can then be rewritten as:

$$h\nu = g\mu_B B_0 \quad (9)$$

where:

$$g = g_e(1 - \sigma) \quad (10)$$

Here,  $g$  is referred to as the  $g$ -factor. A value of  $g$  that is significantly different to the constant  $g_e$  term can give information about the molecular orbital in which the unpaired electron resides. In reality the  $g$ -factor is a second-rank tensor, selection of an appropriate coordinate system, for example Cartesian coordinates, allows the 3x3 matrix to be diagonalized to give  $g_{xx}$ ,  $g_{yy}$ , and  $g_{zz}$ . Another consequence of the interaction between an unpaired electron and atomic nuclei is hyperfine splitting, which arises due to coupling between electronic and nuclear spins. This reveals itself in spectra as multiple peaks, centred at  $h\nu$ , and the so-called ‘‘multiplicity’’ of a transition can be complex.

Spectroscopic methods study the response of a system with respect to some external perturbation, and the energy can therefore be expanded as a Taylor series:

$$E(X) = E(0) + \left. \frac{\partial E}{\partial X} \right|_{X=0} \cdot X + \frac{1}{2!} \left. \frac{\partial^2 E}{\partial X^2} \right|_{X=0} \cdot X^2 + \frac{1}{3!} \left. \frac{\partial^3 E}{\partial X^3} \right|_{X=0} \cdot X^3 \dots \quad (11)$$

where  $X$  is an external perturbation. The calculation of  $g$ -factors is no different in this respect, in that it is the second derivative of the many-electron energy with respect to an external magnetic field and the overall net spin component in a given direction (Eq. 12).

$$g_{xx} = \frac{1}{\mu_B} \left. \frac{\partial^2 E}{\partial B_x \partial S_x} \right|_{S=B=0} \quad (12)$$

As a result of this well-defined expansion, computation of EPR  $g$ -tensors is generally possible by both analytical and numerical methods in most electronic structure packages for a range of quantum chemistry methods, generally HF, DFT, and MP2. Traditionally, magnetic property calculations have suffered from gauge invariance; when using an approximate wavefunction the results of the calculation change depending on the orientation of the molecule in the Cartesian frame of reference. This is negated by using, for example, GaugeInvariant Atom Orbitals (GIAO) which ensure exact gauge invariance, or by using a large enough basis set that the invariance becomes negligible. In reality, unless the choice of gauge origin is very poor, the effects of gauge invariance are not large enough to render a calculation useless, however most modern electronic structure packages offer formally invariant methods and their usage is recommended.

The second property of interest are hyperfine splitting constants, arising from the different possible nuclear and electronic spin configurations. For these properties, several terms need to be computed:

1. The isotropic Fermi contact term, which describes the magnetic interaction between an electron and a nucleus, is required and calculated from:

$$a_{iso}(N) = \left(\frac{4\pi}{3} \langle S_z \rangle^{-1}\right) g_e g_N \beta_e \beta_N \rho(N) \quad (13)$$

where  $\langle S_z \rangle$  is the expectation value of the z-component of the total spin,  $g_e$  and  $g_N$  are the electron and nuclear g-factors, respectively, and  $\beta_e$  and  $\beta_N$  are the electron and nuclear magnetons, respectively. The Fermi contact integral,  $\rho(X)$ , can be computed as:

$$\rho(N) = \sum_{\mu\nu} P_{\mu\nu}^{\alpha-\beta} \varphi_\mu(r_N) \varphi_\nu(r_N) \quad (14)$$

where  $P_{\mu\nu}^{\alpha-\beta}$  is the one-electron spin-density-difference matrix, computed as the difference between the spin density matrices of the  $\alpha$  and  $\beta$  electrons), and evaluation of the overlap of the  $\varphi_\mu$  and  $\varphi_\nu$  basis functions is at nuclear position  $r_x$ . For brevity,  $P_N$  is commonly used in place of  $g_e g_N \beta_e \beta_N$ .

2. The spin dipole component, computed as the expectation value over the spin density:

$$A_{kl}^{dip}(N) = P_N \sum_{\mu,\nu} P_{\mu\nu}^{\alpha-\beta} \langle \varphi_\mu | r_N^{-5} (3\vec{r}_k \vec{r}_{Nl} - \delta_{kl} r_N^2) | \varphi_\nu \rangle \quad (15)$$

where  $\vec{r}_N$  is a vector that points from the nucleus of interest to an electron.

3. The second-order spin-orbit coupling term:

$$A_{\mu\nu}^{orb}(N) = -\frac{1}{2S} P_N \sum_{\mu\nu} \frac{\partial P_{\mu\nu}^{\alpha-\beta}}{\partial B_k} \langle \varphi_\mu | h_l^{SOC} | \varphi_\nu \rangle \quad (16)$$

Two key points about Eq. 13 and 14 are the computed isotropic contact term is dependent on the quality of the spin-density matrices of  $\alpha$  and  $\beta$  electrons, and on the overlap between basis functions at nuclear positions. The quality of the spin-density matrices is generally affected most by the method used to compute them. As all systems with unpaired spins are open shell, restricted MO theory, for example restricted Hartree-Fock (RHF), is not applicable. Its restricted open-shell counterpart, ROHF, is also found to generally perform poorly as only the singly occupied molecular orbital (SOMO) will contribute to  $P_{\mu\nu}^{\alpha-\beta}$ , as the spatially identical doubly occupied orbitals will have zero spin-density difference. This can result in the incorrect prediction of zero hyperfine coupling for atoms in the nodal plane of the SOMO. Unrestricted HF (UHF), on the other hand, optimizes both  $\alpha$  and  $\beta$  orbitals, and can account for spin polarization.

Unfortunately, UHF wavefunctions often suffer from spin contamination, arising from the mixing of higher spin states into the wavefunction, and this too will result in less accurate spin-density matrices. Projected UHF methods can be used to project out spin contamination to improve results.

Alternatively, one may turn instead to methods that suffer less from spin contamination; indeed, most electronic structure packages offer hyperfine coupling constant calculations with some of the most powerful electronic structure theories, for example coupled cluster (CC) methods, as well as with DFT. If CC methods are too expensive, DFT methods are generally robust however, as always, it is recommended the functional of choice is benchmarked for suitability before predictions are made.

The second issue is that of appropriate basis set selection. As the basis set overlap is computed at nuclear positions, those with the largest contributions to the splitting constants describe the core s orbitals. However, the most popular basis sets, for example those of Pople or Dunning, do not describe the core region with the same flexibility as the valence region. This is due to their emphasis on accurate calculations of bonding phenomena, to which core electrons contribute little. As well as this, atomic s orbitals exhibit an electron cusp at the nucleus, which is not well captured by Gaussian-type orbitals (GTO). To that end, basis sets have been developed that systematically improve the description of the core region of electrons, examples being EPR-II or EPR-III, and their usage is recommended. A second practical consideration when using DFT is to ensure that a large numerical grid is employed, to ensure numerical integration remains accurate.

Although not necessarily common when exploring the chemistry of nitroxide radicals, it is possible one may encounter heavy elements, and under these circumstances relativistic effects may become significant. Unlike if bonding interactions are being studied, in which case the relativistic core electrons can be replaced by an effective core potential (ECP) which may include relativistic effects in its parameterisation, accurate EPR calculations generally require the explicit treatment of electrons. As a result, all-electron approximations are available in most electronic packages, and their use is recommended.

### 6.3.2 Simulating EPR Spectra

The computational simulation of EPR spectra depends not only the magnetic properties of the molecule (splitting parameters, spin active nuclei present, linewidth and g tensor values) but also the experimental conditions, such as the type of tumbling regime and whether the spectrum is collected as a continuouswave (cw) EPR spectrum or under pulsed conditions. Many programs have been developed simulate spectra, including Easyspin,<sup>73</sup> Winsim,<sup>74</sup> XSophe,<sup>75</sup> and MoSophe.<sup>76</sup> More specialist programs such as WinMOMD<sup>77</sup> for simulation of slow-motional spectra using the MOMD (microscopic order, macroscopic disorder) model, and optimised SLE solvers employed by Freed<sup>78</sup> at the ACERT Center at Cornell have been employed for more targeted systems. Generally speaking, these programs make use of inputted parameters (splitting parameters, spin active nuclei present, linewidth and g tensor values) in order to construct a parameterised spin Hamiltonian. These can be extracted from the experimental spectrum or, if one is trying to make a first principles prediction, these are provided from the quantum-chemical studies described above. A

quantummechanical approach is then used to simulate the resulting spectrum according to the type of tumbling regime (i.e., isotropic limit, fast motion, slow motion, or rigid limit) and whether the spectrum is collected as a continuous-wave (cw) EPR spectrum or under pulsed conditions. Details of how EPR spectra are simulated are covered in Chapter 4.

### 6.3.3 Selected Applications

**Case Study 1: DFT Calculations of Isotropic Hyperfine Coupling Constants of Nitrogen Aromatic Radicals: The Challenge of Nitroxide Radicals.**<sup>79</sup> In this study, Hermosilla et al.<sup>79</sup> assess the performance of DFT for accurately predicting hyperfine coupling constants, using the PBE0 and B3LYP functionals in conjunction with several basis sets; 6-31G(d), N07D, TZVP, and EPR-III. The study utilised a test set of 38 nitrogen-containing radical species, with 15 of the species nitroxide radicals (Figure 6.5). As a result of the different coupling environments a total of 165 hyperfine splitting constants for <sup>14</sup>N and <sup>1</sup>H nuclei were calculated and compared with experimental data. The study highlights the importance of basis sets when calculating EPR properties, as well as the importance of comparing and contrasting DFT results against HF or more advanced wavefunction methods, as the B3LYP results counter-intuitively suggest that 6-31G(d), rather than the larger, EPR specific EPR-III basis set, was more capable of accurately predicting EPR spectra.

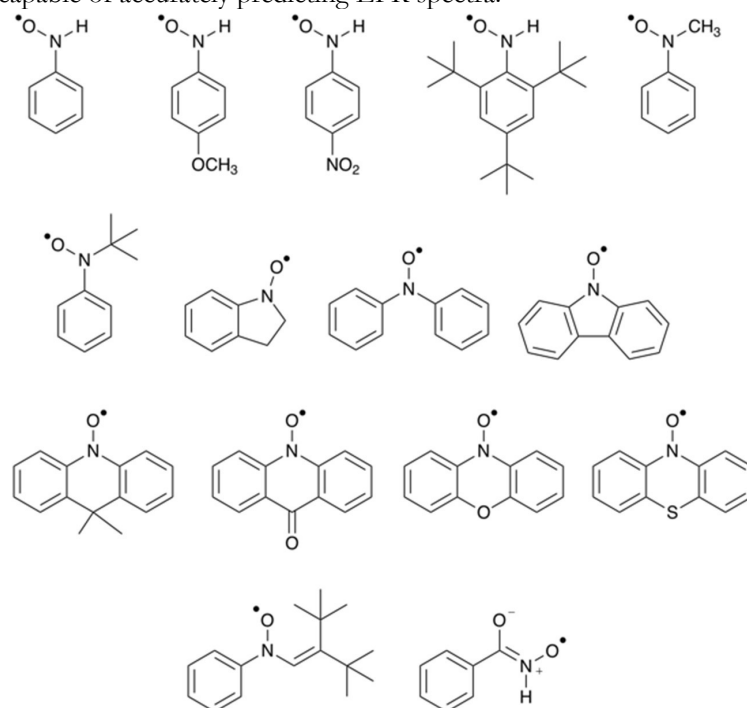
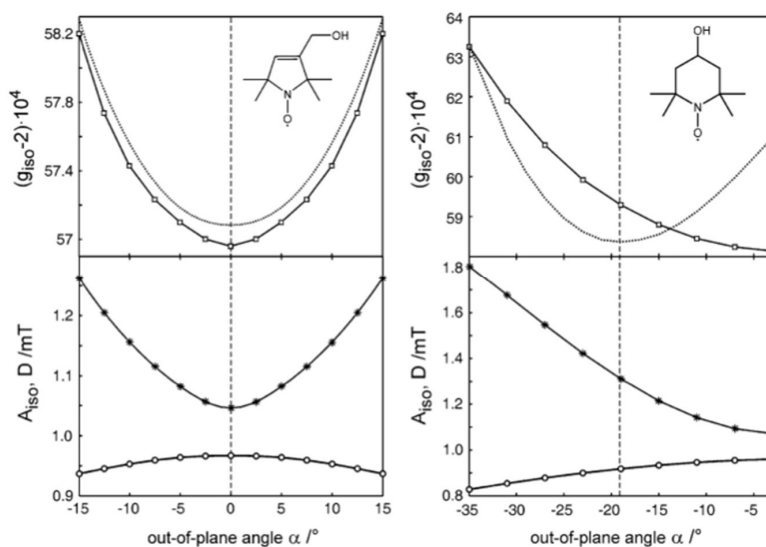


Figure 6.5. Nitroxide radicals studied in ref<sup>79</sup>

**Case Study 2. The temperature dependence of nitroxide spin-label interaction parameters: a high-field EPR study of intramolecular motional contributions.**<sup>80</sup> This study used a combination of high-field W-band EPR and density functional theory calculations to study and explain the temperature

dependence of the  $g$  (anisotropic),  $a$  (hyperfine),  $q$  (quadrupole) tensors of two nitroxides, 3-hydroxymethyl-2,2,5,5-tetramethylpyrrolin-1-oxyl and 4-hydroxy-2,2,6,6-tetramethylpiperidine-N-oxyl, in glass-forming ortho-terphenyl solution. The experimental temperature dependencies were attributed to both the averaging of the anisotropies of the EPR parameters in the glassy matrix, and the intramolecular out-of-plane motion of oxygen in the nitroxide group. This latter mechanism was confirmed via DFT calculations whereby the B1LYP/SVP level of theory was first used to compute the structures associated with harmonic oxygen out-of-plane vibrations, and then the various tensors were calculated at each structure to show how the vibrational motion affected them (Figure 6.6). For this purpose, the SVP basis set was replaced with IGLO-III for computation of the  $a$ - and  $q$ -tensors; while for the  $g$ -tensor LSD/SVP was used in conjunction with RI-SOMF(1X) for the treatment of the spin-orbit coupling operator. Studies such as this highlight the important role of first principles theory in assigning or interpreting complex EPR spectra.



**Figure 6.6.** The calculated  $g_{iso}$  (open square),  $A_{iso}$  (asterisk) and  $D$  (open circle) values as a function of out-of-plane angle  $\alpha$  for 3-hydroxymethyl-2,2,5,5-tetramethylpyrrolin-1-oxyl (left) and 4-hydroxy-2,2,6,6-tetramethylpiperidine-N-oxyl (right). The dotted line shows the relaxed energy profile, and the dashed line indicates the minimum energy angle. Reproduced directly from Ref <sup>80</sup>.

#### 6.4 Predicting Oxidation Potentials

As redox active molecules possessing unique properties and reactivity, nitroxides are utilised in many applications ranging from energy storage devices<sup>81-85</sup> and oxidation catalysts<sup>86-90</sup> to redox mediators for solar-cells<sup>91-94</sup> and super-oxide dismutase mimics.<sup>95, 96</sup> Nitroxides can typically undergo an electrochemically reversible 1-electron oxidation to afford the corresponding oxoammonium cation (see Figure 6.7). In contrast, nitroxide reduction is usually electrochemically irreversible; spontaneous proton transfer from protic impurities rapidly quenching the initially formed oxyamine anion as a hydroxylamine. In this latter case, the highly coupled nature of the rate and equilibrium constants for the underlying elementary processes can make the



direct experimental measurement of a corresponding potential difficult, and computational chemistry offers a valuable alternative to experiment.

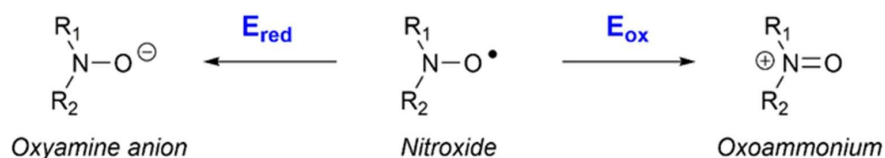


**Figure 6.7.** The oxidation and reduction of a nitroxide of the general form,  $\text{R}_1\text{R}_2\text{N}-\text{O}^\bullet$ .

Even when measurement is possible, the accompanying synthesis can be expensive and time-consuming, and as such computational chemistry offers an attractive means of assessing the utility of a given species prior to experiment. In this respect, the success or failure of a given nitroxide hinges on its precise redox properties; including the electrochemical reversibility of oxidation/reduction and the respective potentials of these electron transfers. For instance, in alcohol oxidation, nitroxides are frequently employed as catalysts in conjunction with a bulk stoichiometric oxidant, such as sodium hypochlorite or ambient oxygen (see Figure 6.8).<sup>97, 98</sup> This bulk oxidant, [O], is used to generate the catalytically active oxoammonium species in situ, which in turn oxidises the substrate alcohol to a ketone. If the oxidation potential of the nitroxide is too high, then the bulk oxidant will be unable to oxidise the initial nitroxide into the catalytically active oxoammonium cation. Conversely, if the oxidation potential of the nitroxide is too low, then the oxoammonium cation will be unreactive towards the alcohol substrate. Moreover, in biochemistry nitroxides are of interest as antioxidants; protecting cells against cytotoxic reactive oxygen species.<sup>99, 100</sup> In vivo, both oxidation and reduction processes involving nitroxides are relevant,<sup>101, 102</sup> and so the ability to predict and rationalise the redox potentials of nitroxides is invaluable for screening novel antioxidants.

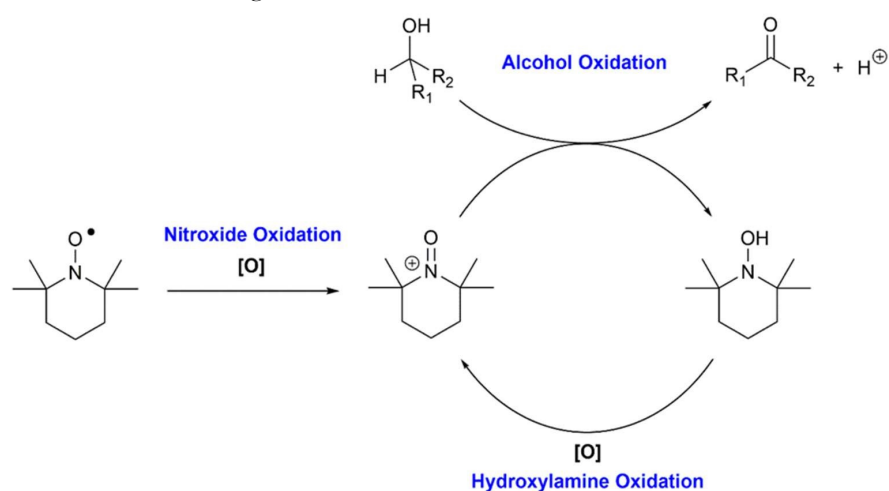


**Figure 6.8.** The nitroxide catalysed oxidation of an alcohol to a ketone in the presence of bulk stoichiometric oxidant [O].

While other references discuss the theoretical evaluation of redox potentials for organic<sup>103, 104</sup> and inorganic<sup>105</sup> species in some detail, we will more briefly outline some of these considerations within the specific context of nitroxide oxidation

and reduction. The theoretical calculations of most thermochemical quantities, including oxidation and reduction potentials, usually take advantage of the Born-Oppenheimer approximation, which partitions the electronic and nuclear wavefunction and so separates the calculation into three steps (Figure 6.9). Initially, the electronic energy of the molecule in its oxidised and reduced form is calculated using normal electronic structure calculations. Next, the entropic contribution from nuclear motion is calculated, usually employing harmonic or quasi-harmonic approximation in conjunction with computed frequencies. Finally, statistical averaging of relevant conformations and solvent corrections are applied, usually by assuming Boltzmann distributions and applying continuum solvent models. For computation of redox potentials, the first step affords the gas phase 0 K adiabatic ionization energy (IE) or electron affinity (EA), the second step computes the (temperature dependent) entropic corrections, while the third step corrects the resulting gas-phase free energy for solvent effects and appropriately weights these quantities according to the population of the individual conformations.

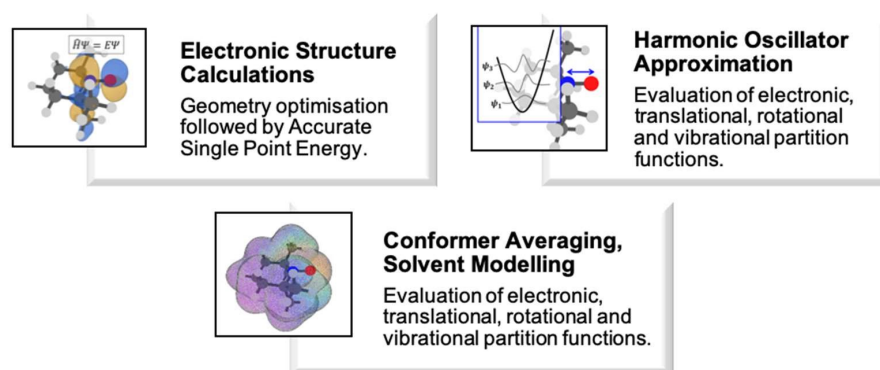
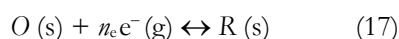


**Figure 6.9.** The three steps involved in the calculation of oxidation and reduction potentials.

The main methodological challenges relate to the first and third steps: in the former case, obtaining a sufficiently accurate description of the electronic energies, albeit within a single reference framework; in the latter, modelling the effects of solvation, particularly for the ionic species. In addition, there is the added complication of converting the solution-phase Gibbs free energies for the half reactions into electrode potentials, which entails choosing appropriate values for the reference electrode, treating the electron in a consistent manner, and considering coupled chemical processes where relevant. Below we introduce the methods (and where relevant equations) for the each of these steps, before examining some of the applications.

#### 6.4.1 Definitions and Key Equations

The standard reduction potential directly measures the thermodynamic feasibility of the general reduction half-reaction.



where O refers to an oxidized reagent, R refers to a reduced reagent,  $n_e$  is the number of electrons exchanged between the oxidized and reduced species, and "s" and "g" refer to species in solution and in the gas phase, respectively. Note

that the charge of O and R are not shown here but must be balanced across the reaction. The absolute reduction potential for this reaction is given by the Nernst equation<sup>106, 107</sup> as

$$\Delta_r G^o(O|R) = -n_e F E_{abs}^o(O|R) \quad (18)$$

where:  $\Delta G(O|R)$  is the Gibbs free energy change for the half reaction, F is the Faraday constant (96485 C mol<sup>-1</sup>), and  $n_e$  is the number of electrons transferred in the half-reaction. To facilitate comparison with experiment, this must be converted to a relative (cell) potential measured against a reference electrode (such Fc/Fc+, Ag/Ag+, the standard hydrogen electrode, etc).

$$E_{rel,REF}^o(O|R) = E_{abs}^o(O|R) - E_{abs}^o(REF) \quad (19)$$

Here  $E_{abs}^o(REF)$  is the absolute reduction potential of the reference electrode and in principle can be calculated the same way, though in practice literature values are available for most references.<sup>103, 104</sup> In choosing a literature value it is important to ensure that the treatment of the electron is consistent in both half reactions so that it cancels from the cell potential. While the electron has no electronic energy as such, it is assumed to have thermal energy and entropy, but the amount differs according to which convention is used. Details of the different conventions are in Refs 103, 104; ultimately, the choice of convention has no impact on the results provided it is applied consistently.

The values of  $E_{rel,REF}^o(O|R)$  yielded from the above equations correspond directly to the experimental half-wave potential for reversible redox processes. However, many species (including nitroxides) can undergo irreversible redox reactions which are often coupled with other spontaneous proton transfer or addition/fragmentation processes. In these situations, experimental cyclic voltammograms (CVs) are complex. One can either fit these experimental CVs with kinetic schemes that take into account the redox processes, the coupled chemical reactions, and diffusion into and out of the double layer. In such cases the computational  $E_{rel,REF}^o(O|R)$  can be compared with the fitted potentials obtained for isolated redox processes. Alternatively, one can use computational chemistry to study the coupled processes as well and yield adjusted half-wave potentials. For instance, in aqueous environments reduction of nitroxide radicals are accompanied by rapid protonation (Figure 6.10). As such, formal reduction processes can be represented by different half reactions, which will depend heavily the nitroxide of interest and on the pH of the solution. Thus, the 1electron reduction of TEMPO<sup>•</sup> generates a TEMPO<sup>-</sup> oxyamine anion, which is rapidly quenched by water (across a range of pH values) to form the corresponding TEMPOH hydroxylamine. However, the TEMPOH hydroxylamine is itself a weak base (conjugate acid pK<sub>a</sub> = 6.9 – 7.5) and may be protonated depending on the pH of the solution. As a result, the half-wave reduction potential observed by experimental measurements is given by:

$$E_{1/2} = E_{red}(X^{\bullet}, 2H^+/H_2X^+) + \frac{RT}{F} \ln(K_1 K_2 + K_1 [H^+] + [H^+]^2) \quad (20)$$

where  $E_{red}(X^{\bullet}, 2H^+/H_2X^+)$ ,  $K_1$  and  $K_2$  are as defined in Figure 6.10.

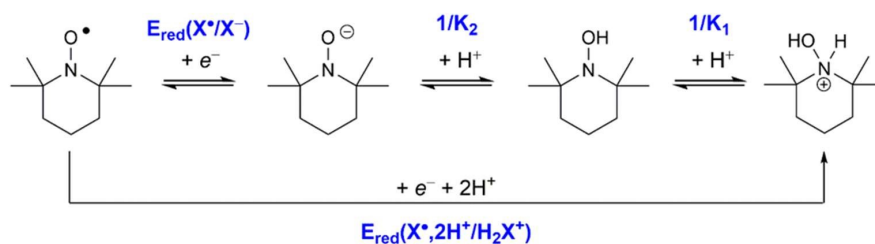


**Figure 6.10.** Chemical processes associated with the reduction of the TEMPO• radical in water.

#### 6.4.2 Electronic Structure Methods and Gas-Phase IEs and EAs

Electronic structure methods are conveniently divided into two categories; wavefunction-based approaches and density functional theory (DFT). Within wavefunction theory there are a hierarchy of different approximations with varying levels of accuracy, some of which were briefly introduced in section 6.2. For redox potentials, single reference methods are usually sufficient. There are three main ‘families’ of correlated single-reference wavefunction methodologies: Møller–Plesset perturbation (MPn) theory<sup>108–114</sup> (e.g. second-order Møller–Plesset corrections, MP2), and configuration interaction methods, for example coupled cluster (CC) theory<sup>115–117</sup> (e.g. single, double and perturbative triple excitations, CCSD(T)) or quadratic configurational interaction with single, double and perturbative triple excitations, QCISD(T).<sup>117–119</sup> While acceptable accuracy will depend largely on context, a sufficiently accurate treatment of electron correlation is achieved in most chemical systems with CCSD(T) or QCISD(T) used in conjunction with large triple zeta basis sets. Such energies will (usually) only differ from corresponding exact values by 1–2 kJ mol<sup>-1</sup>.<sup>120, 121</sup> Thus, CCSD(T) is frequently labelled the “gold-standard” of computational chemistry, as this level accuracy is sufficiently accurate for most (single-reference) applications.

Composite procedures are a notable subclass of wavefunction-based approaches that pragmatically perform basis set extrapolations schemes and/or combine the results of calculations performed at different levels of theory. These procedures are usually as accurate as the large basis set CCSD(T) (or equivalent) calculations that they are attempting to approximate, but only require a fraction of the computational expense.<sup>122–126</sup> The Gaussian composite procedures<sup>122–126</sup> (*Gn*), originally developed by Curtiss and co-workers are among the most popular, and a popular variant of G3 theory is the less computationally intensive G3(MP2)RAD procedure.<sup>127</sup> Other well-known composite procedures include the CBS methods<sup>128–135</sup> developed by Petersson and co-workers, and the *Wn* methods<sup>121, 136–138</sup> formulated by Martin and co-workers. Although not strictly a composite procedure, the F12 approximation<sup>139</sup> in its various manifestations also delivers improved accuracy by significantly reducing errors caused by small basis sets.

Density functional theory (DFT) calculates the energy of a molecule or atomic species using its one-electron density and a functional. The Hohenberg-Kohn Theorems,<sup>140</sup> which form part of the inspiration for DFT, state:

- 1) That the ground state external potential (and thus total electronic energy of the ground state) is a unique functional of the electron density.

- 2) That a density that minimizes the total energy of the ground-state is the exact ground-state density.

Using the electron density to obtain the total energy has been touted as a way of circumventing the poor size scaling of wavefunction based methods. Unfortunately, the first Hohenberg-Kohn Theorem is not constructive but rather an existence proof. As such, it only establishes that the ground state external potential is a unique functional of the electron density and provides no insights into its actual mathematical form. Consequently, the exact DFT functional is unknown.

Modern DFT functionals are based on the Kohn-Sham equations,<sup>141</sup> which cleverly consider the Hamiltonian for a fictitious system of non-interacting electrons that have an overall ground-state density that is identical to the real atomic or molecular system (where the electrons are allowed to interact). Ideally, DFT would be exact and formulated from fundamental physical and mathematical arguments. However, in practice many popular DFT functionals are heavily parametrized using test sets of experimental and (wave-function derived) theoretical data. While current DFT functionals offer reasonable accuracy at low computational cost, they can also fail spectacularly and unexpectedly.<sup>142</sup> Many of the most popular functionals, such as B3LYP, have been found to fail dramatically (often to the extent that results are qualitatively incorrect).<sup>142</sup> Moreover, there is no systematic way to improve DFT results and so choice of functional is quite subjective. Because of this often variable and unpredictable accuracy, DFT should always be employed cautiously in conjunction with appropriate benchmarking.

There are many articles that evaluate the performance of common DFT functions and other wavefunction-based methodology for the calculation of IEs and EAs. For instance, our group examined theoretical procedures for IE and EA calculations on a range of piperidine, pyrrolidine, oxazolidine derivatives, isoindoline, and azaphenalene nitroxides.<sup>143</sup> This study revealed that low cost DFT procedures often carried unacceptably large errors, with B3LYP and MPWB1K carrying mean absolute deviations (MAD) for EAs of 0.23 and 0.40 eV, respectively. Interestingly, these errors are primarily associated with the reaction site and can be largely mitigated using an ONIOM partitioning scheme. For instance B3LYP in conjunction with a G3(MP2)RAD core affords much smaller deviations (around 0.10 eV). Pantazis and co-workers recently examined the IEs of 19 organic species with several methods using CCSD(T)/CBS data as a reference (see Figure 6.11).<sup>144</sup> Despite its enormous popularity in computational organic chemistry, B3LYP once again performs relatively poorly with mean absolute deviations and maximum deviations (MAX) of around 0.40 and 0.70 eV, respectively. M06-2X performs better with a MAD of only 0.11 eV, although it still suffers an unexpectedly large MAX (for phenol) of nearly 1 eV. CCSD(T)/cc-pVTZ offers excellent accuracy, with MAD and MAX values of 0.14 and 0.16 eV, respectively. However, this accuracy is strongly basis set dependent. If a smaller double-zeta basis set (cc-pVDZ) is employed, the MAD and MAX of CCSD(T) increase dramatically to over 0.4 V. CCSD(T)-F12 offers an excellent compromise, with a double-zeta F12 calculation essentially matching the accuracy of standard triple-zeta CCSD(T).

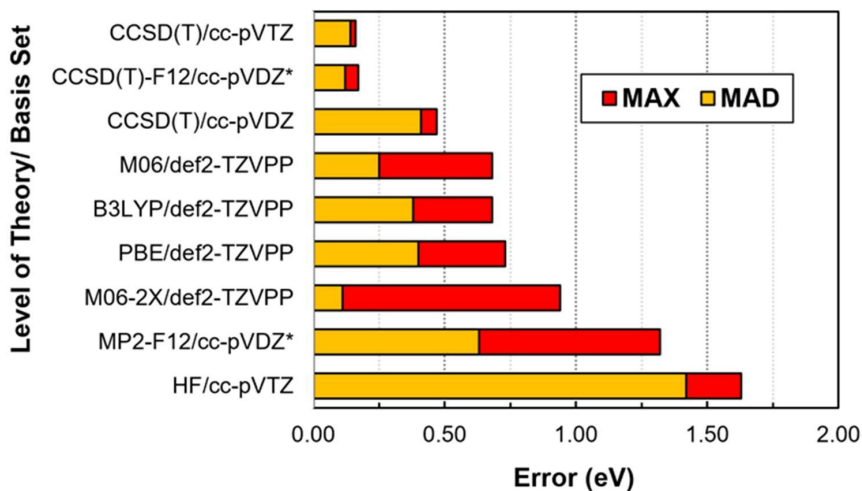


**Figure 6.11.** Mean Absolute Error (MAD) and Maximum Errors (MAX) in Adiabatic Ionization Energies for the 19 organic species in the Pantazis test set, taken from reference <sup>144</sup>. \*Indicates a F12 variant of the standard cc-pVDZ basis set was used.

#### 6.4.3 Solvent Effects and Redox Potentials

To convert gas-phase IEs and EAs to redox potentials, one needs to calculate the Gibbs free energies of solvation, so as to obtain Gibbs free energies in solution. In doing this one also needs to include a term  $RT(\ln V)$  to account for the change of state from 1atm to 1M.<sup>145</sup> The simplest and most computationally efficient methods for calculating solvation Gibbs free energies are continuum models, in which each solute molecule is embedded in a cavity surrounded by a dielectric continuum of permittivity  $\epsilon$ .<sup>146</sup> Continuum models are designed to reproduce bulk or macroscopic behaviour, and can fare extremely well in certain applications including redox potentials.<sup>147</sup> However, the results obtained using continuum models are highly sensitive to the choice of cavities (which are typically parameterised to reproduce the free energies of solvation for a set of small organic molecules). This reliance on empirical parameterisation means the errors can sometimes be unpredictable. Moreover, their accuracy can suffer if there are explicit solute-solvent interactions such as complex formation or hydrogen bonding.<sup>148</sup> Although this problem can be overcome by including a small number of explicit solvent molecules in the ab initio calculation, as in a cluster-continuum model,<sup>149</sup> this adds significantly to the cost of the calculation.

As a result, in small to medium nitroxides (where high-level composite calculations are feasible), the accuracy of redox calculations is usually limited by the accuracy of the continuum solvent model. This is particularly a problem because of the involvement of charged species. For neutral molecules, solvation energies are typically small, and many solvent models are able to compute the solvation energies of neutral molecules with reasonably high accuracy, with errors typically of the order of 5-10 kJ/mol.<sup>150</sup> However, errors in solvation energies for charged systems can be significantly larger (often above 20 kJ/mol; see Figure 6.12). This introduces correspondingly large errors into the resulting redox potentials. Fortunately, errors introduced by solvation models are often

highly systematic (see Figure 6.13); depending on the functionality of anion or cation in question. Note that in Figure 6.13, the superior absolute performance of PCM-UAKS B3LYP is not a general result for other redox systems, and in other studies of nitroxides and or closely related species methods such as SMD or COSMO-RS perform better.<sup>151-156</sup>

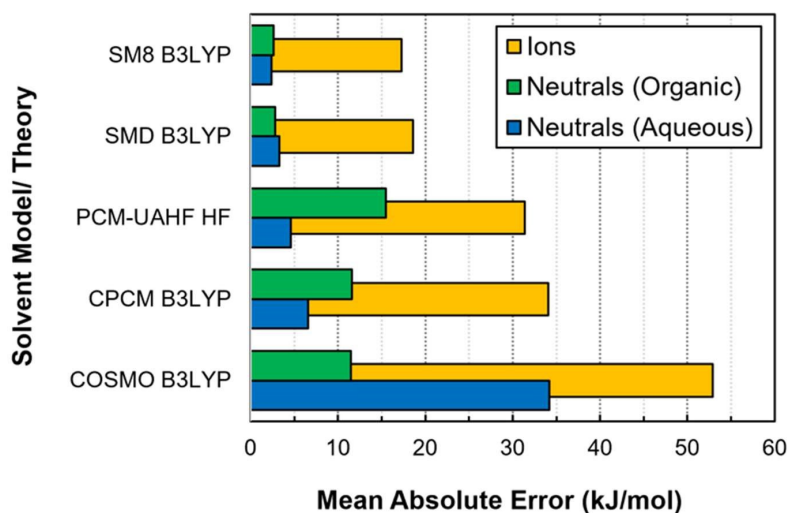


**Figure 6.12.** Typical errors for ionic and neutral species in popular continuum solvation models.

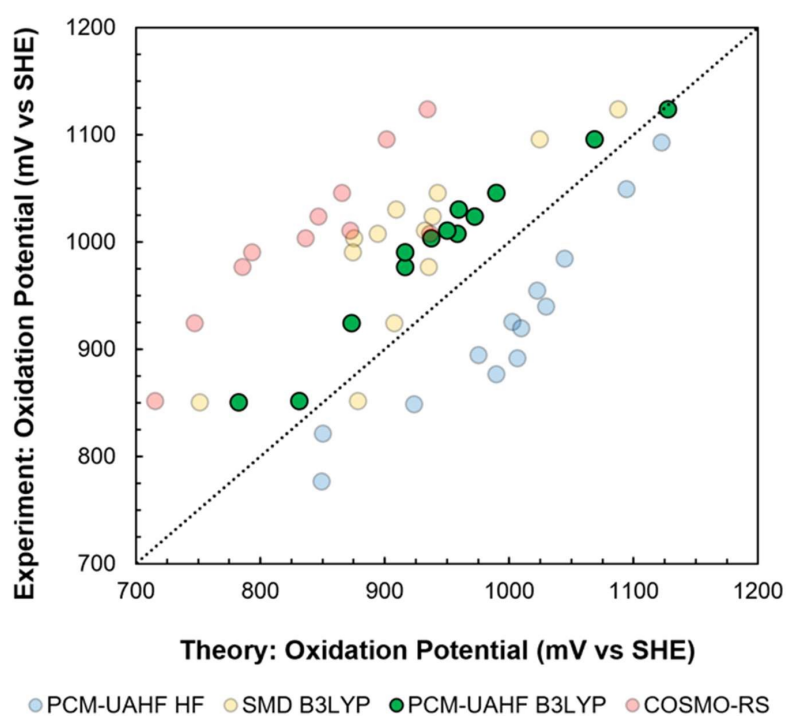


**Figure 6.13.** The performance of different solvent methodologies for the computational prediction of nitroxide oxidation potentials.

Nonetheless, for the most part, errors in solvation energies within a set of related molecules are relatively systematic. As a result, they can be circumvented

somewhat by computing redox potentials in an isodesmic fashion, where relative (rather than absolute) potentials are computed against a structurally similar reference system. The potential of the substrate is then determined by using this relative potential in conjunction with an accurate experimental value for the reference couple (see Figure 6.14). This approach exploits systematic error cancellation by offsetting the errors introduced by sub-optimal solvation modelling of both charged species. While this approach normally delivers more accurate potentials, it relies on the availability of accurate experimental measurements for the reference couple.

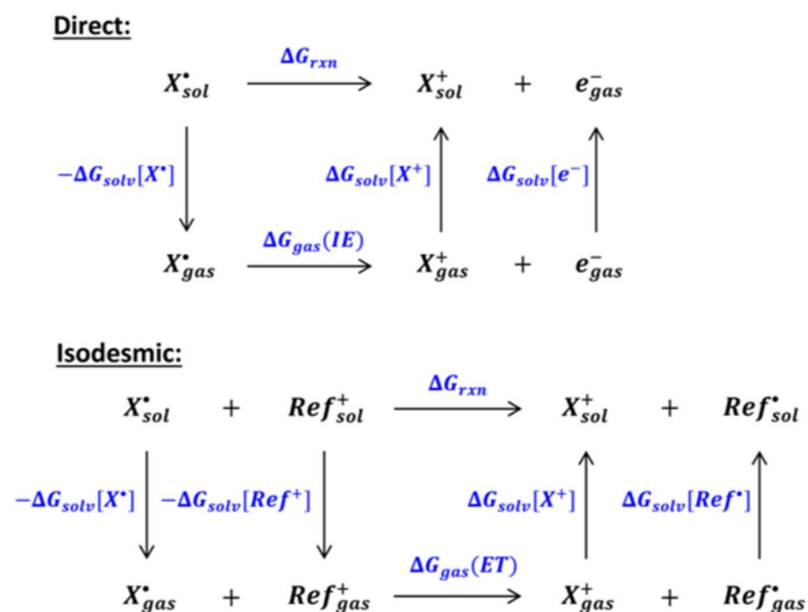


Figure 6.14. Direct vs Isodesmic Oxidation Potential Calculations.

#### 6.4.4 Selected Applications

Computational chemistry offers not only the opportunity predict kinetics and thermodynamics; it can also be used to help interpret the underlying structure-reactivity trends by providing detailed structural information, dipole and quadrupole moments, and other related properties. This in turn is useful in reagent design, as these case studies below illustrate.

**Case Study 1. Computational Design of Cyclic Nitroxides as Efficient Redox Mediators for Dye-Sensitized Solar Cells.**<sup>157</sup> With decreasing global fossil fuels reserves and increasing energy demand, improving the efficiency and cost-effectiveness of renewable energy is becoming an increasing priority. Dye-sensitized solar cells (DSSCs) are particularly promising, as they are less expensive and more flexible than traditional Silicon-based cells. DSSCs are a photoelectrochemical system consisting of two separate electrodes; a mesoporous thin-film semiconductor (usually TiO<sub>2</sub>) with a tethered monolayer of sensitizing dye and a counter electrode (see Figure 6.15). An electrolyte containing a redox mediator is injected between these two electrodes. Light is first absorbed by a dye, then the photoexcited dye (S\*) transfers an electron to TiO<sub>2</sub>. The oxidised dye (S<sup>+</sup>) is reduced by the redox mediator (Md<sup>•</sup>), with the oxidized mediator (Md<sup>+</sup>) diffusing to the counter-electrode. There the oxidised



mediator is reduced by current passing through the cell. As it affects the electrochemical potential at the counter electrode and semiconductor, the redox mediator is a crucial component of the cell.

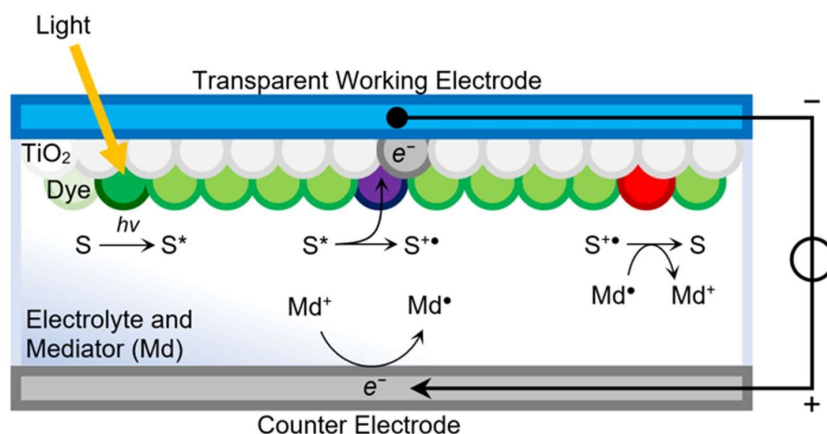


**Figure 6.15.** A simplified depiction of a Dye-Sensitised Solar Cell, showing the principal photoexcitation and electron transfer processes.

Nitroxides are particularly attractive as redox mediators because of their rapid and (usually) reversible redox chemistry, low toxicity, and low corrosivity. They are also characterized by fast rates of both heterogeneous electron-transfer and electron self-exchange reactions. Importantly, their oxidation potentials are also reasonably close to the optimal range of 0.60–0.85 V (versus SHE) and can be further optimised through structural modifications. However, this reversibility is fundamentally dependent on their chemical structure; with some cyclic nitroxides undergoing irreversible ring opening processes or fragmentation (Figure 6.16). Experimental cyclic voltammetry measurements can readily establish the oxidation potential of a given nitroxide and its electrochemical reversibility. Synthesis and characterisation of nitroxides is often time-consuming and expensive. Hence, computational screening is a particularly attractive; allowing for rapid and accurate prediction of the redox properties of candidate nitroxides.

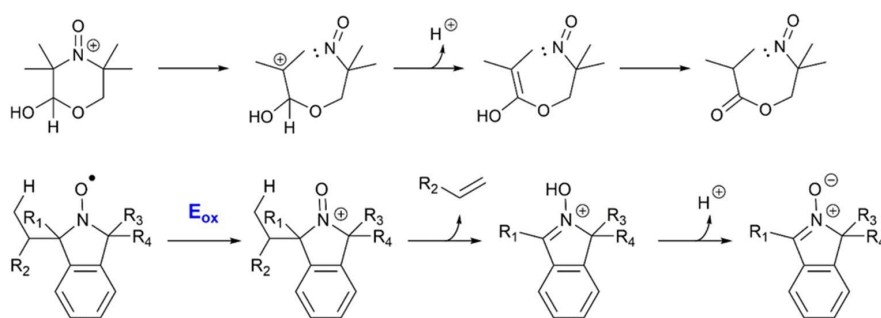
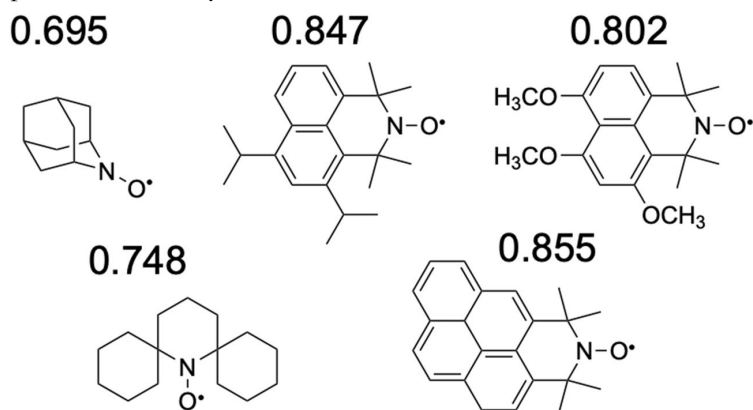


**Figure 6.16.** (Top) Proposed ring opening pathway of a hydroxyl substituted morpholine oxoammonium. The electrochemical oxidation of the corresponding nitroxide is nearly completely irreversible. (Bottom) The generation of isoindoline-derived nitronones via  $\beta$ -fragmentation from the corresponding oxoammonium (with loss of an alkene)

To address this problem, we studied the nitroxide structural features to help guide experimental optimisation of DSSCs.<sup>157</sup> As redox mediators for DSSCs,

nitroxides need to have oxidation potentials of 0.60 –0.85 V (vs SHE) and high stability. It was found that most monocyclic nitroxides had potentials in the correct range, but were susceptible to the ring-opening processes of Figure 6.16. These ring opening processes could be largely suppressed by fusing aromatic rings to piperidine and pyrrolidine nitroxides, leading to azaphenalene and isoindoline ring frameworks. These basic frameworks are resistant to oxidative ring opening, as the initially formed nitroso and carbocation are held near each other by the secondary aromatic scaffold (and rapidly couple). However, their oxidation potentials that are too high for DDSCs (1.02 V and 0.98 V, respectively). One possible solution is replacement of the flanking groups with higher alkyls. While calculations indicate this substitution does appreciably lower the oxidation potential of isoindolines, unfortunately it also facilitates a  $\beta$ -fragmentation process that decomposes the oxoammonium species into a nitronone (Figure 6.16). Aside from modification of the flanking alkyl groups, introduction of electron donating amino substituents onto the aromatic ring also lowered the potential of isoindoline and azaphenalene based nitroxides. However, this moiety can also undergo irreversible oxidation with proton loss to form electrochemically inert products. As such, isomers bearing the  $\text{NH}_2$  group are unsuitable for the present study.

However, it was shown that there are still nitroxides that possess oxidation potentials within the target range and meet the reversibly criteria outlined above. These included an adamantane-like species, piperidines with  $\alpha$ -cyclohexyl groups, TMAO derivatives with alkyl and methoxy substituents, as well a large fused antiaromatic system (Figure 6.17). Latter experimental testing by Nishide and co-workers verified that one of these, the 2-azaadamantan-N-oxyl radical was an exceptional redox mediator, consistent with our theoretical predictions.<sup>158</sup> Employing this mediator in a DSSC, Nishide and co-workers set the benchmark efficiency (for organic radical based mediators) of 8.6%; significantly improving on the previous efficiency of TEMPO-based DSSCs of 5.4%.

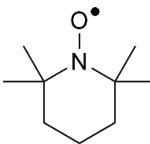
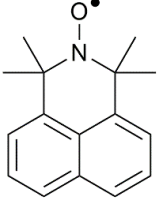
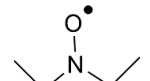
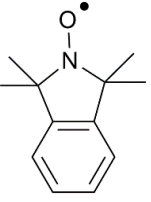


**Figure 6.17.** Proposed redox mediators showing computed potentials in V vs SHE. Figure taken directly from Ref <sup>157</sup>.

**Case Study 2. Effect of heteroatom and functionality substitution on the oxidation potential of cyclic nitroxide radicals; role of electrostatics in electrochemistry.**<sup>159</sup> Computing accurate oxidation potentials is undoubtedly helpful, as it enables the pre-screening of novel nitroxides for specific applications. However, using theory to deduce quantitative (or semi-

quantitative) structure-reactivity or structure-property relationships is arguably even more useful because it allows nitroxides to be rationally designed for a specific purpose. Many theoretical and experimental studies rationalise nitroxide oxidation and reduction potentials using strain-arguments based on ring-size and rigidity.<sup>98, 143, 157, 160, 161</sup> Normally, the basis for such arguments is that the oxoammonium cation, oxyamine anion and nitroxide radical prefer different degrees of planarity around the nitrogen atom. Thus, attaining the optimal geometric rearrangement is hindered to varying extents by size and rigidity of the primary nitroxide ring. To examine strain-based arguments in more detail, we collated literature<sup>143,157</sup> high-level theoretical predictions of the oxidation and reduction potentials of prototypical nitroxides; separately examining the influence of ring contraction and rigidification.

**Table 1.** Relative aqueous oxidation ( $E_{\text{ox}}$ ) and reduction ( $E_{\text{red}}$ ) potentials for piperidine, pyrrolidine, azaphenylene<sup>a</sup> and isoindoline nitroxides. Data taken from Reference ref.<sup>143</sup>

Nitroxide				
$E_{\text{red}}$ (mV)	0.0	+146	-138	-22
$E_{\text{ox}}$ (mV)	0.0	+267	+2	+240

<sup>a</sup>Data for the azaphenylene was subsequently corrected in Ref<sup>157</sup> and we show the corrected data here.

As Table 1 reveals, reduction potentials are significantly lowered by ring-contraction, with a decrease of around 140-180 mV. This indicates the larger piperidine (and azaphenylene) rings are better able to accommodate the geometric changes associated with nitroxide reduction as compared to the smaller pyrrolidine (and isoindoline) rings; consistent with a strain-based argument. Surprisingly, however, ring-size alone does not appreciably influence oxidation potentials; with minimal change moving from piperidine to pyrrolidine (or moving from azaphenylene to isoindoline). While aromatic rigidification does significantly increase oxidation potentials (by 240–260 mV), inexplicably, it also raises the respective reduction potentials (by 120-150 mV). In other words, oxidation potentials are insensitive to ring-size but increase substantially upon rigidification, while reductions potentials are lowered by ring-contraction yet raised by rigidification. Interestingly, rigidification of piperidine through the inclusion of multiple aliphatic frameworks lowers the respective oxidation potential (see Figure 6.17); indicating different effects from aromatic and aliphatic rigidification strategies. Collectively, this behaviour is incompatible with a simple strain-based argument. If attaining the optimal cation or anion geometry is hindered by ring size and rigidity, then why do these parameters appear to operate independently and have unpredictable effects on oxidation and reduction behaviour? Why does rigidification with aromatic (but not aliphatic) frameworks increase nitroxide oxidation potentials?

To address these questions, we recently explored if the fundamental electrostatics could rationalise nitroxide oxidation (and reduction) potentials.<sup>159</sup>

Electrostatic effects can be described using a multipole expansion, which includes contributions from monopole, dipole, quadrupole and octapole (etc) terms. For electronically uncharged substituents, the dipole term is the first nonzero contributor to this expansion and so formed the basis for our initial investigations. The substituent orientation relative to the  $>\text{N}-\text{O}^\cdot$  moiety is crucial, as this axis defines the only component of the dipole moment that will have a non-zero interaction with the charge formed upon oxidation. To decouple the dipole moment of the substituent from that of the  $>\text{N}-\text{O}^\cdot$  group, we used analogues in which the  $>\text{N}-\text{O}^\cdot$  moiety was replaced with a  $\text{CH}_2$  group. This substitution conveniently preserves the relatively fixed orientations of the interacting substituents, as the basic C-C framework of these models is analogous to that of the corresponding nitroxides. Initial investigations revealed that this distance scaled dipole moment was very well correlated with experimental oxidation potentials. However, 3 nitroxides from this initial set possessing  $\pi$ -functionality were found to be significant outliers. This led us to investigate if this behaviour, and more generally the effect of aromatic rigidification on redox potentials (as reported in Table 1), could be electrostatic in origin.

The importance of quadrupole moments in the electrostatic description of molecules with  $\pi$  systems is well known.<sup>162-164</sup> Moreover, truncating the multipole expansion at the dipole term is only valid if the substituent and  $>\text{N}^+=\text{O}$  moiety are sufficiently separated, so at short-range higher order multipole terms may be significant. Inclusion of an appropriately scaled quadrupole term corrects the 3 previous outliers and simultaneously improves the correlation with the experimental oxidation potential. Moreover, this dipole-quadrupole parameter can be applied successfully to a total test set of 35 different  $\alpha$ -tetramethyl substituted nitroxides; comprising of 1 pyrrolidine, 2 pyrrolines, 11 isoindolines, 15 piperidines, 2 morpholines, 3 azaphenylene and 1 azepine (Figure 6.18).<sup>159</sup> Despite the structural diversity of these nitroxides (including different ring sizes and rigidity), good correlation was observed between the distance scaled dipole and quadrupole term and the respective oxidation potential (total  $R^2 = 0.84$ ). Reassuringly, the optimal ratio between the component dipole and quadrupole terms found via a 2-variable regression (1.78:1) is reasonably similar the theoretical ratio predicted in a multipole expansion (2:1). We should caution that due to relatively small separation between the nitroxide moiety and the substituent, higher order multipole moments may also contribute; particularly in more electrostatically complex systems. It is also important to note that this analysis only considers the underlying (gas-phase) electrostatic effects and does not account for other key factors including; induction, ring-strain, through space orbital overlap and solvent effects. Notwithstanding these considerations, this study highlights how nitroxide oxidation potentials can be rationalised with chemical intuition using substituent-based electrostatic arguments.

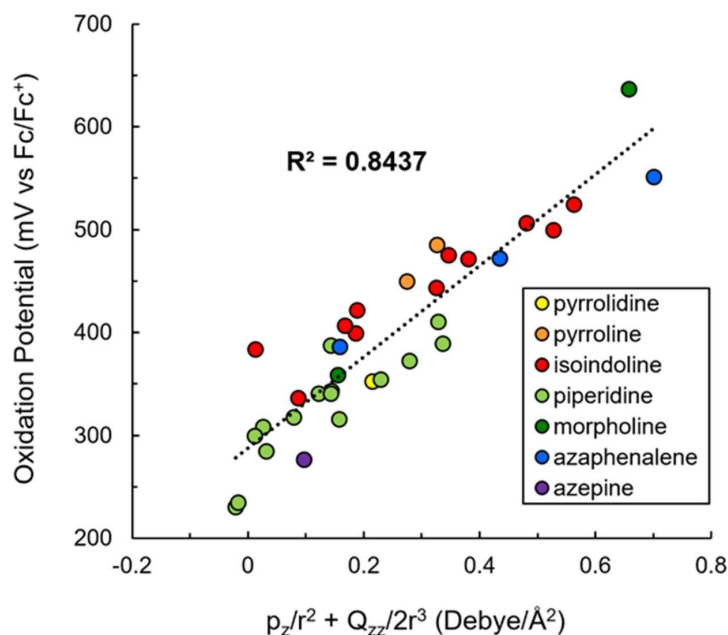


**Figure 6.18.** The generation of isoindoline-derived nitronones via  $\beta$ -fragmentation from the corresponding oxoammonium (with loss of an alkene). Data taken from Ref <sup>159</sup>

Returning briefly to the trends reported in Table 1, we can now fully rationalise these redox potentials in terms of strain and electrostatics. Strain-based effects are clearly a factor in the case of nitroxide reduction (where geometry relaxation is normally more significant). However, rigidification through the inclusion of fused aromatic rings introduces a large quadrupole moment. In the case of isoindolines and azaphenalenes, this quadrupole interacts unfavourably with the forming oxoammonium cation thereby raising the oxidation potential of the corresponding nitroxide. Conversely, this quadrupole interacts favourably with the oxyamine anion and so also raises the corresponding nitroxide reduction potential. This work highlights the often-underappreciated role that throughspace electrostatics has in governing redox behaviour and provides a simple tool for tuning the oxidation behaviour of nitroxide radicals.

## 6.5 Modelling Nitroxide Mediated Polymerisations

Nitroxide mediated polymerization (NMP) was the first successful technique for controlled radical polymerization.<sup>165</sup> Full details of this process and its achievements are outlined in Chapter 7; for the present purposes it is important to note that the key to control rests with: (a) tuning the equilibrium constant for alkoxyamine dissociation to sit within an ideal range whereby there are enough propagating radicals released to sustain a polymerization but not enough for significant chain termination; (b) minimising other chain stopping side reactions. Computational chemistry can assist with both aspects of this design problem and this is illustrated with the case studies outlined below.

### 6.5.1 Methodology

The computational methods used to study NMP are similar to those used for redox processes: high-level single reference methods such as G3(MP2)-RAD with appropriate solvation corrections. An example showing agreement of theory and experiment is provided in Figure 6.19, where theory is obtained using an ONIOM correction to G3(MP2)-RAD and solvent is modelled using the PCM-UAQS continuum model.<sup>166</sup> In this case the Gibbs free energies of reaction agree to within a mean absolute deviation of 4.5 kJ mol<sup>-1</sup>. The kinetics of most of the side reactions in NMP are likewise well described by the same methodology; however, the kinetics of the  $\sigma$ -bond dissociation are, as described in section 6.2.1, a multireference problem. Fortunately modelling the kinetics of alkoxyamine bond dissociation are important for predicting the outcome of an NMP process because the reverse reaction is essentially barrierless and hence the barrier for the forward process is dominated by the thermodynamics.<sup>167</sup>

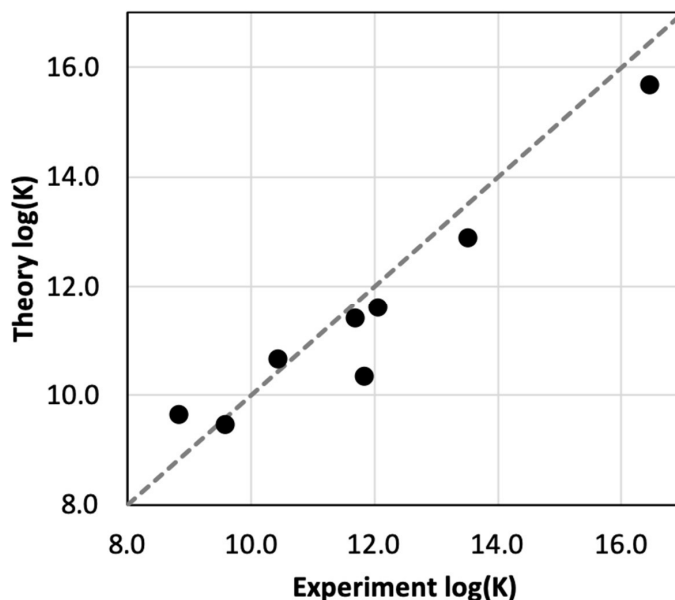


**Figure 6.19.** Comparison of quantum-chemical and experimental equilibrium constants for alkoxyamine dissociation. Theoretical calculations performed using an ONIOM approximation of G3(MP2)-RAD//B3-LYP/6-31G(d) in conjunction with PCM-UAQS solvation energies at the B3-LYP/6-31G(d) level. Data taken from Ref <sup>166</sup>.

### 6.5.2 Selected Applications

**Linear-Free Energy Relationships for Modelling Structure-Reactivity Trends in Controlled Radical Polymerization Macromolecules.**<sup>166, 168, 169</sup> A series of theoretical studies used computational chemistry to develop simple equations for predicting the bond dissociation Gibbs free energy (BDFE) and hence equilibrium constant in nitroxide mediated polymerization as a function of the leaving group and nitroxide. Key to this work was the identification of appropriate descriptors for the steric, resonance and polar properties of the nitroxide and alkyl radical, and statistical analysis to assess which of these factors

were necessary to describe the bond energies. Within a series of alkoxyamines, it was found that the equilibrium constant was well described by the equation<sup>166</sup>

$$\log(\text{Keq}) = -0.10\text{IP} - 0.177\text{RSE} - 0.130\text{RSE}_{\text{nox}} + 38.3 \quad (21)$$

In this equation, IP is the vertical ionization potential of the alkyl radical, RSE is the standard radical stabilization energy the alkyl radical, while  $\text{RSE}_{\text{nox}}$  is a new descriptor for the nitroxide radical, related to the standard radical stabilization energy, but reflecting in this case the flexibility of the nitroxide to the geometric changes associated with formation of an alkoxyamine. In a follow-up study, the linear free energy relationship was expanded to cover multiple types of controlled radical polymerization. The resulting relationship obtained was<sup>168</sup>

$$\text{BDFE}[\text{RX}] = 20.8 \theta[\text{R}] - 9.73 \text{IP}[\text{R}] - 1.10 \text{RSE}[\text{R}] + 192 \theta[\text{X}] + 57.4 \text{EA}[\text{X}] - 62.0 \text{Resonance}[\text{X}] - 250 \quad (22)$$

where the steric descriptors  $\theta[\text{R}]$  and  $\theta[\text{X}]$  are measured as Tolman's cone angle of Cl-R and  $\text{CH}_3\text{-X}$  respectively, the polar descriptors IP[R] and EA[X] are the (gas-phase) ionization energy of  $\text{R}\cdot$  and electron affinity of  $\text{X}\cdot$  respectively, and the radical stability or resonance descriptors RSE[R] and Resonance[X] are measured as the standard radical stabilization energy for  $\text{R}\cdot$  and the inverse HOMO-LUMO energy gap for  $\text{X}\cdot$ . Apart from providing a predictive relationship for the bond energy (and hence equilibrium constant for the controlling equilibrium), the analysis of the descriptor values allows for a comparison of the relative importance of polar, steric and resonance effects in NMP versus atom transfer radical polymerization (ATRP) and reversible addition fragmentation chain transfer (RAFT) (Figure 6.20). From Figure 6.20 it is clear that steric effects are relatively consistent across the different processes, while polar effects are important for ATRP and RAFT, and resonance effects are important for NMP and RAFT. This in turn gives some guidance as to not only what control agent might be important for a particular type of polymer, but what controlled radical polymerization process itself might be necessary to target the right equilibrium constant.

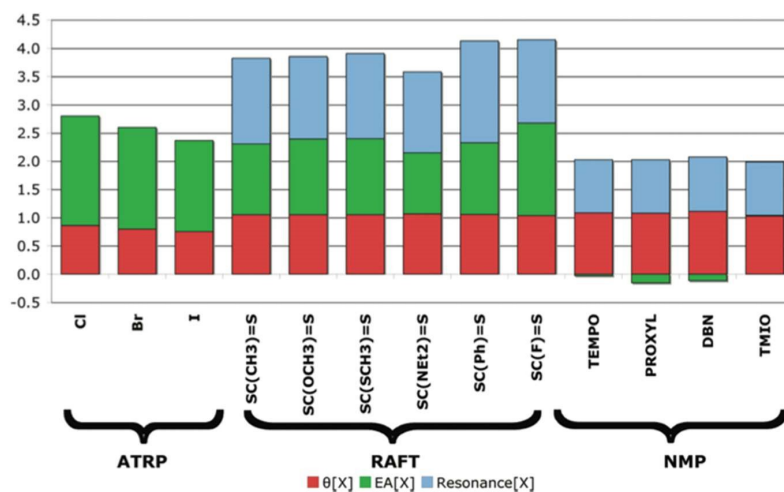


**Figure 6.20.** Values of each of the X-descriptors in dimensionless units (obtained by dividing each value by the average value for that descriptor across the full data set). Figure reproduced directly from Ref. <sup>168</sup>.

## Which Side-Reactions Compromise Nitroxide Mediated Polymerization?

<sup>170</sup> In this work, a combination of quantum chemistry and kinetic modelling (using the software PREDICI) was used to identify the key side reactions in NMP and study how they varied for different combinations of NMP agents (specifically TEMPO, SG1 and DPAIO) and monomer (styrene, methyl acrylate and methyl methacrylate). A variety of side reactions had been proposed to interfere with NMP (Figure 6.21); through first principles modelling, the study was able to show that the main one was an intramolecular alkoxyamine decomposition (often referred to as ‘disproportionation’) via a Cope-type elimination, which was kinetically significant for TEMPO- and SG1-mediated polymerizations of MMA, and not significant for the other systems. The  $\beta$ -scission process was also found to be problematic for propagating radicals bearing an abstractable hydrogen. Interestingly, it was also found that, due to penultimate unit effects, the decomposition of alkoxyamines can occur via principally different mechanisms between the unimeric and polymeric species.

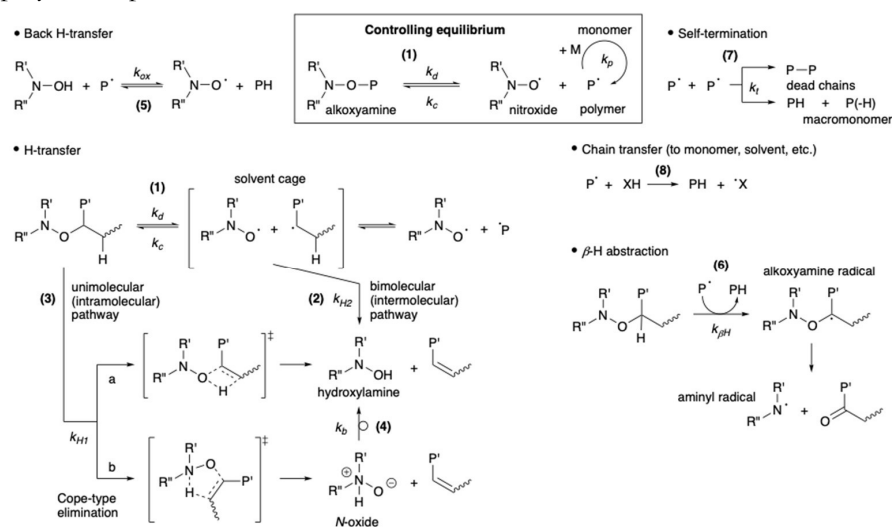
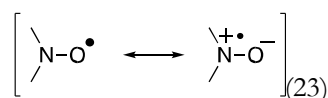


**Figure 6.21.** Nitroxide mediated polymerization and its competing side-reactions. Figure reproduced directly from Ref. <sup>170</sup>.

## Computational Design of pH-Switchable Control Agents for Nitroxide Mediated Polymerization<sup>155, 171-174</sup>

One of the disadvantages of nitroxide mediated polymerization is the relatively high temperatures needed for sufficient alkoxyamine dissociation. Not only does this render polymerization susceptible to side reactions, as seen above, but it also precludes alkoxyamines as a convenient source of carbon-centred radicals in natural product synthesis. Thus, if one could trigger alkoxyamine decomposition under mild conditions in a controlled manner this would be very attractive. One approach is using light and this is outlined below; another is using electrostatic effects. The basic principle behind this latter approach is to take advantage of the dipole associated with the  $\text{N-O}^\bullet$  functionality:





Thus a remote negative charge the nitrogen side of the nitroxide should stabilize this dipole and in doing stabilize the radical. Initial computational and experimental studies showed that indeed deprotonation of the carboxylic acid group in 4-carboxy-TEMPO lowered the gas-phase bond dissociation energies of its corresponding alkoxyamines by around 20 kJ mol<sup>-1</sup>, irrespective of the leaving group.<sup>171, 172</sup> Follow up experimental studies in dichloromethane showed that this “pH-switch” decreased ca. 8.5 kJ mol<sup>-1</sup> due to the increased dielectric constant of the reaction medium and associated decrease in the electrostatic interactions.<sup>174</sup> At that level, while significant, the pH-switch was not large enough to allow 4-carboxy-TEMPO to facilitate NMP at room temperature.<sup>173</sup> Computational studies were thus undertaken to test other nitroxides, known and novel, to see if any would be suitable for room temperature NMP when charged and would be stable when neutral.<sup>173</sup> Design principles used in choosing the test set included synthetic accessibility, increasing the inherent stability of the nitroxide when uncharged, and placing the charge closer to the nitroxide (but without conjugation). Among the successful designs was a carboxy-TIPNO derivative which is indeed predicted to toggle between stability and radical release at room temperature (Figure 6.22). In this study, computational chemistry provided the initial insights behind electrostatic stabilization and its dependence on chemical structure,<sup>171, 172</sup> and subsequently allowed for a large number of molecules to be screened prior to undertaking laborious synthetic work.<sup>173</sup>

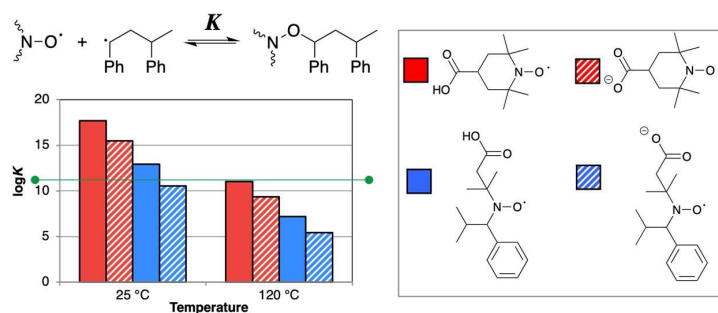


**Figure 6.22.** Change in equilibrium constant (in bulk styrene at 120°C and 25°C) upon deprotonation of 4-carboxy-TEMPO and a TIPNO derivative bearing a remote carboxylic acid group. The green line shows the equilibrium constant of neutral 4-carboxy-TEMPO, which functions well at 120°C and represents a target value for the deprotonated species at room temperature. Above this line the alkoxyamine is too stable to sustain a polymerization; below it too many radicals are released for control. Data taken from Ref. <sup>173</sup>.

## 6.5 Studying Photoactive Nitroxides

Photoactive nitroxides remain an active area of interest, with potential uses as sensors, probes, and as nitroxide-mediated polymerization agents that can be activated under mild conditions.<sup>175-177</sup> Despite the reasonable amount of literature on photoactive nitroxides, and the well-established quenching of fluorescence upon formation of the nitroxide radical species, there is limited literature on exploring their excited states with computational methods.<sup>178</sup> Photoactive nitroxides do, however, exhibit several properties that can guide our approach to how we might explore their excited states. In this section, the different properties, how these properties can lead to different types of reactivity, and how we can model them, will be described.

### 6.6.1 Methodological Aspects

UV-Vis Spectra. Nitroxides like, for example, TEMPO exhibit thermal reactivity in which a stable nitroxide radical is formed, however its  $\sigma$ -bond framework does not lend itself to photoactivity. A widely used approach to increasing light absorption is to introduce highly conjugated chromophore substituents (Figure 6.23).<sup>179-181</sup> These extended  $\pi$ -systems introduce relatively low energy, bright  $\pi\pi^*$  excited states as well as, provided nitrogen and/or oxygen are present, potentially reactive, spectroscopically dark,  $n\pi^*$  states. The increased size of the potential molecules of interest can, however, prevent the application of ab initio excited state methods like, for example, Equation-of-Motion Coupled Cluster (EOM-CCSD)<sup>182</sup> or Algebraic Diagrammatic

Construction (ADC(n)) methods.<sup>183</sup> The extensive conjugation can also give rise to significant correlation effects, for example doubly excited states or multiple low-lying excited states. These states are often difficult, or in the case of doubly excited state impossible, to capture using single-determinant excited state methods, for example time-dependent density functional theory (TD-DFT),<sup>184</sup> or time-dependent Hartree-Fock (TD-HF).<sup>185</sup> Ideally, multireference methods (CASSCF, CASPT2)<sup>186</sup> would be employed, which would be capable of capturing the nature of each excited state and any correlation effects. As with most multireference calculations, however, issues will remain with respect to the size of the active space required to accurately model the excited states, as the significant scaling issues will quickly prevent large molecules/large active spaces from being computationally tractable.

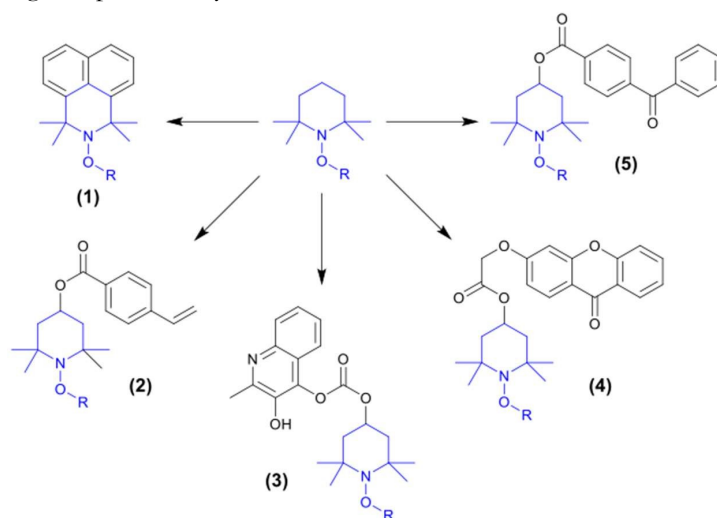


**Figure 6.23.** Examples of TEMPO-derived, photoactive nitroxide compounds, using naphthalene<sup>179</sup> (1), benzoyloxy<sup>180</sup> (2), quinoline<sup>181</sup> (3), xanthone<sup>181</sup> (4), and diphenyl-methanone<sup>181</sup> (5) based chromophores.

Often, the first test of suitability for a particular method is to compute the vertical excitation energies and oscillator intensities for a molecule at its groundstate, equilibrium geometry. Comparison of the computed spectrum against its experimental counterpart serves as a benchmark against which the accuracy of the method can be determined, and can immediately provide insight into the nature of the excited states of interest. When using wavefunction excited

state methods, for example EOM-CCSD or CASSCF, it is important to ensure a large enough basis set is employed, as such methods exhibit a significant dependence between the calculated vertical excitation energy and basis set.<sup>187, 188</sup> At a minimum, a triple-zeta basis set ought to be employed augmented, if possible, with diffuse functions so as to more accurately model the less tightly bound excited state electrons and charge-transfer states. TD-DFT is found to exhibit a smaller basis set dependence, however its accuracy will too benefit from using a large basis set, if possible.<sup>187</sup>

**Excited-State Charge Transfer.** The introduction of chromophores does not necessarily result in the desired photoreactivity. Sometimes, this can be attributed to the separation of the conjugated chromophore and the reactive species by the nitroxide  $\sigma$ -framework, and can result in orbital localization, which in turn gives rise to charge-transfer states (Figure 6.24). To fully model these states, any multireference calculations should include the orbitals on each of the moieties, however this can be difficult if the active space becomes too large. If wavefunction calculations are too expensive to run, it is often necessary to turn to TD-DFT, which is much cheaper. In order to assess the best DFT functional to employ for the best accuracy and performance it may be necessary to consult existing benchmarking literature,<sup>189</sup> which can provide information about functional accuracy relative to the type of property being investigated. An important issue with TD-DFT is, however, its well documented failure when attempting to describe charge-transfer states, which precludes the use of traditional, uncorrected functionals (for example BLYP, B3LYP, or SVWN).<sup>190</sup> It is necessary instead to employ long-range corrected functionals; for example, LC- $\omega$ HPBE or  $\omega$ B97X-D.<sup>191</sup> These functionals include parameters that mitigate self-interaction error in DFT and TD-DFT, and should correctly predict the  $1/R$  asymptotic interaction between the localised charges of the charge-transfer states.

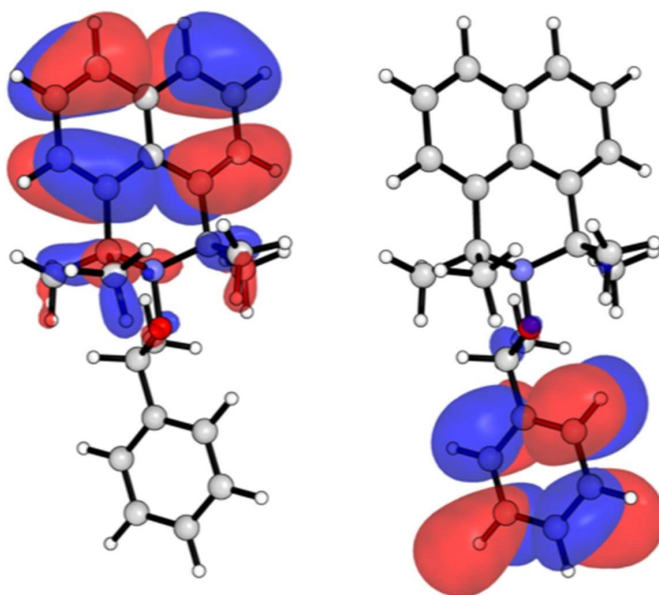


**Figure 6.24.** Orbital localization of  $\pi$ -system across the naphthalene moiety (left), and localization of  $\pi^*$ -system across the styrene moiety (right)

**Non-Adiabatic Excited State Behaviour.** Finally, upon excitation it is possible for the nitroxide molecule to undergo complex internal transfer processes like, for example, intersystem crossing (ISC) between different spin states to surfaces that may be highly reactive.<sup>192</sup> An example could be naphthalene tempo, which can be used as a photoinitiation mediated polymerisation agent.<sup>179</sup> Exciting the molecule could result in efficient ISC to a triplet surface; with the electrons unpaired, it is now easier to form the required reactive radical species.

The phenomena that give rise to efficient population of reactive states, for example conical intersections, can be difficult to model with single-determinant methods; the convergence of two excited state wavefunctions makes the corresponding regions of molecular geometry inherently multideterminant, and are best captured with multireference methods such as CASSCF and CASPT2. As mentioned earlier, however, if such methods are inappropriate for a given system it is often necessary to turn again to TD-DFT. Unfortunately, TD-DFT is unable to correctly describe the  $3N-8$  dimensionality (where  $N$  is the number of atoms) of conical intersections.<sup>193</sup> Despite this, recent work suggests that CAM-B3LYP, M06-2X, and BH&HLYP are capable of qualitatively reproducing the geometries at which conical intersections are found.<sup>194</sup> As well as this, M06-2X and BMK are two functionals found to best reproduce singlet-triplet gaps of the excited states of a range of organic molecules,<sup>19</sup> suggesting that the M06-2X functional at least should be applicable to nitroxide excited states and capable of capturing key aspects of nitroxide photoreactivity.

### 6.6.2 Selected Applications

#### Case Study: Theoretical Study of the Photochemical Initiation in

**Nitroxide-Mediated Photopolymerization.**<sup>178</sup> In their 2014 paper, HuixRotllant et al.<sup>178</sup> employed computational methods to explore the photoinitiation mechanism of nitroxide mediated photopolymerisation. The molecule of interest, shown in Figure 6.25, is expected to exhibit several of the photochemical features described above; charge-transfer from the acetophenone to the tert-butyl moieties, and excited states of different symmetries, i.e.  $\pi\pi^*$  and  $n\pi^*$  states originating from the nitrogen and acyl oxygen groups. It is therefore important to select a method capable of at least qualitatively capturing potential states of interest. To that end, Huix-Rotllant et al.<sup>178</sup> used two methods, (unrestricted) DFT and the second-order extended multireference quasi-degenerate perturbation theory (XMCQDPT2),<sup>195</sup> to give a balanced description of the most likely photochemical processes taking place. The benefit of this approach is the bulk of the computational work can be performed with relatively cheap DFT, and (qualitative) accuracy is ensured by comparison with multireference methods. The active space employed for the multireference calculations contained the  $\pi/\pi^*$  and  $\sigma/\sigma^*$  of interest.

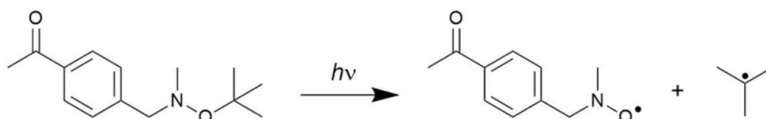


**Figure 6.25.** Photodissociation mechanism investigated by Huix-Rotllant et al.<sup>178</sup>

The study examined the change in several properties; bond dissociation energies, ground- and excited-state equilibrium geometries, and their respective N-O and C-O bond lengths. The study was able to identify the key steps taking place in the photochemical dissociation reaction:

1. Absorption of photon and excitation to  $n \pi^*$  state, localised on acetophenone moiety
2. Singlet-triplet intersystem crossing, localised still on acetophenone
3. Triplet energy delocalisation across alkoxyamine moiety
4. Bond dissociation of three bonds;  $\sigma_{O-C}$  (desirable), and  $\sigma_{N-O}$  and  $\sigma_{N-C}$

### 6.6.3 Concluding remarks.

To conclude, due to their size and complicated photochemical processes, photoactive alkoxyamines present a challenge to current excited state computational methods. However, appropriate application of single- and multideterminant methods should allow for a reliable, qualitative description of their key features. Single-determinant, “black-box” methods should either be correlated wavefunction methods (if possible), or TD-DFT using long-range corrected functionals with some portion of exact exchange. If necessary multireference methods can also be employed, with active spaces consisting of relevant  $\pi$ -,  $\sigma$ -, and  $n$ -orbitals.

### 6.7 Further Applications

The applications of computational chemistry described in this Chapter are by no means exhaustive. For instance, computational chemistry has played an important role in clarifying the mechanism of the Denisov cycle by which hindered amine light stabilizers protect polymers from oxidative damage,<sup>196, 197</sup> and identified a number of key side reactions in this process.<sup>198, 199</sup> These calculations were carried out using high-level single reference procedures, analogous to those used in studies of nitroxide mediated polymerization similar procedures. More recently, computational chemistry supported by experiment has been used to study the oxidative cleavage of alkoxyamines to produce nitroxide radicals and carbocations, both directly and promoted via  $S_N2$  reactions with nucleophiles.<sup>151, 152, 155</sup> These studies used analogous procedures to those used in studies of nitroxide redox chemistry. On the basis of the mechanistic understanding provided by computational chemistry, a new in situ methylation procedure was designed and experimentally demonstrated.<sup>200</sup> This procedure, involving the bench and air stable TEMPO-Me reagent, offers major advantages over existing procedures which typically involve reagents with acute toxicity and high volatility. These are just some of the applications of quantum chemistry in studying nitroxide radical chemistry.

As seen in this chapter, the computational methods for studying nitroxides are many and various and the different types of system and property raise distinct methodological challenges. For instance, high spin systems and many excited states are invariably multi-reference in nature, redox potentials and bond energies while single reference usually require high levels of theory, moreover

solvation effects are a potentially large source of error in redox systems, while EPR properties have their set of methods and require accurate treatments of core electrons, normally unnecessary in other systems. Nonetheless, in all cases, provided appropriated precautions are taken, methods exist to make chemically useful predictions.

### Acknowledgments

MLC gratefully acknowledges support from the Australian Research Council (ARC) Centre of Excellence for Electromaterials Science and an ARC Laureate Fellowship.

### References and Notes

1. S. Sanvito, *Chemical Society Reviews*, 2011, 40, 3336-3355.
2. T. Sugawara and M. M. Matsushita, *Journal of Materials Chemistry*, 2009, 19, 1738-1753.
3. I. Ratera and J. Veciana, *Chemical Society Reviews*, 2012, 41, 303-349.
4. A. J. Wingate and B. W. Boudouris, *Journal of Polymer Science Part A: Polymer Chemistry*, 2016, 54, 1875-1894.
5. M. Abe, *Chemical Reviews*, 2013, 113, 7011-7088.
6. A. Szabo and N. Ostlund, *Modern Quantum Chemistry: Introduction to Advanced Electronic Structure Theory*, Dover Publications, 1996.
7. F. Jensen, *Introduction to Computational Chemistry*, John Wiley & Sons, Inc., 2006.
8. A. J. Cohen, P. Mori-Sánchez and W. Yang, *Chemical Reviews*, 2012, 112, 289-320.
9. D. K. W. Mok, R. Neumann and N. C. Handy, *The Journal of Physical Chemistry*, 1996, 100, 6225-6230.
10. C. J. Cramer, *Essentials of Computational Chemistry: Theories and Models*, Wiley, New York, 2002.
11. P. G. Szalay, T. Müller, G. Gidofalvi, H. Lischka and R. Shepard, *Chemical Reviews*, 2012, 112, 108-181.
12. V. Veryazov, P. Å. Malmqvist and B. O. Roos, *International Journal of Quantum Chemistry*, 2011, 111, 3329-3338.
13. R. Dawes and S. A. Ndengué, *International Reviews in Physical Chemistry*, 2016, 35, 441-478.
14. F. Aiga, *The Journal of Physical Chemistry A*, 2012, 116, 663-669.
15. F. Krausbeck, D. Mendive-Tapia, A. J. W. Thom and M. J. Bearpark, *Computational and Theoretical Chemistry*, 2014, 1040-1041, 14-19.
16. K. Hirao, ed., *Recent Advances in Multireference Methods*, WORLD SCIENTIFIC, 1999.
17. H. J. Werner and P. J. Knowles, *The Journal of Chemical Physics*, 1985, 82, 5053-5063.
18. R. J. Buenker and S. D. Peyerimhoff, *Theoretica chimica acta*, 1974, 35, 33-58.

19. J. Miralles, O. Castell, R. Caballol and J.-P. Malrieu, *Chemical Physics*, 1993, 172, 33-43.
20. V. M. García, M. Reguero and R. Caballol, *Theoretical Chemistry Accounts*, 1997, 98, 50-56.
21. V. M. García, O. Castell, R. Caballol and J. P. Malrieu, *Chemical Physics Letters*, 1995, 238, 222-229.
22. J. Finley, P.-Å. Malmqvist, B. O. Roos and L. Serrano-Andrés, *Chemical Physics Letters*, 1998, 288, 299-306.
23. P. Celani and H.-J. Werner, *The Journal of Chemical Physics*, 2000, 112, 55465557.
24. C. Li and F. A. Evangelista, *The Journal of Chemical Physics*, 2016, 144, 164114.
25. D. I. Lyakh, M. Musiał, V. F. Lotrich and R. J. Bartlett, *Chemical Reviews*, 2012, 112, 182-243.
26. H.-J. Werner, *Molecular Physics*, 1996, 89, 645-661.
27. J. P. Malrieu, R. Caballol, C. J. Calzado, C. de Graaf and N. Guihéry, *Chemical Reviews*, 2014, 114, 429-492.
28. P. Pulay, *International Journal of Quantum Chemistry*, 2011, 111, 3273-3279.
29. J. P. Zobel, J. J. Nogueira and L. González, *Chemical science*, 2017, 8, 14821499.
30. C. Camacho, H. A. Witek and S. Yamamoto, *Journal of Computational Chemistry*, 2009, 30, 468-478.
31. I. Schapiro, K. Sivalingam and F. Neese, *Journal of Chemical Theory and Computation*, 2013, 9, 3567-3580.
32. C. Angeli, M. Pastore and R. Cimiraglia, *Theoretical Chemistry Accounts*, 2007, 117, 743-754.
33. S. Tolstikov, E. Tretyakov, S. Fokin, E. Suturina, G. Romanenko, A. Bogomyakov, D. Stass, A. Maryasov, M. Fedin, N. Gritsan and V. Ovcharenko, *Chemistry – A European Journal*, 2014, 20, 2793-2803.
34. V. Barone, C. Boilleau, I. Cacelli, A. Ferretti, S. Monti and G. Prampolini, *Journal of Chemical Theory and Computation*, 2013, 9, 300-307.
35. V. Barone, C. Boilleau, I. Cacelli, A. Ferretti and G. Prampolini, *Journal of Chemical Theory and Computation*, 2013, 9, 1958-1963.
36. V. Barone, I. Cacelli, P. Cimino, A. Ferretti, S. Monti and G. Prampolini, *The Journal of Physical Chemistry A*, 2009, 113, 15150-15155.
37. V. Barone, I. Cacelli, A. Ferretti and M. Girlanda, *The Journal of Chemical Physics*, 2008, 128, 174303.
38. V. Barone, I. Cacelli, A. Ferretti, S. Monti and G. Prampolini, *Physical Chemistry Chemical Physics*, 2011, 13, 4709-4714.
39. V. Barone, I. Cacelli, A. Ferretti, S. Monti and G. Prampolini, *Journal of Chemical Theory and Computation*, 2011, 7, 699-706.
40. V. Barone, I. Cacelli, A. Ferretti and G. Prampolini, *Physical Chemistry Chemical Physics*, 2009, 11, 3854-3860.
41. V. Barone, I. Cacelli and A. Ferretti, *Physical Chemistry Chemical Physics*, 2018, 20, 18547-18555.
42. C. J. Calzado, C. Angeli, C. de Graaf and R. Caballol, *Theoretical Chemistry Accounts*, 2011, 128, 505-519.

43. G. M. J. Barca, A. T. B. Gilbert and P. M. W. Gill, *Journal of Chemical Theory and Computation*, 2018, 14, 1501-1509.
44. L. Noodleman, C. Y. Peng, D. A. Case and J. M. Mouesca, *Coordination Chemistry Reviews*, 1995, 144, 199-244.
45. L. Noodleman, *The Journal of Chemical Physics*, 1981, 74, 5737-5743.
46. K. Yamaguchi, Y. Takahara and T. Fueno, Dordrecht, 1986.
47. K. Yamaguchi, Y. Takahara, T. Fueno and K. N. Houk, *Theoretica chimica acta*, 1988, 73, 337-364.
48. A. S. Menon and L. Radom, *The Journal of Physical Chemistry A*, 2008, 112, 13225-13230.
49. K. Raghavachari and J. B. Anderson, *The Journal of Physical Chemistry*, 1996, 100, 12960-12973.
50. Y. Kitagawa, T. Saito and K. Yamaguchi, 2018, DOI: 10.5772/intechopen.75726.
51. K. C. Ko, D. Cho and J. Y. Lee, *The Journal of Physical Chemistry A*, 2012, 116, 6837-6844.
52. K. C. Ko, D. Cho and J. Y. Lee, *The Journal of Physical Chemistry A*, 2013, 117, 3561-3568.
53. D. Cho, K. C. Ko and J. Y. Lee, *The Journal of Physical Chemistry A*, 2014, 118, 5112-5121.
54. D. Cho, K. C. Ko and J. Y. Lee, *International Journal of Quantum Chemistry*, 2016, 116, 578-597.
55. M. E. Ali and S. N. Datta, *The Journal of Physical Chemistry A*, 2006, 110, 2776-2784.
56. M. E. Ali and S. N. Datta, *The Journal of Physical Chemistry A*, 2006, 110, 10525-10527.
57. E. I. Izgorodina, D. R. B. Brittain, J. L. Hodgson, E. H. Krenske, C. Y. Lin, M. Namazian and M. L. Coote, *J. Phys. Chem. A*, 2007, 111, 10754-10768.
58. D. Reta Mañeru, A. K. Pal, I. d. P. R. Moreira, S. N. Datta and F. Illas, *Journal of Chemical Theory and Computation*, 2014, 10, 335-345.
59. A. I. Krylov, *Chemical Physics Letters*, 2001, 338, 375-384.
60. A. I. Krylov, *Chemical Physics Letters*, 2001, 350, 522-530.
61. A. I. Krylov and C. D. Sherrill, *The Journal of Chemical Physics*, 2002, 116, 3194-3203.
62. Y. Shao, M. Head-Gordon and A. I. Krylov, *The Journal of Chemical Physics*, 2003, 118, 4807-4818.
63. L. V. Slipchenko and A. I. Krylov, *The Journal of Chemical Physics*, 2002, 117, 4694-4708.
64. S. V. Levchenko and A. I. Krylov, *The Journal of Chemical Physics*, 2003, 120, 175-185.
65. A. A. Golubeva, A. V. Nemukhin, S. J. Klippenstein, L. B. Harding and A. I. Krylov, *The Journal of Physical Chemistry A*, 2007, 111, 13264-13271.
66. T. Tsuchimochi, *The Journal of Chemical Physics*, 2015, 143, 144114.



67. J. Mato and M. S. Gordon, *Physical Chemistry Chemical Physics*, 2018, 20, 2615-2626.
68. X. Zhang and J. M. Herbert, *The Journal of Chemical Physics*, 2015, 143, 234107.
69. D. Casanova and M. Head-Gordon, *Physical Chemistry Chemical Physics*, 2009, 11, 9779-9790.
70. F. Bell, P. M. Zimmerman, D. Casanova, M. Goldey and M. Head-Gordon, *Physical Chemistry Chemical Physics*, 2013, 15, 358-366.
71. M. Song, X. Song and Y. Bu, *Physical Chemistry Chemical Physics*, 2018, 20, 8099-8111.
72. Z. Rolik, L. Szegedy, I. Ladjánszki, B. Ladóczki and M. Kállay, *J. Chem. Phys.*, 2013, 139, 094105.
73. S. Stoll and A. Schweiger, *Journal of Magnetic Resonance*, 2006, 178, 42-55.
74. D. R. Duling, *Journal of Magnetic Resonance, Series B*, 1994, 104, 105-110.
75. D. Wang and G. R. Hanson, *Journal of Magnetic Resonance, Series A*, 1995, 117, 1-8.
76. G. R. Hanson, C. J. Noble and S. Benson, in *High Resolution EPR: Applications to Metalloenzymes and Metals in Medicine*, eds. L. Berliner and G. Hanson, Springer New York, New York, NY, 2009, DOI: 10.1007/9780-387-84856-3\_4, pp. 105-173.
77. K. Khairy, D. Budil and P. Fajer, *Journal of Magnetic Resonance*, 2006, 183, 152-159.
78. D. J. Schneider and J. H. Freed, in *Spin Labeling: Theory and Applications*, eds. L. J. Berliner and J. Reuben, Springer US, Boston, MA, 1989, DOI: 10.1007/978-1-4613-0743-3\_1, pp. 1-76.
79. L. Hermosilla, J. M. García de la Vega, C. Sicero and P. Calle, *J. Chem. Theory Comput.*, 2011, 7, 1169-1179.
80. A. Savitsky, M. Plato and K. Möbius, *Applied Magnetic Resonance*, 2009, 37, 415.
81. T. Janoschka, N. Martin, U. Martin, C. Friebe, S. Morgenstern, H. Hiller, M. D. Hager and U. S. Schubert, *Nature*, 2015, 527, 78.
82. H. Nishide and K. Oyaizu, *Science*, 2008, 319, 737-738.
83. T. Suga, H. Ohshiro, S. Sugita, K. Oyaizu and H. Nishide, *Advanced Materials*, 2009, 21, 1627-1630.
84. T. Janoschka, M. D. Hager and U. S. Schubert, *Advanced Materials*, 2012, 24, 6397-6409.
85. K. Zhang, Y. Hu, L. Wang, J. Fan, M. J. Monteiro and Z. Jia, *Polymer Chemistry*, 2017, 8, 1815-1823.
86. J. B. Gerken and S. S. Stahl, *ACS Central Science*, 2015, 1, 234-243.
87. A. Badalyan and S. S. Stahl, *Nature*, 2016, 535, 406.
88. M. Rafiee, K. C. Miles and S. S. Stahl, *Journal of the American Chemical Society*, 2015, 137, 14751-14757.
89. Q. Cao, L. M. Dornan, L. Rogan, N. L. Hughes and M. J. Muldoon, *Chemical Communications*, 2014, 50, 4524-4543.
90. M. Zhang, C. Chen, W. Ma and J. Zhao, *Angewandte Chemie International Edition*, 2008, 47, 9730-9733.

91. Z. Zhang, P. Chen, T. N. Murakami, S. M. Zakeeruddin and M. Grätzel, *Advanced Functional Materials*, 2008, 18, 341-346.
92. J. Min, J. Won, Y. S. Kang and S. Nagase, *Journal of Photochemistry and Photobiology A: Chemistry*, 2011, 219, 148-153.
93. T. Murakami, F. Kato, K. Oyaizu and H. Nishide, *Journal of Photopolymer Science and Technology*, 2010, 23, 353-355.
94. K. Fumiaki, H. Naoki, M. Takaya, O. Chie, O. Kenichi and N. Hiroyuki, *Chemistry Letters*, 2010, 39, 464-465.
95. B. P. Soule, F. Hyodo, K.-i. Matsumoto, N. L. Simone, J. A. Cook, M. C. Krishna and J. B. Mitchell, *Free Radical Biology and Medicine*, 2007, 42, 1632-1650.
96. T. OFFER, A. RUSSO and A. SAMUNI, *The FASEB Journal*, 2000, 14, 1215-1223.
97. M. B. Lauber and S. S. Stahl, *ACS Catalysis*, 2013, 3, 2612-2616.
98. S. D. Rychnovsky, R. Vaidyanathan, T. Beauchamp, R. Lin and P. J. Farmer, *The Journal of Organic Chemistry*, 1999, 64, 6745-6749.
99. M. Saita, J. Kaneko, T. Sato, S.-s. Takahashi, S. Wada-Takahashi, R. Kawamata, T. Sakurai, M.-C.-i. Lee, N. Hamada, K. Kimoto and Y. Nagasaki, *Biomaterials*, 2016, 76, 292-301.
100. C. Abe, Y. Uto, A. Kawasaki, C. Noguchi, R. Tanaka, T. Yoshitomi, Y. Nagasaki, Y. Endo and H. Hori, *Journal of Controlled Release*, 2014, 182, 67-72.
101. M. C. Krishna, D. A. Grahame, A. Samuni, J. B. Mitchell and A. Russo, *Proceedings of the National Academy of Sciences*, 1992, 89, 5537-5541.
102. Y. Kinoshita, K.-i. Yamada, T. Yamasaki, F. Mito, M. Yamato, N. Kosem, H. Deguchi, C. Shirahama, Y. Ito, K. Kitagawa, N. Okukado, K. Sakai and H. Utsumi, *Free Radical Biology and Medicine*, 2010, 49, 1703-1709.
103. A. V. Marenich, J. Ho, M. L. Coote, C. J. Cramer and D. G. Truhlar, *Physical Chemistry Chemical Physics*, 2014, 16, 15068-15106.
104. J. Ho, M. Coote, C. Cramer and D. Truhlar, in *Organic Electrochemistry: Revised and Expanded*, eds. O. Hammerich and B. Speiser, CRC Press, Taylor and Francis Group, 2015, DOI: 10.1201/b19122-8, pp. 229-259.
105. L. E. Roy, E. Jakubikova, M. G. Guthrie and E. R. Batista, *The Journal of Physical Chemistry A*, 2009, 113, 6745-6750.
106. R. S. Berry, S. A. Rice and J. Ross, *Physical Chemistry*, Second Edition, Oxford University Press, New York, 2000.
107. C. G. Zoski, *Handbook of Electrochemistry*, Elsevier, Amsterdam, 2007.
108. C. Møller and M. S. Plesset, *Phys. Rev.*, 1934, 46, 618-622.
109. M. Head-Gordon, J. A. Pople and M. J. Frisch, *Chem. Phys. Lett.*, 1988, 153, 503-506.
110. J. A. Pople, J. S. Binkley and R. Seeger, *Int. J. Quantum Chem.*, 1976, 10, 1-19.
111. R. Krishnan and J. A. Pople, *Int. J. Quantum Chem.*, 1978, 14, 91-100.
112. P. J. Knowles, J. S. Andrews, R. D. Amos, N. C. Handy and J. A. Pople, *Chem. Phys. Lett.*, 1991, 186, 130-136.
113. W. J. Lauderdale, J. F. Stanton, J. Gauss, J. D. Watts and R. J. Bartlett, *Chem. Phys. Lett.*, 1991, 187, 21-28.

114. W. J. Lauderdale, J. F. Stanton, J. Gauss, J. D. Watts and R. J. Bartlett, *J. Chem. Phys.*, 1992, 97, 6606-6620.
115. G. D. Purvis and R. J. Bartlett, *J. Chem. Phys.*, 1982, 76, 1910-1918.
116. G. E. Scuseria, C. L. Janssen and H. F. Schaefer, *J. Chem. Phys.*, 1988, 89, 7382-7387.
117. J. A. Pople, M. Head-Gordon and K. Raghavachari, *J. Chem. Phys.*, 1987, 87, 5968-5975.
118. J. Gauss and D. Cremer, *Chem. Phys. Lett.*, 1988, 150, 280-286.
119. E. A. Salter, G. W. Trucks and R. J. Bartlett, *J. Chem. Phys.*, 1989, 90, 1752-1766.
120. A. Tajti, P. G. Szalay, A. G. Császár, M. Kállay, J. Gauss, E. F. Valeev, B. A. Flowers, J. Vázquez and J. F. Stanton, *J. Chem. Phys.*, 2004, 121, 11599-11613.
121. A. Karton, E. Rabinovich, J. M. L. Martin and B. Ruscic, *J. Chem. Phys.*, 2006, 125, 144108.
122. J. A. Pople, M. Head-Gordon, D. J. Fox, K. Raghavachari and L. A. Curtiss, *J. Chem. Phys.*, 1989, 90, 5622-5629.
123. L. A. Curtiss, C. Jones, G. W. Trucks, K. Raghavachari and J. A. Pople, *J. Chem. Phys.*, 1990, 93, 2537-2545.
124. L. A. Curtiss, K. Raghavachari, G. W. Trucks and J. A. Pople, *J. Chem. Phys.*, 1991, 94, 7221-7230.
125. L. A. Curtiss, K. Raghavachari, P. C. Redfern, V. Rassolov and J. A. Pople, *J. Chem. Phys.*, 1998, 109, 7764-7776.
126. L. A. Curtiss, P. C. Redfern and K. Raghavachari, *J. Chem. Phys.*, 2007, 126, 084108.
127. D. J. Henry, M. B. Sullivan and L. Radom, *J. Chem. Phys.*, 2003, 118, 48494860.
128. M. R. Nyden and G. A. Petersson, *J. Chem. Phys.*, 1981, 75, 1843-1862.
129. G. A. Petersson, A. Bennett, T. G. Tensfeldt, M. A. Al-Laham, W. A. Shirley and J. Mantzaris, *J. Chem. Phys.*, 1988, 89, 2193-2218.
130. G. A. Petersson and M. A. Al-Laham, *J. Chem. Phys.*, 1991, 94, 60816090.
131. G. A. Petersson, T. G. Tensfeldt and J. A. Montgomery, *J. Chem. Phys.*, 1991, 94, 6091-6101.
132. J. A. Montgomery, J. W. Ochterski and G. A. Petersson, *J. Chem. Phys.*, 1994, 101, 5900-5909.
133. J. W. Ochterski, G. A. Petersson and J. A. Montgomery, *J. Chem. Phys.*, 1996, 104, 2598-2619.
134. J. A. Montgomery, M. J. Frisch, J. W. Ochterski and G. A. Petersson, *J. Chem. Phys.*, 1999, 110, 2822-2827.
135. J. A. Montgomery, M. J. Frisch, J. W. Ochterski and G. A. Petersson, *J. Chem. Phys.*, 2000, 112, 6532-6542.
136. J. M. L. Martin and G. de Oliveira, *J. Chem. Phys.*, 1999, 111, 1843-1856.
137. S. Parthiban and J. M. L. Martin, *J. Chem. Phys.*, 2001, 114, 6014-6029.
138. A. D. Boese, M. Oren, O. Atasoylu, J. M. L. Martin, M. Kállay and J. Gauss, *J. Chem. Phys.*, 2004, 120, 4129-4141.
139. D. Bednarczyk and J. Bednarczyk, *Physics Letters A*, 1978, 64, 409-410.
140. P. Hohenberg and W. Kohn, *Phys. Rev.*, 1964, 136, B864-B871.

141. W. Kohn and L. J. Sham, *Phys. Rev.*, 1965, 140, A1133-A1138.
142. E. I. Izgorodina, M. L. Coote and L. Radom, *J. Phys. Chem. A*, 2005, 109, 7558-7566.
143. J. L. Hodgson, M. Namazian, S. E. Bottle and M. L. Coote, *The Journal of Physical Chemistry A*, 2007, 111, 13595-13605.
144. M. Isegawa, F. Neese and D. A. Pantazis, *Journal of Chemical Theory and Computation*, 2016, 12, 2272-2284.
145. J. Ho, A. Klamt and M. L. Coote, *J. Phys. Chem. A*, 2010, 114, 13442-13444.
146. J. Tomasi, *Theor. Chem. Acc.*, 2004, 112, 184-203.
147. A. V. Marenich, J. Ho, M. L. Coote, C. J. Cramer and D. G. Truhlar, *Phys. Chem. Chem. Phys.*, 2014, 16, 15068-15106.
148. J. Ho and M. L. Coote, *J. Chem. Theory Comput.*, 2009, 5, 295-306.
149. J. R. Pliego Jr. and J. M. Riveros, *J. Phys. Chem. A*, 2001, 105, 7241-7247.
150. A. V. Marenich, C. J. Cramer and D. G. Truhlar, *The Journal of Physical Chemistry B*, 2009, 113, 6378-6396.
151. C. L. Hammill, B. B. Noble, P. L. Norcott, S. Ciampi and M. L. Coote, *The Journal of Physical Chemistry C*, 2019, 123, 5273-5281.
152. B. B. Noble, P. L. Norcott, C. L. Hammill, S. Ciampi and M. L. Coote, *The Journal of Physical Chemistry C*, 2019, 123, 10300-10305.
153. F. J. M. Rogers and M. L. Coote, *The Journal of Physical Chemistry C*, 2019, 123, 20174-20180.
154. F. J. M. Rogers and M. L. Coote, *The Journal of Physical Chemistry C*, 2019, 123, 10306-10310.
155. L. Zhang, E. Laborda, N. Darwish, B. B. Noble, J. H. Tyrell, S. Pluczyk, A. P. Le Brun, G. G. Wallace, J. Gonzalez, M. L. Coote and S. Ciampi, *Journal of the American Chemical Society*, 2018, 140, 766-774.
156. L. Zhang, Y. B. Vogel, B. B. Noble, V. R. Gonçalves, N. Darwish, A. L. Brun, J. J. Gooding, G. G. Wallace, M. L. Coote and S. Ciampi, *Journal of the American Chemical Society*, 2016, 138, 9611-9619.
157. G. Gryn'ova, J. M. Barakat, J. P. Blinco, S. E. Bottle and M. L. Coote, *Chemistry – A European Journal*, 2012, 18, 7582-7593.
158. F. Kato, A. Kikuchi, T. Okuyama, K. Oyaizu and H. Nishide, *Angewandte Chemie*, 2012, 124, 10324-10327.
159. K. Zhang, B. B. Noble, A. C. Mater, M. J. Monteiro, M. L. Coote and Z. Jia, *Physical Chemistry Chemical Physics*, 2018, 20, 2606-2614.
160. J. P. Blinco, J. L. Hodgson, B. J. Morrow, J. R. Walker, G. D. Will, M. L. Coote and S. E. Bottle, *The Journal of Organic Chemistry*, 2008, 73, 67636771.
161. M. Kavala, R. Boča, L. Dlháň, V. Brezová, M. Breza, J. Kožíšek, M. Fronc, P. Herich, L. Švorc and P. Szolcsányi, *The Journal of Organic Chemistry*, 2013, 78, 6558-6569.
162. K. Daze and F. Hof, in *Encyclopedia of Physical Organic Chemistry*, eds. Z. Wang, U. Wille and E. Juaristi, Wiley, 2016, DOI: 10.1002/9781118468586.epoc3001, pp. 1-51.
163. C. R. Martinez and B. L. Iverson, *Chemical Science*, 2012, 3, 2191-2201.

164. A. S. Shetty, J. Zhang and J. S. Moore, *Journal of the American Chemical Society*, 1996, 118, 1019-1027.
165. C. J. Hawker, A. W. Bosman and E. Harth, *Chem. Rev.*, 2001, 101, 3661–3688.
166. J. L. Hodgson, C. Yeh Lin, M. L. Coote, S. R. A. Marque and K. Matyjaszewski, *Macromolecules*, 2010, 43, 3728-3743.
167. J. L. Hodgson, L. B. Roskop, M. S. Gordon, C. Y. Lin and M. L. Coote, *The Journal of Physical Chemistry A*, 2010, 114, 10458-10466.
168. C. Y. Lin, S. R. A. Marque, K. Matyjaszewski and M. L. Coote, *Macromolecules*, 2011, 44, 7568-7583.
169. S. Marque, *The Journal of Organic Chemistry*, 2003, 68, 7582-7590.
170. G. Gryn'ova, C. Y. Lin and M. L. Coote, *Polymer Chemistry*, 2013, 4, 37443754.
171. G. Gryn'ova, D. L. Marshall, S. J. Blanksby and M. L. Coote, *Nature Chemistry*, 2013, 5, 474.
172. G. Gryn'ova and M. L. Coote, *Journal of the American Chemical Society*, 2013, 135, 15392-15403.
173. G. Gryn'ova, L. M. Smith and M. L. Coote, *Physical Chemistry Chemical Physics*, 2017, 19, 22678-22683.
174. M. Klinska, L. M. Smith, G. Gryn'ova, M. G. Banwell and M. L. Coote, *Chemical Science*, 2015, 6, 5623-5627.
175. J. P. Blinco, K. E. Fairfull-Smith, B. J. Morrow and S. E. Bottle, *Australian Journal of Chemistry*, 2011, 64, 373-373.
176. M. Eing, B. T. Tuten, J. P. Blinco and C. Barner-Kowollik, *Chemistry - A European Journal*, 2018, 24, 12246-12249.
177. K. A. Hansen and J. P. Blinco, *Polymer Chemistry*, 2018, 9, 1479-1516.
178. M. Huix-Rotllant and N. Ferre, *Journal of Physical Chemistry A*, 2014, 118, 4464-4470.
179. S. E. Bottle, J.-L. Clement, M. Fleige, E. M. Simpson, Y. Guillaneuf, K. E. Fairfull-Smith, D. Gigmes and J. P. Blinco, *RSC Adv.*, 2016, 6, 8032880333.
180. S. Coiai, E. Passaglia and F. Cicogna, *Polymer International*, 2019, 68, 2763.
181. Y. Guillaneuf, D. Bertin, D. Gigmes, D.-L. Versace, J. Lalevée and J.-P. Fouassier, *Macromolecules*, 2010, 43, 2204-2212.
182. M. Caricato, *Journal of Chemical Theory and Computation*, 2012, 8, 5081-5091.
183. A. Dreuw and M. Wormit, *Wiley Interdisciplinary Reviews: Computational Molecular Science*, 2015, 5, 82-95.
184. R. Ahlrichs and R. Bauernschmitt, *Chemical Physics Letters*, 1996, 256, 454464.
185. M. A. Ball and A. D. McLachlan, *Molecular Physics*, 1964, 7, 501-513.
186. V. Veryazov, P.-A. Malmqvist and B. O. Roos, *International Journal of Quantum Chemistry*, 2011, 111, 3329-3338.
187. A. D. Laurent, A. Blondel and D. Jacquemin, *Theoretical Chemistry Accounts*, 2015, 134, 1-11.
188. M. Schreiber, M. R. Silva-Junior, S. P. A. Sauer and W. Thiel, *Journal of Chemical Physics*, 2008, 128.

189. A. D. Laurent and D. Jacquemin, *International Journal of Quantum Chemistry*, 2013, 113, 2019-2039.
190. A. Dreuw and M. Head-Gordon, *Journal of the American Chemical Society*, 2004, 126, 4007-4016.
191. Y. Jiang, Z. Hu, B. Zhou, C. Zhong, Z. Sun and H. Sun, *The Journal of Physical Chemistry C*, 2019, 123, 5616-5625.
192. W. Domcke and D. R. Yarkony, *Annual Review of Physical Chemistry*, 2012, 63, 325-352.
193. Y. Shu, K. A. Parker and D. G. Truhlar, *Journal of Physical Chemistry Letters*, 2017, 8, 2107-2112.
194. M. Filatov, *Journal of Chemical Theory and Computation*, 2013, 9, 4526-4541.
195. A. A. Granovsky, *Journal of Chemical Physics*, 2011, 134.
196. G. Gryn'ova, K. U. Ingold and M. L. Coote, *Journal of the American Chemical Society*, 2012, 134, 12979-12988.
197. J. L. Hodgson and M. L. Coote, *Macromolecules*, 2010, 43, 4573-4583.
198. M. R. L. Paine, G. Gryn'ova, M. L. Coote, P. J. Barker and S. J. Blanksby, *Polymer Degradation and Stability*, 2014, 99, 223-232.
199. D. L. Marshall, M. L. Christian, G. Gryn'ova, M. L. Coote, P. J. Barker and S. J. Blanksby, *Organic & Biomolecular Chemistry*, 2011, 9, 4936-4947.
200. P. L. Norcott, C. L. Hammill, B. B. Noble, J. C. Robertson, A. Olding, A. C. Bissember and M. L. Coote, *Journal of the American Chemical Society*, 2019, DOI: 10.1021/jacs.9b08634.

## 2.4 Summary and Outlook

The aim of this chapter has been to provide insight into the methodological approaches commonly used to explore photochemical behaviour and nitroxide chemistry. The underlying theory behind these methods, namely DFT and multireference methods, is introduced and summarised in Appendix A.1, this chapter however focuses on what a computational experiment might look like, and the performance, successes, and failings of different methods when applied to different systems.

The main conclusion drawn from this chapter is that computational chemistry is an increasingly indispensable tool for predicting and rationalising the photochemical phenomena of a large range of compounds. Modern density functionals still suffer from self-interaction and charge-transfer errors, and density functional developers are utilising increasingly large test sets in order to minimize average errors. Unfortunately, popular methods like, for example TD-DFT and CASSCF, still largely suffer from the same drawbacks from which they have suffered for many years; namely the failure of TD-DFT for multireference phenomena, and the exponential scaling of CAS methods that give a hard limit to the size of the calculations. As a result, it remains extremely important to assess the performance of a method of choice by consulting either published benchmarking studies, or by performing your own.

This chapter has also provides the foundation and justification for the theoretical methods employed throughout the remainder of this thesis. The size of the systems studied in Chapters 3-6 generally lend themselves to density functional methods, and benchmarking studies for density functionals tend to highlight the sheer number of functionals available in electronic structure software packages, rather than any particularly accurate functional. In general, however, meta-GGA functionals (described in more detail in Appendix A.1) generally provide an acceptable balance of accuracy (or at least, consistency) and computational expense. Of increasing popularity are so-called double hybrid functionals, which include a scaled MP2 energetic component,<sup>10</sup> however the second-order perturbation calculation remains time-consuming and prohibitive, and their continuing development and appearance in the literature is not recipricated by

availability in electronic software packages. A more general move in research towards the development and deployment of predictive algorithms based on artificial intelligence (AI) or machine learning approaches is also driving innovation in, for example, the direct prediction of molecular properties or in the optimization of density functional parameters.<sup>11</sup> Again, however, these techniques are in their infancy and limited to locally developed, unbenchmarked software repositories. In the cases of both AI-driven and double hybrid approaches, however, the fundamental physics of the problems they explore remain unmodelled, and it is unclear to what extent increasingly complex functionals, and increasingly large chemical test sets, can fix the deficiencies of non-correlated wavefunctions when modelling difficult electronic problems. In this respect, quantum computing is the most promising, potentially game-changing technology that could alter the quantum chemistry research landscape. As the electronic wavefunction problem can be represented much more efficiently on a qubit, compared to a traditional bit, quantum computers offer the opportunity to fully realize the correlated wavefunction and allow for its exploration on larger, more interesting chemical systems.<sup>12</sup> Again, unfortunately this technology is not mature enough for a large-scale, high throughput approach generally employed by modern theoretical chemists and supported by, for example, the National Computational Infrastructure (NCI).

As the benchmarking and development of density functionals, wavefunction methods, even basis sets, is either a necessary but secondary aim (in the case of benchmarking), or not an aim at all (i.e. development of new techniques), this thesis employs the M06-2X functional, which is extensively used, reviewed, and benchmarked in the literature. The original publication,<sup>13</sup> in which the development of the functional is reported, has over 14,000 cites, according to the Springer website on which it is hosted and published, and is therefore a safe, tried, and tested functional that will be able to predict many different chemical properties without controversy.

## 2.5 References

- (1) McLachlan, A. D.; Ball, M. A. *Reviews of Modern Physics* **1964**, *36*, 844–855.



- (2) Lischka, H.; Nachtigallová, D.; Aquino, A. J. A.; Szalay, P. G.; Plasser, F.; Machado, F. B. C.; Barbatti, M. *Chemical Reviews* **2018**, *118*, 7293–7361.
- (3) Burke, K.; Werschnik, J.; Gross, E. K. U. *The Journal of Chemical Physics* **2005**, *123*, 62206.
- (4) Roca-Sanjuán, D.; Aquilante, F.; Lindh, R. *Wiley Interdisciplinary Reviews: Computational Molecular Science* **2012**, *2*, 585–603.
- (5) Wodrich, M. D.; Corminboeuf, C.; Schreiner, P. R.; Fokin, A. A.; Schleyer, P. v. R. *Organic Letters* **2007**, *9*, 1851–1854.
- (6) Laurent, A. D.; Jacquemin, D. *International Journal of Quantum Chemistry* **2013**, *113*, 2019–2039.
- (7) Hodgson, J. L.; Namazian, M.; Bottle, S. E.; Coote, M. L. *The Journal of Physical Chemistry A* **2007**, *111*, 13595–13605.
- (8) Huix-Rotllant, M.; Ferre, N. *Journal of Physical Chemistry A* **2014**, *118*, 4464–4470.
- (9) Chumakova, N. A.; Pergushov, V. I. *Mendeleev Communications* **2014**, *24*, 301–303.
- (10) Mardirossian, N.; Head-Gordon, M. *The Journal of Chemical Physics* **2018**, *148*, 241736.
- (11) Mater, A. C.; Coote, M. L. *Journal of Chemical Information and Modeling* **2019**, *59*, 2545–2559.
- (12) Cao, Y.; Romero, J.; Olson, J. P.; Degroote, M.; Johnson, P. D.; Kieferová, M.; Kivlichan, I. D.; Menke, T.; Peropadre, B.; Sawaya, N. P. D.; Sim, S.; Veis, L.; Aspuru-Guzik, A. *Chemical Reviews* **2019**, *119*, 10856–10915.
- (13) Zhao, Y.; Truhlar, D. G. *Theoretical Chemistry Accounts* **2007**, *120*, 215–241.

## 3 Multi-functionalized Anthraquinone-based Photoinitiating Systems

### 3.1 Introduction and Key Findings

It is well established that irradiating materials with UV light can have a detrimental effect on their viability, as the high-energy photons can be absorbed by different chemical components and unfavourable side-reactions can be promoted, leading to photodegradation and photo-oxidation.<sup>1</sup> As discussed in Chapter 1, if the photon absorption is taking place within a biological matrix, high-energy light can also cause mutagenesis. Photoactivation at longer, lower energy wavelengths of light is therefore desirable; however, this needs to be balanced with the absorption behaviour of the chromophoric species and the favourability for the ensuing photoreaction.

To that end, functionalised anthraquinone-based photoinitiating systems offer a simple approach to low-energy light absorption with photoreactivity more often generated by high-energy photons.<sup>2</sup> The large, conjugated aromatic  $\pi$ -system in anthraquinone will inherently exhibit low energy excited states of both  $n_O\pi^*$  and  $\pi\pi^*$  character, and any unstable intermediate species formed during excited state processes are resonance-stabilized. This means anthraquinone-based molecules are able to play sensitisation roles in photoreactions, exhibiting broad absorption profiles and able to interact with a variety of co-initiating species. Whilst there have been several studies into using anthraquinone derivatives for photoinitiation,<sup>3-8</sup> none use computational chemistry to any great extent to explain the experimental results, therefore providing an opportunity to explore these systems with density functional theory.

In this chapter, anthraquinone molecules functionalized with di-, tri-, and tetra-substitution patterns are investigated for efficient photoinitiation of both cationic and radical polymerization reactions. Each publication builds on previous work either by introducing different functional groups in different substitution patterns, or introducing different co-initiators to make either two- or three-component initiator systems. The

effectiveness of each initiating system is studied experimentally, and the role of the chromophoric anthraquinone and subsequent interactions with co-initiating species are studied with quantum chemistry, in order to compare the anthraquinone species with different substitution patterns and to provide insight into the photoinitiation mechanisms. The M06-2X functional has been used extensively in this chapter for a number of reasons; namely it has consistently been shown in benchmarking studies to be effective at predicting oxidation potentials, rate coefficients, as well as excited state properties.<sup>9</sup> Given that this chapter uses all three of these calculations, it is an appropriate functional. It is also worth noting that in this Chapter, and indeed in Chapters 4 and 5, Kohn-Sham (KS) orbitals are used extensively to describe low-lying excited states. Whilst not necessarily “physical”, i.e. KS orbitals are not formally molecular orbitals, the use of KS orbitals in qualitative frontier molecular orbital arguments is accepted practice.<sup>10</sup>

The hydroxy-substituted anthraquinone molecules are found to undergo excited state intramolecular proton transfer reactions; they also exhibit absorption spectra sensitive to internal hydrogen bonding patterns, as well as being able to initiate polymerization reactions. Further investigations into the mechanism for photoinitiation found that, from their low-lying excited states, the anthraquinone molecules are able to form either radical cation or radical anion species, with the relative stabilities of these reactive intermediates dependent on the substitution pattern. Particularly efficient are the three-component initiating systems, which employ diamino-anthraquinones, diphenyliodoniumhexafluorophosphate (Iod), and tertiary amine species. Quantum chemistry calculations were able to demonstrate that, upon irradiation with visible light, the anthraquinone chromophores act as an electron shuttle, able to oxidise and reduce the two co-initiators to form reactive radical species that will subsequently initiate polymerization propagation reactions.

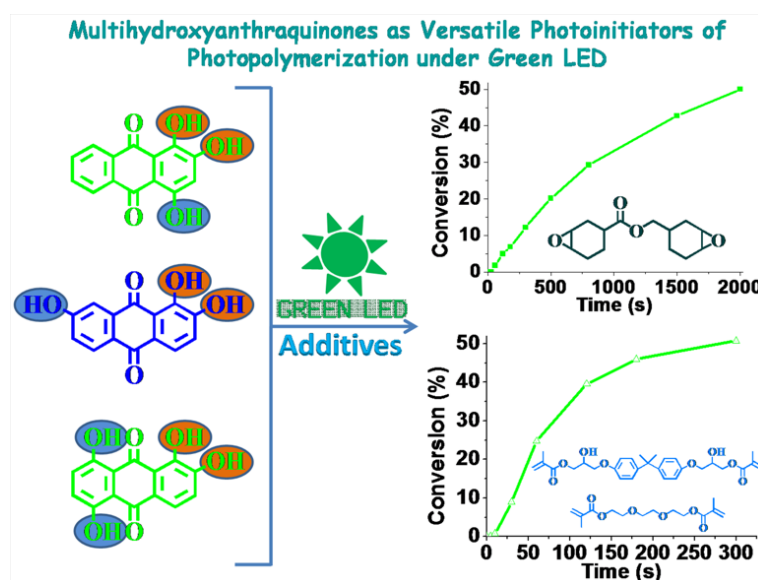
This chapter consists of five publications (Publications 3-7) detailing the experimental and theoretical work performed in order to assess the efficiency and photoexcited behaviour of novel anthraquinone-based initiating systems.

## 3.2 Publication 3

### Multihydroxy-Anthraquinone Derivatives as Free Radical and Cationic Photoinitiators of Various Photopolymerizations under Green LED

Jing Zhang, Nicholas S. Hill, Jacques Laleveé, Jean-Pierre Fouassier, Jiacheng Zhao, Bernadette Graff, Timothy W. Schmidt, Scott H. Kable, Martina H. Stenzel, Michelle L. Coote, and Pu Xiao

*Macromolecular Rapid Communications* **2018**, 1800172



This publication is a peer-reviewed manuscript published in *Macromolecular Rapid Communications*. All computational results and subsequent discussion are my own work. Prof. Michelle Coote assisted with the direction of the theoretical investigations and corrected my draft write-ups. [Supplementary material is available online.](#)

### Statement of Contribution

This thesis is submitted as a Thesis by Compilation in accordance with [https://policies.anu.edu.au/ppi/document/ANUP\\_003405](https://policies.anu.edu.au/ppi/document/ANUP_003405)

I declare that the research presented in this Thesis represents original work that I carried out during my candidature at the Australian National University, except for contributions to multi-author papers incorporated in the Thesis where my contributions are specified in this Statement of Contribution.

Title: Multihydroxy-Anthraquinone Derivatives as Free Radical and Cationic Photoinitiators of Various Photopolymerizations under Green LED

Authors: Jing Zhang, Nicholas S. Hill, Jacques Lalevee, Jean-Pierre Fouassier, Jiacheng Zhao, Bernadette Graff, Timothy W. Schmidt, Scott H. Kable, Martina H. Stenzel, Michelle L. Coote, and Pu Xiao

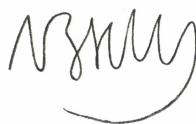
Publication outlet: Macromolecular Rapid Communications

Current status of paper: Published

Contribution to paper: I am the first contributing computational chemistry author. All computational results, mechanistic insight, and subsequent discussion are my own work

Senior author or collaborating authors endorsement: Michelle Coote

Nicholas Hill



20/01/2020

Candidate - Print Name

Signature

Date

### Endorsed

Michelle Coote



20/01/2020

Primary Supervisor – Print Name

Signature

Date



Delegated Authority – Print Name



Signature

20/01/2020

Date



# Multihydroxy-Anthraquinone Derivatives as Free Radical and Cationic Photoinitiators of Various Photopolymerizations under Green LED

Jing Zhang, Nicholas S. Hill, Jacques Lalevée, Jean-Pierre Fouassier, Jiacheng Zhao, Bernadette Graff, Timothy W. Schmidt, Scott H. Kable, Martina H. Stenzel, Michelle L. Coote,\* and Pu Xiao\*

Multihydroxy-anthraquinone derivatives [i.e., 1,2,4-trihydroxyanthraquinone (124-THAQ), 1,2,7-trihydroxyanthraquinone (127-THAQ), and 1,2,5,8-tetrahydroxyanthraquinone (1258-THAQ)] can interact with various additives [e.g., iodonium salt, tertiary amine, *N*-vinylcarbazole, and 2-(4-methoxystyryl)-4,6-bis(trichloromethyl)-1,3,5-triazine] under household green LED irradiation to generate active species (cations and radicals). The relevant photochemical mechanism is investigated using quantum chemistry, fluorescence, cyclic voltammetry, laser flash photolysis, steady state photolysis, and electron spin resonance spin-trapping techniques. Furthermore, the multihydroxy-anthraquinone derivative-based photoinitiating systems are capable of initiating cationic photopolymerization of epoxides or divinyl ethers under green LED, and the relevant photoinitiation ability is consistent with the photochemical reactivity (i.e., 124-THAQ-based photoinitiating system exhibits highest reactivity and photoinitiation ability). More interestingly, multihydroxy-anthraquinone derivative-based photoinitiating systems can initiate free radical crosslinking or controlled (i.e., reversible addition–fragmentation chain transfer) photopolymerization of methacrylates under green LED. It reveals that multihydroxy-anthraquinone derivatives can be used as versatile photoinitiators for various types of photopolymerization reactions.

## 1. Introduction

The discovery of compounds derived from nature for their application as photoinitiators in photopolymerization processes under visible light is of great interest in various fields ranging from imaging, radiation curing, and optics technologies to (bio)medicine, microelectronics, and material science.<sup>[1–10]</sup> Such natural dyes exhibit great potential to act as nontoxic photoinitiators for the fabrication of biocompatible polymeric materials.<sup>[11]</sup> After the absorption of suitable light, natural dyes are promoted to excited states and can then interact with additives through electron (or energy) transfer reactions to yield active species (e.g., cations or radicals) to initiate photopolymerization reactions.<sup>[1–18]</sup> The relevant reactivity between natural dyes and additives is strongly related to their photochemical properties. Recently, curcumin (a yellow-orange natural dye derived from rhizomes of *Curcuma longa*)-based photoinitiating systems have been reported to demonstrate excellent photoinitiation

Dr. J. Zhang, Dr. J. Zhao, Prof. T. W. Schmidt, Prof. S. H. Kable, Prof. M. H. Stenzel, Dr. P. Xiao  
School of Chemistry  
University of New South Wales  
Sydney, NSW 2052, Australia  
E-mail: pu.xiao@anu.edu.au

N. S. Hill, Prof. M. L. Coote  
ARC Centre of Excellence for Electromaterials Science  
Australia  
E-mail: michelle.coote@anu.edu.au

Dr. J. Zhang, N. S. Hill, Prof. M. L. Coote, Dr. P. Xiao  
Research School of Chemistry  
Australian National University  
Canberra, ACT 2601, Australia

Prof. J. Lalevée, Prof. J.-P. Fouassier, B. Graff, Dr. P. Xiao  
Université de Haute-Alsace  
CNRS, IS2M UMR 7361  
F-68100 Mulhouse, France

Prof. J. Lalevée, Prof. J.-P. Fouassier, B. Graff, Dr. P. Xiao  
Université de Strasbourg  
France

Prof. T. W. Schmidt  
ARC Centre of Excellence in Exciton Science  
School of Chemistry  
University of New South Wales  
Sydney, NSW 2052, Australia

The ORCID identification number(s) for the author(s) of this article can be found under <https://doi.org/10.1002/marc.201800172>.

DOI: 10.1002/marc.201800172



ability for the free radical photopolymerization of methacrylates especially under blue light.<sup>[11]</sup> Markedly, the crosslinked poly-methacrylate materials that were produced exhibited no toxicity to human fibroblast HS-27 cells, indicating that curcumin can be an ideal photoinitiator for the production of biocompatible polymers.<sup>[11]</sup> In addition, dihydroxyanthraquinone derivatives and Oil Blue N can also act as blue-light-sensitive and red-light-sensitive photoinitiators of polymerization, respectively.<sup>[19,20]</sup> These promising results prompted us to explore the ability of other natural dyes to initiate photopolymerization, in particular searching for natural photoinitiators that absorb light at different wavelengths. Even though several photoinitiators have been reported to work under green light which can increase the depth of photopolymerization compared with that under blue light,<sup>[21–25]</sup> they were chemically synthesized, rather than derived from natural sources.

9,10-anthraquinone derivatives (AQs) are natural dyes from plants or biological sources and exhibit different light absorption properties depending on the substituent groups.<sup>[26]</sup> Among them, 1,2,4-trihydroxyanthraquinone (124-THAQ; purpurin) is a natural dye found in the roots of madder plant (*Rubia cordifolia*). This natural compound has already found applications in cancer chemotherapy (through the interaction with DNA) and in dyeing of nylon.<sup>[27,28]</sup> 1,2,7-trihydroxyanthraquinone (127-THAQ; anthrapurpurin) has been used to assist the determination of scandium in a nonaqueous medium.<sup>[29]</sup> Another derivative, 1,2,5,8-tetrahydroxyanthraquinone (1258-THAQ; quinalizarin), can act as a cell-permeable inhibitor of protein kinase CK2.<sup>[30]</sup> To the best of our knowledge, there has been no study on the application of these multihydroxy-anthraquinone derivatives as photoinitiating systems for various types of photopolymerizations.

In this paper, the photochemical reactivity between the multihydroxy-anthraquinone derivatives and additives is investigated under the irradiation of a household green light-emitting diode (LED). The ability of the generated active species (e.g., cations or radicals) from these photoinitiating systems to initiate cationic and free radical photopolymerizations under green LED irradiation is ascertained.

## 2. Results and Discussion

### 2.1. Light Absorption Properties of THAQs

As illustrated in Figure 1a and Table S3 in the Supporting Information, the maximum absorption wavelengths ( $\lambda_{\text{max}}$ )

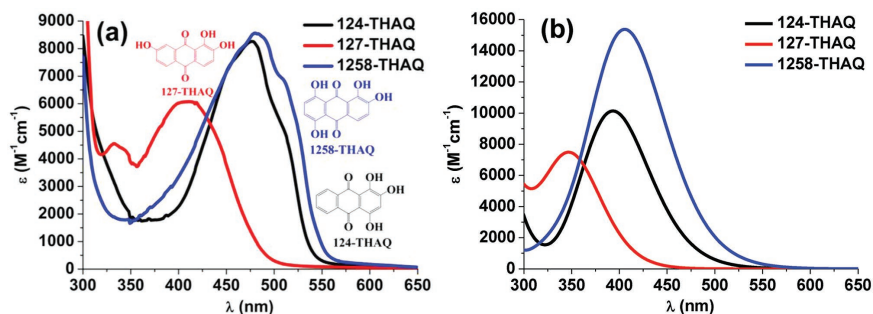


**Figure 1.** a) UV-vis absorption spectra of 124-THAQ, 127-THAQ, and 1258-THAQ in acetonitrile; b) corresponding simulated spectra from TD-DFT calculations.

of the three studied THAQs occur in the visible region. Specifically, 124-THAQ, 127-THAQ, and 1258-THAQ exhibit maximum absorption at 477, 411, and 480 nm with the relevant extinction coefficients 7470, 3230, and 7460  $\text{M}^{-1} \text{cm}^{-1}$ , respectively. Markedly, all three THAQs demonstrate much higher extinction coefficients in the visible light range than the well-known commercial visible-light-sensitive photoinitiator camphorquinone (CQ;  $\lambda_{\text{max}} = 466 \text{ nm}$ ,  $\epsilon_{\text{max}} = 38 \text{ M}^{-1} \text{cm}^{-1}$ ; Figure S5 and Table S3 in the Supporting Information). Overlap between the absorption spectra of both 124-THAQ and 1258-THAQ with the emission spectrum of the household green LED bulb (Figure S6 and Table S3, Supporting Information) is quite high, making them potential photoinitiators under green LED irradiation.

The absorption spectra of the three compounds were also calculated by time-dependent density functional theory (TD-DFT) at the M06-2X/cc-pVTZ level of theory (Figure 1b) and are in good qualitative agreement with the experimental spectra. A previous report<sup>[31]</sup> has recommended systematic scaling of the computational absorption values by  $\approx 1.16$  to correct the systematic overestimation of singlet transition energies at this level of theory, and this indeed results in excellent agreement between the calculated  $\lambda_{\text{max}}$  and the experimental values in the present work (Table S1, Supporting Information).

Both 124-THAQ and 1258-THAQ exhibit a bright  $S_1$  excited state dominated by a HOMO–LUMO,  $\pi\pi^*$  transition. In contrast, 127-THAQ exhibits a dark  $S_1$  excited state dominated by an  $n\pi^*$  transition (Figure S2, Supporting Information). The relative ordering of the low-lying  $\pi\pi^*$  and  $n\pi^*$  states in all three molecules is directly correlated with the extent of intramolecular hydrogen bonding (IHB) present, as bonding between oxygen lone pairs and neighboring hydroxyl groups will stabilize the  $n$  orbitals and shift their participation in electronic transitions to higher energy. As the number of IHBs present is increased, the more dominant the  $\pi\pi^*$  transitions become in the lowest energy excited states. This is confirmed by artificially “turning off” the hydrogen bonding by rotating the OH groups and observing the decrease in the  $\pi\pi^*$  transitions (see the Supporting Information for further details).

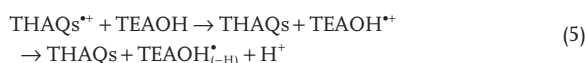
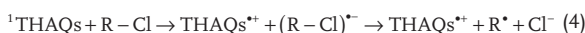
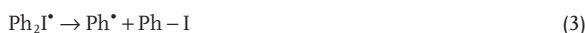
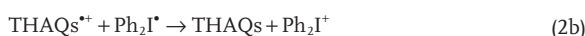
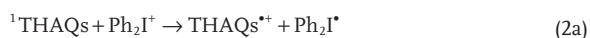
### 2.2. Photochemical Reactivity of THAQs with Additives

It has been reported that the excited states of anthraquinone derivatives (after the light absorption) can interact with various

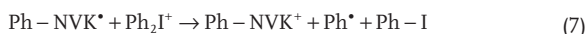
additives [e.g., Iod ( $\text{Ph}_2\text{I}^+$ ), tertiary amine, chlorotriazine, etc.] to generate active species (e.g., cations or radicals).<sup>[19,20]</sup> The fluorescence properties of THAQs are determined by the photo-physics and photochemistry in their excited singlet states. High fluorescence quantum yields arise from stable and long-lived excited states, which enable an efficient interaction between the excited singlet states and other compounds. The fluorescence quantum yields of 124-THAQ, 127-THAQ, and 1258-THAQ are 0.046, 0.00, and 0.013, respectively. As a result, 124-THAQ and 127-THAQ are expected to exhibit highest and lowest reactivity to additives, respectively. The addition of Iod could lead to fluorescence quenching of 124-THAQ in acetonitrile ( $k_q\tau_0 = 3.3 \text{ M}^{-1}$ ). This indicates the occurrence of an electron transfer reaction between the excited singlet state of 124-THAQ and the ground-state Iod. The reaction occurs with almost diffusion controlled kinetics with  $k_q \approx 1.6 \times 10^9 \text{ M}^{-1} \text{ s}^{-1}$  ( $\tau_0$  of 124-THAQ is 2.0 ns). The negative free energy change ( $\Delta G_s = -0.76 \text{ eV}$ ) for the excited singlet state of 124-THAQ ( $^1\text{124-THAQ}$ )/Iod is also consistent with favorable electron transfer from  $^1\text{124-THAQ}$  to Iod. This value is calculated from the classical Rehm–Weller equation<sup>[32]</sup> by using  $E_{\text{ox}}$  (124-THAQ) = 1.41 V (vs saturated calomel electrode (SCE)) measured by cyclic voltammetry,  $E_{\text{red}}$  (Iod) =  $-0.2 \text{ V}$  (vs SCE),<sup>[1]</sup> and singlet state energy  $E_S = 2.37 \text{ eV}$  extracted from the UV–vis absorption and fluorescence emission spectra of 124-THAQ.<sup>[33]</sup> However, the electron transfer quantum yield ( $\Phi_{\text{eT}} = k_q\tau_0 [\text{Iod}]/(1 + k_q\tau_0 [\text{Iod}])$ ); where  $[\text{Iod}] = 4.7 \times 10^{-2} \text{ M}$ ) of 124-THAQ/Iod ( $\Phi_{\text{eT}} = 0.134$ ) is low which would lead to low yield of cations ( $124\text{-THAQs}^+$ ). On the contrary, no fluorescence quenching was observed for 1258-THAQ/Iod indicating the inefficiency of this system. More interestingly, the fluorescence of 124-THAQ can be efficiently quenched by R–Cl ( $k_q\tau_0 = 30.9 \text{ M}^{-1}$ ) which indicates the occurrence of electron transfer between  $^1\text{124-THAQ}$  and R–Cl. Interestingly, the addition of a tiny amount of tertiary amine (TEAOH) into the 124-THAQ solution can quickly turn the solution from yellow to pink indicating the instability of 124-THAQ with TEAOH (see Figure S8c, Supporting Information; the UV–vis absorption of 124-THAQ/TEAOH in acetonitrile is red-shifted to 527 nm compared with 124-THAQ alone (477 nm), and the green light irradiation slightly diminished the light absorption).

In the laser flash photolysis experiment, no triplet state absorption of 124-THAQ was observed in the 400–700 nm range, but the triplet route in the 124-THAQ/additive interaction cannot be ruled out as the negative free energy change  $\Delta G_T$  ( $-0.51 \text{ eV}$ , which is calculated from the classical Rehm–Weller equation<sup>[32]</sup> by using  $E_{\text{ox}}$  (124-THAQ) = 1.41 V (vs SCE) measured by cyclic voltammetry,  $E_{\text{red}}$  (Iod) =  $-0.2 \text{ V}$  (vs SCE),<sup>[1]</sup> and triplet state energy of 124-THAQ  $E_T = 2.12 \text{ eV}$  calculated with TD-DFT at the M06-2X/cc-pVTZ level of theory) indicated the favorability of  $^3\text{124-THAQ}$ /Iod electron transfer reaction. More discussion on the excited state calculations of THAQs is provided in the Supporting Information.

Based on the discussion above, various active species are expected to be produced as demonstrated in the following reactions (1)–(5)



The overall photochemical reactivity of THAQs with additives can be qualitatively estimated using steady state photolysis.<sup>[34]</sup> As demonstrated in Figures S7a and S8d in the Supporting Information, the light absorption of 124-THAQ (in the presence of Iod or R–Cl) decreased slightly during the green light irradiation illustrating the low reactivity of this system. Similarly, 1258-THAQ/Iod system also showed slight decrease of light absorption during the green LED irradiation (Figure S8b, Supporting Information). On the contrary, the nonbleaching of 127-THAQ/Iod combination during the green LED irradiation (Figure S8a, Supporting Information) demonstrated the nonreactivity of this system. More interestingly, the addition of a second additive *N*-vinylcarbazole (NVK) into the 124-THAQ/Iod system significantly affected the relevant steady state photolysis behavior. As illustrated in Figure S7b in the Supporting Information, the baseline of the light absorption of 124-THAQ/Iod/NVK system in acetonitrile ascended dramatically during the green LED irradiation, which can be attributed to the fact that insoluble compound (poly *N*-vinylcarbazole) was produced as indicated in the reactions (6)–(8) which led to the cloudy suspension in the acetonitrile. It also suggested that the produced  $\text{Ph-NVK}^+$  is an efficient cation to initiate the cationic photopolymerization.



Following the electron transfer in the 124-THAQ/Iod system under light irradiation, the generated radicals can be observed directly by the electron spin resonance (ESR) spin-trapping experiment. The hyperfine splitting constants for both the nitrogen ( $a_N$ ) and the hydrogen ( $a_H$ ) of the phenyl-*N*-tert-butyl nitron (PBN)/radical adducts can be used to determine the specific radicals. Specifically, in the 124-THAQ/Iod system,  $a_N = 14.3 \text{ G}$  and  $a_H = 2.2 \text{ G}$  were determined (Figure 2), which can be assigned as PBN/phenyl radical adducts.<sup>[35,36]</sup> This confirms the production of phenyl radicals ( $\text{Ph}^{\cdot}$ ) as in reactions (1)–(3).

### 2.3. THAQ-Based Photoinitiating Systems for Cationic Photopolymerization

As demonstrated in reactions (1)–(3) and (6)–(7) above, THAQ-derived cations ( $\text{THAQs}^+$ ) and NVK-derived cation ( $\text{Ph-NVK}^+$ ) are expected to be generated from THAQs/Iod



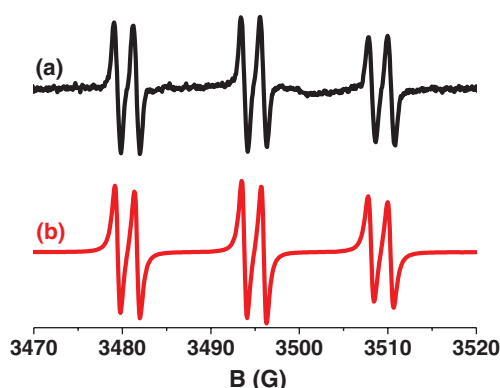


**Figure 2.** ESR spectra of the radicals generated in 124-THAQ/Iod upon light exposure and trapped by PBN in *tert*-butylbenzene: a) experimental and b) simulated spectra.

and THAQs/Iod/NVK photoinitiating systems during green LED irradiation. To study their photoinitiating ability in cationic photopolymerization, experiments with epoxide (EPOX) were first undertaken. As demonstrated in Table S4 in the Supporting Information, Iod alone cannot initiate the cationic photopolymerization of EPOX under the green LED irradiation as Iod can only work under UV light.<sup>[37]</sup> 124-THAQ/Iod was also inefficient under green light, probably due to the low electron transfer quantum yield of 124-THAQ/Iod ( $\Phi_{eT} = 0.134$ ) as discussed above. Similarly, the zero fluorescence quantum yields of 127-THAQ and nonfluorescence quenching of 1258-THAQ/Iod also resulted in the inefficiency of the 127-THAQ (or 1258-THAQ)/Iod system. However, the addition of NVK<sup>[38]</sup> into the 124-THAQ/Iod system significantly promoted the photoinitiation ability of the relevant photoinitiating system and 50% of epoxide conversion was achieved after 2000 s of green light exposure (Figure S9, Supporting Information). Moreover, the cationic photopolymerization reaction of EPOX can also be confirmed by the consumption of epoxy group ( $\approx 790\text{ cm}^{-1}$ ) and the concomitant formation of polyether ( $\approx 1070\text{ cm}^{-1}$ ) and hydroxyl ( $\approx 3430\text{ cm}^{-1}$ ) groups from the IR spectra before and after the photopolymerization (Figure S10, Supporting Information). For 127-THAQ and 1258-THAQ based two-component or three-component photoinitiating systems (Table S4, Supporting Information), nearly no photopolymerization of EPOX was observed, which is in agreement with their photochemical reactivity as discussed above.

Next, it was found that 124-THAQ/Iod system could initiate the cationic photopolymerization of DVE-3 in laminate under green LED irradiation, and 90% of double bond (vinyl group) conversion was attained after 2000 s of photopolymerization (Figure 3). More interestingly, the polymerization rate of DVE-3 was dramatically increased with the addition of NVK into the 124-THAQ/Iod system and 90% conversion was achieved within 500 s using 124-THAQ/Iod/NVK system. The IR spectra of DVE-3 before and after photopolymerization upon exposure to green light further confirmed the reaction of the vinyl group ( $\approx 1620\text{ cm}^{-1}$ ) of DVE-3 (Figure S11, Supporting Information). As reported previously,<sup>[39]</sup> Ph-DVE-3<sup>+</sup> was the initiating species

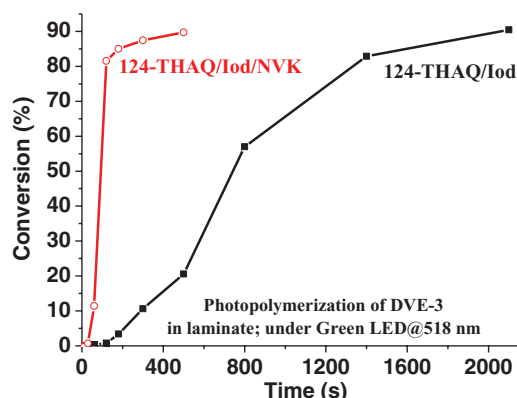
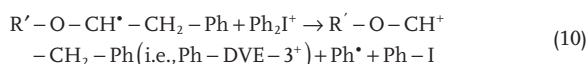
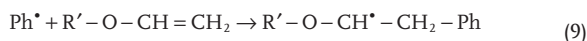


**Figure 3.** Photopolymerization profiles (conversion of double bonds vs polymerization time) of DVE-3 in laminate ( $\approx 20\text{ }\mu\text{m}$  thick) in the presence of 124-THAQ/Iod (0.5%/2% wt%) or 124-THAQ/Iod/NVK (0.5%/2%/3% wt%) upon exposure to green LED@518 nm ( $60\text{ mW cm}^{-2}$ ).

(reactions (9)–(10)) for the polymerization of DVE-3 in the presence of 124-THAQ/Iod while Ph-NVK<sup>+</sup> (reaction (7)) was more efficient to initiate the polymerization when using 124-THAQ/Iod/NVK system.



#### 2.4. THAQ-Based Photoinitiating Systems for Free Radical Photopolymerization

As demonstrated in reactions (1)–(5) above, various radicals (i.e., Ph<sup>•</sup>, TEAOH<sup>•</sup>(<sub>-H</sub>), and R<sup>•</sup>) can be generated from THAQ-based photoinitiating systems during green LED irradiation and would be expected to initiate free radical photopolymerization. Specifically, 124-THAQ/Iod and 1258-THAQ/Iod systems can initiate the free radical photopolymerization of Bis-GMA/TEGDMA blend (typically used as dental resin) under green light as illustrated in Figure 4a, with 124-THAQ/Iod exhibiting higher polymerization rate than that of 1258-THAQ/Iod. More interestingly, R<sup>•</sup> radicals can be produced from the 124-THAQ/R-Cl combination under green light irradiation to initiate the photopolymerization of Bis-GMA/TEGDMA blend (40% of conversion) as indicated in Figure 4b. However, 124-THAQ/TEAOH system was inefficient due to the instability of 124-THAQ in the presence of TEAOH, as discussed above. The photopolymerization profile can be promoted with the three-component photoinitiating system 124-THAQ/R-Cl/TEAOH with higher conversion (51%) attained for Bis-GMA/TEGDMA blend (Figure 4b). The consumption of the monomer double bond ( $\approx 1635\text{ cm}^{-1}$  in the IR spectrum, Figure S12, Supporting Information) clearly demonstrates the photopolymerization of the Bis-GMA/TEGDMA blend. Markedly, THAQ-based photoinitiating systems exhibited higher efficiency than the well-known camphorquinone (CQ)-based system CQ/TEAOH under green LED (Table S4, Supporting Information).

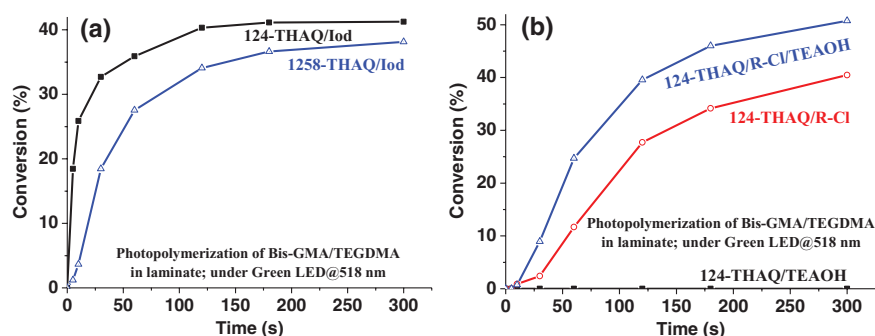


**Figure 4.** Photopolymerization profiles (conversion of double bonds vs polymerization time) of Bis-GMA/TEGDMA blend (70%/30% w/w) in laminate ( $\approx 20 \mu\text{m}$  thick) in the presence of a) THAQs/Iod (0.5%/2% wt%) upon exposure to green LED@518 nm ( $60 \text{ mW cm}^{-2}$ ) and b) 124-THAQ/TEAOH (0.5%/2% wt%), 124-THAQ/R-CI (0.5%/2% wt%), or 124-THAQ/R-CI/TEAOH (0.5%/2%/2% wt%) upon exposure to green LED@518 nm ( $60 \text{ mW cm}^{-2}$ ).

More interestingly, 124-THAQ/Iod/CPADB system is also capable of initiating reversible addition–fragmentation chain transfer (RAFT) photopolymerization of monofunctional methacrylate DEGMEMA under green LED irradiation. Specifically, in the 124-THAQ/Iod/CPADB/DEGMEMA system ([124-THAQ]: [Iod]: [CPADB]: [DEGMEMA] = 0.2: 0.8: 1: 100), well-controlled poly(DEGMEMA) ( $M_n = 1200 \text{ g mol}^{-1}$ ) was produced with a low PDI (1.26) after 12 h of photopolymerization reaction (Figure S13, Supporting Information).

### 3. Conclusion

Multihydroxy-anthraquinone derivatives (124-THAQ, 127-THAQ, and 1258-THAQ) can interact with various additives [e.g., iodonium salt (Iod), tertiary amine (TEAOH), *N*-vinylcarbazole (NVK), and 2-(4-methoxystyryl)-4,6-bis(trichloromethyl)-1,3,5-triazine (R–Cl)] under green LED irradiation to generate active species (e.g., cations and radicals). The photochemical reactivity of these multihydroxy-anthraquinone derivatives/additives is significantly affected by their chemical structures, with 124-THAQ- and 127-THAQ-based systems exhibiting the highest and lowest reactivity, respectively. Consistently, the 124-THAQ/Iod/NVK combination was capable of initiating cationic photopolymerization of EPOX under green LED (50% conversion after 2000 s) and DVE-3 (90% conversion after 500 s). The THAQ-based photoinitiating systems can also initiate free radical photopolymerization of methacrylates (Bis-GMA/TEGDMA) and their photoinitiation ability was even higher than the well-known CQ/TEAOH system upon green LED exposure. Markedly, the controlled photopolymerization (under green light) of monofunctional methacrylate (DEGMEMA) can also be achieved using the 124-THAQ photoinitiating system with the addition of a RAFT agent (CPADB). In summary, multihydroxy-anthraquinone derivatives are versatile photoinitiators under green LED irradiation.

### Supporting Information

Supporting Information is available from the Wiley Online Library or from the author.

### Acknowledgements

P.X. acknowledges funding from the Australian Research Council Future Fellowship (FT170100301) and France–Australia Science Innovation Collaboration Fellowships (Rod Rickards Fellowship Scheme) of the Australian Academy of Science. M.L.C. gratefully acknowledges an ARC Laureate Fellowship (FL170100041), financial support from the ARC Centre of Excellence for Electromaterials Science (CE140100012), and supercomputing time on the National Facility of the National Computational Infrastructure. T.W.S. acknowledges the Australian Research Council for a Future Fellowship (FT130100177). This work was supported by the Australian Research Council (Centre of Excellence in Exciton Science CE170100026).

### Conflict of Interest

The authors declare no conflict of interest.

### Keywords

DFT calculations, green LED, multihydroxy-anthraquinone derivatives, photoinitiator, photopolymerization

Received: February 26, 2018

Revised: March 14, 2018

Published online:

- [1] J.-P. Fouassier, J. Lalevée, *Photoinitiators for Polymer Synthesis-Scope, Reactivity, and Efficiency*, Wiley-VCH Verlag GmbH & Co. KGaA, Weinheim, Germany **2012**.
- [2] J. V. Crivello, *Photoinitiators for Free Radical, Cationic and Anionic Photopolymerization*, 2nd ed., John Wiley & Sons, Chichester **1998**.
- [3] D. C. Neckers, W. Jager, *Photoinitiation for Polymerization: UV and EB at the Millenium*, John Wiley & Sons, Chichester **1999**, p. 410.
- [4] S. Davidson, *Exploring the Science, Technology and Application of UV and EB Curing*, Sita Technology Ltd, London **1999**, p. 290.
- [5] K. Dietliker, *A Compilation of Photoinitiators Commercially Available for UV Today*, Sita Technology Ltd, Edinburgh, London **2002**, p. 250.
- [6] K. D. Belfied, J. V. Crivello, *Photoinitiated Polymerization*. ACS Symposium Series 847, American Chemical Society, Washington DC **2003**.



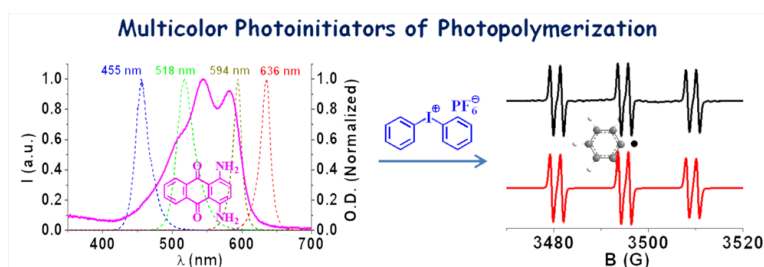
- [7] N. S. Allen, *Photochemistry and Photophysics of Polymer Materials*, Wiley, USA **2010**.
- [8] S. Dadashi-Silab, S. Doran, Y. Yagci, *Chem. Rev.* **2016**, *116*, 10212.
- [9] S. C. Ligon-Auer, M. Schwentenwein, C. Gorsche, J. Stampfl, R. Liska, *Polym. Chem.* **2016**, *7*, 257.
- [10] H. Peng, S. Bi, M. Ni, X. Xie, Y. Liao, X. Zhou, Z. Xue, J. Zhu, Y. Wei, C. N. Bowman, Y.-W. Mai, *J. Am. Chem. Soc.* **2014**, *136*, 8855.
- [11] J. Zhao, J. Lalevee, H. Lu, R. MacQueen, S. H. Kable, T. W. Schmidt, M. H. Stenzel, P. Xiao, *Polym. Chem.* **2015**, *6*, 5053.
- [12] J. Lalevee, J. P. Fouassier, *Dyes and Chromophores in Polymer Science*, ISTE Wiley, London **2015**.
- [13] P. Xiao, J. Zhang, F. Dumur, M. A. Tehfe, F. Morlet-Savary, B. Graff, D. Gigmes, J. P. Fouassier, J. Lalevée, *Prog. Polym. Sci.* **2015**, *41*, 32.
- [14] S. Dadashi-Silab, C. Aydogan, Y. Yagci, *Polym. Chem.* **2015**, *6*, 6595.
- [15] J. Radebner, A. Eibel, M. Leypold, C. Gorsche, L. Schuh, R. Fischer, A. Torvisco, D. Neshchadin, R. Geier, N. Moszner, R. Liska, G. Gescheidt, M. Haas, H. Stueger, *Angew. Chem., Int. Ed.* **2017**, *56*, 3103.
- [16] M. Jin, X. Wu, J. P. Malval, D. Wan, H. Pu, *J. Polym. Sci. Polym. Chem.* **2016**, *54*, 2722.
- [17] M. Jin, M. Yu, Y. Zhang, D. Wan, H. Pu, *J. Polym. Sci. Polym. Chem.* **2016**, *54*, 1945.
- [18] X. Wu, J.-p. Malval, D. Wan, M. Jin, *Dyes Pigm.* **2016**, *132*, 128.
- [19] J. Zhang, J. Lalevee, J. Zhao, B. Graff, M. H. Stenzel, P. Xiao, *Polym. Chem.* **2016**, *7*, 7316.
- [20] P. Xiao, F. Dumur, B. Graff, J. P. Fouassier, D. Gigmes, J. Lalevée, *Macromolecules* **2013**, *46*, 6744.
- [21] J. Zhang, F. Dumur, M. Bouzrati, P. Xiao, C. Dietlin, F. Morlet-Savary, B. Graff, D. Gigmes, J. P. Fouassier, J. Lalevée, *J. Polym. Sci., Part A: Polym. Chem.* **2015**, *53*, 1719.
- [22] P. Xiao, W. Hong, Y. Li, F. Dumur, B. Graff, J. P. Fouassier, D. Gigmes, J. Lalevée, *Polym. Chem.* **2014**, *5*, 2293.
- [23] P. Xiao, M. Frigoli, F. Dumur, B. Graff, D. Gigmes, J. P. Fouassier, J. Lalevée, *Macromolecules* **2014**, *47*, 106.
- [24] M.-A. Tehfe, F. Dumur, B. Graff, D. Gigmes, J.-P. Fouassier, J. Lalevée, *Macromol. Chem. Phys.* **2013**, *214*, 1052.
- [25] M.-A. Tehfe, J. Lalevée, S. Telitel, J. Sun, J. Zhao, B. Graff, F. Morlet-Savary, J.-P. Fouassier, *Polymer* **2012**, *53*, 2803.
- [26] R. Siva, *Curr. Sci.* **2007**, *92*, 916.
- [27] P. Ghosh, G. P. Devi, R. Priya, A. Amrita, A. Sivaramakrishna, S. Babu, R. Siva, *Appl. Biochem. Biotechnol.* **2013**, *170*, 1127.
- [28] D. Gupta, S. Kumari, M. Gulrajani, *Color. Technol.* **2001**, *117*, 328.
- [29] F. G. Sanchez, C. C. Blanco, A. H. Bayona, *Talanta* **1987**, *34*, 345.
- [30] G. Cozza, M. Mazzorana, E. Papinutto, J. Bain, M. Elliott, G. di Maira, A. Gianoncelli, M. A. Pagano, S. Sarno, M. Ruzzene, R. Battistutta, F. Meggio, S. Moro, G. Zagotto, L. A. Pinna, *Biochem. J.* **2009**, *421*, 387.
- [31] S. Markovi, J. Tošovi, *J. Phys. Chem. A* **2015**, *119*, 9352.
- [32] D. Rehm, A. Weller, *Isr. J. Chem.* **1970**, *8*, 259.
- [33] M. A. Tehfe, J. Lalevée, F. Morlet-Savary, B. Graff, N. Blanchard, J. P. Fouassier, *ACS Macro Lett.* **2012**, *1*, 198.
- [34] P. Xiao, F. Dumur, J. Zhang, D. Gigmes, J. P. Fouassier, J. Lalevee, *Polym. Chem.* **2014**, *5*, 6350.
- [35] M. A. Tehfe, J. Lalevée, S. Telitel, E. Contal, F. Dumur, D. Gigmes, D. Bertin, M. Nechab, B. Graff, F. Morlet-Savary, J. P. Fouassier, *Macromolecules* **2012**, *45*, 4454.
- [36] J. Lalevée, N. Blanchard, M. A. Tehfe, F. Morlet-Savary, J. P. Fouassier, *Macromolecules* **2010**, *43*, 10191.
- [37] J. P. Fouassier, *Photoinitiator, Photopolymerization and Photocuring: Fundamentals and Applications*, Hanser Publishers, New York/ Munich/Vienna **1995**.
- [38] J. Lalevée, M.-A. Tehfe, A. Zein-Fakih, B. Ball, S. Telitel, F. Morlet-Savary, B. Graff, J. P. Fouassier, *ACS Macro Lett.* **2012**, *1*, 802.
- [39] P. Xiao, F. Dumur, T. T. Bui, F. Goubard, B. Graff, F. Morlet-Savary, J. P. Fouassier, D. Gigmes, J. Lalevée, *ACS Macro Lett.* **2013**, *2*, 736.

### 3.3 Publication 4

#### Disubstituted Aminoanthraquinone-Based Multicolor Photoinitiators: Photoinitiation Mechanism and Ability of Cationic Polymerization under Blue, Green, Yellow, and Red LEDs

J. Zhang, J. Laleveé, **N. S. Hill**, K. Launay, F. Morlet-Savary, B. Graff, M. H. Stenzel, M.  
L. Coote, and P. Xiao

*Macromolecules* **2018**, *51*, 8165-8173



This publication is a peer-reviewed manuscript published in *Macromolecules*. All computational results, mechanistic insight, and subsequent discussion are my own work. Prof. Michelle Coote assisted with the direction of the theoretical investigations and corrected my draft write-ups. [Supplementary material is available online.](#)

### Statement of Contribution

This thesis is submitted as a Thesis by Compilation in accordance with [https://policies.anu.edu.au/ppi/document/ANUP\\_003405](https://policies.anu.edu.au/ppi/document/ANUP_003405)

I declare that the research presented in this Thesis represents original work that I carried out during my candidature at the Australian National University, except for contributions to multi-author papers incorporated in the Thesis where my contributions are specified in this Statement of Contribution.

Title: Disubstituted Aminoanthraquinone-Based Multicolor Photoinitiators: Photoinitiation Mechanism and Ability of Cationic Polymerization under Blue, Green, Yellow, and Red LEDs

Authors: J. Zhang, J. Lalevee, Nicholas Hill, K. Launay, F. Morlet-Savary, B. Graff, M. H. Stenzel, M. L. Coote, and P. Xiao

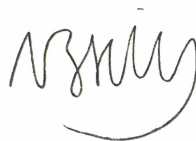
Publication outlet: Macromolecules

Current status of paper: Published

Contribution to paper: I am the first contributing computational chemistry author. All computational results, mechanistic insight, and subsequent discussion are my own work

Senior author or collaborating authors endorsement: Michelle Coote

Nicholas Hill



20/01/2020

Candidate - Print Name

Signature

Date

### Endorsed

Michelle Coote



20/01/2020

Primary Supervisor – Print Name

Signature

Date

Luke Connal



20/01/2020

Delegated Authority – Print Name

Signature

Date

# Disubstituted Aminoanthraquinone-Based Multicolor Photoinitiators: Photoinitiation Mechanism and Ability of Cationic Polymerization under Blue, Green, Yellow, and Red LEDs

J. Zhang,<sup>†,§,⊥</sup> J. Lalevée,<sup>§,||</sup> N. S. Hill,<sup>†,‡</sup> K. Launay,<sup>⊥</sup> F. Morlet-Savary,<sup>§,||</sup> B. Graff,<sup>§,||</sup> M. H. Stenzel,<sup>⊥</sup> M. L. Coote,<sup>\*,†,‡</sup> and P. Xiao<sup>\*,†,§,⊥</sup>

<sup>†</sup>Research School of Chemistry, Australian National University, Canberra, ACT 2601, Australia

<sup>‡</sup>ARC Centre of Excellence for Electromaterials Science

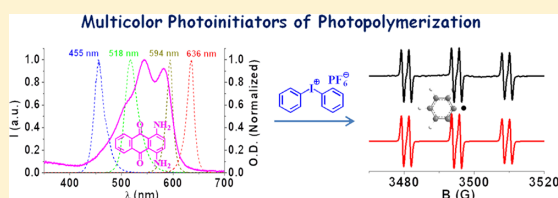
<sup>§</sup>Université de Haute-Alsace, CNRS, IS2M UMR 7361, F-68100 Mulhouse, France

<sup>||</sup>Université de Strasbourg, Strasbourg, France

<sup>⊥</sup>School of Chemistry, University of New South Wales, Sydney, NSW 2052, Australia

## Supporting Information

**ABSTRACT:** The investigation and clarification of the photoinitiation mechanism of novel systems are of importance for the design and development of compounds with high photoinitiation efficiency of photopolymerization. Some disubstituted aminoanthraquinone derivatives have been reported to exhibit interesting photochemical/photophysical properties and have the potential to act as high performance multicolor photoinitiators under the irradiation of various wavelengths of visible light from light-emitting diodes (LEDs). Herein, three disubstituted aminoanthraquinone derivatives, i.e., 1-amino-4-hydroxyanthraquinone, 1,4-diaminoanthraquinone, and 1,5-diaminoanthraquinone, with iodonium salt and *N*-vinylcarbazole as additives, have been investigated. Their photoinitiation mechanism was studied using fluorescence spectroscopy, laser flash photolysis, steady state photolysis, computational quantum chemistry, and electron spin resonance spin trapping techniques. Then, their photoinitiation ability for the cationic photopolymerization of epoxide and divinyl ether monomers under the irradiation of diverse LEDs (i.e., blue, green, yellow, and red LEDs) was investigated. The types and positions of substituents were found to play a vital role in the photoreactivity and photoinitiation ability of the disubstituted aminoanthraquinone derivative-based photoinitiating systems.



## INTRODUCTION

Photopolymerization technology<sup>1–10</sup> is a promising approach in various applications such as 3D printing,<sup>11–21</sup> (bio)medicine, optics technologies, microelectronics, and materials science.<sup>16,22–32</sup> In photopolymerizable formulations, the photoinitiator (PI) plays the significant role of absorbing the light and then triggering the transformation of liquid monomers and resins into solids for the fabrication of various materials.<sup>1,5,33,34</sup> A challenge is to design and develop multicolor PIs of polymerization that can work under the whole visible light range (i.e., blue, green, yellow, and red light), as it can offer the more flexibility and easier accessibility to the photopolymerization processes under any irradiation conditions. Several examples have been reported to work under the panchromatic visible light irradiation (400–700 nm), such as 2,7-di-*tert*-butyldimethyldihydropyrene (DHP),<sup>35</sup> the indanedione derivative D<sub>1</sub>,<sup>36</sup> the polyfunctional thiophene derivative PQXTP,<sup>37</sup> the thioxanthone derivative TX-NPG,<sup>38</sup> and curcumin.<sup>39</sup> However, to the best of our knowledge, none of these reported multicolor PIs exhibit high photoinitiation ability upon exposure to all wavelengths of light, especially long-wavelength irradiation. It is thus desirable

to explore and develop multicolor PIs with high efficiency under the irradiation of light delivered from all colors of light-emitting diodes (LEDs; e.g., blue LED, green LED, yellow LED, and red LED),<sup>40–43</sup> as LEDs have been attracting increasing attention for photopolymerization<sup>44</sup> due to advantages over other light sources such as better light output, higher operating efficiency, safer usage, and lower cost.<sup>1,40,45</sup>

Recently, several 9,10-anthraquinone derivatives have emerged as efficient photoinitiators including 1,8-dihydroxyanthraquinone,<sup>46</sup> 1,2,4-trihydroxyanthraquinone,<sup>47</sup> and oil blue N<sup>48</sup> as blue light-, green light-, and red light-sensitive PIs, respectively. This suggests that the substituents of anthraquinone derivatives can be used to tune their performance as PIs and that anthraquinone derivatives with suitable substituents may act as multicolor PIs. In this study several disubstituted aminoanthraquinone derivatives (DAAQs), i.e., 1-amino-4-hydroxyanthraquinone (AHAQ), 1,4-diaminoanthraquinone

Received: August 15, 2018

Revised: September 11, 2018

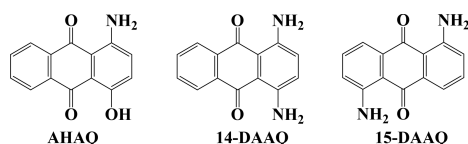
Published: October 5, 2018

(14-DAAQ), and 1,5-diaminoanthraquinone (15-DAAQ), in combination with the additives (i.e., iodonium salt and *N*-vinylcarbazole), are investigated for their photoinitiation mechanism and ability to initiate cationic photopolymerization under blue, green, yellow, and red LED light.

## EXPERIMENTAL SECTION

**Materials.** The investigated disubstituted aminoanthraquinone derivatives (DAAQs), i.e., 1-amino-4-hydroxyanthraquinone (AHAQ), 1,4-diaminoanthraquinone (14-DAAQ), and 1,5-diaminoanthraquinone (15-DAAQ) were obtained from EGA-Chemie KG, Fluka AG, and Sigma-Aldrich, respectively. Their chemical structures are illustrated in Scheme 1. Diphenyliodonium hexafluorophosphate

**Scheme 1. Chemical Structures of the Studied Disubstituted Aminoanthraquinone Derivatives (AHAQ, 14-DAAQ, and 15-DAAQ)**



(Iod) and *N*-vinylcarbazole (NVK) were used as the additives of the disubstituted aminoanthraquinone-based photoinitiating systems, while (3,4-epoxycyclohexane)methyl 3,4-epoxycyclohexylcarboxylate (EPOX) and tri(ethylene glycol) divinyl ether (DVE-3) were used as benchmark monomers (Scheme 2) for cationic photopolymerization. The additives and monomers were all obtained from Sigma-Aldrich.

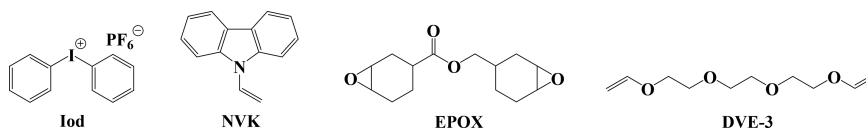
**Computational Methodology.** All electronic structure calculations were performed using the Gaussian 16 software.<sup>49</sup> All closed shell calculations were performed with restricted density functional theory (DFT) calculations, and open-shell calculations were performed with unrestricted DFT, all using the M06-2X<sup>50</sup> functional with the def2-TZVP<sup>51</sup> basis set. Excited states were calculated with time-dependent DFT (TD-DFT) at the M06-2X/def2-TZVP level of theory; in all cases implicit solvent effects were accounted for with the SMD<sup>52</sup> model of acetonitrile.

**Irradiation Sources.** Four different household LED bulbs were used as irradiation devices for photopolymerization reactions: blue LED (emission wavelength centered at 455 nm; incident light intensity: 60 mW cm<sup>-2</sup>), green LED (518 nm; 60 mW cm<sup>-2</sup>), yellow LED (594 nm; 30 mW cm<sup>-2</sup>), and red LED (636 nm; 60 mW cm<sup>-2</sup>).

**Fluorescence Experiments.** The fluorescence properties of DAAQs in acetonitrile were studied using the Varian Cary Eclipse fluorescence spectrophotometer. The fluorescence quenching of DAAQs by Iod was investigated from the classical Stern–Volmer treatment<sup>53</sup> ( $I_0/I = 1 + k_q\tau_0[\text{Iod}]$ ), where  $I_0$  and  $I$  stand for the fluorescent intensity of DAAQs in the absence and the presence of Iod, respectively;  $\tau_0$  stands for the lifetime of DAAQs in the absence of Iod).

**Laser Flash Photolysis.** Nanosecond laser flash photolysis (LFP) experiments were performed using a Q-switched nanosecond Nd:YAG laser ( $\lambda_{\text{exc}} = 355$  nm, 9 ns pulses; energy reduced down to 10 mJ) from Continuum (Minilite) and an analyzing system consisted of a ceramic xenon lamp, a monochromator, a fast photomultiplier, and a transient digitizer (Luzchem LFP 212).<sup>53</sup>

**Scheme 2. Chemical Structures of the Investigated Additives (Iod and NVK) of the Disubstituted Aminoanthraquinone-Based Photoinitiating Systems and Monomers (EPOX and DVE-3) for Cationic Photopolymerization**



8166

DOI: 10.1021/acs.macromol.8b01763  
Macromolecules 2018, 51, 8165–8173

**Steady State Photolysis Experiments.** DAAQs in the presence of Iod in acetonitrile were irradiated with the green LED at 518 nm (60 mW cm<sup>-2</sup>), and the UV–vis spectra were recorded using the Lambda 950 UV/vis/NIR spectrophotometer (PerkinElmer) at different irradiation times.

**Electron Spin Resonance Spin Trapping (ESR-ST) Experiments.** ESR-ST experiments were performed using the Bruker EMX-plus X-Band ESR spectrometer. The radicals were generated at room temperature upon the blue LED exposure under argon and trapped by phenyl-*N*-*tert*-butylnitrone (PBN) according to a procedure<sup>54</sup> described elsewhere in detail. The ESR spectrum simulation was carried out with the WINSIM software.

**Cationic Photopolymerization of Multifunctional Monomers.** The cationic photopolymerization reactions of the multifunctional monomers (EPOX and DVE-3) in the presence of different DAAQ-based photoinitiating systems upon exposure to the various LED bulbs were monitored using ATR-IR (BRUKER, IFS 66/s). To this end, a layer of liquid formulation (~20  $\mu\text{m}$  thick) was coated on the surface of the ATR horizontal crystal, and the ATR-IR spectra of the sample were recorded at different time intervals during the LED irradiation. The evolution of the epoxy group content of EPOX and the double bond content of DVE-3 were followed by ATR-IR spectroscopy using the bands at approximately 790 and 1615 cm<sup>-1</sup>, respectively.<sup>55</sup> The cationic photopolymerization of EPOX was carried out exposed to the air, while the cationic photopolymerization of DVE-3 was conducted in laminate. The degree of epoxy group or double-bond conversion  $C$  at time  $t$  during the photopolymerization is calculated from  $C = (A_0 - A_t)/A_0 \times 100\%$  (where  $A_0$  is the initial peak area before irradiation and  $A_t$  the peak area of the functional groups at time  $t$ ). The conversion  $C$  measured here is not throughout the whole sample thickness as the penetration depth of infrared beam into the sample is ca. 0.5–3  $\mu\text{m}$  for ATR-IR spectroscopy, which is similar to the light penetration, and can thus be used to evaluate the photoinitiation ability of the relevant DAAQ-based photoinitiating systems. The well-known blue light-sensitive camphorquinone-based photoinitiating system was used as a reference.

## RESULTS AND DISCUSSION

**UV–Vis Absorption of DAAQs.** The UV–vis absorption of DAAQs (i.e., AHAQ, 14-DAAQ, and 15-DAAQ) in acetonitrile and their overlap with emission spectra of blue (455 nm), green (518 nm), yellow (594 nm), and red (635 nm) LEDs are demonstrated in Figure 1, while their absorption maxima ( $\lambda_{\text{max}}$ ) and extinction coefficients ( $\epsilon$ ) at  $\lambda_{\text{max}}$  and at the maximum emission wavelengths of different LEDs are summarized in Table 1. As illustrated, AHAQ, 14-DAAQ, and 15-DAAQ exhibit maximum absorption ( $\lambda_{\text{max}}$ ) at 522, 544, and 479 nm, and their corresponding extinction coefficients ( $\epsilon_{\text{max}}$ ) are 11100, 12800, and 9300 M<sup>-1</sup> cm<sup>-1</sup>, respectively. Correspondingly, the colors of AHAQ, 14-DAAQ, and 15-DAAQ are maroon, dark violet, and dark brown-red, respectively. Interestingly, all three DAAQs demonstrate satisfactory overlap with the emission spectra of the blue (455 nm) and green (518 nm) LEDs; i.e., the extinction coefficients at the maximum emission wavelengths of the LEDs are higher than 2000 M<sup>-1</sup> cm<sup>-1</sup> (Table 1). In addition, the light absorption of 14-DAAQ matches well with the emission wavelength of the yellow LED (594 nm), and the extinction coefficient at 594 nm is 8800 M<sup>-1</sup> cm<sup>-1</sup>.

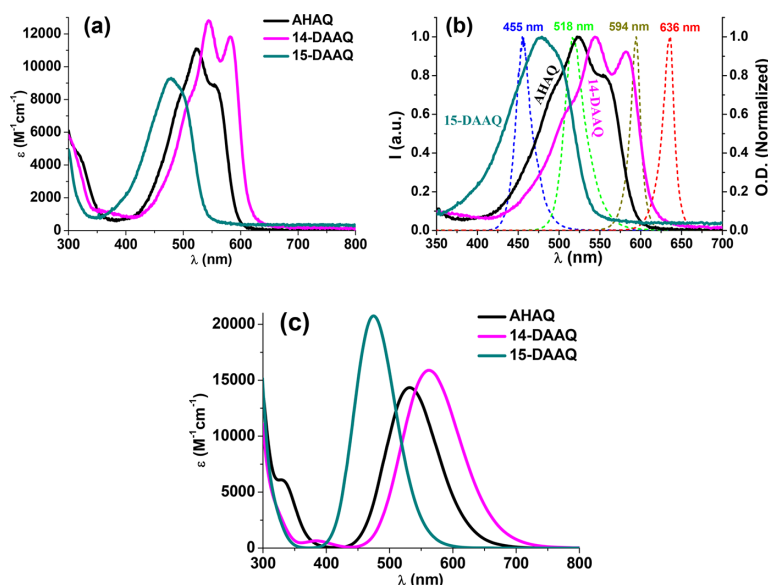


**Figure 1.** (a) UV–vis absorption spectra of AHAQ, 14-DAAQ, and 15-DAAQ in acetonitrile; (b) their overlap with the emission spectra of blue (455 nm), green (518 nm), yellow (594 nm), and red (636 nm) LEDs; (c) adjusted simulated UV–vis absorption spectra of AHAQ, 14-DAAQ, and 15-DAAQ.

**Table 1.** Light Absorption Properties of AHAQ, 14-DAAQ, and 15-DAAQ: Maximum Absorption Wavelengths  $\lambda_{\max}$ ; Extinction Coefficients ( $\epsilon$ ) at  $\lambda_{\max}$  and at the Maximum Emission Wavelengths of the Different LED Bulbs

	$\lambda_{\max}$ (nm)	$\epsilon_{\max}$ ( $M^{-1} cm^{-1}$ )	$\epsilon_{455 nm}^a$ ( $M^{-1} cm^{-1}$ )	$\epsilon_{518 nm}^a$ ( $M^{-1} cm^{-1}$ )	$\epsilon_{594 nm}^a$ ( $M^{-1} cm^{-1}$ )	$\epsilon_{636 nm}^a$ ( $M^{-1} cm^{-1}$ )
AHAQ	522	11100	3300	10700	990	$\sim 0$
14-DAAQ	544	12800	2100	8600	8800	530
15-DAAQ	479	9300	7400	4900	$\sim 360$	$\sim 300$

<sup>a</sup>For maximum emission wavelengths of different LEDs.

Moreover, it also demonstrates the light absorption at the maximum emission wavelength of the red LED (636 nm), but the relevant extinction coefficient is not high ( $530 M^{-1} cm^{-1}$ ). Nonetheless, 14-DAAQ can absorb light from all the investigated LEDs. For 15-DAAQ, the slightly higher baseline of the UV–vis absorption spectrum can be ascribed to its lower solubility in acetonitrile compared to AHAQ and 14-DAAQ. 15-DAAQ can be properly dissolved in the monomer EPOX (Figure S1).

The absorption spectra were also simulated using time-dependent density functional theory (TD-DFT). As found in previous studies,<sup>47</sup> the M06-2X functional is found to overestimate the  $\lambda_{\max}$  values by a factor of  $\sim 1.2$ . Accounting for this overestimation gives simulated UV–vis spectra (Figure 1) in good agreement with the experimental spectra. The  $S_1$  states for AHAQ, 14-DAAQ, and 15-DAAQ are each dominated by  $\pi\pi^*$  transitions, shown in Figure 2. The  $\epsilon_{\max}$  value for 15-DAAQ is also overestimated; however, as the overall peak position is consistent with experiment it is inconsequential.

**Photoinitiation Mechanism of Disubstituted Aminoanthraquinone-Based Photoinitiating Systems.** The photoinitiation mechanism of the investigated disubstituted aminoanthraquinone-based photoinitiating systems DAAQs/Iod was studied using a variety of approaches. The fluorescence emission spectra (related to their excited singlet states) of AHAQ, 14-DAAQ, and 15-DAAQ are illustrated in Figure S2,

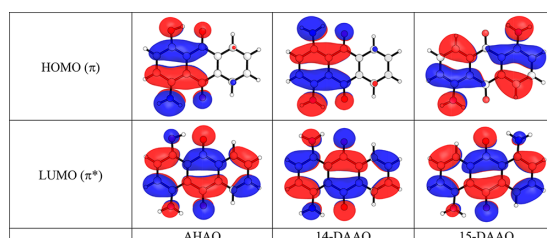


**Figure 2.** Orbitals involved in  $S_0 \rightarrow S_1$ ,  $\pi\pi^*$  transitions of AHAQ, 14-DAAQ, and 15-DAAQ.

and their quantum yields in acetonitrile are 0.0071, 0.0034, and 0.0033, respectively. Interestingly, the fluorescence of 14-DAAQ is dramatically quenched by the addition of Iod as shown in Figure 3a, and the interaction rate constant of  $^{14}\text{DAAQ}/\text{Iod}$  was determined (i.e.,  $k_q \sim 6.0 \times 10^9 M^{-1} s^{-1}$ ) from the Stern–Volmer treatment (Figure 3b; fluorescence lifetime of 14-DAAQ  $\tau_0 \sim 3$  ns). Similarly,  $k_q \sim 1.0 \times 10^9 M^{-1} s^{-1}$  was determined for  $^{15}\text{DAAQ}/\text{Iod}$  interaction (Figure S3b,c; fluorescence lifetime of 15-DAAQ  $\tau_0 \sim 3$  ns). These demonstrate the occurrence of electron transfer between the excited singlet state of 14-DAAQ (or 15-DAAQ) and the ground state of Iod and that the process is diffusion-controlled. However, no obvious fluorescence quenching was observed for the AHAQ with the addition of Iod (Figure S3a), indicating the low efficiency of the



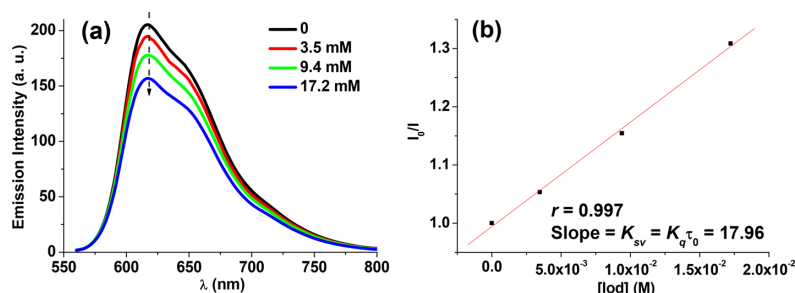


**Figure 3.** (a) Fluorescence spectra of 14-DAAQ as a function of [Iod] in acetonitrile and (b) the relevant Stern–Volmer plot.

interaction of <sup>1</sup>AHAQ/Iod. More interestingly, the electron transfer quantum yields  $[\Phi_{eT} = k_q\tau_0[\text{Iod}]/(1 + k_q\tau_0[\text{Iod}])]$ , where  $[\text{Iod}] = 4.7 \times 10^{-2}$  M in formulations] of <sup>1</sup>14-DAAQ/Iod ( $\Phi_{eT} = 0.46$ ) and <sup>1</sup>15-DAAQ/Iod ( $\Phi_{eT} = 0.12$ ) indicate that the photochemical reactivity of <sup>1</sup>14-DAAQ/Iod is higher than that of <sup>1</sup>15-DAAQ/Iod.

The excited singlet state of aminoanthraquinone derivatives may undergo intersystem crossing to yield the excited triplet states,<sup>56</sup> and the relevant triplet quantum yields are dependent on the number of substituents, their position, and the solvent.<sup>57,58</sup> It has been reported that the triplet quantum yields of 14-DAAQ and 15-DAAQ in toluene can be determined using laser flash photolysis (LFP),<sup>57</sup> but there is no observable triplet formation in the LFP of the investigated DAAQs in acetonitrile in the 400–700 nm range of our study, which can be ascribed to the different polarities of the solvents used.<sup>57,58</sup>

Modeling the electron transfer mechanism for different species of the anthraquinones provides insight into the observed differences in photoinitiating activity. Figure 4

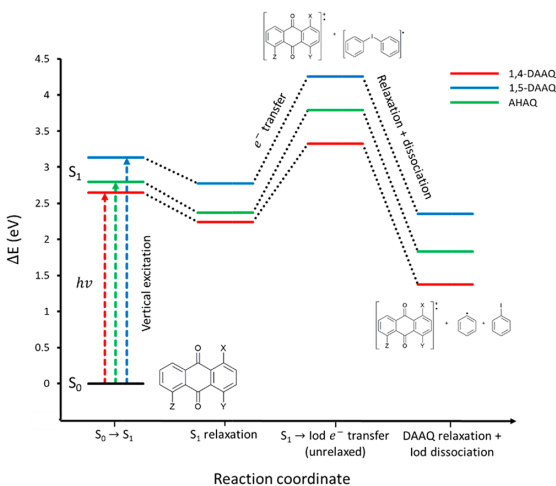


**Figure 4.** Energy level diagram for possible internal energy/electron transfer processes taking place with 14-DAAQ, 15-DAAQ, and AHAQ.

summarizes the electron transfer mechanism for the photoexcited AHAQ, 14-DAAQ, and 15-DAAQ molecules. Table 2 highlights some key energies along the reaction coordinates of AHAQ, 14-DAAQ, and 15-DAAQ.

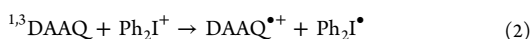
Figure 4 and Table 2 show that 14-DAAQ exhibits the lowest energy pathway to electron transfer to the Iod species,

**Table 2.** Energies for the Energy and Electron Transfer Processes (eV) Shown in Figure 4 and the Change in Gibbs Free Energy (eV) for the Overall Excited State Electron Transfer Reaction

DAAQs	$S_0 \rightarrow S_1$	$S_1 \rightarrow \text{Iod } e^- \text{ transfer (unrelaxed)}$	$\Delta G (S_1 \rightarrow \text{Iod}_{\text{relax}})$
AHAQ	+2.7971	+0.8148	−1.0685
14-DAAQ	+2.6464	+0.5101	−1.3777
15-DAAQ	+3.1338	+1.0032	−0.8724

with a  $S_1 \rightarrow \text{Iod } e^-$  transfer (unrelaxed)  $\Delta E$  of +0.51 eV, almost 0.5 eV lower than for 15-DAAQ; also, at −1.38 eV 14-DAAQ exhibits a greater thermodynamic favorability for the overall excited state electron transfer process. While less efficient, Figure 4 also suggests that both 15-DAAQ and AHAQ should also undergo electron transfer with Iod, whereas experiments show that this is not the case for AHAQ. While both 15-DAAQ and AHAQ suffer from both a relatively high barrier and low thermodynamic favorability to electron transfer, the 15-DAAQ triplet excited state is near the  $S_1$  state, allowing intersystem crossing (Figure S4). This may extend the excited state lifetime, allowing electron transfer to compete with fluorescence. In contrast, the triplet state is less energetically accessible for AHAQ (+0.54 eV above  $S_1$  versus +0.22 for 15-DAAQ). The combined result of these two effects is that fluorescence outcompetes all other processes in AHAQ, preventing electron transfer to Iod.

Based on the above information, the interaction between DAAQs and Iod during the light irradiation can be depicted in the following reactions:



The interaction of DAAQs/Iod under green LED irradiation can be qualitatively investigated using steady state photolysis.<sup>6</sup> As demonstrated in Figure 5, the UV–vis absorption of DAAQs/Iod decreased during irradiation with light. Interestingly, isosbestic points were observed at 452/588 nm, 481/610 nm, and 423/520 nm for AHAQ/Iod, 14-DAAQ/Iod, and 15-DAAQ/Iod, respectively, which indicates that no secondary reactions occurred in reaction 2. The much faster photolysis of 14-DAAQ/Iod than those of the other two systems can be ascribed to its better reactivity during the light irradiation, which is also in agreement with the results of the fluorescence quenching.

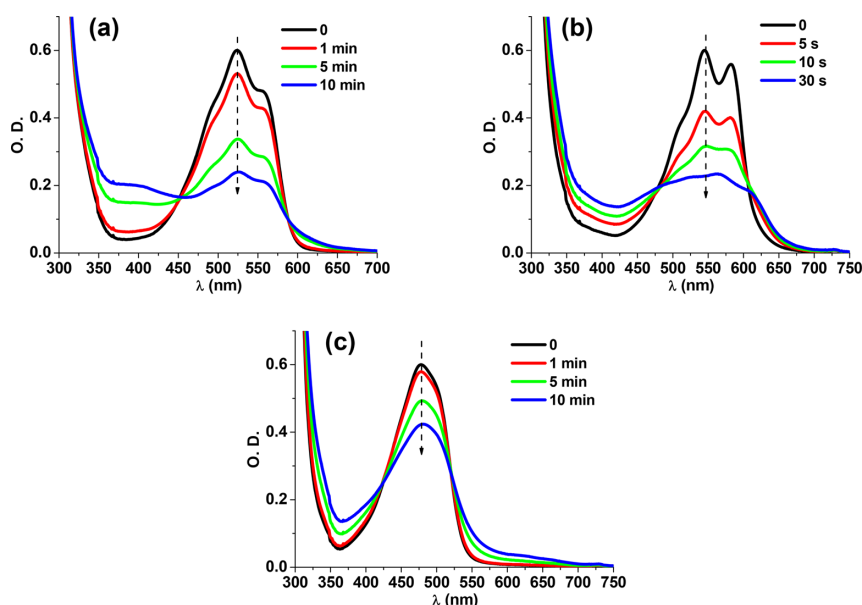


**Figure 5.** Steady state photolysis of (a) AHAQ/Iod, (b) 14-DAAQ/Iod, and (c) 15-DAAQ/Iod in acetonitrile ( $[\text{Iod}] = 15 \text{ mM}$ ); UV-vis spectra recorded at different irradiation times; green LED at 518 nm irradiation ( $60 \text{ mW cm}^{-2}$ ).

More interestingly, the generated radicals from the electron transfer in the DAAQ/Iod systems under light irradiation can be determined using the ESR spin trapping technique. Specifically, the hyperfine splitting constants (HFS) for both the nitrogen ( $a_N$ ) and the hydrogen ( $a_H$ ) of the PBN/radical adducts can be used to determine the types of radicals. Precisely,  $a_N = 14.3 \text{ G}$  and  $a_H = 2.2 \text{ G}$  were measured in the 15-DAAQ/Iod system (Figure 6), which can be assigned to PBN/phenyl radical

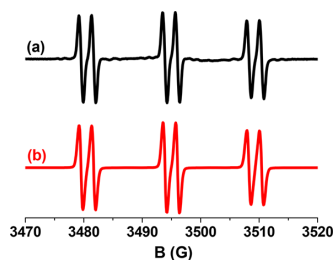
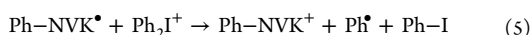


**Figure 6.** ESR spectra of the radicals generated in 15-DAAQ/Iod combination upon the blue LED exposure and trapped by PBN in *tert*-butylbenzene: (a) experimental and (b) simulated spectra.

adducts.<sup>59,60</sup> This further confirmed the generation of phenyl radicals ( $\text{Ph}^\bullet$ ) in reactions 1–3 as indicated above.

**Photoinitiation Ability of Disubstituted Aminoanthraquinone-Based Photoinitiating Systems for Cationic Polymerization.** As expected, the generated DAAQs-derived cations ( $\text{DAAQs}^{\bullet+}$ ) from the DAAQs/Iod systems (reactions 1–3) under light irradiation can initiate the cationic photopolymerization of EPOX. And the photoinitiation ability of these systems can be associated with the relevant light absorption properties of DAAQs, photoreactivity of DAAQs/Iod, and the structures of  $\text{DAAQs}^{\bullet+}$ . As shown in Figure 7 and Table 3, all the DAAQs/Iod systems are capable of initiating

the cationic polymerization of EPOX upon exposure to blue (455 nm) or green (518 nm) LED, which is in agreement with the satisfactory overlap of the light absorption of the studied DAAQs with the emission spectra of the blue (455 nm) and green (518 nm) LEDs. Specifically, 65%–77% epoxy conversions were obtained when using the 14-DAAQ/Iod or 15-DAAQ/Iod photoinitiating systems for 800 s of photopolymerization under blue or green LED. However, the initiation ability of AHAQ/Iod was relatively lower (i.e., <30% of epoxy conversions), which can be ascribed to the lack of obvious fluorescence quenching of AHAQ/Iod system as indicated above. More interestingly, 14-DAAQ/Iod was also efficient for the cationic polymerization of EPOX under yellow (594 nm) and red (636 nm) LEDs, and >55% of epoxy conversions can be achieved after 800 s of photopolymerization. Among the investigated DAAQs/Iod systems, 14-DAAQ/Iod is the only system that can work upon the exposure to all the LEDs: this is in line with the panchromatic light absorption of 14-DAAQ and the high photochemical reactivity of 14-DAAQ/Iod. Notably, the well-known commercial photoinitiator camphorquinone (CQ)-based system CQ/Iod was inefficient under the same conditions, which underlines the high performance of the investigated DAAQ-based systems. Furthermore, the addition of NVK into the DAAQs/Iod systems can promote their photoinitiation ability due to the NVK additive effect<sup>61</sup> as depicted in reactions 4 and 5, with the produced  $\text{Ph-NVK}^+$  is efficient for the cationic photopolymerization.



For instance, >80% epoxy conversions were obtained when using the 15-DAAQ/Iod/NVK system for 800 s of photopolymerization under blue or green LED. Markedly, even >75% of conversions were attained under yellow or red LED with the 14-DAAQ/Iod/NVK system, which is unusual for the cationic

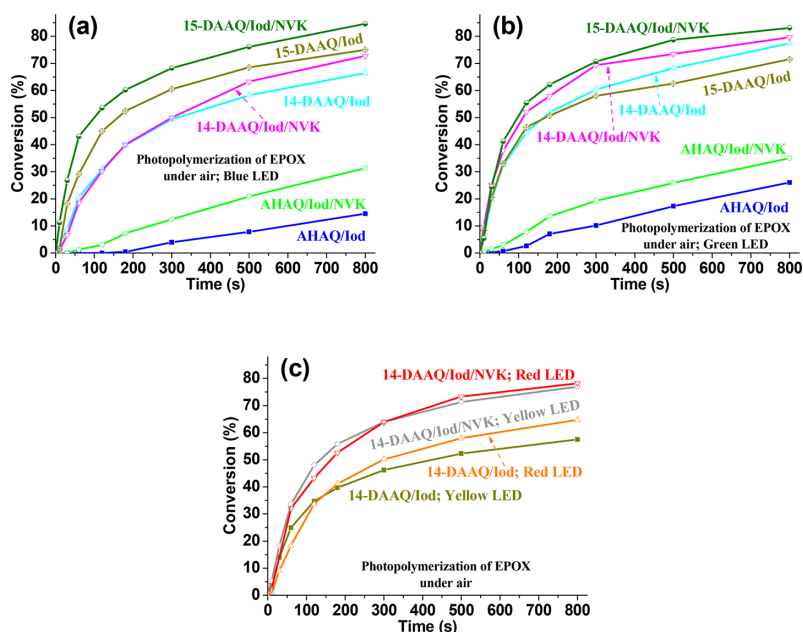


**Figure 7.** Photopolymerization profiles of EPOX under air in the presence of AHAQ, 14-DAAQ, or 15-DAAQ-based PISs upon exposure to (a) blue LED at 455 nm ( $60 \text{ mW cm}^{-2}$ ), (b) green LED at 518 nm ( $60 \text{ mW cm}^{-2}$ ), (c) yellow LED at 594 nm ( $30 \text{ mW cm}^{-2}$ ), and red LED at 636 nm ( $60 \text{ mW cm}^{-2}$ ). AHAQ, 14-DAAQ, or 15-DAAQ: 0.5 wt %; Iod: 2 wt %; NVK: 3 wt %.

**Table 3.** Epoxy Conversions (in %) of Photopolymerization of EPOX Obtained under Air upon Exposure to Different Household LED Devices for 800 s in the Presence of DAAQ-Based PISs (DAAQs or CQ; 0.5 wt %; Iod: 2 wt %; NVK: 3 wt %)

PIS	LED (455 nm)	LED (518 nm)	LED (594 nm)	LED (636 nm)
AHAQ/Iod	15	26	np <sup>a</sup>	np
AHAQ/Iod/NVK	31	35	np	np
14-DAAQ/Iod	66	77	58	65
14-DAAQ/Iod/NVK	73/74 <sup>b</sup>	80	77	78
15-DAAQ/Iod	75	72	np	np
15-DAAQ/Iod/NVK	85/83 <sup>b</sup>	83	np	np
CQ/Iod	np	np	np	np

<sup>a</sup>np: no photopolymerization. <sup>b</sup>After one week storage.

photopolymerization of EPOX under the irradiation of such long-wavelength light. More interestingly, the 14-DAAQ

(or 15-DAAQ)/Iod/NVK system was quite stable in the formulation as the photoinitiation ability did not change significantly after one week storage at room temperature (Table 3).

DAAQ-based photoinitiating systems were also capable of initiating cationic photopolymerization of divinyl ether DVE-3 as shown in reactions (6) – (7) and Figure 8. Specifically, 14-DAAQ/Iod combination can act as a multicolor photoinitiating system, and 78%, 74%, 61%, and 81% of double bond conversions of DVE-3 can be achieved when the photopolymerization reactions were conducted under the irradiation of blue, green, yellow, and red LEDs respectively [Figure 8a]. In addition, 15-DAAQ based photoinitiating systems can also work under blue and green LEDs for the polymerization of DVE-3 as illustrated in Figure 8b, and 78% - 87% of double bond conversions of DVE-3 was attained. The addition of NVK into the photoinitiating systems did not dramatically improve the polymerization profiles, which can be attributed to the fact that the 15-DAAQ/Iod system was already quite

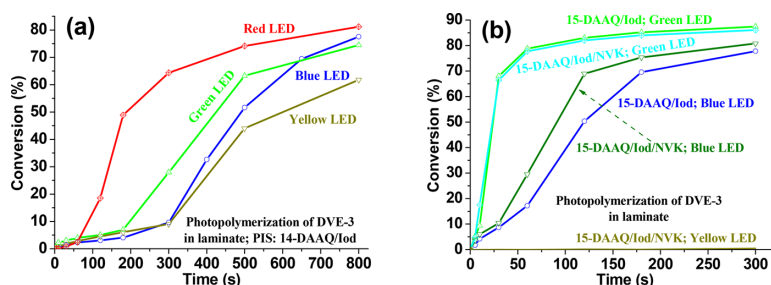
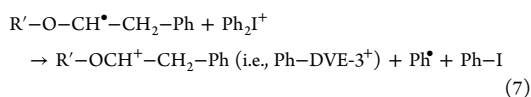
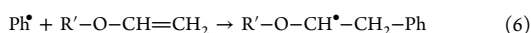


**Figure 8.** Photopolymerization profiles of DVE-3 in laminate in the presence of DAAQ-based PISs (DAAQ: 0.5 wt %; Iod: 2 wt %; NVK: 3 wt %) upon exposure to different LEDs [i.e., blue LED at 455 nm ( $60 \text{ mW cm}^{-2}$ ), green LED at 518 nm ( $60 \text{ mW cm}^{-2}$ ), yellow LED at 594 nm ( $30 \text{ mW cm}^{-2}$ ), and red LED at 636 nm ( $60 \text{ mW cm}^{-2}$ )].

efficient to initiate the cationic polymerization of DVE-3 and there was no significant room for the further improvement of the performance.



## CONCLUSION

The investigation of photoinitiation mechanism of the studied three disubstituted aminoanthraquinone-based photoinitiating systems (PISs) revealed that 14-DAAQ exhibited the highest photoreactivity toward Iod while AHAQ demonstrated the lowest efficiency under the LED irradiation. Phenyl radicals are produced in the initiation process, as confirmed for instance in the 15-DAAQ/Iod combination through the ESR-ST experiments. The types and positions of substituents of the disubstituted aminoanthraquinone derivatives play a significant role in their photoinitiation ability. Specifically, in line with the results of the photoinitiation mechanism study, 14-DAAQ/additives systems can act as efficient multicolour PISs as they were capable of initiating cationic photopolymerization of epoxide and divinyl ether under various LEDs with different emission wavelengths, i.e., blue, green, yellow, and red LEDs, while AHAQ- and 15-DAAQ-based photoinitiating systems can only work under the irradiation of blue and green LEDs. Interestingly, even >80% of epoxy or double-bond conversions can be achieved for the photopolymerization of epoxide and divinyl ether monomers when using the 14-DAAQ- or 15-DAAQ-based photoinitiating systems. The high efficiency of the 14-DAAQ- or 15-DAAQ-based photoinitiating systems can endow them with the potential applications in 3D printing and fabrication of photopolymer-based materials. The ability of the DAAQ-based photoinitiating systems for free radical photopolymerization will be presented in forthcoming papers.

## ASSOCIATED CONTENT

### Supporting Information

The Supporting Information is available free of charge on the ACS Publications website at DOI: 10.1021/acs.macromol.8b01763.

UV-vis absorption spectra of EPOX and 15-DAAQ in EPOX (Figure S1); fluorescence emission spectra of DAAQs (Figure S2); fluorescence quenching of AHAQ and 15-DAAQ by Iod (Figure S3); triplet state energies relative to  $S_1$  state for DAAQs (Figure S4); raw computational data (PDF)

## AUTHOR INFORMATION

### Corresponding Authors

\*E-mail: pu.xiao@anu.edu.au (P.X.).

\*E-mail: michelle.coote@anu.edu.au (M.L.C.).

### ORCID

J. Lalevée: 0000-0001-9297-0335

M. H. Stenzel: 0000-0002-6433-4419

M. L. Coote: 0000-0003-0828-7053

P. Xiao: 0000-0001-5393-7225

### Notes

The authors declare no competing financial interest.

## ACKNOWLEDGMENTS

P.X. acknowledges funding from the Australian Research Council Future Fellowship (FT170100301). M.L.C. gratefully acknowledges a Georgina Sweet ARC Laureate Fellowship (FL170100041) and generous allocations of supercomputing time on the National Facility of the Australian National Computational Infrastructure.

## REFERENCES

- (1) Fouassier, J. P.; Lalevée, J. *Photoinitiators for Polymer Synthesis: Scope, Reactivity, and Efficiency*; Wiley-VCH Verlag GmbH & Co KGaA: Weinheim, 2012.
- (2) Fouassier, J. P. *Photoinitiator, Photopolymerization and Photocuring: Fundamentals and Applications*; Hanser Publishers: New York, 1995.
- (3) Crivello, J. V.; Dietliker, K. *Photoinitiators for Free Radical, Cationic and Anionic Photopolymerization*, 2nd ed.; John Wiley & Sons: Chichester, 1998.
- (4) Scranton, A. B.; Bowman, C. N.; Peiffer, R. W. *Photopolymerization: Fundamentals and Applications*; ACS Symp. Ser. 673; American Chemical Society: Washington, DC, 1997.
- (5) Allen, N. S. *Photochemistry and Photophysics of Polymeric Materials*; Wiley: Hoboken, NJ, 2010.
- (6) Xiao, P.; Zhang, J.; Dumur, F.; Tehfe, M. A.; Morlet-Savary, F.; Graff, B.; Gignes, D.; Fouassier, J. P.; Lalevée, J. Visible light sensitive photoinitiating systems: Recent progress in cationic and radical photopolymerization reactions under soft conditions. *Prog. Polym. Sci.* **2015**, *41*, 32–66.
- (7) Shi, S.; Croutxé-Barghorn, C.; Allonas, X. Photoinitiating systems for cationic photopolymerization: Ongoing push toward long wavelengths and low light intensities. *Prog. Polym. Sci.* **2017**, *65*, 1–41.
- (8) Tasdelen, M. A.; Yagci, Y. Benzodioxinone Photochemistry in Macromolecular Science: Progress, Challenges, and Opportunities. *ACS Macro Lett.* **2017**, *6*, 1392–1397.
- (9) Lauer, A.; Fast, D. E.; Steinkoenig, J.; Kelterer, A.-M.; Gescheidt, G.; Barner-Kowollik, C. Wavelength-Dependent Photochemical Stability of Photoinitiator-Derived Macromolecular Chain Termini. *ACS Macro Lett.* **2017**, *6*, 952–958.
- (10) Ciftci, M.; Yoshikawa, Y.; Yagci, Y. Living Cationic Polymerization of Vinyl Ethers through a Photoinduced Radical Oxidation/Addition/Deactivation Sequence. *Angew. Chem., Int. Ed.* **2017**, *56*, 519–523.
- (11) Ambrosi, A.; Pumera, M. 3D-printing technologies for electrochemical applications. *Chem. Soc. Rev.* **2016**, *45*, 2740–2755.
- (12) Zhang, J.; Xiao, P. 3D printing of photopolymers. *Polym. Chem.* **2018**, *9*, 1530–1540.
- (13) Barner-Kowollik, C.; Bastmeyer, M.; Blasco, E.; Müller, P.; Delaitre, G.; Richter, B.; Wegener, M. 3D Laser Micro- and Nano-Printing: Challenges for Chemistry. *Angew. Chem., Int. Ed.* **2017**, *56*, 15828–15845.
- (14) Donderwinkel, I.; van Hest, J. C. M.; Cameron, N. R. Bio-inks for 3D bioprinting: recent advances and future prospects. *Polym. Chem.* **2017**, *8*, 4451–4471.
- (15) Stansbury, J. W.; Idacavage, M. J. 3D printing with polymers: Challenges among expanding options and opportunities. *Dent. Mater.* **2016**, *32*, 54–64.
- (16) Ligon-Auer, S. C.; Schwentenwein, M.; Gorsche, C.; Stampfl, J.; Liska, R. Toughening of photo-curable polymer networks: a review. *Polym. Chem.* **2016**, *7*, 257–286.
- (17) Xing, J.-F.; Zheng, M.-L.; Duan, X.-M. Two-photon polymerization microfabrication of hydrogels: an advanced 3D printing technology for tissue engineering and drug delivery. *Chem. Soc. Rev.* **2015**, *44*, 5031–5039.
- (18) Gorsche, C.; Seidler, K.; Knaack, P.; Dorfinger, P.; Koch, T.; Stampfl, J.; Moszner, N.; Liska, R. Rapid formation of regulated methacrylate networks yielding tough materials for lithography-based 3D printing. *Polym. Chem.* **2016**, *7*, 2009–2014.

- (19) Pawar, A. A.; Halivni, S.; Waiskopf, N.; Ben-Shahar, Y.; Soreni-Harari, M.; Bergbreiter, S.; Banin, U.; Magdassi, S. Rapid Three-Dimensional Printing in Water Using Semiconductor–Metal Hybrid Nanoparticles as Photoinitiators. *Nano Lett.* **2017**, *17*, 4497–4501.
- (20) Huang, L.; Jiang, R.; Wu, J.; Song, J.; Bai, H.; Li, B.; Zhao, Q.; Xie, T. Ultrafast Digital Printing toward 4D Shape Changing Materials. *Adv. Mater.* **2017**, *29* (1–6), 1605390.
- (21) Han, Y.; Wang, F.; Lim, C. Y.; Chi, H.; Chen, D.; Wang, F.; Jiao, X. High-Performance Nano-Photoinitiators with Improved Safety for 3D Printing. *ACS Appl. Mater. Interfaces* **2017**, *9*, 32418–32423.
- (22) Fouassier, J.-P.; Lalevée, J. *Photoinitiators for Polymer Synthesis-Scope, Reactivity, and Efficiency*; Wiley-VCH Verlag GmbH & Co. KGaA: 2012.
- (23) Crivello, J. V. *Photoinitiators for Free Radical, Cationic and Anionic Photopolymerization*, 2nd ed.; John Wiley & Sons: Chichester, 1998.
- (24) Neckers, D. C.; Jager, W. *Photoinitiation for Polymerization: UV and EB at the Millennium*; John Wiley & Sons: Chichester, 1999; 410 pp.
- (25) Davidson, S. *Exploring the Science, Technology and Application of UV and EB Curing*; Sita Technology Ltd: London, 1999; 290 pp.
- (26) Dietliker, K. A *Compilation of Photoinitiators commercially available for UV today*; Sita Technology Ltd: Edinburgh, London, 2002; 250 pp.
- (27) Belfied, K. D.; Crivello, J. V. *Photoinitiated Polymerization*; ACS Symp. Ser. 847; American Chemical Society: Washington DC, 2003.
- (28) Allen, N. S. *Photochemistry and Photophysics of Polymer Materials*; Wiley: New York, 2010.
- (29) Dadashi-Silab, S.; Doran, S.; Yagci, Y. Photoinduced Electron Transfer Reactions for Macromolecular Syntheses. *Chem. Rev.* **2016**, *116*, 10212–10275.
- (30) Peng, H.; Bi, S.; Ni, M.; Xie, X.; Liao, Y.; Zhou, X.; Xue, Z.; Zhu, J.; Wei, Y.; Bowman, C. N.; Mai, Y.-W. Monochromatic Visible Light “Photoinhibitor”: Janus-Faced Initiation and Inhibition for Storage of Colored 3D Images. *J. Am. Chem. Soc.* **2014**, *136*, 8855–8858.
- (31) Wang, J.; Stanic, S.; Altun, A. A.; Schwentenwein, M.; Dietliker, K.; Jin, L.; Stampfl, J.; Baudis, S.; Liska, R.; Grutzmacher, H. A highly efficient waterborne photoinitiator for visible-light-induced three-dimensional printing of hydrogels. *Chem. Commun.* **2018**, *54*, 920–923.
- (32) Li, Z.; Zou, X.; Zhu, G.; Liu, X.; Liu, R. Coumarin-Based Oxime Esters: Photobleachable and Versatile Unimolecular Initiators for Acrylate and Thiol-Based Click Photopolymerization under Visible Light-Emitting Diode Light Irradiation. *ACS Appl. Mater. Interfaces* **2018**, *10*, 16113–16123.
- (33) Dadashi-Silab, S.; Aydogan, C.; Yagci, Y. Shining a light on an adaptable photoinitiator: advances in photopolymerizations initiated by thioxanthenes. *Polym. Chem.* **2015**, *6*, 6595–6615.
- (34) Rosales, A. M.; Vega, S. L.; DelRio, F. W.; Burdick, J. A.; Anseth, K. S. Hydrogels with Reversible Mechanics to Probe Dynamic Cell Microenvironments. *Angew. Chem., Int. Ed.* **2017**, *56*, 12132–12136.
- (35) Tehfe, M.-A.; Dumur, F.; Vilà, N.; Graff, B.; Mayer, C. R.; Fouassier, J. P.; Gigmès, D.; Lalevée, J. A Multicolor Photoinitiator for Cationic Polymerization and Interpenetrated Polymer Network Synthesis: 2,7-Di-tert-butylidimethyldihydropyrene. *Macromol. Rapid Commun.* **2013**, *34*, 1104–1109.
- (36) Tehfe, M.; Dumur, F.; Graff, B.; Gigmès, D.; Fouassier, J. P.; Lalevée, J. Blue-to-Red Light Sensitive Push-Pull Structured Photoinitiators: Indanedione Derivatives for Radical and Cationic Photopolymerization Reactions. *Macromolecules* **2013**, *46*, 3332–3341.
- (37) Xiao, P.; Dumur, F.; Thirion, D.; Fagour, S.; Vacher, A.; Sallenave, X.; Morlet-Savary, F.; Graff, B.; Fouassier, J. P.; Gigmès, D.; Lalevée, J. Multicolor Photoinitiators for Radical and Cationic Polymerization: Mono vs. Polyfunctional Thiophene Derivatives. *Macromolecules* **2013**, *46*, 6786–6793.
- (38) Tar, H.; Sevinc Esen, D.; Aydin, M.; Ley, C.; Arsu, N.; Allonas, X. Panchromatic Type II Photoinitiator for Free Radical Polymerization Based on Thioxanthone Derivative. *Macromolecules* **2013**, *46*, 3266–3272.
- (39) Zhao, J.; Lalevée, J.; Lu, H.; MacQueen, R.; Kable, S. H.; Schmidt, T. W.; Stenzel, M. H.; Xiao, P. A new role of curcumin: as a multicolor photoinitiator for polymer fabrication under household UV to red LED bulbs. *Polym. Chem.* **2015**, *6*, S053–S061.
- (40) Cordon, C.; Miller, C. *UV-LED: Presented by RadTech-The Association for UV & EB Technology*; RadTech International: 2013.
- (41) Pile, D. Ultraviolet goes solid-state. *Nat. Photonics* **2011**, *5*, 394–395.
- (42) Nakamura, S. The Roles of Structural Imperfections in InGaN-Based Blue Light-Emitting Diodes and Laser Diodes. *Science* **1998**, *281*, 956–961.
- (43) Ponce, F. A.; Bour, D. P. Nitride-based semiconductors for blue and green light-emitting devices. *Nature* **1997**, *386*, 351–359.
- (44) Dietlin, C.; Schweizer, S.; Xiao, P.; Zhang, J.; Morlet-Savary, F.; Graff, B.; Fouassier, J.-P.; Lalevée, J. Photopolymerization upon LEDs: new photoinitiating systems and strategies. *Polym. Chem.* **2015**, *6*, 3895–3912.
- (45) Zhang, J.; Frigoli, M.; Dumur, F.; Xiao, P.; Ronchi, L.; Graff, B.; Morlet-Savary, F.; Fouassier, J. P.; Gigmès, D.; Lalevée, J. Design of Novel Photoinitiators for Radical and Cationic Photopolymerizations under Near UV and Visible LEDs (385, 395 and 405 nm). *Macromolecules* **2014**, *47*, 2811–2819.
- (46) Zhang, J.; Lalevée, J.; Zhao, J.; Graff, B.; Stenzel, M. H.; Xiao, P. Dihydroxyanthraquinone derivatives: natural dyes as blue-light-sensitive versatile photoinitiators of photopolymerization. *Polym. Chem.* **2016**, *7*, 7316–7324.
- (47) Zhang, J.; Hill, N. S.; Lalevée, J.; Fouassier, J.-P.; Zhao, J.; Graff, B.; Schmidt, T. W.; Kable, S. H.; Stenzel, M. H.; Coote, M. L.; Xiao, P. Multihydroxy-Anthraquinone Derivatives as Free Radical and Cationic Photoinitiators of Various Photopolymerizations under Green LED. *Macromol. Rapid Commun.* **2018**, No. 1–6, 1800172.
- (48) Xiao, P.; Dumur, F.; Graff, B.; Fouassier, J. P.; Gigmès, D.; Lalevée, J. Cationic and Thiol-Ene Photopolymerization upon Red Lights Using Anthraquinone Derivatives as Photoinitiators. *Macromolecules* **2013**, *46*, 6744–6750.
- (49) Frisch, M.; Trucks, G.; Schlegel, H.; Scuseria, G.; Robb, M.; Cheeseman, J.; Scalmani, G.; Barone, V.; Petersson, G.; Nakatsuji, H.; Li, X.; Caricato, M.; Marenich, A.; Bloino, J.; Janesko, B.; Gomperts, R.; Mennucci, B.; Hratchian, H.; Ortiz, J.; Izmaylov, A.; Sonnenberg, J.; Williams-Young, D.; Ding, F.; Lipparini, F.; Egidi, F.; Goings, J.; Peng, B.; Petrone, A.; Henderson, T.; Ranasinghe, D.; Zakrzewski, V.; Gao, J.; Rega, N.; Zheng, G.; Liang, W.; Hada, M.; Ehara, M.; Toyota, K.; Fukuda, R.; Hasegawa, J.; Ishida, M.; Nakajima, T.; Honda, Y.; Kitao, O.; Nakai, H.; Vreven, T.; Throssell, K.; Jr, J. M.; Peralta, J.; Ogliaro, F.; Bearpark, M.; Heyd, J.; Brothers, E.; Kudin, K.; Staroverov, V.; Keith, T.; Kobayashi, R.; Normand, J.; Raghavachari, K.; Rendell, A.; Burant, J.; Iyengar, S.; Tomasi, J.; Cossi, M.; Millam, J.; Klene, M.; Adamo, C.; Cammi, R.; Ochterski, J.; Martin, R.; Morokuma, K.; Farkas, O.; Foresman, J.; Fox, D. *Gaussian 16*, revision A.03; Gaussian Inc.: Wallingford, CT, 2016.
- (50) Zhao, Y.; Truhlar, D. G. The M06 suite of density functionals for main group thermochemistry, thermochemical kinetics, non-covalent interactions, excited states, and transition elements: two new functionals and systematic testing of four M06-class functionals and 12 other functionals. *Theor. Chem. Acc.* **2008**, *120*, 215–241.
- (51) Weigend, F.; Ahlrichs, R. Balanced basis sets of split valence, triple zeta valence and quadruple zeta valence quality for H to Rn: Design and assessment of accuracy. *Phys. Chem. Chem. Phys.* **2005**, *7*, 3297–3305.
- (52) Marenich, A. V.; Cramer, C. J.; Truhlar, D. G. Universal Solvation Model Based on Solute Electron Density and on a Continuum Model of the Solvent Defined by the Bulk Dielectric Constant and Atomic Surface Tensions. *J. Phys. Chem. B* **2009**, *113*, 6378–6396.

(53) Lalevée, J.; Blanchard, N.; Tehfe, M. A.; Peter, M.; Morlet-Savary, F.; Gigmes, D.; Fouassier, J. P. Efficient dual radical/cationic photoinitiator under visible light: a new concept. *Polym. Chem.* **2011**, *2*, 1986–1991.

(54) Xiao, P.; Lalevée, J.; Allonas, X.; Fouassier, J. P.; Ley, C.; El Roz, M.; Shi, S. Q.; Nie, J. Photoinitiation Mechanism of Free Radical Photopolymerization in the Presence of Cyclic Acetals and Related Compounds. *J. Polym. Sci., Part A: Polym. Chem.* **2010**, *48*, 5758–5766.

(55) Xiao, P.; Hong, W.; Li, Y.; Dumur, F.; Graff, B.; Fouassier, J. P.; Gigmes, D.; Lalevée, J. Green Light Sensitive Diketopyrrolopyrrole Derivatives used in Versatile Photoinitiating Systems for Photopolymerizations. *Polym. Chem.* **2014**, *5*, 2293–2300.

(56) Borst, H. U.; Kelemen, J.; Fabian, J.; Nepraš, M.; Kramer, H. E. A. Triplet formation in aminoanthraquinones and its importance for the catalytic fading of dye mixtures. *J. Photochem. Photobiol., A* **1992**, *69*, 97–107.

(57) Ritter, J.; Borst, H. U.; Lindner, T.; Hauser, M.; Brosig, S.; Bredereck, K.; Steiner, U. E.; Kühn, D.; Kelemen, J.; Kramer, H. E. A. Substituent effects on triplet yields in aminoanthraquinones: radiationless deactivation via intermolecular and intramolecular hydrogen bonding. *J. Photochem. Photobiol., A* **1988**, *41*, 227–244.

(58) Allen, N. S.; Harwood, B.; McKellar, J. F. Lightfastness and spectroscopic properties of amino-chloroanthraquinones. *J. Photochem.* **1978**, *9*, 559–564.

(59) Tehfe, M. A.; Lalevée, J.; Telitel, S.; Contal, E.; Dumur, F.; Gigmes, D.; Bertin, D.; Nechab, M.; Graff, B.; Morlet-Savary, F.; Fouassier, J. P. Polyaromatic Structures as Organo-Photoinitiator Catalysts for Efficient Visible Light Induced Dual Radical/Cationic Photopolymerization and Interpenetrated Polymer Networks Synthesis. *Macromolecules* **2012**, *45*, 4454–4460.

(60) Lalevée, J.; Blanchard, N.; Tehfe, M. A.; Morlet-Savary, F.; Fouassier, J. P. Green Bulb Light Source Induced Epoxy Cationic Polymerization under Air Using Tris(2,2'-bipyridine)ruthenium(II) and Silyl Radicals. *Macromolecules* **2010**, *43*, 10191–10195.

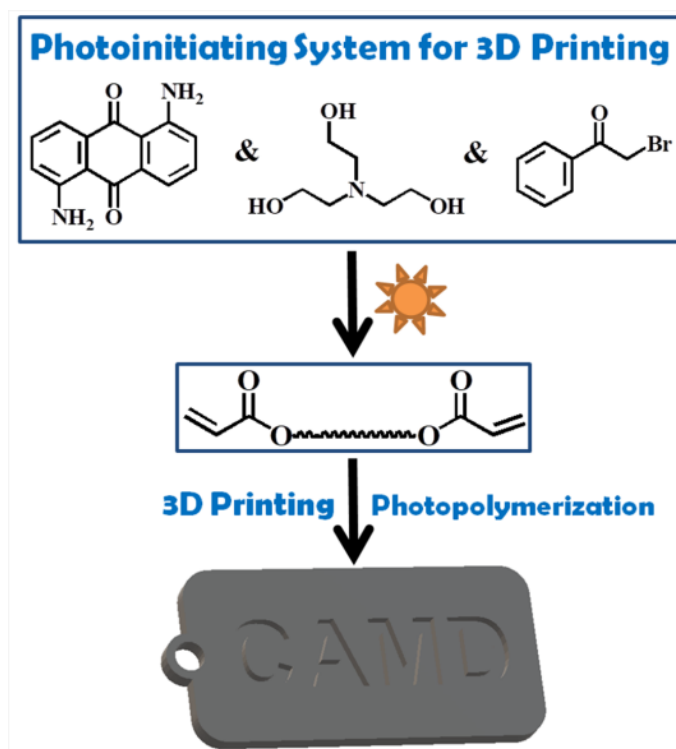
(61) Lalevée, J.; Tehfe, M.-A.; Zein-Fakih, A.; Ball, B.; Telitel, S.; Morlet-Savary, F.; Graff, B.; Fouassier, J. P. N-Vinylcarbazole: An Additive for Free Radical Promoted Cationic Polymerization upon Visible Light. *ACS Macro Lett.* **2012**, *1*, 802–806.

### 3.4 Publication 5

#### Disubstituted Aminoanthraquinone-Based Photoinitiators for Free Radical Polymerization and Fast 3D Printing under Visible Light

J. Zhang, K. Launay, N. S Hill, D. Zhu, N. Cox, J. Langley, J. Laleveé, M. H. Stenzel, M. L. Coote, and P. Xiao

*Macromolecules* **2018**, *51*, 10104-10112



This publication is a peer-reviewed manuscript published in *Macromolecules*. All computational results, mechanistic insight, and subsequent discussion are my own work. Prof. Michelle Coote assisted with the direction of the theoretical investigations and corrected my draft write-ups. [Supplementary material is available online.](#)

### Statement of Contribution

This thesis is submitted as a Thesis by Compilation in accordance with [https://policies.anu.edu.au/ppl/document/ANUP\\_003405](https://policies.anu.edu.au/ppl/document/ANUP_003405)

I declare that the research presented in this Thesis represents original work that I carried out during my candidature at the Australian National University, except for contributions to multi-author papers incorporated in the Thesis where my contributions are specified in this Statement of Contribution.

Title: Disubstituted Aminoanthraquinone-Based Photoinitiators for Free Radical Polymerization and Fast 3D Printing under Visible Light

Authors: J. Zhang, K. Launay, Nicholas S. Hill, D. Zhu, N. Cox, J. Langley, J. Lalevee, M. H. Stenzel, M. L. Coote, and P. Xiao

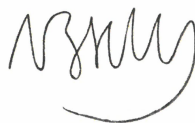
Publication outlet: Macromolecules

Current status of paper: Published

Contribution to paper: I am the first contributing computational chemistry author. All computational results, mechanistic insight, and subsequent discussion are my own work.

Senior author or collaborating authors endorsement: Michelle Coote

Nicholas Hill



20/01/2020

Candidate - Print Name

Signature

Date

#### Endorsed

Michelle Coote



20/01/2020

Primary Supervisor – Print Name

Signature

Date

  
Delegated Authority – Print Name



Signature

20/01/2020

Date



# Disubstituted Aminoanthraquinone-Based Photoinitiators for Free Radical Polymerization and Fast 3D Printing under Visible Light

J. Zhang,<sup>†,‡</sup> K. Launay,<sup>†</sup> N. S. Hill,<sup>‡,§</sup> D. Zhu,<sup>‡</sup> N. Cox,<sup>‡,||</sup> J. Langley,<sup>‡</sup> J. Lalevée,<sup>||,⊥</sup> M. H. Stenzel,<sup>†,||</sup> M. L. Coote,<sup>\*,‡,§,||</sup> and P. Xiao<sup>\*,†,‡,||</sup>

<sup>†</sup>Centre for Advanced Macromolecular Design, School of Chemistry, University of New South Wales, Sydney, NSW 2052, Australia

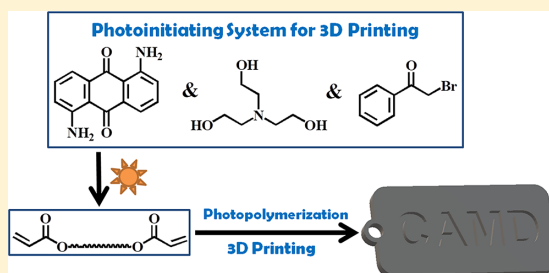
<sup>‡</sup>Research School of Chemistry and <sup>§</sup>ARC Centre of Excellence for Electromaterials Science, Australian National University, Canberra, ACT 2601, Australia

<sup>||</sup>Université de Haute-Alsace, CNRS, IS2M UMR 7361, F-68100 Mulhouse, France

<sup>⊥</sup>Université de Strasbourg, Strasbourg, France

## Supporting Information

**ABSTRACT:** The development of highly efficient and rapid photoinitiating systems for free radical photopolymerization under the irradiation of visible light has attracted increasing attention due to their widespread potential applications in, for example, 3D printing or dental polymers. Unfortunately, currently available visible-light-sensitive photoinitiators are not efficient enough for 3D printing applications suffering from low printing speeds. Here we describe a series of photoinitiating systems consisting of disubstituted aminoanthraquinone derivatives (i.e., 1-amino-4-hydroxyanthraquinone, 1,4-diaminoanthraquinone, and 1,5-diaminoanthraquinone) and various additives (e.g., tertiary amine and phenacyl bromide) toward the free radical photopolymerization of various acrylate monomers (such as commercial 3D resin) under the irradiation of blue to red LEDs. It is shown that the type and position of substituents of the aminoanthraquinone derivative can significantly affect its photoinitiation properties. The most efficient disubstituted aminoanthraquinone derivative-based photoinitiating system was selected and used for the 3D printing of a commercial 3D resin in a 3D printer with polychromatic visible light as the irradiation source. It is shown that its printing speed was dramatically enhanced compared to a commercial photoinitiator 2,4,6-trimethylbenzoyldiphenylphosphine oxide (TPO).



## INTRODUCTION

Free radical photopolymerization has found widespread applications in various fields such as materials science<sup>1–12</sup> and 3D printing.<sup>3,13–22</sup> This technology relies on an efficient photoinitiator (PI) absorbing light to generate free radicals and thus trigger the transformation of liquid monomers/resins into cross-linked solid polymers.<sup>1,2,23,24</sup> In industry, photopolymerization has mainly utilized UV light due to the lack of efficient visible-light-sensitive photoinitiators in the market and indeed is known as “UV curing”.<sup>23,24,27–34</sup> Some efforts have been devoted to the development of photoinitiators/photoinitiating systems applicable to visible light,<sup>7,10,23,25–39</sup> especially from LEDs due to their advantages over other light sources such as safer usage, higher operating efficiency, better light output, and lower cost.<sup>1,40,41</sup> Interestingly, several of them can even be successfully used for 3D printing with 405 nm LEDs.<sup>14,42–46</sup> However, to the best of our knowledge, few visible-light-sensitive PIs have been developed and investigated for fast printing in 3D printers with visible light as irradiation sources, and the printing speed is extremely important to various applications such as in industry.

Recently, a novel 3D printing approach (i.e., continuous liquid interface production (CLIP)) with fast printing speed under UV light irradiation has been reported.<sup>47</sup> By taking advantage of the oxygen inhibition effect, the continuous formation of a solid–liquid interface can be realized, thus avoiding the traditional 3D printing process based on layer-by-layer deposition, accelerating the rate of 3D printing.<sup>47</sup> In this report, several commercial UV-light-sensitive photoinitiators such as TPO, BAPO, Irgacure 184, and Irgacure 369 were used for the photopolymerization of 3D resins during the 3D printing processes under UV light irradiation.<sup>47</sup>

To adapt fast 3D printing with visible light further, the development of efficient visible-light-sensitive photoinitiators is essential. Recently, several disubstituted aminoanthraquinone derivative (DAAQ) [i.e., 1-amino-4-hydroxyanthraquinone (AHAQ), 1,4-diaminoanthraquinone (14-DAAQ), and 1,5-diaminoanthraquinone (15-DAAQ)]-based photoinitiating

Received: October 6, 2018

Revised: November 27, 2018

Published: December 6, 2018

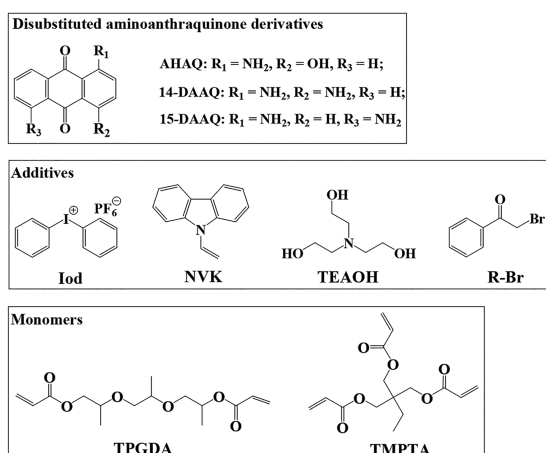
systems were shown to initiate cationic photopolymerization under visible light.<sup>34</sup> Because many important polymerizations occur via radical processes (which are usually faster than cationic polymerization), instead, there remains a need to develop rapid and efficient visible light free radical photoinitiators as well. In this study, we therefore investigate whether these disubstituted aminoanthraquinone derivative-based PISs are capable of initiating the free radical photopolymerization of various acrylate monomers (such as commercial 3D resin) under the irradiation of blue to red LEDs. We assess photoinitiating systems not only under standard photopolymerization conditions but also in a 3D printer with polychromatic visible light as the irradiation source.

## EXPERIMENTAL SECTION

**Materials.** The investigated disubstituted aminoanthraquinone derivatives (DAAQs), i.e., 1-amino-4-hydroxyanthraquinone (AHAQ), 1,4-diaminoanthraquinone (14-DAAQ), and 1,5-diaminoanthraquinone (15-DAAQ), were obtained from EGA-Chemie KG, Fluka AG, and Sigma-Aldrich, respectively. Diphenyliodonium hexafluorophosphate (Iod), *N*-vinylcarbazole (NVK), triethanolamine (TEAOH), and phenacyl bromide (R-Br) were obtained from Sigma-Aldrich and used as the additives of the disubstituted aminoanthraquinone-based photoinitiating systems, while tripropylene glycol diacrylate (TPGDA), trimethylolpropane triacrylate (TMPTA), and EBECRYL 605 (EB605; it is the bisphenol A epoxy diacrylate, EBECRYL 600, diluted 25 wt % with TPGDA) were obtained from Allnex and used as monomers for free radical photopolymerization. The commercial 3D resins (one with 2,4,6-trimethylbenzoyl-diphenyl-phosphineoxide TPO as photoinitiator and the other without any photoinitiator) were obtained from Monocure 3D. The chemical structures of the compounds are illustrated in Scheme 1.

**Irradiation Sources.** Four different household LED bulbs were used as irradiation devices for the free radical photopolymerization reactions: blue LED (emission wavelength centered at 455 nm; incident light intensity: 60 mW cm<sup>-2</sup>), green LED (518 nm; 60 mW cm<sup>-2</sup>), yellow LED (594 nm; 30 mW cm<sup>-2</sup>), and red LED (636 nm; 60 mW cm<sup>-2</sup>).

**Scheme 1. Chemical Structures of the Studied Disubstituted Aminoanthraquinone Derivatives (AHAQ, 14-DAAQ, and 15-DAAQ), Additives (Iod, NVK, TEAOH, and R-Br), and Monomers (TPGDA and TMPTA)**



**Fluorescence Experiments.** The fluorescence properties of DAAQs in acetonitrile were studied using the Varian Cary Eclipse fluorescence spectrophotometer. The fluorescence quenching of DAAQs by the additives (TEAOH or R-Br) was investigated from the classical Stern–Volmer treatment<sup>48</sup> ( $I_0/I = 1 + k_q\tau_0[\text{additive}]$ ), where  $I_0$  and  $I$  stand for the fluorescent intensity of DAAQs in the absence and the presence of additive, respectively;  $\tau_0$  stands for the lifetime of DAAQs in the absence of additive).

**Steady State Photolysis Experiments.** DAAQs in the presence of the additives (TEAOH or R-Br) in acetonitrile were irradiated with the green LED@518 nm (60 mW cm<sup>-2</sup>), and the UV–vis spectra were recorded using the Lambda 950 UV/vis/NIR spectrophotometer (PerkinElmer) at different irradiation times.

**Electron Paramagnetic Resonance Spin Trapping (EPR-ST) Experiments.** EPR-ST experiments were performed using a commercial Bruker E500 spectrometer equipped with an ER4122 SHQ resonator. Samples were loaded into standard X-band EPR tubes of 2.8 mm i.d. The radicals were generated at room temperature upon light exposure under nitrogen and trapped by phenyl-*N*-tert-butyl nitron (PBN) according to the procedure<sup>49</sup> described elsewhere in detail. The EPR spectrum simulation was performed with the WINSIM software.

**Free Radical Photopolymerization of Multifunctional Monomers.** The free radical photopolymerization reactions of the multifunctional monomers (TPGDA, TMPTA EB605, and Monocure 3D resin) in the presence of different DAAQ-based photoinitiating systems upon exposure to the various LED bulbs were monitored using ATR-IR (BRUKER, IFS 66/s). To this end, a layer of liquid formulation (~20 μm thick) was coated on the surface of the ATR horizontal crystal, and the ATR-IR spectra of the sample were recorded at different time intervals during the LED irradiation. The evolutions of the double bond content of TPGDA, TMPTA, EB605, and Monocure 3D resin were all followed by ATR-IR spectroscopy using the bands at about 1635 cm<sup>-1</sup>.<sup>50</sup> The free radical photopolymerization reactions of the investigated monomers were performed in laminate. The degree of double bond-conversion  $C$  at time  $t$  during the photopolymerization is calculated from  $C = (A_0 - A_t)/A_0 \times 100\%$  (where  $A_0$  is the initial peak area before irradiation and  $A_t$  is the peak area of the functional groups at time  $t$ ). The conversion  $C$  measured here is not throughout the whole sample thickness as the penetration depth of infrared beam into the sample is ca. 0.5–3 μm for the ATR-IR spectroscopy, and the conversions measured here can be used to evaluate the photoinitiation ability of the relevant DAAQ-based photoinitiating systems. The well-known blue-light-sensitive camphorquinone-based photoinitiating system was used as a reference.

**3D Printing.** The 3D printing experiments were performed using the M-One 3D printer (MakeX Co. Ltd.) which has a projector as the light irradiation source with the wavelength of polychromatic visible light (400–730 nm; see the emission spectrum in Figure S1 of the Supporting Information; light intensity 3.6 mW/cm<sup>2</sup>).

**Theoretical Procedures.** All electronic structure calculations were performed using the Gaussian 16 software.<sup>51</sup> All calculations were performed with density functional theory (DFT) calculations using the M06-2X<sup>52</sup> functional with the def2-TZVP<sup>53</sup> basis set. Excited state geometries and free energies were calculated with time-dependent DFT (TD-DFT) at the M06-2X/def2-TZVP level of theory; in all cases implicit solvent effects were accounted for with the SMD<sup>54</sup> model of acetonitrile.

## RESULTS AND DISCUSSION

**Generation of Free Radicals from DAAQ-Based Photoinitiating Systems.** It has been reported that DAAQ/Iod-based photoinitiating systems (PISs) are capable of initiating cationic photopolymerization.<sup>34</sup> In the photoinitiation process, free radicals can also be generated from the reduction of Iod by DAAQ with the potential to initiate free radical photopolymerization. Photogeneration of a phenyl radical can be demonstrated using a spin trapping assay. As

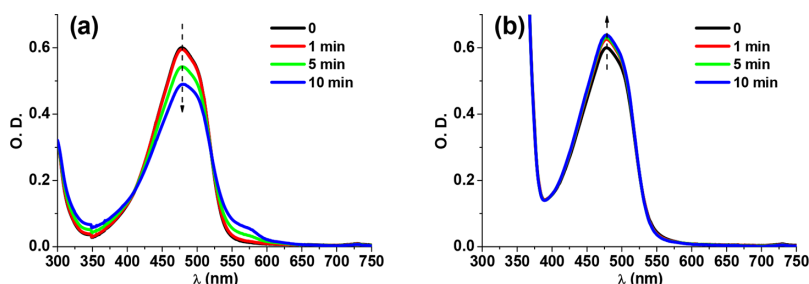


**Figure 1.** Steady state photolysis of (a) 15-DAAQ/TEAOH and (b) 15-DAAQ/R-Br in acetonitrile ( $[\text{TEAOH}] = 45 \text{ mM}$ ;  $[\text{R-Br}] = 35 \text{ mM}$ ); UV-vis spectra recorded at different irradiation time; green LED@518 nm irradiation ( $60 \text{ mW cm}^{-2}$ ).

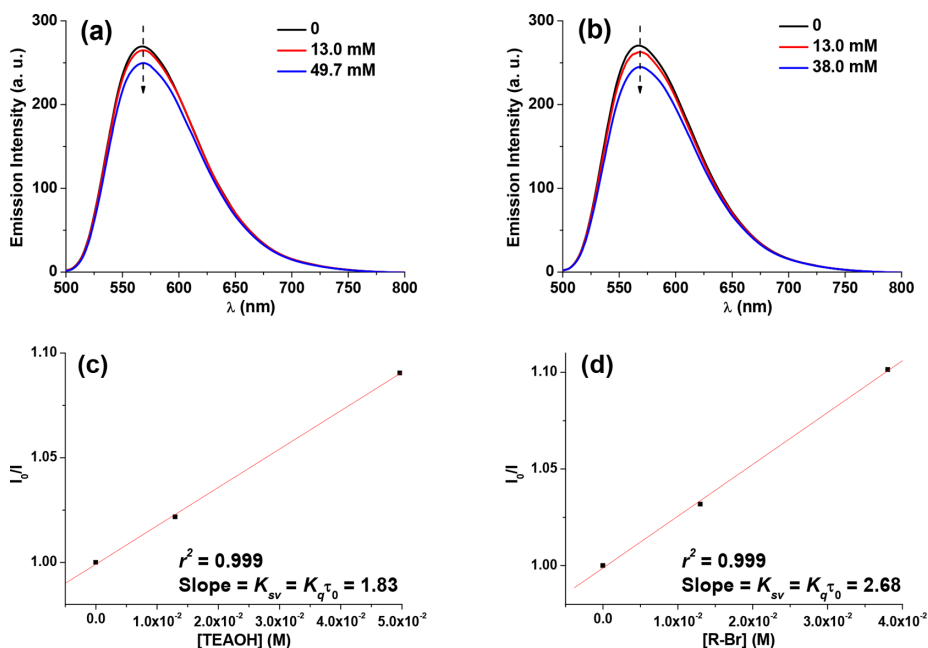


**Figure 2.** Fluorescence spectra of 15-DAAQ as a function of (a)  $[\text{TEAOH}]$  and (b)  $[\text{R-Br}]$  in acetonitrile; the relevant Stern–Volmer plot for the fluorescence quenching of 15-DAAQ by (c) TEAOH and (d) R-Br.

shown in Figure S2, visible light irradiation of the 14-DAAQ/Iod system in the presence of PBN yields a EPR spectrum characteristic of a PBN-phenyl radical adduct,<sup>55,56</sup> with resolved hyperfine splitting constants (HFS) of  $a_{\text{N}} = 14.3 \text{ G}$  for the  $^{14}\text{N}$  nucleus and  $a_{\text{H}} = 2.2 \text{ G}$  for one  $^1\text{H}$  nucleus.

In addition to Iod, it is interesting to investigate other additives and their interaction with DAAQs for the generation of free radicals under the light irradiation. DAAQs/additives with higher photoinitiation efficiency and lower cost compared to the DAAQs/Iod systems are potentially more applicable to industrial production. Tertiary amines (e.g., triethanolamine, TEAOH) and phenacyl bromide (R-Br) are usually used as additives/co-initiators in combination with type II photoinitiators for free radical photopolymerization.<sup>1,48</sup>

The interaction of DAAQs/TEAOH and DAAQs/R-Br systems under the light irradiation were first investigated using steady state photolysis.<sup>25</sup> As demonstrated in Figure 1a, the UV-vis absorption of 15-DAAQ/TEAOH decreased during green LED irradiation. Interestingly, isosbestic points were

observed at 412/520 nm, which indicates that no secondary reactions occurred in reaction 1. The increase of the UV-vis absorption of the 15-DAAQ/R-Br system (Figure 1b) during the green light irradiation also indicates the occurrence of the photochemical reaction and the generation of the photo-product which can absorb at  $\sim 480 \text{ nm}$ . On the contrary, no change was observed for the UV-vis absorption of the AHAQ/TEAOH, 14-DAAQ/TEAOH, and AHAQ/R-Br systems during the green LED irradiation (Figures S3 and S4), implying the low efficiency of the systems. Unusually, the addition of R-Br into the 14-DAAQ solution in acetonitrile can dramatically lead to the decrease of the UV-vis absorption of 14-DAAQ without the light irradiation (Figure S4b), which implies the instability of the 14-DAAQ/R-Br system.

15-DAAQ-based systems were also studied using the fluorescence quenching approach. As illustrated in Figure 2, the fluorescence of 15-DAAQ is quenched by the addition of TEAOH or R-Br, and the interaction rate constants ( $k_{\text{q}}$ ) of  $^{15}\text{-DAAQ/TEAOH}$  and  $^{15}\text{-DAAQ/R-Br}$  determined from

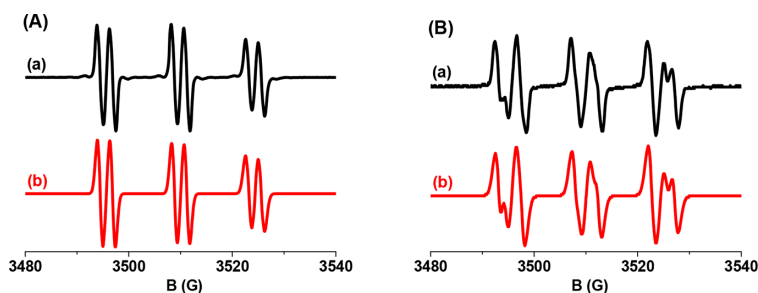


**Figure 3.** EPR spectra of the radicals generated in (A) 15-DAAQ/EDB and (B) 15-DAAQ/EDB/R-Br (ethyl dimethylaminobenzoate (EDB) was used here instead of TEOH to avoid a high polarity of sample preventing EPR analysis) upon the blue LED exposure and trapped by PBN in *tert*-butylbenzene: (a) experimental and (b) simulated spectra.

the Stern–Volmer treatment are  $6.1 \times 10^8$  and  $8.9 \times 10^8 \text{ M}^{-1} \text{ s}^{-1}$ , respectively (fluorescence lifetime of 15-DAAQ  $\tau_0 \sim 3 \text{ ns}$ ). The results demonstrate that the electron transfer occurred in the 15-DAAQ/TEOH and 15-DAAQ/R-Br systems under the light excitation, and the process is diffusion-controlled.

During light irradiation of 15-DAAQ together with additives, radical generation can be detected using the EPR spin trapping technique. Moreover, the type of radical can be determined from the observed HFS of the PBN/radical adduct. For the 15-DAAQ/EDB system (Figure 3A) HFS of  $a_N = 14.3 \text{ G}$  and  $a_H = 2.4 \text{ G}$  were observed indicative of PBN/aminoalkyl radical adducts. For the 15-DAAQ/EDB/R-Br system (Figure 3B) two sets of HFS are observed: (i)  $a_N = 14.3 \text{ G}$  and  $a_H = 2.4 \text{ G}$ <sup>57,58</sup> and (ii)  $a_N = 14.7 \text{ G}$  and  $a_H = 4.6 \text{ G}$ <sup>59,60</sup> indicative of both aminoalkyl and phenacyl radical adducts.

**Photoinitiation Mechanism.** The two- and three-component photoinitiating systems involving DAAQs, TEOH, and R-Br have been modeled computationally to further determine the photoinitiation mechanism. The three-component system is found to perform extremely well when 15-DAAQ is employed as the photoinitiator. The energy levels for the most likely photoinitiation pathway for the three DAAQ derivatives are shown in Figure 4 and clearly demonstrate the thermodynamic favorability when this process takes place with 15-DAAQ. The overall mechanism is shown in Figure 5 and is a redox process in which the excited DAAQ molecules are reduced by the TEOH species present, before being oxidized by the R-Br additive. The first reduction step exhibits a significant thermodynamic favorability, relative to each of the anthraquinones in their S<sub>1</sub> states and a neutral TEOH species, for 15-DAAQ, at  $-65.4 \text{ kJ mol}^{-1}$ , and is much more favorable than equivalent steps for 14-DAAQ and AHAQ at  $-11.0$  and  $-27.5 \text{ kJ mol}^{-1}$ , respectively. The ensuing oxidation step, taking place on the respective ground states of 14-/15-DAAQ and AHAQ, is favorable for both 14-DAAQ and 15-DAAQ ( $-9.8$  and  $-4.6 \text{ kJ mol}^{-1}$ , respectively) but is significantly unfavorable for AHAQ ( $+19.5 \text{ kJ mol}^{-1}$ ). The final step in Figure 4 is the overall reaction free energy change to produce both radical species originating from TEOH and R-Br, for which 15-DAAQ again exhibits the highest thermodynamic favorability; hence, it is the best performing initiator.

The result of this three-component mechanism, especially with 15-DAAQ, is that two different radical species are formed that are available to initiate the polymerization reaction. As well as this, unlike in the two-component systems, the DAAQ species are re-formed and are therefore available for further

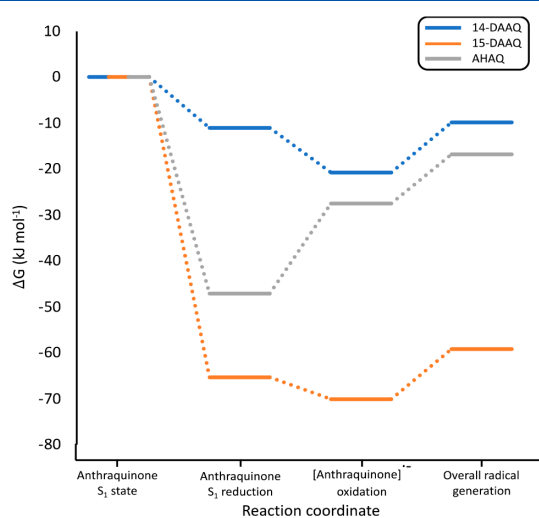


**Figure 4.** Free energy diagram for the photoinitiation pathway for the 14-DAAQ (blue), 15-DAAQ (orange), and AHAQ (gray) initiators in combination with TEOH and R-Br.

photoexcitation. The processes involving 14-DAAQ and AHAQ, however, are found experimentally to be too slow for initiation to take place (as shown in Tables S1–S3). The corresponding photoinitiation mechanisms for the two-component systems are provided in Tables S4 and S5. These mechanisms demonstrate the greater favorability for the DAAQ molecules to interact with TEOH than with R-Br, though both the 15-DAAQ/R-Br and 15-DAAQ/TEOH systems are reactive, though not as effective as the three-component system.

**Free Radical Photopolymerization Using DAAQ-Based Photoinitiating Systems.** Free radicals generated from the DAAQs/Iod (optional NVK),<sup>34</sup> DAAQs/TEOH, DAAQs/R-Br, and DAAQs/TEOH/R-Br systems under light irradiation have the potential to initiate the free radical photopolymerization. Herein the abilities of these systems to initiate different monomers are investigated. As shown in Figure S5 and Table S1, AHAQ- and 14-DAAQ-based PISs were not very efficient for the free radical photopolymerization of TPGDA (double-bond conversions <20% under all conditions): this is in agreement with the results of the steady state photolysis above. Interestingly, 15-DAAQ/Iod/NVK PIS can efficiently initiate the polymerization of TPGDA under the

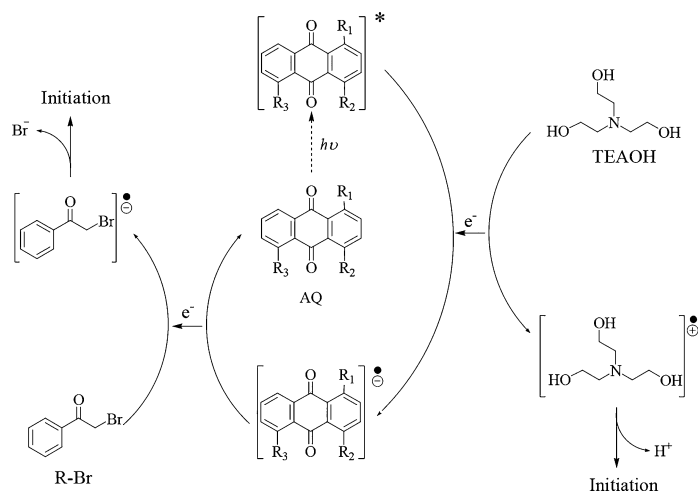


Figure 5. Overall photoinitiation mechanism for DAAQ with TEOAH and R-Br.

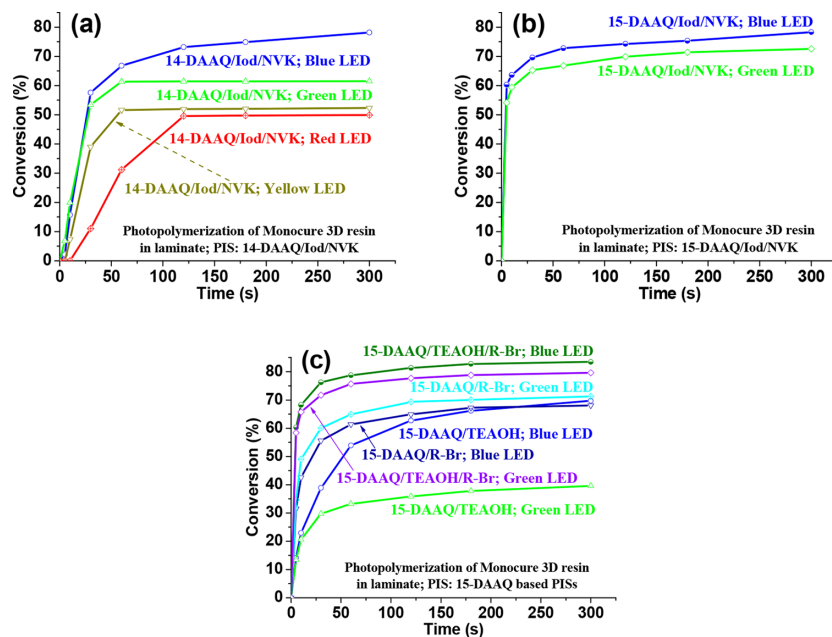


Figure 6. Photopolymerization profiles (double-bond conversions vs time) of Monocure 3D resin (without commercial photoinitiators) in laminate in the presence of DAAQ-based PISs (DAAQ: 0.5 wt %; TEOAH, R-Br, or Iod: 2 wt %; NVK: 3 wt %) upon exposure to different LEDs [i.e., blue LED@455 nm ( $60 \text{ mW cm}^{-2}$ ), green LED@518 nm ( $60 \text{ mW cm}^{-2}$ ), yellow LED@594 nm ( $30 \text{ mW cm}^{-2}$ ), and red LED@636 nm ( $60 \text{ mW cm}^{-2}$ )].

irradiation of both blue and green LEDs and lead to double-bond conversions >60% (Figure S5a). Compared to the well-known blue-light-sensitive commercial camphorquinone (CQ)-based system CQ/Iod, the 15-DAAQ/Iod/NVK system leads to higher polymerization rate but lower double-bond conversions for the polymerization of TPGDA upon the exposure to blue LED. It is interesting that 15-DAAQ/Iod/NVK was efficient under green LED while the CQ/Iod was inefficient, indicating the more versatile character of the 15-DAAQ-based system. The two-component systems 15-DAAQ/TEAOH and 15-DAAQ/R-Br can work as well (Figure

S5b), and their efficiency is even better than CQ/TEAOH under the green LED irradiation. Markedly, the three-component system 15-DAAQ/TEAOH/R-Br exhibited significantly high photoinitiation ability (even faster polymerization rate than CQ/TEAOH system) for TPGDA, and ~80% double-bond conversions can be attained. Similarly, DAAQs-based PISs can also initiate polymerization of the trifunctional acrylate TMPTA (Figure S6 and Table S2), and 15-DAAQ/TEAOH/R-Br demonstrated the highest efficiency (47% of double-bond conversion was achieved under the blue LED

irradiation, even higher than CQ/TEAOH) among all the investigated PISs.

DAAQs-based PISs also exhibited an ability to initiate free radical photopolymerization of the commercial acrylate blend EB605 (i.e., the bisphenol A epoxy diacrylate, EBECRYL 600, diluted 25 wt % with TPGDA) as illustrated in Figure S7 and Table S3. As demonstrated in Figure S7a, 14-DAAQ/Iod can work under blue to red LEDs irradiation, which is in agreement with its panchromatic absorption properties.<sup>34</sup> The higher polymerization efficiency of EB605 compared to TPGDA can be ascribed to its higher viscosity which can counteract the diffusion of oxygen from the atmosphere into the EB605 during the photopolymerization and thus reduce the oxygen inhibition effect. 15-DAAQ-based PISs also demonstrated a photoinitiation ability for EB605 upon the exposure to blue and green LEDs. Specifically, as presented in Figure S7b, >50% of double-bond conversions of EB605 can be achieved with 15-DAAQ/Iod as PIS. Even though the polymerization efficiency with 15-DAAQ/Iod was lower than CQ/Iod under blue LED, it exhibited higher photoinitiation ability under green LED. Moreover, 15-DAAQ/TEAOH, 15-DAAQ/R-Br, and 15-DAAQ/TEAOH/R-Br can also efficiently work under blue and green LEDs (Figure S7c,d); 15-DAAQ/TEAOH/R-Br illustrated the highest photoinitiation ability for the free radical polymerization of EB605, and it is even more efficient than the commercial CQ/TEAOH system.

To estimate the applicability of DAAQ-based PISs in 3D printing, their abilities to initiate the commercial 3D resin (Monocure; acrylate blend) were investigated. As shown in Figure 6 and Table 1, 14-DAAQ/Iod/NVK can work

**Table 1. Double-Bond Conversions (in %) of Photopolymerization of Monocure 3D Resin (without Commercial Photoinitiators) Obtained in Laminate upon Exposure to Different Household LED Devices for 300 s in the Presence of DAAQ-Based PISs (DAAQs: 0.5 wt %; Iod, TEAOH, and R-Br: 2 wt %; NVK: 3 wt %); Monocure 3D Resin (with Commercial Photoinitiator TPO) as Reference<sup>a</sup>**

PIS	LED (455 nm)	LED (518 nm)	LED (594 nm)	LED (636 nm)
14-DAAQ/Iod/NVK	78	61	52	50
15-DAAQ/Iod/NVK	78	72	np	np
14-DAAQ/TEAOH	np	np	np	np
14-DAAQ/R-Br	np	np	np	np
14-DAAQ/TEAOH/R-Br	np	np	np	np
15-DAAQ/TEAOH	70	40	np	np
15-DAAQ/R-Br	68	71	np	np
15-DAAQ/TEAOH/R-Br	83	80	np	np
TPO	np	np	np	np

<sup>a</sup>np: no photopolymerization.

efficiently as a multicolour PIS for the free radical polymerization of the 3D resin under various LEDs (Figure 6a), while 15-DAAQ/Iod/NVK only exhibited the photoinitiation ability under the blue and green LEDs (Figure 6b). 15-DAAQ/Iod/NVK demonstrated a higher efficiency than 14-DAAQ/Iod/NVK under green LED irradiation. As expected, among all the investigated PISs, the 15-DAAQ/TEAOH/R-Br combination showed the highest initiation ability for the free radical

photopolymerization of the 3D resin under blue and green LEDs, and >80% of double-bond conversions of the 3D resin is attained eventually. On the contrary, the 14-DAAQ/TEAOH/R-Br system and 2,4,6-trimethylbenzoyldiphenylphosphine oxide (TPO; the commercial photoinitiator used for the 3D resin) were inefficient for the polymerization of the 3D resin under the irradiation of all studied LEDs.

As the 15-DAAQ/TEAOH/R-Br photoinitiating system exhibited the highest ability to initiate the free radical polymerization of acrylates and the 3D resin, it was used for the 3D printing of a designed keyring with the dimension of 64.0 mm × 30.0 mm × 3.6 mm (Figure 7) via the



**Figure 7.** (a) 3D model of keyring and (b) 3D printed keyring (64.0 mm × 30.0 mm × 3.6 mm) using 15-DAAQ/TEAOH/R-Br (0.5%/2%/2%, wt %) as a photoinitiating system for the polymerization of the 3D resin.

photopolymerization of the 3D resin. The overlap between the absorption spectrum of 15-DAAQ and the emission spectrum of the light source of the 3D printer (Figure 8)

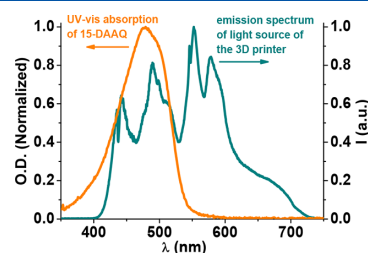


**Figure 8.** UV-vis absorption spectrum of 15-DAAQ and its overlap with the emission spectrum of the light source of the 3D printer.

enables the highly efficient photopolymerization during the 3D printing process. As demonstrated in Table S6, it took 37 min to print the keyring without defect when using TPO (the well-known commercial photoinitiator usually used for 3D printing). Markedly, the printing speed was significantly enhanced when using the 15-DAAQ/TEAOH/R-Br as the photoinitiating system; i.e., the intact keyring can be printed in less than 8 min (Table S7). It indicates that 15-DAAQ/TEAOH/R-Br system can be used as a promising PIS for fast 3D printing.

## CONCLUSION

Free radicals can be generated from the studied DAAQ-based photoinitiating systems (PISs) under light irradiation and have the capability to initiate photopolymerization of various acrylate monomers (TPGDA, TMPTA, EB605, and commercial 3D resin) using a diverse range of LEDs. Interestingly, the 14-DAAQ/Iod system can initiate the free radical polymerization of EB605 (the bisphenol A epoxy diacrylate, EBECRYL 600, diluted 25 wt % with TPGDA) under the irradiation of blue, green, yellow, and red LEDs, which is due to its panchromatic property as a multicolor PIS. Among all the investigated PISs, the 15-DAAQ/TEAOH/R-Br PIS

exhibited the highest efficiency for the free radical photopolymerization under the blue and green LEDs. Time-dependent density functional theory calculations show that this combination demonstrates the highest thermodynamic favorability compared with AHAQ and 14-DAAQ. In addition, there are two different radical species that can be formed to initiate the polymerization reaction, and the 15-DAAQ species can be re-formed and is therefore available for further photoexcitation, which can further enhance the initiation ability of the 15-DAAQ/TEAOH/R-Br PIS. More interestingly, the 15-DAAQ/TEAOH/R-Br PIS can be used for the 3D printing of the commercial 3D resin with the significantly enhanced printing speed compared to that using the commercial photoinitiator TPO.

## ■ ASSOCIATED CONTENT

### Supporting Information

The Supporting Information is available free of charge on the ACS Publications website at DOI: 10.1021/acs.macromol.8b02145.

Emission spectrum of the 3D printer (Figure S1); EPR spectra of the radicals generated in 14-DAAQ/Iod combination (Figure S2); steady state photolysis of AHAQ/TEAOH and 14-DAAQ/TEAOH (Figure S3); steady state photolysis of AHAQ/R-Br and 14-DAAQ/R-Br (Figure S4); photopolymerization profiles of TPGDA in the presence of DAAQ-based PISs (Figure S5); photopolymerization profiles of TMPTA in the presence of DAAQ-based PISs (Figure S6); photopolymerization profiles of EB605 in the presence of DAAQ-based PISs (Figure S7); double-bond conversions of photopolymerization of TPGDA in the presence of DAAQ-based PISs (Table S1); double-bond conversions of photopolymerization of TMPTA in the presence of DAAQ-based PISs (Table S2); double-bond conversions of photopolymerization of EB605 in the presence of DAAQ-based PISs (Table S3); DAAQ photoelectron and proton transfer with TEAOH (Table S4); DAAQ photoelectron donation to R-Br (Table S5); 3D printed keyrings using commercial Monocure 3D resin (TPO as photoinitiator) (Table S6); 3D printed keyrings using commercial Monocure 3D resin with self-designed 15-DAAQ/TEAOH/R-Br photoinitiating system (Table S7); raw computational data (PDF)

## ■ AUTHOR INFORMATION

### Corresponding Authors

\*E-mail: pu.xiao@anu.edu.au (P.X.).

\*E-mail: michelle.coote@anu.edu.au (M.L.C.).

### ORCID

N. Cox: 0000-0002-7815-6115

J. Lalevée: 0000-0001-9297-0335

M. H. Stenzel: 0000-0002-6433-4419

M. L. Coote: 0000-0003-0828-7053

P. Xiao: 0000-0001-5393-7225

### Author Contributions

J.Z. and K.L. contributed equally to this work.

### Notes

The authors declare no competing financial interest.

## ■ ACKNOWLEDGMENTS

P.X. acknowledges funding from the Australian Research Council Future Fellowship (FT170100301). M.L.C. gratefully acknowledges support from the ARC Centre of Excellence for Electromaterials Science, a Georgina Sweet ARC Laureate Fellowship (FL170100041) and generous allocations of supercomputing time on the National Facility of the Australian National Computational Infrastructure. N.C. acknowledges funding from the Australian Research Council (FT140100834). EPR equipment is funded through the ARC LIEF program (LE170100023).

## ■ REFERENCES

- (1) Fouassier, J. P.; Lalevée, J. *Photoinitiators for Polymer Synthesis-Scope, Reactivity, and Efficiency*; Wiley-VCH Verlag GmbH & Co KGaA: Weinheim, 2012.
- (2) Allen, N. S. *Photochemistry and Photophysics of Polymeric Materials*; Wiley: Hoboken, NJ, 2010.
- (3) Neckers, D. C.; Jager, W. *Photoinitiation for Polymerization: UV and EB at the Millennium*; John Wiley & Sons: Chichester, 1999; 410 pp.
- (4) Davidson, S. *Exploring the Science, Technology and Application of UV and EB Curing*; Sita Technology Ltd: London, 1999; 290 pp.
- (5) Dietliker, K. *A Compilation of Photoinitiators commercially available for UV today*; Sita Technology Ltd: Edinburgh, London, 2002; 250 pp.
- (6) Belfied, K. D.; Crivello, J. V. *Photoinitiated Polymerization*; ACS Symp. Ser. 847; American Chemical Society: Washington, DC, 2003.
- (7) Dadashi-Silab, S.; Doran, S.; Yagci, Y. Photoinduced Electron Transfer Reactions for Macromolecular Syntheses. *Chem. Rev.* **2016**, *116*, 10212–10275.
- (8) Ligon-Auer, S. C.; Schwentenwein, M.; Gorsche, C.; Stampfl, J.; Liska, R. Toughening of photo-curable polymer networks: a review. *Polym. Chem.* **2016**, *7*, 257–286.
- (9) Peng, H.; Bi, S.; Ni, M.; Xie, X.; Liao, Y.; Zhou, X.; Xue, Z.; Zhu, J.; Wei, Y.; Bowman, C. N.; Mai, Y.-W. Monochromatic Visible Light “Photoinhibitor”: Janus-Faced Initiation and Inhibition for Storage of Colored 3D Images. *J. Am. Chem. Soc.* **2014**, *136*, 8855–8858.
- (10) Wang, J.; Stanic, S.; Altun, A. A.; Schwentenwein, M.; Dietliker, K.; Jin, L.; Stampfl, J.; Baudis, S.; Liska, R.; Grutzmacher, H. A highly efficient waterborne photoinitiator for visible-light-induced three-dimensional printing of hydrogels. *Chem. Commun.* **2018**, *54*, 920–923.
- (11) Li, Z.; Zou, X.; Zhu, G.; Liu, X.; Liu, R. Coumarin-Based Oxime Esters: Photobleachable and Versatile Unimolecular Initiators for Acrylate and Thiol-Based Click Photopolymerization under Visible Light-Emitting Diode Light Irradiation. *ACS Appl. Mater. Interfaces* **2018**, *10*, 16113–16123.
- (12) Crivello, J. V.; Dietliker, K. *Photoinitiators for Free Radical, Cationic and Anionic Photopolymerization*, 2nd ed.; John Wiley & Sons: Chichester, 1998.
- (13) Ambrosi, A.; Pumera, M. 3D-printing technologies for electrochemical applications. *Chem. Soc. Rev.* **2016**, *45*, 2740–2755.
- (14) Zhang, J.; Xiao, P. 3D printing of photopolymers. *Polym. Chem.* **2018**, *9*, 1530–1540.
- (15) Barner-Kowollik, C.; Bastmeyer, M.; Blasco, E.; Müller, P.; Delaittre, G.; Richter, B.; Wegener, M. 3D Laser Micro- and Nano-Printing: Challenges for Chemistry. *Angew. Chem., Int. Ed.* **2017**, *56*, 15828–15845.
- (16) Donderwinkel, I.; van Hest, J. C. M.; Cameron, N. R. Bio-inks for 3D bioprinting: recent advances and future prospects. *Polym. Chem.* **2017**, *8*, 4451–4471.
- (17) Stansbury, J. W.; Idacavage, M. J. 3D printing with polymers: Challenges among expanding options and opportunities. *Dent. Mater.* **2016**, *32*, 54–64.
- (18) Xing, J.-F.; Zheng, M.-L.; Duan, X.-M. Two-photon polymerization microfabrication of hydrogels: an advanced 3D printing

- technology for tissue engineering and drug delivery. *Chem. Soc. Rev.* **2015**, *44*, 5031–5039.
- (19) Gorsche, C.; Seidler, K.; Knaack, P.; Dorfinger, P.; Koch, T.; Stampfl, J.; Moszner, N.; Liska, R. Rapid formation of regulated methacrylate networks yielding tough materials for lithography-based 3D printing. *Polym. Chem.* **2016**, *7*, 2009–2014.
- (20) Pawar, A. A.; Halivni, S.; Waiskopf, N.; Ben-Shahar, Y.; Soreni-Harari, M.; Bergbreiter, S.; Banin, U.; Magdassi, S. Rapid Three-Dimensional Printing in Water Using Semiconductor–Metal Hybrid Nanoparticles as Photoinitiators. *Nano Lett.* **2017**, *17*, 4497–4501.
- (21) Huang, L.; Jiang, R.; Wu, J.; Song, J.; Bai, H.; Li, B.; Zhao, Q.; Xie, T. Ultrafast Digital Printing toward 4D Shape Changing Materials. *Adv. Mater.* **2017**, *29* (1–6), 1605390.
- (22) Han, Y.; Wang, F.; Lim, C. Y.; Chi, H.; Chen, D.; Wang, F.; Jiao, X. High-Performance Nano-Photoinitiators with Improved Safety for 3D Printing. *ACS Appl. Mater. Interfaces* **2017**, *9*, 32418–32423.
- (23) Dadashi-Silab, S.; Aydogan, C.; Yagci, Y. Shining a light on an adaptable photoinitiator: advances in photopolymerizations initiated by thioxanthenes. *Polym. Chem.* **2015**, *6*, 6595–6615.
- (24) Rosales, A. M.; Vega, S. L.; DelRio, F. W.; Burdick, J. A.; Anseth, K. S. Hydrogels with Reversible Mechanics to Probe Dynamic Cell Microenvironments. *Angew. Chem., Int. Ed.* **2017**, *56*, 12132–12136.
- (25) Xiao, P.; Zhang, J.; Dumur, F.; Tehfe, M. A.; Morlet-Savary, F.; Graff, B.; Gignes, D.; Fouassier, J. P.; Lalevée, J. Visible light sensitive photoinitiating systems: Recent progress in cationic and radical photopolymerization reactions under soft conditions. *Prog. Polym. Sci.* **2015**, *41*, 32–66.
- (26) Shi, S.; Croutxé-Barghorn, C.; Allonas, X. Photoinitiating systems for cationic photopolymerization: Ongoing push toward long wavelengths and low light intensities. *Prog. Polym. Sci.* **2017**, *65*, 1–41.
- (27) Mitterbauer, M.; Haas, M.; Stüger, H.; Moszner, N.; Liska, R. Tetrakis(2,4,6-Trimethylbenzoyl)Silane-A Novel Photoinitiator for Visible Light Curing. *Macromol. Mater. Eng.* **2017**, *302*, 1600536.
- (28) Wu, X.; Jin, M.; Xie, J.; Malval, J.-P.; Wan, D. Molecular Engineering of UV/Vis Light-Emitting Diode (LED)-Sensitive Donor- $\pi$ -Acceptor-Type Sulfonium Salt Photoacid Generators: Design, Synthesis, and Study of Photochemical and Photophysical Properties. *Chem. - Eur. J.* **2017**, *23*, 15783–15789.
- (29) Jin, M.; Yu, M.; Zhang, Y.; Wan, D.; Pu, H. 2,2,2-trifluoroacetophenone-based D- $\pi$ -A type photoinitiators for radical and cationic photopolymerizations under near-UV and visible LEDs. *J. Polym. Sci., Part A: Polym. Chem.* **2016**, *54*, 1945–1954.
- (30) Jin, M.; Wu, X.; Malval, J. P.; Wan, D.; Pu, H. Dual roles for promoting monomers to polymers: A conjugated sulfonium salt photoacid generator as photoinitiator and photosensitizer in cationic photopolymerization. *J. Polym. Sci., Part A: Polym. Chem.* **2016**, *54*, 2722–2730.
- (31) Lalevée, J.; Fouassier, J.-P. *Photopolymerisation Initiating Systems*; Royal Society of Chemistry: 2018; p 586.
- (32) Zhang, X.; Xi, W.; Gao, G.; Wang, X.; Stansbury, J. W.; Bowman, C. N. o-Nitrobenzyl-Based Photobase Generators: Efficient Photoinitiators for Visible-Light Induced Thiol-Michael Addition Photopolymerization. *ACS Macro Lett.* **2018**, *7*, 852–857.
- (33) Zhang, J.; Lalevée, J.; Mou, X.; Morlet-Savary, F.; Graff, B.; Xiao, P. N-Phenylglycine as a Versatile Photoinitiator under Near-UV LED. *Macromolecules* **2018**, *51*, 3767–3773.
- (34) Zhang, J.; Lalevée, J.; Hill, N. S.; Launay, K.; Morlet-Savary, F.; Graff, B.; Stenzel, M. H.; Coote, M. L.; Xiao, P. Disubstituted Aminoanthraquinone-Based Multicolor Photoinitiators: Photoinitiation Mechanism and Ability of Cationic Polymerization under Blue, Green, Yellow and Red LEDs. *Macromolecules* **2018**, *51*, 8165–8173.
- (35) Radebner, J.; Eibel, A.; Leypold, M.; Jungwirth, N.; Pickl, T.; Torvisco, A.; Fischer, R.; Fischer, U. K.; Moszner, N.; Gescheidt, G.; Stueger, H.; Haas, M. Tetraacylstannanes as Long-Wavelength Visible-Light Photoinitiators with Intriguing Low Toxicity. *Chem. - Eur. J.* **2018**, *24*, 8281–8285.
- (36) Eibel, A.; Radebner, J.; Haas, M.; Fast, D. E.; Freißmuth, H.; Stadler, E.; Faschauner, P.; Torvisco, A.; Lamparth, L.; Moszner, N.; Stueger, H.; Gescheidt, G. From mono- to tetraacylgermanes: extending the scope of visible light photoinitiators. *Polym. Chem.* **2018**, *9*, 38–47.
- (37) Radebner, J.; Eibel, A.; Leypold, M.; Gorsche, C.; Schuh, L.; Fischer, R.; Torvisco, A.; Neshchadin, D.; Geier, R.; Moszner, N.; Liska, R.; Gescheidt, G.; Haas, M.; Stueger, H. Tetraacylgermanes: Highly Efficient Photoinitiators for Visible-Light-Induced Free-Radical Polymerization. *Angew. Chem., Int. Ed.* **2017**, *56*, 3103–3107.
- (38) Al Mousawi, A.; Dumur, F.; Garra, P.; Toufaily, J.; Hamieh, T.; Goubard, F.; Bui, T. T.; Graff, B.; Gignes, D.; Fouassier, J. P.; Lalevée, J. Azahelicenes as visible light photoinitiators for cationic and radical polymerization: Preparation of photoluminescent polymers and use in high performance LED projector 3D printing resins. *J. Polym. Sci., Part A: Polym. Chem.* **2017**, *55*, 1189–1199.
- (39) Sangermano, M.; Rodriguez, D.; Gonzalez, M. C.; Laurenti, E.; Yagci, Y. Visible Light Induced Cationic Polymerization of Epoxides by Using Multiwalled Carbon Nanotubes. *Macromol. Rapid Commun.* **2018**, *39*, 1800250.
- (40) Zhang, J.; Frigoli, M.; Dumur, F.; Xiao, P.; Ronchi, L.; Graff, B.; Morlet-Savary, F.; Fouassier, J. P.; Gignes, D.; Lalevée, J. Design of Novel Photoinitiators for Radical and Cationic Photopolymerizations under Near UV and Visible LEDs (385, 395 and 405 nm). *Macromolecules* **2014**, *47*, 2811–2819.
- (41) Cordon, C.; Miller, C. UV-LED: Presented by RadTech-The Association for UV & EB Technology; RadTech International: 2013.
- (42) Al Mousawi, A.; Lara, D. M.; Noirbent, G.; Dumur, F.; Toufaily, J.; Hamieh, T.; Bui, T.-T.; Goubard, F.; Graff, B.; Gignes, D.; Fouassier, J. P.; Lalevée, J. Carbazole Derivatives with Thermally Activated Delayed Fluorescence Property as Photoinitiators/Photoredox Catalysts for LED 3D Printing Technology. *Macromolecules* **2017**, *50*, 4913–4926.
- (43) Al Mousawi, A.; Garra, P.; Sallenave, X.; Dumur, F.; Toufaily, J.; Hamieh, T.; Graff, B.; Gignes, D.; Fouassier, J. P.; Lalevée, J.  $\pi$ -Conjugated Dithienophosphole Derivatives as High Performance Photoinitiators for 3D Printing Resins. *Macromolecules* **2018**, *51*, 1811–1821.
- (44) Al Mousawi, A.; Dumur, F.; Garra, P.; Toufaily, J.; Hamieh, T.; Graff, B.; Gignes, D.; Fouassier, J. P.; Lalevée, J. Carbazole Scaffold Based Photoinitiator/Photoredox Catalysts: Toward New High Performance Photoinitiating Systems and Application in LED Projector 3D Printing Resins. *Macromolecules* **2017**, *50*, 2747–2758.
- (45) Al Mousawi, A.; Poriel, C.; Dumur, F.; Toufaily, J.; Hamieh, T.; Fouassier, J. P.; Lalevée, J. Zinc Tetraphenylporphyrin as High Performance Visible Light Photoinitiator of Cationic Photosensitive Resins for LED Projector 3D Printing Applications. *Macromolecules* **2017**, *50*, 746–753.
- (46) Zhang, J.; Dumur, F.; Xiao, P.; Graff, B.; Bardelang, D.; Gignes, D.; Fouassier, J. P.; Lalevée, J. Structure Design of Naphthalimide Derivatives: Toward Versatile Photoinitiators for Near-UV/Visible LEDs, 3D Printing, and Water-Soluble Photoinitiating Systems. *Macromolecules* **2015**, *48*, 2054–2063.
- (47) Tumbleston, J. R.; Shirvanyants, D.; Ermoshkin, N.; Januszewicz, R.; Johnson, A. R.; Kelly, D.; Chen, K.; Pinschmidt, R.; Rolland, J. P.; Ermoshkin, A.; Samulski, E. T.; DeSimone, J. M. Continuous liquid interface production of 3D objects. *Science* **2015**, *347*, 1349–1352.
- (48) Fouassier, J. P. *Photoinitiator, Photopolymerization and Photocuring: Fundamentals and Applications*; Hanser Publishers: Munich, 1995.
- (49) Xiao, P.; Lalevée, J.; Allonas, X.; Fouassier, J. P.; Ley, C.; El Roz, M.; Shi, S. Q.; Nie, J. Photoinitiation Mechanism of Free Radical Photopolymerization in the Presence of Cyclic Acetals and Related Compounds. *J. Polym. Sci., Part A: Polym. Chem.* **2010**, *48*, 5758–5766.
- (50) Xiao, P.; Hong, W.; Li, Y.; Dumur, F.; Graff, B.; Fouassier, J. P.; Gignes, D.; Lalevée, J. Green Light Sensitive Diketopyrrolopyrrole



Derivatives used in Versatile Photoinitiating Systems for Photopolymerizations. *Polym. Chem.* **2014**, *5*, 2293–2300.

(51) Frisch, M.; Trucks, G.; Schlegel, H.; Scuseria, G.; Robb, M.; Cheeseman, J.; Scalmani, G.; Barone, V.; Petersson, G.; Nakatsuji, H.; Li, X.; Caricato, M.; Marenich, A.; Bloino, J.; Janesko, B.; Gomperts, R.; Mennucci, B.; Hratchian, H.; Ortiz, J.; Izmaylov, A.; Sonnenberg, J.; Williams-Young, D.; Ding, F.; Lipparini, F.; Egidi, F.; Goings, J.; Peng, B.; Petrone, A.; Henderson, T.; Ranasinghe, D.; Zakrzewski, V.; Gao, J.; Rega, N.; Zheng, G.; Liang, W.; Hada, M.; Ehara, M.; Toyota, K.; Fukuda, R.; Hasegawa, J.; Ishida, M.; Nakajima, T.; Honda, Y.; Kitao, O.; Nakai, H.; Vreven, T.; Throssell, K.; Jr, J. M.; Peralta, J.; Ogliaro, F.; Bearpark, M.; Heyd, J.; Brothers, E.; Kudin, K.; Staroverov, V.; Keith, T.; Kobayashi, R.; Normand, J.; Raghavachari, K.; Rendell, A.; Burant, J.; Iyengar, S.; Tomasi, J.; Cossi, M.; Millam, J.; Klene, M.; Adamo, C.; Cammi, R.; Ochterski, J.; Martin, R.; Morokuma, K.; Farkas, O.; Foresman, J.; Fox, D. *Gaussian 16*, revision A.03; Gaussian Inc.: Wallingford, CT, 2016.

(52) Zhao, Y.; Truhlar, D. G. The M06 suite of density functionals for main group thermochemistry, thermochemical kinetics, non-covalent interactions, excited states, and transition elements: two new functionals and systematic testing of four M06-class functionals and 12 other functionals. *Theor. Chem. Acc.* **2008**, *120*, 215–241.

(53) Weigend, F.; Ahlrichs, R. Balanced basis sets of split valence, triple zeta valence and quadruple zeta valence quality for H to Rn: Design and assessment of accuracy. *Phys. Chem. Chem. Phys.* **2005**, *7*, 3297–3305.

(54) Marenich, A. V.; Cramer, C. J.; Truhlar, D. G. Universal Solvation Model Based on Solute Electron Density and on a Continuum Model of the Solvent Defined by the Bulk Dielectric Constant and Atomic Surface Tensions. *J. Phys. Chem. B* **2009**, *113*, 6378–6396.

(55) Tehfe, M. A.; Lalevée, J.; Telitel, S.; Contal, E.; Dumur, F.; Gigmes, D.; Bertin, D.; Nechab, M.; Graff, B.; Morlet-Savary, F.; Fouassier, J. P. Polyaromatic Structures as Organo-Photoinitiator Catalysts for Efficient Visible Light Induced Dual Radical/Cationic Photopolymerization and Interpenetrated Polymer Networks Synthesis. *Macromolecules* **2012**, *45*, 4454–4460.

(56) Lalevée, J.; Blanchard, N.; Tehfe, M. A.; Morlet-Savary, F.; Fouassier, J. P. Green Bulb Light Source Induced Epoxy Cationic Polymerization under Air Using Tris(2,2'-bipyridine)ruthenium(II) and Silyl Radicals. *Macromolecules* **2010**, *43*, 10191–10195.

(57) Xiao, P.; Dumur, F.; Frigoli, M.; Tehfe, M.-A.; Graff, B.; Fouassier, J. P.; Gigmes, D.; Lalevée, J. Naphthalimide Based Methacrylated Photoinitiators in Radical and Cationic Photopolymerization under Visible Light. *Polym. Chem.* **2013**, *4*, 5440–5448.

(58) Zhao, J.; Lalevée, J.; Lu, H.; MacQueen, R.; Kable, S. H.; Schmidt, T. W.; Stenzel, M. H.; Xiao, P. A new role of curcumin: as a multicolor photoinitiator for polymer fabrication under household UV to red LED bulbs. *Polym. Chem.* **2015**, *6*, 5053–5061.

(59) Barclay, L. R. C.; Cromwell, G. R.; Hilborn, J. W. Photochemistry of a model lignin compound. Spin trapping of primary products and properties of an oligomer. *Can. J. Chem.* **1994**, *72*, 35–41.

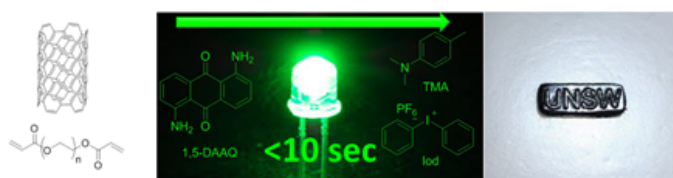
(60) Lalevée, J.; Tehfe, M. A.; Dumur, F.; Gigmes, D.; Blanchard, N.; Morlet-Savary, F.; Fouassier, J. P. Iridium Photocatalysts in Free Radical Photopolymerization under Visible Lights. *ACS Macro Lett.* **2012**, *1*, 286–290.

### 3.5 Publication 6

#### Efficient Photoinitiating System Based on Diaminoanthraquinone for 3D Printing of Polymer/Carbon Nanotube Nanocomposites under Visible Light

Guannan Wang, Nicholas S. Hill, Di Zhu, Pu Xiao, Michelle L. Coote, Martina H. Stenzel

*ACS Applied Polymer Materials* 2019



This publication is a peer-reviewed manuscript published in *Applied Polymer Materials*. All computational results, mechanistic insight, and subsequent discussion are my own work. Prof. Michelle Coote assisted with the direction of the theoretical investigations and corrected my draft write-ups. [Supplementary material is available online](#). The publication also featured as the covering artwork of the journal.

### Statement of Contribution

This thesis is submitted as a Thesis by Compilation in accordance with [https://policies.anu.edu.au/ppi/document/ANUP\\_003405](https://policies.anu.edu.au/ppi/document/ANUP_003405)

I declare that the research presented in this Thesis represents original work that I carried out during my candidature at the Australian National University, except for contributions to multi-author papers incorporated in the Thesis where my contributions are specified in this Statement of Contribution.

Title: Efficient Photoinitiating System Based on Diaminoanthraquinone for 3D Printing of Polymer/Carbon Nanotube Nanocomposites under Visible Light

Authors: Guannan Wang, Nicholas S. Hill, Di Zhu, Pu Xiao, Michelle L. Coote, Martina H. Stenzel

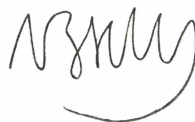
Publication outlet: ACS Applied Polymer Materials

Current status of paper: Published

Contribution to paper: I am the first contributing computational chemistry author. All computational results, mechanistic insight, and subsequent discussion are my own work.

Senior author or collaborating authors endorsement: Michelle Coote

Nicholas Hill



20/01/2020

Candidate - Print Name

Signature

Date

#### Endorsed

Michelle Coote



20/01/2020

Primary Supervisor – Print Name

Signature

Date



Delegated Authority – Print Name



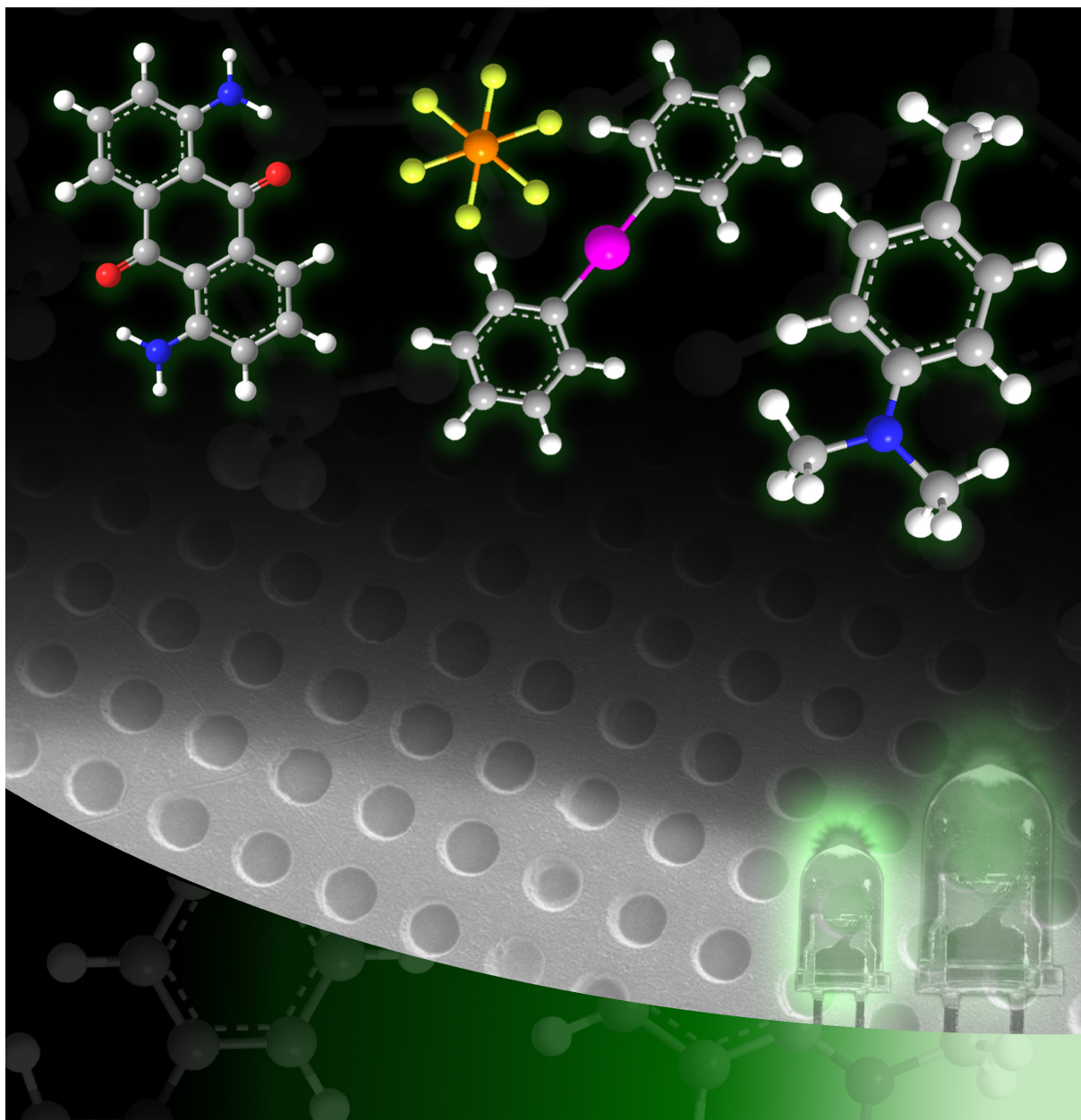
20/01/2020

Signature

Date

# ACS APPLIED POLYMER MATERIALS

May 2019  
Volume 1  
Number 5  
[pubs.acs.org/acscapm](http://pubs.acs.org/acscapm)



 ACS Publications  
Most Trusted. Most Cited. Most Read.

[www.acs.org](http://www.acs.org)

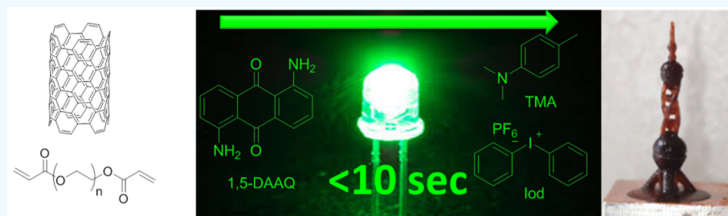
# Efficient Photoinitiating System Based on Diaminoanthraquinone for 3D Printing of Polymer/Carbon Nanotube Nanocomposites under Visible Light

Guannan Wang,<sup>†</sup> Nicholas S. Hill,<sup>‡,§</sup> Di Zhu,<sup>‡</sup> Pu Xiao,<sup>\*,†,‡</sup> Michelle L. Coote,<sup>\*,‡,§</sup> and Martina H. Stenzel<sup>\*,†</sup>

<sup>†</sup>Centre for Advanced Macromolecular Design (CAMD), School of Chemistry, University of New South Wales, Sydney, NSW 2052, Australia

<sup>‡</sup>Research School of Chemistry and <sup>§</sup>ARC Centre of Excellence for Electromaterials Science, Australian National University, Canberra, ACT 2601, Australia

## Supporting Information



**ABSTRACT:** This work reports several 1,5-diaminoanthraquinone (1,5-DAAQ)-based visible-light-sensitive photoinitiating systems (PISs), which can efficiently initiate the free radical photopolymerization of (meth)acrylates under green light delivered from light-emitting diode. The PISs contain three components: 1,5-diaminoanthraquinone, an iodonium salt, and aromatic amines. In one example, polymerization could be efficiently initiated and completed within 10 s with double bond conversions of approximately 80%. The initiating system could also be used in conjunction with reversible addition–fragmentation chain transfer (RAFT) polymerization. Finally, the 1,5-DAAQ/iodonium salt/4-*N,N*-trimethylaniline PIS could be readily employed in the 3D printing process of polymer/carbon nanotube nanocomposites.

**KEYWORDS:** 3D printing, photopolymerization, carbon nanoparticles, three-component photoinitiating systems, green light, LED

## INTRODUCTION

Additive manufacturing (AM), now commonly known as 3D printing, was first developed in the 1980s, when the stereolithography (SLA) patent was published by Charles Hull (1986). In 1987, the first commercially available SLA instrument (Model SLA-1) was produced by the 3D Systems company.<sup>1,2</sup> In its present form, it is characterized by the use of raw materials to produce objects layer-by-layer, with the assistance of computer-assisted design (CAD) software.<sup>3–5</sup> Compared with traditional subtractive manufacturing, 3D printing can produce objects in small quantities or with complex structures economically while reducing waste. At the same time, the CAD interface allows for easy and fast modification of the design.<sup>6</sup> One important 3D printing technique is digital light processing (DLP). DLP 3D printing has a higher resolution in contrast to other 3D printing techniques, such as fused deposition modeling (FDM), selective laser sintering (SLS), or SLA.<sup>5,7</sup> Because the underpinning principle of DLP 3D printing is the photopolymerization of the liquid resins, the development of efficient photoinitiators plays a central role to ensure a high rate of polymerization combined with high polymerization

conversions of monomers to alleviate issues pertaining to unreacted vinyl functionalities.

The two main types of photoinitiators that are commercially available are either sensitive to ultraviolet (UV) light (e.g., trimethylbenzoyl diphenylphosphine oxide (TPO), bis(2,4,6-trimethylbenzoyl)phenylphosphineoxide (BAPO), and isopropylthioxanthone (ITX), etc.) or visible light (e.g., camphorquinone (CQ)-based PISs, eosin Y-based PISs, etc.).<sup>8–10</sup> UV-light-sensitive photoinitiators have the shortcoming that the UV-light source used may not only be an irritant to eyes and skin, but the generation of UV light is a high-energy process, especially when using halogen and mercury lamps as light sources.<sup>11–13</sup> In particular, the preparation of nanocomposites by photopolymerization in the presence of high-performance PISs is hampered, as some nanoparticles such as carbon nanotubes absorb and scatter UV light and therefore slow down or even inhibit the polymerization.<sup>14</sup> Visible light is moreover known to have higher penetration depth, which is

Received: February 13, 2019

Accepted: April 1, 2019

Published: April 1, 2019

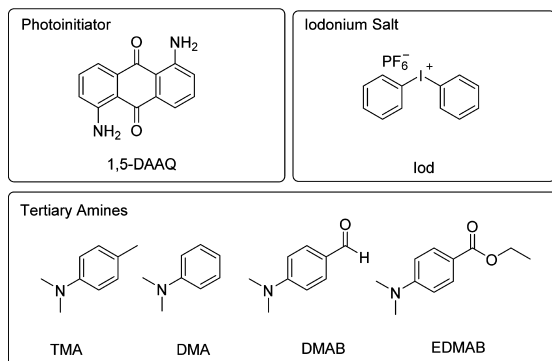
particularly attractive when photocurable formulations contain insoluble inorganic fillers, which can often have a cloudy appearance.

Polymer/carbon nanotube nanocomposites, which can be prepared by *in situ* polymerization<sup>15</sup> including UV photopolymerization,<sup>16–18</sup> have been widely investigated for their high mechanical and thermal stability<sup>17,19</sup> as conductors<sup>16</sup> and as radar absorbing material.<sup>20,21</sup> However, carbon nanotubes can strongly absorb light of shorter wavelength. Therefore, the development of efficient long wavelength light-sensitive photoinitiators for 3D printing nanocomposites is attractive for many applications such as dentistry.<sup>8</sup>

Nonetheless, most of the efficient visible-light photoinitiators available are active at violet or near UV light. Radebner et al. pushed the light wavelength to 470 nm to induce free radical polymerization by employing tetraacyl-stannane, reaching high conversions of round 70% within 18 s.<sup>22</sup> Al Mousawi et al. recently used zinc tetraphenylporphyrin (ZnTPP) as a cationic photoinitiator for 3D printing, polymerizing a monomer mixture within 40 to 50 s under 477 nm light irradiation, with the rate of polymerization decreasing at 530 nm light.<sup>23</sup> Moszner et al. used tetrabenzoylgermane and its derivatives as efficient visible-light photoinitiators (400 to 500 nm) to cure dimethacrylate resins within 20 s with the final monomer conversion reaching around 40 to 50%.<sup>24</sup> Despite these advances, rapid curing at longer wavelengths remains elusive.

In this work, a series of high-performance 1,5-diaminoanthraquinone (1,5-DAAQ)/iodonium salt/aromatic tertiary amines three-component PISs were developed for the free radical photopolymerization of (meth)acrylates under the irradiation of LED at 518 nm (green light) (Scheme 1).

#### Scheme 1. Chemical Structure of Components in PISs<sup>a</sup>



<sup>a</sup>1,5-DAAQ; diphenyliodonium hexafluorophosphate (Iod); ethyl 4-(dimethylamino) benzoate (EDMAB); 4-(dimethylamino) benzaldehyde (DMAB); *N,N*-dimethylaniline (DMA), and 4,*N,N*-trimethylaniline (TMA).

Multicomponent PISs containing a photoinitiator, an iodonium salt, and an amine have attracted a lot of attention due to their high initiation ability (i.e., fast polymerization rate and high monomer conversion) for photopolymerization (Table S1).<sup>25–30</sup> The three-component systems tested so far led to final conversion within a time frame of seconds to minutes using predominantly high-intensity light sources below 500 nm. Recently, 1,5-DAAQ has been identified as an efficient

photoinitiator for polymerization under blue and green household LEDs,<sup>31–36</sup> which inspired us to further develop highly efficient PISs based on the 1,5-DAAQ/Iod/aromatic tertiary amines combinations. Specifically, poly(ethylene glycol) diacrylate (PEGDA, 250 MW) and other (meth)acrylates were polymerized in the presence of four 1,5-DAAQ/Iod/aromatic tertiary amines [i.e., ethyl 4-(dimethylamino)benzoate (EDMAB), 4-(dimethylamino)benzaldehyde (DMAB), *N,N*-dimethylaniline (DMA), and 4,*N,N*-trimethylaniline (TMA)] PISs, in which aromatic tertiary amines vary in their electron density in the amino groups as evidenced by NMR studies (Figure S1). It was identified that highly efficient PIS can initiate the photopolymerization and reach the final conversion within a few seconds upon exposure to the green LED at 518 nm, which was subsequently employed in DLP 3D printing of polymer/carbon nanotube nanocomposites.

#### INITIATION BEHAVIOR OF 1,5-DAAQ-BASED PIS

Prior to the investigation of the 1,5-DAAQ/Iod/aromatic tertiary amines three-component PISs, the 1,5-DAAQ/Iod or 1,5-DAAQ/aromatic tertiary amines two-component PISs were first studied as a control. As illustrated in Figure 1 (a), 1,5-DAAQ/Iod PIS showed a higher efficiency (i.e., higher polymerization rate and final conversion) than that of the 1,5-DAAQ/aromatic tertiary amines PISs. In addition, 1,5-DAAQ/DMA is the most efficient PIS among all the investigated 1,5-DAAQ/aromatic tertiary amines PISs. Specifically, approx-

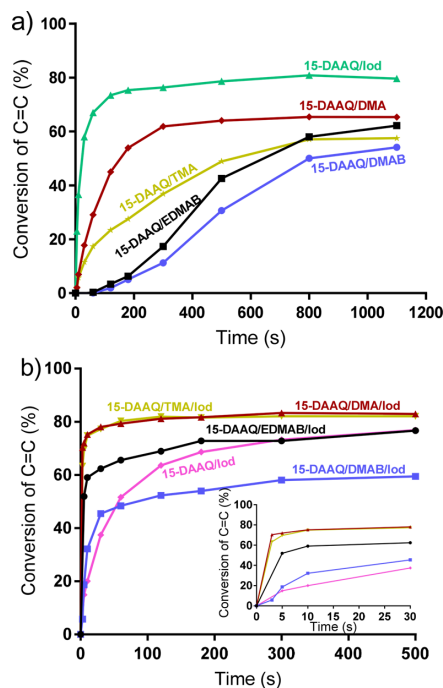


**Figure 1.** Photopolymerization profiles (double bond conversions vs time) of PEGDA (250 MW) in laminate in the presence of (a) 1,5-DAAQ ( $c = 0.023$  M)-based two-component PISs with IOD, EDMAB, DMAB, DMA, or TMA ( $c = 0.164$  M) as additives and (b) 1,5-DAAQ ( $c = 0.023$  M)-based three-component PISs with Iod ( $c = 0.052$  M) and different aromatic tertiary amines ( $c = 0.164$  M) as additives upon exposure to green LED@518 nm ( $60$  mW  $\text{cm}^{-2}$ ).

imately 80 and 60% of double bond conversions can be attained in the presence of 1,5-DAAQ/Iod and 1,5-DAAQ/DMA, respectively, for the photopolymerization of PEGDA (250 MW) under the green LED irradiation.

As shown in Figure 1 (b), the addition of aromatic tertiary amines into 1,5-DAAQ/Iod PIS can accelerate the photopolymerization reactions. And ~80% of final double bond conversions can be achieved for the polymerization of PEGDA (250 MW) in the presence of 1,5-DAAQ/Iod/DMA (or TMA or EDMAB) PISs. More interestingly, 1,5-DAAQ/Iod/DMA and 1,5-DAAQ/Iod/TMA can efficiently initiate the photopolymerization to reach the final double bond conversions within only 10 s. It can be seen that the polymerization rates are directly correlated with the electron densities at the aminoalkyl groups, which can be expressed by the  $^1\text{H}$  NMR chemical shift (Figure S1). Both the TMA and DMA systems are found to be highly efficient in contrast to amines with electron-withdrawing substituents. The EDMAB system is still reasonably fast despite the electron-withdrawing effect. As discussed further below in the mechanism section, the electron-transfer step is faster in TMA and DMA, but the subsequent addition step is more favorable for EDMAB. To put the rate of polymerization into perspective, other three-component systems are tabulated in Table S1, showing that this system is significantly faster or that it can reach a similar rate of polymerizations as other efficient systems but now with the use of a simple household LED. It should be noted that the light intensity chosen here ( $60 \text{ mW cm}^{-2}$ ) will be a determining factor in achieving high rates of polymerization. Lower light intensities will lead to slower reaction rates. The same applies to the concentration of the initiator system, as the reduction of initiator will reduce the amount of radical produced, as it needs to be considered that a three-component reaction will follow high-order kinetics, and therefore, the concentration will play a significant role. Reducing the initiator concentration 10-fold will however still lead to an efficient process (Figure S2).

### FLUORESCENCE QUENCHING EXPERIMENT

The fluorescence emission behavior of 1,5-DAAQ was studied by fluorescence spectrometry. The fluorescence stems from the excited singlet state of 1,5-DAAQ with a 3 ns lifetime.<sup>34</sup> With the addition of tertiary amines, the fluorescence has been quenched with different interaction rate constants. The interaction rate constants were calculated based on the Stern–Volmer equation ( $K_q = 3.127 \times 10^9$ ,  $3.122 \times 10^9$ ,  $3.373 \times 10^9$ , and  $4.707 \times 10^9 \text{ M}^{-1} \text{ s}^{-1}$  for EDMAB, DMAB, DMA, and TMA, respectively) (Figures S3 and S4). The interaction rate constants show the same tendency as the polymerization rates of 1,5-DAAQ/aromatic tertiary amines PISs. The TMA-based two-component PIS has the highest  $K_q$  value and polymerization rate, whereas 1,5-DAAQ/DMAB PIS exhibited the lowest  $K_q$  value and polymerization rate. Compared to 1,5-DAAQ/tertiary amines, 1,5-DAAQ/Iod has a relatively low  $K_q$  value ( $\sim 1 \times 10^9 \text{ M}^{-1} \text{ s}^{-1}$ ),<sup>34</sup> which implies the lower reactivity of 1,5-DAAQ/Iod interaction during light irradiation. However, 1,5-DAAQ/Iod can initiate and regenerate the initiator, whereas 1,5-DAAQ/aromatic amines can initiate (more rapidly) but not regenerate the initiator, resulting in higher efficiencies of the three-component systems over those of two-component systems. The Stern–Volmer plots of 1,5-DAAQ with EDMAB, DMAB, and TMA show a linear relationship with the increase of additive concentrations.

### EPR EXPERIMENTS

During light irradiation, radicals generated from 1,5-DAAQ/Iod/aromatic tertiary amines can be detected using the EPR spin trapping technique. Moreover, the type of radical can be determined from the observed hyperfine splitting (HFS) of the PBN/radical adduct. Specifically, for the 1,5-DAAQ/Iod/EDMAB system (Figure 2) HFS of  $a_N = 14.3 \text{ G}$  and  $a_H = 2.2 \text{ G}$  were observed, indicative of PBN/phenyl radical adducts.<sup>34,37</sup>

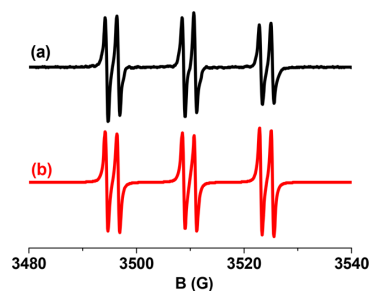


**Figure 2.** EPR spectra of the radicals generated in 1,5-DAAQ/Iod/EDMAB upon light exposure and trapped by PBN in *tert*-butylbenzene: (a) experimental and (b) simulated spectra.

### PHOTOINITIATION CALCULATIONS

Theoretical calculations suggest that the efficiency of the three-component systems arises from a number of desirable features. The first step in the photoinitiation process involves the excited 1,5-DAAQ molecule, which either reduces the Iod species or oxidizes the tertiary amines. Figure 3 shows the

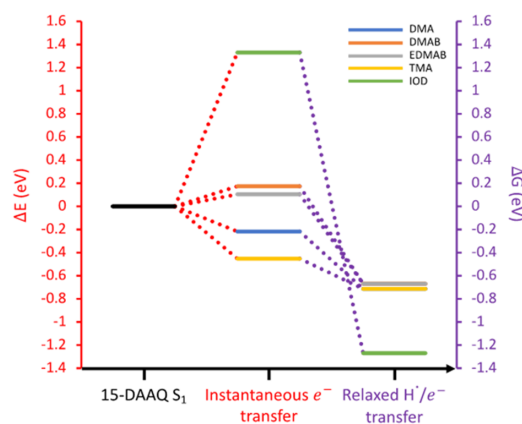


**Figure 3.** Electronic and Gibbs free energy level diagram for electron/hydrogen transfer processes with 1,5-DAAQ, DMA/DMAB/EDMAB/TMA, and Iod.

change in energies relative to the 1,5-DAAQ excited state optimized geometry for these processes, before geometry relaxation of the product is allowed to take place. The energy changes for this process provide an estimate for the relative favorability for electron transfer to the various species and suggest that, in the presence of both tertiary amine and Iod, the 1,5-DAAQ species is more likely to oxidize the amines. From Figure 3, of the four tertiary amine species, DMA and TMA

exhibit negative barriers to electron transfer, reflected experimentally in the highest overall conversion for these two species when paired with Iod. The DMAB and EDMAB tertiary amines' radical cations appear more difficult to form, resulting in a lower conversion; however, the Iod electron transfer is still out-competed for all amine species, hence, the observed acceleration in initiation compared with that of the two-component (1,5-DAAQ/Iod) system.

The second step in Figure 3 is hydrogen atom transfer from the tertiary amine species to 1,5-DAAQ with geometry relaxation allowed to take place. For 1,5-DAAQ/Iod system, the system simply relaxes, and Iod dissociates to a phenyl radical and neutral iodo-phenyl species. Each of the tertiary amine species are found to preferentially lose hydrogen atoms from their tertiary amine-bonded methyl groups. Upon their formation, the tertiary amine radicals can initiate free radical polymerization by reacting with the ethyl acrylate monomer, with each radical exhibiting a similar  $\Delta G$  of activation (Table 1). From Table 1, the different remote groups for each of the

**Table 1.** Gibbs Free Energies ( $\text{kJ mol}^{-1}$ ) of Activation for Hydrogen Abstraction and Radical Addition Reactions with DMA/DMAB/EDMAB/TMA and Phenyl Radical<sup>a</sup>

	DMA	DMAB	EDMAB	TMA	phenyl
hydrogen abstraction ( $\text{kJ mol}^{-1}$ )	+48.4	+50.5	+48.4	+43.1	N/A
radical addition ( $\text{kJ mol}^{-1}$ )	+47.0	+45.6	+42.2	+44.2	+41.3

<sup>a</sup>Calculated at G3(MP2)-RAD.

tertiary amines have a limited impact on their ability to react with monomer units; the difference in observed initiation ability is therefore attributed to the ease with which the respective radicals can be formed.

The reduction of 1,5-DAAQ by tertiary amine results in a 1,5-DAAQ radical, which can subsequently be oxidized by the Iod species to form a phenyl free radical. From here, there are two likely steps involving the phenyl radical: either radical addition to monomer (i.e., initiation) or hydrogen atom abstraction (HA) from another tertiary amine molecule (Table 1). With ethyl acrylate as the monomer unit, phenyl radical-to-monomer addition is generally favored; however, the HA activation energy is calculated independently of the monomer of choice, so the relative HA vs radical addition energies are not necessarily experimentally relevant. The tertiary amine and phenyl radical addition activation energies are, however, within an order of magnitude of each other, suggesting that even if HA does take place to form benzene, the rate of initiation will not decrease.

The overall three-component redox process (Figure 4) results in the formation of reactive free radicals; the only likely competing reaction (i.e., HA between a tertiary amine and phenyl radical) also forms tertiary amine radicals that are as reactive as the phenyl radical. Together, the Iod and tertiary amine components allow for the reformation of neutral 1,5-DAAQ, which can then be re-excited to continue forming initiating radicals. The reader is referred to earlier work that investigated the mechanism of Iod with 1,5-DAAQ in the absence of amine.<sup>36</sup>

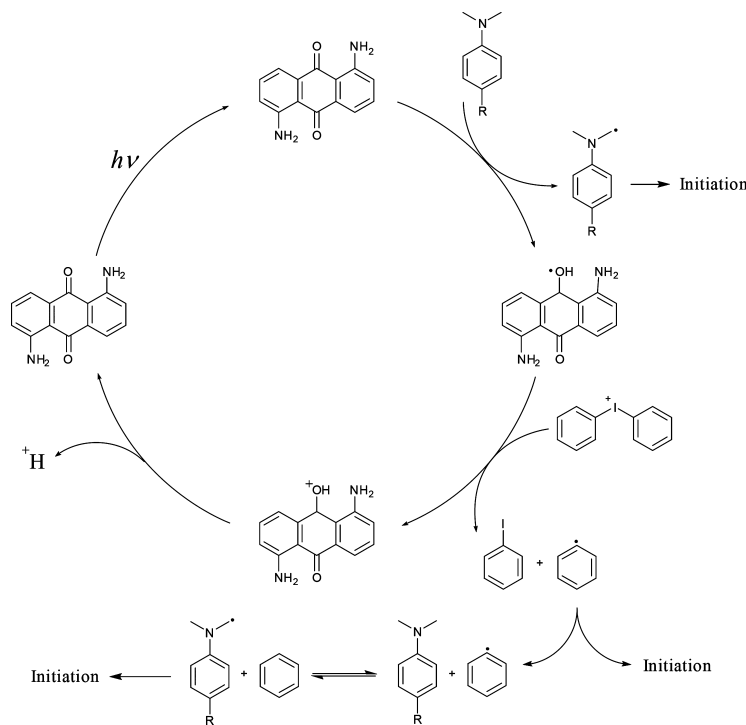


**Figure 4.** Photoinitiation mechanism for 1,5-DAAQ-based three-component systems.



### 3D PRINTING OF POLYMER/MULTIWALL CARBON NANOTUBE (MWCNT) NANOCOMPOSITES

To prepare polymer/MWCNT nanocomposites via 3D printing, the photopolymerization of PEGDA with different amounts of MWCNTs was monitored by FTIR-ATR, using 1,5-DAAQ/Iod/TMA PIS under green LED irradiation. After adding up to 5 wt % of unfunctionalized MWCNTs to PEGDA, no obvious reduction in either polymerization rate or final conversion was observed (Figure 5). However, the

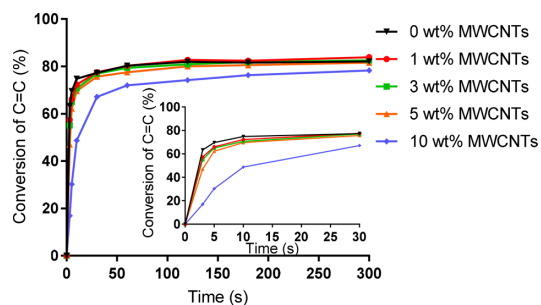


**Figure 5.** Photopolymerization profiles (double bond conversions vs time) of PEGDA (250 MW) with different amounts of MWCNTs (0, 1, 3, 5, or 10 wt %) in laminate in the presence of 1,5-DAAQ/Iod/TMA (0.5/2/2%, wt) upon exposure to green LED@518 nm ( $60 \text{ mW cm}^{-2}$ ).

polymerization rate and the final conversion were slightly decreased for the formulation containing 10 wt % of MWCNTs, probably because of the scattering of the light by MWCNTs (Figure S5). But this is not considered a concern, as an MWCNT content of 10 wt % is beyond what is typically used in various property enhancements such as improvement of mechanical properties and thermal stability.<sup>38–41</sup>

The XY plane resolution of PEGDA with 1,5-DAAQ/Iod/TMA PIS during photopolymerization was investigated by SEM (Figure S6). Specifically, photomasks with different diameter circle patterns were used to cover the light source. Both 80 and 40  $\mu\text{m}$  samples display relatively good resolution, which can ensure the quality of the 3D printing of the formulation.

3D printed objects were obtained using PEGDA as monomer and TMA-based PIS initiator and were printed using a DLP 3D printer with a 5 to 10 s per layer (30–60  $\mu\text{m}$ ) printing speed. For example, the “UNSW” letters in Figure 6 were printed and characterized by profilometry, showing a relatively smooth surface. More objects are shown in Figure S5. Moreover, objects based on nanocomposites with 0.5 wt % MWCNT as fillers were successfully manufactured by 3D printing (Figures 6c and S7). The exposure time to print each layer for the sample with MWCNT is longer than that without MWCNT. The difference between the practical 3D printing time and photopolymerization kinetics (Figure 5) can be ascribed to the different irradiation sources used. The light intensity of the irradiation sources in the 3D printer ( $3.6 \text{ mW cm}^{-2}$ )<sup>36</sup> is much lower than that of the green LED@518 nm ( $60 \text{ mW cm}^{-2}$ ), which can be significantly blocked by the addition of fillers and subsequently decelerated the 3D printing process

### POTENTIAL APPLICATIONS OF 1,5-DAAQ/IOD/AROMATIC TERTIARY AMINE PIS

To investigate the versatility of the 1,5-DAAQ-based PISs, different monomers, such as 1,6-hexanediol diacrylate (HDDA), 1,6-hexanediol dimethacrylate (HDDMA), 2-hydroxyethyl acrylate (HEA), and 2-hydroxyethyl methacrylate (HEMA), were photopolymerized using 1,5-DAAQ/Iod/TMA PIS under green LED irradiation. Similar to PEGDA, the acrylates HEA and HDDA and, to a lesser extent, the methacrylates HDDMA and HEMA can be initiated and polymerized by 1,5-DAAQ/Iod/TMA PIS (Figure S8). Moreover, 1,5-DAAQ/Iod/TMA PIS can also be used in combination with reversible addition–fragmentation chain transfer (RAFT) agent 3-benzylsulfanylthiocarbonylsulfanylpropionic acid (BSPA) for the RAFT photopolymerization poly(ethylene glycol) methyl ether acrylate (PEGMEA). The concentration of 1,5-DAAQ/Iod/TMA (Table S2) was adjusted to suit the RAFT process, where the radical source is used in concentrations well below the RAFT agent concentration to avoid termination reactions.<sup>42</sup> After 6 h, the conversion of PEGMEA reached up to 90%, resulting in polymers with low-molecular-weight distribution ( $\bar{D} = 1.15$ ) (Figure S9). The molecular weight increased with conversions in a linear relationship, highlighting that the PIS is orthogonal

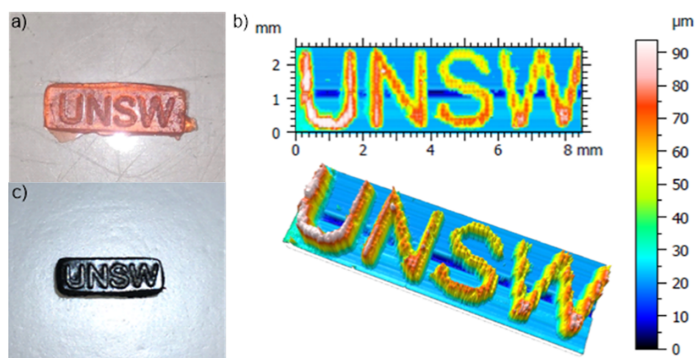


**Figure 6.** (a) Photo of “UNSW” letters with pure PEGDA sample; (b) characterization in 3D by profilometry of “UNSW” letters with pure PEGDA sample; (c) photo of “UNSW” letters with PEGDA with 0.5 wt % CNT sample. Sample was prepared by 3D printing PEGDA with TMA PIS (1,5-DAAQ: 0.5 wt %, Iod: 2.0 wt %, TMA: 2.0 wt %).

to the RAFT process. Because the light intensity used in this work is relatively strong, the potential possibility that the RAFT agent can initiate polymerization itself cannot be ignored.<sup>43</sup> In addition, it is possible that amine can also promote RAFT polymerization.<sup>44</sup> In this research, however, no photopolymerization was observed for the PEGMEA with either RAFT agent (BSPA) alone or the BSPA/TMA system under the irradiation of green LED@518 nm (60 mW/cm<sup>2</sup>) for 6 h (confirmed by <sup>1</sup>H NMR), which indicated the important role and necessity of 15-DAAQ in the photo-initiating system.

## CONCLUSION

Novel three-component visible-light-sensitive photoinitiator systems were developed with the combination of 1,5-DAAQ, iodonium salt (Iod), and different aromatic tertiary amines. The three-component PISs demonstrated much higher polymerization rates for free radical photopolymerization than those of two-component PISs (i.e., 1,5-DAAQ/Iod or 1,5-DAAQ/aromatic tertiary amines). Polymerization processes can be completed within 10 s when using the PISs 1,5-DAAQ/Iod/DMA or 1,5-DAAQ/Iod/TMA, and the final conversions of PEGDA can reach 80%. The acceleration mechanism was investigated by fluorescence quenching, EPR-ST, and quantum chemistry. The application of 1,5-DAAQ/Iod/TMA PIS for the 3D printing of photocurable resin (PEGDA) and polymer/carbon nanotube nanocomposites under visible light was also investigated, which illustrated great potential. Further evaluation of 1,5-DAAQ-based three-component PISs to produce MWCNTs reinforced 3D printed nanocomposites is underway.

## ASSOCIATED CONTENT

### Supporting Information

The Supporting Information is available free of charge on the ACS Publications website at DOI: 10.1021/acsapm.9b00140.

Comparison of different three-component PISs from the literature can be found in Table S1. The concentration of different components during RAFT polymerization can be found in Table S2, whereas <sup>1</sup>H NMR spectra of different tertiary amines can be found in Figure S1. Polymerization rate curve of PEGDA (250 MW) with different PIS concentrations can be found in Figure S2. In addition, fluorescence quenching plots of 1,5-DAAQ with different additives can be found in Figures S3 and S4. UV-vis absorption spectrum of MWCNT in water can be found in Figure S5. SEM images from photomask polymerization are available in Figure S6. 3D printed objects with or without CNT can be found in Figure S7. Potential applications including use of different monomers and application to RAFT polymerization can be found in Figures S8 and S9. Finally, the computational methodology data are in Table S3 (PDF)

## AUTHOR INFORMATION

### Corresponding Authors

\*E-mail: pu.xiao@anu.edu.au. (P.X.)

\*E-mail: michelle.coote@anu.edu.au. (M.L.C.)

\*E-mail: m.stenzel@unsw.edu.au. (M.H.S.)

### ORCID

Michelle L. Coote: 0000-0003-0828-7053

Martina H. Stenzel: 0000-0002-6433-4419

## Author Contributions

The manuscript was written through contributions of all authors. All authors have given approval to the final version of the manuscript.

## Notes

The authors declare no competing financial interest.

## ACKNOWLEDGMENTS

G.W. acknowledges the Chinese Scholarship Council (CSC) for scholarship support. P.X. acknowledges funding from the Australian Research Council Future Fellowship (FT170100301). M.L.C. gratefully acknowledges a Georgina Sweet ARC Laureate Fellowship (FL170100041) and generous allocations of supercomputing time on the National Facility of the Australian National Computational Infrastructure.

## REFERENCES

- (1) Wohlers, T.; Gornet, T. History of Additive Manufacturing. *Wohlers Report 2014*; 2014; p 118.
- (2) Hull, C. W. Apparatus for Production of Three-Dimensional Objects by Stereolithography. US6027324A, 1986.
- (3) Bourell, D. L.; Beaman, J. J.; Leu, M. C.; Rosen, D. W. A Brief History of Additive Manufacturing and The 2009 Roadmap for Additive Manufacturing: Looking Back and Looking Ahead. *Proceedings of RapidTech 2009*, 24–25.
- (4) Wong, K. V.; Hernandez, A. A Review of Additive Manufacturing. *ISRN Mechanical Engineering* **2012**, 2012, 208760.
- (5) Bártolo, P. J. *Stereolithography: Materials, Processes and Applications*; Springer Science & Business Media, 2011.
- (6) Berman, B. 3-D Printing: The New Industrial Revolution. *Business Horiz.* **2012**, 55 (2), 155–162.
- (7) Ligon, S. C.; Liska, R.; Stampfl, J.; Gurr, M.; Mühlaupt, R. Polymers for 3D Printing and Customized Additive Manufacturing. *Chem. Rev.* **2017**, 117, 10212–10290.
- (8) Arikawa, H.; Takahashi, H.; Kanie, T.; Ban, S. Effect of Various Visible Light Photoinitiators on The Polymerization and Color of Light-Activated Resins. *Dent. Mater. J.* **2009**, 28 (4), 454–460.
- (9) Shih, H.; Lin, C. C. Visible Light Mediated Thiol Ene Hydrogelation Using Eosin Y As The Only Photoinitiator. *Macromol. Rapid Commun.* **2013**, 34 (3), 269–273.
- (10) Zhang, J.; Xiao, P. 3D Printing of Photopolymers. *Polym. Chem.* **2018**, 9 (13), 1530–1540.
- (11) Melchels, F. P.; Feijen, J.; Grijpma, D. W. A Review on Stereolithography and Its Applications In Biomedical Engineering. *Biomaterials* **2010**, 31 (24), 6121–6130.
- (12) Shao, J.; Huang, Y.; Fan, Q. Visible Light Initiating Systems for Photopolymerization: Status, Development and Challenges. *Polym. Chem.* **2014**, 5 (14), 4195–4210.
- (13) Endrueit, A.; Johnson, M.; Long, A. Curing of Composite Components by Ultraviolet Radiation: A Review. *Polym. Compos.* **2006**, 27 (2), 119–128.
- (14) Hoyle, C. E. Photocurable Coatings. *Radiation Curing of Polymeric Materials*; ACS Symposium Series; American Chemical Society: Washington, DC, 1990; Vol. 417; p 1.
- (15) Park, S.; Vosguerichian, M.; Bao, Z. A Review of Fabrication and Applications of Carbon Nanotube Film-Based Flexible Electronics. *Nanoscale* **2013**, 5 (5), 1727–1752.
- (16) Fujigaya, T.; Haraguchi, S.; Fukumaru, T.; Nakashima, N. Development of Novel Carbon Nanotube/Photopolymer Nanocomposites with High Conductivity and Application to Nanoimprint Photolithography. *Adv. Mater.* **2008**, 20 (11), 2151.
- (17) Xiong, W.; Liu, Y.; Jiang, L. J.; Zhou, Y. S.; Li, D. W.; Jiang, L.; Silvain, J. F.; Lu, Y. F. Laser-Directed Assembly of Aligned Carbon Nanotubes in Three Dimensions for Multifunctional Device Fabrication. *Adv. Mater.* **2016**, 28 (10), 2002–2009.
- (18) Ushiba, S.; Shoji, S.; Masui, K.; Kuray, P.; Kono, J.; Kawata, S. 3D Microfabrication of Single-Wall Carbon Nanotube/Polymer

Composites by Two-Photon Polymerization Lithography. *Carbon* **2013**, *59*, 283–288.

(19) Liu, Y.; Kumar, S. Polymer/Carbon Nanotube Nano Composite Fibers—A Review. *ACS Appl. Mater. Interfaces* **2014**, *6* (9), 6069–6087.

(20) Zhang, Y.; Li, H.; Yang, X.; Zhang, T.; Zhu, K.; Si, W.; Liu, Z.; Sun, H. Additive Manufacturing of Carbon Nanotube-Photopolymer Composite Radar Absorbing Materials. *Polym. Compos.* **2018**, *39* (S2), E671–E676.

(21) Liang, J. J.; Wang, Y.; Huang, Y.; Ma, Y. F.; Liu, Z. F.; Cai, J. M.; Zhang, C. D.; Gao, H. J.; Chen, Y. S. Electromagnetic Interference Shielding of Graphene/Epoxy Composites. *Carbon* **2009**, *47* (3), 922–925.

(22) Radebner, J.; Eibel, A.; Leypold, M.; Gorsche, C.; Schuh, L.; Fischer, R.; Torvisco, A.; Neshchadin, D.; Geier, R.; Moszner, N.; et al. Tetraacylgermanes: Highly Efficient Photoinitiators for Visible Light Induced Free Radical Polymerization. *Angew. Chem., Int. Ed.* **2017**, *56* (11), 3103–3107.

(23) Al Mousawi, A.; Poriel, C.; Dumur, F. d. R.; Toufaily, J.; Hamieh, T.; Fouassier, J. P.; Lalevée, J. Zinc Tetraphenylporphyrin as High Performance Visible Light Photoinitiator of Cationic Photosensitive Resins for LED Projector 3D Printing Applications. *Macromolecules* **2017**, *50* (3), 746–753.

(24) Moszner, N.; Fischer, U. K.; Lamparth, I.; Fässler, P.; Radebner, J.; Eibel, A.; Haas, M.; Gescheidt, G.; Stueger, H. Tetraacylgermanes As Highly Efficient Photoinitiators for Visible Light Cured Dimethacrylate Resins and Dental Composites. *J. Appl. Polym. Sci.* **2018**, *135* (15), 46115.

(25) Kim, D.; Scranton, A. The Role of Diphenyl Iodonium Salt (DPI) In Three Component Photoinitiator Systems Containing Methylene Blue (MB) and An Electron Donor. *J. Polym. Sci., Part A: Polym. Chem.* **2004**, *42* (23), 5863–5871.

(26) Padon, K. S.; Scranton, A. B. A Mechanistic Investigation of A Three Component Radical Photoinitiator System Comprising Methylene Blue, N Methyl-diethanolamine, and Diphenyliodonium Chloride. *J. Polym. Sci., Part A: Polym. Chem.* **2000**, *38* (11), 2057–2066.

(27) Padon, K. S.; Scranton, A. B. A Mechanistic Investigation of The Three Component Radical Photoinitiator System Eosin Y Spirit Soluble, N Methyl-diethanolamine, and Diphenyliodonium Chloride. *J. Polym. Sci., Part A: Polym. Chem.* **2001**, *39* (5), 715–723.

(28) Kim, D.; Stansbury, J. W. Kinetic Pathway Investigations of Three Component Photoinitiator Systems for Visible Light Activated Free Radical Polymerizations. *J. Polym. Sci., Part A: Polym. Chem.* **2009**, *47* (3), 887–898.

(29) Gómez, M. L.; Previtali, C. M.; Montejano, H. A. Two-and Three-Component Visible Light Photoinitiating Systems for Radical Polymerization Based on Onium Salts: An Overview of Mechanistic and Laser Flash Photolysis Studies. *Int. J. Photoenergy* **2012**, *2012*, 1.

(30) Cook, W. D.; Chen, F. Enhanced Photopolymerization of Dimethacrylates with Ketones, Amines, and Iodonium Salts: The CQ System. *J. Polym. Sci., Part A: Polym. Chem.* **2011**, *49* (23), 5030–5041.

(31) Xiao, P.; Dumur, F.; Graff, B.; Fouassier, J. P.; Gigmès, D.; Lalevée, J. Cationic and Thiol-Ene Photopolymerization upon Red Lights Using Anthraquinone Derivatives as Photoinitiators. *Macromolecules* **2013**, *46*, 6744–6750.

(32) Li, J.; Cui, Y.; Qin, K.; Yu, J.; Guo, C.; Yang, J.; Zhang, C.; Jiang, D.; Wang, X. Synthesis and Properties of A Low-Viscosity UV-Curable Oligomer for Three-Dimensional Printing. *Polym. Bull.* **2016**, *73* (2), 571–585.

(33) Zhang, J.; Hill, N.; Lalevée, J.; Fouassier, J.-P.; Zhao, J.; Graff, B.; Schmidt, T. W.; Kable, S. H.; Stenzel, M. H.; Coote, M. L.; Xiao, P. Multihydroxy-Anthraquinone Derivatives as Free Radical and Cationic Photoinitiators of Various Photopolymerizations under Green LED. *Macromol. Rapid Commun.* **2018**, *39* (19), 1800172.

(34) Zhang, J.; Lalevée, J.; Hill, N. S.; Launay, K.; Morlet-Savary, F.; Graff, B.; Stenzel, M. H.; Coote, M. L.; Xiao, P. Disubstituted Aminoanthraquinone-Based Multicolor Photoinitiators: Photoinitia-

tion Mechanism and Ability of Cationic Polymerization under Blue, Green, Yellow, and Red LEDs. *Macromolecules* **2018**, *51* (20), 8165–8173.

(35) Zhang, J.; Lalevée, J.; Morlet-Savary, F.; Graff, B.; Xiao, P. Photopolymerization Under Various Monochromatic UV/Visible LEDs and IR Lamp: Diamino-anthraquinone Derivatives as Versatile Multicolor Photoinitiators. *Eur. Polym. J.* **2019**, *112*, 591–600.

(36) Zhang, J.; Launay, K.; Hill, N. S.; Zhu, D.; Cox, N.; Langley, J.; Lalevée, J.; Stenzel, M. H.; Coote, M. L.; Xiao, P. Disubstituted Aminoanthraquinone-Based Photoinitiators for Free Radical Polymerization and Fast 3D Printing under Visible Light. *Macromolecules* **2018**, *51* (24), 10104–10112.

(37) Tehfé, M. A.; Lalevée, J.; Telitel, S.; Contal, E.; Dumur, F.; Gigmès, D.; Bertin, D.; Nechab, M.; Graff, B.; Morlet-Savary, F.; Fouassier, J. P. Polyaromatic Structures as Organo-Photoinitiator Catalysts for Efficient Visible Light Induced Dual Radical/Cationic Photopolymerization and Interpenetrated Polymer Networks Synthesis. *Macromolecules* **2012**, *45* (11), 4454–4460.

(38) Deng, H.; Fu, Q.; Bilotti, E.; Peijs, T. The Use of Polymer–Carbon Nanotube Composites in Fibres. *Polymer–Carbon Nanotube Composites* **2011**, 657–675.

(39) Sahoo, N. G.; Cheng, H. K. F.; Cai, J.; Li, L.; Chan, S. H.; Zhao, J.; Yu, S. Improvement of Mechanical and Thermal Properties of Carbon Nanotube Composites Through Nanotube Functionalization and Processing Methods. *Mater. Chem. Phys.* **2009**, *117* (1), 313–320.

(40) Funck, A.; Kaminsky, W. Polypropylene Carbon Nanotube Composites by in Situ Polymerization. *Compos. Sci. Technol.* **2007**, *67* (5), 906–915.

(41) Breuer, O.; Sundararaj, U. Big Returns From Small Fibers: A Review of Polymer/Carbon Nanotube Composites. *Polym. Compos.* **2004**, *25* (6), 630–645.

(42) Stenzel, M. H.; Barner-Kowollik, C. The Living Dead – Common Misconceptions About Reversible Deactivation Radical Polymerization. *Mater. Horiz.* **2016**, *3* (6), 471–477.

(43) McKenzie, T. G.; Fu, Q.; Wong, E. H.; Dunstan, D. E.; Qiao, G. G. Visible Light Mediated Controlled Radical Polymerization in the Absence of Exogenous Radical Sources or Catalysts. *Macromolecules* **2015**, *48* (12), 3864–3872.

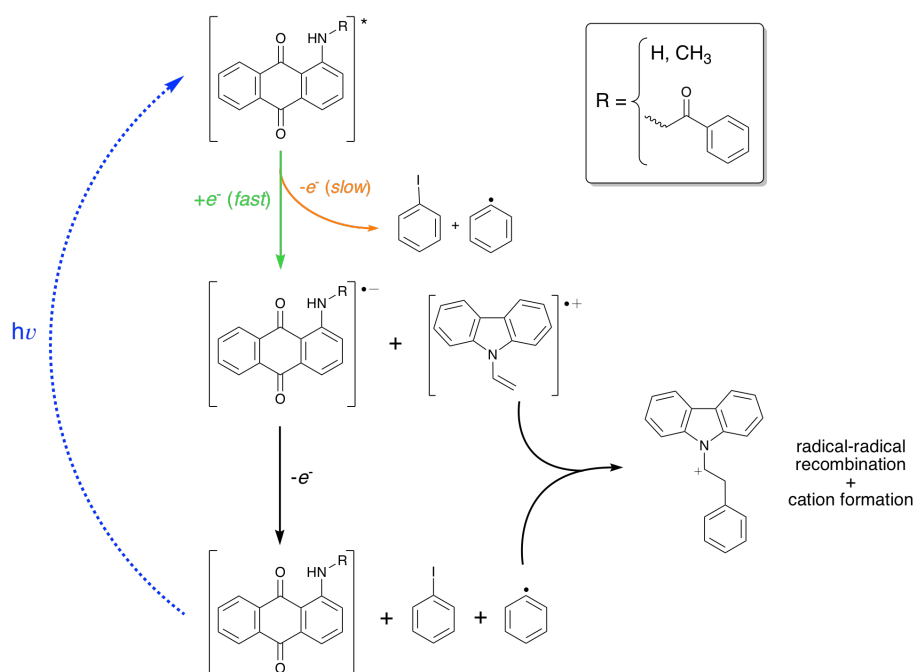
(44) Allegrezza, M. L.; DeMartini, Z. M.; Kloster, A. J.; Digby, Z. A.; Konkolewicz, D. Visible and Sunlight Driven RAFT Photopolymerization Accelerated by Amines: Kinetics and Mechanism. *Polym. Chem.* **2016**, *7* (43), 6626–6636.

### 3.6 Publication 7

#### Photoinitiation Mechanism and Ability of Monoamino-Substituted Anthraquinone Derivatives as Cationic Photoinitiators of Polymerization under LEDs

Jing Zhang, Jacques Lalevee, **Nicholas S. Hill**, Xiaotong Peng, Di Zhu, Jonathon Kiehl, Fabrice Morlet-Savary, Martina H. Stenzel, Michelle L. Coote, Pu Xiao

*Macromolecular Rapid Communications* 2019



This publication is a peer-reviewed manuscript published in *Macromolecular Rapid Communications*. All computational results, mechanistic insight, and subsequent discussion are my own work. Prof. Michelle Coote assisted with the direction of the theoretical investigations and corrected my draft write-ups. [Supplementary material is available online.](#)

### Statement of Contribution

This thesis is submitted as a Thesis by Compilation in accordance with [https://policies.anu.edu.au/ppi/document/ANUP\\_003405](https://policies.anu.edu.au/ppi/document/ANUP_003405)

I declare that the research presented in this Thesis represents original work that I carried out during my candidature at the Australian National University, except for contributions to multi-author papers incorporated in the Thesis where my contributions are specified in this Statement of Contribution.

Title: Photoinitiation Mechanism and Ability of Monoamino-Substituted Anthraquinone Derivatives as Cationic Photoinitiators of Polymerization under LEDs

Authors: Jing Zhang, Jacques Lalevee, Nicholas S. Hill, Xiaotong Peng, Di Zhu, Jonathon Kiehl, Fabrice Morlet-Savary, Martina H. Stenzel, Michelle L. Coote, Pu Xiao

Publication outlet: Macromolecular Rapid Communications

Current status of paper: ~~Not Yet Submitted/Submitted/Under Revision/~~Accepted/Published

Contribution to paper: I am the first contributing computational chemistry author. All computational results, mechanistic insight, and subsequent discussion are my own work

Senior author or collaborating authors endorsement: Michelle Coote

Nicholas Hill



20/01/2020

Candidate - Print Name

Signature

Date

### Endorsed

Michelle Coote



20/01/2020

Primary Supervisor – Print Name

Signature

Date

Luke Connell



20/01/2020

Delegated Authority – Print Name

Signature

Date



# Photoinitiation Mechanism and Ability of Monoamino-Substituted Anthraquinone Derivatives as Cationic Photoinitiators of Polymerization under LEDs

Jing Zhang, Jacques Lalevée, Nicholas S. Hill, Xiaotong Peng, Di Zhu, Jonathan Kiehl, Fabrice Morlet-Savary, Martina H. Stenzel, Michelle L. Coote,\* and Pu Xiao\*

The design and development of photoinitiating systems applicable to UV or even visible light delivered from light-emitting diodes (LEDs) has been attracting increasing attention due to their great potential applications in various fields. Compared to the strategy of synthesizing novel compounds, the exploration of existing chemicals with interesting photochemical/ photophysical properties for their usage as photoinitiators is more appealing and easily commercialized. Nevertheless, a number of compounds such as monoamino-substituted anthraquinone derivatives, which are intensively investigated for their photophysical and photochemical properties, have seldom been studied for their roles as photoinitiators under LED irradiation. Herein, three monoamino-substituted anthraquinone derivatives, that is, 1-aminoanthraquinone, 1-(methylamino)anthraquinone and 1-(benzamido)anthraquinone, are studied for their potential as photoinitiators. The photoinitiation mechanism of these monoamino-substituted anthraquinone derivatives, when combined with iodonium salt, is first clarified using computational quantum chemistry, fluorescence, steady-state photolysis, and electron spin resonance spin-trapping techniques. Then, their photoinitiation ability for the cationic photopolymerization of epoxide and divinyl ether monomers is also investigated.

the fabrication of various materials such as inks, coatings, adhesives, varnishes, and microelectronics in industry.<sup>[3-6]</sup> However, for broader uptake, it is important to find photoinitiators capable of responding efficiently to LEDs instead of the traditional mercury lamps due to their higher operating efficiency, better light output, safer usage, and lower cost.<sup>[7,8]</sup> While several newly synthesized efficient photoinitiators applicable to UV to red light delivered from LEDs have recently been published,<sup>[9-12]</sup> it remains desirable to find cheaper compounds for industrial applications. In evaluating compounds, it is important to thoroughly investigate their photochemical mechanism as well as their photoinitiation efficiency in polymerization.

Recently, several 9,10-anthraquinone derivatives (AQs)<sup>[13]</sup> such as 1,8-dihydroxyanthraquinone,<sup>[14]</sup> 1,2,4-trihydroxyanthraquinone<sup>[15]</sup> and diaminoanthraquinones<sup>[16,17]</sup> have emerged as efficient photoinitiators of polymerization under LEDs. However, the effect of amino substituents on the photochemical properties of AQs has seldom been studied. Herein, we investigate the photoinitiation mechanism and efficiency of three monoamino-substituted anthraquinone derivatives (Scheme 1), that is, 1-aminoanthraquinone (AAQ), 1-(methylamino)anthraquinone (MAAQ), and 1-(benzamido)anthraquinone (BAAQ), along with various additives,

An efficient photoinitiator (PI), which absorbs a certain wavelength of light to generate an active species (e.g., cation or free radical), is an essential component in photopolymerization technology.<sup>[1,2]</sup> This technology is based on the fast transformation of liquid monomers/resins into highly crosslinked solid polymers under light irradiation, and it finds applications in

stituents on the photochemical properties of AQs has seldom been studied. Herein, we investigate the photoinitiation mechanism and efficiency of three monoamino-substituted anthraquinone derivatives (Scheme 1), that is, 1-aminoanthraquinone (AAQ), 1-(methylamino)anthraquinone (MAAQ), and 1-(benzamido)anthraquinone (BAAQ), along with various additives,

Dr. J. Zhang, X. Peng, D. Zhu, Dr. P. Xiao  
Research School of Chemistry  
Australian National University  
Canberra, ACT 2601, Australia  
E-mail: pu.xiao@anu.edu.au

N. S. Hill, Prof. M. L. Coote  
ARC Centre of Excellence for Electromaterials Science  
Research School of Chemistry  
Australian National University  
Canberra, ACT 2601, Australia  
E-mail: michelle.coote@anu.edu.au

The ORCID identification number(s) for the author(s) of this article can be found under <https://doi.org/10.1002/marc.201900234>.

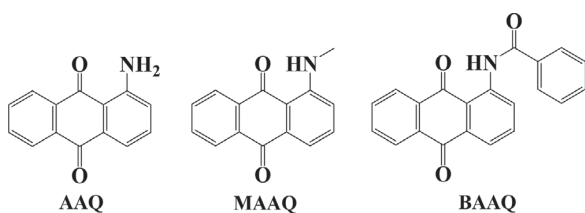
Dr. J. Zhang, Prof. J. Lalevée, Dr. F. Morlet-Savary, Dr. P. Xiao  
Université de Haute-Alsace, CNRS  
IS2M UMR 7361, F-68100 Mulhouse, France

Prof. J. Lalevée, Dr. F. Morlet-Savary  
Université de Strasbourg  
France

Dr. J. Zhang, J. Kiehl, Prof. M. H. Stenzel, Dr. P. Xiao  
School of Chemistry  
University of New South Wales  
Sydney, NSW 2052, Australia

Dr. J. Zhang  
Department of Chemical Engineering  
Monash University  
Clayton, Victoria 3800, Australia

DOI: 10.1002/marc.201900234



**Scheme 1.** Chemical structures of the studied monoamino-substituted anthraquinone derivatives (AAQ, MAAQ and BAAQ).

to initiate cationic photopolymerization under UV, blue, and green LED bulbs. These monoamino-substituted anthraquinone derivatives were selected as they are low-cost and easily prepared.

The UV–vis absorption of AAQs (i.e., AAQ, MAAQ, and BAAQ) in acetonitrile and their overlap with emission spectra of UV (392 nm), blue (455 nm), and green (518 nm) LEDs are illustrated in **Figure 1**, while their absorption maxima ( $\lambda_{\text{max}}$ ) and extinction coefficients ( $\epsilon$ ) at  $\lambda_{\text{max}}$  and at the maximum emission wavelengths of the LEDs are presented in Table S1, Supporting Information. AAQ, MAAQ, and BAAQ demonstrate absorption maxima ( $\lambda_{\text{max}}$ ) at 465, 522, and 406 nm with the relevant extinction coefficients of 7380, 1700, and 3930  $\text{M}^{-1} \text{cm}^{-1}$  respectively. These peaks overlap with the emission spectra of the UV (392 nm), blue (455 nm), and green (518 nm) LEDs respectively [Figure 1b; and Table S1, Supporting Information].

To understand these differences in photochemical behavior, time-dependent density functional theory (TD-DFT) calculations were undertaken. Each of the investigated AAQs exhibit bright  $\pi\pi^*$  transitions that correspond to the broad absorption peaks observed in Figure 1a, and the change in substitution pattern is found to have a significant impact on the molecules' excited states. Moving from AAQ to MAAQ results in a red-shift in the  $\pi\pi^*$  state; according to TD-DFT calculations, there is no change in energy of the  $n\pi^*$  states. In contrast to AAQ and MAAQ, BAAQ exhibits significant orbital contribution from the benzamido substituent in both the  $n\pi^*$  and  $\pi\pi^*$  excited states. The result of this is two dark  $n\pi^*$  states at approximately the same wavelength as the  $\pi\pi^*$  states of AAQ and BAAQ, followed by a lower wavelength bright  $\pi\pi^*$  state, the orbitals of which (Figure S1, Supporting Information) suggest a large amount of charge transfer from the benzamido  $\pi$

system to the anthraquinone  $\pi^*$  system. Whilst these are inefficient transitions, the low-lying  $n\pi^*$  states do give BAAQ access to the higher energies required to undergo the redox processes that form the reactive initiating species.

The AAQ, MAAQ, and BAAQ undergo fluorescence emission associated with their excited singlet states (see Figure S2, Supporting Information) with fluorescence quantum yields of 0.0095, 0.0063, and 0.0145, respectively. Interestingly, the addition of diphenyliodonium hexafluorophosphate (Iod) into the solutions of AAQ or MAAQ in acetonitrile can quench their fluorescence emission [e.g., Figure S3a, Supporting Information]. No fluorescence quenching was observed for  $^1\text{BAAQ}/\text{Iod}$ . The interaction rate constant of  $^1\text{AAQ}/\text{Iod}$  ( $k_q > 1.8 \times 10^9 \text{ M}^{-1} \text{ s}^{-1}$ ) can be obtained from the Stern–Volmer treatment [Figure S3b, Supporting Information, fluorescence lifetime of AAQ  $\tau_0 < 3 \text{ ns}$ ]. Similarly,  $k_q > 1.2 \times 10^9 \text{ M}^{-1} \text{ s}^{-1}$  was obtained for  $^1\text{MAAQ}/\text{Iod}$  interaction. These indicate that quenching is diffusion-controlled and there is an electron transfer reaction between the excited singlet state of AAQ or MAAQ and the ground-state of Iod. Furthermore, the electron transfer quantum yields ( $\Phi_{\text{eT}} = k_q \tau_0 [\text{Iod}] / (1 + k_q \tau_0 [\text{Iod}])$ ;<sup>[1]</sup> where  $[\text{Iod}] = 4.7 \times 10^{-2} \text{ M}$ ) of  $^1\text{AAQ}/\text{Iod}$  ( $\Phi_{\text{eT}} = 0.20$ ) and  $^1\text{MAAQ}/\text{Iod}$  ( $\Phi_{\text{eT}} = 0.14$ ) demonstrate the higher photochemical reactivity of  $^1\text{AAQ}/\text{Iod}$  than that of  $^1\text{MAAQ}/\text{Iod}$ .

The lack of electron transfer between BAAQ and Iod is twofold in its origin; the first is the general unfavorability for electron transfer from low-lying excited states, and the second is the stability of the resulting radical cation. For the AAQ and MAAQ species, these effects are compensated for by the delocalization of the radical cation orbital across the anthraquinone moiety. However, with BAAQ, the radical cation is initially localized on the phenyl moiety. This results in a radical cation stabilized to a lesser degree than those on the AAQ and MAAQ species, and a greater amount of geometry relaxation upon formation of the BAAQ radical cation. The net result is that BAAQ is unable to compensate for the unfavorable energetics of electron transfer. This is reflected in the electron transfer rate coefficients for these species (Table S2, Supporting Information).

The overall photochemical behavior of AAQs/Iod interaction under blue LED irradiation can be qualitatively investigated using steady state photolysis experiments.<sup>[2]</sup> As illustrated in Figure S4, Supporting Information, the UV–vis absorption of AAQ/Iod or MAAQ/Iod decreased during light irradiation. Interestingly, isobestic points were observed at 438/509 nm and

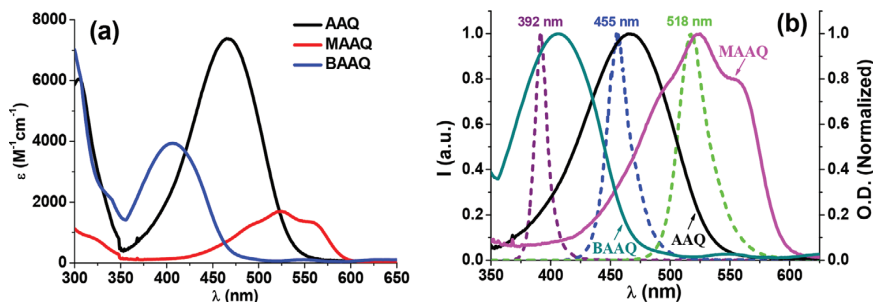


**Figure 1.** a) UV–vis absorption spectra of AAQ, MAAQ and BAAQ in acetonitrile and b) their overlap with the emission spectra of UV (392 nm), blue (455 nm), and green (518 nm) LED bulbs.

448/584 nm for AAQ/Iod and MAAQ/Iod, respectively, which indicated that no secondary reactions occurred in the electron transfer between the excited singlet state and Iod. In addition, the bleaching of AAQ/Iod was slower than that of MAAQ/Iod under light irradiation [Figure S4a versus S4b, Supporting Information]. But the lower extinction coefficient of MAAQ (compared to that of AAQ) would diminish its photoreactivity with Iod. For BAAQ/Iod, the UV-vis absorption increased upon the light exposure, indicating the generation of new species with higher extinction coefficient, which may explain the lack of electron transfer with Iod.

The reaction between AAQ or MAAQ with Iod gives rise to AAQ-derived cations (AAQs<sup>+</sup>) that can initiate the cationic photopolymerization of EPOX under blue LED irradiation. Conversions of epoxy groups increased with the increasing of Iod concentration in the AAQ/Iod system with 13% conversion attained after 780 s of irradiation (Figure S5 and Table S3, Supporting Information). To further confirm this mechanism, ESR spin trapping was used in conjunction with a phenyl-*N*-tert-butyl nitron (PBN) radical trap. Hyperfine coupling constants for nitrogen and hydrogen of  $a_N = 14.3$  G and  $a_H = 2.2$  G were

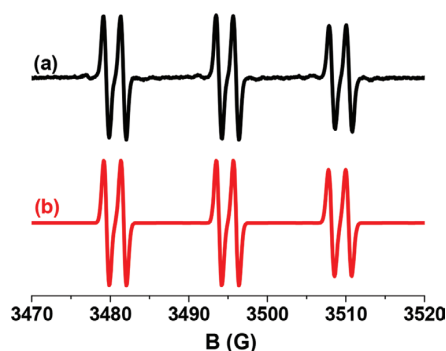
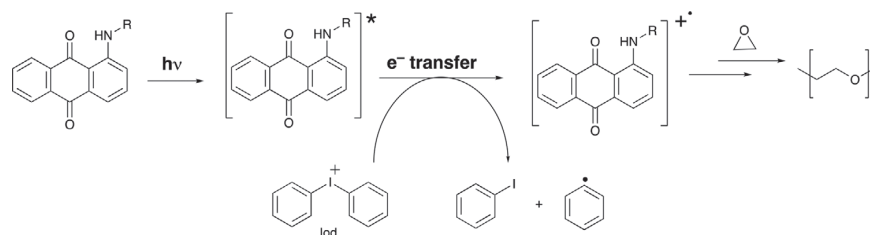
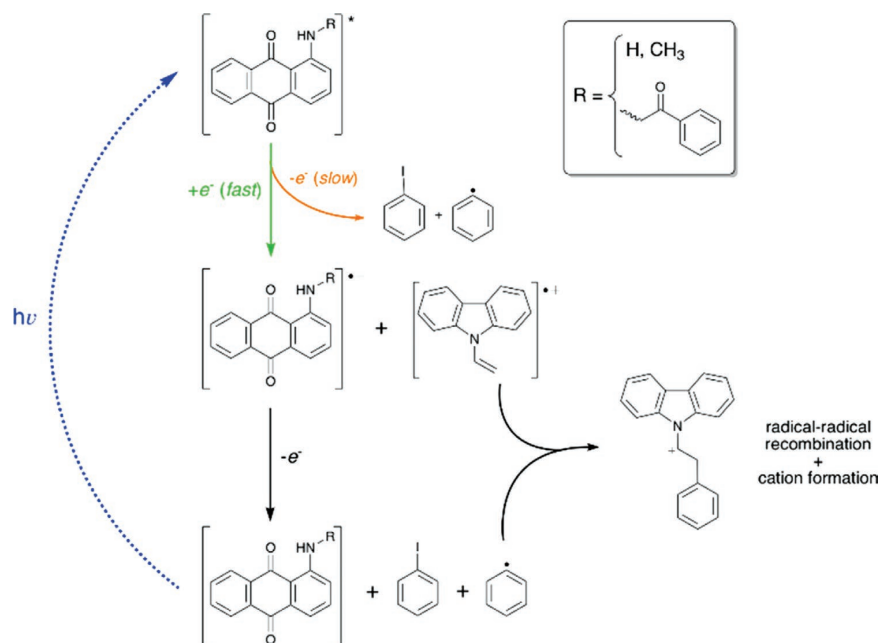


**Figure 2.** ESR spectra of the radicals generated in AAQ/Iod combination upon the blue LED exposure and trapped by PBN in *tert*-butylbenzene: a) experimental and b) simulated spectra.

measured in the AAQ/Iod system (Figure 2), which can be assigned to PBN/phenyl radical adducts.<sup>[18,19]</sup> Therefore, the overall initiation mechanism for AAQs/Iod systems is shown in Scheme 2.



**Scheme 2.** Proposed polymerization initiation mechanism of epoxide with the AAQs/Iod system.



**Scheme 3.** Electron transfer mechanism between AAQs, Iod, and NVK.





Alternatively, the addition of a second additive NVK into the AAQ-based photoinitiating system can further promote the photoinitiation ability due to the NVK additive effect,<sup>[20]</sup> with 42% epoxy conversion can be achieved when using the AAQ/Iod/NVK (0.5%/2%/3%, wt) system under the same irradiation conditions. The most likely electron transfer pathway of the AAQs/Iod/NVK systems can also be determined by the estimation of electron transfer rate constants of AAQs/Iod and AAQs/NVK using standard Marcus theory.<sup>[21]</sup> As illustrated in Table S2, Supporting Information, upon the introduction of NVK the fastest electron transfer reaction involves the reduction of the excited AAQs and corresponding oxidation of NVK. The resulting AAQs radical anions can then undergo a subsequent oxidation by Iod, resulting in the reformation of the AAQs, a phenyl radical, and iodobenzene. The phenyl radical can then undergo radical recombination with the NVK radical cation, resulting in a reactive NVK cation species that can initiate the cationic polymerization of EPOX. Scheme 3 summarizes the overall photoinitiation mechanism.

The AAQ-based photoinitiating systems can also initiate the cationic photopolymerization of EPOX under green LED irradiation (Figure S6 and Table S4, Supporting Information), but the photoinitiation ability (polymerization rate and conversion) with green LEDs was lower than that with blue LED, for example, 30% of epoxy conversion was obtained when using the AAQ/Iod/NVK (0.5%/2%/3%, wt) system for 780 s of photopolymerization under green LED. As demonstrated in Figure 3, MAAQ/Iod/NVK and BAAQ/Iod/NVK photoinitiating systems were also capable of initiating cationic photopolymerization of EPOX under blue LED irradiation. Among them, the MAAQ-based system exhibited lowest photoinitiation ability (epoxy conversion = 12% after 780 s of photopolymerization) due to its lowest extinction coefficient and weakest overlap of its light absorption with the emission spectrum of blue LED (Table S1, Supporting Information).

Interestingly, the BAAQ-based system demonstrated the highest photoinitiation ability (epoxy conversion = 53% after 780 s of photopolymerization under blue LED). This is despite its poor performance in the fluorescence quenching experiment with Iod and despite the weaker overlap between BAAQ light absorption and the emission spectrum of blue LED than

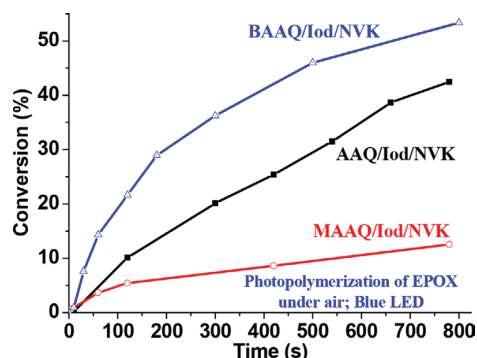


**Figure 3.** Photopolymerization profiles of EPOX under air in the presence of different AAQs-based PISs (i.e., AAQ/Iod/NVK, MAAQ/Iod/NVK and BAAQ/Iod/NVK) upon exposure to Blue LED@455 nm (60 mW cm<sup>-2</sup>). AAQs: 0.5 wt%, Iod: 2 wt%, NVK: 3 wt%.

that of AAQ. This is evidence that the low-lying  $n\pi^*$  states of BAAQ provide it with sufficient energy to undergo electron transfer in the three component systems, where the key reaction is reduction of BAAQ by NVK, not oxidation by Iod. This is confirmed by the efficient fluorescence quenching of BAAQ by NVK [Figure S3c,d, Supporting Information] and no fluorescence quenching of BAAQ/Iod, that is, the electron transfer quantum yield ( $\Phi_{eT} = kq\tau_0 [NVK]/(1 + kq\tau_0 [NVK])$ ; where  $[NVK] = 0.155 \text{ M}$ ) of <sup>1</sup>BAAQ/NVK is  $\Phi_{eT} = 0.85$  while  $\Phi_{eT} = 0$  for <sup>1</sup>BAAQ/Iod. In addition, the electron transfer quantum yields of <sup>1</sup>AAQ/NVK ( $\Phi_{eT} = 0.82$ ) and <sup>1</sup>MAAQ/NVK ( $\Phi_{eT} = 0.72$ ) are lower than that of <sup>1</sup>BAAQ/NVK ( $\Phi_{eT} = 0.85$ ). The high relative photoinitiation performance of BAAQ is due to the delocalization of the radical anion across the anthraquinone moiety. This gives BAAQ an advantage over AAQ and particularly MAAQ in this reaction (Figure 4). As well as this, the inefficient electron transfer between  $\pi\pi$  and  $n\pi^*$  states (arising from El Sayed's rules<sup>[22]</sup>), delays BAAQ from undergoing fluorescence, and reduces its competition with electron transfer. UV LED irradiation also leads to more efficient cationic photopolymerization of EPOX using the BAAQ/Iod/NVK system (due to the more intense overlap between BAAQ light

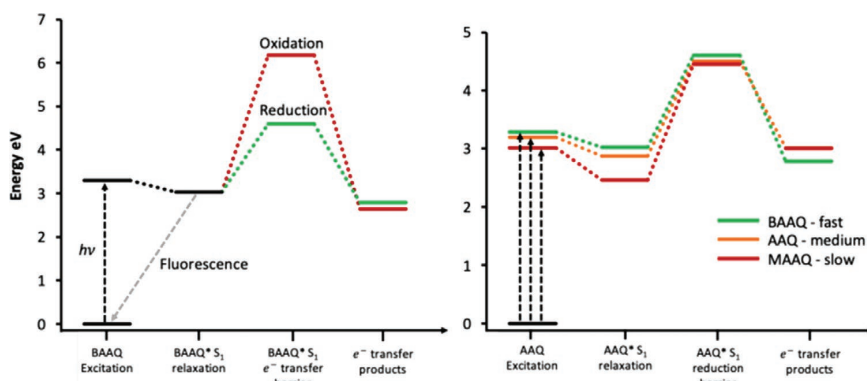


**Figure 4.** Left shows the competition between oxidation by Iod (unfavorable) and reduction by NVK (favorable) for BAAQ. Right compares the energetics of the reduction reaction for the three AAQs.

absorption and the emission spectrum of UV LED) than that of blue LED and 62% of epoxy conversion can be achieved after 780 s of photopolymerization as shown in Figure S7, Supporting Information.

The AAQ-based systems were also able to initiate cationic photopolymerization of DVE-3 (Figure S8, Supporting Information). Specifically, 87% and 78% of double bond conversions can be attained for the 780 s of photopolymerization of DVE-3 using AAQ/Iod system under blue LED and green LED respectively. The addition of NVK can further improve the photopolymerization rate which can be ascribed to the higher efficiency of Ph-NVK<sup>+</sup> than that of Ph-DVE-3<sup>+</sup>. Radicals, however, cannot initiate the polymerization of DVE-3 as confirmed in Figure S9, Supporting Information: no polymerization can be observed when using AAQ/TEAOH or AAQ/TEAOH/R-Br systems in which only radicals can be efficiently generated.<sup>[23]</sup> As illustrated in Figure S10, Supporting Information, MAAQ-based photoinitiating systems were inefficient for the polymerization of DVE-3.

In conclusion, this work demonstrates that the photoinitiation mechanism and ability of monoamino-substituted anthraquinone derivatives (when combined with Iod) depend strongly on the type of amino substituents. The cations generated from the AAQs-based photoinitiating systems can initiate cationic photopolymerization of epoxide and divinyl ether monomers under UV, blue, or green LEDs, and BAAQ-based system exhibits highest photoinitiation efficiency under UV and blue LEDs.

## Supporting Information

Supporting Information is available from the Wiley Online Library or from the author.

## Acknowledgements

P.X. acknowledges funding from the Australian Research Council (ARC) Future Fellowship (FT170100301). M.L.C. gratefully acknowledges support from the ARC Centre of Excellence for Electromaterials Science (CE140100012), a Georgina Sweet ARC Laureate Fellowship (FL170100041) and generous allocations of supercomputing time on the National Facility of the Australian National Computational Infrastructure.

## Conflict of Interest

The authors declare no conflict of interest.

## Keywords

anthraquinone, cationic photopolymerization, light-emitting diodes (LED), photoinitiation mechanism, photoinitiators

Received: May 14, 2019

Revised: June 3, 2019

Published online:

- [1] J. P. Fouassier, J. Lalevée, *Photoinitiators for Polymer Synthesis-Scope, Reactivity, and Efficiency*, Wiley-VCH Verlag GmbH & Co KGaA, Weinheim **2012**.
- [2] P. Xiao, J. Zhang, F. Dumur, M. A. Tehfe, F. Morlet-Savary, B. Graff, D. Gigmes, J. P. Fouassier, J. Lalevée, *Prog. Polym. Sci.* **2015**, *41*, 32.
- [3] F. Marquardt, M. Bruns, H. Keul, Y. Yagci, M. Möller, *Chem. Commun.* **2018**, *54*, 1647.
- [4] E. Blasco, M. Wegener, C. Barner-Kowollik, *Adv. Mater.* **2017**, *29*, 1604005.
- [5] S. C. Ligon-Auer, M. Schwentenwein, C. Gorsche, J. Stampfl, R. Liska, *Polym. Chem.* **2016**, *7*, 257.
- [6] S. Dadashi-Silab, S. Doran, Y. Yagci, *Chem. Rev.* **2016**, *116*, 10212.
- [7] C. Cordon, C. Miller, *UV-LED: Presented by RadTech-The Association for UV & EB Technology*, RadTech International **2013**.
- [8] S. Nakamura, *Science* **1998**, *281*, 956.
- [9] J. Wang, S. Stanic, A. A. Altun, M. Schwentenwein, K. Dietliker, L. Jin, J. Stampfl, S. Baudis, R. Liska, H. Grützmacher, *Chem. Commun.* **2018**, *54*, 920.
- [10] J. Radebner, A. Eibel, M. Leypold, C. Gorsche, L. Schuh, R. Fischer, A. Torvisco, D. Neshchadin, R. Geier, N. Moszner, R. Liska, G. Gescheidt, M. Haas, H. Stueger, *Angew. Chem., Int. Ed.* **2017**, *56*, 3103.
- [11] J. Zhang, F. Dumur, P. Xiao, B. Graff, D. Bardelang, D. Gigmes, J. P. Fouassier, J. Lalevée, *Macromolecules* **2015**, *48*, 2054.
- [12] H. Tar, D. S. Esen, M. Aydin, C. Ley, N. Arsu, X. Allonas, *Macromolecules* **2013**, *46*, 3266.
- [13] R. Siva, *Curr. Sci.* **2007**, *92*, 916.
- [14] J. Zhang, J. Lalevée, J. Zhao, B. Graff, M. H. Stenzel, P. Xiao, *Polym. Chem.* **2016**, *7*, 7316.
- [15] J. Zhang, N. S. Hill, J. Lalevée, J.-P. Fouassier, J. Zhao, B. Graff, T. W. Schmidt, S. H. Kable, M. H. Stenzel, M. L. Coote, P. Xiao, *Macromol. Rapid Commun.* **2018**, *39*, 1800172.
- [16] J. Zhang, K. Launay, N. S. Hill, D. Zhu, N. Cox, J. Langley, J. Lalevée, M. H. Stenzel, M. L. Coote, P. Xiao, *Macromolecules* **2018**, *51*, 10104.
- [17] J. Zhang, J. Lalevée, N. S. Hill, K. Launay, F. Morlet-Savary, B. Graff, M. H. Stenzel, M. L. Coote, P. Xiao, *Macromolecules* **2018**, *51*, 8165.
- [18] M. A. Tehfe, J. Lalevée, S. Telitel, E. Contal, F. Dumur, D. Gigmes, D. Bertin, M. Nechab, B. Graff, F. Morlet-Savary, J. P. Fouassier, *Macromolecules* **2012**, *45*, 4454.
- [19] J. Lalevée, N. Blanchard, M. A. Tehfe, F. Morlet-Savary, J. P. Fouassier, *Macromolecules* **2010**, *43*, 10191.
- [20] J. Lalevée, M.-A. Tehfe, A. Zein-Fakih, B. Ball, S. Telitel, F. Morlet-Savary, B. Graff, J. P. Fouassier, *ACS Macro Lett.* **2012**, *1*, 802.
- [21] J. Stubbe, D. G. Nocera, C. S. Yee, M. C. Y. Chang, *Chem. Rev.* **2003**, *103*, 2167.
- [22] A. D. McNaught, A. Wilkinson, *IUPAC Compendium of Chemical Terminology*, 2nd ed., Blackwell Scientific Publications, Oxford **1997**.
- [23] P. Xiao, F. Dumur, D. Thirion, S. Fagour, A. Vacher, X. Sallenave, F. Morlet-Savary, B. Graff, J. P. Fouassier, D. Gigmes, J. Lalevée, *Macromolecules* **2013**, *46*, 6786.

### 3.7 Implications and Applications

In this series of papers, a range of anthraquinone derivatives were synthesised and assessed for their polymerization photoinitiation efficiency, in conjunction with different additives. The substitution patterns of the anthraquinones was found to have a profound effect on their excited state properties and ability to initiate either radical or cationic polymerization reactions.

In particular, the different substitution positions and types of functional groups used had a large effect on the absorption spectrum of anthraquinone. Whilst invariably the spectra were dominated by  $\pi\pi^*$  transitions arising from the  $\pi$ -system on the anthraquinone, when hydroxy-anthraquinone derivatives were studied, for example, the presence (or absence) of hydrogen bonds altered the dominance of  $\pi\pi^*$  and  $n_o\pi^*$  transitions in the  $S_1$  excited state. As well as this, the favourability for excited state oxidation or reduction, in the presence of co-initiating species, could also be altered according to amino- and hydroxy-substitution patterns. As a result, substituted anthraquinone derivatives are a robust and flexible set of photoinitiators, capable of initiating polymerization reactions under mild conditions.

As the choice of functionalisation pattern allows for the selective stabilisation or destabilisation of radical cation or radical anion formation, substituted anthraquinone chromophores are explored in Chapter 5 for nitroxide mediated photopolymerisation applications. These studies expand on anthraquinone photochemistry, and again highlight their chemical flexibility.

Finally, (photo)chemical trends observed experimentally with the anthraquinone derivatives were well captured by quantum chemistry, therefore allowing the effectiveness of potential candidate systems to be rapidly assessed.

### 3.8 References

- (1) Rånby, B. G.; Rabek, J. F., *Photodegradation, Photo-Oxidation, and Photostabilization of Polymers: Principles and Applications*; Wiley-Interscience publication; John Wiley & Sons: 1975.

- (2) Xiao, P.; Zhang, J.; Dumur, F.; Tehfe, M. A.; Morlet-Savary, F.; Graff, B.; Gimes, D.; Fouassier, J. P.; Lalevée, J. *Progress in Polymer Science* **2015**, *41*, 32–66.
- (3) Xiao, P.; Dumur, F.; Graff, B.; Fouassier, J. P.; Gimes, D.; Lalevée, J. *Macromolecules* **2013**, *46*, 6744–6750.
- (4) Pullen, G. K.; Allen, N. S.; Edge, M.; Weddell, I.; Swart, R.; Catalina, F.; Navaratnam, S. *European Polymer Journal* **1996**, *32*, 943–955.
- (5) Ledwith, A.; Ndaalio, G.; Taylor, A. R. *Macromolecules* **1975**, *8*, 1–7.
- (6) Encinas, M. V.; Majmud, C.; Lissi, E. A. *Journal of Polymer Science Part A: Polymer Chemistry* **1990**, *28*, 2465–2474.
- (7) Allen, N. S.; Pullen, G.; Shah, M.; Edge, M.; Weddell, I.; Swart, R.; Catalina, F. *Polymer* **1995**, *36*, 4665–4674.
- (8) Tozuka, M.; Igarashi, T.; Sakurai, T. *Polymer Journal* **2009**, *41*, 709.
- (9) Laurent, A. D.; Jacquemin, D. *International Journal of Quantum Chemistry* **2013**, *113*, 2019–2039.
- (10) Stowasser, R.; Hoffmann, R. *Journal of the American Chemical Society* **1999**, *121*, 3414–3420.

## 4 Strategies for the Rational Modification of Photochemical Properties

### 4.1 Introduction and Key Findings

In Chapter 3, functionalized anthraquinones with co-initiators were explored as a route to visible light photoinitiation. These systems may not be universally applicable to all cationic and free radical polymerizations, for example due to solubility issues. This chapter therefore focuses on exploring a different strategy for altering and improving photochemical processes with different functional groups. Examples of functional groups explored are: increasing conjugation by attaching unsaturated carbon chains/aromatic rings to the original chromophore moiety,<sup>1</sup> introduction of Lewis acids<sup>2</sup> or, as is reported the first time in this thesis, acid/base functional groups that can form charged species. These charged functional groups are able to alter the stabilities of  $n_O\pi^*$  and  $\pi\pi^*$  excited states via through-space, electrostatic interactions.

Until recently, the prevailing view of electrostatic effects in chemistry was limited to that of redox chemistry, in which the application of a relatively small voltage bias can have an order-of-magnitude effect on the measured redox current. In spectroscopy, electrostatic effects give rise to the Stark effect, the name given to the phenomenon by which excited state energies change upon the application of an external, oriented electric field.<sup>3</sup> These two applications of electric fields are mature areas of research. Seminal work by, among others, Shaik,<sup>4,5</sup> and Ciampi and Coote<sup>6-9</sup> has opened up the possibility of employing electric fields as a way of stabilizing charge-separated contributors in ordinarily covalent transition states. This effect has been explored in Diels-Alder reactions both experimentally and by theoretical means. The magnitude of the effect of introducing an electric field is highly dependent on the relative orientation between the applied electric field and the property that is to be manipulated. In the electrostatic catalysis of a Diels-Alder reaction, this property is the transition state dipole (Figure 4.1). The effect of the electric field is maximized when the angle between the dipole

moment and the applied electric field approaches 0°. It is also worth noting that alignment effects in the strong-field regime have been explored by Corkum and others,<sup>10,11</sup> however this chapter focusses on photochemistry suitable for synthesis, i.e. visible light initiation with low wattage lamps, rather than in an ultrafast laser spectroscopy setup.

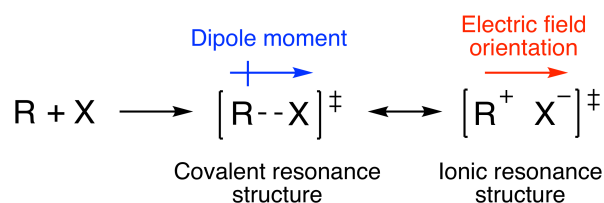


Figure 4.1: The two resonance structures of a model transition state. The ionic structure is susceptible to electric fields and can therefore be (de)stabilized by their introduction

Whilst relatively easy to study with computational chemistry, in which an external electric field can be included in the overall electronic Hamiltonian to mimic its effect,<sup>12</sup> introducing an oriented electric field to a chemical reaction experimentally presents a significant synthetic challenge. Aragonès *et al* demonstrated electrostatic catalysis by attaching the diene and dienophilic components of a Diels-Alder reaction to different sides of a scanning tunneling microscope (STM), across which a voltage bias was then applied. This surface-based approach is unsuitable for solution-based, bulk chemical reactions due to the random distribution of the molecules. An alternative approach is to install some charged functional group on the reacting system itself, which can be used as a local, or internal, oriented electric field.<sup>13-16</sup> This approach mitigates the random distribution of molecular orientation as the relative orientation of the electric field will, by design, be predictable. Computational chemistry is an invaluable tool for the design of such molecules, and has been employed with some success.<sup>17</sup> The required direction of the internal field (i.e. positive or negative charge) can be evaluated, as can the most favourable position for the functional group so as to maximize the desired through-space effect.

A natural extension to the application of charged functional groups is to apply them to the excited states of molecules. The simplest picture of an excited state is one in which an electron has been promoted in a molecule in its Aufbau configuration to an

antibonding orbital. Excited states generally exhibit changes in dipole moments ( $\Delta\mu$ ) and polarizability ( $\Delta\alpha$ ), two properties that will respond, or influence the response, to an electric field.<sup>18</sup> As previously mentioned, exploiting the Stark effect is a well established spectroscopic method for exploring the excited states of a chemical system, however for the first time electrostatic effects are studied as a generally applicable means of altering the photochemistry of a particular molecule in a chemically sensible and useful manner.

Publication 8 details the investigation into applying an internal oriented electric field, in the form of a so-called “pH switch”, to acetophenone, in order to assess and rationalize any observed effects on its excited state energies. The study found that a positive charge stabilizes the  $n_O\pi^*$  state and destabilizes the  $\pi\pi^*$  state, for both singlet and triplet states, and that a negative charge has the opposite effect. As well as this, the effect of a positive charge was not found to be completely equal and opposite to that of a negative charge. This was rationalized by the difference in polarizability between the two types of excited state. Furthermore, the effects were confirmed to be electrostatic in origin by two independent approaches, and the effect of including solvent was also assessed. Whilst increasingly polar solvent will attenuate the electrostatic effects, the opposing effect on  $\pi\pi^*$  and  $n_O\pi^*$  states can lead to a net doubling of the overall electrostatic effect.

The second publication in this chapter, Publication 9, is an extension of the investigations performed in Publication 8. Here, Irgacure 2959 (I2959) is studied, and is used as a case study against which electric fields can be assessed against Lewis acid complexation, and increasing conjugation. I2959 is a water soluble, Norrish Type I photoinitiator that has recently found use in 3D-bioprinting applications.<sup>19–24</sup> I2959 provides an opportunity to improve a photochemical system by:

1. Altering photon absorption wavelength to that which is more desirable and effective
2. Decreasing singlet/triplet gaps of different symmetry states

### 3. Increasing water solubility by inclusion of extra polar functional groups

From this study,  $\pi\pi^*$  and  $n\pi^*$  states were again found to be altered in opposite directions, depending on the field direction, and the size of the effect was also found to be similar in magnitude to that of increasing conjugation and Lewis acid complexation. Significantly, introducing charged functional groups is the only method that gives chemists a choice as to whether to stabilize or destabilize particular excited states.

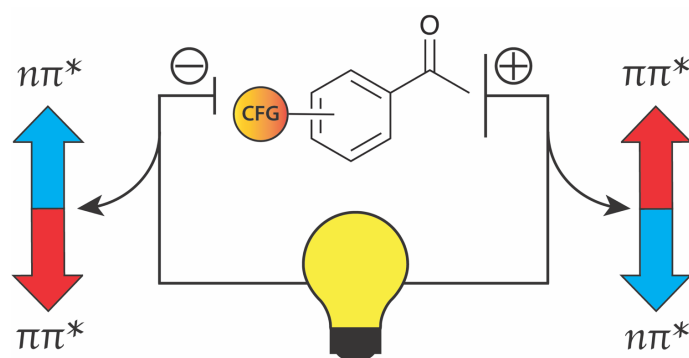


## 4.2 Publication 8

### Internal Oriented Electric Fields as a Strategy for Selectively Modifying Photochemical Reactivity

Nicholas S. Hill, Michelle L. Coote

*Journal of the American Chemical Society* **2018**, *140*, 17800-17804



This publication is a peer-reviewed manuscript published in *Journal of the American Chemical Society*. All computational results and subsequent discussion are my own work. Prof. Michelle Coote assisted with the direction of the theoretical investigations and corrected my draft write-ups. [Supplementary material is available online.](#)

### Statement of Contribution

This thesis is submitted as a Thesis by Compilation in accordance with [https://policies.anu.edu.au/pp/document/ANUP\\_003405](https://policies.anu.edu.au/pp/document/ANUP_003405)

I declare that the research presented in this Thesis represents original work that I carried out during my candidature at the Australian National University, except for contributions to multi-author papers incorporated in the Thesis where my contributions are specified in this Statement of Contribution.

Title: Internal Oriented Electric Fields as a Strategy for Selectively Modifying Photochemical Reactivity

Authors: Nicholas Hill, Michelle Coote

Publication outlet: Journal of the American Chemical Society

Current status of paper: Published

Contribution to paper: I am the first contributing computational chemistry author. All computational results, mechanistic insight, and subsequent discussion are my own work

Senior author or collaborating authors endorsement: Michelle Coote

Nicholas Hill



20/01/2020

Candidate - Print Name

Signature

Date

### Endorsed

Michelle Coote



20/01/2020

Primary Supervisor – Print Name

Signature

Date

Luke Connal  
Delegated Authority – Print Name



20/01/2020

Date

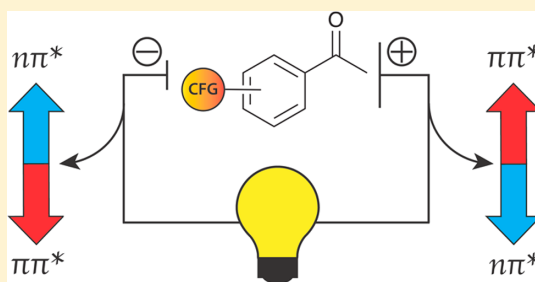
# Internal Oriented Electric Fields as a Strategy for Selectively Modifying Photochemical Reactivity

Nicholas S. Hill and Michelle L. Coote\*<sup>✉</sup>

ARC Centre of Excellence for Electromaterials Science, Research School of Chemistry, Australian National University, Canberra, Australian Capital Territory 2601, Australia

**S** Supporting Information

**ABSTRACT:** Time-dependent density functional theory calculations have been performed on acetophenone derivatives to explore the possibility of using charged functional groups as internal electric fields, the orientation of which can be altered to change photochemical behavior at will. Results demonstrate that nonconjugated charged groups can significantly alter, by up to  $-1.44$  eV, the stabilities of excited states. Specifically, a nonconjugated negatively charged group in the para position will destabilize the  $n\pi^*$  and stabilize the  $\pi\pi^*$  transitions, while a positively charged group will do the opposite. These electrostatic effects can be tuned by moving these substituents into the meta and ortho positions. Through use of acids and bases, these charged groups can be switched on or off with pH, allowing for selective alteration of the energy levels and photochemical reactivity. Solvent effects are shown to attenuate the electric field effect with increasing dielectric permittivity; however electrostatic effects are shown to remain significant even in quite polar solvents. Using charged functional groups to deliver the position-dependent electrostatic (de)stabilization effects is therefore a potential route to improving the efficiency of desirable photochemical processes.



## INTRODUCTION

Until relatively recently, electrostatic effects were largely thought to be applicable only to redox chemistry, where reactions involve electron transfer and as such respond predictably to an external voltage bias. However, work by Shaik, Coote, and others have highlighted the ability of carefully oriented electric fields to catalyze and alter non-electrochemical chemical reactions.<sup>1–3</sup> Specifically, the relative stability of the high-energy charge-separated resonance contributors of the transition state can be altered significantly upon introduction of electrostatic effects, which in turn can alter the reaction barrier. The magnitude of an electrostatic effect is dependent on the polarities involved, the strength of the applied field, and, importantly, the direction of the field relative to the reaction axis dipole.

This direction dependence introduces complexities when attempting to apply oriented external electric fields (OEEFs) on a large scale to solution-based chemistry. To date these challenges have been overcome on the nanoscale using surface chemistry techniques in conjunction with scanning tunneling microscopy,<sup>4,5</sup> but movement toward larger scale systems involving electrodes or charged insulators has been limited to unimolecular reactions and/or surface-tethered systems.<sup>5–7</sup> A more promising approach to applying electrostatic effects to solution chemistry is by introduction of charged functional groups (CFGs) to a specific region of a molecule.<sup>8</sup> Typically these CFGs are Brønsted acids and bases in their relevant

protonation states, although charged ligands,<sup>9</sup> Lewis acids,<sup>10</sup> and ionic aggregates<sup>11</sup> are also recognized as having potential as electrostatic catalysts.

Despite this recent attention, studies into the applicability of CFGs have focused primarily on ground state, thermal reactions. In this work their application to excited state chemistry is explored. Photochemistry is a promising avenue for application of electrostatic effects due to the presence of electron density in high-energy antibonding orbitals, orbitals that are inherently more diffuse and polarizable than ground state equivalents. As well as this, under mild conditions photoactive molecules can give selective access to reactions that are extremely unfavorable in the ground state, and therefore the ability to tune and enhance photochemical reactivity is highly desirable. Current approaches to changing the photochemical behavior of molecules focus on increasing the amount of conjugation in the molecule to red-shift absorption,<sup>12</sup> although Lewis acid complexation has also been found to induce similar effects.<sup>13</sup> However, increasing conjugation to an extent where absorption is shifted significantly can result in excitation character in regions of a molecule too far from the desired reaction center to be useful, while Lewis acid complexation was found to reduce the initiation efficiency. Introduction of CFGs could provide a

Received: November 8, 2018

Published: November 23, 2018

more balanced approach to tuning a molecule's photochemistry based on the following considerations:

- $\pi\pi^*$  and  $n\pi^*$  excited states exhibit different dipole moments and can therefore be targeted independently of each other;
- the stabilities of different states can be increased or decreased by introduction of either a positively or negatively charged group;
- the magnitude of the resultant electrostatic effect can be tuned by changing the position of the CFG on the molecule.

This study does not aim to fully explore the excited state properties, which often requires high-level, multireference *ab initio* calculations.<sup>14</sup> Instead, time-dependent density functional theory (TD-DFT) is employed to demonstrate that vertical excitation energies can be changed at will with electrostatic effects. For simplicity, acetophenone has been taken as a model system, as it is the simplest in the class of aromatic ketone photoinitiators, and TD-DFT is found to reproduce the correct ordering of its excited states.<sup>15</sup> Herein we show that the inclusion of (nonconjugated) charged functional groups can be used to selectively stabilize or destabilize its various transitions according to the sign of the charge and its location.

## COMPUTATIONAL METHODOLOGY

All calculations were performed using time-dependent density functional theory (DFT) with the Gaussian 16 electronic structure package.<sup>16</sup> Geometries were optimized with the M06-2X<sup>17</sup> exchange–correlation functional with the 6-31+G(d,p) basis set; TD-DFT calculations of excited states were also performed at M06-2X/6-31+G(d,p). Solvent effects (toluene, dichloromethane, acetonitrile, H<sub>2</sub>O) were considered with the SMD continuum solvent model.<sup>18</sup> All energies given are from the conformationally searched, global minimum energy structures in both gas and solvent phases, unless stated otherwise. Carboxylate pH switches for the  $n\pi^*$  and  $\pi\pi^*$  transitions were calculated with a range of basis sets for benchmarking purposes, finding that the switches predicted by 6-31+G(d,p) were consistent with both larger and smaller basis sets.

## RESULTS AND DISCUSSION

The photochemistry of acetophenone is known to change depending on whether it is excited to  $n\pi^*$   $S_1$ , upon which it will fluoresce, or to  $\pi\pi^*$   $S_2$ , which will give rise to radical generation via the mechanism shown in Figure 1.<sup>19</sup> The  $n\pi^*$   $S_1$  transitions involve electron donation from the lone pair on oxygen to the  $\pi^*$  orbital of the phenyl to form a charge-separated biradical,<sup>13</sup> while the  $\pi\pi^*$   $S_2$  involves excitation from the  $\pi$ -bonding orbital to its antibonding orbital. The  $n\pi^*$  state can undergo dissociation but only after intersystem crossing to the triplet ( $n\pi^*$   $T_1$ ). The relative energies of the various states influence the population of the dissociative  $n\pi^*$   $T_1$  state and can thus have a major impact on the efficiency of acetophenone as a photoinitiator.

Charged functional groups were added to the acetophenone phenyl ring in combination with a methylene spacer group to prevent direct  $\pi$ -conjugation between the charged group and the orbitals on the acetophenone fragment. This separation does not completely prevent through-bond effects such as sigma donation or withdrawal, but will to a first approximation help to isolate the electrostatic effects from other orbital effects. Deprotonated carboxylic acid groups were used to form negative charges, and protonated tertiary amine groups were used to form positive charges (Figure 2). Groups were placed

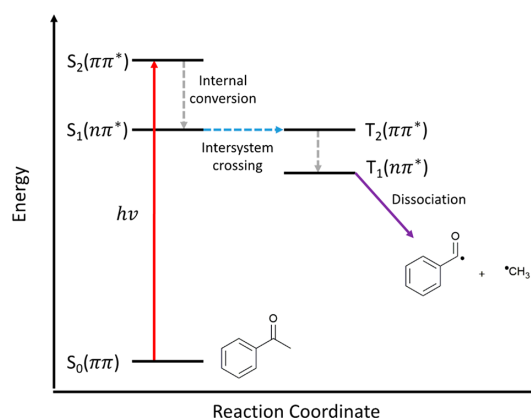


Figure 1. Energy level diagram highlighting excited state radiationless processes in acetophenone that give rise to radical dissociation.

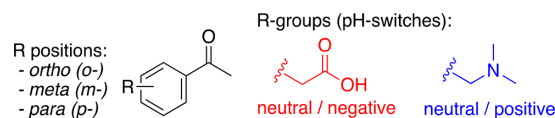


Figure 2. CFM-functionalized acetophenone.

in the ortho, meta, and para positions, and it should be noted that upon conformational optimization, the two ortho positions are equivalent to each other, as are the two meta positions.

**Singlet States.** The formation of charges on the carboxylate and amino groups to acetophenone results in stabilization/destabilization effects that vary as a function of ring position (Figure 3) and protonation state. For the singlet states, positive charge is found to stabilize the  $^1n\pi^*$  and destabilize the  $^1\pi\pi^*$  state, except at the ortho position, where the  $^1\pi\pi^*$  state is stabilized. To understand these effects, it is helpful to examine the electronic structure of the excited states.

As is well known,<sup>20</sup> the  $^1n\pi^*$  state is associated with a dipole with a significant charge-transfer contribution (Scheme 1), and hence appropriately placed charged groups should be able to electrostatically stabilize this dipole. From Scheme 1 it is clear that substituents in the para position should be best aligned with the dipole and hence most effective, and this alignment is poorer in the meta and, to a greater extent, the ortho position. It is also clear from Scheme 1 that a negatively charged carboxylate will destabilize the dipole and the positively charged protonated amine will stabilize it. This is consistent with the trends observed in Figure 3.

In contrast, the negatively charged carboxylate group is found to have the opposite effect on transition energies; deprotonation drastically stabilizes the  $\pi\pi^*$  state at all positions on the acetophenone ring, while the  $n\pi^*$  transition is destabilized. The result of this large stabilization upon deprotonation, based on the transition orbitals for the  $S_1$  states for both acetophenone and its carboxylate-functionalized equivalents (Figure S1, Supporting Information), is that the ordering of the  $n\pi^*$  and  $\pi\pi^*$  states actually inverts between the meta and para positions. More generally, the opposing effects of charge on the  $n\pi^*$  and  $\pi\pi^*$  transitions provide a strategy for, say, red-shifting one with respect to the other.

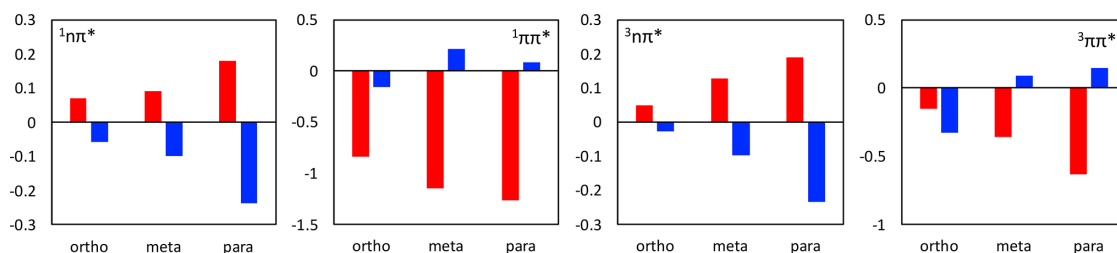
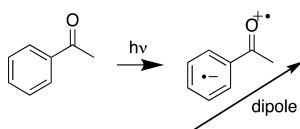


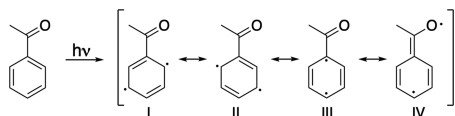
**Figure 3.** Change in  ${}^1n\pi^*$ ,  ${}^1\pi\pi^*$ ,  ${}^3n\pi^*$ , and  ${}^3\pi\pi^*$  vertical excitation energies (eV), upon charge formation (i.e., deprotonation of COOH, red, or protonation of NMe<sub>2</sub>, blue) relative to the corresponding neutral systems.

#### Scheme 1. Charge-Separated Representation of the ${}^1n\pi^*$ Excited State



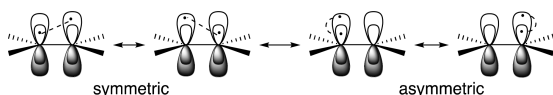
To understand the  $\pi\pi^*$  effects in more detail, we turn to valence bond (VB) theory. Scheme 2 shows the primary

#### Scheme 2. Resonance Contributors to the $S_2$ $\pi\pi^*$ State



resonance contributors to the  ${}^1\pi\pi^*$  state. While there are no apparent dipoles as drawn, VB studies of simpler compounds such as ethylene<sup>21</sup> show that additional “asymmetric” contributors can contribute as much as a quarter of the VB wave function (Scheme 3). In a symmetrical compound such

#### Scheme 3. VB Contributors to the First Singlet Excited State of Ethylene, Adapted from Ref 21



as ethylene this results in no net dipole, as both asymmetric contributors are degenerate; it does, however, explain the highly polarizable nature of the  $\pi\pi^*$  excited state. However, in acetophenone, the equivalent asymmetric VB structures for IV would involve a choice between a net negative charge on the electronegative oxygen or a net positive charge. The former would be more stable, and this contributor would thus carry more weight, giving the excited acetophenone a net dipole in which the para-carbon is delta positive and the oxygen is delta negative. As a result, one would expect a negatively charged group to stabilize the  $\pi\pi^*$  state and the positively charged group to destabilize it, in accordance with observations in Figure 3. At the same time, the  $\pi\pi^*$  state remains highly polarizable, and this polarizability enhances the stabilizing effects of the negative charge and diminishes the destabilizing effects of the positive charge, analogous to the asymmetry seen previously in ground state electrostatic catalysis.<sup>22,23</sup>

In the ortho position, the positively charged group lowers the  ${}^1\pi\pi^*$  transition, in opposition to the other trends. This is because upon protonation the ortho-amino group forms a hydrogen bond between the N–H and the carbonyl moiety (Figure S1, Supporting Information). This bond is not possible in the neutral species (lacking the proton) and thus results in a net stabilization despite the destabilizing electrostatic effects. Removal of the hydrogen bond by selecting a higher energy conformation without the hydrogen bond present returns the pH switch to the predicted trend of (de)stabilization. However, the lowest conformer results, i.e., the conformer with the H-bond, are presented here, as they highlight how different intramolecular interactions can prevent a designed electric field effect from taking place.

**Triplet States.** Acetophenone is an example of a molecule that exhibits an intersystem crossing (ISC) to its triplet excited states, regardless of whether it is excited to the  $S_1$  or  $S_2$  states. ISC is favored in situations where the  $S_n$  and  $T_n$  states have different orbital symmetries; for example  ${}^1n\pi^* \rightarrow {}^3\pi\pi^*$  ISC is more efficient than  ${}^1\pi\pi^* \rightarrow {}^3\pi\pi^*$  ISC.<sup>24</sup> Tuning the triplet energies of acetophenone is undoubtedly unnecessary, due to the near-degenerate  ${}^1n\pi^*/{}^3\pi\pi^*$  states. However, examining the triplet excited states of acetophenone functionalized with (un)charged groups suggests that these transition energies can also be altered with OEFs (Figure 3).

For the  $n\pi^*$  transitions the electrostatic effects in the singlet and triplet states are essentially identical. For the  $\pi\pi^*$  transitions, however, there are differences with the electrostatic effects on the triplet states generally smaller than the corresponding singlet states. This is likely due to TD-DFT inadequacies,<sup>25,26</sup> rather than an electric field effect. As we move further into the excited state manifold with the  $T_2(\pi\pi^*)$  state (inaccessible with open-shell calculations), these errors are likely exacerbated. A more thorough exploration of the excited states with high-level multireference calculations would provide more insight into the true behavior of the triplet states; however this is beyond the scope of the current work. It is sufficient to conclude here that electrostatic effects on the triplet  $n\pi^*$  and  $\pi\pi^*$  are qualitatively in line with those on the corresponding singlet states.

**Isolation of Electrostatic Effects.** While the CH<sub>2</sub> linker prevents  $\pi$ -conjugation between the pH-switchable group and the acetophenone, hyperconjugation between the phenyl ring and CH<sub>2</sub>–R  $\sigma$  bond (where R is COOH or NMe<sub>2</sub>) is possible. Indeed, in the lowest energy conformations of the various neutral and charged species this CH<sub>2</sub>–R  $\sigma$  bond is clearly orthogonal to the phenyl ring, allowing for orbital overlap with the  $\pi$  system (Figure S1, Supporting Information). Formation of a charge on R can stabilize or destabilize the C–R sigma\*

orbital and, hence, indirectly enhance or diminish hyperconjugation.

To separate through-bond orbital effects and through-space electrostatic effects, two independent approaches can be used: application of an increasingly large external electric field to the protonated form of the lowest energy deprotonated carboxylate structure and removal of the  $\text{CH}_2$  spacer group to instead terminate the carboxylate and acetophenone groups with hydrogen atoms. The external electric field was applied to the neutral form of the lowest energy *m*-carboxy-substituted structure. Moving from the protonated to the deprotonated, charged form of the carboxylate structure results in a large change in the overall dipole moment, and the electric field was applied along the axis in which this change was largest (Figure S4, Supporting Information). Figure 4 shows the destabilization of the  ${}^1n\pi^*$  transition and stabilization of the  ${}^1\pi\pi^*$  transition is almost totally recovered at a field strength of  $1.6 \times 10^{-2}$  au.

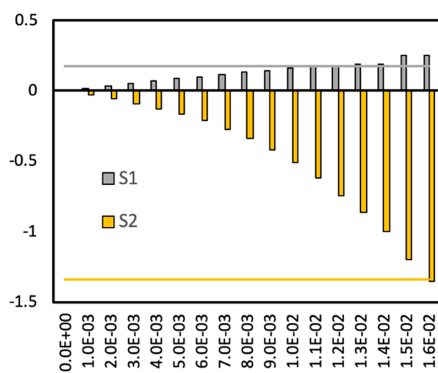


**Figure 4.** Change in  ${}^1n\pi^*$  and  ${}^1\pi\pi^*$  vertical excitation energies on uncharged, *m*-carboxy-functionalized acetophenone with increasing static electric field strength.

The external electric field calculations in Figure 5 still include any through-bond sigma effects, which can be removed by deleting the methyl spacer group, i.e., studying an equivalent complex of  $\text{HC}(\text{O})\text{O}^-$  (or  $\text{H}_2\text{NMe}_2^+$ ) and acetophenone (Figure 5) and comparing the excitation energies of the resulting protonated and deprotonated forms. To be as consistent as possible when the  $\text{CH}_2$  linker was removed, the positions of all conserved atoms were held constant, the missing bonds were capped with hydrogens, and these were added using standard default bond lengths and angles. Figure 5 confirms that electrostatic effects persist in the absence of a sigma-bonded connection between the charged group and the acetophenone and also suggests the sigma effects are attenuating the electrostatic field in the case of the  ${}^1\pi\pi^*$  transition for the carboxylate-substituted compound. This is consistent with the idea that, when connected by a  $\text{CH}_2$  linker, the charge is also diminishing hyperconjugative stabilization of the excited state.

**Solvent Effects.** Calculations so far have focused primarily on electrostatic effects exhibited in the gas phase; however, in real systems solvation is a key concern for future application of OEFs, as high-polarity solvents, for example, acetonitrile and water, significantly attenuate through-space OEFS.<sup>23</sup> It is therefore necessary to find a balance between solubility and polarity for the charged species, and dichloromethane ( $\epsilon =$

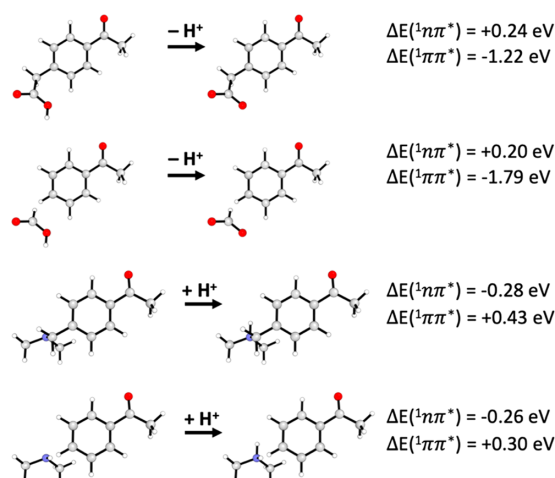


**Figure 5.** Removal of methylene spacer groups demonstrates the through-space effect deprotonation has on the  ${}^1n\pi^*$  and  ${}^1\pi\pi^*$  transition energies.

8.93) has previously been found to be satisfactory.<sup>27</sup> The effect of solvation on the change in energy of the  ${}^1n\pi^*$  and  ${}^1\pi\pi^*$  states, relative to uncharged para-substituted acetophenone, is shown in Figure 6 for a range of solvents. There is a significant

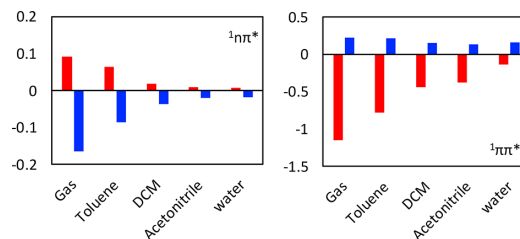


**Figure 6.** Change in  ${}^1n\pi^*$  and  ${}^1\pi\pi^*$  vertical excitation energies upon charge formation (i.e., deprotonation of  $\text{COOH}$ , red, or protonation of  $\text{NMe}_2$ , blue) for para-substituted acetophenone as a function of increasing solvent polarity.

reduction in both stabilization and destabilization effects for both states, as solvent polarity is increased. Promisingly, the electrostatic effects for negative carboxylate remain significant in both dichloromethane and even acetonitrile ( $\epsilon = 35.7$ ), exhibiting changes in  ${}^1\pi\pi^*$  energy of  $-0.53$  and  $-0.47$  eV, respectively. This suggests that electrostatic effects on photochemistry could remain large and usable in a range of solvation environments.

## CONCLUSIONS

To conclude, electrostatic effects have been found to originate from the introduction of CFGs to acetophenone. These effects have a significant effect on the stability of  ${}^1\pi\pi^*$  transitions and a smaller opposite effect on  ${}^1n\pi^*$  transitions. Specifically, a nonconjugated negatively charged group in the para position will destabilize the  ${}^1n\pi^*$  and stabilize the  ${}^1\pi\pi^*$ , while a positively charged group will do the opposite. These electrostatic effects can be tuned by moving these substituents into the meta and ortho positions and/or increasing their distance from the acetophenone through the use of additional linkers. Given the

position dependence for both the magnitude and direction of the effective (de)stabilizing field, it should be possible to enhance the efficiency of low-yielding photochemical processes. As well as this, unlike effects on ground states,<sup>23,27</sup> electrostatic effects are found to remain significant even in quite polar solvents, such as acetonitrile. This is likely due to the increased sensitivity to electric fields exhibited by the more diffuse antibonding orbitals. This gives great promise for the general application of this approach to solvated photochemical systems.

## ■ ASSOCIATED CONTENT

### ● Supporting Information

The Supporting Information is available free of charge on the ACS Publications website at DOI: 10.1021/jacs.8b12009.

Geometries and total energies for all structures in this work (PDF)

## ■ AUTHOR INFORMATION

### Corresponding Author

\*michelle.coote@anu.edu.au

### ORCID

Michelle L. Coote: 0000-0003-0828-7053

### Notes

The authors declare no competing financial interest.

## ■ ACKNOWLEDGMENTS

The authors acknowledge financial support from the Australian Research Council (ARC) Centre of Excellence for Electromaterials Science, an ARC Laureate Fellowship (to M.L.C.), generous supercomputing time from the National Computational Infrastructure, and helpful discussions with Kam Fung.

## ■ REFERENCES

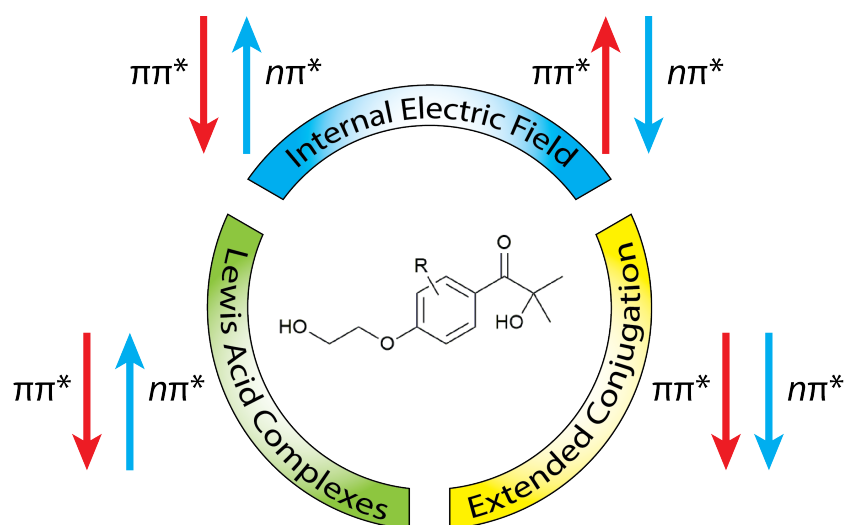
- (1) Ciampi, S.; Darwish, N.; Aitken, H. M.; Diez-Perez, I.; Coote, M. L. Harnessing Electrostatic Catalysis in Single Molecule, Electrochemical and Chemical Systems: A Rapidly Growing Experimental Tool Box. *Chem. Soc. Rev.* **2018**, *47* (14), 5146–5164.
- (2) Shaik, S.; Mandal, D.; Ramanan, R. Oriented Electric Fields as Future Smart Reagents in Chemistry. *Nat. Chem.* **2016**, *8* (12), 1091–1098.
- (3) Shaik, S.; Ramanan, R.; Danovich, D.; Mandal, D. Structure and Reactivity/Selectivity Control by Oriented-External Electric Fields. *Chem. Soc. Rev.* **2018**, *47* (14), 5125–5145.
- (4) Aragonès, A. C.; Haworth, N. L.; Darwish, N.; Ciampi, S.; Bloomfield, N. J.; Wallace, G. G.; Diez-Perez, I.; Coote, M. L. Electrostatic Catalysis of a Diels–Alder Reaction. *Nature* **2016**, *531* (7592), 88–91.
- (5) Zhang, L.; Laborda, E.; Darwish, N.; Noble, B. B.; Tyrell, J. H.; Pluczyk, S.; Le Brun, A. P.; Wallace, G. G.; Gonzalez, J.; Coote, M. L.; et al. Electrochemical and Electrostatic Cleavage of Alkoxyamines. *J. Am. Chem. Soc.* **2018**, *140* (2), 766–774.
- (6) Akamatsu, M.; Sakai, N.; Matile, S. Electric-Field-Assisted Anion- $\pi$  Catalysis. *J. Am. Chem. Soc.* **2017**, *139* (19), 6558–6561.
- (7) Gorin, C. F.; Beh, E. S.; Kanan, M. W. An Electric Field-Induced Change in the Selectivity of a Metal Oxide-Catalyzed Epoxide Rearrangement. *J. Am. Chem. Soc.* **2012**, *134* (1), 186–189.
- (8) Gryn'ova, G.; Marshall, D. L.; Blanksby, S. J.; Coote, M. L. Switching Radical Stability by PH-Induced Orbital Conversion. *Nat. Chem.* **2013**, *5* (6), 474–481.
- (9) Yue, L.; Wang, N.; Zhou, S.; Sun, X.; Schlagen, M.; Schwarz, H. The Electric Field as a “Smart” Ligand in Controlling the Thermal Activation of Methane and Molecular Hydrogen. *Angew. Chem., Int. Ed.* **2018**, *57*, 1–6.
- (10) Jiang, J. Y.; Smith, L. M.; Tyrell, J. H.; Coote, M. L. Pulsed Laser Polymerisation Studies of Methyl Methacrylate in the Presence of AlCl<sub>3</sub> and ZnCl<sub>2</sub>—Evidence of Propagation Catalysis. *Polym. Chem.* **2017**, *8* (38), 5948–5953.
- (11) Schwarz, H.; Shaik, S.; Li, J. Electronic Effects on Room-Temperature, Gas-Phase C–H Bond Activations by Cluster Oxides and Metal Carbides: The Methane Challenge. *J. Am. Chem. Soc.* **2017**, *139* (48), 17201–17212.
- (12) Le Guennic, B.; Jacquemin, D. Taking Up the Cyanine Challenge with Quantum Tools. *Acc. Chem. Res.* **2015**, *48* (3), 530–537.
- (13) Noble, B. B.; Mater, A. C.; Smith, L. M.; Coote, M. L. The Effects of Lewis Acid Complexation on Type I Radical Photoinitiators and Implications for Pulsed Laser Polymerization. *Polym. Chem.* **2016**, *7*, 6400.
- (14) Blancafort, L. Photochemistry and Photophysics at Extended Seams of Conical Intersection. *ChemPhysChem* **2014**, *15* (15), 3166–3181.
- (15) Huix-Rotllant, M.; Ferre, N. Triplet State Photochemistry and the Three-State Crossing of Acetophenone within Time-Dependent Density-Functional Theory. *J. Chem. Phys.* **2014**, *140* (13), 134305.
- (16) Frisch, M. J.; Trucks, G. W.; Schlegel, H. B.; Scuseria, G. E.; Robb, M. A.; Cheeseman, J. R.; Scalmani, G.; Barone, V.; Petersson, G. A.; Nakatsuji, H.; et al. *Gaussian 16*, Revision A.03; Gaussian Inc.: Wallingford, CT, 2016.
- (17) Zhao, Y.; Truhlar, D. G. The M06 Suite of Density Functionals for Main Group Thermochemistry, Thermochemical Kinetics, Noncovalent Interactions, Excited States, and Transition Elements: Two New Functionals and Systematic Testing of Four M06-Class Functionals and 12 Other Fun. *Theor. Chem. Acc.* **2008**, *120*, 215–241.
- (18) Marenich, A. V.; Cramer, C. J.; Truhlar, D. G. Universal Solvation Model Based on Solute Electron Density and on a Continuum Model of the Solvent Defined by the Bulk Dielectric Constant and Atomic Surface Tensions. *J. Phys. Chem. B* **2009**, *113*, 6378–6396.
- (19) Huix-Rotllant, M.; Siri, D.; Ferré, N. Theoretical Study of the Photochemical Generation of Triplet Acetophenone. *Phys. Chem. Chem. Phys.* **2013**, *15* (44), 19293–19300.
- (20) Zimmerman, H. E.; Alabugin, I. V. Excited State Energy Distribution and Redistribution and Chemical Reactivity; Mechanistic and Exploratory Organic Photochemistry. *J. Am. Chem. Soc.* **2000**, *122* (5), 952–953.
- (21) Wu, W.; Zhang, H.; Braida, B.; Shaik, S.; Hiberty, P. C. The V State of Ethylene: Valence Bond Theory Takes up the Challenge. *Theor. Chem. Acc.* **2014**, *133* (3), 1–13.
- (22) Gryn'ova, G.; Coote, M. L. Directionality and the Role of Polarization in Electric Field Effects on Radical Stability. *Aust. J. Chem.* **2016**, *70*, 367.
- (23) Gryn'ova, G.; Coote, M. L. Origin and Scope of Long-Range Stabilizing Interactions and Associated SOMO-HOMO Conversion in Distonic Radical Anions. *J. Am. Chem. Soc.* **2013**, *135* (41), 15392–15403.
- (24) McNaught, A. D.; A, W. *IUPAC. Compendium of Chemical Terminology*, 2nd ed.; Blackwell Scientific Publications, 1997.
- (25) Jacquemin, D.; Perp, E. A.; Ciofini, I.; Adamo, C.; Electrochimie, L.; Cnrs-enscp, U. M. R. Assessment of Functionals for TD-DFT Calculations of Singlet-Triplet Transitions. *J. Chem. Theory Comput.* **2010**, *6*, 1532–1537.
- (26) Laurent, A. D.; Jacquemin, D. TD-DFT Benchmarks: A Review. *Int. J. Quantum Chem.* **2013**, *113* (17), 2019–2039.
- (27) Klinska, M.; Smith, L. M.; Gryn'ova, G.; Banwell, M. G.; Coote, M. L. Experimental Demonstration of PH-Dependent Electrostatic Catalysis of Radical Reactions. *Chem. Sci.* **2015**, *6* (10), 5623–5627.

### 4.3 Publication 9

#### Strategies for Red-Shifting Type I Photoinitiators: Internal Electric Fields vs Lewis Acids vs Increasing Conjugation

Nicholas S. Hill, Michelle L. Coote

*Australian Journal of Chemistry* 2019



This publication is a peer-reviewed manuscript published in *Australian Journal of Chemistry*. All computational results and subsequent discussion are my own work. The article was also featured on the cover of the journal. Prof. Michelle Coote assisted with the direction of the theoretical investigations and corrected my draft write-ups. [Supplementary material is available online.](#)



### Statement of Contribution

This thesis is submitted as a Thesis by Compilation in accordance with [https://policies.anu.edu.au/ppl/document/ANUP\\_003405](https://policies.anu.edu.au/ppl/document/ANUP_003405)

I declare that the research presented in this Thesis represents original work that I carried out during my candidature at the Australian National University, except for contributions to multi-author papers incorporated in the Thesis where my contributions are specified in this Statement of Contribution.

Title: Strategies for Red-Shifting Type I Photoinitiators: Internal Electric Fields vs Lewis Acids vs Increasing Conjugation

Authors: Nicholas Hill, Michelle Coote

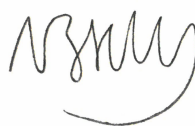
Publication outlet: Australian Journal of Chemistry

Current status of paper: Published

Contribution to paper: I am the first contributing computational chemistry author. All computational results, mechanistic insight, and subsequent discussion are my own work

Senior author or collaborating authors endorsement: Michelle Coote

Nicholas Hill



20/01/2020

Candidate - Print Name

Signature

Date

### Endorsed

Michelle Coote



20/01/2020

Primary Supervisor – Print Name

Signature

Date



Delegated Authority – Print Name



Signature

20/01/2020

Date

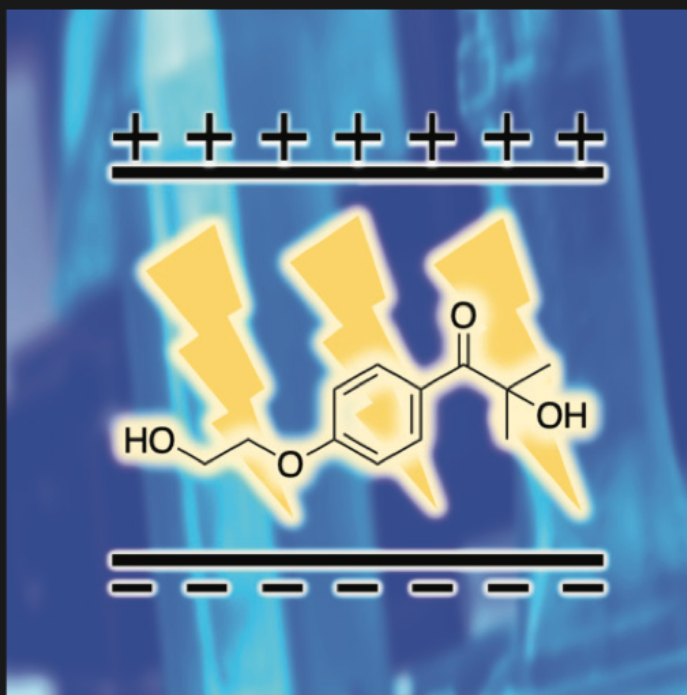
Vol. 72(8) 2019 Pages 561-648

Vol. 72, No. 8, 2019

# AUSTRALIAN JOURNAL OF CHEMISTRY

AN INTERNATIONAL JOURNAL FOR CHEMICAL SCIENCE

## RACI Awards 2017-19



AUSTRALIAN JOURNAL OF CHEMISTRY - AN INTERNATIONAL JOURNAL FOR CHEMICAL SCIENCE

CSIRO PUBLISHING

[www.publish.csiro.au/journals/ajc](http://www.publish.csiro.au/journals/ajc)

# Strategies for Red-Shifting Type I Photoinitiators: Internal Electric Fields versus Lewis Acids versus Increasing Conjugation\*

Nicholas S. Hill<sup>A</sup> and Michelle L. Coote<sup>A,B</sup>

<sup>A</sup>ARC Centre of Excellence for Electromaterials Science, Research School of Chemistry, Australian National University, Canberra, ACT 2601, Australia.

<sup>B</sup>Corresponding author. Email: michelle.coote@anu.edu.au

Time-dependent density functional theory calculations were performed on derivatives of Irgacure 2959, a water-soluble, acetophenone-type photoinitiator, in order to assess the relative merits and drawbacks of three distinct ways of modifying its photochemistry: Lewis acid complexation, changing the amount of conjugation in the molecule, and application of an internal electric field through inclusion of a remote charged functional group. The effectiveness of each of the three methods was evaluated against the magnitude of the change in energy of the excited states. Internal electric fields were shown to provide the best method for targeting specific excited states in a controlled and rational manner. The other strategies also had significant effects but it was more difficult to independently target different transitions. Nonetheless, for the specific case of Irgacure 2959, we predict that its complexation with  $Mg^{2+}$  ions in a range of solvents will both red-shift the initiator's absorbance while improving its efficiency and it is thus a promising candidate for testing as a visible light photoinitiator.

Manuscript received: 9 June 2019.

Manuscript accepted: 12 July 2019.

Published online: 31 July 2019.

## Introduction

Over the past few years, much attention has focussed on harnessing electric fields – either externally or via the internal fields generated by charged functional groups – to modify chemical reactivity.<sup>[1,2]</sup> During the course of such work, it has been noted that polarizable molecules, such as resonance-stabilized radicals, show particularly large sensitivities to electric field effects.<sup>[3,4]</sup> As many excited states are highly polarizable, this raises the prospect of selectively manipulating these states with electric fields.

Recently, we used time-dependent density functional theory (TD-DFT) to investigate if electric fields offer a route for tuning the photochemical behaviour of acetophenone (**1**, Chart 1) and, by extension, other similar Type I photoinitiating compounds.<sup>[5]</sup> The study highlighted how the introduction of a non-conjugated charged functional group can either stabilize or destabilize  $n\pi^*$  and  $\pi\pi^*$  excited states. Moreover, the two types of state are affected in opposite directions depending on the sign of the charge, and there is a significant dependence of the magnitude of the electrostatic effect on ring position, thus allowing tuning of the effect. This is important if one wishes to, say, red-shift a photoinitiator without compromising its efficiency.

In the present work, we aim to assess the relative merits of using such electrostatic effects to modify photoinitiation behaviour when compared with more traditional approaches based on resonance. In particular, it is well known that extending the  $\pi$ -system of a photoactive compound will decrease the  $\pi-\pi^*$

excitation energy and hence provide a means of red-shifting excitations into the  $\pi^*$  system.<sup>[6]</sup> Moreover, aromatic systems with conjugated lone pair donors respond to pH changes, as these determine if the lone pair is available for resonance with the aromatic ring. One such example is the pH-dependent UV-vis spectrum of F<sub>420</sub>.<sup>[7]</sup> A related approach is to change the extent of resonance by coordinating Lewis acids with conjugated lone pair donor and/or  $\pi$ -acceptor groups. For example, we recently showed that Lewis acids could red-shift the absorption spectra and alter the photoinitiation behaviour of the popular Type I photoinitiators methyl-4'-(methylthio)-2-morpholinopropiophenone (MMMP) and 2,2-dimethoxy-2-phenylacetophenone (DMPA).<sup>[8]</sup>

To compare these different approaches, in the present work we attempt to improve the commercial Type I photoinitiator Irgacure 2959 (I2959, **2** in Chart 1). Recently, I2959 has found use in 3D bioprinting,<sup>[9–11]</sup> a process that involves the printing of biological material to form a specific tissue shape. Initially, the printable material is in the form of a 'bio-ink', a liquid-like

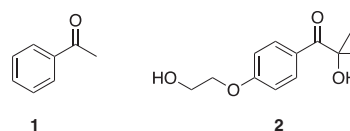


Chart 1. Chemical structures of acetophenone (**1**) and Irgacure 2959 (**2**).

\*Michelle L. Coote is the winner of the 2019 RACI Physical Division Medal.

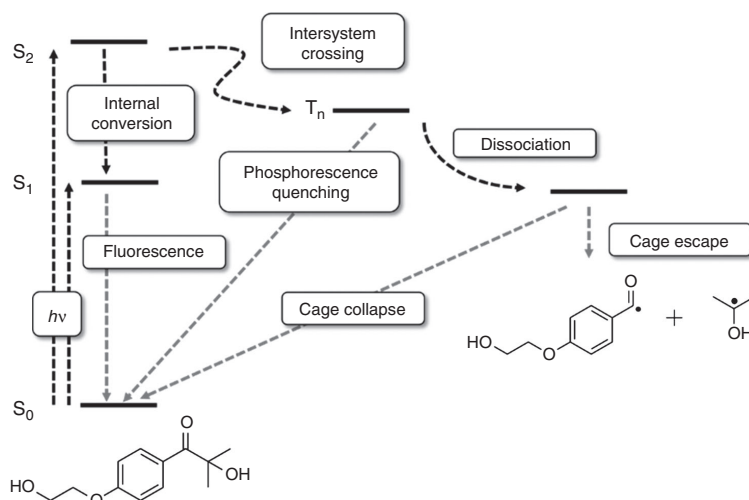


Fig. 1. Jablonski diagram describing Type I photoinitiation of acetophenone.

mixture of cellular material, monomer, and photoinitiator. At the point of printing, the ink is irradiated with UV light in order to initiate a polymerization curing reaction that hardens the ink so that a three-dimensional tissue can be additively built. UV light does, however, have a detrimental effect on the cell viability within the 3D-printed tissue, as the high-energy photons can be absorbed by the cells with damaging consequences. Moreover, I2959 exhibits a reasonably low quantum yield of photolysis, at  $\Phi = 0.29$ .<sup>[12]</sup> Although visible-light photoinitiators exist,<sup>[13–15]</sup> to date, the initiators used are not as attractive as I2959 for bioprinting applications owing to their poor solubility in water.

Summing up, I2959 exhibits several properties that make it useful in 3D-printing applications; however, these properties could be improved. In particular, the necessity for damaging UV irradiation can be altered by lowering the energies of the reactive states; the efficiency of the electronic transitions could be improved, which would result in a higher value of  $\Phi$ , and I2959's solubility in water can be increased. Herein, we investigate if, and to what extent, this can be achieved through the use of remote charged functional groups, or through other strategies including Lewis acid complexation or more direct modifications to the chromophore such as extending the  $\pi$  system.

## Theoretical Procedures

Although more accurate multireference methods are required to fully explore excited-state properties, here we are primarily interested in systematic effects on vertical excitation energies. Literature studies have shown that TD-DFT can reproduce these excitation energies for organic molecules in general<sup>[16]</sup> and acetophenone in particular.<sup>[17]</sup> Thus, as in our previous study,<sup>[5]</sup> the M06-2X density functional<sup>[18]</sup> was used for all ground- and excited-state calculations. Every species was extensively conformer-searched in order to locate the global minimum energy structure; structures were optimized with the 6-31+G(d,p) basis set, on which TD-DFT calculations were performed. Where relevant, solvent effects were considered with the SMD implicit continuum solvent model.<sup>[19]</sup> All calculations were performed with the *Gaussian 16 Revision A* electronic structure software package.<sup>[20]</sup>

## Results and Discussion

### Photochemistry of Unfunctionalized I2959

Like acetophenone, I2959 exhibits  $S_1(n\pi^*)$  and  $S_2(\pi\pi^*)$  excited states and several low-lying triplet excited states. Experimentally, I2959 exhibits  $\lambda_{\text{max}}$  at 273 nm; at these wavelengths, the predominant excited state transition will be to the  $S_2(\pi\pi^*)$  state, and the reactive triplet excited state has  $^3\pi\pi^*$  and  $^3n\pi^*$  character.<sup>[12]</sup> TD-DFT calculations suggest, however, that the  $S_1(n\pi^*)$  state at  $\sim 305$  nm has a nearby  $T_2(n\pi^*)$  at  $\sim 337$  nm and  $T_1(\pi\pi^*)$  at 348 nm. According to El Sayed selection rules,<sup>[21]</sup> the most efficient intersystem crossing (ISC) will take place from the  $S_1(n\pi^*)$  to the  $T_1(\pi\pi^*)$  surface. Fig. 1 is a simple diagram describing Type I photoinitiation, and the different internal processes that can take place on photoexcitation. A simple approach to improving the initiation efficiency of I2959 would therefore be to reduce the  $S_1/T_1$  energy gap, resulting in a red-shift in the required wavelength of light for initiation ( $S_1$  rather than  $S_2$  is being targeted), and the different symmetries of the states would allow the efficient population of the  $T_1$  state.

### Effect of Increasing $\pi$ -Conjugation

The effect of increasing conjugation of the photoactive moiety of I2959 was investigated with the structures shown in Fig. 2. Increasing the amount of  $\pi$ -conjugation present in a molecule is the most commonly adopted method to altering photochemistry. As this is a through-bond orbital effect, rather than a through-space electric field effect, this approach ought to be the most robust to solvent effects and so gas-phase energies were studied for simplicity. To explore these effects, three ways of increasing conjugation were evaluated; by fusing either an extra phenyl ring or an antiaromatic ring system to the original I2959 phenyl moiety, or by replacing the non-equivalent H-atoms with increasingly large unsaturated alkyl chains or a benzene ring. It is noted that these structural changes would likely decrease rather than increase water solubility but they are considered here to provide a baseline as to what effects are possible with changes to  $\pi$ -conjugation.

The changes in the gas-phase energies of the  $S_1$ ,  $S_2$ , etc., states on the introduction of these functional groups relative to

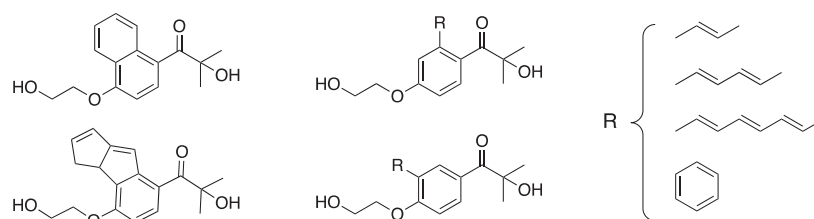


Fig. 2. Extended conjugative groups introduced into I2959.

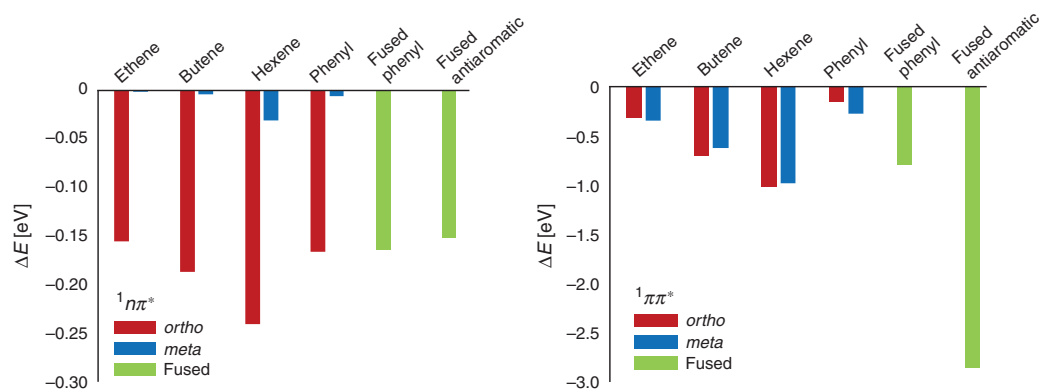


Fig. 3. Change in gas-phase vertical excitation energies of the  ${}^1n\pi^*$  and  ${}^1\pi\pi^*$  states on increasing the conjugation in I2959. Note that the *meta* value for the  ${}^1n\pi^*$  transition with ethene is essentially zero.

that of I2959 are shown in Fig. 3. Owing to the presence of the phenyl ring in I2959, introducing further conjugation in the form of an extra phenyl moiety, or a long alkyl chain, is found to have only a limited effect on the energies of the  $S_1$  states; in fact, at the *meta* positions, the effects are negligible (Fig. 3). In contrast, extending the  $\pi$  system greatly lowers the energy of the  $\pi\pi^*$  transitions. This is particularly pronounced with the fused antiaromatic rings, which become aromatic in the excited state.

The net result of introducing more conjugation to I2959 is primarily to lower (red-shift) the energies for  $\pi\pi^*$  transitions, with minimal effect on the  $n\pi^*$  transitions, thus closing the gap with the  $\pi\pi^*$  states. Unfortunately, although this does red-shift the absorption of the initiator, it is unlikely to improve initiator efficiency. For instance, with the addition of butene at the *meta* position, for example, the  $S_1(n\pi^*)$  to  $S_2(\pi\pi^*)$  is reduced from 0.61 eV in I2959 to 0.15 eV. This small energy gap may allow the efficient population of the  $n\pi^*$  state via the bright  $\pi\pi^*$  state; however, the corresponding triplet excited states have also been stabilized, and are now further away in energy from the singlet states. The red-shifting of the  ${}^1\pi\pi^*$  state is particularly profound on the addition of a fused antiaromatic unit, resulting in a 2.85 eV reduction in energy in the gas phase, and a 2.58 eV lowering in water. The  $n\pi^*$  states are stabilized to a much lower extent, and therefore whereas the absorption of I2959 in this case would be significant in the visible light region, TD-DFT calculations do not suggest this would lead to efficient photoinitiation.

#### Effect of Lewis Acid Complexation

In order to assess the potential application of Lewis acid (LA) complexation to alter the photochemistry of I2959, three metal

chloride species were investigated:  $ZnCl_2$ ,  $MgCl_2$ , and  $CaCl_2$ . The counterions were chosen for computational efficiency and because they had been used in our previous experimental study of the effect of LA complexation on MMMP and DMPA.<sup>[8]</sup> Depending on the conditions, other counterions could be used to enhance solubility and, particularly if non-coordinating, will have little impact on the results. It should also be added some of the reaction conditions studied (e.g. gas phase) are not practical but are included to better understand trends in the data.

There are two possible binding modes between I2959 and LA species, and each LA was modelled in both  $LA^{2+}$  and  $LACl_2$  forms in order to determine the I2959-LA complex most prevalent in different solvent environments. The thermodynamic calculations are summarized in Tables S1–S4 in the Supplementary Material, and show that for each of the LA species, the most favourable complexation position is to the acyl oxygen site (Fig. 4).

With the complexation mode of the LA with I2959 established, TD-DFT calculations were performed in order to assess the effect of their introduction on I2959 excited states. Fig. 5 shows the change in vertical excitation energy of the three excited states of interest on complexation relative to uncomplexed I2959 (Tables S10–S12, Supplementary Material). The calculations show that the  $n\pi^*$  states are destabilized and the  $\pi\pi^*$  states are stabilized by the presence of LAs. This is consistent with our previous experimental and theoretical study of the effects of zinc chloride ( $ZnCl_2$ ) and aluminium chloride ( $AlCl_3$ ) on MMMP and DMPA.<sup>[8]</sup> In the present work, we find that  $MgCl_2$  complexation has the most significant effect on the stability of the excited states of I2959. The observed splitting in stability between the  $n\pi^*$  and  $\pi\pi^*$  states arises from the

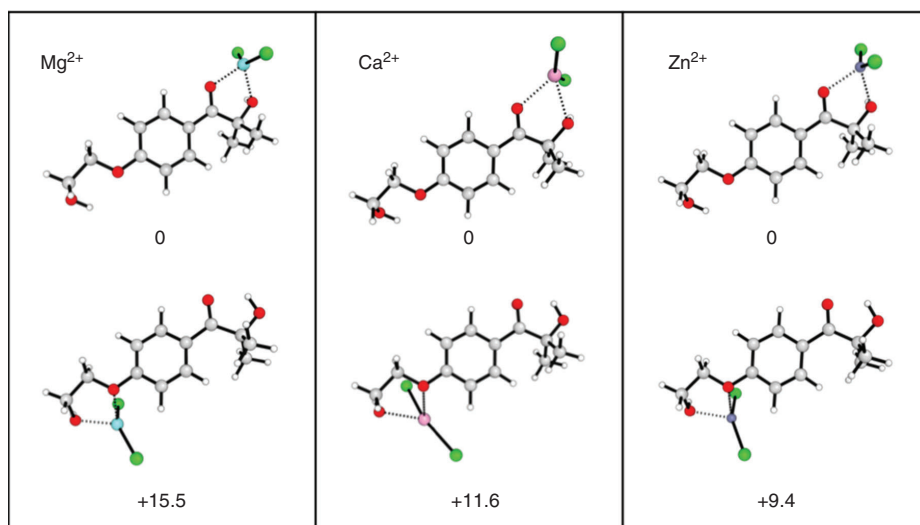


**Fig. 4.** Gas-phase Lewis acid complex structures and relative free energies ( $\text{kJ mol}^{-1}$ ) for  $\text{MgCl}_2$  (left),  $\text{CaCl}_2$  (middle), and  $\text{ZnCl}_2$  (right). In each case, the top structure is the minimum energy complex at the carbonyl and nearby alcohol, whereas the lower structure is the minimum energy complex at the ether and its nearby alcohol.

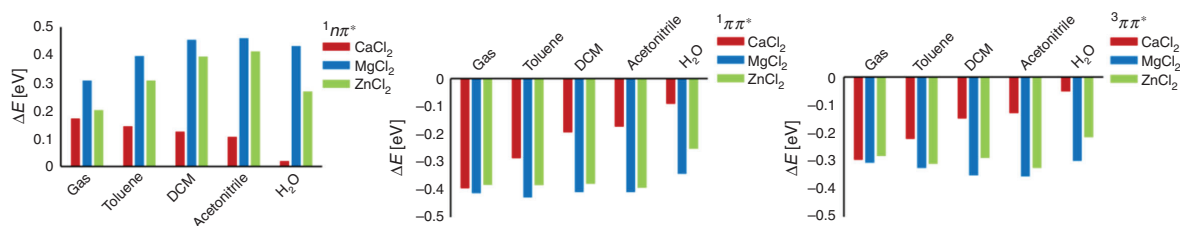


**Fig. 5.** Change in  ${}^1n\pi^*$ ,  ${}^1\pi\pi^*$ , and  ${}^3\pi\pi^*$  vertical excitation energies (eV) on Lewis acid complexation.

difference in their respective Lewis basicities;<sup>[8]</sup>  $n\pi^*$  transitions involve moving an electron from the ketone oxygen  $n$ -orbitals into the  $\pi^*$ -system, resulting in a net less Lewis-basic ketone oxygen and conversely,  $\pi\pi^*$  transitions involve moving an electron from the  $\pi$ -system into  $\pi^*$ -orbitals that have some ketone delocalization, resulting in an increase in Lewis basicity at the ketone oxygen.

Compared with the remote charged functional groups (below), the complexation of LAs does not allow specific states to be selectively altered in energy based on their position or direction of charge, with complexation limited to only destabilizing the  $n\pi^*$  and vice versa for the  $\pi\pi^*$  states. As a result, their effects can be a bit hit-and-miss. For instance, in our previous study,<sup>[8]</sup> LAs red-shifted the excitation energies but caused a deterioration in initiator efficiency by prolonging triplet lifetimes. Nonetheless, the calculations presented here suggest that introduction of  $\text{MgCl}_2$  offers a promising route to increasing photoinitiation efficiency of Irgacure. On closer inspection of the excited states of the  $\text{MgCl}_2$ -I2959 complex in water, it is found the (de)stabilization of its excited states results in the ordering of the  ${}^1n\pi^*$  and  ${}^1\pi\pi^*$  states to swap, while the energy gap between the  ${}^1\pi\pi^*$  and  ${}^3n\pi^*$  states shrinks from 0.97 to 0.18 eV. If found experimentally to be accurate, this change in order of the excited states would allow the efficient population of the bright  ${}^1\pi\pi^*$  state, followed by efficient ISC to the  ${}^3n\pi^*$  to form radical species.

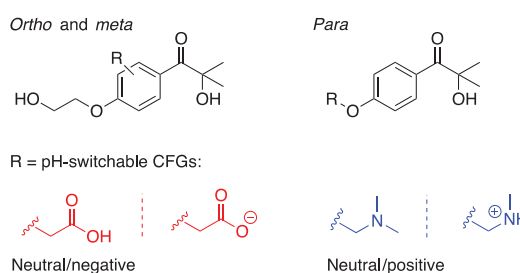


**Fig. 6.** CFG-functionalised I2959.

#### Effect of Remote Charged Functional Groups

Previous work demonstrated that the attachment of non-conjugated charged functional groups (CFGs), i.e. acid and base groups that can be (de)protonated to form a charge, results in a ring-position-dependent electric field effect that can (de)stabilize  $n\pi^*$  and  $\pi\pi^*$  excited states, depending on the charge formed.<sup>[5]</sup> In I2959, the effect of attaching the carboxylic acid (CA) and tertiary amine (TA) groups at the *ortho* and *meta* positions of the phenyl ring, and replacing the alcohol group at the end of the alkyl chain as a pseudo-*para* position (Fig. 6) was investigated in solvents with increasingly large dielectric constants (Fig. 7). The *para* position was altered in a slightly

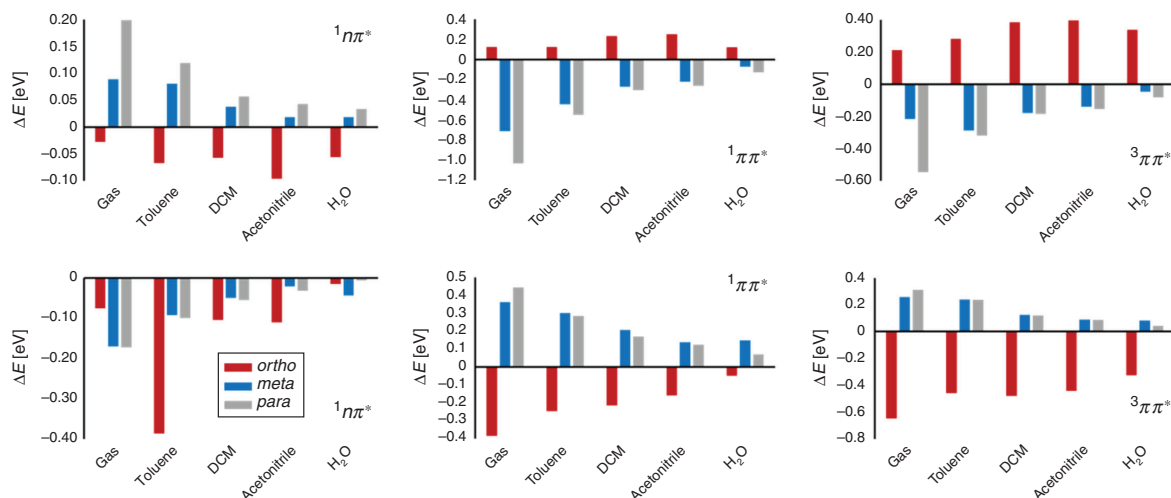


Fig. 7. Change in  ${}^1n\pi^*$ ,  ${}^1\pi\pi^*$ , and  ${}^3\pi\pi^*$  vertical excitation energies (eV) on charge formation of  $\text{COO}^-$  (top row) or  $\text{NMe}_2\text{H}^+$  (bottom row).

different manner than the *ortho* and *meta* positions; in the case of the former, CFGs were introduced either by adding an acyl oxygen group to the  $-\text{CH}_2\text{OH}$  moiety or swapping the alcohol group for a tertiary amine group. For the *ortho* and *meta* positions,  $-\text{CH}_2\text{COOH}$  and  $-\text{CH}_2\text{NMe}_2$  groups were used. The difference in  $\text{p}K_a$  values of the CA and alkyl-OH groups of I2959 would be sufficient to allow selective deprotonation of the CA.

Fig. 7 includes the change in  ${}^1n\pi^*$ ,  ${}^1\pi\pi^*$ , and  ${}^3\pi\pi^*$  vertical excitation energies on the formation of the charged species in the following solvent phases: gas, toluene, dichloromethane, acetonitrile, and water. Interestingly, there is a distinct *ortho/meta/para* (de)stabilization pattern different to that which has been reported previously.<sup>[5]</sup> Here, moving from the *ortho* to the *meta* positions results in a complete inversion in the effect of introducing either a positive or negative charged group. As well as this, the effect of applying a charged functional group is generally maximized at the *para* position. The reason for the observed anomalous results for the  ${}^1n\pi^*$  state on introduction of an  $\text{NMe}_2\text{H}^+$  group is the presence of an internal hydrogen bond between it and the *n*-orbitals of the acyl moiety, which is countering the expected electrostatic destabilization of the  $n\pi^*$  excited state.

Given we wish to increase photoinitiation efficiency by lowering the  $S_1(n\pi^*)$  and raising the  $T_1(\pi\pi^*)$  states in energy, this is best achieved with a negative charge at the *ortho* position. Indeed, this results in a pH switch significant enough to make the  ${}^1n\pi^*$  and  ${}^3\pi\pi^*$  states degenerate in all solvents except water; even then, the resulting singlet–triplet energy gap  $\Delta E$  is reduced from  $\sim 0.5$  to  $\sim 0.1$  eV (see Supplementary Material for relevant vertical excitation energies). The convergence of these chosen excited states suggests that introducing remote charge to I2959 or, in fact, any molecule with photochemistry arising from excited states of differing symmetries is a practical and powerful method for manipulating photochemistry.

Finally, although the introduction of a positively charged group by the protonation of an amine substituent appears to be an ineffective approach to internal electric field introduction owing to spurious hydrogen-bond formation, it is important to remember that the amine group could instead be replaced with a quaternary ammonium salt. Such structures would not exhibit the unwanted internal hydrogen bond, and could be employed

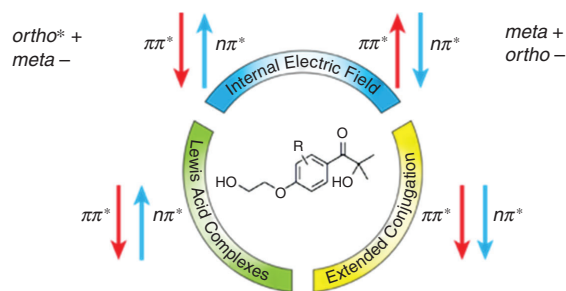


Fig. 8. Summary of calculated effects on the photochemistry of I2959 on introduction of extra functional groups. As noted in the text, the *ortho* positively charged groups stabilize the  $n\pi^*$  through a spurious hydrogen-bonding reaction that could be avoided through use of an alternative functional group to carry the positive charge.

when a low pH environment (required to form  $\text{COO}^-$ ) is inappropriate.

## Conclusions

TD-DFT calculations were performed on functionalized Irgacure I2959, a water-soluble Type I photoinitiator, in order to identify practical strategies for red-shifting its excitation energies while maintaining or improving its photoinitiation efficiency. Fig. 8 summarizes the main results and recommendations, which are also outlined below:

- Extending the  $\pi$ -system will red-shift the UV-vis spectrum, but owing to the  $\pi\pi^*$  states being stabilized and the  $n\pi^*$  being relatively unaffected, it would lead to a decline in photoinitiation efficiency.
- Including LAs to complex with the photoinitiator is a simple strategy that red-shifts  $\pi\pi^*$  transitions and blue-shifts  $n\pi^*$  transitions. The net effect on initiator efficiency varies considerably with the system but we predict that the  $\text{Mg}^{2+}$  complex of I2959 should exhibit the most significantly affected excited state energies, and therefore be a promising candidate as an efficient visible light photoinitiator.

- Including remote (non-conjugated) charged functional groups to electrostatically alter the transition energies is a very powerful strategy that can give more precise control through choice of charge and location. For I2959, best results would be achieved by inclusion of a  $\text{CH}_2\text{C}(\text{O})\text{O}^-$  group in the ortho position.

Work is under way to investigate these designs experimentally for the specific case of Irgacure I2959, but we also stress that the general findings can be applied to manipulation of other photochemical systems.

### Supplementary Material

Further computational results, including total energies and optimized geometries of all species, are available on the Journal's website.

### Conflicts of Interest

The authors declare no conflicts of interest.

### Acknowledgements

MLC gratefully acknowledges a Georgina Sweet ARC Laureate Fellowship (FL170100041), financial support from the ARC Centre of Excellence for Electromaterials Science (CE140100012), and generous allocations of supercomputing time on the National Facility of the Australian National Computational Infrastructure.

### References

- [1] S. Shaik, R. Ramanan, D. Danovich, D. Mandal, *Chem. Soc. Rev.* **2018**, *47*, 5125. doi:10.1039/C8CS00354H
- [2] S. Ciampi, N. Darwish, H. M. Aitken, I. Díez-Perez, M. L. Coote, *Chem. Soc. Rev.* **2018**, *47*, 5146. doi:10.1039/C8CS00352A
- [3] G. Gryn'ova, M. L. Coote, *J. Am. Chem. Soc.* **2013**, *135*, 15392. doi:10.1021/JA404279F
- [4] G. Gryn'ova, M. L. Coote, *Aust. J. Chem.* **2017**, *70*, 367. doi:10.1071/CH16579
- [5] N. S. Hill, M. L. Coote, *J. Am. Chem. Soc.* **2018**, *140*, 17800. doi:10.1021/JACS.8B12009
- [6] D. P. Hagberg, T. Marinado, K. M. Karlsson, K. Nonomura, P. Qin, G. Boschloo, T. Brinck, A. Hagfeldt, L. Sun, *J. Org. Chem.* **2007**, *72*, 9550. doi:10.1021/JO701592X
- [7] A. E. Mohamed, F. H. Ahmed, S. Arulmozhiraja, C. Y. Lin, M. C. Taylor, E. R. Krausz, C. J. Jackson, M. L. Coote, *Mol. Biosyst.* **2016**, *12*, 1110. doi:10.1039/C6MB00033A
- [8] B. B. Noble, A. C. Mater, L. M. Smith, M. L. Coote, *Polym. Chem.* **2016**, *7*, 6400. doi:10.1039/C6PY01445C
- [9] W. Schuurman, P. A. Levett, M. W. Pot, P. R. van Weeren, W. J. A. Dhert, D. W. Hutmacher, F. P. W. Melchels, T. J. Klein, J. Malda, *Macromol. Biosci.* **2013**, *13*, 551. doi:10.1002/MABI.201200471
- [10] B. J. Klotz, D. Gawlitta, A. J. W. P. Rosenberg, J. Malda, F. P. W. Melchels, *Trends Biotechnol.* **2016**, *34*, 394. doi:10.1016/J.TIBTECH.2016.01.002
- [11] K. S. Lim, B. S. Schon, N. V. Mekhileri, G. C. J. Brown, C. M. Chia, S. Prabakar, G. J. Hooper, T. B. F. Woodfield, *ACS Biomater. Sci. Eng.* **2016**, *2*, 1752. doi:10.1021/ACSBIOMATERIALS.6B00149
- [12] S. Jockusch, M. S. Landis, B. Freiermuth, N. J. Turro, *Macromolecules* **2001**, *34*, 1619. doi:10.1021/MA001836P
- [13] J. Zhang, M. Frigoli, F. Dumur, P. Xiao, L. Ronchi, B. Graff, F. Morlet-Savary, J. P. Fouassier, D. Gigmes, J. Lalevée, *Macromolecules* **2014**, *47*, 2811. doi:10.1021/MA500612X
- [14] S. Shi, C. Croutxé-Barghorn, X. Allonas, *Prog. Polym. Sci.* **2017**, *65*, 1. doi:10.1016/J.PROGPOLYMSCI.2016.09.007
- [15] J. Kabatc, M. Zasada, J. Paczkowski, *J. Polym. Sci. A Polym. Chem.* **2007**, *45*, 3626. doi:10.1002/POLA.22112
- [16] D. Jacquemin, I. Duchemin, X. Blase, *J. Chem. Theory Comput.* **2015**, *11*, 5340. doi:10.1021/ACS.JCTC.5B00619
- [17] M. Huix-Rotllant, N. Ferre, *J. Chem. Phys.* **2014**, *140*, 134305. doi:10.1063/1.4869802
- [18] Y. Zhao, D. G. Truhlar, *Theor. Chem. Acc.* **2008**, *120*, 215. doi:10.1007/S00214-007-0310-X
- [19] A. V. Marenich, C. J. Cramer, D. G. Truhlar, *J. Phys. Chem. B* **2009**, *113*, 6378. doi:10.1021/JP810292N
- [20] M. J. Frisch, G. W. Trucks, H. B. Schlegel, G. E. Scuseria, M. A. Robb, J. R. Cheeseman, G. Scalmani, V. Barone, G. A. Petersson, H. Nakatsuji, X. Li, M. Caricato, A. V. Marenich, J. Bloino, B. G. Janesko, R. Gomperts, B. Mennucci, H. P. Hratchian, J. V. Ortiz, A. F. Izmaylov, J. L. Sonnenberg, D. Williams-Young, F. Ding, F. Lipparini, F. Egidi, J. Goings, B. Peng, A. Petrone, T. Henderson, D. Ranasinghe, V. G. Zakrzewski, J. Gao, N. Rega, G. Zheng, W. Liang, M. Hada, M. Ehara, K. Toyota, R. Fukuda, J. Hasegawa, M. Ishida, T. Nakajima, Y. Honda, O. Kitao, H. Nakai, T. Vreven, K. Throssell, J. A. Montgomery Jr, J. E. Peralta, F. Ogliaro, M. J. Bearpark, J. J. Heyd, E. N. Brothers, K. N. Kudin, V. N. Staroverov, T. A. Keith, R. Kobayashi, J. Normand, K. Raghavachari, A. P. Rendell, J. C. Burant, S. S. Iyengar, J. Tomasi, M. Cossi, J. M. Millam, M. Klene, C. Adamo, R. Cammi, J. W. Ochterski, R. L. Martin, K. Morokuma, O. Farkas, J. B. Foresman, D. J. Fox, *Gaussian 16 Revision A.03* **2016** (Gaussian Inc.: Wallingford, CT)
- [21] A. D. McNaught, A. Wilkinson, *IUPAC Compendium of Chemical Terminology*, 2nd edn **1997** (Blackwell Scientific Publications: Oxford).



## 4.4 Implications and Applications

To date, electric fields in photochemistry have been largely confined to Stark spectroscopy, or electrochromism, an area of physics and chemistry that studies how materials behave when subjected to large voltages. This area of research has led to materials with interesting properties, for example smart glasses, which will change their opacity when a voltage is applied. However, this type of chemistry often results in the formal oxidation/reduction of the molecules of the material, which can have significantly different optical properties from their original states. Here, it is shown how static electric fields can be applied in a milder manner, in which certain photochemical properties are enhanced, or tuned, rather than switched on or off from electron transfer reactions.

The studies found that introducing neutral acid or base groups, in conjunction with methyl spacer groups, had very little effect on the photochemical properties of two Type I photoinitiators, acetophenone and Irgacure 2959. Upon formation of the protonated/deprotonated charged species, however, it is found that the energies of their excited states were altered significantly, and that  $n_O\pi^*$  and  $\pi\pi^*$  states were altered in opposite directions. The (de)stabilization of these two types of excited state was dependent on the sign of the charge, i.e. positively charged base groups had an opposite effect compared to negatively charged acid groups; the electric field origin of these effects was further confirmed by a) removal of methyl spacer linkers to form two fragments, and b) application of an external electric field to uncharged species. Finally, these calculations were repeated in a range of solvents with increasingly large dielectric constants, and whilst high dielectric solvents (for example  $H_2O$ ) attenuate the electric field effects, they do remain significant. It is worth noting here that implicit solvent models were used in both Publications 8 and 9; it is understood that implicit solvation is imperfect, and that a range of different effects arising from solvent may be missing from the chemical model. However, “proper” modelling of solvation environments is a long-standing problem in quantum chemistry; this chapter serves to highlight the potential power of electric fields in harnessing photochemical phenomena in a controlled manner. The ultimate test, as it always is when designing molecules, will be whether these effects are

present upon synthesis and experimental testing.

The significance of these effects, in particular the “splitting” of the  $n_O\pi^*$  and  $\pi\pi^*$  states for a given field direction, is that the internal excited states of a molecule can be moved further apart or closer together, as required. This means singlet and triplet states of different symmetries (states which can undergo fast intersystem crossing) can be moved closer together, potentially resulting in higher quantum yields under lower intensity light. It also allows for the possibility to red-shift the reactive states which a molecule may need to be excited into in order to react, and this may prevent photochemical side reactions as high energy light can be avoided.

The next step in this area of research is to synthesize the functionalized molecules designed in either of these two papers. Doing so will allow for the electric field effects to be assessed experimentally and correlated against predicted results obtained from quantum chemistry, and to begin to rationalize the accuracy and merits in the conceptually simple approach to the modelling performed in the two publications. This work is currently underway.

## 4.5 References

- (1) Marian, C. M.; Gilka, N. *Journal of Chemical Theory and Computation* **2008**, *4*, 1501–1515.
- (2) Noble, B. B.; Mater, A. C.; Smith, L. M.; Coote, M. L. *Polymer Chemistry* **2016**, *7*, 6400.
- (3) Bublitz, G. U.; Boxer, S. G. *Annual Review of Physical Chemistry* **1997**, *48*, 213–242.
- (4) Shaik, S.; Mandal, D.; Ramanan, R. *Nature Chemistry* **2016**, *8*, 1091–1098.
- (5) Shaik, S.; Ramanan, R.; Danovich, D.; Mandal, D. *Chemical Society Reviews* **2018**, *47*, 5125–5145.
- (6) Aragonès, A. C.; Haworth, N. L.; Darwish, N.; Ciampi, S.; Bloomfield, N. J.; Wallace, G. G.; Diez-Perez, I.; Coote, M. L. *Nature* **2016**, *531*, 88–91.
- (7) Zhang, L.; Vogel, Y. B.; Noble, B. B.; Gonc, V. R.; Darwish, N.; Brun, A. L.; Gooding, J. J.; Wallace, G. G.; Coote, M. L.; Ciampi, S. *Journal of the American Chemical Society* **2016**, *138*, 9611–9619.
- (8) Zhang, L.; Laborda, E.; Darwish, N.; Noble, B. B.; Tyrell, J. H.; Pluczyk, S.; Le Brun, A. P.; Wallace, G. G.; Gonzalez, J.; Coote, M. L.; Ciampi, S. *Journal of the American Chemical Society* **2018**, *140*, 766–774.

- (9) Ciampi, S.; Darwish, N.; Aitken, H. M.; Díez-Perez, I.; Coote, M. L. *Chemical Society Reviews* **2018**, *47*, 5146–5164.
- (10) Litvinyuk, I. V.; Lee, K. F.; Dooley, P. W.; Rayner, D. M.; Villeneuve, D. M.; Corkum, P. B. *Physical Review Letters* **2003**, *90*, 233003.
- (11) Kanai, T.; Minemoto, S.; Sakai, H. *Nature* **2005**, *435*, 470–474.
- (12) Hush, N. S.; Reimers, J. R. *Journal of Physical Chemistry* **1995**, *99*, 15798–15805.
- (13) Gryn'ova, G.; Marshall, D. L.; Blanksby, S. J.; Coote, M. L. *Nature Chemistry* **2013**, *5*, 474–481.
- (14) Gryn'ova, G.; Coote, M. L. *Journal of the American Chemical Society* **2013**, *135*, 15392–15403.
- (15) Aitken, H. M.; Coote, M. L. *Physical Chemistry Chemical Physics* **2018**, *20*, 10671–10676.
- (16) Blyth, M. T.; Coote, M. L. *The Journal of Organic Chemistry* **2019**, *84*, 1517–1522.
- (17) Klinska, M.; Smith, L. M.; Gryn'ova, G.; Banwell, M. G.; Coote, M. L. *Chemical Science* **2015**, *6*, 5623–5627.
- (18) Heid, E.; Hunt, P. A.; Schröder, C. *Physical Chemistry Chemical Physics* **2018**, *20*, 8554–8563.
- (19) Rouillard, A. D.; Berglund, C. M.; Lee, J. Y.; Polacheck, W. J.; Tsui, Y.; Bonassar, L. J.; Kirby, B. J. *Tissue engineering. Part C, Methods* **2011**, *17*, 173–179.
- (20) Bartnikowski, M.; Bartnikowski, N. J.; Woodruff, M. A.; Schrobback, K.; Klein, T. J. *Acta Biomaterialia* **2015**, *27*, 66–76.
- (21) O'Connell, C. D. et al. *Biofabrication* **2016**, *8*, 015019.
- (22) Yue, K.; Trujillo-de Santiago, G.; Alvarez, M. M.; Tamayol, A.; Annabi, N.; Khademhosseini, A. *Biomaterials* **2015**, *73*, 254–271.
- (23) Klotz, B. J.; Gawlitta, D.; Rosenberg, A. J. W. P.; Malda, J.; Melchels, F. P. W. *Trends in Biotechnology* **2016**, *34*, 394–407.
- (24) Soman, P.; Chung, P. H.; Zhang, A. P.; Chen, S. *Biotechnology and Bioengineering* **2013**, *110*, 3038–3047.

# 5 Theoretical Exploration and Rational Design of Nitroxide Mediated Photopolymerization and Photoalkylation Reactions

## 5.1 Introduction and Key Findings

Nitroxide-mediated polymerization (NMP)<sup>1</sup> is one of the three commonly used approaches to perform controlled, or “pseudo-living”, polymerization reactions.<sup>2</sup> In a controlled polymerization, there is a dynamic equilibrium between the dormant and active forms of the radical reagents (Figure 5.1). In NMP, this dynamic equilibrium heavily favours the dormant, unreactive alkoxyamine, and the resulting propagation reaction proceeds in a temporally controlled manner. This control allows for the formation of polymer chains with a narrow molecular weight distribution, and predetermined functionalities and topologies.

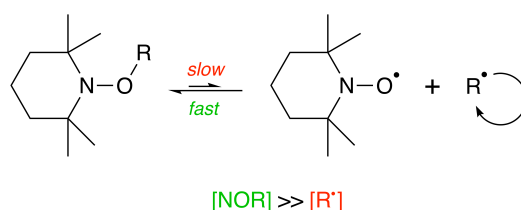


Figure 5.1: Dynamic equilibrium in nitroxide-mediated polymerization

Controlled radical polymerizations aim to limit unwanted side reactions with a low overall concentration of propagating radicals. However, the high temperatures required in NMP (the polymerization of styrene mediated by 2,2',6,6'-tetramethylpiperidine-*N*-oxyl is carried out at 125 °C)<sup>3</sup> results in side reactions involving the nitroxide moiety which can subsequently deactivate the polymerization. The elevated temperatures, high reaction cost, and lack of control over side reactions severely limits the effectiveness and application of NMP,<sup>4,5</sup> and its improvement remains an active area of research. A photochemical approach<sup>6</sup> (nitroxide mediated photopolymerization, or PNMP) is appealing as the milder conditions under which homolysis can take place will prevent thermal side

reactions and reduce the working temperature of the overall polymerization.

Computational chemistry is an important tool for investigating how and why nitroxide reactions may not be proceeding as designed, and is especially necessary in this chapter as the introduction of photoexcited states complicates the overall PNMP process. As well as this, there are limited computational studies into PNMP. That which has been performed<sup>7</sup> utilises TD-DFT and second-order extended multireference quasi-degenerate perturbation theory (XMCQDPT2)<sup>8</sup> to examine photochemical initiation by homolysis. The study only utilises a simple chemical model; one that includes an acetophenone chromophore and a tert-butyl leaving group. As a result, this model does not consider the stability of different monomer units, nor any different cleavage pathways, only homolytic cleavage.

From both a computational and an experimental perspective, PNMP remains a relatively unexplored and unoptimized field of chemistry. The aim of this chapter is to explore different cleavage pathways that may be accessible to light-activated alkoxyamines, provide a rationale as to why experiments can point to the products of PNMP but not demonstrate controlled polymerization behaviour, and identify strategies as to how this chemistry can be manipulated.

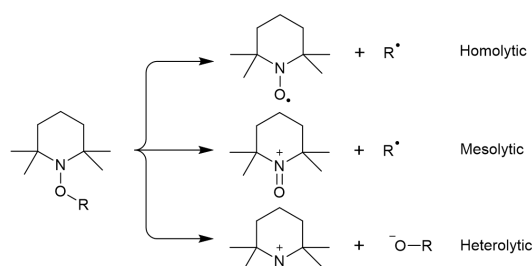
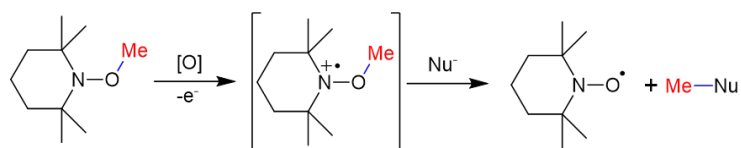


Figure 5.2: Potential cleavage products of an activated nitroxide species. The activation step is not shown, but could be thermal<sup>9</sup> or light energy,<sup>6</sup> or oxidation<sup>10</sup>

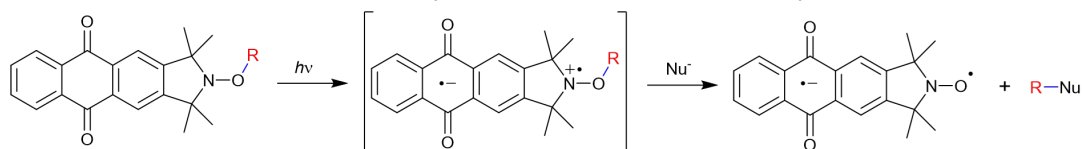
In Publication 10, two alkoxyamines are explored using ground- and excited-state methods. One of the systems has been shown to undergo homolysis under UV irradiation, and the second set of alkoxyamines have been shown to give uncontrolled free-radical polymerization reactions.<sup>6</sup> The inclusion of a photo-mesolytic-type cleavage pathways is explored for the first time, and can be used to rationalize the performance of a class of alkoxyamines for PNMP, as well as the monomer-dependent performance

of these molecules.

The second publication, Publication 11, centres on the rational design of compounds that can undergo cleavage reactions as described in Publication 10 upon irradiation of light. Specifically, alkoxyamines bonded to an anthraquinone chromophore are studied, as in Publications 3-7 the substitution pattern of anthraquinones has been shown to alter their photochemical properties, and in Publications 8 and 9 electric fields are also shown to alter these properties. The substitution dependence is taken advantage of in Publication 11, as amino and alcohol groups, and charged functional groups, are employed to alter the energies and charge separation of  $n_N\pi^*$  states. As the properties of the  $n_N\pi^*$  excited state are altered, it is demonstrated how the resulting molecules can be used for PNMP and other synthetic reactions.



(a) Electrochemical methylation mechanism studied by Coote *et al*<sup>10</sup>



(b) Photochemical alkylation procedure employing photoactive nitroxides (Publication 11)

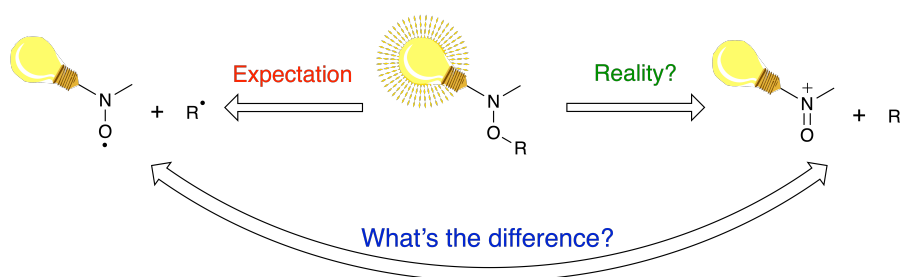
Figure 5.3: Activated nitroxide molecules for *in situ* methylation/alkylation

## 5.2 Publication 10

### Mesolytic versus Homolytic Cleavage in Photochemical Nitroxide Mediated Polymerization

Nicholas S. Hill, Melinda J. Fule, Jason Morris, Jean-Louis Clement, Yohann Guillaneuf, Didier Gimes, Michelle L. Coote

*Macromolecules* **2020**, 53, 1567–1572.



This is manuscript that has been published to *Macromolecules* for peer review. All computational results and subsequent discussion of are my own work. Prof. Michelle Coote assisted with the direction of the theoretical investigations and corrected my draft write-ups. Prof. Yohann Guillaneuf and Dr Jason Morris provided experimental direction and insightful discussions into photonitroxide chemistry. [Supplementary material is available online.](#)

### Statement of Contribution

This thesis is submitted as a Thesis by Compilation in accordance with [https://policies.anu.edu.au/ppi/document/ANUP\\_003405](https://policies.anu.edu.au/ppi/document/ANUP_003405)

I declare that the research presented in this Thesis represents original work that I carried out during my candidature at the Australian National University, except for contributions to multi-author papers incorporated in the Thesis where my contributions are specified in this Statement of Contribution.

Title: Mesolytic versus Homolytic Cleavage in Photochemical Nitroxide Mediated Polymerization

Authors: Nicholas S. Hill, Melinda J. Fule, Jason Morris, Jean-Louis Clement, Yohann Guillaneuf, Didier Gignes, Michelle L. Coote

Publication outlet: Macromolecules

Current status of paper: Published

Contribution to paper: I am the first contributing computational chemistry author. All computational results, mechanistic insight, and subsequent discussion are my own work

Senior author or collaborating authors endorsement: Michelle Coote

Nicholas Hill



14/05/2020

Candidate - Print Name

Signature

Date

#### Endorsed

Michelle Coote



14/05/2020

Primary Supervisor – Print Name

Signature

Date

Luke Connal



14/05/2020

Delegated Authority – Print Name

Signature

Date



## Mesolytic Versus Homolytic Cleavage in Photochemical Nitroxide-Mediated Polymerization

Nicholas S. Hill, Melinda J. Fule, Jason Morris, Jean-Louis Clément, Yohann Guillauneuf, Didier Gigmes, and Michelle L. Coote\*



Cite This: *Macromolecules* 2020, 53, 1567–1572



Read Online

ACCESS |



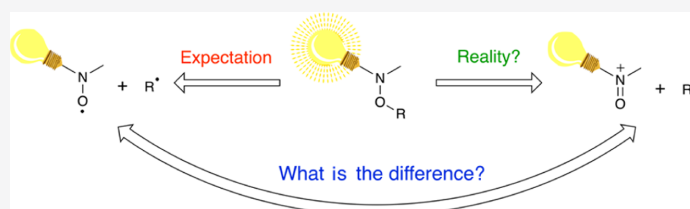
Metrics & More



Article Recommendations



Supporting Information



**ABSTRACT:** Time-dependent density functional theory calculations have been performed to study the photocleavage reactions of chromophore-functionalized alkoxyamines in nitroxide-mediated photopolymerization. Two case studies were considered: azaphenylene derivatives and benzophenone-based alkoxyamines. For the azaphenylene derivatives, we show that the expected homolysis pathway is actually inaccessible. Instead, these alkoxyamines exhibit low-lying  $n, \pi^*$  excited states that exhibit an electronic structure about the nitroxide moiety similar to that of the formally oxidized radical cation. As a result, the cleavage of these alkoxyamines can be described as mesolytic-like rather than homolytic. As with formally oxidized species, mesolytic cleavage can result in the production of either carbon-centered radicals or carbocations, with only the former resulting in radical polymerization. Here, the cleavage products are found to be dependent on the respective radical/cation stabilities of the monomer units of choice (styrene, ethyl propanoate, and ethyl isobutyrate). In contrast to the azaphenylene derivatives, in the benzophenone-based alkoxyamines, conjugation between the nitroxide and chromophore moieties appears to facilitate homolysis because of the ideal alignment of singlet and triplet states of different symmetries.

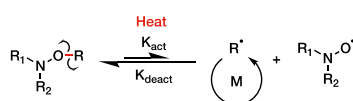
### INTRODUCTION

Methods for controlling the molecular weight and architecture in free-radical polymerization have broad applications in the synthesis of smart materials for use in applications ranging from drug delivery to lithography.<sup>1,2</sup> One such technique is nitroxide-mediated polymerization (NMP).<sup>3–6</sup> In this process, control is achieved through a dynamic equilibrium between the dormant alkoxyamine and the active propagating radical (Scheme 1). By minimizing the concentration of active propagating radicals with respect to the population of dormant alkoxyamines, bimolecular termination is minimized with respect to chain growth, while imparting a synthetically useful

nitroxide functionality on the chain end. However, a key drawback of NMP is the requirement for elevated temperatures, which can lead to side reactions that deactivate the dynamic equilibrium upon NMP, depends.<sup>7</sup>

To address this problem, the use of light, rather than heat, to activate the alkoxyamine has been explored.<sup>8–10</sup> However, while the so-called photo-nitroxide-mediated polymerization (PNMP) has shown extremely promising results in certain systems, overall the results have been mixed, with some systems displaying control, others displaying noncontrolled polymerization, and some displaying no reaction at all. For example, while azaphenylene derivatives are effective PNMP agents for styrene polymerization, alkoxyamines containing chromophores such as 9,10-diphenylanthracene and 9,10-bis-(phenylethynyl) anthracene undergo fluorescence instead.<sup>11</sup> A better understanding of the photochemical processes is

**Scheme 1. Controlling Equilibrium for NMP, Where an Alkoxyamine is Thermally Cleaved Into the Active Transient Carbon Centered Radical and the Persistent Nitroxide Radical.**



Received: January 20, 2020

Revised: February 6, 2020

Published: February 26, 2020

involved, and their dependence on chemical structures is essential to the design of more effective PNMP agents.

To date, it has been assumed that PNMP occurs via energy transfer from the chromophore to the breaking of the NO–R bond on the triplet surface, so as to cause homolysis in the same manner as standard NMP.<sup>8,12</sup> This reactive process is in competition with various nonreactive processes, as represented in Figure 1. However, mesolytic cleavage (Scheme 2) is a

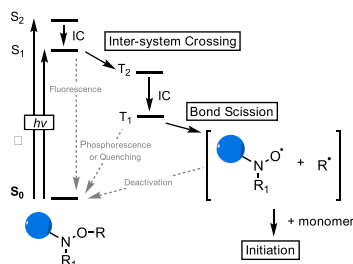
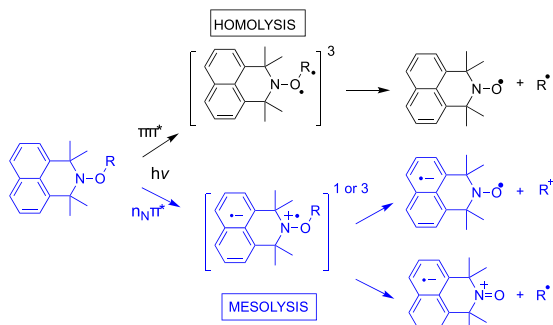


**Figure 1.** (A) Simplified Jablonski diagram showing the photochemical processes leading to homolytic cleavage and the competing nonreactive relaxation processes.

#### Scheme 2. Alternative Homolysis (Black) and mesolysis (Blue) Pathways Demonstrated for an Azaphenylene<sup>a</sup>



<sup>a</sup>Mesolytic cleavage can result in either a carbocation or a carbon-centered radical depending on their relative stabilities and those of the nitroxide and oxoammonium.

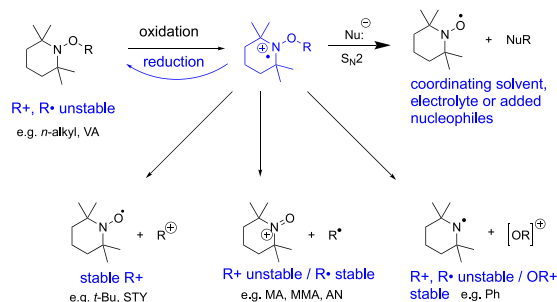
conceivable alternative which could help explain some of the unexpected failures of PNMP agents. The excited state capable of leading to mesolytic cleavage is the  $n_N\pi^*$  state, on either the singlet or triplet surface. This excited state results in the transfer of a nonbonding electron from the nitrogen atom into the  $\pi^*$ -system of the chromophore, resulting in a biradical charge-separated state. The radical cation centered on the nitrogen therefore possesses the valency necessary for mesolysis.

As shown in Scheme 2, mesolytic cleavage results in the formation of a radical and a cation, with the ultimate location of these species dependent on their respective stabilities, that is, nitroxide radical and carbocation versus oxoammonium cation and carbon-centered radical. In these situations, it is unclear if the propagating species and nitroxide can recouple to reform the dormant species. However, it is likely that if a carbon-centered radical is formed, the zwitterionic nitroxide fragment could relax back to a nitroxide, allowing controlled radical polymerization to proceed. If, however, a carbocation is

formed, cationic polymerization may occur with fate of the nitroxide radical anion dependent on protic impurities.

Interestingly, the local  $[\text{NO-R}]^{\bullet+}$  environment in the  $n_N\pi^*$  state directly resembles that of formally oxidized alkoxyamines, which have recently been shown to undergo mesolytic cleavage. Experiments have shown that the exact specific cleavage behavior depends on the leaving group and the presence or absence of nucleophiles including coordinating solvents such as acetonitrile (see Scheme 3).<sup>13–16</sup> As seen in

#### Scheme 3. Effect of R on the Oxidation Behavior of TEMPO-Based Alkoxyamines<sup>a</sup>



<sup>a</sup>Included among the R groups are models of the propagating species in polymerizations of vinyl acetate (VA,  $\text{CH}_2\text{OCOCH}_3$ ), styrene (STY,  $\text{CH}(\text{CH}_3)\text{Ph}$ ), methyl acrylate (MA,  $\text{C}(\text{CH}_3)\text{COOCH}_3$ ), methyl methacrylate (MMA,  $\text{C}(\text{CH}_3)_2\text{COOCH}_3$ ), and acrylonitrile (AN,  $\text{CH}(\text{CH}_3)\text{CN}$ ).<sup>13</sup>

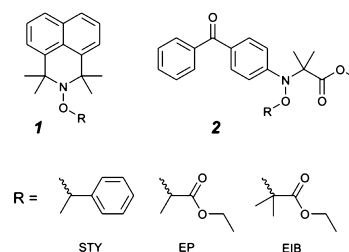
Scheme 3, in the oxidized species at least, cleavage to a carbon-centered radical is expected for acrylate and methacrylate polymerizations but not for styrene which will produce carbocations.

Summing up, while it has been assumed until now that PNMP proceeds via energy transfer and standard homolytic cleavage, the possibility of mesolytic cleavage and its implications has not been explored. If it occurs, this has significant implications for the success or failure of PNMP as it can lead to species other than carbon-centered propagating radicals being produced. In this work, we use computational chemistry to study the cleavage pathways in two key PNMP families, azaphenalenenes (1) and benzophenone-based nitroxides (2), with a view to better informing reagent design (Scheme 4).

#### COMPUTATIONAL METHODOLOGY

All electronic structure calculations were performed with density functional theory (DFT) or its excited-state extension,

#### Scheme 4. Test Set Considered



time-dependent DFT (TD-DFT), using the Gaussian 16.C01 software package.<sup>17</sup> The M06-2X functional<sup>18</sup> was used for both types of calculations, as it has been shown to perform well when describing free-radical processes and the excited states of organic chromophores. The 6-31+G(d,p) basis set was employed for all calculations, and the SMD universal solvent model<sup>19</sup> was used for solvent-phase electronic energies. The solvent used was ethyl ethanoate, as it is a solvent that will exhibit properties similar to that of bulk acrylate monomers. TD-DFT chosen for investigating the excited states of the alkoxyamines as multireference calculations, requiring a large active space that includes  $n_N/O$ ,  $\pi$  and  $\pi^*$ , and  $\sigma$  orbitals for a proper description of the dissociation pathways, is too expensive for these systems. M06-2X has, however, been shown to give good agreement with respect to predicting the ordering of states of differing symmetries and at predicting singlet–triplet gaps.<sup>20</sup> Although calculations of accurate excited-state free energies are not possible with TD-DFT, enough information about the character and therefore reactivity of the excited states is possible.

## RESULTS AND DISCUSSION

**Azaphenalenenes (1).** To explore the likelihood of homolytic versus mesolytic cleavage, TD-DFT calculations were first used to construct Jablonski diagrams for a family of 6-azaphenalenenes (Figure 2). 6-Azaphenalenenes have been shown

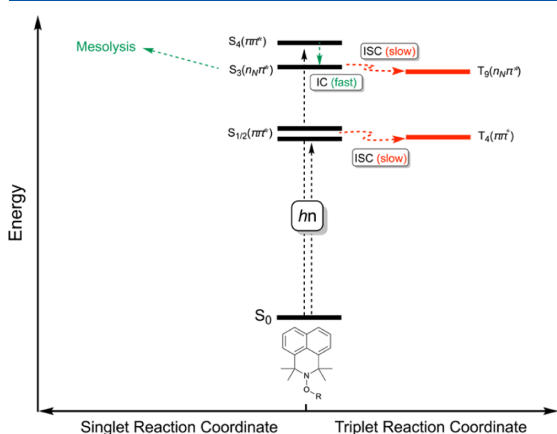


**Figure 2.** Simplified Jablonski diagram for azaphenalenenes functionalized with R groups shown in Scheme 4. Characters of the low-lying states are found to be independent of the R group as they are localized on the azaphenalene moiety. Radiative processes are not shown but they can be expected to compete with radiationless processes.

to be effective PNMP agents for styrene polymerization but not for (meth)acrylates,<sup>11</sup> although this latter result was attributed to side reactions rather than problems in the photodissociation. In the present work, styrene, methyl acrylate, and methyl methacrylate were modeled using unimeric R-groups of styrene (STY), ethyl propanoate, and ethyl isobutyrate, respectively. Qualitative results for each of the three leaving groups are shown in Figure 3; the low-lying states are localized to the chromophore, and the characters of these states are found to be independent of the R-group. The vertical excitation energies change only minimally with the R-group.

In the azaphenalenenes, the first singlet excited state is a  $\pi\pi^*$  transition centered on the chromophore. However, the accompanying triplet state nearest in energy (average  $\Delta E_{S-T}(\pi\pi^*) = -0.07$  eV between R-groups) is also of  $\pi\pi^*$  character rather than of  $n_N\pi^*$  character. Intersystem crossing (ISC) between the singlet and triplet states of the same symmetry does not occur,<sup>21</sup> and so the reactive  $^3\pi\pi^*$  state is inaccessible. Thus, populating the bright  $^1\pi\pi^*$  would not result in any reaction as the valency around the nitroxide moiety will remain unchanged. Instead, for dissociation to occur, only mesolytic cleavage from  $S_3$  (average  $\Delta E_{S-T}(n_N\pi^*) = -0.05$  eV) is available. In the azaphenalene derivatives, population of the dark  $n_N\pi^*$  state is likely possible by first populating the bright  $S_4(\pi\pi^*)$  state which lies relatively close in energy to the  $S_3(n_N\pi^*)$  state (average  $\Delta E = +0.3$  eV). As a result, mesolysis, if it occurs, is the only possible reactive outcome in this family of reagents.

While TD-DFT is sufficiently reliable to draw this qualitative conclusion, it is not sufficiently accurate for predicting quantitative reaction energies. As described above, accurate alternatives such as multireference methods are cost-prohibitive for these large systems. To qualitatively assess the likely mesolytic cleavage behavior, we can instead examine the ground state of formally oxidized species. Figure 3 shows the

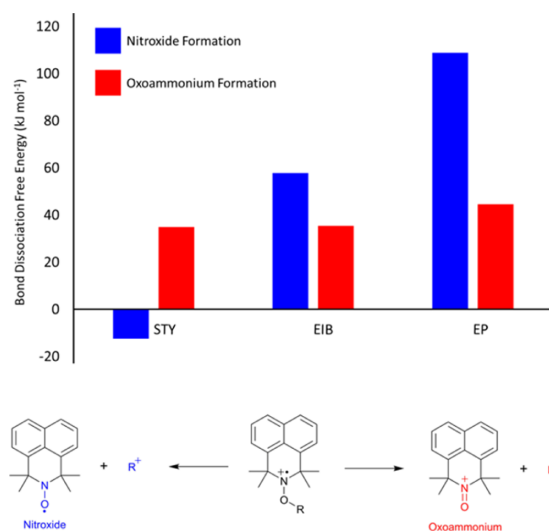


**Figure 3.** Bond dissociation Gibbs free energies for the (ground state) oxidized 6-azaphenalenenes, showing results as a function of the leaving group for mesolytic cleavage to a nitroxide radical and a carbocation and cleavage to an oxoammonium and a carbon-centered radical.

computed bond dissociation Gibbs free energies for mesolytic cleavage to a nitroxide radical and a carbocation and cleavage to an oxoammonium and a carbon-centered radical.

From Figure 3, it is seen that the styrene-derivative of oxidized 6-azaphenalene prefers to undergo cleavage to a carbocation, while the (meth)acrylates prefer to cleave to a radical. Moreover, the energetic cost of cleavage is the least for the styrene leaving group and the most for the acrylate leaving group, as one might expect based on both radical and carbocation stability considerations. This is consistent with experimental observations for the oxidative cleavage of the corresponding TEMPO-based analogues.<sup>13–16</sup> If the results

above were to be applied also to the corresponding excited-state mesolytic cleavage, it would suggest that styrene actually undergoes photoinitiated cationic polymerization with this PNMP agent (which would still be consistent with the observed control) and the acrylates in particular struggle to undergo cleavage at all, which could help explain the failed experiments with this monomer.

While most of the trends in the calculations of Figure 3 would be mirrored in the excited-state mesolysis energies, there are two important differences: (1) the excited states are higher in energy, and this additional energy helps to overcome the otherwise unfavorable Gibbs free energies requirements; (2) the chromophore bears a remote negative charge which is able to electrostatically interact with the nitroxide functionality. This latter effect would preferentially stabilize the oxoammonium over the nitroxide and systematically reduce the mesolytic cleavage energies for carbon-centered radical production.

In order to assess the potential impact of the negative charge that will be present in the charge-separated, biradical  $n_N\pi^*$  excited state, a negatively charged  $BF_4$  ion was introduced to the azaphenalene-styrene radical cation system. The difference in reaction free energies for styrene/azaphenalene radical/cation formation with and without the  $BF_4$  salt is shown in Table 1. Table 1 clearly shows how the electrostatic interaction

**Table 1. Reaction Free Energies ( $\text{kJ mol}^{-1}$ ) for Azaphenalene–Styrene Mesolysis with and without  $BF_4$  Present**

product	STY radical	STY cation	$\Delta\Delta G_{\text{rad-cat}}^0$
no $BF_4$	+35.0	−12.5	+47.4
with $BF_4$	+55.7	+70.5	−14.8

between the negative  $BF_4$  salt and positive radical cation stabilizes the formation of the oxoammonium and the styrene radical.

One could consider the formally oxidized species and the zwitterionic  $BF_4$  salt as limiting cases, with the true behavior somewhere in between the two. While quantitative results are not possible without prohibitive multireference calculations, one can conclude that mesolysis is the only available pathway for these systems. For (meth)acrylates, carbon-centered radicals are preferred over carbocations, while for styrene, the two pathways are in reasonably close competition and cations should not be ruled out.

**Benzophenone Derivatives (2).** The benzophenone-based alkoxyamines have been shown to initiate photopolymerization of *n*-butyl acrylate with a partial living character.<sup>9</sup> In contrast to the azaphenalenes, the chromophore is directly bonded to the nitroxide moiety making them a better candidate for direct homolysis via energy transfer.

Indeed, examining the excited states from TD-DFT highlights some clear differences between the benzophenone (Figure 4) and azaphenalene (Figure 2) derivatives. For the azaphenalenes, TD-DFT predicts singlet and triplet states of the same symmetry close in energy, suggesting that ISC to the triplet manifold would be uncompetitive, relative to reactivity from the singlet states. For the benzophenone derivatives, however, this is not the case, with singlet and triplet states of different symmetries predicted to be near-degenerate in energy. In contrast to azaphenalene derivatives, this would allow for efficient population of low-lying triplet states, resulting in

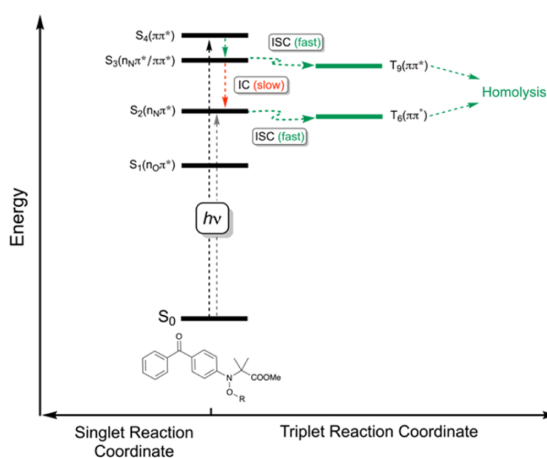


**Figure 4.** Simplified Jablonski diagram for R-functionalized benzophenone derivatives shown in Scheme 4.

triplet photoreactivity similar to that of acetophenone. In addition to this, population of the  $^1n_N\pi^*$  state, which would possess the correct valency for mesolysis, is

1. Difficult to populate because of the transition being symmetry-forbidden and no other singlet states being close in energy (slow internal conversion)
2. Likely unreactive; Figure 5 shows that the BDFEs for mesolysis of the formally oxidized benzophenone

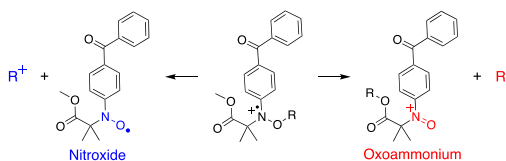
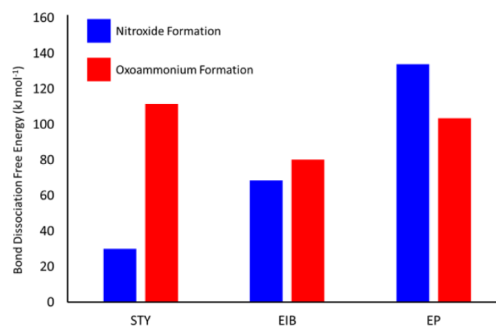


**Figure 5.** Bond dissociation Gibbs free energies for cleavage of oxidized benzophenone nitroxide and oxoammonium species.

derivatives suggest that even upon oxidation, cleavage to either a nitroxide or oxoammonium is unfavorable (except for with styrene as an R group).

Summing up, in contrast to the azaphenalenes, for the benzophenone derivatives, the triplet  $\pi\pi^*$  state can be populated, while the  $n_N\pi^*$  state is difficult to populate and likely to be in any case unreactive. Hence, triplet reactivity and

bond homolysis, rather than mesolysis, is the preferred pathway for these systems.

## CONCLUSIONS

Theoretical calculations have been performed which highlight the potential role of mesolytic cleavage in describing the cleavage pathways of photoactive NMP agents. Mesolytic cleavage can be used to explain the monomer-dependent performance of PNMP. The radical rearrangement upon mesolytic-like cleavage can regenerate the nitroxide radical (when mesolysis produces R<sup>•</sup>) or the hydroxylamine (when mesolysis produces R<sup>+</sup>). However, analogous to type II photoinitiators such as anthraquinones, electron transfer reactions with additives (or impurities) such as amines, halides, and so forth<sup>22</sup> can compete and negatively impact the radical–radical recombination required for “living” polymerization reactions.

The consequences of this study are as follows:

1. Conjugation between the nitroxide and chromophore moieties appears to facilitate homolysis because of the ideal alignment of singlet and triplet states of different symmetries. However, it must be noted that such conjugation can also promote side reactions such as N–O homolysis or beta-fragmentation (on the second alkyl group bearing the nitroxide).<sup>9</sup>
2. When there is no conjugation between the nitroxide and the chromophore, a low-lying, charge-separated  $n_N\pi^*$  excited state is accessible, which possesses the valency around the nitroxide to undergo mesolytic rather than homolytic cleavage.
3. The choice of the monomer remains important when designing PNMP agents: as with thermally-initiated NMP, acrylate derivatives still suffer from side-reactions and poor “living” behavior.
4. The mesolytic pathway may lend itself to other synthetically useful photoreactions, outside that of NMP applications, analogous to our recent use of formally oxidized alkoxyamines as in situ methylation agents.<sup>15</sup> Indeed, this trapping of the  $n_N\pi^*$  intermediate with a strong nucleophile would provide a practical experimental test of these findings. Work in this direction is currently underway.

## ASSOCIATED CONTENT

### Supporting Information

The Supporting Information is available free of charge at <https://pubs.acs.org/doi/10.1021/acs.macromol.0c00134>.

Raw energies for cleavage reactions, raw vertical excitation energies and dominant character, and gas phase structure cartesian coordinates (PDF)

## AUTHOR INFORMATION

### Corresponding Author

Michelle L. Coote – ARC Centre of Excellence for Electromaterials Science, Research School of Chemistry, Australian National University, Canberra, Australian Capital Territory 2601, Australia; [orcid.org/0000-0003-0828-7053](https://orcid.org/0000-0003-0828-7053); Email: [michelle.coote@anu.edu.au](mailto:michelle.coote@anu.edu.au)

### Authors

Nicholas S. Hill – ARC Centre of Excellence for Electromaterials Science, Research School of Chemistry, Australian National

University, Canberra, Australian Capital Territory 2601, Australia

Melinda J. Fule – ARC Centre of Excellence for Electromaterials Science, Research School of Chemistry, Australian National University, Canberra, Australian Capital Territory 2601, Australia

Jason Morris – Aix Marseille Univ, CNRS, ICR UMR 7273, 13397 Marseille, France

Jean-Louis Clément – Aix Marseille Univ, CNRS, ICR UMR 7273, 13397 Marseille, France

Yohann Guillauneuf – Aix Marseille Univ, CNRS, ICR UMR 7273, 13397 Marseille, France; [orcid.org/0000-0002-5390-1553](https://orcid.org/0000-0002-5390-1553)

Didier Gignes – Aix Marseille Univ, CNRS, ICR UMR 7273, 13397 Marseille, France; [orcid.org/0000-0002-8833-8393](https://orcid.org/0000-0002-8833-8393)

Complete contact information is available at:

<https://pubs.acs.org/doi/10.1021/acs.macromol.0c00134>

## Funding

Australian Research Council (CE140100012, FL170100041).

## Notes

The authors declare no competing financial interest.

## ACKNOWLEDGMENTS

The authors acknowledge financial support from the Australian Research Council (ARC) Centre of Excellence for Electromaterials Science, an ARC Laureate Fellowship (to M.L.C.) and generous supercomputing time from the National Computational Infrastructure.

## REFERENCES

- (1) Matyjaszewski, K.; Spanswick, J. Controlled/Living Radical Polymerization. *Mater. Today* **2005**, *8*, 26–33.
- (2) Matyjaszewski, K. Architecturally Complex Polymers with Controlled Heterogeneity. *Science* **2011**, *333*, 1104.
- (3) Hawker, C. J.; Bosman, A. W.; Harth, E. New Polymer Synthesis by Nitroxide Mediated Living Radical Polymerizations. *Chem. Rev.* **2001**, *101*, 3661–3688.
- (4) Grubbs, R. B. Nitroxide-Mediated Radical Polymerization: Limitations and Versatility. *Polym. Rev.* **2011**, *51*, 104–137.
- (5) Bertin, D.; Gignes, D.; Marque, S. R. A.; Tordo, P. Kinetic Subtleties of Nitroxide Mediated Polymerization. *Chem. Soc. Rev.* **2011**, *40*, 2189–2198.
- (6) Nicolas, J.; Guillauneuf, Y.; Lefay, C.; Bertin, D.; Gignes, D.; Charleux, B. Nitroxide-Mediated Polymerization. *Prog. Polym. Sci.* **2013**, *38*, 63–235.
- (7) Gryn'ova, G.; Lin, C. Y.; Coote, M. L. Which Side-Reactions Compromise Nitroxide Mediated Polymerization? *Polym. Chem.* **2013**, *4*, 3744.
- (8) Chen, M.; Zhong, M.; Johnson, J. A. Light-Controlled Radical Polymerization: Mechanisms, Methods, and Applications. *Chem. Rev.* **2016**, *116*, 10167–10211.
- (9) Guillauneuf, Y.; Bertin, D.; Gignes, D.; Versace, D.-L.; Lalevée, J.; Fouassier, J.-P. Toward Nitroxide-Mediated Photopolymerization. *Macromolecules* **2010**, *43*, 2204–2212.
- (10) Morris, J.; Telitel, S.; Fairfull-Smith, K. E.; Bottle, S. E.; Lalevée, J.; Clément, J.-L.; Guillauneuf, Y.; Gignes, D. Novel Polymer Synthesis Methodologies Using Combinations of Thermally- and Photochemically-Induced Nitroxide Mediated Polymerization. *Polym. Chem.* **2015**, *6*, 754–763.
- (11) Bottle, S. E.; Clément, J.-L.; Fleige, M.; Simpson, E. M.; Guillauneuf, Y.; Fairfull-Smith, K. E.; Gignes, D.; Blinco, J. P. Light-Active Azaphenylene Alkoxyamines: Fast and Efficient Mediators of a Photo-Induced Persistent Radical Effect. *RSC Adv.* **2016**, *6*, 80328–80333.

(12) Huix-Rotllant, M.; Ferré, N. Theoretical Study of the Photochemical Initiation in Nitroxide-Mediated Photopolymerization. *J. Phys. Chem. A* **2014**, *118*, 4464–4470.

(13) Hammill, C. L.; Noble, B. B.; Norcott, P. L.; Ciampi, S.; Coote, M. L. Effect of Chemical Structure on the Electrochemical Cleavage of Alkoxyamines. *J. Phys. Chem. C* **2019**, *123*, 5273–5281.

(14) Noble, B. B.; Norcott, P. L.; Hammill, C. L.; Ciampi, S.; Coote, M. L. Mechanism of Oxidative Alkoxyamine Cleavage: The Surprising Role of the Solvent and Supporting Electrolyte. *J. Phys. Chem. C* **2019**, *123*, 10300–10305.

(15) Norcott, P. L.; Hammill, C. L.; Noble, B. B.; Robertson, J. C.; Olding, A.; Bissember, A. C.; Coote, M. L. TEMPO–Me: An Electrochemically Activated Methylating Agent. *J. Am. Chem. Soc.* **2019**, *141*, 15450–15455.

(16) Zhang, L.; Laborda, E.; Darwish, N.; Noble, B. B.; Tyrell, J. H.; Pluczyk, S.; Le Brun, A. P.; Wallace, G. G.; Gonzalez, J.; Coote, M. L.; et al. Electrochemical and Electrostatic Cleavage of Alkoxyamines. *J. Am. Chem. Soc.* **2018**, *140*, 766–774.

(17) Frisch, M. J.; Trucks, G. W.; Schlegel, H. B.; Scuseria, G. E.; Robb, M. A.; Cheeseman, J. R.; Scalmani, G.; Barone, V.; Petersson, G. A.; Nakatsuji, H.; et al. *Gaussian 16*, Revision C.01; Gaussian, Inc., 2016.

(18) Zhao, Y.; Truhlar, D. G. The M06 Suite of Density Functionals for Main Group Thermochemistry, Thermochemical Kinetics, Noncovalent Interactions, Excited States, and Transition Elements: Two New Functionals and Systematic Testing of Four M06-Class Functionals and 12 Other Function. *Theor. Chem. Acc.* **2007**, *120*, 215–241.

(19) Marenich, A. V.; Cramer, C. J.; Truhlar, D. G. Universal Solvation Model Based on Solute Electron Density and on a Continuum Model of the Solvent Defined by the Bulk Dielectric Constant and Atomic Surface Tensions. *J. Phys. Chem. B* **2009**, *113*, 6378–6396.

(20) Jacquemin, D.; Perpète, E. A.; Ciofini, I.; Adamo, C.; Electrochimie, L.; Cnrs-enscp, U. M. R. Assessment of Functionals for TD-DFT Calculations of Singlet-Triplet Transitions. *J. Chem. Theory Comput.* **2010**, *6*, 1532–1537.

(21) McNaught, A. D.; Wilkinson, A. *IUPAC Compendium of Chemical Terminology*, 2nd ed.; Blackwell Scientific Publications, 1997.

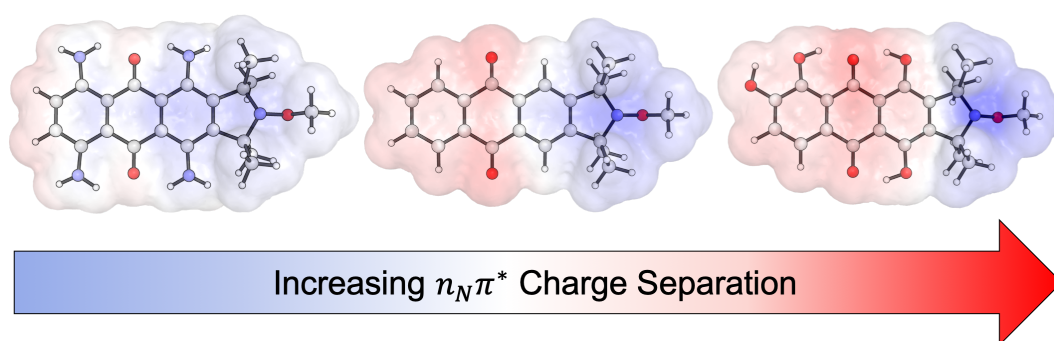
(22) Zhang, J.; Launay, K.; Hill, N. S.; Zhu, D.; Cox, N.; Langley, J.; Lalevé, J.; Stenzel, M. H.; Coote, M. L.; Xiao, P. Disubstituted Aminoanthraquinone-Based Photoinitiators for Free Radical Polymerization and Fast 3D Printing under Visible Light. *Macromolecules* **2018**, *51*, 10104–10112.

### 5.3 Publication 11

#### Rational Design of Photo-cleavable Alkoxyamines for Polymerization and Synthesis: Promotion and Deactivation of Cleavage Pathways

Nicholas S. Hill, Michelle L. Coote

*Physical Chemistry Chemical Physics* - Submitted 2020



This is manuscript that has been submitted to the *Physical Chemistry Chemical Physics* for peer review. All computational results and subsequent discussion of are my own work. Prof. Michelle Coote assisted with the direction of the theoretical investigations and corrected my draft write-ups. Prof. Yohann Guillaneuf and Dr Jason Morris provided experimental direction and insightful discussions into photonitroxide chemistry. Supplementary material is in Appendix A.2.

### Statement of Contribution

This thesis is submitted as a Thesis by Compilation in accordance with [https://policies.anu.edu.au/ppi/document/ANUP\\_003405](https://policies.anu.edu.au/ppi/document/ANUP_003405)

I declare that the research presented in this Thesis represents original work that I carried out during my candidature at the Australian National University, except for contributions to multi-author papers incorporated in the Thesis where my contributions are specified in this Statement of Contribution.

Title: Rational Design of Photo-cleavable Alkoxyamines for Polymerization and Synthesis: Promotion and Deactivation of Cleavage Pathways

Authors: Nicholas S. Hill, Michelle L. Coote

Publication outlet: Physical Chemistry Chemical Physics

Current status of paper: Submitted

Contribution to paper: I am the first contributing computational chemistry author. All computational results, mechanistic insight, and subsequent discussion are my own work

Senior author or collaborating authors endorsement: Michelle Coote

Nicholas Hill



14/05/2020

Candidate - Print Name

Signature

Date

### Endorsed

Michelle Coote



14/05/2020

Primary Supervisor – Print Name

Signature

Date

Luke Connal



14/05/2020

Delegated Authority – Print Name

Signature

Date





PCCP

**Rational Design of Photo-cleavable Alkoxyamines for  
Polymerization and Synthesis**

Journal:	<i>Physical Chemistry Chemical Physics</i>
Manuscript ID	Draft
Article Type:	Paper
Date Submitted by the Author:	n/a
Complete List of Authors:	Coote, Michelle; Australian National University, Research School of Chemistry Hill, Nicholas; Australian National University, Research School of Chemistry

SCHOLARONE™  
Manuscripts

## Rational Design of Photo-cleavable Alkoxyamines for Polymerization and Synthesis

Nicholas S. Hill<sup>a</sup> and Michelle L. Coote<sup>a\*</sup>

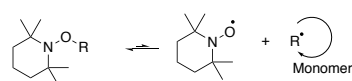
Received 00th January 20xx,  
Accepted 00th January 20xx

DOI: 10.1039/x0xx00000x

Theoretical calculations have been performed in order to investigate the impact of different substitution patterns on predicted photoreactivity of alkoxyamines fused to an anthraquinone chromophore. Amino and hydroxy groups (similar to those which have been previously synthesized) are introduced and their effect on excited state energies and charge transfer is assessed. Analogous to formally oxidized alkoxyamines, the charge-separated  $n_{\text{N}}\pi^*$  state can undergo mesolytic cleavage or bimolecular or  $S_{\text{N}}2$  reactions with nucleophiles, according to the substitution patterns and other reagents present. While homolytic cleavage is in principle promoted by triplet  $\pi\pi^*$  states, the accessible  $\pi\pi^*$  triplet states in this system are centered on the chromophore and unreactive. We show that the reactive  $n_{\text{N}}\pi^*$  state, which bears a negative charge, is stabilized by hydroxy substitution while amino substitution will destabilize it. After mesolysis to a carbon centred radical, the nitroxide radical re-forms; however, when carbocations are produced the remaining open-shell singlet is stable and unable to undergo coupling with the carbocation.

### Introduction

Nitroxide-mediated polymerization (NMP) is an important industrial process, used for controlling the molecular weight and architecture in free-radical polymerization.<sup>1–3</sup> It works by establishing a dynamic equilibrium between the active propagating radical and a dormant alkoxyamine (Scheme 1).



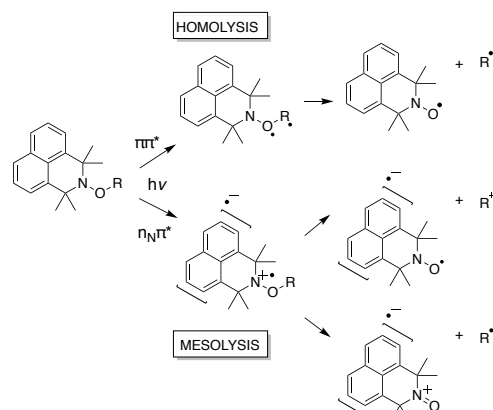
Scheme 1. Nitroxide mediated polymerization

A key drawback with nitroxide mediated polymerization, however, is the requirement for elevated temperatures can promote unwanted side reactions.<sup>4–13</sup> As a result, the development of photochemical NMP (PNMP) is an important goal as the activation of the nitroxide species by light, rather than thermal energy, can occur at ambient reaction conditions that will reduce energy costs as well as the prevalence of side reactions.<sup>14–16</sup>

Unfortunately, the development of effective PNMP agents for a wide range of monomer units has proven difficult, with recent experimental work demonstrating that NMP-like reactivity is highly dependent on both the choice of chromophore and choice of monomer unit.<sup>14–20</sup> Recently we studied two systems that are able to control some but not all classes of monomer tested,<sup>15, 17</sup> and have shown that this variable behaviour may be in part due to a preference for mesolytic rather than homolytic dissociation (Scheme 2).<sup>21</sup> Mesolytic cleavage, which occurs from the  $n_{\text{N}}\pi^*$  rather than  $\pi\pi^*$  or  $n_{\text{O}}\pi^*$  excited states, results in the formation of a radical and a cation. The ultimate location of these species is dependent on the respective stabilities of these species, i.e. nitroxide radical and carbocation versus oxoammonium

cation and carbon-centred radical. Only the former pathway leads to effective PNMP, the latter at best leading to initiation of cationic polymerization.

Whilst potentially detrimental to NMP reactivity, the prevalence of mesolytic cleavage does offer synthetic opportunities. Recently, experimental and theoretical work demonstrated that oxidized alkoxyamines are capable of alkylating, even methylating, nucleophiles under oxidative conditions.<sup>22–25</sup> These processes required formal oxidation, performed electrochemically. A simpler approach would be to use PNMP agents primed to undergo mesolytic cleavage. Here, we aim to design organic, photoactive alkoxyamines that can be tuned to enhance mesolytic cleavage, for use in photochemical alkylation reactions.

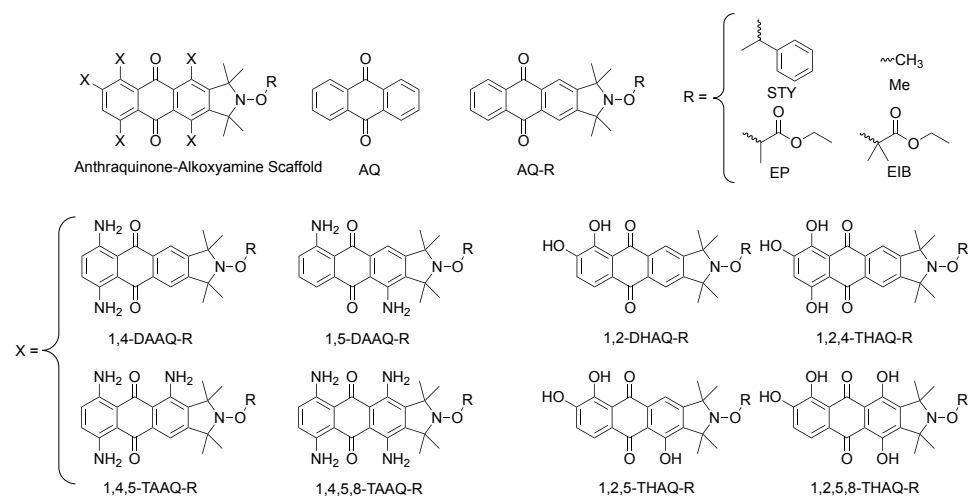


Scheme 2. Alternative homolysis and mesolysis photocleavage pathways of azaphenolenes, as studied in Ref 21. Note that the diradical of the  $\pi\pi^*$  is drawn across the O–R bond to emphasize that diradicals centered on the chromophore do not undergo homolytic cleavage.

<sup>a</sup> ARC Centre of Excellence for Electromaterials Science, Research School of Chemistry, Australian National University, Canberra ACT 2601 Australia

\* Footnotes relating to the title and/or authors should appear here.

Electronic Supplementary Information (ESI) available: [Supplementary figures and complete computational details.]. See DOI: 10.1039/x0xx00000x



**Scheme 3.** Anthraquinone-Alkoxyamine substitution variations considered in this study.

## COMPUTATIONAL METHODOLOGY

Electronic structure calculations were performed with the Gaussian 16.E01 software package.<sup>26</sup> All open- and closed-shell SCF calculations were performed with density functional theory (DFT), and excited state energies and electrostatic surfaces were obtained with TD-DFT. As in our previous study,<sup>21</sup> the meta-GGA, M06-2X density functional<sup>27</sup> was employed alongside the 6-31+G(d,p) basis set for all types of calculation, as this combination of functional and basis set has been shown to produce ground and excited state energies with qualitative accuracy.<sup>28</sup> Solvent effects were obtained with the SMD universal solvent model,<sup>29</sup> using ethyl ethanoate as the solvation environment so as to mimic a bulk acrylic monomer-like solvent. For ground state reactions, gas-phase Gibbs free energies were calculated using ideal gas partition functions and combined with solvation energies so as to obtain solution Gibbs free energies via thermocycle; for the excited states, energies in solution were obtained directly. Free energies were also obtained directly for the singlet-triplet energy gaps, to ensure the correct states were being optimised.

## RESULTS AND DISCUSSION

### Excited States of Anthraquinone-Alkoxyamines

As our initial test set, we considered the anthraquinone-alkoxyamines in Scheme 3. These species are simple derivatives of known PNMP agents<sup>14-20</sup> but use a chromophore that is an established Type II photoinitiator that can be tuned through ring substitution.<sup>30-34</sup> As leaving groups we consider models of the propagating radical in

styrene (STY), ethyl propanoate (EP) and ethyl isobutyrate (EIB) polymerization, as well as methyl (Me), so as to evaluate the potential for photoactivated methylation. For brevity, the different structures are named throughout to reflect the substitution of the anthraquinone moiety.

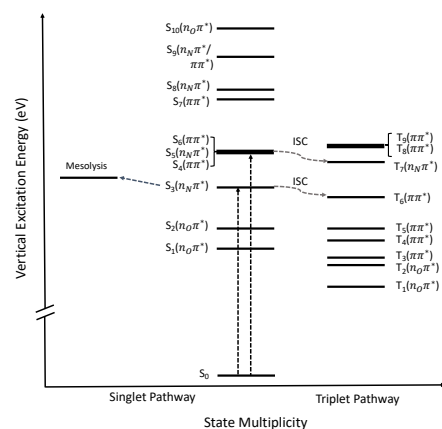


**Figure 1.** Simplified Jablonski diagram for AQ-Me

Figure 1 shows a simplified Jablonski diagram for AQ-Me. The extensive conjugation, keto groups, and nitrogen heteroatom present in the alkoxyamines studied give rise to  $\pi\pi^*$ ,  $n_O\pi^*$ , and  $n_N\pi^*$  low-lying excited states, respectively. The  $\pi\pi^*$  and  $n_O\pi^*$  states are centred on the anthraquinone moiety and are thus unreactive toward NO-R scission. TD-DFT calculations show that the energies of these states are largely unaffected upon introduction of the 2,2,5,5-tetramethyl-1-pyrrolidinyloxy moiety, due to the lack of

conjugation between the different sources of electrons (Figure 2). Although centred on the N–O group, the energy of the lowest  $n_N\pi^*$  states, are also relatively unaffected by the different R-groups bonded to the alkoxyamine moiety (Figure 2).

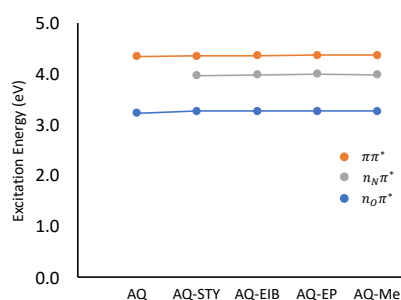


**Figure 2.**  $n_O\pi^*$ ,  $n_N\pi^*$ , and  $\pi\pi^*$  excited state energies for anthraquinone, and alkoxyamine-based derivatives.

The excited state capable of leading to mesolytic NO–R cleavage is the  $n_N\pi^*$  state. As seen in Figure 1, this can occur directly from  $S_3(n_N\pi^*)$ , or via intersystem crossing from  $S_7(\pi\pi^*)$  to  $T_7(n_N\pi^*)$ . The  $n_N\pi^*$  excited state results in the transfer of a non-bonding electron from the nitrogen atom into the  $\pi^*$ -system of the anthraquinone, resulting in a biradical charge-separated state. The radical cation centred on the nitrogen therefore possesses the valency necessary for mesolysis. This phenomenon is shown in Figure 3, an electrostatic potential (ESP) difference plot that shows that, upon excitation to the  $n_N\pi^*$  state, there is a build-up of negative charge on the anthraquinone moiety and a concomitant build-up of positive charge around the nitrogen atom.

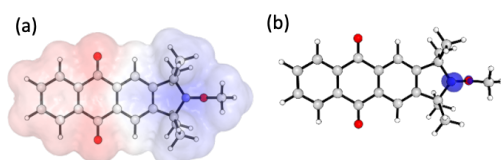


**Figure 3** a) Change in electrostatic potential upon excitation to  $\pi\pi^*$  excited state of methyl-anthraquinone-alkoxyamine. Blue regions correspond to a decrease in electrostatic potential, and red regions correspond to an increase in electrostatic potential, upon excitation. b) Spin density of methyl-anthraquinone-alkoxyamine radical cation.

However, compared with the equivalent, formally oxidized radical cation (Figure 3b), the positive charge shown in Figure 3a is more diffuse. This raises an interesting conundrum. On the one hand, as the  $n_N\pi^*$  state becomes increasingly stabilised and increasingly charge-separated, the properties around the N–O–R moiety should approach that of the formally oxidized radical cation, and mesolysis should be promoted. On the other, as seen in Figure 1,

stabilization of  $S_3(n_N\pi^*)$  would in principle bring its energy closer to that of  $T_6(\pi\pi^*)$ , and thus would be expected to promote intersystem crossing to the triplet manifold and thus to unreactive  $\pi\pi^*$  and  $n_O\pi^*$  triplet states. A solution to this problem is to stabilize  $S_3(n_N\pi^*)$  to such an extent that its energy drops significantly below  $T_6(\pi\pi^*)$ . This is the aim of the next section.

#### Effect of Hydroxy- and Amino- Functionalisation on Anthraquinone and Anthraquinone-Alkoxyamine Properties

There are two ways of increasing the charge-separation and stabilizing  $n_N\pi^*$ : stabilizing the formation of either the radical anion or cation. Due to the limited scope for structural variation around the nitrogen, it is simpler to stabilize the anthraquinone  $\pi$ -system and radical anion. This stabilization will be demonstrated by a decrease in vertical excitation energy of the  $n_N\pi^*$  state, an increase in the component of the excited state dipole moment along the vector that describes the change in electron density, and an increase in localization of the radical cation on the nitrogen atom. Our previous work employing anthraquinone derivatives for visible light photoinitiation highlighted the role of substitution in stabilizing key radical anion and radical cation intermediates necessary for Type II initiation.<sup>30–34</sup> Here, similar substitution patterns are used with the anthraquinone-alkoxyamines and their subsequent effects are assessed (Figure 4).

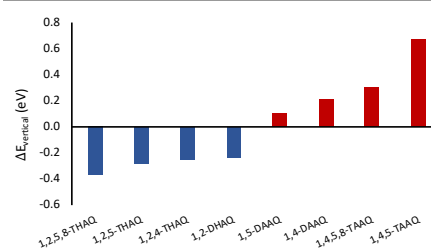


**Figure 4.** Average change in  $n_N\pi^*$  excitation energy (eV), relative to unfunctionalized anthraquinone-alkoxyamine, for amine (red) and hydroxyl (blue) functionalized (STY-, EP-, EIB-, Me-) anthraquinone-alkoxyamine

Figure 4 shows that amine and hydroxyl groups have opposite effects on the  $n_N\pi^*$  vertical excitation energies; specifically, hydroxyl groups stabilise, and amine groups destabilise, this excited state. These effects of substitution are best demonstrated in Figure 5, which clearly shows the blue, positive charge density being “pushed” from the anthraquinone onto the alkoxyamine moiety, as the functionalization pattern moves from amine to alcohol groups. This is a clear indication that the extent of charge separation is increasing with the increase in stability of the radical anion, and the reactivity of the 1258-THAQ  $n_N\pi^*$  state should resemble that of the formally oxidized species more closely than that of 1458-TAAQ or unfunctionalized AQ. As predicted, the observed (de)stabilization of these

states is also observed in the size of the  $n_N\pi^*$  state dipole (Table 1) In each case, the results of the extreme cases, 1458-tetraaminoanthraquinone alkoxyamine and 1258-tetrahydroxyanthraquinone alkoxyamine are shown; other structures studied are shown in the SI.

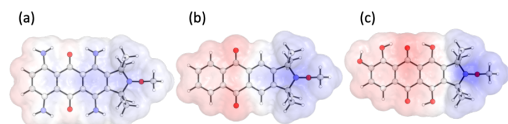


**Figure 5.** Change in electrostatic potential upon excitation to  $n_N\pi^*$  excited state of methyl-anthraquinone-alkoxyamine derivatives with (a) amino substitution, (b) no substitution, (c) hydroxyl substitution.

**Table 1.** Ground and excited state dipole moment x-components, corresponding to the direction of charge transfer upon excitation to  $n_N\pi^*$  state

State	1458-TAAQ-Me	AQ-Me	1258-THAQ-Me
$S_0$	0.4351	0.4797	0.1408
$S_n(n_N\pi^*)$	3.0294	7.6674	8.0705

It is clear that the  $n_N\pi^*$  state is significantly stabilised upon hydroxy substitution due to the sigma withdrawing properties of the hydroxy groups; conversely the electron donating amino substituents destabilize it. While stabilization of  $n_N\pi^*$  makes it more accessible and more reactive to mesolysis, it is important to consider competing intersystem crossing to the triplet manifold. To this end, simplified Jablonski diagrams for the two extreme cases, 1458-tetraaminoanthraquinone alkoxyamine and 1258-tetrahydroxyanthraquinone alkoxyamine are shown in

Figure 6. In both cases the orbitals are re-ordered compared with the unsubstituted anthraquinone alkoxyamine with the net effect that the  $^1n_N\pi^* - ^3\pi\pi^*$  increases. This increase will limit ISC and promote reactivity on the singlet surface, which is then favoured by hydroxy substitution.

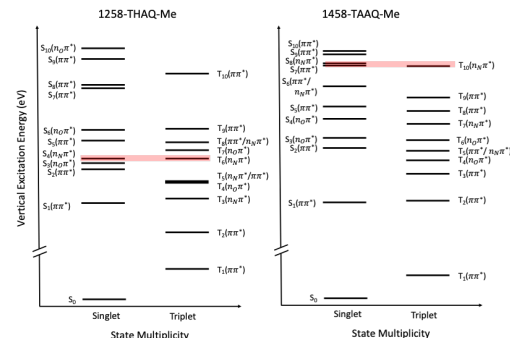


**Figure 6.** Simplified Jablonski diagrams for 1258-THAQ-Me and 1458-TAAQ-Me. The highlighted red bar shows the lowest  $S_1(n_N\pi^*)$  state and nearest triplet state. In each case they have the same orbital symmetry and intersystem crossing would be expected to be slow based on El-Sayed rules.

#### Promotion of Alkylation.

Recently we showed that oxidized TEMPO-methyl is a potent in situ methylating agent in the presence of nucleophiles.<sup>25</sup> Quantum chemistry calculations suggest an  $S_N2$  mechanism, resulting in the transfer of a methyl cation to form the methylated nucleophile and the corresponding nitroxide radical. The activation barrier of the  $S_N2$  reaction is shown to be significantly decreased upon oxidation, compared with the same reaction on the ground state singlet surface. Closed and open-shell calculations on the ground state and radical cation anthraquinone alkoxyamines, respectively, demonstrate that similar catalysis of the  $S_N2$  methylation mechanism can be expected upon formal oxidation (Figure 7).

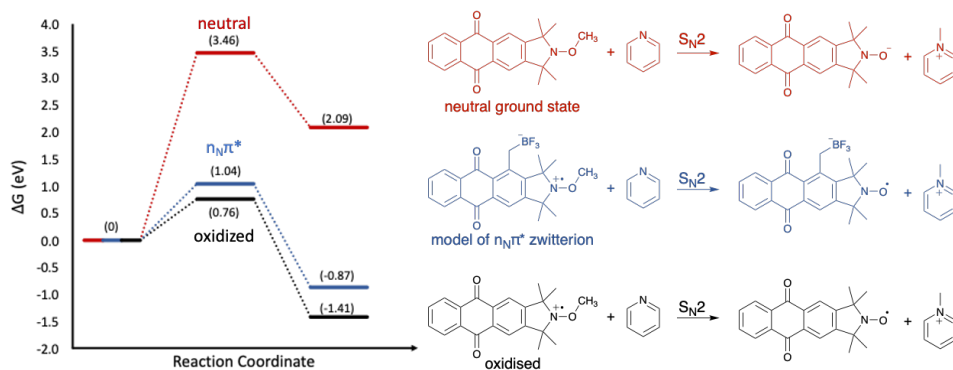


**Figure 7.**  $S_N2$  mechanism and relative free energies for ground state (red), oxidized (black), and zwitterionic (blue) anthraquinone-alkoxyamine.

In reality, the  $n_N\pi^*$  excited state exists as a zwitterionic biradical species, however accurately modelling this species is difficult with standard DFT methods, hence the exploration of the radical cation species. To that end, for the final  $S_N2$  methylation reaction a negatively charged boron trifluoride ( $BF_3$ ) functional group is attached to the anthraquinone moiety close to the nitroxide moiety, resulting in a through-space electrostatic stabilization effect of the localized radical cation. The relative energies for the zwitterionic reaction are also shown in Figure 7. Due to the stabilization of the anthraquinone-alkoxyamine-methyl radical cation the activation energy of the  $S_N2$  reaction increases slightly, however the calculations suggest that the positive-negative electrostatic interaction would not drastically alter the photoreactivity around the alkoxyamine.

#### On the Fate of the Anthraquinone-centred Radical Anion

So far, calculations and discussion have focussed on the formation of the initial charge-separated  $n_N\pi^*$  state that can undergo mesolysis. Here, the potential deactivation of the radical anion that forms on the anthraquinone is addressed. From Figure 8, there are two “products” for the two mesolytic cleavage pathways; the formal product that features a radical anion localized on the anthraquinone moiety and the corresponding radical/oxoammonium, and their potential relaxation resonance structures, with either an anion or radical localised on the alkoxyamine moiety.

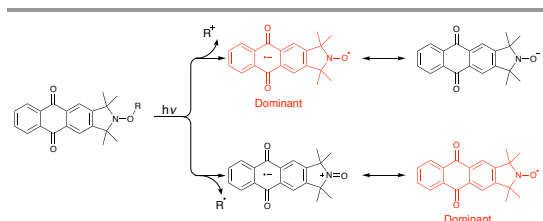


**Figure 8.** Formal products of photo-mesolysis and isoelectronic resonance structures.

The cleavage pathway from the singlet  $n_N\pi^*$  to form a carbocation and the negatively charged biradical is simple to explore with DFT, as the two resonance structures are well represented by two different spin multiplicities; the oxygen centred anion is a closed-shell singlet, and the biradical anion an open-shell singlet. Performing these calculations on unfunctionalized anthraquinone-alkoxyamine, as well as 1,4,5-TAAQ and 1,2,5,8-THAQ, reveals that in each case the open-shell singlet biradical is more stable than the closed-shell oxygen-centred anion. Using a broken symmetry DFT approach, whereby the converged triplet biradical SCF state is used as an initial guess for a subsequent open-shell singlet calculation, reveals the singlet biradical state to sit 70.2, 93.6 and 134.9 kJ mol<sup>-1</sup> below the closed shell species for 1,4,5-TAAQ, AQ and 1,2,5,8-THAQ respectively. The consequence of the stability of the singlet biradical is the lack of ionic recombination between the carbocation and oxygen centred anion, as the nitroxide

radical will persist. The radical anion, however, could be oxidised by coinicators as has been reported previously.<sup>30-34</sup> For the radical zwitterion, open-shell DFT calculations are more difficult as both resonance structures exhibit the same charge and spin multiplicity. Indeed, using Intermediate Neglect of Differential Overlap (INDO) occupancy guess simply results in convergence to the nitroxide radical SCF solution for each of the three species, suggesting that there is no low-lying zwitterionic solution present. Time-dependent approaches are also not viable due to severe spin-contamination issues when performed on open-shell species. However, given the apparent stability of the nitroxide radical, relaxation upon mesolysis to this species would allow for continued controlled radical polymerization. Alternatively, in an alkylation reaction the nitroxide would be inert.

#### CONCLUSIONS

To conclude, a range of anthraquinone-functionalized alkoxyamines have been studied using DFT and TD-DFT, and predictions have been made about their respective (photo)reactivities. With good leaving groups, these reagents undergo mesolytic cleavage which is favoured by hydroxyl-functionalization. The products of mesolytic cleavage are either carbon-centred radicals or carbocations, with the only the former favouring nitroxide-mediated polymerization. Based on our experimental studies of oxidative cleavage, radical formation is expected to occur for (meth)acrylate polymerizations, while for styrene polymerization cationic products may be implicated. More importantly, the methyl alkoxyamines are predicted to be excellent candidates for photochemical methylation, analogous to our recently published electrochemical procedure.<sup>25</sup> Synthetic work in this direction is currently underway.

#### Conflicts of interest

There are no conflicts to declare.

#### Acknowledgements

The authors acknowledge financial support from the Australian Research Council (ARC) Centre of Excellence for Electromaterials Science, an ARC Laureate Fellowship (to M.L.C.), generous supercomputing time from the National Computational Infrastructure, and helpful discussions with Yohann Guillaneuf, Didier Gimes, and Jason Morris.

#### Notes and references

1. D. Bertin, D. Gimes, S. R. A. Marque and P. Tordo, *Chem. Soc. Rev.*, 2011, **40**, 2189-2198.
2. R. B. Grubbs, *Polym. Rev.*, 2011, **51**, 104-137.
3. C. J. Hawker, A. W. Bosman and E. Harth, *Chem. Rev.*, 2001, **101**, 3661-3688.

4. C. Dire, J. Belleney, J. Nicolas, D. Bertin, S. Magnet and B. Charleux, *J. Polym. Sci. A Polym. Chem.*, 2008, **46**, 6333-6345.
5. M. Souaille and H. Fischer, *Macromolecules*, 2001, **34**, 2830-2838.
6. A. Goto and T. Fukuda, *Macromolecules*, 1999, **32**, 618-623.
7. C. Burguière, M.-A. Dourges, B. Charleux and J.-P. Vairon, *Macromolecules*, 1999, **32**, 3883-3890.
8. D. Benoit, V. Chaplinski, R. Braslau and C. J. Hawker, *J. Am. Chem. Soc.*, 1999, **121**, 3904-3920.
9. G. S. Ananchenko and H. Fischer, *J. Polym. Sci. A Polym. Chem.*, 2001, **39**, 3604-3621.
10. Y. Guillauneuf, D. Gignes, S. R. A. Marque, P. Tordo and D. Bertin, *Macromol. Chem. Phys.*, 2006, **207**, 1278-1288.
11. M. Edeleva, S. R. A. Marque, K. Kabytaev, Y. Guillauneuf, D. Gignes and E. Bagryanskaya, *J. Polym. Sci. A Polym. Chem.*, 2013, **51**, 1323-1336.
12. G. S. Ananchenko, M. Souaille, H. Fischer, C. Le Mercier and P. Tordo, *J. Polym. Sci. A Polym. Chem.*, 2002, **40**, 3264-3283.
13. G. Gryn'ova, C. Y. Lin and M. L. Coote, *Polym. Chem.*, 2013, **4**, 3744-3754.
14. M. Chen, M. Zhong and J. A. Johnson, *Chem. Rev.*, 2016, **116**, 10167-10211.
15. Y. Guillauneuf, D. Bertin, D. Gignes, D.-L. Versace, J. Lalevée and J.-P. Fouassier, *Macromolecules*, 2010, **43**, 2204-2212.
16. J. Morris, S. Telitel, K. E. Fairfull-Smith, S. E. Bottle, J. Lalevée, J.-L. Clément, Y. Guillauneuf and D. Gignes, *Polym. Chem.*, 2015, **6**, 754-763.
17. S. E. Bottle, J.-L. Clément, M. Fleige, E. M. Simpson, Y. Guillauneuf, K. E. Fairfull-Smith, D. Gignes and J. P. Blinco, *RSC Adv.*, 2016, **6**, 80328-80333.
18. Y. Guillauneuf, D.-L. Versace, D. Bertin, J. Lalevée, D. Gignes and J.-P. Fouassier, *Macromol. Rapid Commun.*, 2010, **31**, 1909-1913.
19. M. Herder and J.-M. Lehn, *J. Am. Chem. Soc.*, 2018, **140**, 7647-7657.
20. M. Huix-Rotllant and N. Ferre, *J. Phys. Chem. A*, 2014, **118**, 4464-4470.
21. N. S. Hill, M. J. Fule, J. Morris, J.-L. Clément, Y. Guillauneuf, D. Gignes and M. L. Coote, *Macromolecules*, 2020, **53**, 1567-1572.
22. L. Zhang, E. Laborda, N. Darwish, B. B. Noble, J. H. Tyrell, S. Pluczyk, A. P. Le Brun, G. G. Wallace, J. Gonzalez, M. L. Coote and S. Ciampi, *J. Am. Chem. Soc.*, 2018, **140**, 766-774.
23. C. L. Hammill, B. B. Noble, P. L. Norcott, S. Ciampi and M. L. Coote, *J. Phys. Chem. C*, 2019, **123**, 5273-5281.
24. B. B. Noble, P. L. Norcott, C. L. Hammill, S. Ciampi and M. L. Coote, *J. Phys. Chem. C*, 2019, **123**, 10300-10305.
25. P. L. Norcott, C. L. Hammill, B. B. Noble, J. C. Robertson, A. Olding, A. C. Bissember and M. L. Coote, *J. Am. Chem. Soc.*, 2019, **141**, 15450-15455.
26. M. J. Frisch, G. W. Trucks, H. B. Schlegel, G. E. Scuseria, M. A. Robb, J. R. Cheeseman, G. Scalmani, V. Barone, G. A. Petersson, H. Nakatsuji, X. Li, M. Caricato, A. Marenich, J. Bloino, B. G. Janesko, R. Gomperts, B. Mennucci, H. P. Hratchian, J. V. Ortiz, A. F. Izmaylov, J. L. Sonnenberg, D. Williams-Young, F. Ding, F. Lipparini, F. Egidi, J. Goings, B. Peng, A. Petrone, T. Henderson, D. Ranasinghe, V. G. Zakrzewski, J. Gao, N. Rega, G. Zheng, W. Liang, M. Hada, M. Ehara, K. Toyota, R. Fukuda, J. Hasegawa, M. Ishida, T. Nakajima, Y. Honda, O. Kitao, H. Nakai, T. Vreven, K. Throssell, J. A. Montgomery Jr., J. E. Peralta, F. Ogliaro, M. Bearpark, J. J. Heyd, E. Brothers, K. N. Kudin, V. N. Staroverov, T. Keith, R. Kobayashi, J. Normand, K. Raghavachari, A. Rendell, J. C. Burant, S. S. Iyengar, J. Tomasi, M. Cossi, J. M. Millam, M. Klene, C. Adamo, R. Cammi, J. W. Ochterski, R. L. Martin, K. Morokuma, O. Farkas, J. B. Foresman and D. J. Fox, *Gaussian 09, Revision E.01*, Gaussian, Inc., Wallingford CT, 2016.
27. Y. Zhao and D. G. Truhlar, *Theor. Chem. Acc.*, 2008, **120**, 215-241.
28. A. D. Laurent and D. Jacquemin, *Int. J. Quantum Chem.*, 2013, **113**, 2019-2039.
29. A. V. Marenich, C. J. Cramer and D. G. Truhlar, *J. Phys. Chem. B*, 2009, **113**, 6378-6396.
30. G. N. Wang, N. S. Hill, D. Zhu, P. Xiao, M. L. Coote and M. H. Stenzel, *ACS Appl. Polym. Mat.*, 2019, **1**, 1129-1135.
31. J. Zhang, N. Hill, J. Lalevee, J. P. Fouassier, J. C. Zhao, B. Graff, T. W. Schmidt, S. H. Kable, M. H. Stenzel, M. L. Coote and P. Xiao, *Macromol. Rapid Commun.*, 2018, **39**, 6.
32. J. Zhang, J. Lalevee, N. S. Hill, K. Launay, F. Morlet-Savary, B. Graff, M. H. Stenzel, M. L. Coote and P. Xiao, *Macromolecules*, 2018, **51**, 8165-8173.
33. J. Zhang, J. Lalevee, N. S. Hill, X. T. Peng, D. Zhu, J. Kiehl, F. Morlet-Savary, M. H. Stenzel, M. L. Coote and P. Xiao, *Macromol. Rapid Commun.*, 2019, **40**, 5.
34. J. Zhang, K. Launay, N. S. Hill, D. Zhu, N. Cox, J. Langley, J. Lalevee, M. H. Stenzel, M. L. Coote and P. Xiao, *Macromolecules*, 2018, **51**, 10104-10112.

## 5.4 Implications and Applications

This chapter has highlighted how photoinitiation of PNMP agents by homolysis cannot be assumed to be the dissociation mechanism upon irradiation. Instead, a mesolytic-type cleavage behaviour is possible and could give rise to either nitroxide radicals or oxoammonium cations, as well as varying, monomer-dependent polymerization behaviour. This information can be incorporated into future designs of photoactive alkoxyamines, as access to the reactive  $n_N\pi^*$  state ought to be avoided for PNMP applications. However, photoactively inducing radical cation-like reactivity around the nitroxide moiety may allow for reactions more closely resembling alkylation, rather than free radical polymerization, as is explored in Publication 11.

Anthraquinone-functionalized alkoxyamines can have their  $n_N\pi^*$  excited state reactivity altered by mimicking the functionalization patterns used in Chapter 3; anthraquinone functionalization is also a well-established synthetic target and therefore the experimental testing of these predictions is feasible. A future direction of this work is to mimic the effects on charge-separation with charged functional groups, as explored in Chapter 4. There are several key design criteria arising from this study:

1. The reactive  $n_N\pi^*$  state is the main state of interest, and chromophoric alkoxyamines are likely to exhibit these low-lying states
2. Affecting the reactivity of the nitroxide moiety directly is impractical, as the functional groups surrounding the nitroxide will affect the useful nitroxide chemistry. The chromophore is therefore the ideal target for functionalization
3. Amine groups are found to stabilize radical cation formation on the anthraquinone moiety, and therefore destabilizes the  $n_N\pi^*$  state and reduces charge-separation within the state. Alcohol groups have the opposite effect; stabilising radical anion formation, stabilising the  $n_N\pi^*$  state and increasing charge-separation
4. Internal electric fields also have a significant effect on the stability of the  $n_N\pi^*$  state. Following the same trends as outlined in Chapter 4, a positive charge in line



with the direction of the charge-transfer should form a sequence that reinforces the charge transfer, and vice versa for negative charges, and is the next system to study:

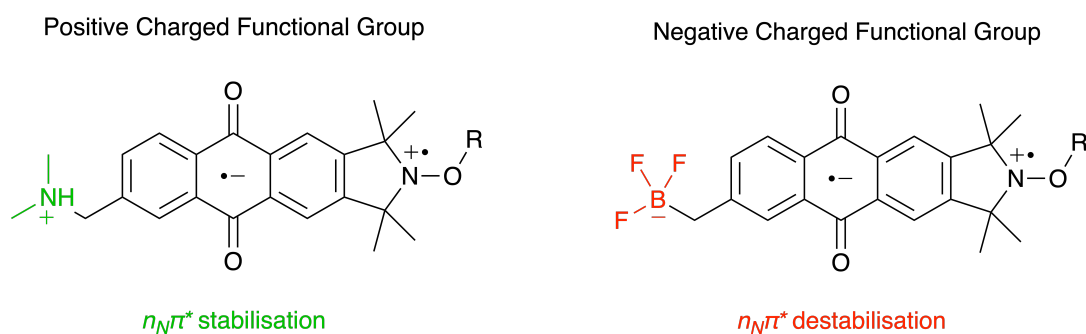


Figure 5.4: Potential electrostatic (de)stabilization of  $n_N\pi^*$  excited state for further research

The applications of this work are varied and flexible, depending on the desired reactivity. Where PNMP is required, amine groups or an appropriately positioned negatively charged functional group can be employed, in order to reduce the biradical-like, charge-transfer character of the  $n_N\pi^*$  state. This will promote reactivity more closely resembling that of the singlet ground state, which has been shown with theory to be unreactive towards alkylation. As the molecule would be in an excited state the delayed mesolytic reactivity can allow for the relevant internal processes that lead to homolytic cleavage to take place, and NMP reactivity to take place. On the other hand, a gentle alkylation, potentially even methylation, procedure may be desired. In such cases, functionalization of the anthraquinone with either alcohol or positively charged functional groups will promote mesolytic reactivity in the  $n_N\pi^*$  state.

Anthraquinone molecules, then, are a highly flexible scaffold whose chemistry can be easily altered. As well as this, the types of functionalization that can be used remain effective in different solvent environments. Specifically, amine- and hydroxy-anthraquinones have already been shown to be soluble in bulk monomer and acetonitrile, and CFGs offer an effective approach to control when pH changes are tolerable. Further work is required to synthesize the functionalized anthraquinone-alkoxyamines and test their photoreactivity, and this work is ongoing.

## 5.5 References

- (1) Moad, G.; Rizzardo, E. *Macromolecules* **1995**, *28*, 8722–8728.
- (2) Nicolas, J.; Guillaneuf, Y.; Bertin, D.; Gigmes, D.; Charleux, B. *Progress in Polymer Science* **2012**, *3*, 277–350.
- (3) Fukuda, T.; Terauchi, T.; Goto, A.; Ohno, K.; Tsujii, Y.; Miyamoto, T. *Macromolecules* **1996**, *29*, 6393–6398.
- (4) Gryn'ova, G.; Lin, C. Y.; Coote, M. L. *Polymer Chemistry* **2013**, *4*, 3744.
- (5) Marshall, D. L.; Gryn, G.; Coote, M. L.; Barker, P. J.; Blanksby, S. J. *International Journal of Mass Spectrometry* **2015**, *378*, 38–47.
- (6) Guillaneuf, Y.; Bertin, D.; Gigmes, D.; Versace, D. L.; Lalevée, J.; Fouassier, J. P. *Macromolecules* **2010**, *43*, 2204–2212.
- (7) Huix-Rotllant, M.; Ferre, N. *Journal of Physical Chemistry A* **2014**, *118*, 4464–4470.
- (8) Granovsky, A. A. *The Journal of Chemical Physics* **2011**, *134*, 214113.
- (9) Hodgson, J. L.; Roskop, L. B.; Gordon, M. S.; Lin, C. Y.; Coote, M. L. *The Journal of Physical Chemistry A* **2010**, *114*, 10458–10466.
- (10) Norcott, P. L.; Hammill, C. L.; Noble, B. B.; Robertson, J. C.; Olding, A.; Bissember, A. C.; Coote, M. L. *Journal of the American Chemical Society* **2019**, *141*, 15450–15455.

## 6 Mechanistic Insights into Organo- and Lewis Acid Catalysis

### 6.1 Introduction and Key Findings

So far, the photochemical behaviour of a variety of molecules has been manipulated with different types of chemistry, including the introduction of co-initiating species. These co-initiators have been shown to improve desirable photochemical properties and photoinitiation abilities, but can also have a significant effect on ground-state reactions that can take place between reaction components. This chapter therefore details studies into the catalysis of a thermally initiated polymerization reaction by addition of Lewis acids, and the thermal hydrolysis of a biologically relevant reaction.

In the past, the effect of adding Lewis acids to polymerization reactions has been investigated as a means of propagation catalysis and as potential stereocontrol reagents,<sup>1</sup> as well as a simple approach to altering the light absorption properties of photoinitiators.<sup>2,3</sup> The catalysis of propagation reactions generally arises from Lewis acid complexation to the propagating radical species, resulting in an increase in polar character between the radical chain end and incoming monomer unit. In this respect, the addition of Lewis acids offer a cheap and simple method for lower-temperature thermal reactivity. However, Lewis acids can suffer from poor solubility and low binding specificities which limit their effectiveness and general applicability.

The binding of Lewis acids to polymer chains and/or monomer units can not only result in propagation catalysis, but can have a significant effect on the microstructure of the resulting polymer chain. The orientation of side-groups along a polymer chain, known as tacticity, has profound consequences on the mechanical properties of polymer compounds but has proven difficult to control in free radical polymerization.<sup>4</sup> While achieving highly stereo-regular polymer chains from free-radical polymerization reactions is not impossible, it is not generally achieved by design, nor is there a single, generalizable approach to controlling tacticity.

The difficulty in controlling tacticity arises at the propagating radical chain end, which is a planar,  $sp^2$ -hybridized carbon atom able to rotate freely, preventing the formation of a stereospecific polymer backbone (the so-called “fast interconversion scheme”<sup>5</sup> is described in more detail in Publication 12). Lewis acid complexation, rather than being introduced to alter the kinetics of radical addition steps, can potentially prevent, or slow down, the free rotation and introduce tacticity control. Unfortunately, extensive investigations into this approach<sup>6</sup> demonstrate that the simple introduction of Lewis acids is not enough for tacticity control.

An example where this approach has been successful is studied computationally in Publication 12. This study explains how Lewis acids induce stereocontrol in a copolymerization reaction and increase our understanding of how Lewis acids may be employed successfully in future reactions.

The final publication in this thesis, Publication 13, is an experimental and computational investigation into the catalysis of a hydrolysis reaction (Figure 6.1a). This reaction employs an enzyme-inspired, artificial catalytic triad (ACT) (Figure 6.1b) in conjunction with micellar catalysis. Solvent effects on organic reactions are well established,<sup>Parker1969</sup> and in Chapters 4 and 5 their importance is related to the balance between the size of an internal electric field (large in low polarity solvents), and the solubility of the overall system (low in low polarity solvents). To that end, micellar and enzyme catalysis, with their dynamic, high- and low-polarity solvation environments present an opportunity to introduce electrostatic effects in a practical and effective manner that limits negative solvation effects.

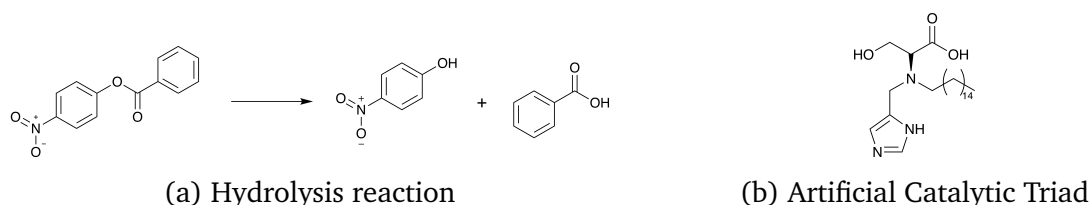


Figure 6.1: Systems studied with quantum chemistry in Publication 13

It is well known that in biological systems, proteins are able to catalyse biologically important reactions by taking advantage of their own solubility in water, the predomi-

nant solvent environment in cells, whilst providing a hydrophobic pocket for improved reactant solubility.<sup>7</sup> It is therefore difficult to beat the biological enzyme catalysis, however, there are disadvantages that can prevent their widespread application:<sup>8</sup>

1. Enzymes are highly selective and difficult to design
2. Whilst stable and active under physiological conditions, i.e. over a temperature range of 20-40°C and pH range of 6-8, outside of these conditions enzymes can be rendered inactive or, at worst, irreversibly denatured

The design and synthesis of an ACT/micelle co-catalyst has not, therefore, been performed so as to match the catalytic ability of biological enzymes, but to instead to keep the core reactivity exhibited by functional groups within the enzyme itself. The ACT is based on the functional groups present in the hydrophobic pocket of hydrolase enzymes, namely the histidine, aspartate, and serine amino acids.<sup>9</sup> The key functional groups present in these amino acids are installed on a flexible tertiary amine scaffold, allowing the functional groups to orient themselves so as to introduce reactivity. The inclusion of micelles is aimed at introducing some element of micelle catalysis<sup>10,11</sup> to complement the ACT. A micelle is a self-assembled aggregate of amphiphilic monomers, in aqueous solutions monomers usually possess polar, water-soluble headgroups and long, apolar hydrophobic alkyl chains. When the concentration of monomers is above the critical micelle concentration, or c.m.c., the formation of micelles is spontaneous. Like enzymes, micelles exhibit a hydrophilic surface that allows solvation by water, and a hydrophobic, low polarity core that will solvate organic reactants for catalysis. As well as this, a key part of micellar catalysis is the localization of organic reactants, important as whilst the overall concentration of the reactants may be low, the local concentrations can be much higher, due to more favourable solvation environment.

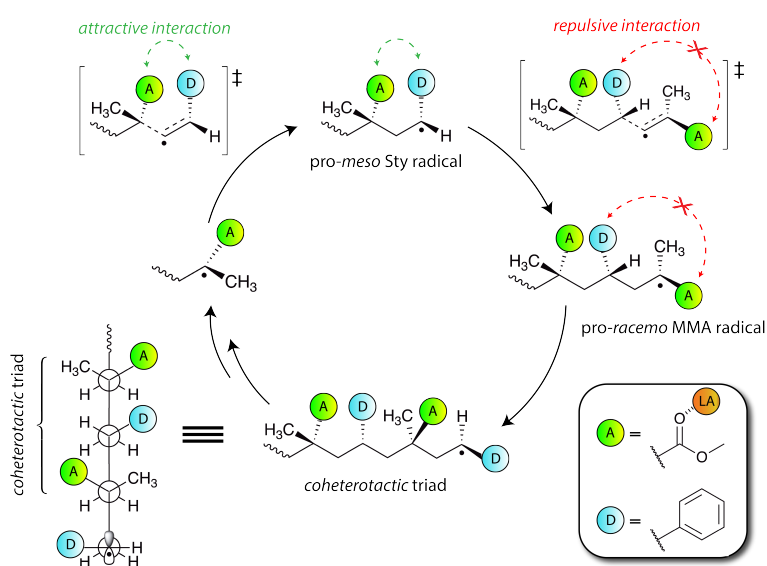
In this publication, quantum chemistry was used to deduce the likely catalytic mechanism of the ACT molecule in order to explain the observed increase in rate of the hydrolysis reaction. These calculations were supported by molecular dynamics calculations that were able to describe and model the micelle structures to a much greater extent than quantum chemistry could, due to the size of the systems investigated.

## 6.2 Publication 12

### Mechanistic Insights into Lewis Acid Mediated Sequence- and Stereo-Control in Radical Copolymerization

Nicholas S. Hill, Benjamin B. Noble, Michelle L. Coote

*Reversible Deactivation Radical Polymerization: Mechanisms and Synthetic Methodologies*, 2018, 41-61



This publication is a peer-reviewed manuscript published as a book chapter in *Reversible Deactivation Radical Polymerization: Mechanisms and Synthetic Methodologies*. All computational results and subsequent discussion are my own work. Prof. Michelle Coote assisted with the direction of the theoretical investigations and corrected my draft write-ups. [Supplementary material is available online.](#)

### Statement of Contribution

This thesis is submitted as a Thesis by Compilation in accordance with [https://policies.anu.edu.au/ppl/document/ANUP\\_003405](https://policies.anu.edu.au/ppl/document/ANUP_003405)

I declare that the research presented in this Thesis represents original work that I carried out during my candidature at the Australian National University, except for contributions to multi-author papers incorporated in the Thesis where my contributions are specified in this Statement of Contribution.

Title: Mechanistic Insights into Lewis Acid Mediated Sequence- and Stereo-Control in Radical Copolymerization

Authors: Nicholas S. Hill, Benjamin B. Noble, Michelle L. Coote


Publication outlet: Reversible Deactivation Radical Polymerization: Mechanisms and Synthetic Methodologies

Current status of paper: Published

Contribution to paper: I am the first contributing computational chemistry author. The majority of the computational results, mechanistic insight, and subsequent discussion are my own work

Senior author or collaborating authors endorsement: Michelle Coote

Nicholas Hill



20/01/2020

Candidate - Print Name

Signature

Date

### Endorsed

Michelle Coote



20/01/2020

Primary Supervisor – Print Name

Signature

Date



Delegated Authority – Print Name



Signature

20/01/2020

Date

## Chapter 2

# Mechanistic Insights into Lewis Acid Mediated Sequence- and Stereo-Control in Radical Copolymerization

Nicholas S. Hill, Benjamin B. Noble, and Michelle L. Coote\*

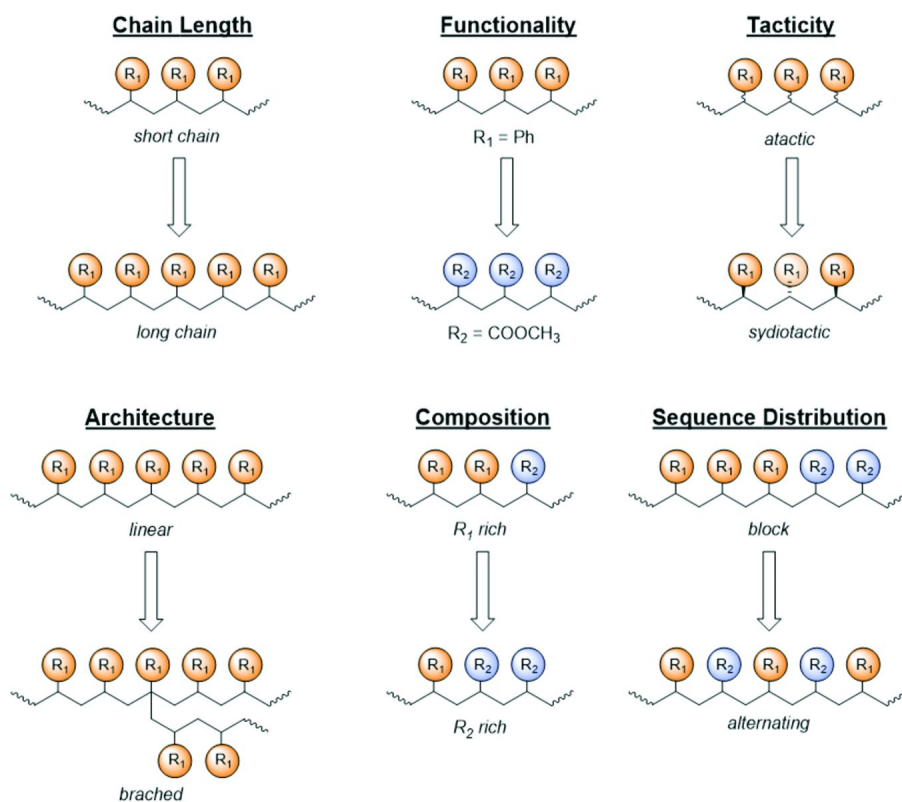
ARC Centre of Excellence in Electromaterials Science,  
Research School of Chemistry, Australian National University,  
Canberra ACT 2601, Australia

\*E-mail: michelle.coote@anu.edu.au.

Theoretical calculations have been performed to model the effects of a model Lewis acid, boron trichloride ( $\text{BCl}_3$ ) on the radical copolymerization of methyl methacrylate (MMA) and styrene (Sty). These calculations suggest that the high degree of alternation observed in the copolymer sequence distribution cannot be attributed to either ternary monomer complexes nor radical-monomer complexes. These complexes were not found to be sufficiently stable, particularly in the presence of competing solvation by toluene. However, this alternation can be satisfactorily explained via an enhanced cross-propagation mechanism, which originates from the matched donor/acceptor electronic character of the  $\text{MMA}(\text{BCl}_3)/\text{Sty}$  system.

A long-term goal for both academic and industrial chemists is to control the structure and resultant properties of macromolecules. There are a variety of chemical and physical properties that can be tuned via structural modifications to suit a specific application. Such modifications might include alterations to the chemical functionality of the side-chain(s), the molecular weight distribution (MWD), tacticity/stereochemistry or architecture of the resultant polymer (see Scheme 1). Additionally, in copolymers, sequence distribution and composition can also be altered. The feasibility of these structural modifications is usually heavily dependent on the type of polymerization procedure(s) used.





*Scheme 1. Idealized Modifications of Various Aspects of (Co)polymer Microstructure*

For decades, radical polymerization was regarded as the least precise polymerization process. Structural control in conventional radical polymerization is plagued by random bimolecular termination reactions (radical-radical combination and disproportionation), which leads to polydisperse products with little (if any) tacticity or chain-end control. This lack of microstructural control limits the utility of free-radical polymerization in precision polymer synthesis. However, the development of ‘living’ radical polymerizations has led to unprecedented levels of structural control, with popular examples including: nitroxide-mediated polymerization (NMP) (1–6), atom-transfer radical polymerization (ATRP) (7–9), and reversible addition-fragmentation chain-transfer (RAFT) polymerization (10–16). The specific chemical components of each process are different, however all three utilize an equilibrium between dormant and active polymer chains to lower the concentration of propagating radicals. This greatly reduces the incidence of bimolecular termination, relative to the overall number of polymer chains, and allows for the synthesis of polymers with well-defined MWDs and highly specialized architectures (including block copolymers, brushes, stars etc.) (17, 18).

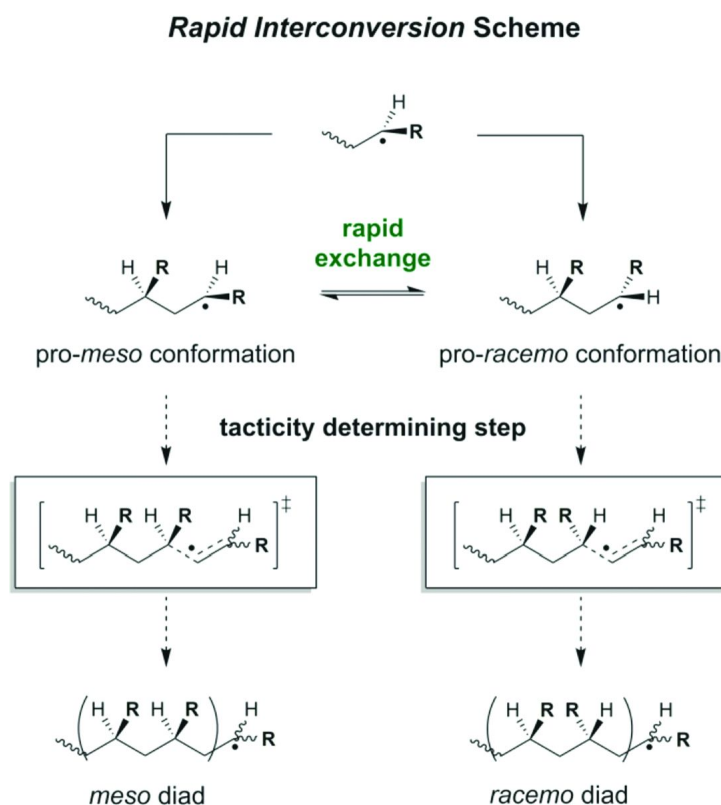
Living radical polymerization reactions give chemists a high degree of control over a variety of structural features for a wide range of different monomers. Unfortunately, complete control over all aspects of polymer structure remains elusive. Of interest, and difficulty, is the achievement of control over the unit-by-unit sequence of copolymers and their stereochemistry. Sequence control is desirable as it gives access to copolymers with macroscopic properties that can be tuned by altering the sequence of the monomers, rather than their identity. Progress towards sequence control has been made through, for example, the use of brush copolymers (19) and single monomer unit addition (SUMI)-RAFT techniques (20), however such processes are significantly more complex and less robust than standard NMP, RAFT, or ATRP. Stereocontrol in radical polymerization also remains notoriously difficult, although some notable progress has been made in certain monomer systems (21, 22).

The mechanism of tacticity control in most radical-based polymerizations is described by the rapid interconversion scheme (RIS) (see Scheme 2) (23). In the RIS, tacticity of the polymer chain is determined by the relative orientation of the terminal and penultimate side-chain during monomer addition. This scheme also illustrates how, in an unmediated reaction, control over the stereochemistry of the polymer chain is lost. Due to the low energy rotational barrier between *pro-meso* and *pro-racemo* conformations (compared with the tacticity defining radical addition reaction) and their near degeneracy, radical polymerization typically results in predominantly atactic polymer (23).

This does not, however, mean that stereospecificity in radical polymerization is entirely unachievable. The 2009 review by Satoh and Kamigaito (21) highlights key methodologies that have been previously used with varying degrees of success. One such route is that of Lewis acid (LA)-mediated polymerization whereby a LA is used to bind to the polymer side-chain (23). This interaction instils some conformational preference upon the propagating polymer terminus that affects the relative stability of *pro-meso* and *pro-racemo* conformations. The effects of LA on free radical polymerization reactions are, however, varied and largely inconsistent. Depending on the LA, monomer and specific reaction conditions, degrees of stereocontrol can range from  $\Delta m = 70\%$  to essentially nothing (e.g.  $\Delta m = 1-2\%$ ) (24, 25).

Moreover, LA have been shown to affect several other aspects of the polymerization. As early as 1957, it was reported that the addition of LiCl results in the acceleration of acrylonitrile (AN) polymerisation (26), an example of LA acting as a catalyst for the polymerization reaction. Recent pulsed laser polymerization studies have confirmed their ability to act as propagation catalysts (27, 28). Matumoto *et al.* suggested the polymerisation of MMA was amenable to tacticity control by stereospecifically bound  $\text{MgBr}_2$  (29), and in a more recent study we showed that the presence of LA can also result in a red-shift in the absorbance spectrum of a radical photoinitiator and affect initiation rates (30). Finally, and of specific interest to the development of sequence control, LA have been observed to alter the sequence distribution of copolymers, typically increasing their alternating tendency (31–36). The assumption, then, that a LA will passively bind to the propagating radical and otherwise be a spectator in the ensuing reaction is not necessarily valid. Understanding the mechanism by which

LAs influence radical polymerization would greatly assist in designing effective stereo- and sequence control systems.



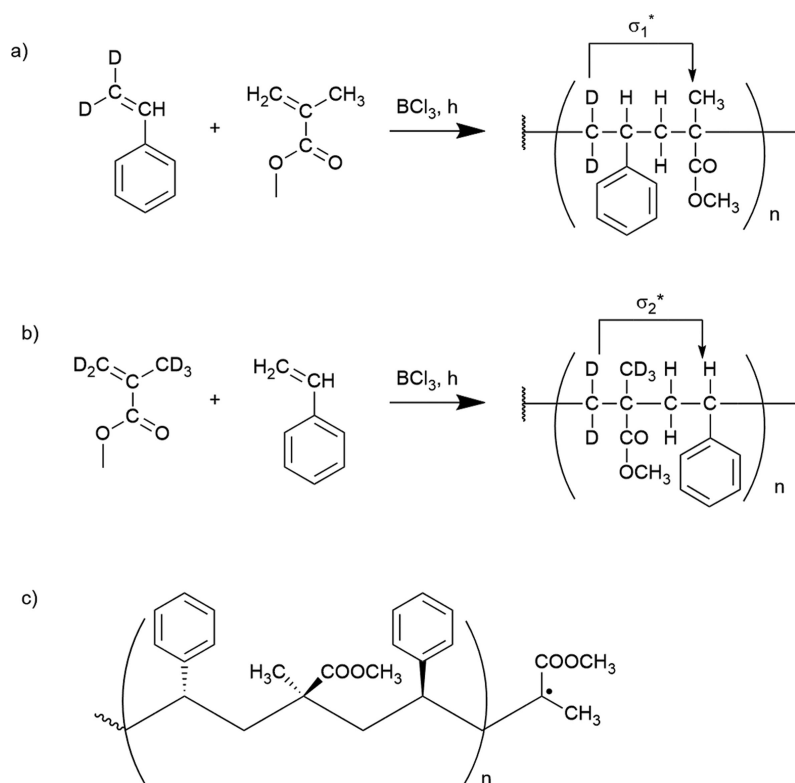
*Scheme 2. The Mechanism of Tacticity Determination Assuming Rapid Interconversion of the Intermediate Pro-meso and Pro-racemo Conformations*

To this end, in the present work we use theory to clarify the mechanism of an intriguing system in which boron trichloride ( $\text{BCl}_3$ ) was shown affect both the sequence distribution and stereochemistry of the radical copolymerization of methyl methacrylate (MMA) and styrene (Sty) (36, 37). In particular, Gotoh *et al.* (37) noted a remarkable increase in coheterotacticity, upon addition of stoichiometric amounts of boron trichloride ( $\text{BCl}_3$ ) to the copolymerization of methyl methacrylate (MMA) and styrene (Sty). The addition of  $\text{BCl}_3$  resulted in polymer cotacticity ratios of  $mm/mr/rr = 1/89/10$  and  $4/85/11$  for the St- and MMA-centered triads, respectively. An elegant follow up study by the authors (38) used deuterated monomers to determine the coisotactic parameters, or probability of isotactic diad formation. Determination of these “Bovey  $\sigma$  parameters (33)”, given as  $\sigma_1^*$  and  $\sigma_2^*$ , allowed the authors to determine the favoured propagation process involved in forming the coheterotactic polymer.

The deuterated analogue reactions and coheterotactic propagation processes are given in Scheme 3a and b. The experimentally obtained  $\sigma_1^*$  and  $\sigma_2^*$  values are 0.09 and 0.85, respectively, which means that the presence of  $\text{BCl}_3$  results in:

1. Sty monomer addition to an MMA radical resulting in a *racemo* diad
2. MMA monomer to Sty radical resulting in formation of a *meso* diad

The coheterotactic polymer therefore has the structure shown in Scheme 3c. As noted by the authors, the  $\sigma_1^*$  and  $\sigma_2^*$  parameters are determined independently of any assumed polymerisation mechanism. This means that the effect of the addition of  $\text{BCl}_3$  on the tacticity is unambiguous, although the actual role of the LA remains unclear.



Scheme 3. (a) Deuterated Analogue Sty-MMA Copolymerization Performed to Determine the Coisotactic Parameter of Sty Radical to MMA Monomer Addition, Where 100% *Meso*-Diad Formation Gives  $\sigma_1^* = 1$ . (b) The equivalent coisotactic parameter,  $\sigma_2^*$ , for MMA radical to Sty monomer addition. (c) Experimentally obtained heterotactic triad unit of poly(MMA-*alt*-Sty).

The experimental work performed by Gotoh *et. al.* clearly demonstrates that BCl<sub>3</sub> has unique effects on this copolymerization, imparting both sequence- and stereo-control (37, 38). At the same time, other examples of heterotactic control in radical-based polymerizations are exceedingly rare. To explore the success of this particular Lewis acid, several questions must be answered; what is the preferred binding mode of the BCl<sub>3</sub> molecule? What is happening to the propagating radical upon binding that results in the observed catalysis? Why does the addition of BCl<sub>3</sub> result in stereocontrol? Why does sequence control only require a catalytic concentration of BCl<sub>3</sub>, while heterotactic control requires stoichiometric concentrations of LA? Such an understanding will provide desirable characteristics that can be included when designing future reactions, as well as clues as to why the addition of BCl<sub>3</sub> (and other LA) doesn't necessarily lead to stereocontrol and/or sequence control in other systems.

### Computational Methodology

Standard *ab initio* molecular orbital theory and density functional theory (DFT) calculations were carried out using Gaussian 09 (39) with the exception of CCSD(T) calculations, which were performed using Molpro 2015 (40, 41), Geometries of all species were optimised at the M06-2X (42) level of theory using the 6-31+G(d,p) basis set and frequencies, entropies and thermal corrections were also calculated at this level of theory. Improved single-point energies were calculated using the high-level composite *ab initio* G3(MP2,CC) method (43). Adiabatic ionization potentials and electron affinities were calculated with G3(MP2,CC)(+), a variation of standard G3(MP2,CC) where calculations with the 6-31G(d) basis set are replaced with 6-31+G(d). High-level calculations were utilized in conjunction with the ONIOM approximation (44, 45) for larger systems, with UMP2 used to model remote substituents effects. Similar methodology has been shown to accurately reproduce the kinetics and thermodynamics of a range of radical reactions (23, 46–48). Vibrational analyses were performed on all geometries to verify the nature of the stationary points, and to calculate the gas-phase partition functions and associated thermal and entropic corrections. Gas phase free energies were then corrected to the solution phase using Gibbs free energies of solvation, calculated using the COSMO-RS model (49–51). The ADF package (52) was used to compute COSMO-RS solvation free energies on solution-phase geometries at the BP/TZP level of theory (as it was parameterized for), and the remaining parameters were kept as default values (53). The atomic radius of Boron was taken as 2.05 Å by scaling the van der Waals radius by 117%, as recommended by Klamt and co-workers (54, 55). Having obtained the solution-phase Gibbs free activation barriers, rate coefficients were calculated via standard transition state theory (56).

## Results and Discussion

### Binding Modes and Lewis Basicity

Sty and MMA monomer possess several possible Lewis donor sites and so we rigorously examined all possible interactions between these monomers and  $\text{BCl}_3$ . Intuitively, one would expect the strongest interaction to be between  $\text{BCl}_3$  and the O-acyl portion of the methoxy ester, although binding to the O-methoxy group or to the C=C bond could also be envisaged. For Sty monomer, complexation could feasibly occur through either the C=C bond or the aromatic ring. However, despite an exhaustive search, no stable minima between  $\text{BCl}_3$  and Sty monomer was found. Similarly, no stable complex with the C=C bond of MMA monomer was located. This is perhaps unsurprising, as  $\text{BCl}_3$  is a very hard Lewis acid and so minimal interactions with soft (and weak) Lewis bases would be anticipated. However,  $\text{BCl}_3$  can bind to either of the oxygen atoms present in the methoxy ester side-chain of MMA. In total this yields four possible structures; s-cis and s-trans conformations for both O-acyl and O-methoxy coordinated complexes (see Figure 1). Consistent with expectations, both O-acyl complexes are highly favored, with the s-cis isomer being the most thermodynamically stable complex. Thus, other modes of coordination were not examined henceforth.

In an MMA/Sty copolymerization, there are 3 functionally distinct methyl ester moieties: those of the monomer, the radical terminus and polymer side-chains. To determine if there is a preference for  $\text{BCl}_3$ -complexation to a particular ester moiety, relative binding free energies to various unimeric MMA models were calculated (see Figure 2). These results indicate that the most Lewis basic ester side-chain is that of the propagating polymer radical terminus and thus preferential binding of  $\text{BCl}_3$  at this site is anticipated. Moreover, the  $\text{BCl}_3$  binds more strongly to the ester-moiety of MMA monomer compared to a unimeric MMA side-chain segment. These results suggest that if only catalytic concentrations of  $\text{BCl}_3$  were present, the LA would likely detach from the ester side-chains of the polymer backbone. However, we should caution that the  $\pi$ -ester interaction (vide infra), which occurs in larger polymer chain models would likely reduce this selectivity for chain-end and monomer binding.

### Mechanistic Origins of Sequence Control

There are several previous examples of increased alternation in copolymer sequence distribution upon the introduction of Lewis acids (31–36), with the effect normally ascribed to one of three possible mechanisms (see Scheme 4) (35). The first mechanism is via the formation of a ternary monomer complex composed of the LA bound acceptor and donor monomer. As depicted in Scheme 4, alternation originates from the addition of this ternary complex to the propagating polymer terminus, with sequential (but very rapid) addition of the donor monomer followed by the acceptor (or vice versa). The second and arguably the most frequently cited mechanism is through enhanced cross propagation (35, 57–61), whereby the LA alters the reactivity of the acceptor monomer and radical such that cross propagation is significantly favoured over homopropagation (62). The third mechanism is via the formation a radical-monomer complex, between either

the LA bound acceptor radical and donor monomer (as depicted in Scheme 4) (63). To discriminate between these mechanisms, we first explored the stability of ternary monomer and radical-monomer complexes before examining the effects of LA complexation on cross propagation.

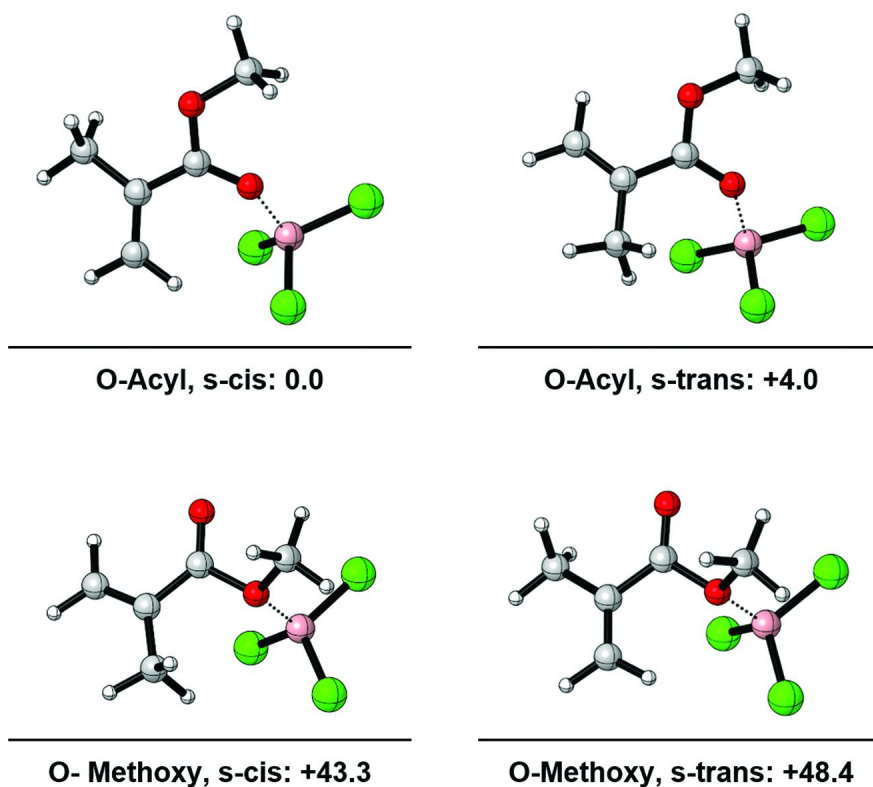


Figure 1. Optimised geometries and relative free energies ( $\text{kJ mol}^{-1}$ ) of different binding modes between  $\text{BCl}_3$  and MMA monomer at  $-95\text{ }^\circ\text{C}$  in toluene.

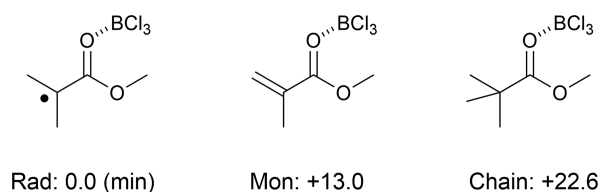
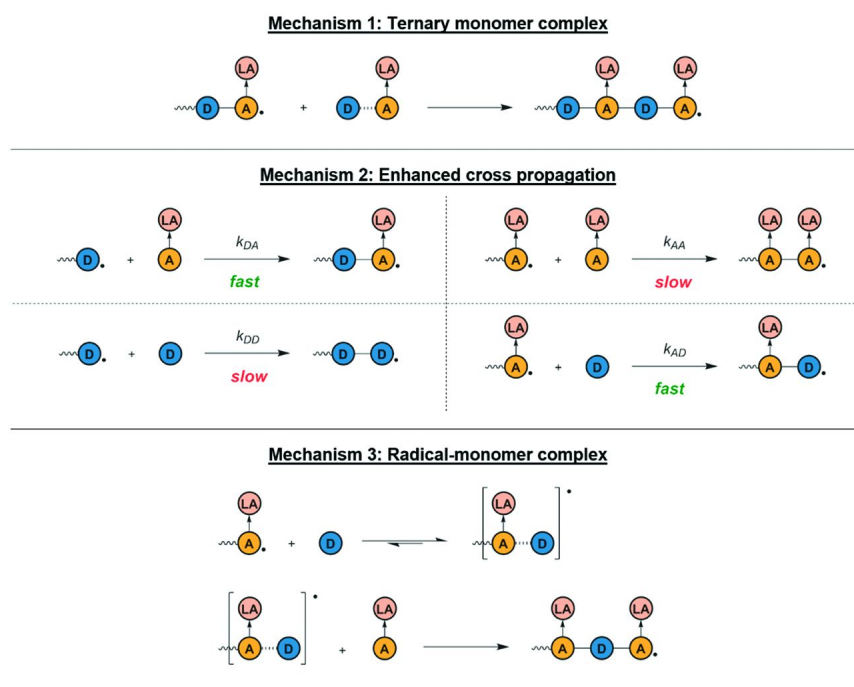


Figure 2. Chemical structures of various unimeric MMA models and their corresponding relative free binding energies ( $\text{kJ mol}^{-1}$ ) to  $\text{BCl}_3$  at  $-95\text{ }^\circ\text{C}$  in toluene.



*Scheme 4. Three Previously Proposed Mechanisms to Explain the Increased Tendency Towards Alternation with LA Inclusion. (A: acceptor monomer, D: donor monomer, LA: Lewis acid)*

### Potential Role of Ternary Monomer and Radical-Monomer Complexes

A ternary monomer complex was proposed by Gotoh *et al.* as the origin of sequence and stereocontrol in the  $\text{BCl}_3$ -mediated MMA/Sty copolymerisation (31). However, other authors have argued that ternary monomer complexes are not, in general, sufficiently stable to explain alternation (64). Moreover, trapping experiments by Tirrell and co-workers found no evidence for concerted monomer addition in a prototypical donor-acceptor copolymerization (chloroethyl vinyl ether and N-phenylmaleimide) (65). Nevertheless, the low polymerization temperatures used by Gotoh *et al.* in their study (i.e.  $-95\text{ }^\circ\text{C}$ ) should enhance the thermodynamic stability of such complexes, which are enthalpically favorable but entropically disfavored. To ascertain the potential importance of ternary monomer complexes, we predicted their stability using high-level theoretical calculations (see Figure 3). As illustrated by Figure 3, formation of a ternary monomer complex is essentially thermoneutral compared with the separated MMA( $\text{BCl}_3$ ) and Sty monomer in toluene at  $-95\text{ }^\circ\text{C}$ . These calculations suggest that formation of the ternary monomer complex formation would be feasible under reaction conditions. However, it should be noted that continuum solvation models usually carry errors of approximately  $4\text{ kJ mol}^{-1}$  for neutral solutes (66).



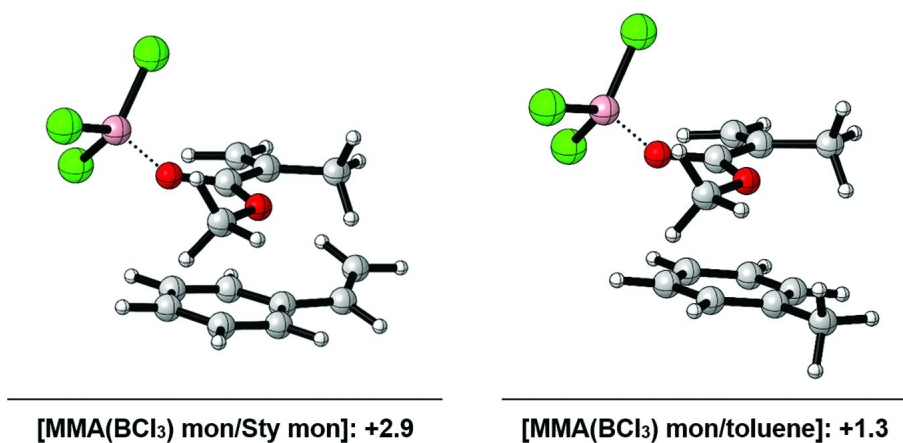


Figure 3. Optimised geometries and binding free energies ( $\text{kJ mol}^{-1}$ ) of the  $\text{MMA}(\text{BCl}_3)/\text{Sty}$  ternary monomer complex and an analogous  $\text{MMA}(\text{BCl}_3)/\text{toluene}$  complex in bulk toluene at  $-95\text{ }^\circ\text{C}$ .

The combination of computational uncertainty and the weak absolute interaction energy makes it difficult to ascertain how prevalent ternary complexes might be under experimental conditions. Thus, we further evaluated the plausibility of this mechanism by assessing the relative strength of the competing complex formed with toluene. Crucially, the relative binding energy of Sty monomer and toluene to  $\text{BCl}_3$  should have a smaller error because of the structural similarities of both donor species. While previous work on pKa prediction has noted that continuum solvent models often carry significant absolute errors, relative solvation energies for solutes that are structurally similar is much less prone to error (66). Moreover, to form a significant amount of ternary monomer complex, the interaction between  $\text{BCl}_3$ -bound MMA monomer and Sty monomer would have to be significantly stronger than the comparable interaction with toluene. If there is not a sufficient thermodynamic preference, then the large molar excess of toluene relative to Sty monomer would disrupt the formation of the ternary monomer complex. As illustrated by Figure 3, the strength of the interaction between  $\text{MMA}(\text{BCl}_3)$  and toluene is slightly stronger than the respective interaction  $\text{MMA}(\text{BCl}_3)$  and Sty monomer. Since the molar ratio of toluene to Sty monomer is over 75:1 under the experimental conditions used, it is unlikely that a ternary monomer complex would be present at significant concentrations.

While noting the weak interaction energy for ternary monomer complexes, analogous radical-monomer complexes should not be automatically discounted. Indeed, the presence of the conjugate radical has been noted to significantly alter the Bronsted (23) and Lewis basicities (67) of carboxylic acid/ ester functional groups. However, we found that a  $\text{BCl}_3$ -complexed unimeric MMA radical had an interaction with Sty monomer that was only marginally stronger (by  $2.9\text{ kJ mol}^{-1}$ )

than that of complexed MMA monomer. This weak interaction would also likely be compounded with similarly poor selectivity for interaction with Sty compared to explicit toluene solvent.

### Enhanced Cross Propagation

Given the thermodynamic instability of the ternary monomer and radical-monomer complexes, enhanced cross-propagation is the remaining plausible mechanism for sequence control. LA complexation can dramatically affect both intrinsic radical stability and the polar characteristics of radical reactions. Indeed, we recently found  $\text{AlCl}_3$  complexation could change the radical stabilization energies (RSEs) of certain photoinitiator derived radicals by as much as  $50 \text{ kJ mol}^{-1}$  (68). Moreover, the reactivity of these radicals could be altered by as much as 8 orders of magnitude through LA coordination (68).  $\text{AlCl}_3$  was also shown to be an excellent propagation catalyst in MMA homopolymerization (69). To explore the effect of  $\text{BCl}_3$  complexation, we calculated reaction barriers and rate coefficients at  $-95^\circ\text{C}$  in toluene for the elementary addition reactions in a Sty/MMA copolymerization assuming a terminal model (see Table 1). We then assessed the impact of  $\text{BCl}_3$  complexation at different ester moieties on these addition barriers and the corresponding solution-phase rate coefficients. While it is well known that the terminal model fails to properly describe unmediated Sty/MMA copolymerization (70), these prototypical reactions are used simply to assess the feasibility of an enhanced cross propagation mechanism.

**Table 1. Calculated Kinetic, Thermodynamic and Polar Parameters at  $-95^\circ\text{C}$  in Toluene for Prototypical Homo- and Cross-Propagation Reactions of Sty and MMA in the Presence and Absence of  $\text{BCl}_3$**

Radical	Monomer	$\Delta G^\ddagger$ ( $\text{kJ mol}^{-1}$ )	$k_{\text{add}}$ ( $\text{L mol}^{-1} \text{ s}^{-1}$ )	$\Delta H_{\text{rxn}}$ ( $\text{kJ mol}^{-1}$ )	$\text{IE}_r + \text{EA}_m$ (eV)	$\text{IE}_m + \text{EA}_r$ (eV)
MMA	Sty	46.5	$8.63 \times 10^{-2}$	-103.2	8.17	7.23
MMA/ $\text{BCl}_3$	Sty	31.9	$1.65 \times 10^3$	-100.8	7.00	4.87
Sty	MMA	48.8	$1.83 \times 10^{-2}$	-85.4	7.02	8.85
Sty	MMA/ $\text{BCl}_3$	25.8	$1.01 \times 10^5$	-109.3	4.82	8.58
MMA	MMA	45.0	$2.37 \times 10^{-1}$	-95.5	8.06	8.40
MMA/ $\text{BCl}_3$	MMA/ $\text{BCl}_3$	31.2	$2.64 \times 10^3$	-128.8	5.60	5.77
Sty	Sty	51.4	$3.16 \times 10^{-3}$	-87.9	7.13	7.68

As Table 1 indicates, unmediated Sty/MMA reactions have addition rate coefficients which are consistent with the random nature of the corresponding copolymerization. The unimeric MMA radical has similar reactivity towards both MMA and Sty monomer, with addition barriers of  $45.0$  and  $46.5 \text{ kJ mol}^{-1}$ , respectively. Similarly, the unimeric Sty radical is comparably reactive towards both MMA and Sty monomer, with addition barriers of  $48.8$  and  $51.4 \text{ kJ mol}^{-1}$ , respectively.  $\text{BCl}_3$  complexation significantly catalyzes both Sty/MMA cross propagation reactions, with corresponding rate coefficient increases of

4-7 orders of magnitude. Interestingly, the Sty radical/MMA monomer cross propagation reaction is catalyzed significantly more than the corresponding MMA radical/Sty monomer. Consistent with previous results for other Las (67, 69), BCl<sub>3</sub>-complexation also lowers the barrier for MMA homopropagation, albeit by a smaller amount. Thus, it is clear that LA complexation results in enhanced cross-propagation, which in turn leads to the alternating behaviour.

The reactivity of the respective radicals and the influence of BCl<sub>3</sub>-complexation can be rationalized by considering the enthalpic and polar characteristics of these reactions. Many radical-based addition reactions obey the Bell–Evans–Polanyi principle (71, 72) and thus  $\Delta H_{\text{rxn}}$  values can be used to infer reactivity changes originating from general enthalpic effects (e.g. intrinsic radical stability). The sum of the radical ionization energy and monomer electron affinity ( $IE_r + EA_m$ ) and the converse sum of radical electron affinity and monomer ionization energy ( $IE_m + EA_r$ ) is frequently used to assess the importance of polar-effects in radical addition reactions. Non-negligible charge transfer in the transition state is indicated by values of  $< 7$  to  $8$  eV, with lower values signifying greater polar stabilization of the transition state (73). To assist in rationalizing these kinetic results, we also calculated both the gas-phase reaction enthalpy ( $\Delta H_{\text{rxn}}$ ) and polar terms ( $IE_r + EA_m$  and  $IE_m + EA_r$ ) for these elementary reactions (see Table 1).

The unmediated cross-propagation reactions are not significantly favoured over the corresponding homopropagation reaction because neither the polar nor the enthalpic effects are significantly different. BCl<sub>3</sub> complexation at the conjugate methyl ester dramatically increases the electrophilicity of MMA radicals and monomer (decreasing their electron affinities by around 2 eV). This results in strong charge transfer stabilization for reactions with the relatively nucleophilic Sty monomer and radicals. Complexation of BCl<sub>3</sub> enthalpically stabilizes the forming MMA radical and consequently increases the favourability of Sty radical addition ( $\Delta H_{\text{rxn}}$  increases by 25 kJ mol<sup>-1</sup>). In contrast, complexed MMA radical addition to Sty monomer is marginally less enthalpically favoured due to this stabilization. This difference in enthalpic favourability can be used to rationalise the greater increase in reactivity for Sty radical cross-propagation ( $\sim 7$  orders of magnitude increase in  $k_{\text{add}}$ ), compared to MMA radical cross-propagation ( $\sim 4$  orders of magnitude).

Interestingly, while BCl<sub>3</sub> greatly enhances the alternation behaviour of Sty-based radicals, it appears to catalyse both homo- and cross-propagation for MMA-based radicals. This suggests that using a unimeric propagating MMA-radical is likely too simplistic and more sophisticated models are required to provide quantitative agreement with experiment. However, these prototypical models confirm the significant impact of BCl<sub>3</sub> on the propagation kinetics and reveal the fundamental origins of alternation.

### Mechanistic Origins of Coheterotactic Specificity

To determine the origins of coheterotactic specificity, we next examined interactions between the phenyl and methyl ester side-chains in various model systems. According to the rapid interconversion scheme, tacticity is determined

by the relative arrangement of the terminal and penultimate side-chains with respect to the macromolecular backbone. However, interactions between the side-chains of the terminal unit and incoming monomer must also be examined, as these interactions can interfere with those of the terminal and penultimate groups and indeed have been shown to be kinetically dominant in other systems (67). To examine the relative strength of the interactions between the terminal-penultimate and terminal-monomer side-chains, we studied the conformational preferences of the dimeric radicals and corresponding transition structures. Specifically, we examined if these side-chains preferred to be in a *syn* (interacting) or *anti* (non-interacting) orientation.

For the MMA(BCl<sub>3</sub>)-Sty radical, there is a strong terminal-penultimate side-chain interaction, with the *syn* conformation favored by 4.6 kJ mol<sup>-1</sup> (see Figure 4). The terminal-monomer interaction in the Sty radical system is significantly weaker, with the *syn* conformation still favored but only by 1.8 kJ mol<sup>-1</sup>. Meanwhile, for the Sty-MMA(BCl<sub>3</sub>) radical, there is no significant terminal-penultimate side-chain interaction, with the *syn* conformation favored by only 0.3 kJ mol<sup>-1</sup> (see Figure 5). However, there is a very strong interaction between the terminal MMA(BCl<sub>3</sub>) side-chain and that of incoming Sty monomer. Indeed, we were unable to find transition state conformations where the terminal and monomer side-chains were not interacting. Collectively, these results indicate that the conformational preferences of propagating Sty radicals are largely dictated by the interactions between the terminal and penultimate side-chains. Conversely, the conformational preferences of propagating MMA(BCl<sub>3</sub>) radicals are largely dictated by the interactions between the terminal and monomer side-chains.

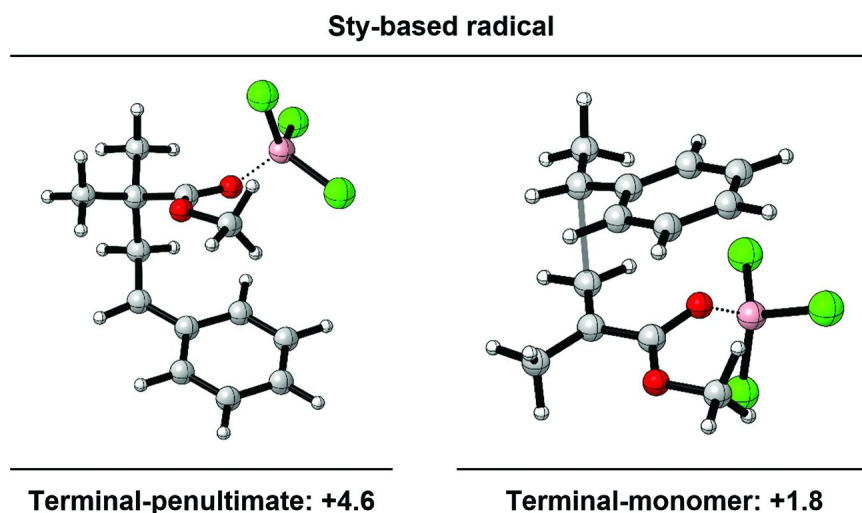
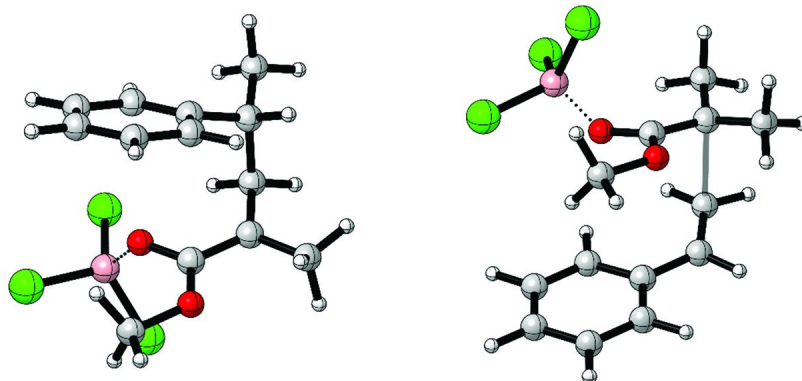


*Figure 4. The strength of terminal-penultimate and terminal-monomer interactions in Sty-based radicals. This is evaluated by comparing the stability of *syn* (side-chains interacting) and *anti* (side-chains not interacting) conformations of the respective dimer and propagating transition structure.*

### MMA( $\text{BCl}_3$ )-based radical



**Terminal-penultimate: +0.3**

**Terminal-monomer: > 10.0**

Figure 5. The strength of terminal-penultimate and terminal-monomer interactions for MMA( $\text{BCl}_3$ ) radicals. This is evaluated by comparing the stability of syn (side-chains interacting) and anti (side-chains not interacting) conformations of the respective dimer and propagating transition structure.

The differing strength of terminal-penultimate and terminal-monomer interactions for each type of radical is intriguing. The electrostatic potential surfaces (ESPs) of the  $\text{BCl}_3$ -complexed methyl ester and phenyl groups are illustrated in Figure 6. We should note that similar ESPs are observed for the side-chains of the terminal radical and polymer chain. That is, the presence of a conjugate radical or a fully saturated alkane (instead of an allylic  $-\text{CH}=\text{CH}_2$  or  $-\text{CCH}_3=\text{CH}_2$  moiety) does not qualitatively alter these surfaces. The face of the phenyl substituent carries a large negative electrostatic potential because of the relatively large quadrupole created by the aromatic  $\pi$ -system. As Figure 7 illustrates, the terminal phenyl side-chain in the MMA( $\text{BCl}_3$ )-Sty radical is positioned around the methoxy methyl region of the methyl ester. In contrast, the penultimate phenyl substituent in the Sty-MMA( $\text{BCl}_3$ ) radical is situated around the acyl O region of the terminal ester side-chain. In other words, the rigidity of the (forming) polymer backbone limits interactions between the adjacent substituents to two different electropositive regions of the ester side-chain, which are centered around the O-acyl atom and methoxy methyl group. The methyl region is significantly more electropositive than the acyl region and consequently the  $\pi$ -methyl interaction is significantly more stabilizing than the  $\pi$ -acyl interaction.

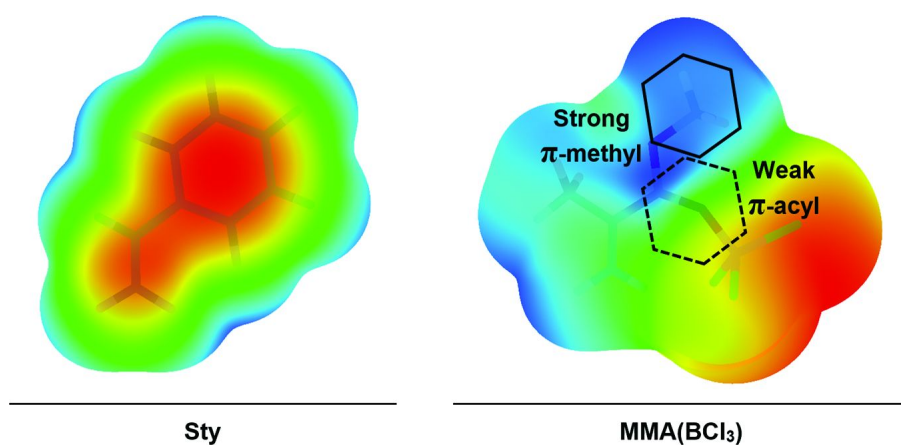


Figure 6. Electrostatic potential surfaces (ESPs) of Sty and MMA(BCl<sub>3</sub>) monomer. The two possible positions of phenyl interaction are illustrated on the MMA(BCl<sub>3</sub>) surface. Darker regions depict areas of greater negative (Left: Sty) or positive (Right: MMA(BCl<sub>3</sub>)) electrostatic potential.

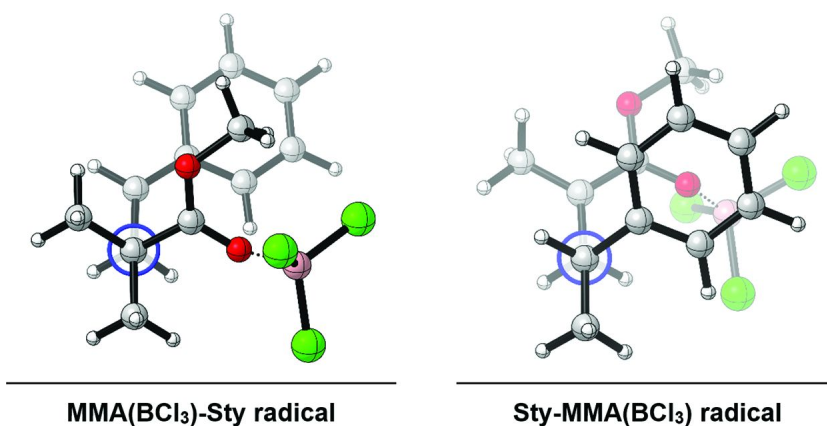


Figure 7. Newman projections of the MMA(BCl<sub>3</sub>)-Sty and Sty-MMA(BCl<sub>3</sub>) radicals highlighting the different relative positioning of the methyl ester and phenyl side-chains.

Having established the dominant pair-wise interactions using dimer models, we then examined the conformational preferences of larger more realistic trimeric radicals (see Figure 8). Unsurprisingly, the MMA(BCl<sub>3</sub>)-Sty-MMA(BCl<sub>3</sub>) radical adopts a linear pro-*racemo* arrangement, which is consistent with the notion that the terminal-penultimate interaction is weak and repulsive for MMA(BCl<sub>3</sub>)

radicals. Crucially, this *pro-racemo* arrangement also leaves the terminal ester side-chain free to interact with incoming Sty monomer. In contrast, the Sty-MMA(BCl<sub>3</sub>)-Sty radical adopts a linear *pro-meso* arrangement, which is consistent with the idea that the terminal-penultimate interactions determine the conformation of the Sty based radicals.

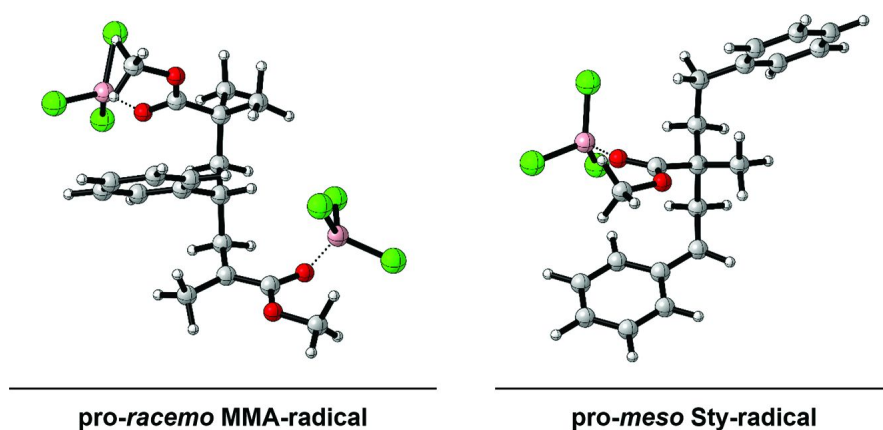
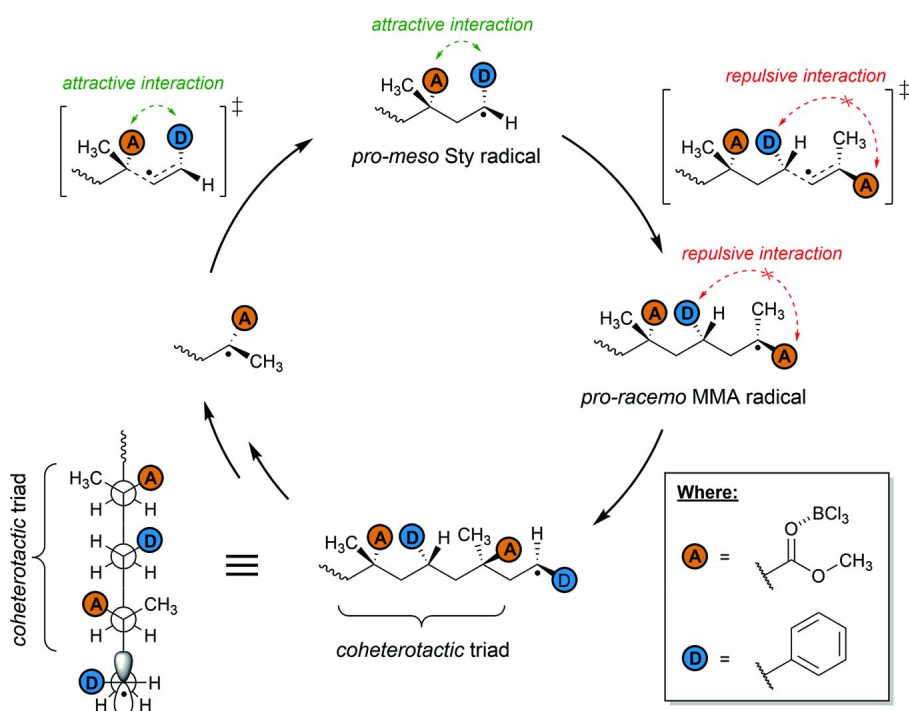


Figure 8. The lowest energy accessible conformations for MMA(BCl<sub>3</sub>)-Sty-MMA(BCl<sub>3</sub>) and Sty-MMA(BCl<sub>3</sub>)-Sty radicals.

The alternating *pro-racemo/pro-meso* conformational preference would lead to alternating *racemo/meso* cross-propagation (see Scheme 5) and hence the coheterotactic microstructure observed by Gotoh and co-workers (74, 75) (see Scheme 3c). This mechanism is consistent with the observation that catalytic quantities of BCl<sub>3</sub> can induce alternation (36) but not coheterotactic control (37). Specifically, the *pro-meso* conformational preference observed for propagating Sty radicals results from interactions between the terminal phenyl and penultimate ester substituents. If the penultimate ester substituent is not complexed with BCl<sub>3</sub>, then no appreciable selectivity for either *pro-meso* or *pro-racemo* conformations was observed. Moreover, the *pro-racemo* conformational preference of MMA-based radicals is also reduced if the antepenultimate ester is not complexed with BCl<sub>3</sub>, as the penultimate phenyl side-chain can interact more effectively with the terminal ester substituent. In other words, sequence control only requires BCl<sub>3</sub>-complexation of the terminal and monomer side-chains, while stereocontrol requires the complexation of the penultimate and antepenultimate substituents as well.



Scheme 5. A Simplified Mechanism of Coheterotactic Selectivity for  $\text{BCl}_3$ -Mediated MMA/Sty Copolymerization.

## Conclusions

To conclude, high-level *ab initio* calculations have been used to investigate the origin of sequence and stereo-control of the  $\text{BCl}_3$  mediated copolymerization of MMA and styrene. It is found that the high degree of alternation can be attributed to an enhanced cross-propagation mechanism. Moreover, the dramatic increase in reactivity calculated for  $\text{BCl}_3$ -complexed MMA monomer units and MMA radical chain-ends agrees with the experimental observation that alternation only requires the addition of a catalytic amount of  $\text{BCl}_3$ . Coheterotactic control is found to originate from  $\pi$ -stacking interactions between the  $\text{BCl}_3$  complexed methyl-esters and the phenyl groups; these interactions result in the terminal ester moiety of a MMA radical chain end preferentially interacting with the  $\pi$ -system of the incoming styrene monomer unit, rather than the preceding styrene unit. Conversely, the styrene radical chain end exhibits a strong preference for the ester moiety present in the preceding MMA unit, with no significant interaction with incoming MMA monomer. Collectively, these two effects result in cross-propagation reactions that strongly favour coheterotacticity. Unlike alternation, for which only a catalytic amount of  $\text{BCl}_3$  is required, coheterotacticity



requires a stoichiometric amount. This can be reconciled by the fact that for stereocontrol to be imparted, there is a requirement for BCl<sub>3</sub> to be bound to the penultimate and antepenultimate chain units; there would be no thermodynamic or kinetic preference for this to be the case if only a small amount of BCl<sub>3</sub> is present.

## Acknowledgments

MLC gratefully acknowledges financial support from the Australian Research Council through an ARC Laureate Fellowship, and generous allocations of supercomputing time on the National Facility of the National Computational Infrastructure.

## References

1. Solomon, D. H.; Rizzardo, E.; Cacioli, P. *Polymerization process and polymers produced thereby*. 4,581,429, 1985.
2. Georges, M. K.; Veregin, R. P. N.; Kazmaier, P. M.; Hamer, G. K. *Macromolecules* **1993**, *26*, 2987–2988.
3. Hawker, C. J.; Bosman, A. W.; Harth, E. *Chem. Rev.* **2001**, *101*, 3661–3688.
4. Gimes, D. *Nitroxide Mediated Polymerization: From Fundamentals to Applications in Materials Science*; The Royal Society of Chemistry: U.K., 2016.
5. Grubbs, R. B. *Polym. Rev.* **2011**, *51*, 104–137.
6. Nicolas, J.; Guillaneuf, Y.; Lefay, C.; Bertin, D.; Gimes, D.; Charleux, B. *Prog. Polym. Sci.* **2013**, *38*, 63–235.
7. Matyjaszewski, K.; Wang, J.-S. *(Co)polymers and a novel polymerization process based on atom (or group) transfer radical polymerization*. 5,763,548, 1995.
8. Wang, J. S.; Matyjaszewski, K. *J. Am. Chem. Soc.* **1995**, *117*, 5614–5615.
9. Tsarevsky, N. V.; Matyjaszewski, K. *Chem. Rev.* **2007**, *107*, 2270–2299.
10. Le, T.; Moad, G.; Rizzardo, E.; Thang, S. H. *Polymerization with Living Characteristics*. 7,250,479, 2007.
11. Chiefari, J.; Chong, Y. K.; Ercole, F.; Krstina, J.; Jeffery, J.; Le, T. P. T.; Mayadunne, R. T. A.; Meijs, G. F.; Moad, C. L.; Moad, G.; Rizzardo, E.; Thang, S. H. *Macromolecules* **1998**, *31*, 5559–5562.
12. Moad, G.; Rizzardo, E.; Thang, S. H. *Accounts. Chem. Res.* **2008**, *41*, 1133–1142.
13. Delduc, P.; Tailhan, C.; Zard, S. Z. *J. Chem. Soc. Chem. Comm.* **1988**, 308–310.
14. Zard, S. Z. *Angew. Chem., Int. Ed.* **1997**, *36*, 673–685.
15. Zard, S. Z. *Aust. J. Chem.* **2006**, *59*, 663–668.
16. Zard, S. Z. *J. Phys. Org. Chem.* **2012**, *25*, 953–964.
17. Matyjaszewski, K.; Tsarevsky, N. V. *Nat. Chem.* **2009**, *1*, 276–288.
18. Matyjaszewski, K.; Tsarevsky, N. V. *J. Am. Chem. Soc.* **2014**, *136*, 6513–6533.

19. Feng, H.; Lu, X.; Wang, W.; Kang, N.-G.; Mays, J. *Polymers* **2017**, *9*, 494.
20. Moad, G.; Guerrero-Sanchez, C.; Haven, J. J.; Keddie, D. J.; Postma, A.; Rizzardo, E.; Thang, S. H. In *Sequence-Controlled Polymers: Synthesis, Self-Assembly, and Properties*; American Chemical Society: 2014; Vol. 1170, pp 133–147.
21. Satoh, K.; Kamigaito, M. *Chem. Rev.* **2009**, *109*, 5120–5156.
22. Noble, B. B.; Coote, M. L. In *Advances in Physical Organic Chemistry*; Williams, I. H., Williams, N. H., Eds.; Academic Press, 2015; Vol. 49, pp 189–258.
23. Noble, B. B.; Coote, M. L. In *Controlled Radical Polymerization: Mechanisms*; American Chemical Society, 2015; Vol. 1187, pp 51–72.
24. Suito, Y.; Isobe, Y.; Habaue, S.; Okamoto, Y. *J. Polym. Sci., Part A* **2002**, *40*, 2496–2500.
25. Isobe, Y.; Suito, Y.; Habaue, S.; Okamoto, Y. *J. Polym. Sci., Part A* **2003**, *41*, 1027–1033.
26. Bamford, C. H. *Proc. R. Soc. London A, Ser. A Math. Phys. Sci.* **1957**, *241*, 364–375.
27. Noble, B. B.; Smith, L. M.; Coote, M. L. *Polym. Chem.* **2014**, *5*, 4974–4983.
28. Jiang, J. Y.; Smith, L. M.; Tyrell, J. H.; Coote, M. L. *Polym. Chem.* **2017**, *8*, 5948–5953.
29. Matsumoto, A.; Nakamura, S. *J. Appl. Polym. Sci.* **1999**, *74*, 290–296.
30. Noble, B. B.; Mater, A. C.; Smith, L. M.; Coote, M. L. *Polym. Chem.* **2016**, *7*, 6400–6412.
31. Hirooka, M.; Yabuuchi, H.; Morita, S.; Kawasumi, S.; Nakaguchi, K. *J. Polym. Sci., Part B* **1967**, *5*, 47–55.
32. Hirooka, M.; Yabuuchi, H.; Iseki, J.; Nakai, Y. *J. Polym. Sci., Part A* **1968**, *6*, 1381–1396.
33. Hirai, H. *J. Polym. Sci. Macromol. Rev.* **1976**, *11*, 47–91.
34. Hirai, H.; Tanabe, T.; Koinuma, H. *J. Polym. Sci., Part A* **1980**, *18*, 203–222.
35. Lutz, J.-F.; Kirci, B.; Matyjaszewski, K. *Macromolecules* **2003**, *36*, 3136–3145.
36. Hirai, H.; Takeuchi, K.; Komiyama, M. *J. Polym. Sci., Part A* **1981**, *19*, 2581–2594.
37. Yaeko, G.; Tadashi, I.; Naokuni, K.; Naoki, T.; Hidefumi, H. *Chem. Lett.* **1990**, *19*, 2157–2160.
38. Yaeko, G.; Mihoko, Y.; Masato, N.; Naoki, T.; Hidefumi, H. *Chem. Lett.* **1991**, *20*, 53–56.
39. Frisch, J.; Trucks, G. W.; Schlegel, H. B. S., G. E.; Robb, M. A.; Cheeseman, J. R.; Scalmani, G.; Barone, V.; Mennucci, B.; Petersson, G. A.; Nakatsuji, H.; Caricato, M.; Li, X.; Hratchian, H. P.; Izmaylov, A. F.; Bloino, J.; Zheng, G.; Sonnenberg, J. L.; Hada, M.; Ehara, M.; Toyota, K.; Fukuda, R.; Hasegawa, J.; Ishida, M.; Nakajima, T.; Honda, Y.; Kitao, O.; Nakai, H.; Vreven, T.; Montgomery, J. A.; Peralta, J., J. E.; Ogliaro, F.; Bearpark, M.; Heyd, J. J.; Brothers, E.; Kudin, K. N.; Staroverov, V. N.; Keith, T.; Kobayashi, R.; Normand, J.; Raghavachari, K.; Rendell, A.; Burant, J. C.; Iyengar, S. S.; Tomasi, J.; Cossi, M.; Rega, N.; Millam, J. M.; Klene, M.; Knox, J. E.; Cross, J. B.; Bakken, V.; Adamo, C.; Jaramillo, J.; Gomperts,

- R.; Stratmann, R. E.; Yazyev, O.; Austin, A. J.; Cammi, R.; Pomelli, C.; Ochterski, J. W.; Martin, R. L.; Morokuma, K.; Zakrzewski, V. G.; Voth, G. A.; Salvador, P.; Dannenberg, J. J.; Dapprich, S.; Daniels, A. D.; Farkas, O.; Foresman, J. B.; Ortiz, J. V.; Cioslowski, J.; Fox, D. J. *Gaussian 09*, Rev. D; Gaussian, Inc.: Wallingford CT, 2013.
40. Werner, H.-J.; Knowles, P. J.; Knizia, G.; Manby, F. R.; Schütz, M. *WIREs Comput. Mol. Sci.* **2012**, *2*, 242–253.
  41. Werner, H.-J.; Knowles, P. J.; Knizia, G.; Manby, F. R.; Schütz, M.; Celani, P. G. W.; Kats, D. K., T.; Lindh, R.; Mitrushenkov, A.; Rauhut, G. S., K. R.; Adler, T. B. A., R. D.; Bernhardsson, A.; Berning, A. C., D. L.; Deegan, M. J. O.; Dobbyn, A. J.; Eckert, F.; Goll, E.; Hampel, C.; Hesselmann, A.; Hetzer, G.; Hrenar, T.; Jansen, G.; Köppl, C.; Liu, Y.; Lloyd, A. W.; Mata, R. A.; May, A. J.; McNicholas, S. J.; Meyer, W.; Mura, M. E.; Nicklass, A.; O'Neill, D. P.; Palmieri, P.; Peng, D.; Pflüger, K.; Pitzer, R.; Reiher, M.; Shiozaki, T.; Stoll, H.; Stone, A. J.; Tarroni, R.; Thorsteinsson, T.; Wang, M. *MOLPRO*, version 2015.1, a package of ab initio programs; 2015.
  42. Zhao, Y.; Truhlar, D. G. *Theor. Chem. Acc.* **2008**, *120*, 215–241.
  43. Curtiss, L. A.; Raghavachari, K.; Redfern, P. C.; Baboul, A. G.; Pople, J. A. *Chem. Phys. Lett.* **1999**, *314*, 101–107.
  44. Izgorodina, E. I.; Brittain, D. R. B.; Hodgson, J. L.; Krenske, E. H.; Lin, C. Y.; Namazian, M.; Coote, M. L. *J. Phys. Chem. A* **2007**, *111*, 10754–10768.
  45. Coote, M. L.; Krenske, E. H.; Izgorodina, E. I. *Macromol. Rapid Commun.* **2006**, *27*, 473–497.
  46. Lin, C. Y.; Hodgson, J. L.; Namazian, M.; Coote, M. L. *J. Phys. Chem. A* **2009**, *113*, 3690–3697.
  47. Noble, B. B.; Coote, M. L. *Int. Rev. Phys. Chem.* **2013**, *32*, 467–513.
  48. Lin, C. Y.; Izgorodina, E. I.; Coote, M. L. *Macromolecules* **2010**, *43*, 553–560.
  49. Klamt, A. *J. Phys. Chem.* **1995**, *99*, 2224–2235.
  50. Klamt, A.; Jonas, V.; Bürger, T.; Lohrenz, J. C. *J. Phys. Chem. A* **1998**, *102*, 5074–5085.
  51. Klamt, A. *COSMO-RS: from quantum chemistry to fluid phase thermodynamics and drug design*; Elsevier, 2005.
  52. Louwen, J. N.; C. C. Pye; van Lenthe, E.; McGarrity, E. S.; Xiong, R.; Sandler, S. I.; Burnett, R. I. In *ADF2014 COSMO-RS, SCM, Theoretical Chemistry*; Vrije Universiteit: Amsterdam, The Netherlands, 2014; <http://www.scm.com>.
  53. Pye, C. C.; Ziegler, T.; Van Lenthe, E.; Louwen, J. N. *Can. J. Chem.* **2009**, *87*, 790–797.
  54. Klamt, A.; Jonas, V.; Bürger, T.; Lohrenz, J. C. W. *J. Phys. Chem. A* **1998**, *102*, 5074–5085.
  55. Klamt, A.; Eckert, F. *Fluid Phase Equilib.* **2000**, *172*, 43–72.
  56. Truhlar, D. G.; Garrett, B. C.; Klippenstein, S. J. *J. Phys. Chem.* **1996**, *100*, 12771–12800.
  57. Bamford, C. H.; Malley, P. J. *J. Polym. Sci., Part C* **1981**, *19*, 239–247.
  58. Afchar-Momtaz, J.; Polton, A.; Tardi, M.; Sigwalt, P. *Eur. Polym. J.* **1985**, *21*, 1067–1073.

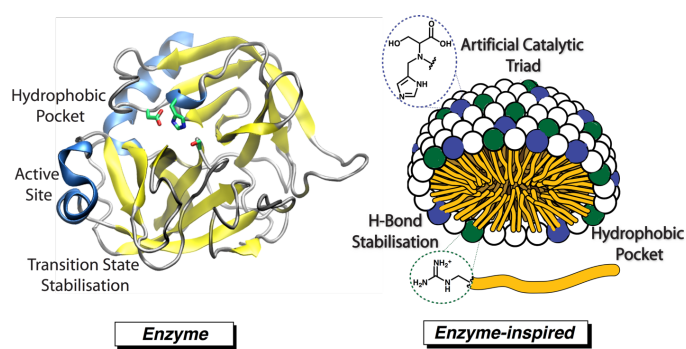
59. Hill, D. J. T.; O'Donnell, J. H.; O'Sullivan, P. W. *Macromolecules* **1985**, *18*, 9–17.
60. Zubov, V. P.; Lachinov, M. B.; Ignatova, E. V.; Georgiev, G. S.; Golubev, V. B.; Kabanov, V. A. *J. Polym. Sci., Part A* **1982**, *20*, 619–638.
61. Hill, D. J. T.; O'Donnell, J. J.; O'Sullivan, P. W. *Prog. Polym. Sci.* **1982**, *8*, 215–275.
62. Golubev, V. B.; Zubov, V. P.; Georgiev, G. S.; Stoyachenko, I. L.; Kabanov, V. A. *J. Polym. Sci., Part A* **1973**, *11*, 2463–2487.
63. Hirooka, M. *J. Polym. Sci., Part B* **1972**, *10*, 171–176.
64. Bamford, C. H. In *Alternating Copolymers*; Cowie, J. M. G., Ed.; Plenum Press: New York, 1985.
65. Jones, S. A.; Tirrell, D. A. *Macromolecules* **1986**, *19*, 2080–2082.
66. Ho, J.; Coote, M. L. *Theor. Chem. Acc.* **2009**, *125*, 3.
67. Noble, B. B.; Smith, L. M.; Coote, M. L. *Polym. Chem.* **2014**, *5*, 4974–4983.
68. Noble, B. B.; Mater, A. C.; Smith, L. M.; Coote, M. L. *Polym. Chem.* **2016**, *7*, 6400–6412.
69. Jiang, J. Y.; Smith, L. M.; Tyrell, J. H.; Coote, M. L. *Polym. Chem.* **2017**, *8*, 5948–5953.
70. Coote, M. L.; Davis, T. P. *Prog. Polym. Sci.* **1999**, *24*, 1217–1251.
71. Evans, M. G.; Polanyi, M. *J. Chem. Soc. Faraday Trans.* **1936**, *32*, 1333–1360.
72. Bamford, C. H. *Proc. R. Soc. London, Ser. A Math. Phys. Sci.* **1957**, *241*, 364–375.
73. Fischer, H.; Radom, L. *Angew. Chem., Int. Ed.* **2001**, *40*, 1340–1371.
74. Yaeko, G.; Tadashi, I.; Naokuni, K.; Naoki, T.; Hidefumi, H. *Chem. Lett.* **1990**, *19*, 2157–2160.
75. Yaeko, G.; Mihoko, Y.; Masato, N.; Naoki, T.; Hidefumi, H. *Chem. Lett.* **1991**, *20*, 53–56.

## 6.3 Publication 13

### A Multi-Functional Surfactant Catalyst Inspired by Hydrolyases

Mitchel D. Nothling, Zeyun Xiao, **Nicholas S. Hill**, Mitchell T. Blyth, Ayana Bhaskaran, Marc-Antoine Sani, Andrea Espinosa-Gomez, Kevin Ngov, Jonathon White, Tim Buscher, Frances Separovic, Megan O'Mara, Michelle L. Coote, Luke A. Connal

*Science Advances* 2020, 6



This publication is a peer-reviewed manuscript published in *Science Advances*. All quantum chemistry computational results and subsequent discussion are my own work, with molecular dynamics calculations and discussion performed by Mr. Mitchell Blyth. Prof. Michelle Coote assisted with the direction of the theoretical investigations and corrected my draft write-ups, and Dr. Luke Connal also provided valuable insight into the direction of the study. Dr Mitchel Nothling and Dr Zeyun Xiao provided the experimental results. [Supplementary material is available online.](#)

### Statement of Contribution

This thesis is submitted as a Thesis by Compilation in accordance with [https://policies.anu.edu.au/ppi/document/ANUP\\_003405](https://policies.anu.edu.au/ppi/document/ANUP_003405)

I declare that the research presented in this Thesis represents original work that I carried out during my candidature at the Australian National University, except for contributions to multi-author papers incorporated in the Thesis where my contributions are specified in this Statement of Contribution.

Title: A Multi-Functional Surfactant Catalyst Inspired by Hydrolyases

Authors: Mitchel D. Nothling, Zeyun Xiao, Nicholas S. Hill, Mitchell T. Blyth, Ayana Bhaskaran, Marc-Antoine Sani, Andrea Espinosa-Gomez, Kevin Ngov, Jonathon White, Tim Buscher, Frances Separovic, Megan O'Mara, Michelle L. Coote, Luke A. Connal

Publication outlet: Science Advances

Current status of paper: Published

Contribution to paper: I am the first contributing computational chemistry author. The quantum chemistry computational results, mechanistic insight, and subsequent discussion are my own work

Senior author or collaborating authors endorsement: Michelle Cootes

Nicholas Hill



14/05/2020

Candidate - Print Name

Signature

Date

#### Endorsed

Michelle Coote



14/05/2020

Primary Supervisor – Print Name

Signature

Date

Luke Connal



14/05/2020

Delegated Authority – Print Name

Signature

Date

## CHEMISTRY

## A multifunctional surfactant catalyst inspired by hydrolases

Mitchell D. Nothling<sup>1</sup>, Zeyun Xiao<sup>2</sup>, Nicholas S. Hill<sup>3</sup>, Mitchell T. Blyth<sup>3</sup>, Ayana Bhaskaran<sup>3</sup>, Marc-Antoine Sani<sup>4</sup>, Andrea Espinosa-Gomez<sup>1</sup>, Kevin Ngov<sup>1</sup>, Jonathan White<sup>4</sup>, Tim Buscher<sup>5</sup>, Frances Separovic<sup>4</sup>, Megan L. O'Mara<sup>3</sup>, Michelle L. Coote<sup>6</sup>, Luke A. Connal<sup>3\*</sup>

The remarkable power of enzymes to undertake catalysis frequently stems from their grouping of multiple, complementary chemical units within close proximity around the enzyme active site. Motivated by this, we report here a bioinspired surfactant catalyst that incorporates a variety of chemical functionalities common to hydrolytic enzymes. The textbook hydrolase active site, the catalytic triad, is modeled by positioning the three groups of the triad (-OH, -imidazole, and -CO<sub>2</sub>H) on a single, trifunctional surfactant molecule. To support this, we recreate the hydrogen bond donating arrangement of the oxyanion hole by imparting surfactant functionality to a guanidinium headgroup. Self-assembly of these amphiphiles in solution drives the collection of functional headgroups into close proximity around a hydrophobic nano-environment, affording hydrolysis of a model ester at rates that challenge  $\alpha$ -chymotrypsin. Structural assessment via NMR and XRD, paired with MD simulation and QM calculation, reveals marked similarities of the co-micelle catalyst to native enzymes.

## INTRODUCTION

The impressive catalytic power of enzymes, as well as their remarkable stereo-, regio- and substrate specificity, has underpinned the evolution of life on Earth. Much research has been directed at elucidating the structure and function of enzymes, and it is now well accepted that many enzymes use a complex suite of covalent, electrostatic, hydrogen bonding (H-bonding), and directional interactions to undertake catalysis (1–7). Notably, it is the well-defined combination of multiple chemical interactions within the enzyme protein structure that gives rise to their unrivalled rate enhancement (8). In the study of enzyme function and in the development of new catalysts, a major target for researchers has been the design of simpler, small-molecule enzyme models that incorporate one or more of these interactions. An understanding that enzymes, as Knowles (9) suggests, are “not different, just better” has driven the exploration of such model materials, although the realization of substantial reaction rate enhancements remains extremely challenging. The field of enzyme mimicry based on active-site structure has been widely examined, with pioneering work by Breslow (10), Cram (11, 12), and Rebek (13) and their co-workers introducing the idea of synthetic binding pockets that may attract and partition substrates similarly to native enzymes (14).

Hydrolytic enzymes (hydrolases) as an enzyme family have received significant focus due to their ubiquity in living systems and their increasing industrial relevance (15, 16). In particular, the serine proteases are an important hydrolase class that have been the target of enzyme-mimicking efforts, with the digestive protease  $\alpha$ -chymotrypsin an illustrative example of controlling multiple chemical interactions

(10, 17–19). At the core of the protein structure lies a relatively small functional area, the active site, which mediates their important reactions. The active site of chymotrypsin-like hydrolases is often composed of a hydrophobic binding pocket that contains three spatially close amino acid residues, histidine, aspartate, and serine, known as the catalytic triad (20, 21). In addition, the important functional role of the active-site residues is frequently supported by nearby complementary residues that participate in H-bonding with reaction intermediates and transition states to reduce the activation energy of the catalytic reaction. In many serine proteases, two nearby peptide N–H moieties undertake this role in a region known as the oxyanion hole (22). The combination of a hydrophobic pocket, the catalytic triad residues, and the oxyanion hole in the hydrolases collectively affords hydrolysis of select substrates at rates approaching the diffusion limit (23). A long-standing challenge for researchers is to imitate the unique structural features of hydrolases in a synthetic catalyst system. Progress in synthetic polymer chemistry has afforded abiotic macromolecules that can self-assemble to afford unique internal environments and functionalities, similar to native enzymes (24–26). In particular, the collapse or folding of polymeric chains—termed foldamers—into single-chain nanoparticles represents a powerful approach to mimic the tertiary structure of biopolymers (27, 28). However, the influence of synergizing multiple chemical and physical interactions into an effective catalyst design remains mostly an open question (26).

The challenge we have targeted is to combine these multiple enzyme properties—the active-site chemistry, hydrophobic environment, and transition-state stabilization—into a single enzyme-inspired catalytic system. We do this by using the ubiquitous method of self-assembling amphiphiles to recreate the macromolecular architecture of enzymes by forming micelles. Micellar catalysis has been an active research area, including work that aims to mimic the hydrophobic binding pocket of enzymes with the internal, low-polarity environment of micelles (29–32). Early work by Kunitake *et al.* (33, 34), Ihara *et al.* (35), and Tonellato (36, 37) illustrated the benefit of functionalized surfactant headgroups for undertaking both inter- and intramolecular cooperative catalysis. However, to the best

Copyright © 2020  
The Authors, some  
rights reserved;  
exclusive licensee  
American Association  
for the Advancement  
of Science. No claim to  
original U.S. Government  
Works. Distributed  
under a Creative  
Commons Attribution  
NonCommercial  
License 4.0 (CC BY-NC).

Downloaded from <http://advances.sciencemag.org/> on May 13, 2020

<sup>1</sup>Department of Chemical and Biomolecular Engineering, The University of Melbourne, Melbourne, VIC 3010, Australia. <sup>2</sup>Chongqing Institute of Green and Intelligent Technology, Chinese Academy of Sciences, Chongqing 400714, P. R. China. <sup>3</sup>Research School of Chemistry, Australian National University, Canberra, ACT 2601, Australia. <sup>4</sup>School of Chemistry, Bio21 Institute, The University of Melbourne, Melbourne, VIC 3010, Australia. <sup>5</sup>Department of Chemistry and Biochemistry, University of California, Santa Barbara, Santa Barbara, CA 93106, USA. <sup>6</sup>ARC Centre of Excellence for Electromaterials Science, Research School of Chemistry, Australian National University, Canberra, ACT 2601, Australia.

\*Corresponding author. Email: [luke.connal@anu.edu.au](mailto:luke.connal@anu.edu.au)

of our knowledge, no previous study has combined the three groups of the catalytic triad into the headgroup of a surfactant—and furthermore including transition-state stabilization groups into a co-micellar system. Herein, we report a bioinspired catalyst that contains an imidazole, a hydroxyl, and a carboxylate group in close proximity on a single molecule to give an artificial catalytic triad (ACT) (Fig. 1). The simple, high-yielding, and modular synthesis allows fine adjustment to the relative positioning of the catalytic functional groups, yielding a surfactant-type molecule with a catalytic triad functionalized headgroup that can form a co-micelle capsule in solution. Furthermore, inspired by the active site of native enzymes, which is supported by an oxyanion hole, these ACT surfactants have then been coassembled with a guanidine headgroup 16-carbon surfactant. Such a cosurfactant is capable of donating strong, bifurcated H-bonding and is critical to assist the ACT in catalysis by undertaking supporting interactions with the catalyst-substrate complex. This approach is a simple and scalable synthesis for the creation of a multifunctional, synthetic self-assembled catalytic system inspired by the properties of serine proteases.

## RESULTS AND DISCUSSION

We found inspiration in the power of micellar self-assembly to drive the collection of multiple functionalities into a confined environment, analogous to the protein folding of enzymes. In this way, the assembly

of surfactants, which contain the functional units associated with hydrolase activity (i.e., hydroxyl, imidazole, carboxylate, and H-bond donors) as headgroup, could direct these units into close proximity to undertake bioinspired catalysis. We reasoned that a loss in ideal functional group placement and rigidity in a micellar system may be compensated by an increased number of active sites and flexibility in catalyst placement. Therefore, our first target was the preparation of a functionalized surfactant containing the three groups of the catalytic triad (Fig. 1A).

To achieve this, we used the readily available amino acid L-serine to provide a primary hydroxyl (as the serine residue does in the natural enzyme; Fig. 1C) and a carboxylate group to act as an activator. Attaching 2-formyl imidazole to the primary amine of L-serine via reductive amination is then used to introduce the third component of the catalytic triad, the basic imidazole unit. This straightforward synthesis quantitatively results in a bioinspired trifunctional molecule (an ACT) with each of the three groups of the catalytic triad positioned in close proximity on the same structure. Addition of surfactant functionality is then achieved via the addition of *n*-hexadeca-1-ol to the secondary amine of the ACT by way of a second reductive amination, resulting in a 16-carbon ACT surfactant (ACT-C<sub>16</sub>) (38). This two-step strategy represents a powerful route toward highly functional, enzyme-inspired molecules from readily available starting materials, and its modularity enables fine adjustment to the relative positioning of functional groups.

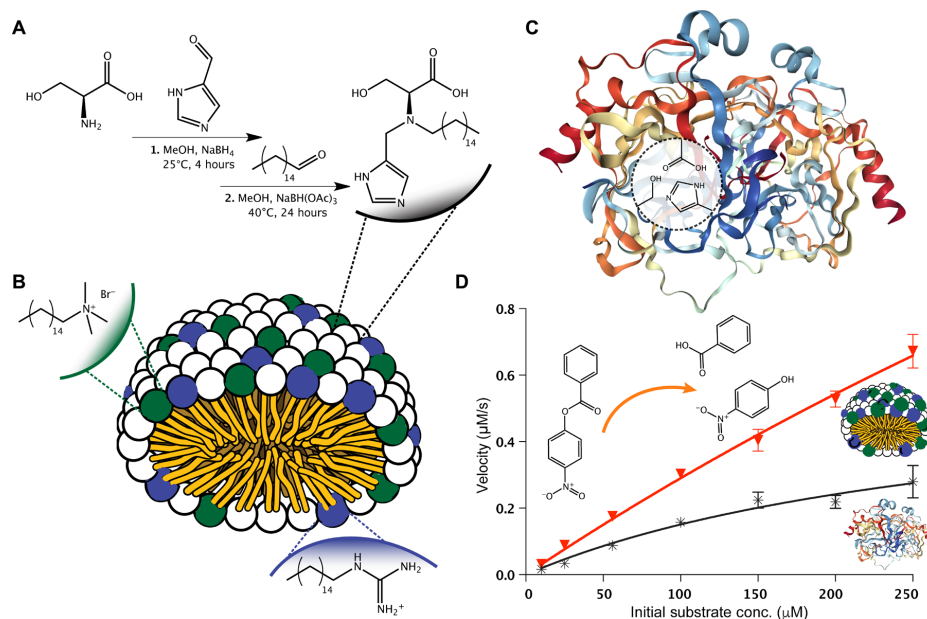


**Fig. 1. A hydrolase-inspired cosurfactant catalyst.** (A) Straightforward preparation of a novel surfactant incorporating an ACT of hydroxyl, carboxylate, and imidazole units as headgroup. (B) Self-assembly of the ACT surfactant with cosurfactants [hexadecyl guanidinium hydrochloride (Guan-C<sub>16</sub>) and cetyltrimethylammonium bromide (CTAB)] yields a functionalized micelle with an internal hydrophobic core as a mimic of native hydrolase binding pockets. (C) The active site of a common hydrolase,  $\alpha$ -chymotrypsin, highlighting a similar hydrophobic pocket and a catalytic triad of active residues to that of the ACT-surfactant system (74). (D) The ACT-surfactant coassembly displays an enhanced esterolytic effect for a model substrate when directly compared with the native enzyme  $\alpha$ -chymotrypsin. (Data points are the mean of at least three independent experiments, and error bars represent SEM.)



With the active site-inspired ACT-C<sub>16</sub> in hand, we sought to further extend our design to incorporate a cosurfactant with H-bonding capability as mimicry of the oxyanion hole. We selected guanidine for this role, whose dual N—H bonds are capable of bifurcated H-bond formation, and which has been shown to participate in a variety of nucleophilic and general base catalysis roles, including in native proteins (Fig. 1B) (39–41). In addition, a guanidine-based surfactant has been shown to increase self-assembly properties due to enhanced H-bond formation between the guanidine headgroups, an advantageous trait to potentially complement the ACT surfactant during catalysis (42). The guanidine-containing surfactant hexadecyl guanidinium chloride (Guan-C<sub>16</sub>) was prepared according to prior literature under mild conditions in quantitative yields, with purification by a single recrystallization step (43).

Assessment of the self-assembly of Guan-C<sub>16</sub> in borate buffer [0.1 M (pH 9.0), 25°C] by the pyrene fluorescence technique revealed a critical micelle concentration (CMC) of 0.28 mM, with the material precipitating at higher concentrations (fig. S1). In contrast, the assessment of the CMC of ACT-C<sub>16</sub> proved inconclusive because of a low aqueous solubility at room temperature. To address the low solubility of both bioinspired surfactants, we added the common cationic surfactant cetyltrimethylammonium bromide (CTAB) to a buffered mixture of ACT-C<sub>16</sub> and Guan-C<sub>16</sub> (ACT-C<sub>16</sub>:Guan-C<sub>16</sub>:CTAB = 0.002:0.3:0.8 mM), resulting in a clear solution. These concentrations were selected to (i) ensure micelle formation by targeting a value just above the CMC of both CTAB and Guan-C<sub>16</sub> and (ii) provide a low, catalytic amount of ACT, such that substrate turnover and saturation kinetics could be targeted during catalytic assessment. The complete dissolution of both bioinspired surfactants on the addition of CTAB provides support for their inclusion into a three-component co-micelle system.

Hydrolysis of a model ester substrate [*p*-nitrophenol benzoate (PNB)] was used to examine the catalytic effect of the three-component surfactant system, which releases the chromogenic product *p*-nitrophenol (Fig. 1D). Enhanced PNB hydrolysis was observed across a broad range of initial substrate concentrations (10 to 250 μM, equating to a catalyst loading of 0.1 to 22 mole percent), with an ACT substrate turnover rate of 1.90 s<sup>-1</sup> calculated under Michaelis-Menten kinetics (table S1). Compared with the uncatalyzed reaction without any surfactant addition, this represents an approximately 16,000-fold rate enhancement. Excluding any of the three surfactants from the co-micellar assembly resulted in a significantly reduced catalytic effect, particularly when excluding CTAB, which appears pivotal in maintaining solubility of Guan-C<sub>16</sub> and ACT surfactants. An equivalent concentration of CTAB was added to all assays to ensure a consistent comparison between catalysts, as CTAB can contribute to background ester hydrolysis. Subsequent assessment of the native protease  $\alpha$ -chymotrypsin under the same reaction conditions revealed a sevenfold lower substrate turnover rate, highlighting the power of our bioinspired approach under the model conditions. However, the observed Michaelis constant  $K_M$  for the enzyme (0.3 mM) is also lower than that for the bioinspired micelle system (1.47 mM). This result may indicate either a lower binding affinity of the micellar catalyst with the ester substrate or an additional contribution of the cosurfactants toward hydrolysis, separate from that undertaken by the ACT. Under the assay conditions, the latter hypothesis would seem more likely, increasing the apparent saturation concentration of the ACT due to the known general base catalysis performed by both CTAB and guanidinium (discussed below). In

addition, saturation of the co-micellar construct with the hydrophobic substrate may alter the physical characteristics of the catalytic system, affecting the observed catalysis at higher substrate loading and reducing esterolytic efficiency. It must also be noted that the natural substrate of  $\alpha$ -chymotrypsin (proteins, specifically hydrophobic peptide bonds) is decidedly different from the *p*-nitrophenyl model substrate used here, and the basic pH of our assay procedure places the native enzyme at a disadvantage during a direct comparison (44, 45). However, because of convenience for monitoring the hydrolysis spectrophotometrically and the short reaction times, this comparison is frequently made in the literature and provides an insight into the important role of supporting environmental effects for optimizing active-site chemistry. The benzoate ester was examined here as a more stable and challenging model substrate compared with the more commonly explored *p*-nitrophenyl acetate, and the high observed turnover value supports the power of a bioinspired cosurfactant system (46).

#### Active-site mimicry

With the impressive catalytic power of the three-component bioinspired micellar system established, we were drawn to examine the structure and mechanism of the ACT and guanidine surfactants in more detail. First, an examination of the ACT was made to assess the presence of interfunctional group interactions and a mechanism of substrate attack in comparison to the native catalytic triad of  $\alpha$ -chymotrypsin. To investigate the participation of the three functional groups of the ACT in catalysis, several control surfactants were prepared and assayed, each excluding a functional group of the ACT (fig. S2). Significantly, a 12-fold reduction in catalytic effect was observed for each of the control structures containing only two functional groups of the ACT when combined with CTAB. This result provides evidence for the concerted action of all three groups during ACT catalysis. However, it must be noted that for the control structure containing imidazole and carboxylate groups (but excluding hydroxyl), an approximately 10% increase in esterolysis was observed above the CTAB background. This finding is consistent with results reported previously where the imidazole unit of histidine can undertake general base hydrolysis of activated substrates (47–49).

To determine the functional group separation in the ACT, a single crystal of an ACT-C<sub>8</sub> surfactant was grown in water and elucidated via x-ray diffraction (XRD). The solid-phase structure of ACT-C<sub>8</sub> provides information on the functional group interactions (including separation distances), which may affect the solution-phase chemistry of the ACT surfactant. The resolved structure was compared with the well-studied catalytic triad of  $\alpha$ -chymotrypsin (Fig. 2, A and B). Similar to the native enzyme, the three functional groups (hydroxyl, imidazolyl, and carboxyl) of the ACT are observed to be spatially close. Intramolecular H-bonding was observed between the carboxyl and imidazolyl groups in the ACT, a phenomenon typical of the enzyme active site. The distance between the carboxyl (O) and imidazolyl (N) of the ACT is 2.72 Å, which is relatively short and is approaching the separation of these groups in the native enzyme (2.64 Å) (50). In the native enzyme, however, H-bonding between the Ser-OH and His-N groups is also observed, whereas this was not detected in the solid-state structure of ACT-C<sub>8</sub>. This is due to the ACT hydroxyl group forming an intermolecular H-bond with the carboxyl group of a nearby ACT molecule. The interaction between the carboxyl and imidazolyl groups in the ACT occurs between the anti lone pair of the carboxyl-O and the imidazolyl-N as opposed to

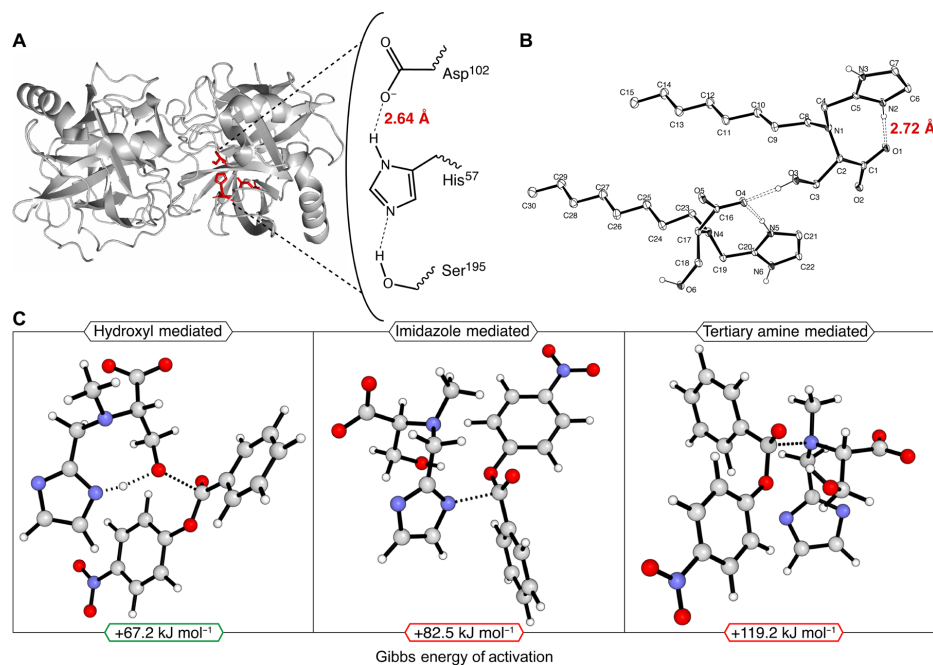


**Fig. 2. An ACT.** (A) The catalytic triad of active-site residues in  $\alpha$ -chymotrypsin, highlighting the close proximity of each unit, facilitated by H-bonding (50). (B) A similarly close proximity of functional groups in the ACT surfactant is observed via single-crystal XRD, emphasizing the power of positioning active groups on a single, trifunctional molecule. (C) Assessment of the substrate carbonyl attack by the ACT surfactant (identified as rate-determining) via QM computation reveals a preferred pathway common to native enzymes, whereby the high-energy transition state is established by the nucleophilic ACT hydroxyl group.

the *syn* pair interaction that is observed in the enzyme active site (51). The exposed *syn* lone pair of the carboxyl group now has increased basicity due to this interaction, which may provide an alternative method for substrate attack by the ACT via general base catalysis. Further mechanistic alternatives that implicate the imidazole group in nucleophilic attack have also been suggested earlier by Bruice *et al.* (52), Johnson (53), and Jencks (54). Such a mechanism involves substrate carbonyl attack by the imidazolyl-N, followed by acyl transfer to water, although the studied systems lack the additional -OH and -COOH functional groups present in the ACT.

To provide further insight into the potential catalytic mechanism of the ACT surfactant, we performed quantum mechanical (QM) calculations of the model esterolytic reaction on the ACT headgroup. The rate-determining step of this process was determined to be the formation of a charged quaternary intermediate, where the ACT becomes covalently attached to the carbonyl carbon of PNB following an initial nucleophilic attack (fig. S3). The formation of a similar enzyme-substrate quaternary transition state also constitutes the rate-determining step during enzymatic catalysis (55). To determine the ACT functional group that undertakes substrate attack, we modeled the Gibbs free energy of activation of the addition reaction for the three strongest nucleophilic groups present on the ACT (i.e., the hydroxyl, the tertiary amine, and the imidazole) (Fig. 2C). Under the assay conditions, the lowest energy transition state was observed for the ACT-substrate complex formed via attack by the hydroxyl

group (+67.2 kJ mol<sup>-1</sup>), again similar to the mechanism of the native enzyme. Furthermore, for this transition state to be established, the imidazole group must be located nearby to accept the hydroxyl-H upon the addition to the carbonyl of PNB. Frequency analysis of this transition state confirms a bimodal frequency, corresponding to the O→C addition with a concomitant H→N transfer. All calculations performed on geometries that did not have the hydroxyl and imidazole groups next to each other failed to find a transition-state structure, offering support for a concerted action between the hydroxyl and imidazolyl groups to affect catalysis.

#### Hydrophobic pocket

A key design feature of the ACT-surfactant system is the development of an internal hydrophobic region via micelle self-assembly. In addition, the formation of micelles may serve additional roles in catalysis, including drawing multiple functional groups together and tuning their reactivity, as well as attracting and partitioning lipophilic substrates (29). Inspired by previous reports of enhanced hydrolytic catalysis in a low-polarity environment, we sought to investigate the effect of micelle aggregation on the interaction and catalytic activity of the ACT (56, 57).

The functional group interactions of the ACT appear to be tuned by the inclusion of the ACT surfactant into a co-micelle system with CTAB when analyzed by one-dimensional (1D) and 2D <sup>1</sup>H nuclear magnetic resonance (NMR) (Fig. 3, A and B). Analysis of ACT-C<sub>8</sub>

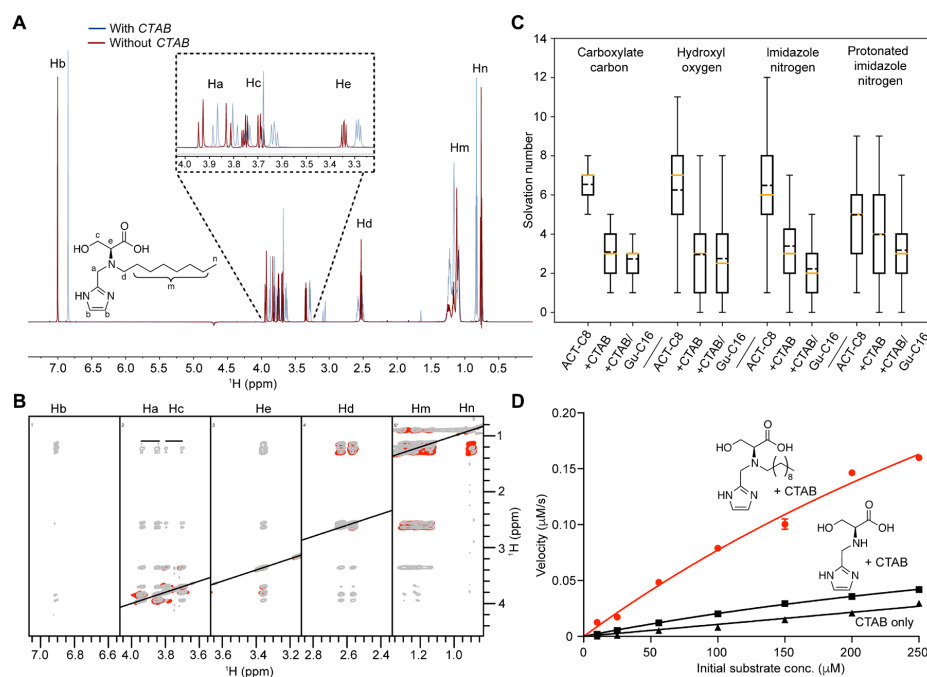


**Fig. 3. Mimicking the hydrophobic pocket.** (A) Analysis of the eight-carbon ACT surfactant via  $^1\text{H}$  NMR reveals changes to the ACT proton environment in the presence (blue line) and the absence (red line) of *d*-CTAB micelles. (B) Five hundred-millisecond  $^1\text{H}$  NOESY (gray) and 100-ms TOCSY (red) 2D spectra of ACT-C<sub>8</sub> in the presence of *d*-CTAB micelles. Strong through-space interactions between Hb and Hm and the absence of interaction between Hb and He/Hc indicate a preferential orientation of the imidazole ring toward the hydrophobic core of the micelle. (C) Solvation number of key ACT-C<sub>8</sub> functional groups predicted by MD simulation, in the absence of cosurfactants (ACT-C<sub>8</sub>), upon the addition of CTAB (+CTAB), and upon the addition of both surfactants (+CTAB and Guan-C<sub>16</sub>). The average number of water molecules surrounding each functional group decreased reliably upon the addition of surfactant and cosurfactant, indicating an increasingly hydrophobic environment. (D) Michaelis-Menten kinetics profile of PNB esterolysis catalyzed by the ACT-C<sub>8</sub> surfactant, ACT (nonsurfactant), or CTAB only. An increased catalytic effect was observed when incorporating amphiphilic character into the ACT structure by enhancing interaction with CTAB micelles. [Assay conditions: 25°C; 0.1 M borate buffer (pH 9.0), [catalyst] = 2.24 μM; [CTAB] = 0.8 mM; [substrate] = 10 to 250 μM.] (Data points are the mean of at least three independent experiments, and error bars represent SEM.)

both with and without the addition of deuterated CTAB (*d*-CTAB) (0.8 mM) highlights a significant change in  $^1\text{H}$  chemical shift in the presence of *d*-CTAB micelles, indicating insertion of the ACT surfactant into the micelle. The most significant shift was observed for the imidazole ring protons (Hb; see Fig. 3A for annotations), 0.15 parts per million (ppm) upfield compared with the CTAB-free system, which may be due to an orientation of these protons into a more hydrophobic environment, such as the core of the *d*-CTAB micelle. This is supported by total correlation spectroscopy (TOCSY) and nuclear Overhauser effect spectroscopy (NOESY) spectra, which confirm strong through-space interactions between Hb and the acyl chain protons (Hm) of the surfactant tail (Fig. 3B). Weak through-space interactions were also observed between Hb and the imidazolyl-adjacent methylene protons (Ha) and between Hb and the closest acyl protons (Hd), which is expected considering the proximity imposed by the compound chemical structure. With the lack of interaction between Hb and the hydroxyl-adjacent methylenes (Hc), it is likely that the imidazole ring is buried into the micelle while the hydroxyl group is facing away toward the aqueous solution. This is further supported by the weaker through-space interactions between Hc and Hd or Hm. The NOESY/TOCSY results indicate some

interaction between all three ACT functional groups as well as between the ACT groups and the surfactant alkyl chain.

The incorporation of ACT surfactant into the CTAB micelle was also suggested by molecular dynamics (MD) simulation. Upon incorporation into the micelle, MD simulation highlighted a marked decrease in the number of water molecules surrounding each of the key functional groups the ACT-C<sub>8</sub> surfactant (Fig. 3C). This effect was enhanced for the ACT-C<sub>16</sub> surfactant, whose longer alkyl chain resulted in a deeper incorporation into the micellar assembly. In the absence of CTAB, the ACT surfactants were not observed to form persistent aggregates over 100 ns of simulation, suggesting that the ACT is only incorporated into a hydrophobic environment in the presence of cosurfactants (fig. S4). Also observed were changes to the interactions between functional groups of the ACT surfactants upon incorporation into the micelle (figs. S11 and S12). The intramolecular distance between functional groups of the ACT was altered following micelle assembly, establishing closer interactions between the imidazole ring and the carboxylate and hydroxyl moieties of the ACT, consistent with experimental NOESY data (vide supra). In addition, micelle incorporation resulted in a substantial shift in the separation distribution between the hydroxyl group and the imidazole

ring toward shorter-range interactions. Combined with the available solvation and NMR data, this suggests a significant contribution by the micelle self-assembly process to tune the electrostatic interactions and local nano-environment of the ACT functional groups.

To examine the impact of ACT-surfactant self-assembly on catalysis, we also assayed the ACT headgroup (without an alkyl chain) for PNB esterolysis (Fig. 3D). The ACT molecule displays excellent water solubility in isolation, and it is likely that this material would be poorly incorporated into a micellar assembly. A significant reduction in catalysis was observed for the ACT molecule compared with the ACT-C<sub>8</sub> surfactant, when assessed in combination with CTAB. This result provides insight into the environmental effects, which help to facilitate catalysis, whereby positioning of the ACT close to the hydrophobic PNB substrate is achieved through the addition of surfactant functionality to the ACT and subsequent self-assembly. Without surfactant functionality, the ACT unit is likely to be distributed broadly in solution, limiting the kinetics of substrate interaction and catalysis. In addition, a reduced catalytic

effect was observed when moving from a longer alkyl chain surfactant ACT-C<sub>16</sub> to the shorter alkyl chain ACT-C<sub>8</sub>, further emphasizing the effect of catalyst environment. These assay findings offer support to both the computational and NMR results, highlighting the impact of localizing the ACT into a micelle environment for tuning functional group interactions and enhancing catalysis.

### H-bond cosurfactant

While the active site and hydrophobic pocket are essential functional components in enzymatic reactions, stabilization of transition states via H-bonding is a key stage common in biocatalysis. We proposed that the localization of a strongly H-bond donating group (i.e., guanidinium) nearby to the ACT headgroup within a micelle assembly may assist catalysis, similar to the role of the oxyanion hole in  $\alpha$ -chymotrypsin. Excluding the Gu-C<sub>16</sub> from the cosurfactant system resulted in an approximately fourfold decrease in catalytic activity, highlighting the strong contribution of Gu-C<sub>16</sub> to effect catalysis (Fig. 4D). Examination of the cosurfactant system containing only

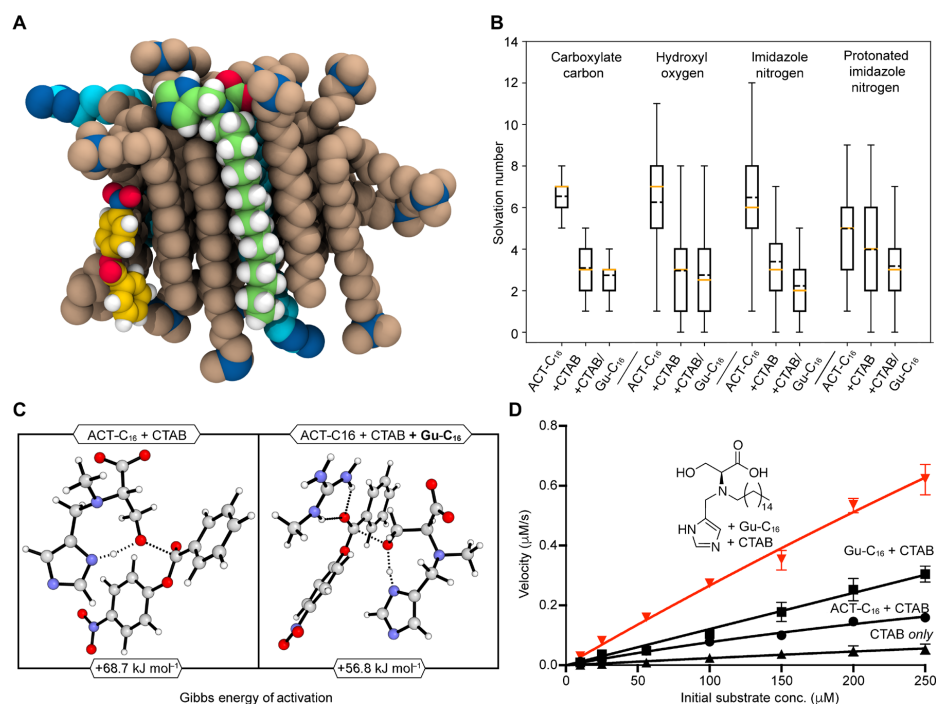


**Fig. 4. Enhancing catalysis by incorporating a guanidine-based surfactant.** (A) Cross section of a representative micelle observed via MD simulation, highlighting both catalyst and substrate incorporated into the hydrophobic core following aggregation of CTAB and Guan-C<sub>16</sub> cosurfactants. The catalytic groups of ACT-C<sub>16</sub> (lime green) are largely buried in the micelle environment. CTAB and Guan-C<sub>16</sub> molecules are shown in tan and cyan van der Waals representation, respectively, with hydrogen atoms omitted for clarity. PNB is shown in yellow. Nitrogen atoms are shown in dark blue, and oxygen atoms are shown red. (B) Solvation number of the ACT-C<sub>16</sub> polar functional groups predicted by MD simulation, in the absence of cosurfactants (ACT-C<sub>16</sub>), upon the addition of CTAB (+CTAB), and upon the addition of both surfactants (+CTAB and Guan-C<sub>16</sub>). The average number of water molecules surrounding each functional group was markedly decreased upon the addition of both cosurfactants, indicating enhanced incorporation of ACT-C<sub>16</sub> into the hydrophobic micelle core. (C) QM simulation of the model esterolysis reaction revealed a decrease in Gibbs activation energy of 11.9 kJ mol<sup>-1</sup> when Guan-C<sub>16</sub> is incorporated into the cosurfactant system. This corresponds to an approximately two orders of magnitude increase in the rate of substrate addition to ACT-C<sub>16</sub> (rate-determining step). (D) Michaelis-Menten kinetics profile of PNB esterolysis catalyzed by ACT-C<sub>16</sub> in a cosurfactant system with CTAB and Guan-C<sub>16</sub>. Incorporation of all three cosurfactants into the catalyst assembly resulted in enhanced catalysis compared with the single- or two-component systems. (Data points are the mean of at least three independent experiments, and error bars represent SEM.)

Gu-C<sub>16</sub> and CTAB revealed a higher catalytic effect than for the ACT-C<sub>16</sub>/CTAB system. This may be due to the higher concentration of Gu-C<sub>16</sub> used in the assay compared with ACT-C<sub>16</sub> (0.3 mM versus 0.002 mM, respectively) and indicates that the guanidinium surfactant by itself is also capable of facilitating hydrolysis, potentially via combined general base catalysis and induced micellar catalysis at the charged assembly interface. The strong, bifurcated H-bond donation of guanidinium could also serve to activate the carbonyl to attack by alternative nucleophilic species in solution; such has been reported in ring-opening polymerizations (40, 58). Despite this, the highest rate enhancement was observed for the three-component system, which gives support for the concerted action of the guanidinium and ACT headgroups in catalysis. Although other Lewis acid structures may perform similar tasks, we believe that the guanidinium headgroup offers benefits, such as facile synthesis, double H-bond donation, and a high pKa.

To further probe the cooperation between the ACT and guanidinium surfactants, we conducted computational modeling on the co-micelle assembly and catalytic mechanism. Assessment via MD simulation revealed the aggregation of Guan-C<sub>16</sub> with CTAB, ACT surfactant, and PNB substrate into a co-micellar assembly, whose size, morphology, and composition are consistent with previous literature (Fig. 4A and figs. S4 to S6) (59). The average aggregation number of the micelles was observed to increase upon the addition of the Guan-C<sub>16</sub> cosurfactant, which may be a result of increased availability of surfactants, rather than insufficient simulation time. In all cases, the composition of the assembly following the addition of Guan-C<sub>16</sub> affected the solvation of the key ACT functional groups, with consistently increased solvation numbers pointing toward a deeper inclusion of the ACT into the micellar aggregate (Fig. 4B). This effect may also be a result of charge-screening effects afforded to the catalyst by the cationic Gu-C<sub>16</sub> headgroup, potentially illustrating electrostatic contact between the ACT and guanidinium units. In contrast, no preferential interaction between the guanidinium group and the acyl group of the PNB substrate was observed during simulation, although this does not preclude the possibility of catalytically relevant transition-state stabilization interactions between the two groups. Rather, this may suggest that the additional rate enhancement afforded by Gu-C<sub>16</sub> may arise from an electronic interaction with the ACT, as well as physically allowing the catalyst to bury further into the micelle environment.

To provide deeper insight into the origin of the increased rate enhancement on the addition of Gu-C<sub>16</sub> to the co-micelle system, we introduced a positively charged guanidinium headgroup to the QM calculations of the model assay reaction. Subtle changes to the rate-determining transition-state structures were observed when the guanidinium headgroup is positioned proximate to the acyl group of the PNB substrate (Fig. 4C). More specifically, the guanidinium unit formed a bifurcated H-bond with the carbonyl oxygen of PNB, withdrawing electron density from the scissile carbon and lowering the barrier for nucleophilic attack by the ACT. As a result, the Gibbs energy of the rate-determining intermediate was reduced by  $-11.9$  kJ mol<sup>-1</sup>, which corresponds to an approximately two orders of magnitude increase in the rate of ACT→PNB addition. This result reflects the enhanced catalysis observed experimentally on the addition of Gu-C<sub>16</sub> to the co-micellar assembly. Because of a lack of rigidity in the micelle structure and the dynamic nature of headgroup interactions, this remarkable rate enhancement is not fully reflected in the experimental assay results. However, there is clear potential

for a supporting H-bond donor to complement the catalysis of the ACT, and further study exploring optimal group arrangements is ongoing.

## CONCLUSION

In summary, we report the development of a bioinspired cosurfactant micelle system that undertakes hydrolysis of a model ester substrate via a proposed mechanism similar to native enzymes. Drawing inspiration from the catalytic triad, oxyanion hole, and hydrophobic binding pocket common to many hydrolases, the co-micelle assembly collects multiple functional groups into close proximity around a macromolecular capsule to affect catalysis. Structural assessment via XRD, <sup>1</sup>H NMR, and 2D <sup>1</sup>H NMR supports the close interaction of the three groups of the ACT, as well as highlighting the importance of surfactant functionality for optimizing the local nano-environment. Furthermore, computational modeling via QM calculations and MD simulation further support the close relationship between functional groups in the co-micelle catalyst and the notable similarity of the catalytic mechanism to native enzymatic reactions. Highly functional surfactants hold promise for the future design of multifunctional, enzyme-inspired catalysts, although much work remains to be done before we may realize a true model of these incredibly complex natural proteins.

## MATERIALS AND METHODS

### General information

All commercially obtained solvents and reagents were used without further purification. Analytical thin-layer chromatography was carried out on Merck silica gel 60 F<sub>254</sub> glass plates, and flash chromatography was performed on Merck silica gel 60 (70 to 230 mesh).

Visualization was accomplished with short-wave ultraviolet (UV) light and/or KMnO<sub>4</sub> staining solution followed by gentle heating. Surfactants were purified by preparative reverse-phase high-performance liquid chromatography (RP-HPLC) on a Biotage SP1 HPFC Flash Purification System using a reverse-phase Biotage SNAP Cartridge (KP-C18-HS, 60 g). For synthesis characterization, <sup>1</sup>H and <sup>13</sup>C solution-state NMR were recorded on a Varian Unity Inova 500 (500 MHz for <sup>1</sup>H and 125 MHz for <sup>13</sup>C) or a Varian Unity Inova AS600 (600 MHz for <sup>1</sup>H and 150 MHz for <sup>13</sup>C) spectrometer. Chemical shifts  $\delta$  are reported relative to the resonance signal of <sup>1</sup>H or <sup>13</sup>C cores of tetramethylsilane and in parts per million. The <sup>1</sup>H spectra were calibrated by setting the solvent peaks, caused by remaining traces of protons, to values known from the literature ( $\delta$ CHCl<sub>3</sub> = 7.26 ppm,  $\delta$ CD<sub>3</sub>OH = 4.87 ppm, and  $\delta$ D<sub>2</sub>O = 4.79 ppm). The coupling constants  $J$  are reported in hertz.

### CMC measurements—Pyrene method

According to the literature (60), a pyrene stock solution was prepared by dissolving pyrene (5 mg) in methanol (10 ml) and diluting 20-fold with methanol. Pyrene was stored under an inert atmosphere at 4°C, and stock solutions were prepared fresh each day. Surfactant stock solutions (~0.1 M) were prepared in dimethyl sulfoxide (DMSO) or borate (pH 9.0) (Na<sub>2</sub>B<sub>4</sub>O<sub>7</sub>·10H<sub>2</sub>O) buffer according to the individual surfactant solubilities. For the fluorescence assay, an appropriate volume of surfactant stock solution (surfactant final concentration range, 0.01 to 0.8 mM) was transferred to a quartz fluorescence cuvette. Pyrene stock solution (50  $\mu$ l) and either deionized water or borate buffer (pH 9.0) were added to the cuvette for a final volume

of 2.5 ml. In the cases where the surfactant was dissolved in DMSO, a small aliquot of DMSO was added to the cuvette to maintain a constant DMSO concentration for all surfactant concentrations [final DMSO concentration, <1% (v/v)]. The fluorescence emission spectrum of pyrene was measured immediately after mixing using an emission wavelength scanning mode from 360 to 400 nm over 90 s. The excitation wavelength was 334 nm (slit width, 8 nm), and emission slit width was 2 nm. The first and third fluorescent vibrational peaks ( $I_1$  and  $I_3$ ) were recorded at 373 and 384 nm, respectively, and the ratio was plotted against surfactant concentration for the CMC calculations. The midpoint of the inflection of  $I_1/I_3$  versus surfactant concentration was taken as the CMC value in all cases (fig. S1).

#### Esterolysis assay with *p*-nitrophenyl benzoate (representative assay for the three-component catalyst)

Catalyst (ACT surfactant, 2.24  $\mu$ M) was dissolved with cetyl ammonium bromide (CTAB; 0.8 mM) and hexadecylguanidinium chloride (Gu-C<sub>16</sub>; 0.3 mM) in a borate (Na<sub>2</sub>B<sub>4</sub>O<sub>7</sub>·10H<sub>2</sub>O) buffer at pH 9 ( $c_{\text{buffer}} = 100$  mM) with vigorous stirring. Control reactions lacking either CTAB, ACT surfactant, or Gu-C<sub>16</sub> were also conducted with the same concentrations. A stock solution of substrate *p*-nitrophenyl benzoate was made up in acetonitrile and added to the buffered solution containing surfactants ( $c_{\text{substrate,initial}} = 10, 25, 56, 100, 150,$  and  $250$   $\mu$ M). A small aliquot of acetonitrile was added to the reference cell to maintain consistency [acetonitrile concentration, <5% (v/v)]. Following mixing, the reaction was immediately monitored via UV light absorption at 405 nm at room temperature in a Cary 60 UV-visible spectrophotometer (Agilent). The kinetics of ester substrate consumption was calculated via nonlinear regression using the plotting software GraphPad Prism 8, under an assumption of Michaelis-Menten kinetics. The background hydrolysis rate without the addition of catalyst or surfactants was determined using a first-order rate assumption, where  $k_{\text{cat}}$  is equal to the  $k_{\text{hydrolysis}}$  for the reaction.

For the enzyme-catalyzed control reaction,  $\alpha$ -chymotrypsin (from bovine pancreas type II, lyophilized powder, Sigma-Aldrich) (2.2  $\mu$ M) was dissolved as received in borate (Na<sub>2</sub>B<sub>4</sub>O<sub>7</sub>·10H<sub>2</sub>O) buffer at pH 9 ( $c_{\text{buffer}} = 100$  mM), containing CTAB (0.8 mM). A stock solution of substrate *p*-nitrophenyl benzoate was made up in acetonitrile and added to the buffered solution containing surfactants ( $c_{\text{substrate,initial}} = 10, 25, 56, 100, 150,$  and  $250$   $\mu$ M), as per the surfactant experiments above. The hydrolysis reaction was assessed over 10 min and compared directly with the results of the cosurfactant systems.

#### X-ray crystallography of ACT-C<sub>8</sub> surfactant

The crystal data of the ACT-C<sub>8</sub> surfactant were collected on a charge-coupled device diffractometer using Cu-K $\alpha$  radiation (graphite crystal monochromator = 1.54184 Å). The structure was solved by direct methods (SHELXT) and difference Fourier synthesis. Thermal ellipsoid plots were generated using the program ORTEP-3 integrated within the WinGX suite of programs. C<sub>15</sub>H<sub>27</sub>N<sub>3</sub>O<sub>3</sub>;  $M = 297.39$ ,  $T = 130.0(2)$  K,  $\lambda = 1.54184$  Å; monoclinic, space group  $P2_1$ ;  $a = 12.9624(5)$ ,  $b = 8.4191(3)$ ,  $c = 14.9957(6)$  Å,  $\beta = 93.510(3)$ ,  $V = 1633.44(11)$  Å<sup>3</sup>,  $Z = 4$ ,  $Z' = 2$ ,  $D_c = 1.209$  Mg M<sup>-3</sup> (Cu-K $\alpha$ ) = 0.685 mm<sup>-1</sup>,  $F(000) = 648$ ; crystal size, 0.65 mm by 0.21 mm by 0.03 mm.  $\theta_{\text{max}} = 76.48$ , 9264 reflections measured, 4774 independent reflections ( $R_{\text{int}} = 0.058$ ), the final  $R = 0.0567$  [ $I > 2\sigma(I)$ , 4459 data], and  $wR(F^2) = 0.1559$  (all data) Goodness-of-fit = 1.073, absolute structure parameter 0.0(2). Cambridge Crystallographic Data Centre code: 1900732.

#### NMR of ACT-C<sub>8</sub> surfactant

NMR samples were prepared by either dissolving ACT-C<sub>8</sub> in buffer [50 mM borate (pH 9.0), 0.05 mM DSS (4,4-dimethyl-4-silapentane-1-sulfonic acid), 10% (v/v) D<sub>2</sub>O] or in 75 mM deuterated CTAB [50 mM borate (pH 9.0), 0.05 mM DSS, 10% (v/v) D<sub>2</sub>O] to reach a final compound concentration of ca. 5 mM. NMR spectra were obtained at 298 K on an 800-MHz Bruker Avance II equipped with a TCI CryoProbe. Chemical shifts were referenced to DSS at 0 ppm. Data were processed in TopSpin (Bruker) and analyzed using the CCPNmr Analysis program (Laue 2005 Proteins 59, 687). <sup>1</sup>H homonuclear correlation spectroscopy, TOCSY (mixing time  $\tau_{\text{mix}} = 100$  ms), and NOESY ( $\tau_{\text{mix}} = 100$  and 500 ms) were run using 4000 and 512 points in the direct and indirect dimensions, respectively.

#### Synthetic procedures

##### Reductive amination of *L*-serine with 1*H*-imidazole-2-carboxaldehyde (preparation of ACT molecule)

*L*-Serine (1.05 g, 10 mmol, 1.00 eq) and sodium hydroxide (420 mg, 10.5 mmol, 1.05 eq) were dissolved in methanol ( $c_{\text{L-serine}} \approx 85$  mM), and 1*H*-imidazole-2-carboxaldehyde or 1*H*-imidazole-4-carboxaldehyde (1.06 g, 11 mmol, 1.10 eq) was added to the solution with stirring. The mixture was stirred at 40°C for 30 min and afterward allowed to cool down to room temperature over 4 hours while stirring. Sodium borohydride (605.3 mg, 16 mmol, 1.60 eq) was added slowly, and the reaction mixture was stirred at room temperature for 30 min. Glacial acetic acid was added dropwise until the mixture reached approximately pH 4 to 5, and the resulting suspension was stirred at room temperature for a further 10 min. The product was obtained as the precipitate by filtration and washing with methanol. ACT was collected as a fine, white solid (yield 99%).

[ACT (2-imidazole isomer)] <sup>1</sup>H NMR (600 MHz; D<sub>2</sub>O, 298 K):  $\delta = 7.23$  (s, 2H, aromatic), 4.31 ( $d$ ,  $^2J = 15.1$  Hz, 1H, CHHN), 4.23 ( $d$ ,  $^2J = 15.1$  Hz, 1H, CHHN), 3.95 to 3.77 ( $m$ , 2H, CH<sub>2</sub>OH), 3.56 (dd,  $^3J = 5.3$  Hz,  $^2J = 4.1$  Hz, 1H, CHCO<sub>2</sub><sup>-</sup>). MS [electrospray ionization (ESI)] was calculated for C<sub>7</sub>H<sub>11</sub>N<sub>3</sub>O<sub>3</sub>H<sup>+</sup> ([M + H]<sup>+</sup>): 186.09. Found: 186.09.

[ACT (4-imidazole isomer)] <sup>1</sup>H NMR (400 MHz, CD<sub>3</sub>OD, 298 K):  $\delta = 7.66$  (s, 1H, Im), 7.17 (s, 1H, Im), 4.15 (d,  $J = 13.9$  Hz, 1H, CH<sub>2</sub>OH), 4.11 (d,  $J = 13.9$  Hz, 1H, CH<sub>2</sub>OH), 3.84 (dd,  $J = 12.9, 3.9$  Hz, 1H, CH<sub>2</sub>Im), 3.78 (dd,  $J = 12.9, 3.9$  Hz, 1H, CH<sub>2</sub>Im), 3.57 (t,  $J = 7.4, 3.8$  Hz, 1H, CHCH<sub>2</sub>OH). MS (ESI) was calculated for C<sub>7</sub>H<sub>11</sub>N<sub>3</sub>O<sub>3</sub>H<sup>+</sup> ([M + H]<sup>+</sup>): 186.09. Found: 186.09.

##### Preparation of *n*-octan-1-ol from *n*-octan-1-ol

According to the literature (61), *n*-Octan-1-ol (1.3 g, 10 mmol, 1.0 eq) was dissolved in dichloromethane ( $c_{\text{alcohol}} \approx 65$  mM), and pyridinium dichromate (4.5 g, 12 mmol, 1.2 eq) was added to the solution portionwise. The mixture was stirred at room temperature for 8 hours. The suspension was filtered through filter paper and a short silica pad. The solid residue was washed several times with diethyl ether. The solvents were removed in vacuo, and the crude product was purified by flash chromatography (hexane/ethyl acetate = 19:1) to yield a waxy colorless solid (819 mg, 64%). <sup>1</sup>H NMR (400 MHz, CDCl<sub>3</sub>, 298 K):  $\delta = 9.74$  (t,  $J = 1.9$  Hz, 1H, CHO), 2.40 (td,  $J = 7.4, 1.9$  Hz, 2H, CH<sub>2</sub>CHO), 1.60 (m, CH<sub>2</sub>, 2H), 1.35 to 1.19 (m, CH<sub>2</sub>, 8H), 0.86 (t,  $J = 6.8$  Hz, 3H).

##### Preparation of *n*-hexadecan-1-ol from *n*-hexadecan-1-ol

1-Hexadecanol (5.00 g, 20.6 mmol, 1.00 eq) was dissolved with stirring in dichloromethane (150 ml). Pyridinium dichromate (9.40 g,

25.0 mmol, 1.20 eq) was added portionwise, and the mixture was stirred for a further 5 hours. The suspension was filtered over a short silica pad and washed several times with dichloromethane and ethyl acetate, and the filtrate was dried in vacuo. Purification of the crude product by column chromatography (hexane/ethyl acetate = 19:1) yielded target aldehyde as a colorless solid (3.69 g, 15.3 mmol, 74%). <sup>1</sup>H NMR (500 MHz, CDCl<sub>3</sub>, 298 K): δ = 9.76 (t, <sup>3</sup>J = 1.9 Hz, 1H, CHO), 2.41 (td, <sup>3</sup>J = 7.4 Hz, <sup>2</sup>J = 1.9 Hz, 2H, CH<sub>2</sub>CHO), 1.66 to 1.58 (m, 2H, CH<sub>2</sub>), 1.35 to 1.21 (m, 24H, CH<sub>2</sub>), 0.88 (t, <sup>3</sup>J = 6.9 Hz, 3H, CH<sub>3</sub>).

#### Reductive amination of ACT with *n*-octan-1-al (preparation of ACT-C<sub>8</sub> surfactant)

The corresponding ACT (1.00 eq) and sodium hydroxide (1.05 eq) were dissolved in methanol (*c*<sub>precursor</sub> ≈ 100 mM). *n*-Octan-1-al (1.20 eq) and sodium triacetoxyborohydride (1.40 eq) were added to the solution, and the mixture was stirred at 40°C for 2 hours. Another two batches of *n*-octan-1-al (2 × 1.20 eq) and sodium triacetoxyborohydride (2 × 1.40 eq) were added to the solution every 2 hours, and after 4 hours, the mixture was left to stir at 40°C for a further 20 hours. The reaction was quenched with glacial acetic acid, and the solvents were removed in vacuo. The crude product was washed with ethyl acetate and purified by RP-HPLC with an H<sub>2</sub>O/acetonitrile gradient (19:1→1:19). (Both derivatives a pale-yellow solid, 2-isomer = 60%, 4-isomer = 84%). (ACT-C<sub>8</sub> 2-isomer) <sup>1</sup>H NMR (500 MHz; D<sub>2</sub>O, 298 K): δ = 7.78 (s, 1H, Im), 7.32 (s, 1H, Im), 4.34 to 4.18 (m, 2H, ImCH<sub>2</sub>N), 4.00 to 3.82 (m, 2H, CH<sub>2</sub>OH), 3.57 (dd, <sup>3</sup>J = 6.9 Hz, <sup>2</sup>J = 5.2 Hz, 1H, CHCO<sub>2</sub>H), 2.86 to 2.70 (m, 2H, CH<sub>2</sub>CH<sub>2</sub>N), 1.44 to 1.30 (m, 2H, CH<sub>2</sub>CH<sub>2</sub>N), 1.24 to 1.03 (m, 10H, CH<sub>2</sub>), 0.75 (t, <sup>3</sup>J = 6.8 Hz, 3H, CH<sub>3</sub>). MS (ESI) was calculated for C<sub>15</sub>H<sub>27</sub>N<sub>3</sub>O<sub>3</sub>H<sup>+</sup> ([M + H]<sup>+</sup>): 298.21. Found: 298.24.

#### Reductive amination of ACT with *n*-hexadecan-1-al (preparation of ACT-C<sub>16</sub> surfactant)

The corresponding ACT (185 mg, 1.0 mmol, 1.00 eq) was dissolved in methanol and glacial acetic acid (*c*<sub>amino acid precursor</sub> ≈ 12.3 M) with stirring at 60°C. C<sub>16</sub> aldehyde (360 mg, 1.5 mmol, 1.50 eq) was added, and the reaction was mixed for 20 min. Sodium triacetoxyborohydride (420 mg, 2.0 mmol, 2.0 eq) was added carefully to the solution, and stirring was continued at 60°C for 4 hours. Another batch of aldehyde (360 mg, 1.5 mmol, 1.50 eq) and Sodium triacetoxyborohydride (420 mg, 2.0 mmol, 2.0 eq) was added, and the mixture was stirred at 60°C for a further 24 hours. The reaction was quenched with water, and the solvents were removed in vacuo at elevated temperature. The crude product was extracted with methanol and washed several times with ethyl acetate before being purified by reverse-phase column chromatography (H<sub>2</sub>O/methanol = 19:1→1:19→0:1) to yield ACT-C<sub>16</sub> surfactant (213 mg, 0.52 mmol, 52%). <sup>1</sup>H NMR (400 MHz, CD<sub>3</sub>OD, 298 K): δ = 7.77 (s, 1H, Im); 7.35 (s, 1H, Im); 4.51 (d, *J* = 13.9 Hz, 1H, CH<sub>2</sub>OH); 4.42 (d, *J* = 13.9 Hz, 1H, CH<sub>2</sub>OH), 4.17 (dd, *J* = 12.9, 3.9 Hz, 1H, CH<sub>2</sub>Im), 4.05 (dd, *J* = 12.9, 3.9 Hz, 1H, CH<sub>2</sub>Im); 3.82 (dd, *J* = 7.4, 3.8 Hz, 1H, CHCH<sub>2</sub>OH); 2.24 (t, *J* = 7.4 Hz, 1H, CH<sub>2</sub>N); 1.57 (p, *J* = 7.2 Hz, 2H, CH<sub>2</sub>CH<sub>2</sub>N); 1.40 to 1.22 (m, 26H, CH<sub>2</sub>); 0.88 (t, *J* = 7.2 Hz, 3H, CH<sub>3</sub>). MS (ESI) was calculated for C<sub>23</sub>H<sub>43</sub>N<sub>3</sub>O<sub>3</sub>H<sup>+</sup> ([M + H]<sup>+</sup>): 410.33. Found: 410.34.

#### 1-Hexadecylguanidinium chloride (Gu-C<sub>16</sub>)

According to the literature (43), 1-hexadecylamine (723 mg, 3.0 mmol, 1.0 eq) was dissolved in methanol (15 ml) at 40°C with stirring. 1H-pyrazole-1-carboxamide hydrochloride (438 mg, 3.0 mmol,

1.0 eq) was added, and stirring was continued at 40°C for 3 days. Solvent was removed in vacuo, and the crude product was washed three times with hot acetone to yield target surfactant Gu-C<sub>16</sub> as a colorless solid (850 mg, 2.9 mmol, 97%). <sup>1</sup>H NMR (400 MHz, CD<sub>3</sub>OD, 298 K): δ = 3.14 (t, *J* = 7.1 Hz, 2H), 1.56 (p, *J* = 7.2 Hz, 2H), 1.41 to 1.22 (m, 26H), 0.87 (m, 3H). MS (ESI) was calculated for C<sub>17</sub>H<sub>33</sub>N<sub>3</sub>H<sup>+</sup> ([M + H]<sup>+</sup>): 284.30. Found: 284.32.

#### Preparation of (OH-COOH) control structure [(S)-3-hydroxy-2-(octylamino)propanoic acid]

L-serine (210 mg, 2.0 mmol, 1.0 eq) was suspended in 15 ml of methanol at 50°C, and sodium hydroxide (88 mg, 1.4 mmol, 1.1 eq) was added with stirring. 1-Octanal (310 mg, 2.4 mmol, 1.2 eq) was then added, and the reaction was mixed overnight at room temperature. NaBH<sub>4</sub> (150 mg, 4.0 mmol, 2.0 eq) was then added, and the reaction mixture was stirred for a further 1 hour at room temperature. Concentrated hydrochloric acid (32%, ~0.7 ml) was added to quench the reaction mixture, the suspension was filtered, and solvent was removed in vacuo. The crude product was washed with ethyl acetate and then purified via reverse-phase column chromatography (MeOH/H<sub>2</sub>O 19:1→0:1) to yield target structure (239 mg, 1.1 mmol, 54%). <sup>1</sup>H NMR (400 MHz; CD<sub>3</sub>OD, 298 K): δ = 3.93 (dd, *J* = 11.8, 4.0 Hz, 2H, CH<sub>2</sub>OH), 3.82 (dd, *J* = 11.8, 6.4 Hz, 2H, CH<sub>2</sub>OH), 3.46 (dd, *J* = 6.4, 4.0 Hz, 1H, CHCH<sub>2</sub>OH), 2.95 (m, 2H, CH<sub>2</sub>NH), 1.67 (p, *J* = 7.6 Hz, 2H), 1.38 to 1.13 (m, 10H, CH<sub>2</sub>), 0.97 to 0.80 (m, 3H, CH<sub>3</sub>). MS (ESI) was calculated for C<sub>11</sub>H<sub>23</sub>NO<sub>3</sub>H<sup>+</sup> ([M + H]<sup>+</sup>): 218.17. Found: 218.19.

#### Preparation of (Im-COOH) control structure

##### [(R)-3-(1H-imidazol-5-yl)-2-(octylamino)propanoic acid]

L-histidine (620.8 mg, 4.0 mmol, 1.0 eq) was suspended in 20 ml of methanol at 50°C, and sodium hydroxide (168 mg, 4.2 mmol, 1.1 eq) was added with stirring. 1-Octanal (620 mg, 4.8 mmol, 1.2 eq) was then added, and the reaction was mixed overnight at room temperature. NaBH<sub>4</sub> (300 mg, 8.0 mmol, 2.0 eq) was then added, and the reaction mixture was stirred for a further 1 hour at room temperature. Concentrated hydrochloric acid (32%, ~1.0 ml) was added to quench the reaction mixture, the suspension was filtered, and the solvent was removed in vacuo. The crude product was washed with ethyl acetate and a small volume of water and then purified via reverse-phase column chromatography (MeOH/H<sub>2</sub>O 19:1→0:1) to yield target structure (639 mg, 2.4 mmol, 60%). <sup>1</sup>H NMR (400 MHz; CD<sub>3</sub>OD, 298 K): δ = 8.74 (s, 1H, Im); 7.38 (s, 1H, Im); 3.71 to 3.60 (m, 1H, CHCOOH), 3.54 to 3.43 (m, 2H, CH<sub>2</sub>Im), 3.08 to 2.97 (m, 2H, CH<sub>2</sub>NH), 1.47 to 1.35 (m, 2H, CH<sub>2</sub>CH<sub>2</sub>NH), 1.31 to 1.07 (m, 10H, CH<sub>2</sub>); 0.79 to 0.7 (m, 3H, CH<sub>3</sub>). MS (ESI) was calculated for C<sub>14</sub>H<sub>25</sub>N<sub>3</sub>O<sub>2</sub>H<sup>+</sup> ([M + H]<sup>+</sup>): 268.20. Found: 268.21.

#### Preparation of (Im-OH) control structure [(R)-3-(1H-imidazol-5-yl)-2-(octylamino)propan-1-ol]

L-histidinol dihydrochloride (430 mg, 2.0 mmol, 1.0 eq) was suspended in 15 ml of methanol at 50°C, and sodium hydroxide (180 mg, 4.2 mmol, 2.1 eq) was added with stirring. The cloudy suspension was filtered, 1-octanal (260 mg, 2.1 mmol, 1.05 eq) was then added, and the reaction was mixed overnight at room temperature. NaBH<sub>4</sub> (90 mg, 2.4 mmol, 1.2 eq) was then added, and the reaction mixture was stirred for a further 1 hour at room temperature. Concentrated hydrochloric acid (~0.6 ml) was added to quench the reaction mixture, the suspension was filtered, and the solvent was removed in

vacuo. The crude product was washed several times with ethyl acetate, extracted into methanol, and purified via reverse-phase column chromatography (MeOH/H<sub>2</sub>O 19:1→0:1) to yield target structure (214 mg, 0.8 mmol, 42%). <sup>1</sup>H NMR (400 MHz; CD<sub>3</sub>OD, 298 K): δ = 8.81 (s, 1H, Im); 7.43 (s, 1H, Im); 4.40 to 4.34 (m, 2H, CH<sub>2</sub>OH), 4.18 to 4.07 (m, 2H, CH<sub>2</sub>Im); 3.42 (dd, *J* = 7.4, 3.8 Hz, 1H, CHCH<sub>2</sub>OH); 3.11 to 2.97 (m, 2H, CH<sub>2</sub>CH<sub>2</sub>N); 2.23 to 2.06 (m, 2H, CH<sub>2</sub>CH<sub>2</sub>N); 1.39 to 1.10 (m, 26H, CH<sub>2</sub>); 0.80 (t, *J* = 7.2 Hz, 3H, CH<sub>3</sub>). C<sub>14</sub>H<sub>26</sub>N<sub>3</sub>O<sup>+</sup> ([M - H]<sup>+</sup>): 252.22. Found: 252.21.

### Computational procedures

#### Quantum mechanics

All electronic structure calculations were performed with the Gaussian 16, Revision A.03 (62) software package. All density functional theory calculations were performed using the M06-2X functional (63) in conjunction with the 6-31+G(d,p) basis set. Implicit solvent effects for all calculations performed were obtained using the SMD (solvent model density) (64) solvation model for water. The ACT molecules were truncated by replacement of the extended alkyl chains with a single methyl group and conformationally searched to locate the global minimum energy structure; guanidine was also truncated by replacement of the extended alkyl chain with a single methyl group, so as to determine the possible role of the positively charged head-group. All entropies, zero-point vibrational energies, and thermal corrections were scaled by recommended scale factors (65); vibrational analysis was performed on all geometries to confirm (i) the absence of imaginary frequencies for minimum energy structures and (ii) the presence of a single imaginary frequency for transition-state structures.

#### Molecular dynamics

MD simulations were performed using the GROMACS 2018.1 engine with parameters from the GROMOS54a7 force field (66, 67). All-atom parameter sets for each surfactant (CTAB, molid 10929; Gu-C16, molid 306970), uncharged catalyst (ACT-C8, molid 306428; ACT-C16, molid 306429), charged catalyst (ACT-C8, molid 306968; ACT-C16, 306969), and substrate (PNB, molid 9503) corresponding to the predicted ionization states at pH 9 were obtained using the Automated Topology Builder V.2.2 (68). To remove any conformational bias from the system setup, triplicate systems were prepared in which molecules of substrate, catalyst, and surfactant were randomly orientated in a cubic dodecahedron box at the relative concentrations used in experimental assays (table S2) and solvated with a 7-nm buffer of explicit simple point-charge water. The concentration of surfactant species was increased 10-fold to facilitate sampling. Ions were added as required to neutralize overall system charge. The initial configuration was relaxed using standard steepest descent minimization using at least 1000 steps before being equilibrated for 10 ns in the isothermal-isobaric (*NpT*) ensemble to stabilize the system density. Each catalytic system (simulations 1 to 20; table S2) was allowed to self-assemble for 100 ns under *NpT*. Single CTAB controls (simulations 21 to 25; table S2) were run at various concentrations under the same conditions for 300 ns each. Periodic boundary conditions were used, and long-range electrostatics were calculated using the particle-mesh Ewald method with a cutoff of 14 Å (69). The temperature in all simulations was set to 300 K and controlled via the v-rescale thermostat (70); the initial velocities of all particles were randomly generated. Pressure coupling was handled with the Berendsen barostat during equilibration and with the Parrinello-Rahman barostat for dynamics. The LINCS (Linear Constraint

Solver) algorithm (71) was used to constrain bonds in conjunction with an integration time step of 2 fs. All trajectory images were produced in VMD (visual molecular dynamics) (72). All data were visualized using Python.

#### Aggregation numbers and component ratios

Micelle aggregation numbers and component ratios were calculated using a Python program using MDTraj (73) written for this purpose that recursively considers the neighbors of each micelle component within a given cutoff to define an aggregate, until no more neighbors are found. A 3-Å cutoff was used, and all micelle components in the simulation box were found using this scheme. Micelle aggregation numbers reported (figs. S4 and S5) are for a single frame of each replicate after 100 ns, after periodicity was considered. Component ratios are reported as the sample mean across replicates at 100 ns, after combining data from simulations run at different protonation states, in fig. S6.

#### Hydration number

Hydration numbers were calculated by searching for solvent molecules near a given atom within a cutoff of 4 Å, which was determined to be optimal by generating radial distribution functions (fig. S10) for the solvent surrounding each atom of interest from simulations containing only the catalyst in water. Data reported are the distribution for each simulation over the whole simulation time, as reported in table S2. The hydration numbers of catalytically relevant atoms of interest are given in figs. S7 to S9.

#### Intramolecular distances

Intramolecular distances between relevant atoms of the catalysts were measured as the Cartesian distance between the groups at each frame of the final trajectory, after considering periodic boundary conditions. The intramolecular distances of each catalyst monomer were considered separately, and the overall distance data reported are the distributions over the total simulation time of each set of replicates (figs. S11 and S12).

### SUPPLEMENTARY MATERIALS

Supplementary material for this article is available at <http://advances.sciencemag.org/cgi/content/full/6/14/eaaz0404/DC1>

### REFERENCES AND NOTES

1. A. Warshel, P. K. Sharma, M. Kato, Y. Xiang, H. Liu, M. H. M. Olsson, Electrostatic basis for enzyme catalysis. *Chem. Rev.* **106**, 3210–3235 (2006).
2. J. McMurry, T. P. Begley, *The Organic Chemistry of Biological Pathways* (Roberts and Company Publishers, Englewood, Colorado, USA, 2005).
3. A. J. Kirby, Efficiency of proton transfer catalysis in models and enzymes. *Acc. Chem. Res.* **30**, 290–296 (1997).
4. F. M. Menger, Enzyme reactivity from an organic perspective. *Acc. Chem. Res.* **26**, 206–212 (1993).
5. D. E. Koshland, The key-lock theory and the induced fit theory. *Angew. Chem. Int. Ed. Engl.* **33**, 2375–2378 (1995).
6. A. J. Kirby, Enzyme mechanisms, models, and mimics. *Angew. Chem. Int. Ed. Engl.* **35**, 706–724 (1996).
7. X. Zhang, K. N. Houk, Why enzymes are proficient catalysts: Beyond the Pauling paradigm. *Acc. Chem. Res.* **38**, 379–385 (2005).
8. D. L. Purich, *Enzyme Kinetics: Catalysis and Control: A Reference of Theory and Best-Practice Methods* (Elsevier Science, 2010).
9. J. R. Knowles, Enzyme catalysis: Not different, just better. *Nature* **350**, 121–124 (1991).
10. R. Breslow, Biomimetic chemistry and artificial enzymes: Catalysis by design. *Acc. Chem. Res.* **28**, 146–153 (1995).
11. D. J. Cram, J. M. Cram, *Container Molecules and Their Guests* (Royal Society of Chemistry, 1994).
12. D. J. Cram, H. E. Katz, I. B. Dicker, Host-guest complexation. 31. A transacylase partial mimic. *J. Am. Chem. Soc.* **106**, 4987–5000 (1984).
13. D. M. Rudkevich, G. Hilmersson, J. Rebek, Self-folding cavitands. *J. Am. Chem. Soc.* **120**, 12216–12225 (1998).



14. M. D. Nothing, Z. Xiao, A. Bhaskaran, M. T. Blyth, C. Bennett, M. L. Coote, L. A. Connal, Synthetic catalysts inspired by hydrolytic enzymes. *ACS Catalysis* **9**, 168–187 (2019).
15. H. Neurath, Proteolytic enzymes, past and future. *Proc. Natl. Acad. Sci. U.S.A.* **96**, 10962–10963 (1999).
16. O. Kirk, T. V. Borcher, C. C. Fuglsang, Industrial enzyme applications. *Curr. Opin. Biotechnol.* **13**, 345–351 (2002).
17. M. L. Bender, F. J. Kezdy, Mechanism of action of proteolytic enzymes. *Annu. Rev. Biochem.* **34**, 49–76 (1965).
18. L. Polgár, The catalytic triad of serine peptidases. *Cell. Mol. Life Sci.* **62**, 2161–2172 (2005).
19. A. R. Buller, C. A. Townsend, Intrinsic evolutionary constraints on protease structure, enzyme acylation, and the identity of the catalytic triad. *Proc. Natl. Acad. Sci. U.S.A.* **110**, E653–E661 (2013).
20. L. Polgár, Structure and function of serine proteases, in *New Comprehensive Biochemistry*, A. Neuberger, K. Brocklehurst, Eds. (Elsevier, Amsterdam, The Netherlands, 1987), chap. 3, vol. 16, pp. 159–200.
21. R. Wiczorek, K. Adamala, T. Gasperi, F. Politicelli, P. Stano, Small and random peptides: An unexplored reservoir of potentially functional primitive organocatalysts. The case of seryl-histidine. *Life* **7**, 19 (2017).
22. R. Ménard, A. C. Storer, Oxyanion hole interactions in serine and cysteine proteases. *Biol. Chem. Hoppe Seyler* **373**, 393–400 (1992).
23. A. J. Barrett, J. F. Woessner, N. D. Rawlings, *Handbook of Proteolytic Enzymes* (Elsevier Science, London, United Kingdom, 2012).
24. C. J. Hawker, K. L. Wooley, The convergence of synthetic organic and polymer chemistries. *Science* **309**, 1200–1205 (2005).
25. Y. Chi, S. T. Scroggins, J. M. J. Fréchet, One-pot multi-component asymmetric cascade reactions catalyzed by soluble star polymers with highly branched non-interpenetrating catalytic cores. *J. Am. Chem. Soc.* **130**, 6322–6323 (2008).
26. M. D. Nothing, A. Ganesan, K. Condic-Jurkic, E. Pressly, A. Davalos, M. R. Gotrik, Z. Xiao, E. Khoshdel, C. J. Hawker, M. L. O'Mara, M. L. Coote, L. A. Connal, Simple design of an enzyme-inspired supported catalyst based on catalytic triad. *Chem* **2**, 732–745 (2017).
27. Y. Liu, S. Pujals, P. J. M. Stals, T. Paulöhr, S. I. Presolski, E. W. Meijer, L. Albertazzi, A. R. A. Palmans, Catalytically active single-chain polymeric nanoparticles: Exploring their functions in complex biological media. *J. Am. Chem. Soc.* **140**, 3423–3433 (2018).
28. H. Rothfuss, N. D. Knöfel, P. W. Roesky, C. Barner-Kowollik, Single-chain nanoparticles as catalytic nanoreactors. *J. Am. Chem. Soc.* **140**, 5875–5881 (2018).
29. J. H. Fendler, E. J. Fendler, *Catalysis in Micellar and Macromolecular Systems* (Academic Press, New York, 1975).
30. C. A. Bunton, F. Nome, F. H. Quina, L. S. Romsted, Ion binding and reactivity at charged aqueous interfaces. *Acc. Chem. Res.* **24**, 357–364 (1991).
31. C. J. O'Connor, R. E. Ramage, A. J. Porter, Surfactant systems as enzyme models. *Adv. Colloid Interface Sci.* **15**, 25–70 (1981).
32. S. Taşcıoğlu, Micellar solutions as reaction media. *Tetrahedron* **52**, 11113–11152 (1996).
33. T. Kunitake, Y. Okahata, T. Sakamoto, Multifunctional hydrolytic catalyses. 8. Remarkable acceleration of the hydrolysis of p-nitrophenyl acetate by micellar bifunctional catalysts. *J. Am. Chem. Soc.* **98**, 7799–7806 (1976).
34. T. Kunitake, S. Shinkai, Catalysis by micelles, membranes and other aqueous aggregates as models of enzyme action. *Adv. Phys. Org. Chem.* **17**, 435–487 (1980).
35. Y. Ihara, M. Nango, Y. Kimura, N. Kuroki, Multifunctional micellar catalysis as a model of enzyme action. *J. Am. Chem. Soc.* **105**, 1252–1255 (1983).
36. U. Tonellato, Catalysis of ester hydrolysis by cationic micelles of surfactants containing the imidazole ring. *J. Chem. Soc. Perkin Trans. 2* **1976**, 771–776 (1976).
37. U. Tonellato, Functional micellar catalysis. Part 2. Ester hydrolysis promoted by micelles containing the imidazole ring and the hydroxy-group. *J. Chem. Soc. Perkin Trans. 2* **1977**, 821–827 (1977).
38. A. F. Abdel-Magid, K. G. Carson, B. D. Harris, C. A. Maryanoff, R. D. Shah, Reductive amination of aldehydes and ketones with sodium triacetoxymethylborohydride. Studies on direct and indirect reductive amination procedures. *J. Org. Chem.* **61**, 3849–3862 (1996).
39. E. J. Corey, M. J. Grogan, Enantioselective synthesis of  $\alpha$ -amino nitriles from N-benzhydryl imines and HCN with a chiral bicyclic guanidine as catalyst. *Org. Lett.* **1**, 157–160 (1999).
40. R. C. Pratt, B. G. Lohmeijer, D. A. Long, R. M. Waymouth, J. L. Hedrick, Triazabicyclodecene: A simple bifunctional organocatalyst for acyl transfer and ring-opening polymerization of cyclic esters. *J. Am. Chem. Soc.* **128**, 4556–4557 (2006).
41. N. J. V. Lindgren, L. Geiger, J. Razkin, C. Schmuck, L. Baltzer, Downsizing of enzymes by chemical methods: Arginine mimics with low pKa values increase the rates of hydrolysis of RNA model compounds. *Angew. Chem. Int. Ed.* **48**, 6722–6725 (2009).
42. M. Miyake, K. Yamada, N. Oyama, Self-assembly of guanidine-type surfactant. *Langmuir* **24**, 8527–8532 (2008).
43. S. El Hankari, P. Hessemann, Guanidinium vs ammonium surfactants in soft-templating approaches: Nanostructured silica and zwitterionic i-silica from complementary precursor-surfactant ion pairs. *Eur. J. Inorg. Chem.* **2012**, 5288–5298 (2012).
44. F. M. Menger, M. Ladika, Origin of rate accelerations in an enzyme model: The p-nitrophenyl ester syndrome. *J. Am. Chem. Soc.* **109**, 3145–3146 (1987).
45. M. L. Bender, M. J. Gibian, D. J. Whelan, The alkaline pH dependence of chymotrypsin reactions: Postulation of a pH-dependent intramolecular competitive inhibition. *Proc. Natl. Acad. Sci. U.S.A.* **56**, 833–839 (1966).
46. F. Richter, R. Blomberg, S. D. Khare, G. Kiss, A. P. Kuzin, A. J. T. Smith, J. Gallaher, Z. Pianowski, R. C. Helgeson, A. Grjasnow, R. Xiao, J. Seetharaman, M. Su, S. Vorobiev, S. Lew, F. Forouhar, G. J. Kornhaber, J. F. Hunt, G. T. Montelione, L. Tong, K. N. Houk, D. Hilvert, D. Baker, Computational design of catalytic dyads and oxyanion holes for ester hydrolysis. *J. Am. Chem. Soc.* **134**, 16197–16206 (2012).
47. P. Nieri, S. Carpi, S. Fogli, B. Polini, M. C. Breschi, A. Podestà, Cholinesterase-like organocatalysis by imidazole and imidazole-bearing molecules. *Sci. Rep.* **7**, 45760 (2017).
48. A. J. Kirby, R. E. Marriott, Mechanism of RNA cleavage by imidazole. Catalysis vs medium effects. *J. Am. Chem. Soc.* **117**, 833–834 (1995).
49. R. Breslow, How do imidazole groups catalyze the cleavage of RNA in enzyme models and in enzymes? Evidence from "negative catalysis". *Acc. Chem. Res.* **24**, 317–324 (1991).
50. H. Tsukada, D. M. Blow, Structure of  $\alpha$ -chymotrypsin refined at 1.68 Å resolution. *J. Mol. Biol.* **184**, 703–711 (1985).
51. S. C. Zimmerman, J. S. Korthals, K. D. Gramer, Syn and anti-oriented imidazole carboxylates as models for the histidine-aspartate couple in serine proteases and other enzymes. *Tetrahedron* **47**, 2649–2660 (1991).
52. T. C. Bruice, R. Lapinski, Imidazole catalysis. IV. <sup>1</sup> The reaction of general bases with p-nitrophenyl acetate in aqueous solution. *J. Am. Chem. Soc.* **80**, 2265–2267 (1958).
53. S. L. Johnson, General base and nucleophilic catalysis of ester hydrolysis and related reactions. *Adv. Phys. Org. Chem.* **5**, 237–330 (1967).
54. W. P. Jencks, *Catalysis in Chemistry and Enzymology* (Dover, 1987).
55. D. M. Blow, Structure and mechanism of chymotrypsin. *Acc. Chem. Res.* **9**, 145–152 (1976).
56. K. Adamala, J. W. Szostak, Competition between model protocells driven by an encapsulated catalyst. *Nat. Chem.* **5**, 495–501 (2013).
57. F. M. Menger, C. E. Portnoy, Chemistry of reactions proceeding inside molecular aggregates. *J. Am. Chem. Soc.* **89**, 4698–4703 (1967).
58. S. E. Felder, M. J. Redding, A. Noel, S. M. Grayson, K. L. Wooley, Organocatalyzed ROP of a glucopyranoside derived five-membered cyclic carbonate. *Macromolecules* **51**, 1787–1797 (2018).
59. J. Chen, J. Hao, Molecular dynamics simulation of cetyltrimethylammonium bromide and sodium octyl sulfate mixtures: Aggregate shape and local surfactant distribution. *Phys. Chem. Chem. Phys.* **15**, 5563–5571 (2013).
60. A. Dominguez, A. Fernandez, N. Gonzalez, E. Iglesias, L. Montenegro, Determination of critical micelle concentration of some surfactants by three techniques. *J. Chem. Educ.* **74**, 1227 (1997).
61. G. Dutheil, M. P. Webster, P. A. Worthington, V. K. Aggarwal, Stereocontrolled synthesis of carbon chains bearing contiguous methyl groups by iterative boronic ester homologations: Application to the total synthesis of (+)-faranol. *Angew. Chem. Int. Ed. Engl.* **48**, 6317–6319 (2009).
62. M. J. Frisch, G. W. Trucks, H. B. Schlegel et al., GAUSSIAN 16, Revision A.03, Gaussian, Inc., Wallingford, CT, 2009.
63. Y. Zhao, D. G. Truhlar, The M06 suite of density functionals for main group thermochemistry, thermochemical kinetics, noncovalent interactions, excited states, and transition elements: Two new functionals and systematic testing of four M06-class functionals and 12 other fun. *Theor. Chem. Acc.* **120**, 215–241 (2007).
64. A. V. Marenich, C. J. Cramer, D. G. Truhlar, Universal Solvation Model Based on Solute Electron Density and on a Continuum Model of the Solvent Defined by the Bulk Dielectric Constant and Atomic Surface Tensions. *J. Phys. Chem. B* **113**, 6378–6396 (2009).
65. I. M. Alecu, J. Zheng, Y. Zhao, D. G. Truhlar, Computational thermochemistry: Scale factor databases and scale factors for vibrational frequencies obtained from electronic model chemistries. *J. Chem. Theory Comput.* **6**, 2872–2887 (2010).
66. N. Schmid, A. P. Eichenberger, A. Choutko, S. Riniker, M. Winger, A. E. Mark, W. F. van Gunsteren, Definition and testing of the GROMOS force-field versions 54A7 and 54B7. *Eur. Biophys. J.* **40**, 843–856 (2011).
67. M. J. Abraham, M. Murtola, R. Schulz, S. Páll, J. C. Smith, B. Hess, E. Lindahl, GROMACS: High performance molecular simulations through multi-level parallelism from laptops to supercomputers. *SoftwareX* **1–2**, 19–25 (2015).
68. K. B. Kozlars, M. Stroet, A. K. Malde, A. E. Mark, Testing and validation of the automated topology builder (ATB) version 2.0: Prediction of hydration free enthalpies. *J. Comput. Aided Mol. Des.* **28**, 221–233 (2014).
69. U. Essmann, L. Perera, M. L. Berkowitz, T. Darden, H. Lee, L. G. Pedersen, A smooth particle mesh Ewald method. *J. Chem. Phys.* **103**, 8577–8593 (1995).
70. G. Bussi, D. Donadio, M. Parrinello, Canonical sampling through velocity rescaling. *J. Chem. Phys.* **126**, 014101 (2007).
71. B. Hess, P-LINCS: A Parallel Linear Constraint Solver for Molecular Simulation. *J. Chem. Theory Comput.* **4**, 116–122 (2008).

72. W. Humphrey, A. Dalke, K. Schulten, VMD: Visual molecular dynamics. *J. Mol. Graph.* **14**, 33–38 (1996).
73. R. T. McGibbon, K. A. Beauchamp, M. P. Harrigan, C. Klein, J. M. Swails, C. X. Hernández, C. R. Schwantes, L.-P. Wang, T. J. Lane, V. S. Pande, MDTraj: A modern open library for the analysis of molecular dynamics trajectories. *Biophys. J.* **109**, 1528–1532 (2015).
73. A. Prlić, A. R. Bradley, J. M. Duarte, P. W. Rose, A. S. Rose, Y. Valasatava, NGL viewer: Web-based molecular graphics for large complexes. *Bioinformatics* **34**, 3755–3758 (2018).

**Acknowledgments**

**Funding:** Funding from the U.S. Army International Technology Centre Pacific (ITC-PAC FA5209-14-C-0017 and the Australian Research Council (ARC)(DP200100535) is gratefully acknowledged (to L.A.C. and M.L.O.). M.D.N. and L.A.C. acknowledge the Australia Science Endowment Fund (SIEF) for a John Stoker postgraduate Scholarship, as well as an Endeavour Research Fellowship and Australian Nanotechnology Network Overseas Travel Fellowship (to M.D.N.). M.L.C. acknowledges financial support from the ARC Centre of Excellence for Electromaterials Science (CE140100012), an ARC Laureate Fellowship (FL170100041), and supercomputing time from the National Computational Infrastructure. **Author contributions:**

M.D.N., Z.X., A.B., A.E.-G., K.N., and T.B. conducted the synthesis and catalysis studies. M.A.-S. conducted the NMR studies. J.W. conducted the XRD studies. N.S.H. and M.T.B. conducted the computational studies. M.D.N., F.S., M.L.O., M.L.C., and L.A.C. conceived the concepts and designed the experiments. All authors contributed to the manuscript preparation and editing. **Competing interests:** The authors declare that they have no competing interests. **Data and materials availability:** All data needed to evaluate the conclusions in the paper are present in the paper and/or the Supplementary Materials. Additional data related to this paper may be requested from the authors.

Submitted 7 August 2019

Accepted 8 January 2020

Published 1 April 2020

10.1126/sciadv.aaz0404

**Citation:** M. D. Nothing, Z. Xiao, N. S. Hill, M. T. Blyth, A. Bhaskaran, M.-A. Sani, A. Espinosa-Gomez, K. Ngov, J. White, T. Buscher, F. Separovic, M. L. O'Mara, M. L. Coote, L. A. Connal, A multifunctional surfactant catalyst inspired by hydrolases. *Sci. Adv.* **6**, eaaz0404 (2020).

## A multifunctional surfactant catalyst inspired by hydrolases

Mitchell D. Nothling, Zeyun Xiao, Nicholas S. Hill, Mitchell T. Blyth, Ayana Bhaskaran, Marc-Antoine Sani, Andrea Espinosa-Gomez, Kevin Ngov, Jonathan White, Tim Buscher, Frances Separovic, Megan L. O'Mara, Michelle L. Coote and Luke A. Connal

*Sci Adv* 6 (14), eaaz0404.  
DOI: 10.1126/sciadv.aaz0404

ARTICLE TOOLS	<a href="http://advances.sciencemag.org/content/6/14/eaaz0404">http://advances.sciencemag.org/content/6/14/eaaz0404</a>
SUPPLEMENTARY MATERIALS	<a href="http://advances.sciencemag.org/content/suppl/2020/03/30/6.14.eaaz0404.DC1">http://advances.sciencemag.org/content/suppl/2020/03/30/6.14.eaaz0404.DC1</a>
REFERENCES	This article cites 66 articles, 4 of which you can access for free <a href="http://advances.sciencemag.org/content/6/14/eaaz0404#BIBL">http://advances.sciencemag.org/content/6/14/eaaz0404#BIBL</a>
PERMISSIONS	<a href="http://www.sciencemag.org/help/reprints-and-permissions">http://www.sciencemag.org/help/reprints-and-permissions</a>

Downloaded from <http://advances.sciencemag.org/> on May 13, 2020

Use of this article is subject to the [Terms of Service](#)

*Science Advances* (ISSN 2375-2548) is published by the American Association for the Advancement of Science, 1200 New York Avenue NW, Washington, DC 20005. The title *Science Advances* is a registered trademark of AAAS.

Copyright © 2020 The Authors, some rights reserved; exclusive licensee American Association for the Advancement of Science. No claim to original U.S. Government Works. Distributed under a Creative Commons Attribution NonCommercial License 4.0 (CC BY-NC).

## 6.4 Implications and Applications

In the two publications presented in this chapter, quantum chemistry has been employed in order to accurately model two types of organic reaction, free radical polymerization and hydrolysis, which are catalysed using two different approaches. Throughout this thesis, photochemical reactions have been altered by the introduction of external stimuli, be they electric fields or secondary (and tertiary) components. It is important to understand how these new, more complex systems behave and how their chemistry can be altered, and provide a baseline of knowledge upon which more computationally challenging, photochemical investigations can be built.

The first publication studied the catalysis and tacticity control of a styrene and methyl methacrylate copolymerization with  $\text{BCl}_3$  present. The propagation catalysis was confirmed to arise from the increase in polarity of methyl methacrylate, either has a radical chain end or monomer unit, upon complexation with  $\text{BCl}_3$ . This complexation was found to significantly decrease the relevant transition state activation energies. Coheterotacticity was found to arise from pairwise  $\pi$ -stacking interactions between  $\text{BCl}_3$ -complexed methyl methacrylate and styrene. This study highlights the difficulty in achieving coheterotacticity and the possible effects of introducing Lewis acids; catalysis is achieved with small amounts of  $\text{BCl}_3$  as only a single methyl methacrylate is required to be complexed in order to undergo rapid radical addition to a styrene unit. For tacticity to be obtained, however, a stoichiometric amount of  $\text{BCl}_3$  is required, in order to promote and maintain the alternating attractive/repulsive pairwise  $\pi$ -stacking interactions. In a different reaction, however, the addition of too much Lewis acid may promote side-reactions and result in a polymer difficult to clean. As well as this, the tacticity is dependent on the presence of the styrene  $\pi$ -system, so is not generally applicable to all monomer types.

The second publication studied the ability of an enzyme-inspired catalytic triad coupled with micelles to catalyse the hydrolysis of *p*-nitrophenyl benzoate. Here, a significant challenge lay in the complexity of the experimental conditions; micelles are typically composed of thousands of lipids and the solvent environment will alter between

being predominantly water at the edge of the micelle, to a predominantly “alkane” environment internally in the micelle. A full quantum chemical treatment of such a large and complex system is unfeasible due to computing limitations. The computational problem was therefore split into two parts: a molecular dynamics study into the behaviour of the micelles and the localization of reactants, and a quantum mechanical investigation using a truncated model system to capture the core interactions and reactivity between the artificial catalytic triad, a guanidinium headgroup, and *p*-nitrophenyl benzoate.

From the quantum mechanical small model, it was found that the core reactivity of the artificial catalytic triad and *p*-nitrophenyl benzoate was a bimodal transition state, corresponding to the hydroxyl group of the former adding to the  $sp^2$  hybridized carbon centre of the latter, via the deprotonated imidazole ring on the artificial catalytic triad. This process is further enhanced by a positively charged guanidinium headgroup of a neighbouring cosurfactant, due to its positive charge stabilising the localized negative charge forming on the acyl oxygen in the transition state. This charge stabilization corresponds to an increase in reaction rate of several orders of magnitude, and is therefore a significant and highly useful effect. The molecular dynamics study provided further evidence for this reactivity, finding that the required three species for catalytic reaction will localize at the surface of the micelles. This approach to catalysis is a general approach, and is currently being applied to transesterification and polymerization reactions. As well as this, electrostatic interactions were found to play a significant role in the hydrolysis catalysis, highlighting how micellar environments are a potentially effective route to introducing charge to other reactions that can take advantage of electric fields.

## 6.5 References

- (1) Noble, B. B.; Coote, M. L. In *Advances in Physical Organic Chemistry, First Edition*, First Edit, 2015, pp 189–258.
- (2) Noble, B. B.; Mater, A. C.; Smith, L. M.; Coote, M. L. *Polymer Chemistry* **2016**, *7*, 6400.
- (3) Hill, N. S.; Coote, M. L. *Australian Journal of Chemistry* **2019**, *72*, 627–632.

- (4) Kamigaito, M.; Satoh, K. *Macromolecular* **2008**, *41*, 269–276.
- (5) Noble, B. B.; Coote, M. L. In *Controlled Radical Polymerization: Mechanisms*; ACS Symposium Series, Vol. 1187; American Chemical Society: 2015, pp 3–51.
- (6) Isobe, Y.; Nakano, T.; Okamoto, Y. *Journal of Polymer Science Part A: Polymer Chemistry* **2001**, *39*, 1463–1471.
- (7) Garcia-Viloca, M.; Gao, J.; Karplus, M.; Truhlar, D. G. *Science* **2004**, *303*, 186–195.
- (8) Steiner, K.; Schwab, H. *Computational and structural biotechnology journal* **2012**, *2*, e201209010.
- (9) Dodson, G.; Wlodawer, A. *Trends in Biochemical Sciences* **1998**, *23*, 347–352.
- (10) Rathman, J. F. *Current Opinion in Colloid & Interface Science* **1996**, *1*, 514–518.
- (11) Sorella, G. L.; Strukul, G.; Scarso, A. *Green Chemistry* **2015**, *17*, 644–683.

## 7 General Conclusions

A wide range of chemical systems have been studied throughout this thesis, from which several conclusion have been drawn. These are summarized below.

### 7.1 Summary of Key Findings

1. Recent literature employing excited state computational methods has been extensively reviewed, and served as a guide and justification for the choice of methods used throughout this thesis. The review finds that TD-DFT remains a popular method for excited state calculations, much more so than *ab initio*, wavefunction methods due to the expense and difficulty associated with the latter. Moreover, the M06-2X functional has been consistently found to provide reasonably accurate results for both thermal and photo-reactions, and has therefore been used extensively throughout this thesis. As well as this, the application of quantum chemistry to nitroxide molecules has been discussed, and many of the approaches to modelling chemistry used throughout this body of work can be found in this methodological review.
2. The application of functionalized anthraquinone molecules to visible light photoinitiation has been studied, and quantum chemistry provided detailed insight into how these systems behave upon irradiation with light, and how they interact co-initiating species. The photochemical pathways were modelled and how the excited anthraquinone derivatives were able to sensitize radical or cationic co-initiator molecules was determined. The full photochemical cycles for these systems, some involving three different components, have been fully elucidated and their observed reactivities rationalized. The anthraquinones were found to be excited state “electron pumps”, able to act as either electron sinks or electron donors depending on the substitution pattern used and the co-initiators present.
3. Internal electric fields, generated by acid or base functional groups that can be

charged or neutral depending on their protonation state, have for the first time been applied to Type I radical photoinitiators. First, the effect of introducing charged functional groups was assessed using acetophenone as the model photoinitiator, finding that  $n_O\pi^*$  and  $\pi\pi^*$  excited states split in opposite directions, depending on the direction of the applied field. Further calculations were performed to confirm the electrostatic origin of the observed effects. Secondly, these effects were applied to Irgacure 2959, a radical photoinitiator that finds use in 3D bioprinting applications. Irgacure 2959 suffers from poor solubility in water as well as low quantum yields of initiation, and was used as a system that could be improved with electric fields. Once again, the  $n_O\pi^*$  and  $\pi\pi^*$  excited states were split in opposite directions, and the singlet and triplet states of different symmetries were shown to be able to be moved closer together energetically, therefore providing a route to alter photochemical reactions in a predetermined manner. Finally, these effects were compared against more thoroughly explored ways of altering photochemistry, namely Lewis acid complexation and increasing conjugation. Both of these approaches altered the photo-absorption of Irgacure 2959, but not in a controlled manner.

4. Development of effective PNMP agents has proven difficult as both the chromophore and monomer unit are found to affect the observed reactivity of the systems upon irradiation with light. Two theoretical studies have therefore been performed; the first considers a mesolytic-type pathway for cleavage upon irradiation, and in the second new photoactive alkoxyamines have been designed, which employ functionalization patterns that have been studied in Chapters 3 and 4. Mesolytic cleavage is a new rationale for observed PNMP agent photoreactivity, and is identified as a reason for the inconsistent performance of this class of molecules. It has also been shown computationally that using amine/hydroxyl groups or electric fields will significantly alter the charge-transfer properties of the low-lying  $n_N\pi^*$  excited state, and the chemistry that this state can exhibit. Depending on the application and solvent environment, radical or mesolytic cleavage



pathways can be selectively chosen with different functional groups, and can be used with a variety of different monomer units attached to the nitroxide moiety.

5. The introduction of extra compounds to a reaction may not only alter photochemical properties, but may also alter ground-state, thermal reactivity. To that end, the effect of introducing Lewis acids to the copolymerization of styrene and methyl methacrylate, which has been studied extensively experimentally, was modelled using quantum chemistry, in order to determine how and why  $\text{BCl}_3$  induces propagation catalysis and coheterotacticity. The attractive/repulsive pairwise interactions observed in the chemical model was found to satisfactorily explain the observed effects, and also provides insight into why these Lewis acid effects are not ubiquitous. Finally, the ability of quantum chemistry to describe large, complex solvation environments was studied with a guanidine, artificial catalytic triad, and *p*-nitrophenyl benzoate system. Here, quantum chemistry was able to elucidate the most likely catalytic pathway, and rationalize the observed catalysis of the hydrolysis reaction.

## 7.2 Future Work

Quantum chemistry has been used extensively to explain experimental results and to design new molecules, and it is now important to highlight how the knowledge obtained can be utilized in the future.

With respect to the anthraquinone visible light photoinitiators, the importance of including secondary and tertiary co-initiating species is shown, as their presence allows for the initiating cycle to be closed, allowing for the continuing reformation of the anthraquinone molecules for reinitiation. Their inclusion is also an avenue of research for the anthraquinone-based nitroxide species studied in Chapter 5, as mesolytic pathways are expected to be important and the presence of co-initiators may encourage the exclusive formation of radical, rather than cationic, species.

Chapter 6 also presents publications that couple experimental results with computational modelling. In each case, theoretical modelling was used to elucidate likely

reaction mechanisms, thereby identifying the origin of observed catalysis and, for Publication 12, how polymer tacticity control is achieved. The research and development of chemical techniques that truly achieve stereocontrol in polymer synthesis remains an outstanding problem in polymer chemistry, and the future directions to achieving this is outside the scope of this thesis. However,  $\pi$ -stacking interactions and Lewis acid catalysis are powerful effects as:

- (a) Monomer molecules usually exhibit unsaturated bonds, required for radical formation and propagation, and can be used for  $\pi$ -stacking effects
- (b) Many Lewis acids are simple molecules, soluble in bulk monomer solutions, and can exhibit a range of (non-)covalent interactions and binding modes

However, reviews by Satoh and Kamigaito<sup>1</sup> and Noble and Coote<sup>2</sup> suggest that addition of Lewis acids is not a simple solution to tacticity control.

The future direction of the development of enzyme-inspired, artificial catalytic triads is clearer; their effectiveness at catalysing both industrially and biologically relevant reactions should be investigated. The introduction of heteroatoms to the key functional groups is also worth investigating as the altering, for example, the nucleophilicity of the alcohol moiety may have a dramatic effect on the observed catalysis. The impact of introducing heteroatoms can be evaluated by computational chemistry and compared to the catalytic pathways of the original ACT, and this research is ongoing.

In Chapters 4 and 5, and contrary to the studies in Chapters 3 and 6, several different molecules have been rationally designed, and their chemical properties predicted, with only theoretical chemistry. The most significant effect is the introduction of charged functional groups, which has been shown computationally to significantly alter the energies of excited states of differing symmetries in a predictable manner. The first challenge that must be met is the synthesis of photoactive molecules that are functionalized with acid/base groups at an appropriate position with a methyl spacer unit. In order to determine the reliability of the theoretical calculations these first molecules do not necessarily need to be photoinitiators, as electrostatic (de)stabilization (exhibited by

UV shifts upon charge formation) and solvent effects (size of UV shift as a function of solvent polarity) are simple to measure. Once the electric field effects are established experimentally, more complex photochemical phenomena like, for example, the effect on photoinitiation can be investigated.

Finally, the identification of mesolytic cleavage in photoactivated alkoxyamines as a possible pathway and source of poor performance in photo-NMP agents allows for their continuing development. Experimental confirmation of the mesolytic pathway is the first challenge, and can likely be achieved by careful selection of monomers that can only undergo cationic polymerization, therefore leaving no room for potential homolytic/mesolytic competition. The formation of polymer in such a combination would clearly demonstrate mesolytic cleavage. The anthraquinone scaffold has been shown to be simple to functionalize and calculations in Publication 11 have shown how hydroxyl and amine groups can increase or decrease  $n_N\pi^*$  excited state charge transfer, respectively. Significant charge transfer is linked to mesolytic cleavage, and therefore tuning charge transfer can allow for the selection of different cleavage pathways as appropriate.

### 7.3 References

- (1) Kamigaito, M.; Satoh, K. *Chemical Reviews* **2009**, *109*, 5120–5156.
- (2) Noble, B. B.; Coote, M. L. In *Advances in Physical Organic Chemistry, First Edition*, First Edit, 2015, pp 189–258.

# A Appendices

## A.1 Quantum Chemistry and Theoretical Procedures

### Introduction

With the increase in speed and decrease in cost of high-performance computing in the second half of the 20th century, computational chemistry has become an increasingly important tool for modern chemists. When applied properly, quantum chemistry can provide insight into reactions that would otherwise be difficult to elucidate using standard experimental procedures. Molecular structures can be linked to observed reactivities, allowing for reaction mechanisms to be determined and routes for further optimization to be explored. The role of a computational chemist is, then, to construct a suitable potential energy surface (PES), which takes into account all of the relevant chemical structures, lowest energy conformers of reactants, intermediates, and transition states. With these structures, subsequent calculations can be performed in order to generate the frequencies associated with the structures, necessary for the calculation of gas-phase partition functions and Gibbs energies, or the PES can be improved by using high-level single-point energies. This thesis also has a focus on excited state computational chemistry, in which ground-state methods are extended to molecules with non-Aufbau electron configurations. The aim of this appendix is to provide a brief overview of the methods used throughout this thesis, and to highlight how they have been used.

More detailed discussions into theoretical chemistry can be found in books by Jensen,<sup>1</sup> or Cramer,<sup>2</sup> among others.

### *Ab initio* methods

“*Ab initio*” generally refers to the class of methods based on the fundamental equation in quantum mechanics; the time-independent Schrödinger equation (Equation A1).<sup>3</sup>

$$\hat{H}\Psi = E\Psi \quad (\text{A1})$$

Equation A1 describes how the Hamiltonian operator ( $\hat{H}$ ) acting on a system's wavefunction ( $\Psi$ ) returns an observable, in this case the energy ( $E$ ), of the system. When applied to a molecular system, the Hamiltonian operator is composed of kinetic and potential energy terms:

$$\hat{H} = \hat{T} + \hat{V} \quad (\text{A2})$$

The kinetic energy,  $\hat{T}$ , arises from nuclear and electron motion:

$$\hat{T} = - \sum_i \frac{\hbar}{2m_e} \nabla_i^2 - \sum_k \frac{\hbar}{2m_k} \nabla_k^2 \quad (\text{A3})$$

where  $\hbar$  is the reduced Planck constant,  $i$  runs over electrons,  $k$  runs over nuclei,  $m_e$  and  $m_k$  are the masses of the electron and nuclei  $k$ , respectively, and  $\nabla_i^2$  is the Laplacian operator with the form:

$$\nabla_i^2 = \frac{\partial^2}{\partial x_i^2} + \frac{\partial^2}{\partial y_i^2} + \frac{\partial^2}{\partial z_i^2} \quad (\text{A4})$$

The potential energy term,  $\hat{V}$ , arises from nuclei-nuclei, electron-electron, and electron-nuclear electrostatic interactions:

$$\hat{V} = - \sum_i \sum_k \frac{e^2 Z_k}{r_{ik}} + \sum_{i < j} \frac{e^2}{r_{ij}} + \sum_{k < l} \frac{e^2 Z_k Z_l}{r_{kl}} \quad (\text{A5})$$

where  $e$  is the charge of the electron,  $Z_l$  is the atomic number of nuclei  $l$ , and  $r_{ik}$  is the distance between particles  $i$  and  $j$ .

The potential energy operator (Eq. A5) contains pairwise interactions between nuclei and electrons present in a molecule, terms that correlate the motion of the particles and renders the wavefunction extremely difficult to express. In order to simplify the Hamiltonian, the Born-Oppenheimer approximation<sup>4</sup> is introduced which, assuming that nuclear motion is extremely slow compared to electronic motion, holds nuclei

stationary. The result of this approximation is the disappearance of the nuclear kinetic energy term and a constant nuclear repulsion term, and now only the electronic wavefunction (Eq. A6) needs to be computed across frozen nuclear geometries.

$$(H_{el} + V_N)\Psi_{el}(\mathbf{q}_i; \mathbf{q}_k) = E_{el}\Psi_{el}(\mathbf{q}_i; \mathbf{q}_k) \quad (\text{A6})$$

The introduction of the Born-Oppenheimer approximation leads to the concept of a “potential energy surface” (PES), which is defined as the electronic energy,  $E_{el}$ , across all possible nuclei geometries. Using potential energy surfaces it is possible to define stationary points as equilibrium or transition state structures, which provide chemists with physical arguments of chemical processes. However, in its current form, the electronic wavefunction remains analytically insoluble; in particular, the electron-electron repulsion term remains analytically insoluble for many-electron systems, and requires further treatment in order to be of any great use.

### Hartree-Fock

The simplest approach to solving the many-electron wavefunction is the Hartree-Fock (HF) method;<sup>5-9</sup> such is its success in doing so even today it remains the cornerstone upon which the most accurate wavefunction methods are built. The core assumption of HF is that the many-electron wavefunction can be expressed as the product of independent, one-electron wavefunctions, also known as molecular orbitals (MO):

$$\Psi_{HP} = \psi_1\psi_2, \psi_3\dots\psi_N \quad (\text{A7})$$

In this form, the Hartree-product wavefunction (Eq. A7) does not obey the Pauli exclusion principle, which states that electronic wavefunctions must be antisymmetric with respect to their coordinates. In order to satisfy this principle, the electronic wavefunction is reconstructed as a Slater determinant (Eq. A8).

$$\Psi_{el} = \frac{1}{\sqrt{N!}} \begin{vmatrix} \psi_1(r_1) & \psi_1(r_2) & \dots & \psi_1(r_N) \\ \psi_2(r_1) & \psi_2(r_2) & \dots & \psi_2(r_N) \\ \vdots & \vdots & \ddots & \vdots \\ \psi_N(r_1) & \psi_N(r_2) & \dots & \psi_N(r_N) \end{vmatrix} \quad (\text{A8})$$

In order to obtain the one-electron wavefunctions, it is assumed that each MO can be represented as a linear combination of atomic orbitals (LCAO) (Eq. A9).

$$\psi_i(r_i) = \sum_{\mu} C_{\mu i} \chi_{\mu}(r_i) \quad (\text{A9})$$

where  $C_{\mu i}$  is the molecular orbital coefficient, and  $\chi_{\mu}$  are the basis functions used to describe the atomic orbitals.

HF is also a variational, self-consistent field (SCF) method. The variational theorem (Eq. A10) describes how the expectation value of the energy,  $E$ , can only be greater than or equal to the exact energy,  $E_{exact}$ .

$$\langle E \rangle = \langle \Psi | \hat{H} | \Psi \rangle \geq E_{exact} \quad (\text{A10})$$

The variational theorem is a powerful concept as it provides a target for any wavefunction calculations; that is, the lower the energy of the wavefunction, the better the wavefunction guess. The HF wavefunction can be considered converged, and therefore optimal, when no step in the calculation results in a lower energy wavefunction. An SCF procedure is employed in order to optimize the wavefunction, the steps of which are:

1. Define the relevant nuclear coordinates
2. Obtain a trial set of non-optimal MO coefficients to compute the Fock operator (one-electron Hamiltonian)
3. Solve the electronic Schrödinger wave equation to obtain the energy and a new set of MO coefficients

4. If the new MO coefficients are different to those used in previous steps, repeat from Step 2 until the change in wavefunction energy and MO coefficients are less than some arbitrary threshold

Depending on the total electron spin of the molecular system, one of several different HF “flavours” may need to be employed. The simplest spin system is that which has no unpaired electrons, for which Restricted Hartree-Fock (RHF) is used. In RHF, each spatial molecular orbital is used to form two spin-orbitals:

$$\chi_i(r, \omega) = \begin{cases} \psi_j(r)\alpha(\omega) \\ \psi_j(r)\beta(\omega) \end{cases} \quad (\text{A11})$$

where  $\alpha$  and  $\beta$  are spin-functions representing “spin up” and “spin down” electrons. This approach is not appropriate, however, in systems that possess unpaired electrons, examples of which in this thesis are radical species (one unpaired electron in a singly occupied molecular orbital), and triplet species (two unpaired electrons). In order to properly describe such systems, RHF was generalized to unrestricted Hartree-Fock (UHF), which allows electrons of  $\alpha$  and  $\beta$  electrons to be described by different spatial functions.

The drawback of employing a UHF wavefunction is that, compared to a RHF wavefunction, it is artificially “mixed” with higher energy electronic spin states, known as spin contamination. The extent of spin contamination can be monitored via the total spin squared operator,  $\hat{S}^2$ , of which spin contaminated wavefunctions will not be pure eigenvalues. For systems that are suffering from significant spin contamination, it may be necessary to employ the final common HF method, restricted open-shell Hartree-Fock (ROHF). In simple terms, ROHF uses elements of RHF and UHF in its formalism, where all paired electrons are treated in a manner analogous to RHF, and unpaired electrons are treated with singly occupied, unrestricted MOs.

HF represents the first steps towards describing the quantum mechanical nature of chemical systems, and remains the least expensive computational method for the optimization of MO coefficients. Due to the one-electron wavefunctions used in its for-



malism, HF is a mean-field theory and neglects the instantaneous Columbic interaction between electrons, termed electron correlation. Electron correlation is defined as the difference between the HF energy,  $E_{HF}$ , and the exact energy,  $E_{exact}$  (Eq. A12).

$$E_{exact} = E_{HF} + E_{correlation} \quad (\text{A12})$$

Whilst the electron correlation energy is only a small proportion of a system's total energy (typically <1%), it is extremely sensitive to electronic structure and can give rise to large errors when calculating reaction and activation energies. More complex, so-called post-HF methods are therefore employed to recover electron correlation in order to give more accurate electronic energies.

### Basis Sets

Before exploring post-HF methods, it is important to first describe basis sets, without which computational electronic structure calculations would not be practical. As described in Eq. A9, each molecular orbital is formed using the LCAO approach and are a linear combination of basis functions. Collectively, these basis functions form a basis set, and are used to describe the electronic probability density as a function of electron-nuclei distance.<sup>10</sup> When choosing an appropriate basis function, it is important to consider its chemical relevance; it should predict high electron density close to the atomic nuclei and low electron density at larger distances. As well as this, the functional form must be such that the respective integrals appearing in HF calculations can be evaluated in an efficient manner. There are two predominant types of functions used for basis sets; Slater-type orbitals (STO) and Gaussian-type orbitals (GTO). STO basis functions (functional form in Eq. A13a) benefit from closely resembling hydrogenic atomic orbitals, and therefore require fewer functions than GTOs (Eq. A13b), for similar levels of accuracy. Unfortunately, the mathematical form of STOs gives rise to complex integrals with no analytical solution; their numerical evaluation is time consuming, and

this prevents their widespread usage in electronic structure codes.

$$\chi_{abc}^{STO}(x, y, z) = Nx^a y^b z^c e^{-\alpha r} \quad (\text{A13a})$$

$$\chi_{abc}^{GTO}(x, y, z) = Nx^a y^b z^c e^{-\alpha r^2} \quad (\text{A13b})$$

where  $a$ ,  $b$ , and  $c$  define the angular momentum of the atomic orbital, and  $\alpha$  defines its width.

Despite giving rise to integrals that have analytical solutions which can be efficiently computed, GTOs do not exhibit either the correct electron radial decay, as  $\exp(-\alpha r^2)$  decays more rapidly than the  $\exp(-\alpha r)$  term found in STOs, or the electron cusp found at the nuclear-electron boundary. As a result, most basis sets use a linear combination of Gaussian functions to more accurately model the properties of atomic orbitals; this linear combination is known as a contracted basis function, the individual Gaussian functions are known as primitive Gaussians.

The simplest basis sets are known as minimal basis sets, and only use a single contracted basis function per atomic orbital. Examples of original minimal basis sets are the STO- $n$ G set,<sup>11</sup> in which each STO is approximated with  $n$  primitive Gaussians. These basis sets are too inflexible to accurately describe chemical bonding and do not give sufficiently accurate or reliable results. In order to improve the accuracy and flexibility of the basis set, it is possible to model the atomic orbitals using two, rather than one, basis function. Such a basis set is called double-zeta basis set; one that uses three basis functions per atomic orbital is called triple-zeta, and so on. In pursuit of computational efficiency it is important to remember that chemical bonding only involves the valence orbitals; it is not therefore necessary to model the core atomic orbitals with more than one basis function, but it is necessary to maintain the flexibility of using multiple basis functions for the valence orbitals. These are known as split-valence basis sets, the most popular of which are the Pople basis sets,<sup>12</sup> the naming of which follows A-BCG for double-zeta, or A-BCDG for triplet-zeta basis sets. Here, A refers to the number of primitive Gaussians used to describe each of the core basis function, and B, C, and D

refer to the number of primitive Gaussian functions comprising the valence orbital basis functions. A commonly used basis set, for example, is the 6-31G Pople basis set. Another popular family of basis sets are those by Dunning,<sup>13-17</sup> which follow the naming scheme cc-pVnZ. Here, *n* can be D (double-zeta), T (triple-zeta), Q (quintuple-zeta), and so on. These basis sets are designed to systematically approach the complete basis set (CBS) limit as they get larger; that is, after employing increasingly large basis sets it is possible to extrapolate the resulting energy to that which would be obtained with an infinitely large, infinitely flexible basis set.

It is often necessary to introduce, or “augment”, basis sets with extra functions that further increase their flexibility and accuracy. Two types of functions are used, polarization functions and diffuse functions; both can be used in conjunction with the other. Polarization functions include angular momentum functions higher than the occupied valence orbitals. These functions allow the MOs to become more asymmetric as necessary, and more fully describe the electron probability density. With Pople basis sets, the inclusion of polarization functions is shown by either a “\*”, a “d”, or a “p”, which signify:

- 6-31G\* or 6-31G(d) - d polarization functions are added to heavy (non-Hydrogen) atoms
- 6-31G\*\* or 6-31G(d,p) - as above, with p polarization functions added to Hydrogen atoms

Diffuse functions are Gaussians that decay much more slowly than those used normally to construct a basis function; these functions are necessary when describing molecules with a more loosely bound electron density than a neutral species, for example anions or excited states. Their inclusion in a Pople basis sets is demonstrated by a “+” sign, for example 6-31+G\*, which describes a basis set with a d-type polarization function and a s- and p-type diffuse function on heavy atoms. Dunning basis sets use the “aug” (augmented) suffix, for example aug-cc-pVDZ.

The selection of an appropriate basis set is extremely important when performing

quantum chemistry calculations, as the inclusion, or lack thereof, of suitable basis functions can drastically alter the energies and structures that may be obtained. Generally speaking, when it comes to basis set choice bigger is almost always better, but for large structures and/or high-level calculations this may not always be feasible and in such cases results obtained with smaller basis sets should be treated with some caution.

### Post-Hartree-Fock Methods

There are three oft-used post-HF methods, each with their advantages and drawbacks; Møller-Plesset perturbation theory (MP $n$ ),<sup>18–25</sup> Coupled Cluster (CC),<sup>26–29</sup> and configuration interaction (CI).<sup>30</sup> The accuracy of each of these three methods can be systematically increased by extending their respective wavefunction expansions, however only CC and CI methods will eventually return the exact solution to the electronic Schrödinger equation, within an exact basis set. These methods are non-variational but are size consistent; i.e. the sum of the energies of  $N$  species at “infinite” separation in a single calculation is equal to the sum of the individual energies of the  $N$  species (Eq. A14).

$$E(A + B) = E(A) + E(B) \tag{A14}$$

The most popular variants of these post-HF methods are:

1. Second-order Møller-Plesset perturbation theory (MP2)
2. Coupled cluster with single, double, and perturbative triple excitations (CCSD(T))
3. Quadratic configuration interaction with single, double, and perturbative triple excitations (QCISD(T))

CCSD(T) is generally regarded as the “gold standard” of electronic structure methods, however each of these three methods suffer from exponential scaling issues as higher-order expansions are included. Specifically, MP $n$  methods scale at  $O(N^{n+3})$ , CCSD/QCISD at  $O(N^6)$ , and CCSD(T)/QCISD(T) at  $O(N^7)$ ; these scaling issues limit post-HF methods to small to medium sized molecules. As well as this, high-level wavefunction methods often exhibit a strong basis set dependence; that is, the computed

energies will change significantly as the basis set size is increased. Despite this dependence, application of a suitably large basis set may not always be possible.

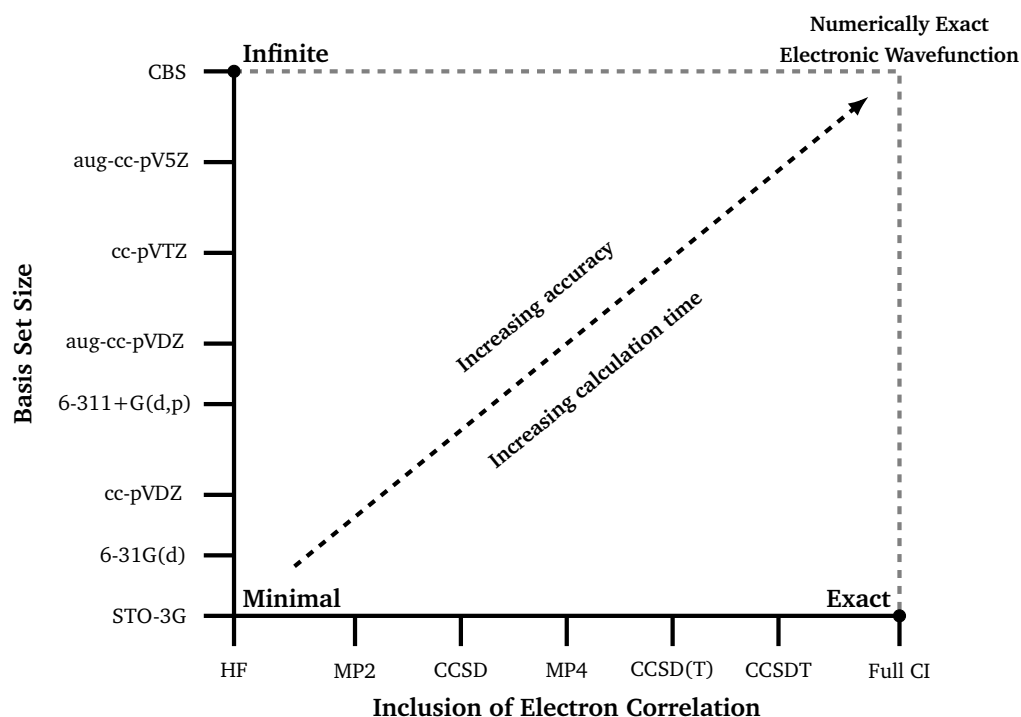


Figure A.1: Pople diagram illustrating how commonly available basis sets and wavefunction methods approach the numerically exact solution to the electronic Schrödinger equation

As a result of the expense of most post-HF methods, most modern computational chemists will employ different strategies to best approach the most accurate wavefunction energies with minimal computational cost. For example, one common approach is to optimize molecular geometries, i.e. find molecule geometry that has the lowest possible electronic energy, at a “low level” of theory, either using a small basis set or cheap electronic structure theory, or both. The subsequent structure can then be used for a high-level calculation, and is acceptable as geometry optimizations are more dependent on electronic energy gradients, rather than correlation energy to which single-point calculations are highly sensitive. In many medium sized system this approach may not be feasible, for example a CCSD(T) calculation with a large enough basis set, e.g. cc-pVTZ, may be too large for available computational resources. A successful approach to extending these higher-accuracy methods to larger systems is to employ a composite procedure.

Figure A.1 is a Pople diagram, illustrating how modern electronic structure theories and basis sets approach the numerically exact solution to the TISE; Full Configuration Interaction within the Complete Basis Set (CBS).

## Density Functional Theory

As discussed above, post-HF methods are capable of high accuracy but suffer from severe scaling issues. Post-HF energies are necessary, however, due to the importance of correlation when exploring chemical reactions. It is therefore desirable to have a formalism that can capture some, or all, of electron correlation, but not suffer from the same scaling issues of *ab initio* methods. Density functional theory (DFT) is an exact approach to solving the time-independent Schrödinger equation (Eq. A1). From the first Hohenberg-Kohn theorem,<sup>31</sup> the ground-state external potential,  $\nu_{ext}(\mathbf{r})$ , and therefore the total electronic energy, is a unique functional of the electron density  $\rho(\mathbf{r})$ . Unlike *ab initio*, wavefunction methods DFT is dependent on a constant number of variables and should not, therefore, suffer from severe scaling issues. Unfortunately, however, the first Hohenberg-Kohn theorem is an existence proof, and does not provide the form of the exact functional that determines the ground-state potential.

Modern DFT arises from the Kohn-Sham equations,<sup>32</sup> which greatly simplify the electron-electron interaction term in the Hamiltonian by using a “fictitious” system of non-interacting electrons that have the same ground-state density as a “real” system of interacting electrons. The electronic energy,  $E_e[\rho(\mathbf{r})]$ , can then be expressed in the form:

$$E_e[\rho(\mathbf{r})] = T_{ni}[\rho(\mathbf{r})] + V_{ne}[\rho(\mathbf{r})] + V_{ee}[\rho(\mathbf{r})] + E_{XC}[\rho(\mathbf{r})] \quad (\text{A15})$$

Where  $T_{ni}[\rho(\mathbf{r})]$  is the kinetic energy of the non-interacting electrons,  $V_{ne}[\rho(\mathbf{r})]$  and  $V_{ee}[\rho(\mathbf{r})]$  are the nuclear-electron and classical electron-electron interactions, respectively. The final term,  $E_{XC}[\rho(\mathbf{r})]$ , is known as the exchange-correlation functional (XCF), and is required to correct the non-interacting nature of the first three terms to that of an interacting, real electron system. The true form of  $E_{XC}[\rho(\mathbf{r})]$  is unknown, and its definition remains an ongoing and challenging area of research for contemporary theoretical

chemists. The varying accuracy of different XCF functionals, and the different ways in which they are formulated, gives rise to large errors when calculating electronic properties. Unlike wavefunction methods like, for example, CCSD and CCSDT, DFT cannot be systematically extended to include higher-order electron configurations that approach the solution to the TISE. Appropriate selection of XCFs is therefore extremely important, as is benchmarking the functional against high-level, *ab initio* data.

Throughout this thesis, the exchange-correlation functional of choice has generally been M06-2X,<sup>33</sup> a global-hybrid meta-GGA (generalized gradient approximation) functional.<sup>34</sup> In DFT the exchange-correlation functional,  $E_{XC}[\rho(\mathbf{r})]$ , is often expressed as the sum of exchange,  $E_X[\rho(\mathbf{r})]$ , and correlation,  $E_C[\rho(\mathbf{r})]$ , functionals (Eq. A16).

$$E_{XC}[\rho(\mathbf{r})] = E_X[\rho(\mathbf{r})] + E_C[\rho(\mathbf{r})] \quad (\text{A16})$$

A meta-GGA functional employs three functions in an attempt to accurately model the exchange energy of a molecule. The first is the local spin-density approximation (LSDA), which describes the exchange functional of a uniform electron gas (UEG). This approximation is insufficient for molecules, which invariably exhibit inhomogeneous electron density distributions. The second function is the generalized gradient approximation, which introduces inhomogeneity to the electron density by including the density gradient,  $\nabla\rho$ . Thirdly, meta-GGA functionals use the Laplacian of the gradient,  $\nabla^2\rho$ , to include second-derivative information. More specifically, M06-2X uses the spin kinetic energy density,  $\tau_r$  (Eq. A17), as it is related to the Laplacian but more numerically stable in its computation.

$$\tau(\mathbf{r}) = \frac{1}{2} \sum_i^{\text{occup}} |\nabla\psi_i(\mathbf{r})|^2 \quad (\text{A17})$$

where  $\psi$  are the Kohn-Sham orbitals.

A global-hybrid functional takes a final step towards the exchange energy of a molecule by further splitting the  $E_X[\rho(\mathbf{r})]$  functional into some portion of “exact”, or non-local, HF exchange, and local DFT (meta-GGA) exchange (Eq. A18). The term

“global” means the proportion of HF vs DFT exchange does not change through space. In M06-2X,  $a$  is defined as 0.54.

$$E_X^{GH} = aE_X^{HF} + (1 - a)E_X^{DFT} \quad (\text{A18})$$

This exchange functional is then combined with an appropriate correlation functional to give the global-hybrid meta-GGA exchange-correlation functional in its entirety.

M06-2X has been used extensively in this thesis due to its success in modelling a wide range of chemical reactions, being capable of capturing chemical trends and even activation energies in excellent agreement with those obtained with high-level methods. As throughout this thesis qualitative, rather than quantitative, insight was generally required, M06-2X was found to be a flexible and wholly appropriate functional of choice.

### Composite Procedures

Composite procedures are powerful methods that can achieve near-chemical accuracy, at a fraction of the cost of the methods they aim to approximate. There are a large number of composite procedures available, and all involve indirectly obtaining a high level of theory with large basis set by combining different *ab initio* methods with different sized basis sets, in conjunction with theoretical and empirical corrections. The only composite procedures employed in this thesis are variants of the G3(MP2) procedure,<sup>35</sup> which is summarized below:

$$E_{G3(MP2)-RAD} = (U/R)CCSD(T)/6-31G(d) + MP2/G3MP2Large - MP2/6-31G(d) + SO + HLC \quad (\text{A19})$$

Where  $SO$  is a spin-orbit correction,  $HLC$  is a high-level correction term, and  $G3MP2Large$  is the modified version of the 6-311+G(3df,2p) basis set. In this thesis, G3(MP2)-RAD energies were used with structures and frequencies calculated with the M06-2X density functional.



## Excited State Methods

So far, we have only considered methods that provide the energy of electronic ground states. Methods that calculate the energies of excited states have also been used, and are introduced below.

An electronic excited state is one in which a molecule is not in its lowest possible energy electron configuration, and is generated upon the absorption of a photon of light of an appropriate wavelength. These states present a challenge for the SCF procedure as the variational principle, and all of the accompanying algorithmic developments, will drive any excited state wavefunction guess back to the ground state configuration. This is known as variational collapse and, except in certain favourable situations, prevents access to electronic excited states. In order to obtain excited state wavefunctions, then, there are two dominant approaches; multireference *ab initio* methods and time-dependent methods.

**Multiconfiguration Self Consistent Field (MCSCF).** Two of the most commonly used multireference methods are the complete-active space SCF (CASSCF) method,<sup>36,37</sup> and its second-order perturbation theory counterpart CASPT2.<sup>38</sup> CASPT2 in particular is used in excited state benchmarking studies as the gold-standard method against which other methods are compared. Both methods use a linear combination configuration state functions (CSF), each representing the possible electronic excitations, to variationally optimize the MO coefficients in order to model the exact electronic wavefunction (Eq. A20). The resulting multideterminant wavefunction is more balanced and accurate than single-determinant methods, for example HF or DFT, when there are (quasi-)degenerate states, as there often are in excited states.

$$\Psi_{exact} = a_1\Phi_1 + a_2\Phi_2 + \dots + a_N\Phi_N \quad (\text{A20})$$

Where  $\Psi_{exact}$  is the exact electronic wavefunction within a limited basis set and the Born-Oppenheimer approximation,  $a_i$  are the coefficients representing the contribution of each determinant to the expansion, and  $\Phi_i$  are the CSFs.

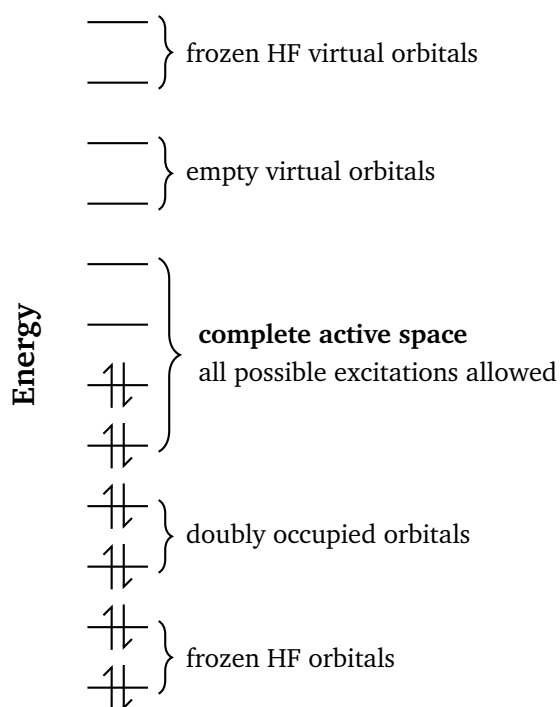


Figure A.2: Different orbital subspaces in a CASSCF calculation. Frozen orbitals are not relaxed from the original HF calculation, doubly occupied and empty virtual orbitals are relaxed but their occupancies are enforced, and the active space spans the region of orbitals that are fully correlated

As each of set of CSFs represents every possible electronic excitation, the number of CSFs increases exponentially with the number of electrons and/or orbitals. To limit this combinatorial explosion, CASSCF/CASPT2 use a truncated orbital space of “active” electrons (Fig. A.2), which is defined prior to the multireference calculation and includes the orbitals of relevance to the process being modelled (e.g. photon absorption, bond formation/dissociation). The strength of CASPT2, compared to CASSCF, is the incorporation of dynamic correlation into the final electronic energy.

There are, however, several disadvantages to using either CAS method; first, neither method are “black box”, in that they require the manual selection of an appropriate active space. This selection is not an exact procedure, and often relevant orbitals may appear high (or low) in the virtual (occupied) orbital manifold. As well as this, while truncated active spaces allow for relatively large molecules to be treated with CAS methods, the ultimate size of the active space is limited to approximately 18 electrons in 18 orbitals which may not allow for the selection of an appropriate active space.

**Time-dependent Density Functional Theory (TD-DFT).** Another extremely popular method is TD-DFT, the excited state extension to DFT.<sup>39,40</sup> Whereas MCSCF methods formally construct the multideterminant wavefunction, solving it iteratively to obtain a new set of MOs, in TD-DFT an external, time-dependent electric field,  $\mathbf{E}$ , is applied to the ground state density (Eq. A21). When the molecular polarizability matrix,  $\langle a \rangle$ , is examined as a function of incident frequency,  $\omega$ , so-called “poles” in the frequency-dependent polarizability are obtained when  $\omega$  is in resonance with the energy difference of the ground,  $E_0$ , and excited,  $E_i$ , states (Eq. A22).

$$\mathbf{E} = \mathbf{r} \cos(\omega t) \quad (\text{A21})$$

Where  $\mathbf{r}$  is the position vector, and  $t$  is time.

$$\langle a \rangle_\omega = \sum_{i \neq 0}^{\text{states}} \frac{|\langle \Phi_0 | \mathbf{r} | \Phi_i \rangle|^2}{\omega - (E_i - E_0)} \quad (\text{A22})$$

Where  $|\langle \Phi_0 | \mathbf{r} | \Phi_i \rangle|^2$  is the transition dipole moment. This approach does not produce an excited state wavefunction, however most modern electronic structure packages include analytical gradients for TD-DFT energies, allowing for the computation of excited state equilibrium and transition state geometries, as well as frequencies for free energy calculations. Time-dependent HF (TD-HF) is the wavefunction equivalent to TD-DFT, however the implicit inclusion of correlation in the DFT orbitals generally makes TD-DFT more accurate for low-lying excited states. The computational cost of TD-DFT, compared to multireference and other variations of single-determinant wavefunction excited state methods, is modest and it can therefore be applied to relatively large systems.

Despite the relatively low cost and black-box nature of TD-DFT (all that needs to be specified is the number, and spin, of states to be computed), as with CASSCF and CASPT2 there are several disadvantages to the method. Whilst the inclusion of correlation in the DFT formalism is advantageous, it does leave TD-DFT sensitive to the exchange-correlation functional of choice. In particular, functionals that do not include

non-local, HF exchange generally suffer in accuracy compared to those that do and, if not identified and corrected for, TD-DFT is notorious for underestimating the transition energies of charge-transfer excited states. As well as this, TD-DFT is necessarily single-determinant and only considers single electronic excitations, resulting in inaccuracies when doubly (or higher) excited states need to be considered, or when multideterminant, non-adiabatic processes are prevalent. The non-systematic failures of TD-DFT and different functionals means their benchmarking against high-level theories is necessary and an ongoing area of research.

### **Solvent Effects**

In order to model a chemical system as accurately as possible, it is generally necessary to consider solvation effects. Gas phase energies are often insightful and suitable for predicting chemical trends, but are not always appropriate when trying to recreate experimental results. One approach to modelling solvent effects is so-called *explicit solvation*, which involves the direct inclusion of solvent molecules in a calculation. A key issue with this approach, however, is the slow convergence of solvation energy with respect to the number of explicit solvent molecules due to the formation of solvation shells surrounding the molecule(s) of interest. In a water environment, for example, where hydrogen bonds are prevalent, the formation of solvation shells introduces “edge effects”, arising from non-hydrogen bonded water molecules. To limit the influence of these nonphysical edge effects, the number of molecules included in the calculation can quickly become unfeasibly high. As well as this, in excited state calculations, the presence of explicit solvent molecules can give rise to low-lying, solute to solvent charge-transfer states that are artefacts of the type of calculation, rather than physically reasonable excited states.

Phenomena like, for example, solvatochromism,<sup>41</sup> where the UV-vis absorption of a molecule changes depending on the solvent environment, means the quantum mechanical treatment of solvent effects remains desirable. To that end, in this thesis *implicit* solvent models were used instead. In an implicit solvent model, the electronic wave-

function problem is reduced to just the solute molecule. Implicit solvent models give atomic detail, and the solute resides within an electrostatic cavity surrounded by dielectric medium that represents the solvent. The Gibbs free energy of solvation is given by:

$$\Delta G_{solv} = \Delta G_{cav} + \Delta G_{disp-rep} - \Delta G_{el} \quad (\text{A23})$$

where  $\Delta G_{cav}$  is the free energy change upon formation of the solvent cavity,  $\Delta G_{disp-rep}$  is the free energy change from dispersive and repulsive interactions between the solvent and solute, and  $\Delta G_{el}$  is the free energy change from electrostatic interactions.

Throughout this thesis the Universal Solution Model, known as SMD,<sup>42</sup> is used, which uses:

1.  $\epsilon$  to describe the relative permittivity of the solvent
2. A self-consistent reaction field (SCRF) treatment, using the polarized continuous quantum mechanical charge density of the solute, for electrostatic contributions
3. Intrinsic atomic Coulomb radii for the solvent accessible surface and atomic surface tension coefficients, for non-electrostatic contributions

The benefit of the SMD model is the use of the quantum mechanical electron density in its formalism, meaning the treatment of more complex electron systems, for example radicals, than those that employ more approximate methods.<sup>43</sup> All implicit solvent models are necessarily approximate, however, and therefore their usage in this thesis has been to capture photochemical/reaction trends, rather than for accurate, quantitative modelling.

## Conclusion

To conclude, the field of computational chemistry is full of different methods, density functionals, basis sets, and solvent models. With these techniques, we can model a wealth of different properties that describe the behaviour of chemical systems, to varying degrees of accuracy. Unfortunately, however, the choice of which method and which

basis set can be difficult, especially if chemical accuracy is required as the the necessary approaches rapidly become inapplicable. In this thesis DFT methods have generally been favoured over wavefunction methods as the increases in accuracy did not compensate for the resultant increase in computational expense.

## References

- (1) Jensen, F., *Introduction to Computational Chemistry*; John Wiley & Sons, Inc.: New York, 2006.
- (2) Cramer, C. J., *Essentials of Computational Chemistry: Theories and Models*; 3; John Wiley & Sons: New York, 2004; Vol. 31.
- (3) Schrödinger, E. *Physical Review* **1926**, *28*, 1049–1070.
- (4) Born, M.; Oppenheimer, R. *Annalen der Physik* **1927**, *389*, 457–484.
- (5) Hartree, D. R. *Mathematical Proceedings of the Cambridge Philosophical Society* **1928**, *24*, 89–110.
- (6) Hartree, D. R. *Mathematical Proceedings of the Cambridge Philosophical Society* **1928**, *24*, 111–132.
- (7) Hartree, D. R. *Mathematical Proceedings of the Cambridge Philosophical Society* **1928**, *24*, 426–437.
- (8) Fock, V. *Zeitschrift für Physik* **1930**, *62*, 795–805.
- (9) Roothaan, C. C. J. *Reviews of Modern Physics* **1951**, *23*, 69–89.
- (10) Jensen, F. *Wiley Interdisciplinary Reviews: Computational Molecular Science* **2013**, *3*, 273–295.
- (11) Hehre, W. J.; Stewart, R. F.; Pople, J. A. *The Journal of Chemical Physics* **1969**, *51*, 2657–2664.
- (12) Ditchfield, R.; Hehre, W. J.; Pople, J. A. *The Journal of Chemical Physics* **1971**, *54*, 724–728.
- (13) Dunning, T. H. *The Journal of Chemical Physics* **1989**, *90*, 1007–1023.
- (14) Kendall, R. A.; Dunning, T. H.; Harrison, R. J. *The Journal of Chemical Physics* **1992**, *96*, 6796–6806.
- (15) Woon, D. E.; Dunning, T. H. *The Journal of Chemical Physics* **1993**, *98*, 1358–1371.
- (16) Peterson, K. A.; Woon, D. E.; Dunning, T. H. *The Journal of Chemical Physics* **1994**, *100*, 7410–7415.
- (17) Wilson, A. K.; van Mourik, T.; Dunning, T. H. *Journal of Molecular Structure: THEOCHEM* **1996**, *388*, 339–349.
- (18) Møller, C.; Plesset, M. S. *Physical Review* **1934**, *46*, 618–622.
- (19) Frisch, M. J.; Head-Gordon, M.; Pople, J. A. *Chemical Physics Letters* **1990**, *166*, 281–289.

- (20) Frisch, M. J.; Head-Gordon, M.; Pople, J. A. *Chemical Physics Letters* **1990**, *166*, 275–280.
- (21) Head-Gordon, M.; Pople, J. A.; Frisch, M. J. *Chemical Physics Letters* **1988**, *153*, 503–506.
- (22) Head-Gordon, M.; Head-Gordon, T. *Chemical Physics Letters* **1994**, *220*, 122–128.
- (23) Pople, J. A.; Seeger, R.; Krishnan, R. *International Journal of Quantum Chemistry* **1977**, *12*, 149–163.
- (24) Pople, J. A.; Binkley, J. S.; Seeger, R. *International Journal of Quantum Chemistry* **1976**, *10*, 1–19.
- (25) Raghavachari, K.; Pople, J. A.; Replogle, E. S.; Head-Gordon, M. *The Journal of Physical Chemistry* **1990**, *94*, 5579–5586.
- (26) Bartlett, R. J.; Purvis, G. D. *International Journal of Quantum Chemistry* **1978**, *14*, 561–581.
- (27) Purvis, G. D.; Bartlett, R. J. *The Journal of Chemical Physics* **1982**, *76*, 1910–1918.
- (28) Scuseria, G. E.; Janssen, C. L.; Schaefer, H. F. *The Journal of Chemical Physics* **1988**, *89*, 7382–7387.
- (29) Scuseria, G. E.; Schaefer, H. F. *The Journal of Chemical Physics* **1989**, *90*, 3700–3703.
- (30) Pople, J. A.; Head-Gordon, M.; Raghavachari, K. *The Journal of Chemical Physics* **1987**, *87*, 5968–5975.
- (31) Hohenberg, P.; Kohn, W. *Physical Review* **1964**, *136*, B864–B871.
- (32) Kohn, W.; Sham, L. J. *Physical Review* **1965**, *140*, A1133–A1138.
- (33) Zhao, Y.; Truhlar, D. G. *Theoretical Chemistry Accounts* **2007**, *120*, 215–241.
- (34) Yu, H. S.; Li, S. L.; Truhlar, D. G.; Yu, H. S.; Li, S. L.; Truhlar, D. G. *The Journal of Chemical Physics* **2016**, *145*, 130901.
- (35) Henry, D. J.; Sullivan, M. B.; Radom, L. *Journal of Chemical Physics* **2003**, *118*, 4849–4860.
- (36) Roos, B. O.; Taylor, P. R.; Sigbahn, P. E. M. *Chemical Physics* **1980**, *48*, 157–173.
- (37) Siegbahn, P. E. M.; Almlöf, J.; Heiberg, A.; Roos, B. O. *The Journal of Chemical Physics* **1981**, *74*, 2384–2396.
- (38) Andersson, K.; Roos, B. O. *Int. J. Quantum Chem.* **1993**, *45*, 591–607.
- (39) Ahlrichs, R.; Bauernschmitt, R. *Chemical Physics Letters* **1996**, *256*, 454–464.
- (40) Maitra, N. T. *Journal of Chemical Physics* **2016**, *144*.
- (41) Marini, A.; Muñoz-Losa, A.; Biancardi, A.; Mennucci, B. *Journal of Physical Chemistry B* **2010**, *114*, 17128–17135.
- (42) Marenich, A. V.; Cramer, C. J.; Truhlar, D. G. *Journal of Physical Chemistry B* **2009**, *113*, 6378–6396.
- (43) Tomasi, J.; Mennucci, B.; Cammi, R. *Chemical Reviews* **2005**, *105*, 2999–3093.

## A.2 Supporting Information: Rational Design of Photo-cleavable Alkoxyamines for Polymerization and Synthesis: Promotion and Deactivation of Cleavage Pathways

### Rational Design of Photo-cleavable Alkoxyamines for Polymerization and Synthesis: Promotion and Deactivation of Cleavage Pathways

Nicholas S. Hill, Michelle L. Coote\*

ARC Centre of Excellence for Electromaterials Science, Research School of Chemistry, Australian National University, Canberra, Australian Capital Territory, 2601, Australia

\*Correspondence: [michelle.coote@anu.edu.au](mailto:michelle.coote@anu.edu.au)

### Supplementary Information

#### Table of Contents

Raw Energies .....	S2
Raw Vertical Excitation Energies and Dominant Character .....	S3
Gas Phase Structure Cartesian Coordinates .....	S4



Supplementary Figures

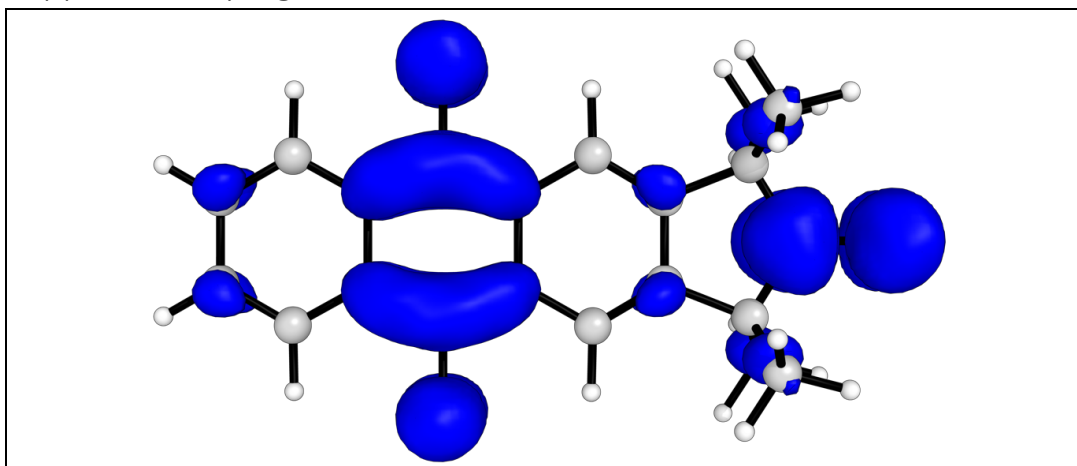


**Figure S1.** Spin density of anthraquinone-alkoxyamine triplet anion

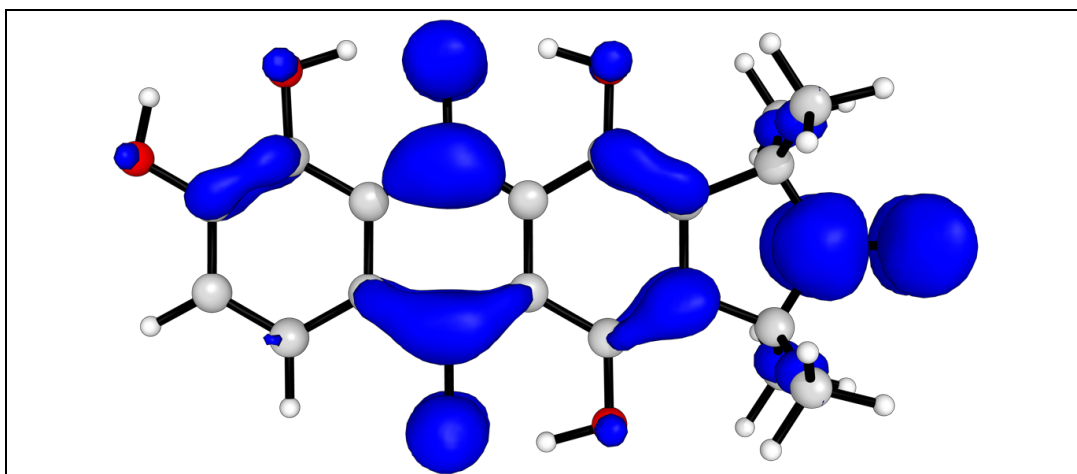


**Figure S2.** Spin density of 1,2,5,8-THAQ triplet anion

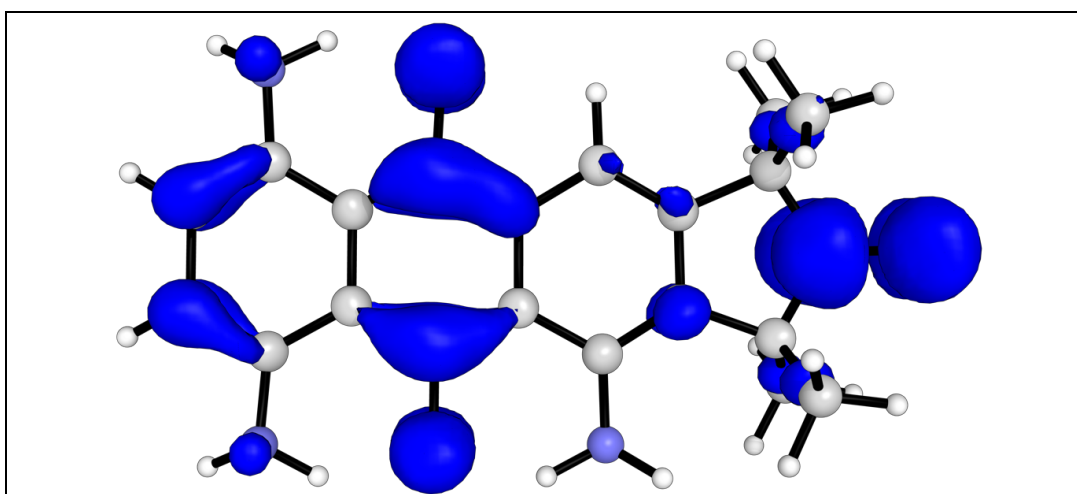


**Figure S3.** Spin density of 1,4,5-TAAQ triplet anion

## Raw Energies

**Table S1.** Free energy components of all reported species

Structure	Gas			Solvent Electronic Energy (H)
	Zero-point Vibrational Energy (kJ mol <sup>-1</sup> )	Gibbs Free Energy (H)	Electronic Energy (H)	
Aq-STY	1284.7707	-1362.714547	-1363.147108	-1363.176845
Aq-STY radical cation	1283.1448	-1362.44675	-1362.877206	-1362.96369
Aq-EIB	1331.5978	-1438.130226	-1438.576377	-1438.605936
Aq-EIB radical cation	1330.2664	-1437.858393	-1438.30392	-1438.389465
Aq-EP	1256.9638	-1398.861173	-1399.278837	-1399.308678
Aq-EP radical cation	1256.9586	-1398.585688	-1399.003086	-1399.09057
Aq-Me	993.2202	-1092.551213	-1092.879409	-1092.902015
Aq-Me radical cation	994.2860	-1092.278009	-1092.605827	-1092.6926
1,2-DHAQ Aq-STY	1308.7470	-1513.126329	-1513.565931	-1513.596034
1,2-DHAQ Aq-EIB	1355.2516	-1588.542485	-1588.995826	-1589.026144
1,2-DHAQ Aq-EP	1281.1956	-1549.271507	-1549.697381	-1549.728315
1,2-DHAQ Aq-Me	1017.2067	-1242.962938	-1243.298124	-1243.321234
1,2,4-THAQ Aq-STY	1321.0531	-1588.334607	-1588.778172	-1588.808301
1,2,4-THAQ Aq-EIB	1367.3783	-1663.7508	-1664.208035	-1664.238335
1,2,4-THAQ Aq-EP	1293.3047	-1624.479857	-1624.909579	-1624.940506
1,2,4-THAQ Aq-Me	1029.2861	-1318.171263	-1318.51032	-1318.533403
1,2,5-THAQ Aq-STY	1322.1555	-1588.335024	-1588.779229	-1588.807749
1,2,5-THAQ Aq-EIB	1367.3144	-1663.75249	-1664.2089	-1664.237625
1,2,5-THAQ Aq-EP	1294.4951	-1624.480247	-1624.910728	-1624.940242
1,2,5-THAQ Aq-Me	1030.5087	-1318.171696	-1318.511383	-1318.533137
1,2,5,8-THAQ Aq-STY	1334.7939	-1663.540073	-1663.988305	-1664.015939
1,2,5,8-THAQ Aq-EIB	1382.1761	-1738.955443	-1739.418822	-1739.446483
1,2,5,8-THAQ Aq-EP	1309.6530	-1699.679723	-1700.116553	-1700.144401
1,2,5,8-THAQ Aq-Me	1043.1987	-1393.3772	-1393.720968	-1393.741813
1,5-DAAQ Aq-STY	1373.3381	-1473.376057	-1473.839381	-1473.8713
1,5-DAAQ Aq-EIB	1420.0344	-1548.792278	-1549.269672	-1549.301551
1,5-DAAQ Aq-EP	1347.1325	-1509.516822	-1509.967483	-1509.999591
1,5-DAAQ Aq-Me	1081.3977	-1203.214213	-1203.572913	-1203.597966
1,4-DAAQ Aq-STY	1370.1582	-1473.37495	-1473.838512	-1473.871804
1,4-DAAQ Aq-EIB	1418.1396	-1548.792402	-1549.268696	-1549.302015
1,4-DAAQ Aq-EP	1345.6826	-1509.516401	-1509.966516	-1510.000035
1,4-DAAQ Aq-Me	1078.2551	-1203.212036	-1203.570975	-1203.597153
1,4,5-TAAQ Aq-STY	1416.7762	-1528.70211	-1529.180522	-1529.214581
1,4,5-TAAQ Aq-EIB	1463.0219	-1604.117969	-1604.611276	-1604.64391
1,4,5-TAAQ Aq-EP	1390.9345	-1564.847844	-1565.314161	-1565.347666
1,4,5-TAAQ Aq-Me	1124.5789	-1258.54067	-1258.914224	-1258.941346
1,4,5,8-TAAQ Aq-STY	1462.0248	-1584.020974	-1584.51564	-1584.55009

1,4,5,8-TAAQ Aq-EIB	1510.4923	-1659.437017	-1659.947741	-1659.981403
1,4,5,8-TAAQ Aq-EP	1437.4259	-1620.161661	-1620.645389	-1620.67928
1,4,5,8-TAAQ Aq-Me	1170.3883	-1313.860758	-1314.250538	-1314.278712
AQ-NO radical	886.6340	-1052.69662	-1052.984009	-1053.00927
AQ-NO cation	889.4054	-1052.428996	-1052.719091	-1052.806342
AQ-NO anion	877.8209	-1052.723509	-1053.009311	-1053.087975
Pyridine	235.2370	-248.123997	-248.1861964	-248.1957941
Methyl-pyridine cation	332.9927	-287.746132	-287.8470342	-287.9292132
Methyl-pyridine cation	344.7885	-287.93308	-288.0288912	-288.039927
AQ-Me-Pyridine TS (ground state)	1225.5824	-1340.38196	-1340.789026	-1340.874367
AQ-Me-Pyridine TS (radical cation)	1230.2303	-1340.577063	-1340.982771	-1340.982784
AQ-BF <sub>3</sub> -Me radical	1067.4275	-1455.652501	-1455.997519	-1456.020173
AQ-BF <sub>3</sub> -Me-Pyridine TS (radical)	1309.5435	-1703.692401	-1704.123802	-1704.198845
AQ-BF <sub>3</sub> -NO radical	964.8818	-1415.931595	-1416.242903	-1416.323595
AQ-BF <sub>3</sub> -NO cation	968.6831	-1415.763854	-1416.07797	-1416.137472

## Raw Vertical Excitation Energies

**Table S2.** Vertical excitation energies for all reported functionalized species

Species		$n_N\pi^*$	$\pi\pi^*$
AQ-STY	14-DAAQ	4.1777	2.6689
	15-DAAQ	4.0611	3.118
	145-TAAQ	4.6377	2.6317
	1458-TAAQ	4.2553	2.4451
	12-DHAQ	3.5078	3.808
	125-THAQ	3.6511	3.3336
	124-THAQ	3.7212	3.1384
AQ-EIB	1258-THAQ	3.6288	2.9949
	14-DAAQ	4.1907	2.6585
	15-DAAQ	4.0847	3.1157
	145-TAAQ	4.7111	2.627
	1458-TAAQ	4.2867	2.4416
	12-DHAQ	3.8223	3.5042
	125-THAQ	3.7318	3.3321
AQ-EP	124-THAQ	3.7369	3.1354
	1258-THAQ	3.6729	3.003
	14-DAAQ	4.1947	2.6585
	15-DAAQ	4.0899	3.118
	145-TAAQ	4.6461	2.6256
	1458-TAAQ	4.2911	2.4442
	12-DHAQ	3.8272	3.4988
AQ-EP	125-THAQ	3.6693	3.3322
	124-THAQ	3.7425	3.1306
	1258-THAQ	3.4881	3.0031
	125-THAQ	3.6693	3.3322

AQ-ME	14-DAAQ	4.189	2.6502
	15-DAAQ	4.0801	3.1034
	145-TAAQ	4.6082	2.6183
	1458-TAAQ	4.2798	2.4549
	12-DHAQ	3.8161	3.5001
	125-THAQ	3.7316	3.3344
	124-THAQ	3.7316	3.1307
	1258-THAQ	3.6389	3.0008

**Table S3.** Vertical excitation energies of unfunctionalized species

Species	$n_N\pi^*$	$\pi\pi^*$	$n_O\pi^*$
AQ	N/A	4.3443	3.226
AQ-STY	3.963	4.3512	3.2686
AQ-EIB	3.9837	4.3585	3.2678
AQ-EP	3.9923	4.3654	3.264
AQ-ME	3.978	4.3661	3.2622

## Open shell singlet vs triplet Mulliken Charges and Spin Densities

**Table S4.** Mulliken charge and spin densities of unfunctionalized anthraquinone-alkoxyamine

Atom	Open shell singlet biradical		Triplet biradical	
	Charge	Spin density	Charge	Spin density
C	-0.10846	-0.031765	-0.108436	0.031738
C	-0.10846	-0.031765	-0.108436	0.031738
C	0.112076	-0.005695	0.112151	0.00574
C	0.120078	-0.039274	0.120094	0.039206
C	0.120078	-0.039274	0.120094	0.039206
C	0.112076	-0.005695	0.112151	0.00574
C	-0.19528	-0.109268	-0.195363	0.111049
C	0.128339	-0.041434	0.12829	0.042139
C	0.128337	-0.041434	0.128288	0.042139
C	-0.19528	-0.109268	-0.195363	0.111049
C	0.164102	-0.005781	0.164232	0.006026
C	-0.714141	-0.05293	-0.714051	0.009406
C	-0.71413	-0.05293	-0.714049	0.009406
C	0.164102	-0.005781	0.164232	0.006026
O	-0.640164	-0.224921	-0.640125	0.224845
O	-0.640165	-0.224921	-0.640125	0.224845
C	0.401988	-0.002567	0.40223	0.04158
N	-0.41681	0.500614	-0.417318	0.493929
C	0.401987	-0.002568	0.402229	0.04158
O	0.0613	0.47028	0.061469	0.47018
C	0.2046	0.014093	0.204442	0.003107
C	0.204618	0.014096	0.20446	0.003111
C	0.204599	0.014092	0.204442	0.003107
C	0.204619	0.014096	0.204461	0.00311

**Table S5.** Mulliken charge and spin densities of 1,2,5,8-THAQ

Atom	Open shell singlet biradical		Triplet biradical	
	Charge	Spin density	Charge	Spin density

C	-0.175843	-0.071941	-0.176068	0.021774
C	-0.312048	-0.122344	-0.311778	0.070176
C	-0.042553	-0.017077	-0.042552	0.025053
C	-0.225538	-0.003295	-0.225717	0.012635
C	-0.311924	0.050501	-0.311813	-0.043246
C	-0.141847	-0.059469	-0.14175	0.065041
C	0.598017	-0.203833	0.598045	0.205617
C	0.367266	0.035231	0.367386	-0.035187
C	-0.206979	-0.021696	-0.206978	0.021625
C	0.139214	-0.114884	0.139191	0.116965
C	-0.348862	-0.050467	-0.348857	0.050311
C	0.195531	-0.044854	0.195505	0.04481
C	0.208096	-0.017196	0.20814	0.017041
C	-0.089107	-0.02531	-0.089052	0.025315
O	-0.793857	-0.156254	-0.793845	0.156139
O	-0.653962	-0.158507	-0.653987	0.158495
C	0.249899	0.004971	0.250301	0.025933
C	0.312623	0.001919	0.312927	0.033723
O	-0.128055	-0.006786	-0.128036	0.007028
O	-0.094833	-0.011844	-0.094728	0.011974
O	-0.166806	-0.007497	-0.166785	0.00749
O	-0.157636	-0.006407	-0.157619	0.006405
N	-0.393451	0.499972	-0.394056	0.492257
O	0.084843	0.471493	0.084978	0.470661
C	0.273622	0.008378	0.273385	0.008222
C	0.273602	0.008376	0.273366	0.008216
C	0.270263	0.009407	0.270167	0.007766
C	0.270327	0.009416	0.270231	0.00776

**Table S6.** Mulliken charge and spin densities of 1,4,5-TAAQ

Atom	Open shell singlet biradical		Triplet biradical	
	Charge	Spin density	Charge	Spin density
C	-0.779981	-0.037047	-0.780185	-0.008391
C	-0.432664	-0.07917	-0.432413	0.025587
C	0.49416	0.005561	0.4942	-0.009174
C	-0.353045	-0.005702	-0.353309	0.002228
C	-0.120744	-0.069384	-0.120495	0.071977
C	0.10312	-0.032459	0.103398	0.035732
C	-0.150756	-0.124366	-0.150857	0.12737
C	0.278006	0.022269	0.278132	-0.022206
C	0.42895	0.020539	0.428892	-0.020804
C	0.08615	-0.132708	0.086109	0.133476
C	-0.376592	-0.025833	-0.376571	0.025706
C	-0.322193	-0.016399	-0.322274	0.01645
C	0.177023	-0.07443	0.177023	0.074515
C	-0.025163	-0.084493	-0.025073	0.084333
O	-0.659081	-0.19665	-0.658968	0.196494
O	-0.70716	-0.165554	-0.707232	0.165631
C	0.260135	-0.006685	0.260211	0.057495
C	0.35315	-0.005622	0.353579	0.02496
N	0.091742	-0.002654	0.091674	0.003953
N	-0.0164	-0.015079	-0.016351	0.01507
N	-0.001887	-0.014135	-0.001885	0.01414

N	-0.432343	0.502511	-0.432763	0.495317
O	0.065143	0.470673	0.065248	0.470552
C	0.211326	0.02057	0.211128	0.004463
C	0.231488	0.01706	0.231458	-0.003378
C	0.294439	0.011759	0.294226	0.009538
C	0.303178	0.017431	0.3031	0.008968

## Gas Phase Structure Cartesian Coordinates

AQ

C -5.5542621361 2.8671730276 -0.0005707914  
C -5.5553928268 1.4702787275 -0.0003878167  
C -4.3520608958 0.7711036819 -0.0001580017  
C -3.1406451909 1.4648425269 -0.0001114188  
C -3.1395090298 2.8687008519 -0.000294055  
C -4.3498002778 3.5643996518 -0.0005235729  
C -1.8609362499 3.6386818962 -0.0002545815  
C -0.5836115571 2.8666324118 0.0001367729  
C -0.5847476451 1.4627739964 0.000319575  
C -1.8633203812 0.6927930205 0.0001231641  
C 0.6278041074 3.5603712248 0.0003156014  
C 0.6255435961 0.767075508 0.0006813128  
C 1.8311359877 2.8611963207 0.000674359  
C 1.830005553 1.464301978 0.00085741  
O -1.8599489237 4.8583305143 -0.0002826175  
O -1.8643074414 -0.526855549 0.0004335117  
H -6.4933700431 3.4114803037 -0.0007498234  
H -6.4953804575 0.9274922326 -0.0004249258  
H -4.3359622897 -0.3139435 -0.0000159935  
H -4.3319453568 4.6494193146 -0.0006642678  
H 0.611705495 4.6454184319 0.0001691855  
H 0.6076888647 -0.3179442134 0.0008177362  
H 2.7711236541 3.4039828062 0.0008120227  
H 2.7691134445 0.919994835 0.0011372148

Aq-STY

C 0.7608793167 -1.5780146054 -6.6399304016  
C -0.5510961627 -1.6401042634 -6.1622310263  
C -0.8966922406 -0.9900335953 -4.9824137902  
C 0.0693910445 -0.2737871363 -4.2736895683  
C 1.385531441 -0.2116376599 -4.752905148  
C 1.7271523349 -0.8658869411 -5.937718598  
C 2.4416240203 0.5468117488 -4.016475131  
C 2.0475904993 1.2345062594 -2.7523087163  
C 0.727935208 1.1728706136 -2.2715653202  
C -0.3266470179 0.4167630976 -3.008834384  
C 0.3794787565 1.8220142723 -1.0852696761  
C 1.3550303525 2.52802586 -0.3939307328  
C 2.6611405179 2.5886124748 -0.8707404348  
C 3.0206047466 1.9461524997 -2.0476226643  
O 3.5838034875 0.6004133952 -4.4358640953

O -1.4711401892 0.3627431548 -2.5962655553  
H 1.0268463045 -2.0866117235 -7.561093867  
H -1.3025245801 -2.1969060675 -6.7129591521  
H -1.9078949303 -1.0223344781 -4.590150798  
H 2.7525831483 -0.801940217 -6.2867898229  
H -0.6484188717 1.7558826347 -0.7395650791  
C 1.2046352261 3.3222861476 0.8806608435  
C 3.5246639052 3.4363185825 0.0297992603  
H 4.031347034 1.9764051439 -2.4452059437  
N 2.6453860996 3.5890150493 1.2454095402  
C 4.8187108439 2.7008834165 0.386920378  
C 3.8561087184 4.7657581759 -0.6642458311  
C 0.5143772413 2.4817630326 1.9587019448  
C 0.391686799 4.5963933611 0.6122521941  
O 2.7848363692 4.8988257183 1.7580314241  
C 3.2347448992 4.9524497047 3.1231898367  
C 4.6128993851 4.343655079 3.3110754477  
C 2.1816963599 4.4357180598 4.0840178042  
C 2.2887787472 3.2056360551 4.7337659107  
H 3.1646277439 2.5836420807 4.5794606006  
C 1.266222084 2.7529329941 5.5678292703  
H 1.3595630873 1.7901868575 6.0607541045  
C 0.1247662214 3.5274884021 5.7614373207  
H -0.67220351 3.1726821041 6.4073812872  
C 0.0140559435 4.7660743284 5.127440827  
H -0.8679979596 5.3800935608 5.2807944222  
C 1.0400756598 5.2148468666 4.3008822072  
H 0.9560353136 6.1788906597 3.8037640054  
H 4.5940731777 1.7904294864 0.949058379  
H 5.4791686402 3.334549507 0.9816927469  
H 5.3571679467 2.4263553389 -0.5258696473  
H 2.9515305284 5.3158225571 -0.9329328011  
H 4.4180337107 4.5552315747 -1.579574148  
H 4.4634527149 5.3982934487 -0.0135916428  
H 1.1345798339 1.6206033499 2.2206580422  
H -0.4496671605 2.1214544481 1.5842363443  
H 0.3245588713 3.0685944384 2.8592640891  
H 0.2834952645 5.1782952512 1.5297073819  
H -0.603324469 4.3105150683 0.257029875  
H 0.8631880058 5.2254176983 -0.1462867282  
H 3.3086585004 6.0366720647 3.2701371382  
H 5.3281504915 4.842040484 2.651533372  
H 4.6072520277 3.2767179925 3.0788362974  
H 4.9425585177 4.4781525883 4.3453284084

Aq-STY radical cation

C 0.569465629 -1.2147661101 -6.8928359072  
C -0.5435859756 -1.6676441625 -6.180190352  
C -0.74914475 -1.2571080433 -4.866813685  
C 0.160468623 -0.3896758217 -4.2604197377  
C 1.28027153 0.0659460084 -4.9773508979

C 1.4803829451 -0.349910985 -6.2943612984  
C 2.2687636341 0.9905466608 -4.3605821582  
C 2.028104185 1.422400698 -2.9423542011  
C 0.9120018684 0.9679466259 -2.2279328126  
C -0.0822616692 0.0335935082 -2.8555733594  
C 0.6989621606 1.3727615694 -0.9091083328  
C 1.6138187223 2.2366920979 -0.3268228154  
C 2.7213072079 2.6907595047 -1.0392705212  
C 2.9441785401 2.2918903382 -2.348035919  
O 3.2442224959 1.3965502225 -4.9610116262  
O -1.042754031 -0.3488277582 -2.2162921932  
H 0.724997161 -1.5380021853 -7.9167638455  
H -1.2507364632 -2.3419410309 -6.6517236095  
H -1.6065901835 -1.5963826565 -4.2950175006  
H 2.3514065367 0.0139815659 -6.829325942  
H -0.1784963379 0.9968579472 -0.3889576419  
C 1.5533147768 2.7782822018 1.087565875  
C 3.5626998634 3.6323433938 -0.2223289247  
H 3.7980724502 2.6271774406 -2.9311028158  
N 2.8461265339 3.5631912961 1.0903237031  
C 4.9984238086 3.1427711538 -0.0036932643  
C 3.5310859115 5.0670325834 -0.7648148405  
C 1.5433394539 1.633370633 2.1020612259  
C 0.3683367494 3.7331318794 1.2854292013  
O 3.1969670868 4.5219143684 1.9051971727  
C 3.3554696324 4.3721687673 3.4052246972  
C 4.1829559055 3.1412386157 3.7021315904  
C 2.0517775609 4.5658974625 4.1301938085  
C 1.5441989268 3.6211271995 5.0231356433  
H 2.0848562208 2.6997711118 5.2205917661  
C 0.3404779687 3.8606290635 5.6871025366  
H -0.0467542184 3.123001822 6.3818720069  
C -0.3550505766 5.0465158568 5.4659334643  
H -1.2903982207 5.2311857141 5.9836858224  
C 0.1626156953 6.0081070883 4.5951030429  
H -0.3656611446 6.9425327958 4.4383103978  
C 1.365619677 5.7722487503 3.9404238525  
H 1.7736981867 6.5230430458 3.2674437363  
H 5.0112167266 2.132779374 0.4144337126  
H 5.5382239352 3.8269300454 0.6564015829  
H 5.5091351951 3.1220075789 -0.9697083818  
H 2.5038552043 5.4273768038 -0.8597853938  
H 3.9854726846 5.0607022688 -1.7585288909  
H 4.0997623651 5.7408707187 -0.1217566253  
H 2.4185988456 0.9901468434 1.9809225033  
H 0.6532048653 1.0307356028 1.9033697152  
H 1.4710697329 2.0017219359 3.1247394489  
H 0.2897320947 4.0668458689 2.3205886509  
H -0.5392916806 3.1816810476 1.0256390375  
H 0.4428911579 4.5984942861 0.6220462738  
H 3.9702839833 5.2644231343 3.5481969133



H 5.0940492869 3.1476592046 3.1005046144  
H 3.6428126302 2.2108717297 3.5239114406  
H 4.4750988958 3.1730333197 4.7550000573

Aq-EIB

C 0.6623087776 -1.8920325531 -6.1472596426  
C -0.6278074522 -1.9216000695 -5.6106076367  
C -0.9289554876 -1.1793129 -4.4738325256  
C 0.0598789658 -0.4026753682 -3.8675992973  
C 1.3540843616 -0.3729208517 -4.4060626087  
C 1.6511436944 -1.1200913341 -5.5471267612  
C 2.4334046762 0.4489477011 -3.7798270277  
C 2.0862937199 1.2374374616 -2.5613076267  
C 0.7887372712 1.2079308673 -2.021146658  
C -0.2884981632 0.3859867019 -2.6470402744  
C 0.4842392137 1.9509156806 -0.8787360498  
C 1.4812408956 2.717710412 -0.2907908355  
C 2.7653186993 2.7474891555 -0.8268824744  
C 3.0812364202 2.0114234314 -1.9606189977  
O 3.5569012026 0.4732710393 -4.2492490737  
O -1.4130079974 0.3573038155 -2.1806965121  
H 0.8935679403 -2.4726051842 -7.0346016252  
H -1.3970519554 -2.5250284193 -6.0818426962  
H -1.9224192315 -1.1848256694 -4.0374368994  
H 2.6603274713 -1.0795990999 -5.9438028468  
H -0.5275270796 1.9079677369 -0.4848973399  
C 1.3771291447 3.6073931741 0.9232024323  
C 3.6590141628 3.6718458522 -0.0377979826  
H 4.0741660114 2.0147669715 -2.4019396378  
N 2.8265427118 3.9307786131 1.1910472235  
C 4.9676390892 2.9738434047 0.3392352589  
C 3.9554850942 4.9370282532 -0.8561809476  
C 0.7856900711 2.832691246 2.1058652389  
C 0.5186870778 4.8412358562 0.6153569734  
O 2.9688079972 5.2855533538 1.567472136  
C 3.4367723755 5.4871030687 2.9068077013  
H 4.7654812281 2.1027156735 0.9680515829  
H 5.6320768398 3.6531963477 0.8765776976  
H 5.4893936107 2.6422411977 -0.5642691775  
H 3.0375480365 5.4648161588 -1.1249044506  
H 4.4725641253 4.6481152411 -1.7764096672  
H 4.5937575638 5.6204636652 -0.2917911397  
H 1.4580285073 2.0222725408 2.4002286259  
H -0.1837875612 2.4060774923 1.8282726733  
H 0.6186817449 3.4976209987 2.9546973812  
H 0.4656827266 5.4948995431 1.4885950986  
H -0.4915213743 4.5092875328 0.3555206678  
H 0.9228770543 5.4082214269 -0.2268946812  
C 3.6018413646 7.0022521541 2.9920881908  
H 4.3518872164 7.3202947596 2.2634706569  
H 3.9326822831 7.2935272705 3.9928495177

H 2.6507678778 7.4914107471 2.7747240183  
C 2.313321057 5.0938476178 3.8829062434  
O 1.2293696003 5.6306236008 3.8935350501  
O 2.6566759257 4.1151428607 4.7259458823  
C 1.6640078743 3.738236651 5.696447256  
C 2.2535502633 2.6233026625 6.5313200603  
H 0.7593033672 3.4222245163 5.1688942078  
H 1.4117902835 4.6194907466 6.2938392795  
H 2.5034052279 1.7645459597 5.9035341804  
H 1.5300848282 2.3036225495 7.2856045233  
H 3.1606879247 2.9581979818 7.0401070785  
C 4.7441098982 4.7650023527 3.1869154797  
H 5.5079711492 5.1408262069 2.5002458865  
H 4.6310535678 3.6880163689 3.0591050408  
H 5.0684981109 4.9627148274 4.2113598501

Aq-EIB radical cation

C 0.644708161 -1.7929942543 -6.3487214352  
C -0.4828853328 -2.1263415353 -5.594234089  
C -0.706290071 -1.5193645806 -4.3623525442  
C 0.1998574573 -0.5739460028 -3.8801026674  
C 1.33431056 -0.2386424045 -4.639200932  
C 1.5524684693 -0.8516078192 -5.8737281998  
C 2.3198714722 0.7637566912 -4.1539621151  
C 2.058675276 1.4103989273 -2.8237014092  
C 0.9284442308 1.0764442659 -2.0672854964  
C -0.0614346354 0.0598430465 -2.560447283  
C 0.6946140008 1.6826306724 -0.8308116743  
C 1.6066424561 2.6201971134 -0.3735990783  
C 2.7325029719 2.9520424782 -1.1274667476  
C 2.9733498474 2.3556908755 -2.3544439102  
O 3.3091809076 1.0670237407 -4.7913183847  
O -1.0329073432 -0.2174354126 -1.8847431706  
H 0.8140282032 -2.2692652379 -7.308704373  
H -1.1875494753 -2.8609977137 -5.969471741  
H -1.5752682425 -1.7633210114 -3.760166808  
H 2.4345912427 -0.5778985818 -6.4431399728  
H -0.1960376341 1.399177046 -0.2761270592  
C 1.5144802592 3.4141519509 0.9121317129  
C 3.5786782802 3.9895847667 -0.4385626156  
H 3.8402980005 2.5898401888 -2.9668081669  
N 2.8702009917 4.0729079909 0.873152243  
C 5.0193721261 3.5330270851 -0.1850562968  
C 3.5459323435 5.3568801706 -1.1394081117  
C 1.2983398978 2.5109034068 2.126580995  
C 0.4442851676 4.517956402 0.8007366985  
O 3.2816390612 5.0571759915 1.6353164796  
C 3.5896361586 4.8904141645 3.0880492247  
H 5.0445697829 2.5760076201 0.3420129217  
H 5.567097044 4.2903215291 0.3822876968  
H 5.5128822083 3.40640941 -1.1517815771

H 2.521054666 5.6974888179 -1.2984719645  
H 4.0264038005 5.2439714407 -2.1142655338  
H 4.0938461394 6.1009192727 -0.557868858  
H 2.0448516544 1.715056295 2.1679055628  
H 0.3180713242 2.0423244719 2.0080368473  
H 1.2783296975 3.0611463786 3.068188298  
H 0.451693749 5.1698627108 1.6735571912  
H -0.524430735 4.0165827119 0.7242115826  
H 0.5916935825 5.1080358126 -0.1060525393  
C 4.44455688 6.1229460353 3.3615690778  
H 5.3685095968 6.0716550011 2.7809907538  
H 4.6969191018 6.1488247028 4.4245469118  
H 3.8963126446 7.0313906895 3.1037203698  
C 2.298627881 5.045870785 3.8996103497  
O 1.3682323187 5.7238821856 3.5406803142  
O 2.3876164965 4.4124709173 5.0590122078  
C 1.2758631459 4.6004878955 5.9794195749  
C 1.6065812136 3.844931135 7.2441784669  
H 0.371581582 4.2274396632 5.4905796602  
H 1.1578973819 5.6738882518 6.1461486153  
H 1.7350277143 2.7792937983 7.0417893166  
H 0.789161453 3.9630122185 7.9590873067  
H 2.5203434106 4.2309086239 7.7010756639  
C 4.3491373005 3.5964453483 3.3112088964  
H 5.2557386867 3.5925441437 2.7027653622  
H 3.7494710309 2.7144367563 3.0825991938  
H 4.6337644395 3.5443529563 4.3631252591

Aq-EP

C 0.8891628951 -1.8049347421 -6.4907112389  
C -0.3903453558 -1.9711704615 -5.9535878095  
C -0.7497447706 -1.3069707102 -4.7858293809  
C 0.1699716801 -0.472137239 -4.1488866296  
C 1.4535551848 -0.3055477848 -4.687587516  
C 1.8092498599 -0.9745434475 -5.8599726944  
C 2.4593184557 0.5810200056 -4.0280989425  
C 2.0505858842 1.2836422738 -2.7765946473  
C 0.764025905 1.1169758629 -2.2360327861  
C -0.2398946515 0.2306181222 -2.895343035  
C 0.4004383181 1.7782973604 -1.0597802838  
C 1.3274911646 2.6042420003 -0.4409330382  
C 2.603475114 2.7727503044 -0.9822579562  
C 2.977501675 2.1179146853 -2.145921853  
O 3.5739538222 0.7241433499 -4.4975489825  
O -1.3553263659 0.0836942181 -2.429557275  
H 1.1659588013 -2.3248110739 -7.4023337864  
H -1.1056997298 -2.6201757504 -6.4485718581  
H -1.7364482215 -1.4187190766 -4.348388538  
H 2.8088003458 -0.8283040967 -6.256152708  
H -0.599460471 1.6245472084 -0.6634976057  
C 1.1629047166 3.4109499124 0.8263602945

C 3.4003503715 3.7533336813 -0.1593404947  
H 3.9644130192 2.228958271 -2.5868667676  
N 2.5893735654 3.7819150598 1.0953858791  
C 4.8072797157 3.2602771521 0.1780263853  
C 3.483068362 5.1039627816 -0.8887129437  
C 0.6390295122 2.5395435184 1.971521753  
C 0.2352246171 4.6149668293 0.6189073963  
O 2.7053001755 5.0531644364 1.6917405955  
C 3.3089418309 4.9826743891 2.9671116984  
H 4.7623206881 2.2848064296 0.6680902636  
H 5.2941948518 3.9730705895 0.8529085341  
H 5.4213377699 3.1809064237 -0.7247611019  
H 2.4921431789 5.4974684552 -1.1235174821  
H 4.0286370925 4.9666219664 -1.8273720617  
H 4.0113956622 5.8378038027 -0.2761812445  
H 1.3140038806 1.6970206463 2.1427248257  
H -0.3561079419 2.152332344 1.7291091094  
H 0.553175754 3.1318216409 2.8852429809  
H 0.1973592739 5.2089236099 1.5349658759  
H -0.7701564012 4.2523644999 0.3831625008  
H 0.5710600223 5.2501478586 -0.2035698725  
C 4.1141100547 6.2633094057 3.1653104565  
H 4.9009049834 6.3188611677 2.4092423887  
H 4.569614398 6.2793685142 4.1579898342  
H 3.4598560125 7.1322397312 3.0552614169  
C 2.2491589883 4.8839650104 4.05945376  
O 1.0942280364 5.2144796492 3.9428615581  
O 2.7835065667 4.4216553843 5.1981975286  
C 1.8909639528 4.3421667271 6.3244528206  
C 2.6882329766 3.8123580985 7.4954596192  
H 1.0582129073 3.683949875 6.0598207379  
H 1.4832244953 5.3388381166 6.5168141268  
H 3.093321005 2.8229642081 7.270334152  
H 2.0445448404 3.7321166424 8.3751280367  
H 3.5181024335 4.4822913212 7.7330871722  
H 3.950139092 4.0972908418 3.0237988326

Aq-EP radical cation

C 0.5702838077 -1.6250368098 -6.5169630102  
C -0.4796055418 -2.0808253267 -5.7158325815  
C -0.6656246926 -1.557801083 -4.4400167172  
C 0.2001653841 -0.5740252292 -3.9604237141  
C 1.2564405473 -0.1153786417 -4.7664983015  
C 1.4374652696 -0.6446589605 -6.0449676755  
C 2.1969362126 0.9312552085 -4.2855336191  
C 1.9770579913 1.4853170676 -2.9065026485  
C 0.9253948493 1.027796316 -2.1034981481  
C -0.0198829528 -0.0320122697 -2.5934897816  
C 0.7294235012 1.5479107463 -0.8218710058  
C 1.600889514 2.5235529268 -0.3666975157  
C 2.6490272553 2.9801606423 -1.1680880859

C 2.850641688 2.470434621 -2.4400144716  
O 3.1186651415 1.3415082208 -4.9628532601  
O -0.9239609176 -0.4149235721 -1.8770936347  
H 0.7107751092 -2.0363471213 -7.5110265526  
H -1.1528284952 -2.8453887486 -6.0890069728  
H -1.4742360437 -1.8973701406 -3.8011617834  
H 2.2592097196 -0.2764136644 -6.6502954811  
H -0.1025475591 1.1702314861 -0.233194819  
C 1.5272580726 3.2499571204 0.9611638484  
C 3.4697817183 4.0353863254 -0.4713948085  
H 3.6570604398 2.8012156539 -3.0894277897  
N 2.8302615815 3.9954965182 0.8730891465  
C 4.945277315 3.652322218 -0.3083433844  
C 3.316937048 5.4347125621 -1.086007614  
C 1.4478336747 2.2977071112 2.1556094622  
C 0.3774767799 4.2761033761 0.9585327039  
O 3.3017660335 4.874006798 1.7211326949  
C 3.4724267558 4.5078931943 3.1331335125  
H 5.0478257654 2.67860667 0.1779183905  
H 5.4784218768 4.415291869 0.2639791787  
H 5.3963289599 3.5883131799 -1.3014592139  
H 2.2659229138 5.7123395288 -1.1861035806  
H 3.7648843019 5.4150904443 -2.0824827437  
H 3.8370906629 6.1794060301 -0.4797108272  
H 2.3210702689 1.6423127423 2.2078259461  
H 0.5673470428 1.6672520604 2.0096053626  
H 1.3101960378 2.823849306 3.1028926105  
H 0.4046652467 4.9133255331 1.8425959568  
H -0.5574697379 3.7087608224 0.9440418998  
H 0.4123551876 4.8947189167 0.0596043404  
C 4.7562615647 5.1943850718 3.5671428304  
H 5.6013304046 4.8211357891 2.9863038918  
H 4.9294664257 4.9771867571 4.6231947236  
H 4.6698918371 6.2752105287 3.4339732653  
C 2.2819141217 5.0124045508 3.9425516595  
O 1.4813413626 5.8170174396 3.5390131033  
O 2.3024852958 4.4593674425 5.1441825651  
C 1.2770460721 4.9042443617 6.0783827063  
C 1.5134742498 4.1812545053 7.3825483124  
H 0.3034447681 4.6722503827 5.6388069683  
H 1.3630124358 5.9891044714 6.1752752867  
H 1.4395556355 3.0997111875 7.2496579985  
H 0.758078768 4.4912173279 8.1081943972  
H 2.4984465645 4.4212648951 7.7885190809  
H 3.5557827606 3.4216116405 3.1956478989

Aq-Me

C 0.9028986996 -2.0177450782 -6.1665972649  
C -0.3732905981 -2.1556390731 -5.613879808  
C -0.7304446723 -1.4210494529 -4.4883632559  
C 0.1882749072 -0.5439233093 -3.9095468772

C 1.4685219714 -0.4055924676 -4.4640206263  
C 1.8219452281 -1.1452621002 -5.5938014811  
C 2.4731544023 0.5250043549 -3.8664548589  
C 2.0680914088 1.301204515 -2.6575229102  
C 0.785184148 1.1625754513 -2.1018860112  
C -0.2186118526 0.234168179 -2.7006623879  
C 0.4236954407 1.8947685648 -0.9669919013  
C 1.3514567517 2.7577547323 -0.4048659935  
C 2.6282600914 2.8957388166 -0.9578740864  
C 2.997228841 2.1728700108 -2.0816145381  
O 3.5841291727 0.6449619564 -4.3504816133  
O -1.3316445547 0.1138292981 -2.2214826873  
H 1.1780646411 -2.5928498542 -7.0449153631  
H -1.0877828648 -2.8376790395 -6.0635761267  
H -1.7145860762 -1.509747044 -4.0400003963  
H 2.8188942973 -1.0199033627 -6.0034463209  
H -0.5744369663 1.7638640071 -0.5581364154  
C 1.1905813169 3.6655645835 0.7916953668  
C 3.4363396964 3.9082909603 -0.180998696  
H 3.9825834355 2.2562983953 -2.5318167275  
N 2.6208687896 3.9842356118 1.0643107745  
C 4.8371839508 3.4068487622 0.1728386718  
C 3.5438649347 5.231021161 -0.9563150024  
C 0.6013078688 2.9489675762 2.0075552754  
C 0.320290006 4.8825858521 0.4399444292  
O 2.756011467 5.2359209175 1.6886462237  
C 3.3312697634 5.0723866918 2.9758155191  
H 4.7751239069 2.4689276123 0.7295477826  
H 5.3519764399 4.1517438402 0.7880926164  
H 5.4341810961 3.2496809469 -0.731200106  
H 2.5673035259 5.6057617255 -1.2668822045  
H 4.147206197 5.0704008928 -1.8550625419  
H 4.0265237051 5.9898344111 -0.3364532759  
H 1.2139268138 2.0839461886 2.2719506261  
H -0.4219818177 2.6167141258 1.8053735806  
H 0.5678607289 3.6345682608 2.8603449261  
H 0.3091001766 5.5880280551 1.2737335954  
H -0.7027811864 4.5461378443 0.2457920928  
H 0.6802683273 5.4017816838 -0.4496670981  
H 4.3267555934 4.6220115451 2.9072016624  
H 2.6983215188 4.4459398651 3.612604204  
H 3.4053113289 6.0771333863 3.3974792295

Aq-Me radical cation

C 0.7656839956 -1.9434680994 -6.188959717  
C -0.4772618108 -2.0996956118 -5.5705386312  
C -0.7803727048 -1.3849643235 -4.4158369183  
C 0.1616586788 -0.5090867814 -3.8747031724  
C 1.412479165 -0.3518681655 -4.497123692  
C 1.7097070923 -1.0719824947 -5.6548423286  
C 2.4388519872 0.5725040012 -3.947342629

C 2.0923247257 1.3364744553 -2.7003398755  
C 0.8467538785 1.179133652 -2.080378114  
C -0.1865195459 0.2426771923 -2.6406447561  
C 0.5344320383 1.8913541526 -0.9206276314  
C 1.4848716142 2.7564394875 -0.402536571  
C 2.724538405 2.915458369 -1.0222726323  
C 3.0441170216 2.2104161175 -2.1713782817  
O 3.5267666202 0.7250682167 -4.4663170732  
O -1.2600086095 0.1247580676 -2.0832326254  
H 0.9966559411 -2.5033330631 -7.0890710732  
H -1.2096429516 -2.7805613173 -5.9912999032  
H -1.7394588686 -1.4913477328 -3.9197260708  
H 2.6809108929 -0.9356121242 -6.1190368274  
H -0.4440423236 1.7411509294 -0.4710220203  
C 1.3247374905 3.6277178126 0.8294422184  
C 3.5975211784 3.9073268627 -0.2977593026  
H 4.0006645351 2.307764882 -2.6783979615  
N 2.7119221529 4.2073252116 0.8649923524  
C 4.903697885 3.3026611705 0.2297302713  
C 3.8479796978 5.1890729093 -1.1034278374  
C 1.0060919531 2.7907489804 2.0747433686  
C 0.3015031948 4.7481951363 0.5843173276  
O 3.1429014521 5.1812626227 1.6227097174  
C 2.6323489802 5.3180812363 2.9742036664  
H 4.7101967679 2.4060419658 0.8237082445  
H 5.4526142531 4.0339711361 0.8277317627  
H 5.5225656088 3.0207105159 -0.6256134206  
H 2.9081973264 5.6367967022 -1.4353138734  
H 4.4317297985 4.9227731944 -1.9878096652  
H 4.4148274443 5.9136884154 -0.515216077  
H 1.8266946707 2.108603744 2.3115151653  
H 0.1250109925 2.185773665 1.8470732256  
H 0.7662285962 3.4029712426 2.9447863905  
H 0.1878399919 5.4120160637 1.4431709371  
H -0.6654992627 4.2729782478 0.3988275627  
H 0.5667146113 5.3355507613 -0.2973961501  
H 2.8477559022 4.4024064862 3.5255434406  
H 1.5690950852 5.5494253215 2.9636155773  
H 3.2026144523 6.1547007861 3.3704636035

1,2-DHAQ Aq-STY

C -4.0297027918 2.48205407 0.0543584543  
C -3.9307090098 1.1135754537 -0.1771085063  
C -2.692437521 0.5015760453 -0.3266528754  
C -1.5391204504 1.281698516 -0.2424570062  
C -1.639742691 2.6647527669 -0.0091172395  
C -2.8898932936 3.269843791 0.1412371805  
C -0.4222035805 3.5074695611 0.084943356  
C 0.8904440696 2.8580271107 -0.0698117372  
C 1.0042399998 1.4679087167 -0.3046617141  
C -0.2092011999 0.6155843087 -0.4032478352

C 2.0488027383 3.6346953522 0.0180348768  
C 3.3158104117 3.029965221 -0.1269240855  
C 3.4127319342 1.6668693618 -0.3564870347  
C 2.2562497358 0.8875172274 -0.4451510728  
O -0.5111224176 4.7218528565 0.2882690715  
O -0.1330028284 -0.5836154598 -0.6073390191  
C -5.4720623388 2.914093465 0.1569676696  
C -5.2979017741 0.4825669034 -0.2632703444  
H -2.5843077684 -0.5640553938 -0.5089323565  
H -2.9343602686 4.3402609586 0.3208502204  
O 2.0617959788 4.9626088864 0.2378239849  
O 4.4250778009 3.7918136823 -0.0396334004  
H 4.3994536986 1.2293597403 -0.4636085198  
H 2.3156822186 -0.1803950496 -0.6245359959  
H 1.1250559214 5.2578008952 0.3199917808  
H 4.1592522936 4.7097385516 0.1216486103  
N -6.1802443708 1.5851305453 0.2656848671  
O -7.3844350119 1.6120435621 -0.4734982194  
C -8.5695674224 1.4370135523 0.3234044728  
C -5.868556162 3.7227768105 -1.0859971182  
C -5.6918520857 3.7553239396 1.4175904589  
C -5.3801332208 -0.7544628938 0.6344261574  
C -5.6006814582 0.0918774576 -1.717604733  
H -9.3413126345 1.4500312516 -0.4555449212  
H -5.7314658272 3.1475866701 -2.0045295761  
H -5.2402045045 4.617444125 -1.139139571  
H -6.913805931 4.0311188786 -1.020565105  
H -5.502395047 3.154065891 2.3105828505  
H -6.7103867493 4.1448138421 1.4627357523  
H -5.0067288218 4.6098406014 1.4152470489  
H -5.2400486783 -0.4727804062 1.6815111172  
H -4.6013687285 -1.4716966057 0.3561546675  
H -6.3439702921 -1.2548519888 0.5246863076  
H -5.5501786102 0.9549315681 -2.385129529  
H -6.5969419431 -0.347731799 -1.7976715778  
H -4.8607056851 -0.6442999943 -2.0466911354  
C -8.6112024534 0.0906547307 1.0237367279  
C -8.8200532539 2.6265597306 1.2296592631  
C -9.2450375001 3.8267573127 0.6496882702  
H -9.4162027457 3.8633491311 -0.4240827623  
C -9.4353485061 4.9675652487 1.4241173856  
H -9.7601440397 5.8926530255 0.9579863992  
C -9.2127221495 4.916988195 2.8011555649  
H -9.3601984615 5.8035290389 3.409908487  
C -8.8089639324 3.7215617661 3.3913050128  
H -8.6376728664 3.6750370735 4.4623150893  
C -8.6144479302 2.5829458738 2.6090331813  
H -8.283590136 1.6632707417 3.0807163196  
H -8.5230350426 -0.7107409477 0.2855520196  
H -9.5622299875 -0.0265712543 1.5511883044  
H -7.7953266778 -0.0048622126 1.7431120609



1,2-DHAQ Aq-EIB

C -4.0297778033 2.6131410094 0.005167818  
C -3.9774716572 1.2222753093 -0.0121888163  
C -2.7600719882 0.5534696927 -0.0054245409  
C -1.5810197725 1.2988039305 0.0159591353  
C -1.6349491889 2.7037261674 0.0325832342  
C -2.8647781905 3.3668617469 0.0282871693  
C -0.3893695486 3.5098076743 0.0575496055  
C 0.9011044826 2.8008809681 0.067177155  
C 0.9683610696 1.3880354968 0.0503954061  
C -0.2729237502 0.5718152026 0.0218926598  
C 2.0852041559 3.5424253497 0.0934554511  
C 3.3317381571 2.880327264 0.1030969059  
C 3.3828895805 1.4956740921 0.0865628686  
C 2.2006297706 0.7512899283 0.0602324783  
O -0.4387062665 4.7432053705 0.0701693155  
O -0.2373970371 -0.6462317907 0.0036281419  
C -5.4571612222 3.1016632107 -0.0303046372  
C -5.3637426023 0.6306000077 -0.0642824049  
H -2.6881917601 -0.5305832841 -0.0174581658  
H -2.8729821638 4.4531399584 0.0421605678  
O 2.1430818213 4.8870165942 0.1110454737  
O 4.4661830985 3.6085964825 0.1283422872  
H 4.3546855661 1.0139708145 0.0945688703  
H 2.224335599 -0.3328802027 0.0471057508  
H 1.2170794255 5.2235746163 0.1011546344  
H 4.2318342453 4.548952466 0.1380941774  
N -6.2175222207 1.8314051606 0.2469064044  
O -7.3974785909 1.8134654209 -0.5300747199  
C -8.6144580662 1.6965560501 0.2185952233  
C -5.7707856421 3.7207245117 -1.4001225132  
C -5.70604414 4.1288971548 1.0763063235  
C -5.5397079834 -0.4264471214 1.0289534649  
C -5.625889739 0.0282194524 -1.4517093929  
C -9.6965223738 1.9201516665 -0.8383033576  
C -8.7278991443 2.7010533436 1.3512643808  
C -8.7823538892 0.274715088 0.7776134399  
H -5.6120074884 3.0063548025 -2.2110062543  
H -5.1106076523 4.5789653197 -1.5594020176  
H -6.8078058441 4.0614153869 -1.4389633928  
H -5.5417995574 3.6774272096 2.0581232141  
H -6.7257968022 4.5148831913 1.0293486211  
H -5.0237146751 4.9770741733 0.9595852816  
H -5.3752422657 0.0174183391 2.0136697642  
H -4.8264270212 -1.2446886244 0.8836567579  
H -6.5439071462 -0.8512149918 1.0024981419  
H -5.4698774725 0.7663412111 -2.2422579885  
H -6.6500035161 -0.3423106622 -1.516762833  
H -4.9283124482 -0.8000234941 -1.6137470297  
O -8.6350558978 -0.65835246 -0.1753383717

C -8.8399355722 -2.0209590819 0.2371483924  
C -8.360305051 -2.9095401423 -0.8893493074  
O -9.0642514455 0.0142512415 1.922610189  
H -9.5678659594 1.2188812531 -1.6647514755  
H -9.6163002142 2.9419387243 -1.2182795251  
H -10.6891578562 1.7827619786 -0.4003487861  
H -8.7163148233 3.7120373042 0.9360859931  
H -7.907259697 2.5807871615 2.0596840845  
H -9.6686611042 2.5475228279 1.8836108934  
H -9.9045654625 -2.158266302 0.4513799526  
H -8.2891264355 -2.1977705161 1.1656619655  
H -8.8950224232 -2.6852064864 -1.815585048  
H -8.5319385356 -3.9581398767 -0.6333554398  
H -7.2900098637 -2.7664862893 -1.0620855756

1,2-DHAQ Aq-EP

C -3.9966477107 2.5450894798 -0.0969563907  
C -3.909731473 1.1516191335 -0.108287659  
C -2.6769127886 0.5158617537 -0.0605101475  
C -1.5186758761 1.2929751722 -0.0003354577  
C -1.608765775 2.6955292372 0.0172503273  
C -2.85459228 3.3283369021 -0.031646747  
C -0.3854468932 3.5328391055 0.0887989495  
C 0.9215604661 2.857043459 0.1408228589  
C 1.0251961347 1.4464313335 0.1224033457  
C -0.1932131296 0.5994336567 0.0492109656  
C 2.084862473 3.6281371203 0.2098394758  
C 3.3467573731 2.9976387679 0.260198013  
C 3.4335320636 1.6147774786 0.2412258731  
C 2.2721252 0.8408992394 0.1724012682  
O -0.4671495038 4.764381232 0.1037959082  
O -0.1265219054 -0.6172430556 0.0293196035  
C -5.4345100315 2.9866935026 -0.209478728  
C -5.2828659594 0.5247334277 -0.1792702922  
H -2.5759845063 -0.5659044967 -0.0666173078  
H -2.8930265852 4.413993707 -0.0172551498  
O 2.1081775102 4.973671054 0.2331576202  
O 4.4608524894 3.7540662216 0.3263635634  
H 4.4164146207 1.1577696306 0.2809166314  
H 2.3237140589 -0.2422690419 0.1567453493  
H 1.1751303873 5.2872568289 0.1928628942  
H 4.2028485394 4.6882550864 0.3296513244  
N -6.1366760227 1.7131027168 0.1322050101  
O -7.3755229237 1.6661854012 -0.5364668044  
C -8.4596167737 1.6535711708 0.377062885  
C -5.7171480534 3.5023751117 -1.6297589742  
C -5.8229120984 4.0527173343 0.8148086405  
C -5.464925059 -0.533514965 0.9124278046  
C -5.5495516208 -0.0913777044 -1.5594340088  
C -9.6553445434 2.267830847 -0.3407208425  
C -8.8246695365 0.248996594 0.8438691534

H -5.4631946273 2.7598219694 -2.3887450407  
H -5.1118007003 4.3960835718 -1.8097731165  
H -6.7723527186 3.7622631689 -1.7381196905  
H -5.6087759992 3.7044897273 1.8279088782  
H -6.8938296415 4.2687469311 0.7340108491  
H -5.2799094991 4.9856279018 0.6324104006  
H -5.3071833888 -0.0918084996 1.8990344712  
H -4.7542969971 -1.3545373937 0.7711133347  
H -6.4729505121 -0.9527337896 0.8680890079  
H -5.3797559111 0.6253747551 -2.365507263  
H -6.583880375 -0.4391492473 -1.6112773247  
H -4.8742551365 -0.9398807328 -1.7087997743  
O -8.6506100282 -0.6708372989 -0.1133449759  
C -8.9958406688 -2.0209337824 0.2440604729  
C -8.5234713844 -2.9151191679 -0.8809761045  
O -9.2771565972 0.0080790544 1.9377992602  
H -9.8699037331 1.7073370715 -1.2542676436  
H -9.4272591064 3.3024877306 -0.607818805  
H -10.5355641832 2.2512685935 0.3063261298  
H -10.0784367611 -2.0746277059 0.393910542  
H -8.5147203239 -2.2646272845 1.1963826004  
H -8.9907634253 -2.628227633 -1.8261889678  
H -8.7840833287 -3.9542145408 -0.6644646844  
H -7.437978177 -2.847081862 -0.9953771809  
H -8.1958870433 2.2200160205 1.2746656695

1,2-DHAQ Aq-Me

C -4.0907549644 2.6091763938 -0.0363218929  
C -4.0453089869 1.2144415466 -0.119536512  
C -2.8330530777 0.5402281597 -0.1314026439  
C -1.6500603446 1.2790844734 -0.0605628417  
C -1.6966852973 2.6811481289 0.0234292111  
C -2.9235151854 3.3530181816 0.036860767  
C -0.4467128853 3.4773475195 0.1025667236  
C 0.8399996976 2.761429742 0.0911224625  
C 0.8994793488 1.3507853778 0.0068433751  
C -0.3460851251 0.5447881395 -0.073287339  
C 2.0279774017 3.4934991553 0.1654441511  
C 3.2705012226 2.8238846936 0.1557021086  
C 3.313964079 1.4413346846 0.0727460848  
C 2.1277961654 0.7065036771 -0.0015145961  
O -0.4895643584 4.7088025264 0.1759512114  
O -0.3172079718 -0.6712995003 -0.1475181098  
C -5.520230824 3.0968255865 -0.0667841399  
C -5.4403477308 0.6431841118 -0.2128011808  
H -2.7668322328 -0.5425311285 -0.1923195221  
H -2.9271670511 4.4372303919 0.1056229855  
O 2.0933497926 4.8353521139 0.2488577224  
O 4.4088328237 3.5429573737 0.2278641037  
H 4.2828348807 0.9537650796 0.0674173191  
H 2.1452435377 -0.3759065193 -0.0668451513

H 1.1694843719 5.1776127531 0.2468064356  
H 4.1798909309 4.483287059 0.27944449815  
N -6.2304600594 1.8229509185 0.2401828074  
O -7.523570792 1.8134843102 -0.3093604878  
C -8.4875370316 1.7193796324 0.7283956439  
C -5.860578211 3.7041812363 -1.4369523201  
C -5.8259250951 4.1132486773 1.0343388606  
C -5.674996293 -0.5147477453 0.7583472656  
C -5.7444061287 0.1819765318 -1.6472067973  
H -9.4595799542 1.7157672838 0.2306237773  
H -8.4189102034 2.5752974543 1.40749377  
H -8.3584541738 0.796120991 1.3022607323  
H -5.6175219917 3.0279491229 -2.2580312243  
H -5.2845276397 4.6246555437 -1.5732726636  
H -6.9253338279 3.9424264219 -1.4863802909  
H -5.5937494579 3.6917830073 2.015117391  
H -6.8867513003 4.3818317576 1.0054066145  
H -5.2454553824 5.0301937042 0.8899751234  
H -5.4668397033 -0.1989559717 1.7832316023  
H -5.0366022174 -1.3680701102 0.5081994883  
H -6.716327169 -0.8459703965 0.6933285084  
H -5.549669534 0.9656922594 -2.3809979926  
H -6.7912605934 -0.1185662817 -1.7289882454  
H -5.1090214578 -0.6753980684 -1.8893572767

1,2,4-THAQ Aq-STY

C -3.9105548785 2.5083059995 0.1201162324  
C -3.8093088545 1.1388389485 -0.1059134217  
C -2.5707222573 0.5285937778 -0.257406428  
C -1.419045429 1.3128155463 -0.1803663032  
C -1.5214085228 2.6970392222 0.0480976345  
C -2.772362527 3.2992815146 0.2002398733  
C -0.3043575159 3.5390343438 0.133850616  
C 1.003619267 2.8870661498 -0.0249384818  
C 1.1034644033 1.4829605878 -0.2570243238  
C -0.0919586605 0.6557683707 -0.3423150302  
C 2.1492666775 3.6619437133 0.0542403499  
C 3.4265929634 3.050235782 -0.0966364034  
C 3.5332953284 1.6977818446 -0.3204036944  
C 2.3729118035 0.9014126464 -0.4027925465  
O -0.3912882439 4.7556832275 0.3336488486  
O -0.029806802 -0.564507662 -0.5437076966  
C -5.3534893948 2.9374237981 0.2250411989  
C -5.1753199498 0.5043810684 -0.1843108853  
H -2.4621385586 -0.5374421575 -0.4356895027  
H -2.8182598667 4.3703100255 0.3758122222  
O 2.1716234787 4.990209867 0.2686008789  
O 4.5250103753 3.8204644184 -0.0162473099  
H 4.5071553986 1.2361315175 -0.4344737467  
O 2.5458655673 -0.4039862518 -0.6217476607

H 1.2340243837 5.2869559635 0.3545887116  
H 4.2514175337 4.7369802904 0.1432090204  
H 1.6527008684 -0.8209296878 -0.6536043387  
N -6.0582670473 1.6074453664 0.3425401383  
O -7.2647752102 1.627853946 -0.3928049624  
C -8.4470880777 1.4541099955 0.408780182  
C -5.7551397991 3.7389284511 -1.0210170125  
C -5.5709848407 3.7847203615 1.4819999928  
C -5.2517734474 -0.7283691398 0.7197951463  
C -5.4823717848 0.1059611418 -1.6356363231  
H -9.2211241156 1.4604302877 -0.3679555344  
C -8.4828750753 0.1117548339 1.1170947198  
H -5.620180053 3.1591507984 -1.936966297  
H -5.128542641 4.6343705746 -1.0809667424  
H -6.8006782189 4.0458209663 -0.9537459292  
H -5.3758233954 3.1889811501 2.3774467541  
H -6.5906591743 4.1709620945 1.5291187984  
H -4.8888536122 4.6415615481 1.4721744204  
H -5.108460475 -0.4413587275 1.7649839795  
H -4.4728464114 -1.4456756193 0.4420874709  
H -6.2150831006 -1.2309805897 0.6160347945  
H -5.4354423188 0.965626397 -2.3077624547  
H -6.4783060962 -0.3352784825 -1.7098990376  
H -4.7426392106 -0.6309771748 -1.9635822169  
C -8.6978582428 2.6484041009 1.3085757843  
C -9.1258767555 3.8444679828 0.722300633  
H -9.2992705599 3.8743733497 -0.3513229009  
C -9.3168064829 4.9894435941 1.4903854621  
H -9.6440535406 5.9112224381 1.0194288737  
C -9.0916486585 4.9472713387 2.8672953565  
H -9.2397126352 5.8370275349 3.471182946  
C -8.6849276239 3.7559329954 3.4637634284  
H -8.5119177383 3.7160152143 4.5347603932  
C -8.4898385568 2.6130934788 2.6878411408  
H -8.1570774351 1.6965395672 3.1643133357  
H -8.3961311311 -0.693887121 0.3833795048  
H -9.4315321055 -0.0043014359 1.6490225513  
H -7.6639810158 0.0221859182 1.8338357909

1,2,4-THAQ Aq-EIB

C -3.9163810767 2.6850663337 0.0131754331  
C -3.8635387161 1.2940776225 0.0280525057  
C -2.646342206 0.6256700096 0.0498798691  
C -1.4675996972 1.3728911369 0.0533661618  
C -1.5216803301 2.7782667516 0.0378603744  
C -2.7517913193 3.4399466965 0.0188043245  
C -0.2755024816 3.5813504635 0.0437470586  
C 1.0095314254 2.8685031329 0.0667699506  
C 1.0609122074 1.4427373753 0.080681228  
C -0.1626540183 0.6536153097 0.0742359248  
C 2.1817560116 3.606781649 0.0735101256

C 3.4380596157 2.9358631481 0.0942625323  
C 3.4980648075 1.5622875242 0.1074168448  
C 2.3103458875 0.8027340898 0.1007595961  
O -0.3212185462 4.8164182839 0.0294892274  
O -0.1432318314 -0.5843877944 0.0849654505  
C -5.3438357444 3.1721982677 -0.0337865011  
C -5.2494083322 0.7006745786 -0.010437142  
H -2.5756972065 -0.4582306999 0.0626311511  
H -2.760138405 4.5262370833 0.0076570678  
O 2.2499183614 4.9504944735 0.0615183551  
O 4.5629559734 3.6709310653 0.1002687407  
H 4.4559333411 1.0555439614 0.1229373881  
O 2.4385459378 -0.5257586828 0.1141452453  
H 1.3229598657 5.2893925069 0.0462202374  
H 4.3217080532 4.6100587395 0.0900305867  
H 1.5314822101 -0.912539045 0.1074066441  
N -6.1048012894 1.908196491 0.2696569501  
O -7.2811742749 1.8710617079 -0.511868276  
C -8.501588609 1.7739587945 0.2342517654  
C -5.6559634421 3.7616845276 -1.4168998477  
C -5.5928097848 4.2228729749 1.0507280564  
C -5.4260317636 -0.3286717292 1.1088612131  
C -5.5097294924 0.0638110075 -1.3827304494  
C -9.5788118358 1.9659114487 -0.8336727007  
C -8.620906576 2.8103484324 1.3371121451  
C -8.6697520427 0.3685309323 0.8330807497  
H -5.4966407342 3.0299023575 -2.2120283221  
H -4.9956717344 4.6163013748 -1.5940169402  
H -6.6929346966 4.1013789592 -1.4639707812  
H -5.4296413729 3.7920718698 2.0419751027  
H -6.6121921702 4.6086095396 0.9950982842  
H -4.9097702832 5.0678951275 0.9167299569  
H -5.261876835 0.1395590781 2.0822833967  
H -4.7132930426 -1.1508622414 0.9843704001  
H -6.4305217726 -0.7532278364 1.0926337183  
H -5.3541370304 0.7824361214 -2.1911528793  
H -6.5333260396 -0.3094251346 -1.4393602005  
H -4.8112163118 -0.7675015655 -1.5237564518  
O -8.5199103811 -0.5910975977 -0.0927720174  
C -8.7257724903 -1.9415929528 0.3574799242  
C -8.2419008776 -2.8614870309 -0.7417070186  
O -8.9533548063 0.1405384799 1.9845127071  
H -9.444606041 1.2422182309 -1.6396365989  
H -9.4989971068 2.9769149372 -1.2415624916  
H -10.5732922389 1.8384776552 -0.3969194417  
H -8.6066616076 3.8090575188 0.8932065149  
H -7.8042458924 2.7100390797 2.0531820012  
H -9.5646043953 2.6723854626 1.8685145474  
H -9.7911323355 -2.0730957588 0.5716796538  
H -8.1783602274 -2.0917992343 1.2926549381  
H -8.7735351257 -2.6638055628 -1.6757521979

H -8.4138681141 -3.9024970634 -0.4566746034  
H -7.1710810129 -2.7227423824 -0.9147891878

1,2,4-THAQ Aq-EP

C -3.8834624852 2.6237073021 -0.1229801907  
C -3.8009705218 1.2304970461 -0.076769129  
C -2.5703931742 0.5930978207 -0.0041024465  
C -1.4097812205 1.3696559017 0.0224512086  
C -1.4952783709 2.7724968442 -0.0175230318  
C -2.7392117934 3.4058696462 -0.091048349  
C -0.2685499326 3.6046062889 0.0181821405  
C 1.0309661101 2.9227628823 0.0944772384  
C 1.1144570014 1.4989773845 0.1325686782  
C -0.0898132232 0.6816311225 0.0981349518  
C 2.1850217561 3.6883616262 0.1282462383  
C 3.4550693411 3.0473995771 0.2005436896  
C 3.5460170071 1.6759796672 0.2371392159  
C 2.3768706232 0.8887543835 0.2035762564  
O -0.3426932572 4.8378403301 -0.0162477075  
O -0.0427516615 -0.5552499498 0.1292793391  
C -5.3198622663 3.0648230022 -0.252319534  
C -5.1763062419 0.605809769 -0.1195907875  
H -2.4742778046 -0.4882234014 0.0344562348  
H -2.7741093824 4.4913010701 -0.1212019095  
O 2.2227625729 5.0328905638 0.0974576661  
O 4.5619700126 3.8085369161 0.2318176825  
H 4.5141958708 1.1920608731 0.2919099442  
O 2.5350508605 -0.4359312859 0.2420540125  
H 1.2894700909 5.3500536754 0.0468756561  
H 4.3000393235 4.7415393257 0.1977204242  
H 1.6379914022 -0.8441580408 0.2118526758  
N -6.0254310809 1.8090870805 0.143668898  
O -7.2657159138 1.7387795992 -0.5199928996  
C -8.3481567615 1.7684037152 0.3953206334  
C -5.6022232946 3.5208430171 -1.692966663  
C -5.7035727119 4.1745579791 0.7262724561  
C -5.3602258485 -0.405355915 1.0155800142  
C -5.4477181677 -0.0664026759 -1.472393995  
C -9.5424863666 2.3584835357 -0.3447124053  
C -8.7185748789 0.3856972864 0.9195241962  
H -5.3508938828 2.7463392839 -2.420235843  
H -4.9949323963 4.4046924006 -1.9110044567  
H -6.6568918598 3.7784717422 -1.8111381611  
H -5.4892640979 3.8690851013 1.7530358892  
H -6.7739548292 4.3899838902 0.6375286254  
H -5.15826371 5.0973414924 0.5037759446  
H -5.1994486653 0.0764412564 1.98274093  
H -4.6529989551 -1.2343751526 0.9076090004  
H -6.3698561454 -0.8222752941 0.9901026437  
H -5.2774656939 0.6154287029 -2.3080925949  
H -6.4832641917 -0.4126749955 -1.5075064236

H -4.7755779111 -0.9227078487 -1.5874754969  
O -8.5487405349 -0.5734412129 0.0009034601  
C -8.9007634313 -1.9060422422 0.413495806  
C -8.4368794952 -2.8476427965 -0.6757812986  
O -9.1712852388 0.1919237322 2.0226575468  
H -9.7613793339 1.7624165996 -1.234399763  
H -9.3103899769 3.380437321 -0.653932295  
H -10.4214837555 2.3722040677 0.3040364313  
H -9.9832025195 -1.9471895741 0.5682537665  
H -8.4183150714 -2.1138342924 1.3736240824  
H -8.9056300721 -2.5966323865 -1.6304253623  
H -8.7025090813 -3.8756317832 -0.4166214083  
H -7.351393268 -2.7904582293 -0.7960953846  
H -8.0800114955 2.369676255 1.2686139593

1,2,4-THAQ Aq-Me

C -3.9910981372 2.6672089094 -0.042427599  
C -3.9463454041 1.269876264 -0.0619273493  
C -2.734794456 0.5950959016 -0.0391075093  
C -1.5516289013 1.3371551622 0.0018218473  
C -1.5975614208 2.7420536096 0.0215451974  
C -2.8240261909 3.4135275877 0.0003202389  
C -0.346942691 3.5370196454 0.0687396108  
C 0.933759611 2.816483517 0.0938785392  
C 0.9768081274 1.3906318507 0.0735405193  
C -0.2511755727 0.6097512364 0.0273734261  
C 2.1098414568 3.5471637433 0.1381134861  
C 3.3618219416 2.8682212605 0.1634863552  
C 3.4137597317 1.4944016082 0.1443731684  
C 2.2218995938 0.7426372562 0.0991548353  
O -0.3857291255 4.7722537784 0.085871035  
O -0.2391115451 -0.6282121228 0.0087134275  
C -5.4198594564 3.1540900323 -0.0984012893  
C -5.3417273066 0.6962896455 -0.1330631756  
H -2.6702712463 -0.4892139482 -0.0500890197  
H -2.8270261636 4.4997063336 0.0198859194  
O 2.1858928736 4.890369395 0.1602299425  
O 4.4905633794 3.5961750008 0.2064063509  
H 4.3682086115 0.9814078951 0.1639134664  
O 2.3421619209 -0.5865689702 0.0824925754  
H 1.2611769618 5.2350021708 0.1393341352  
H 4.2548174644 4.5367256991 0.2137905145  
H 1.4332029509 -0.9675044955 0.0507991352  
N -6.1315029085 1.8960204019 0.264908643  
O -7.4236797047 1.8625270659 -0.2853664546  
C -8.3894480006 1.8181340713 0.7542496304  
C -5.7563278722 3.6987874421 -1.4956558534  
C -5.7267618956 4.2200494885 0.9545280873  
C -5.5806749903 -0.4165967179 0.8883369491  
C -5.6430353154 0.1719231375 -1.5462058961  
H -9.3606074426 1.79207522 0.2555111355



H -8.3210351101 2.7049396197 1.392481369  
H -8.2621129751 0.9226427885 1.3708791317  
H -5.5124315526 2.9858413469 -2.2847811993  
H -5.1790177132 4.6115512246 -1.6723617907  
H -6.8207041197 3.9355900423 -1.5580559498  
H -5.4970822037 3.8437873652 1.9540958803  
H -6.7872377375 4.4878179541 0.9109471904  
H -5.1453207588 5.1290362352 0.7695154083  
H -5.373623234 -0.0559800582 1.8985546619  
H -4.9443463296 -1.2820044565 0.6775151046  
H -6.6227689856 -0.747565877 0.8361569422  
H -5.4455439534 0.9217099162 -2.3138955383  
H -6.6902132804 -0.1302528911 -1.6167229893  
H -5.0086509239 -0.6964712853 -1.7484422463

1,2,5-THAQ Aq-STY

C -3.8665172543 2.5133432857 0.1479303805  
C -3.802586276 1.1612847259 -0.1188694353  
C -2.5611711652 0.5376077753 -0.3390472901  
C -1.3853019879 1.3135751478 -0.2486269418  
C -1.4850898379 2.6950944581 0.0455800827  
C -2.7153551656 3.3016888233 0.239305995  
C -0.2614353767 3.5301521919 0.1477184187  
C 1.044050782 2.8846229653 -0.0651384826  
C 1.1421697003 1.5064561982 -0.3644139851  
C -0.0776630093 0.6761433274 -0.4705062315  
C 2.2083544295 3.6492716571 0.0292193215  
C 3.4679302966 3.0429618134 -0.1733127212  
C 3.5494518203 1.6908753103 -0.466032834  
C 2.3857781485 0.9233268181 -0.5617297138  
O -0.3375180354 4.7347777215 0.4049241575  
O 0.009185427 -0.5277727403 -0.7409814457  
C -5.2986890702 2.9753425283 0.2620291754  
C -5.1765889113 0.5403047506 -0.1784696032  
O -2.535029206 -0.7654238134 -0.6386764908  
H -2.7533850498 4.3652976274 0.4515928441  
O 2.2356783847 4.9649535555 0.3067700226  
O 4.5832790741 3.7925395114 -0.0791497511  
H 4.5299284482 1.252408742 -0.6166231731  
H 1.302685158 5.2618946564 0.4231751189  
H 4.3293815004 4.7044612992 0.1294819344  
H 2.4348190918 -0.135410332 -0.7905159137  
H -1.5874226102 -1.0215827394 -0.7572063865  
N -6.0425937467 1.6678353481 0.3378902139  
O -7.2276584446 1.7385241787 -0.4283191781  
C -8.4337784347 1.5835687175 0.340008621  
C -5.6611476707 3.8181208334 -0.9692459893  
C -5.5021997385 3.7966662535 1.5384366811  
C -5.2760787287 -0.6669587802 0.7602006227  
C -5.5033946551 0.118453874 -1.6175131429  
H -9.1879361134 1.6293282772 -0.4548654985

C -8.5272179125 0.229243448 1.0192969945  
H -5.5398194321 3.2495501286 -1.8944688777  
H -5.0031921508 4.6920594496 -1.007043531  
H -6.6956108738 4.1602252807 -0.9031405759  
H -5.3285402766 3.1736429706 2.4197744038  
H -6.5132915829 4.2047256479 1.5882270689  
H -4.8007708863 4.6376037992 1.5559253052  
H -5.1276346538 -0.3485831152 1.7960462686  
H -4.5173413873 -1.4076315682 0.4993888386  
H -6.2571405303 -1.137684598 0.6731879676  
H -5.4647021604 0.9692490791 -2.3019884382  
H -6.5033685417 -0.3173486928 -1.6698589155  
H -4.7706758275 -0.6279954027 -1.9356696009  
C -8.6709902186 2.7662988459 1.2592487273  
C -9.0457775367 3.9876429411 0.6888725608  
H -9.1905800983 4.0454392093 -0.3878369935  
C -9.220053555 5.1219973773 1.476480592  
H -9.5055436063 6.0634699911 1.0174358929  
C -9.0324398262 5.0439426701 2.8574344616  
H -9.1677886815 5.9252971512 3.4764869674  
C -8.6794954459 3.8278698017 3.4378332078  
H -8.5358243324 3.7598299277 4.5117649085  
C -8.5002215775 2.6958553604 2.642365286  
H -8.208560144 1.7596393788 3.1071370104  
H -8.4292708171 -0.5639991367 0.2735460471  
H -9.4981270338 0.1255094634 1.5124205394  
H -7.7386326836 0.106976625 1.764274502

1,2,5-THAQ Aq-EIB

C -3.817532214 2.7150045675 -0.1040977822  
C -3.7913737161 1.3369276729 0.0113166825  
C -2.5671657265 0.6534288257 0.0918691864  
C -1.3702794023 1.4035541972 0.0896233328  
C -1.432962469 2.8139895457 -0.0107619553  
C -2.6468870411 3.4761087053 -0.1145683471  
C -0.1864175513 3.6215778512 -0.0129152956  
C 1.1018243212 2.9182407064 0.0943918132  
C 1.1636370755 1.5092003225 0.1910175328  
C -0.0775831842 0.7047658988 0.1845162553  
C 2.2861355276 3.6574428734 0.1008522  
C 3.5296338733 2.9950801613 0.2039479553  
C 3.5753661348 1.6132505645 0.2981732295  
C 2.391661655 0.8709491024 0.2912149943  
O -0.2311799709 4.8515963517 -0.1018008821  
O -0.022643229 -0.5284152297 0.257569376  
C -5.2360322261 3.2036311548 -0.2699871968  
C -5.183719779 0.752747224 -0.0175840671  
O -2.5770969322 -0.6820085454 0.1564301494  
H -2.6550136589 4.5579045807 -0.2010258299  
O 2.3486212983 4.9980103013 0.0136402505  
O 4.6645794046 3.7203616454 0.2094222872

H 4.5440720032 1.1318191589 0.3761728165  
H 1.4243838654 5.3338210707 -0.0543134906  
H 4.4356478464 4.6593275682 0.1350498899  
H 2.4127817214 -0.2107004365 0.3637243242  
H -1.6370825159 -0.98166903 0.210752807  
N -5.9913198549 2.0013846946 0.1921619648  
O -7.2343846449 1.9505526166 -0.4658031101  
C -8.3801017592 1.8431105846 0.3960192431  
C -5.4875305383 3.5851772361 -1.7389456889  
C -5.5497353709 4.4010686096 0.6257536919  
C -5.4346384609 -0.2005015231 1.1549196326  
C -5.4442774564 0.0390598015 -1.3518423839  
C -9.5269946684 2.363627302 -0.4722721757  
C -8.2623870513 2.6217713771 1.69530131  
C -8.6800442522 0.3690524953 0.7158397449  
H -5.2450552805 2.7670839196 -2.4194149591  
H -4.8598541393 4.4437373937 -1.9973844872  
H -6.5355665198 3.8571903283 -1.8817823765  
H -5.4344480758 4.1346740909 1.6792571064  
H -6.5750920221 4.7394934322 0.4527629766  
H -4.8827646558 5.2370949882 0.3924753443  
H -5.2612740363 0.3153591558 2.1030066922  
H -4.7729521763 -1.0667221159 1.0905069761  
H -6.4678174889 -0.556660713 1.1433633182  
H -5.2063516374 0.6762374363 -2.2061299072  
H -6.4943942051 -0.2503393193 -1.4158983487  
H -4.8121952309 -0.8524889548 -1.4003315133  
O -8.5768321554 -0.4143960044 -0.3655668302  
C -8.8631753215 -1.8082155773 -0.156023551  
C -8.6860872737 -2.510792838 -1.4840593365  
O -9.0225343118 -0.0405376713 1.8002326633  
H -9.5521783145 1.824913906 -1.421962897  
H -9.3682535401 3.4276083155 -0.6684701067  
H -10.4841260107 2.2353770291 0.0408869895  
H -8.1431270735 3.6846476213 1.4781455091  
H -7.4123257392 2.2769223941 2.284711618  
H -9.1734734889 2.4766259109 2.2784665088  
H -9.8821273432 -1.9008542544 0.2310039482  
H -8.1795144283 -2.1925707898 0.6081758311  
H -9.3582581482 -2.0902935868 -2.2360164001  
H -8.912201769 -3.5742658133 -1.3717507266  
H -7.6581506663 -2.4123382871 -1.8418465065

1,2,5-THAQ Aq-EP

C -3.8194072663 2.6756315894 -0.1312364927  
C -3.7738147229 1.2929153824 -0.1449970883  
C -2.5397638136 0.6231434756 -0.1159465979  
C -1.3545813544 1.3877752849 -0.0397741895  
C -1.4380133034 2.8004367963 -0.0060033861  
C -2.6611257519 3.451816444 -0.0575121505  
C -0.2036906959 3.6224941998 0.079272653

C 1.0943731672 2.9308344956 0.1265420653  
C 1.1769150778 1.5199829526 0.0880851026  
C -0.0519840952 0.7018684882 -0.0010027663  
C 2.2674881419 3.6830587738 0.2100477975  
C 3.5204015083 3.0319969524 0.2552680039  
C 3.5864462474 1.6483017407 0.2165623474  
C 2.4140017182 0.8929758013 0.1327893477  
O -0.2669039526 4.8544591685 0.1095311969  
O 0.0206709369 -0.5318348804 -0.0419907186  
C -5.2428188889 3.154893784 -0.2727298292  
C -5.1567472801 0.6881126587 -0.2146686217  
O -2.5308767241 -0.712617778 -0.170988939  
H -2.6867172754 4.5367793047 -0.040293721  
O 2.310488121 5.0265092181 0.2523387646  
O 4.6443385044 3.7697208477 0.3356212698  
H 4.5620112079 1.1758049592 0.2525827963  
H 1.3818744147 5.3543751132 0.2125596467  
H 4.4018420194 4.7081039926 0.3508571461  
H 2.4509912006 -0.1902274097 0.1014042778  
H -1.586900276 -1.0028867546 -0.1383999127  
N -5.9880897692 1.9062307635 0.0577858765  
O -7.2057721117 1.8846333461 -0.650577203  
C -8.3182660691 1.9290688661 0.2269592173  
C -5.4731553772 3.6676203041 -1.7038449372  
C -5.61996571 4.2403863919 0.7352970368  
C -5.3889798861 -0.329231666 0.9078267762  
C -5.4227505416 0.041423524 -1.5801793298  
C -9.4731190306 2.5496104641 -0.5498446112  
C -8.7357674847 0.5513756198 0.7286152867  
H -5.2315726936 2.9058457896 -2.4479700384  
H -4.8312890634 4.5363038172 -1.8799344369  
H -6.515368385 3.9651036895 -1.8378576201  
H -5.4410654336 3.8928121537 1.7554689014  
H -6.6814075123 4.4886996235 0.6279970326  
H -5.0447007904 5.1551104773 0.5597457209  
H -5.2045482144 0.1343086 1.8801641795  
H -4.7271942035 -1.189618071 0.7857716728  
H -6.4238183908 -0.6787230053 0.8782999837  
H -5.2490481498 0.7413229859 -2.4006771578  
H -6.459858017 -0.2984891296 -1.6266723846  
H -4.7502162608 -0.812358975 -1.7019414135  
O -8.5619199369 -0.4041221516 -0.192153551  
C -8.9435908799 -1.733588735 0.20339631  
C -8.4528280446 -2.6778777067 -0.871753145  
O -9.2247133743 0.3606592234 1.8169338048  
H -9.672106523 1.965060711 -1.4517573267  
H -9.209565344 3.5690013253 -0.841950436  
H -10.3742693051 2.5762356615 0.0674002421  
H -10.0312582823 -1.7622642639 0.320240313  
H -8.4967123049 -1.949680505 1.1786767046  
H -8.8826001191 -2.4172221864 -1.8421160544

H -8.7424064393 -3.7028274811 -0.6262127573  
H -7.3630300866 -2.6352980143 -0.9511409443  
H -8.06949313 2.5179639523 1.1143462859

1,2,5-THAQ Aq-Me

C -3.9477766141 2.676788811 -0.0345473361  
C -3.9334055631 1.2924463447 -0.0692024645  
C -2.7167152897 0.593251462 -0.0805845916  
C -1.5117964587 1.3282934749 -0.0241872864  
C -1.5608511679 2.7420888236 0.0282183996  
C -2.7691902117 3.4233638818 0.0178667606  
C -0.3053414602 3.5334269846 0.0913909527  
C 0.9769062253 2.8108263561 0.096210218  
C 1.0245140567 1.3990885058 0.0391378018  
C -0.2256200998 0.6112888872 -0.0271866453  
C 2.1696518993 3.5338408769 0.1578114268  
C 3.4071784529 2.8526188465 0.1628169052  
C 3.4389147669 1.4683055153 0.1064838008  
C 2.2467989963 0.7422656651 0.0443860025  
O -0.3377841425 4.7661062277 0.1386892854  
O -0.183313531 -0.623053068 -0.0845387611  
C -5.3664424998 3.1902191379 -0.109709004  
C -5.3328278194 0.7285332057 -0.1372527297  
O -2.7441331284 -0.7416122768 -0.1529250728  
H -2.7675722491 4.5082319041 0.0510738901  
O 2.245919335 4.8753815015 0.2147128407  
O 4.5503274976 3.56251883 0.2226412448  
H 4.4033807203 0.9722982261 0.111824563  
H 1.3244381207 5.2250392836 0.2033599305  
H 4.3306902317 4.506074511 0.2554103189  
H 2.256615561 -0.3410677292 -0.0004128258  
H -1.8083470973 -1.0570400894 -0.1481288671  
N -6.1104227265 1.9487200311 0.2350378334  
O -7.3860475763 1.938782082 -0.3541993035  
C -8.3841301879 1.9229342278 0.6548019359  
C -5.6597426843 3.7419935138 -1.5141535731  
C -5.6687056971 4.2620021506 0.9386059369  
C -5.6072388221 -0.3557450911 0.9080558025  
C -5.6330599218 0.1795900327 -1.5403811307  
H -9.3396079508 1.9117740433 0.1258915531  
H -8.3185729301 2.8141118333 1.287461368  
H -8.2945538793 1.0311848003 1.2830841774  
H -5.4227929855 3.0168596775 -2.2946017208  
H -5.0527983715 4.6367587035 -1.683666319  
H -6.7154719021 4.0092031031 -1.5968820041  
H -5.4637249307 3.8804908257 1.9415874916  
H -6.7230866392 4.5495377276 0.8777711346  
H -5.0673167439 5.1600920485 0.7643933592  
H -5.3746913772 0.0164921396 1.9089295389  
H -5.0130802525 -1.2491804935 0.7060953409  
H -6.6675808541 -0.6259003035 0.8722648702

H -5.4630727041 0.9266352201 -2.3177850145  
H -6.6737390641 -0.1472359209 -1.5975334355  
H -4.97820033 -0.6753044509 -1.7304265985

1,2,5,8-THAQ Aq-STY

C -3.8354593542 2.5540231864 -0.2412167135  
C -3.7670036861 1.2153987999 0.039418136  
C -2.5257550801 0.5772057829 0.292840675  
C -1.3558749781 1.3399320809 0.2274872505  
C -1.4250347295 2.7384184755 -0.0652332601  
C -2.6659369429 3.3523544519 -0.2882946491  
C -0.20764067 3.5364864587 -0.1194052216  
C 1.0868673456 2.8833252349 0.1110894292  
C 1.1645467526 1.5013076319 0.4004952602  
C -0.0659956646 0.6874434667 0.4781812604  
C 2.2644824937 3.634229301 0.0473685858  
C 3.510990567 3.0085871575 0.2676785836  
C 3.5707363656 1.6528546105 0.5497023977  
C 2.3965050866 0.900329215 0.6168780295  
O -0.2472877365 4.7672934205 -0.3601023185  
O 0.0015648868 -0.5198415746 0.7497562437  
C -5.2638048088 3.016694884 -0.409557573  
C -5.1395079802 0.5895494039 0.0952706338  
O -2.5246228138 -0.724929466 0.5963495656  
O -2.8019234701 4.6615326927 -0.5296190106  
O 2.323555053 4.9527739374 -0.2159164647  
O 4.6383867287 3.7430505848 0.2018131798  
H 4.5429083577 1.2012946552 0.7147234079  
H 1.4028995062 5.2737517745 -0.3450329412  
H 4.4024109854 4.6605699927 -0.0028320686  
H 2.4257907513 -0.1606963517 0.8379972054  
H -1.5787550194 -0.9878971883 0.7353704396  
H -1.9036889972 5.0624583689 -0.53209731  
N -6.0125608708 1.7048024497 -0.4266078419  
O -7.1793268255 1.8024252693 0.3633378378  
C -8.4014923897 1.6106780489 -0.3708305357  
C -5.4618059067 3.7477268197 -1.7423001669  
C -5.6487006275 3.9280897134 0.7636735762  
C -5.4613229909 0.1791965587 1.5390181227  
C -5.2279585577 -0.6245833526 -0.8367488296  
H -9.1381463932 1.6962471649 0.4370807865  
C -8.5087706773 0.223718009 -0.9789001568  
H -5.2665209349 3.0650727039 -2.5742309846  
H -4.7839880567 4.6013235036 -1.8071081925  
H -6.4872823645 4.1124204652 -1.8261300684  
H -5.5583004467 3.4054776303 1.7195096664  
H -6.6792732399 4.2693825974 0.6513540097  
H -4.9853046484 4.7969289503 0.7646966001  
H -5.4287767974 1.039656796 2.2120660603  
H -4.7259765796 -0.5606027754 1.865432353  
H -6.4594048448 -0.2601430893 1.5951680364

H -5.0885040732 -0.3087685429 -1.8746876795  
H -6.2045446203 -1.1029252082 -0.7431344191  
H -4.4622092642 -1.3575671734 -0.5760777007  
C -8.660343268 2.744579095 -1.3443206391  
C -9.020652799 3.9944121904 -0.8293373611  
H -9.1391510296 4.1081444549 0.2461092346  
C -9.2127732862 5.0868851899 -1.6700508173  
H -9.4850590207 6.0516519057 -1.2533676409  
C -9.0594682511 4.9370060054 -3.0491638968  
H -9.2085682632 5.7854916961 -3.7095752705  
C -8.7221927528 3.6916839067 -3.5741859434  
H -8.6048010957 3.5677723134 -4.6463118642  
C -8.5237275493 2.6023008398 -2.7257815186  
H -8.2434439153 1.6432816484 -3.1489946294  
H -8.377239024 -0.5319068132 -0.1997784614  
H -7.7477616591 0.0701069216 -1.74615062  
H -9.4960599251 0.0899431198 -1.4305537978

1,2,5,8-THAQ Aq-EIB

C -3.8573543715 2.7347129155 -0.1795450832  
C -3.8240194436 1.3664224937 -0.2155066001  
C -2.5980820255 0.6560854231 -0.1713990145  
C -1.4068300443 1.3840188694 -0.1011747035  
C -1.4390980296 2.8134697519 -0.0575765228  
C -2.6652050644 3.4934465192 -0.0889239849  
C -0.1982395109 3.57219389 0.029174018  
C 1.0804305716 2.8514193272 0.0570822009  
C 1.1217521505 1.4383728916 0.0132602703  
C -0.1311770973 0.6592916975 -0.0595774541  
C 2.2793987087 3.5667487611 0.1297519185  
C 3.5108614269 2.8760981115 0.1562090495  
C 3.5347215108 1.4909809632 0.1120608361  
C 2.3392472952 0.7731291557 0.0413220918  
O -0.2059836497 4.8257287652 0.079418797  
O -0.0955498725 -0.5788339354 -0.0843367145  
C -5.2743345842 3.2593445025 -0.2121495537  
C -5.2119025718 0.7766842789 -0.2400813741  
O -2.6341964839 -0.6802724651 -0.1886291498  
O -2.7666712741 4.8268139746 -0.0250348436  
O 2.3742043161 4.9082876769 0.1786045724  
O 4.6588167659 3.5772596082 0.2253732408  
H 4.4960394238 0.989333629 0.1343169427  
H 1.4620594859 5.2746212816 0.1575528963  
H 4.447449063 4.5229273529 0.2471112275  
H 2.3404331504 -0.3105641988 0.0072344406  
H -1.6951604565 -0.9947805196 -0.1541368266  
H -1.8563037829 5.1955108074 0.0321748392  
N -6.0674408074 1.9982914827 -0.4621248913  
O -7.1913768172 1.9580118563 0.3930524932  
C -8.4545369199 1.9351128962 -0.2811294548  
C -5.4599830519 4.2311717989 -1.3840114405

C -5.6196333166 3.9436271436 1.1162481212  
C -5.4841953208 0.0690027801 1.0949295394  
C -5.3925388857 -0.1780770968 -1.425043657  
C -9.4613729372 2.0352540526 0.8648705813  
C -8.6753824273 0.5961304061 -1.0021159198  
C -8.6260161045 3.0710412443 -1.2739929279  
H -5.2928170348 3.7095583141 -2.3306671203  
H -4.7556101315 5.0612229367 -1.3000279862  
H -6.4720582122 4.6387321685 -1.3854720025  
H -5.515541299 3.2530989673 1.9569644511  
H -6.649562296 4.3075311325 1.0995297291  
H -4.9449281737 4.7910880677 1.2601187447  
H -5.362818494 0.7597911632 1.9339628538  
H -4.7708655011 -0.7523042143 1.2054289792  
H -6.5017583748 -0.3223358888 1.1144898626  
H -5.1542824115 0.336157855 -2.3600614354  
H -6.4295017146 -0.5129384501 -1.4784282486  
H -4.7440217405 -1.0504108343 -1.3171183754  
O -8.4818134482 -0.4512034909 -0.1869573101  
C -8.7119639841 -1.7504741074 -0.7594376335  
C -8.1446618706 -2.7729959752 0.2005146272  
O -9.0310969957 0.4860614215 -2.1509748302  
H -10.4823741772 1.9535963314 0.4818479721  
H -9.3446988854 3.0043960526 1.3570629595  
H -9.2849870778 1.2405064988 1.5920481823  
H -9.6275210253 3.0326512975 -1.7077144487  
H -7.8994506558 2.9898384927 -2.0830882327  
H -8.5004518835 4.0239477431 -0.7521674702  
H -8.2317855703 -1.7955768142 -1.7411685819  
H -9.7893730227 -1.8728228078 -0.9097566114  
H -7.0640643969 -2.6422931785 0.3056571502  
H -8.3360838371 -3.7810262239 -0.1762339437  
H -8.6047668032 -2.6768745501 1.1871607591

1,2,5,8-THAQ Aq-EP

C -3.8597271152 2.7099007539 -0.1708941974  
C -3.8170081166 1.3419899981 -0.2182588977  
C -2.5861511263 0.6399796956 -0.1846684855  
C -1.3997498903 1.3759944738 -0.1168233437  
C -1.4416201041 2.804776635 -0.0625374759  
C -2.672697443 3.476330789 -0.0798603602  
C -0.2053463907 3.5714565157 0.0223065558  
C 1.0784804754 2.8595109069 0.0354095529  
C 1.1290857437 1.4471442677 -0.0193355865  
C -0.1188385641 0.659964019 -0.0884437334  
C 2.2729920877 3.5825255477 0.1048493105  
C 3.5093115821 2.9001220225 0.1168936904  
C 3.5422734574 1.5155463304 0.0620975854  
C 2.3512364922 0.7900797316 -0.0051941727  
O -0.2215926386 4.8243775259 0.0829483246  
O -0.074860179 -0.5777103575 -0.1211942955



C -5.2810709388 3.2230302759 -0.1795621293  
C -5.2008932935 0.7427145865 -0.2433842815  
O -2.6130097064 -0.6964653146 -0.2085741766  
O -2.7836937322 4.8081495191 -0.0017032101  
O 2.3588950209 4.9242697686 0.1633166829  
O 4.6529186207 3.6085727658 0.1829472785  
H 4.5071031754 1.0203517005 0.0734574388  
H 1.4441634349 5.284433983 0.1517185103  
H 4.4353524254 4.5525796878 0.2138835791  
H 2.3596367258 -0.2933015075 -0.0472832006  
H -1.6715392703 -1.0045840218 -0.1819526319  
H -1.8758616706 5.1832306249 0.0526995307  
N -6.0607922702 1.961708349 -0.4611158864  
O -7.1997948598 1.9051977596 0.3761423725  
C -8.4298063402 1.8614874562 -0.3391433648  
C -5.4939273069 4.2277308869 -1.3173288831  
C -5.6186340825 3.8620461652 1.1737042417  
C -5.4717193301 0.0273304375 1.0875240593  
C -5.3745054004 -0.2092198308 -1.4316570155  
C -8.6418328996 0.5249259079 -1.0537490529  
C -8.6577167855 3.0197082632 -1.288026295  
H -5.3201169355 3.7422882241 -2.2818029018  
H -4.8094475454 5.0713108898 -1.2089332684  
H -6.5158747622 4.6099672808 -1.2991916534  
H -5.5030675424 3.1454046703 1.9906878971  
H -6.6498288973 4.2216626523 1.1779335793  
H -4.9460898298 4.7074164645 1.3394332068  
H -5.3547101514 0.7132771285 1.9310180525  
H -4.7554864583 -0.7919184785 1.1947848034  
H -6.4879634241 -0.3680683848 1.1028926672  
H -5.1541037314 0.3137384268 -2.3661036346  
H -6.4046178274 -0.5654696374 -1.4778498526  
H -4.7090016757 -1.0696978106 -1.3329212126  
O -8.4797396504 -0.5112866992 -0.2190296361  
C -8.6916075446 -1.8181474003 -0.7824306371  
C -8.1529094534 -2.8284418186 0.2064024758  
O -8.9621365271 0.4074540745 -2.211745638  
H -9.6600650228 2.9506108509 -1.7160607588  
H -7.9351670595 2.9914201071 -2.1048758606  
H -8.5690122904 3.9624509245 -0.7427692789  
H -8.1820224636 -1.8744620973 -1.7486431747  
H -9.7639556147 -1.9431552749 -0.9633738036  
H -7.075806838 -2.6965220603 0.3411963666  
H -8.3337203584 -3.8411184236 -0.1630149749  
H -8.6415024753 -2.7194905612 1.1777937121  
H -9.1660957073 1.8868606344 0.4737654881

1,2,5,8-THAQ Aq-Me

C -3.9310249706 2.746095665 -0.0424573516  
C -3.916340582 1.373222451 0.0021200179  
C -2.7001545787 0.6508484843 0.0370506155

C -1.498425765 1.3657669149 -0.0001024132  
C -1.5119590732 2.7956496891 -0.04681338  
C -2.7304737014 3.4909545866 -0.0556581342  
C -0.2595057305 3.5404426421 -0.0716218902  
C 1.0108235033 2.8043510778 -0.0643360215  
C 1.033701847 1.3910183283 -0.0191307459  
C -0.2301106718 0.6268949255 0.024431131  
C 2.2198728521 3.50539629 -0.100183338  
C 3.443148455 2.7999429695 -0.0937148008  
C 3.4490141317 1.4146249888 -0.0497632406  
C 2.2434002969 0.7112482398 -0.0115858151  
O -0.2511925235 4.7942906485 -0.099253253  
O -0.2095083576 -0.6101539251 0.0812467688  
C -5.3446935233 3.2789285646 -0.0009517642  
C -5.3174213765 0.814262753 0.0765114367  
O -2.7569779735 -0.6828077674 0.1142927535  
O -2.8214031841 4.8266487259 -0.0650338561  
O 2.3315167612 4.8459122713 -0.1423505309  
O 4.6010413751 3.4872809783 -0.129774261  
H 4.4043873682 0.9013187046 -0.0453378088  
H 1.4232079711 5.2225213652 -0.1378738945  
H 4.4016996613 4.4354344934 -0.1563347676  
H 2.2306244037 -0.3723184824 0.0245976273  
H -1.8237111388 -1.0121979944 0.1245305548  
H -1.9087141581 5.1908212067 -0.0781787729  
N -6.0940804958 2.0271787646 -0.310601005  
O -7.3617759762 2.0329535279 0.2950135145  
C -8.3747523811 1.985598524 -0.6982533732  
C -5.6503903683 4.3075757 -1.0928770402  
C -5.6469491788 3.8819457554 1.3797065048  
C -5.6068662612 0.291602243 1.4923889232  
C -5.5955438554 -0.2880207692 -0.9489993402  
H -9.321918669 1.9935881448 -0.1545116107  
H -8.2966645836 1.0732091483 -1.2978194289  
H -8.3177138709 2.8548822989 -1.3609771078  
H -5.4085769168 3.898108147 -2.0769066579  
H -5.0856246945 5.2279347214 -0.9326525036  
H -6.7187072877 4.544672783 -1.0664652486  
H -5.4554989568 3.1703590175 2.1852168713  
H -6.6947138774 4.1860585245 1.4299451883  
H -5.0117457671 4.7593798673 1.5295844836  
H -5.4338799666 1.0564232381 2.2519759383  
H -4.9508729115 -0.5591017803 1.6962047154  
H -6.6472201834 -0.03361333 1.5610688402  
H -5.3652744693 0.0662938157 -1.9569032505  
H -6.6569090598 -0.5522918267 -0.9057872727  
H -5.0045715867 -1.1800253097 -0.7331260058

1,5-DAAQ Aq-STY

C -5.2706448306 2.5302385779 0.1573922348  
C -5.1927643245 1.1811134643 -0.1072396596

C -3.9360401944 0.5620253559 -0.3388248052  
C -2.7684995445 1.3752018353 -0.2392723592  
C -2.8959989599 2.7533642869 0.0589383348  
C -4.1341755368 3.3380826501 0.2493705751  
C -1.7006065205 3.6506270673 0.1756769751  
C -0.3668703905 3.0765019065 -0.0290430214  
C -0.2351398737 1.7044635509 -0.3396165619  
C -1.4336806741 0.8089840744 -0.4660095249  
C 0.8005324125 3.8799099532 0.078228991  
C 1.0072789496 1.127225534 -0.5405039364  
C 2.0580610244 3.2654240284 -0.1302492353  
C 2.1543223649 1.9233981719 -0.4317551814  
O -1.8703730697 4.8409954955 0.4395277299  
O -1.2527295789 -0.3739895827 -0.7578790535  
C -6.701360299 2.991924252 0.2764739144  
C -6.5755647901 0.5554559976 -0.1368008141  
N -3.8467314109 -0.7615131409 -0.6345095167  
H -4.1891329153 4.3999203391 0.4621652489  
N 0.7505843338 5.2039420481 0.3711265799  
H 2.9537832025 3.8752578987 -0.0485544978  
H 3.1341731655 1.4819496751 -0.5861416919  
H -0.1460266079 5.6451366954 0.5183434405  
H 1.6034359696 5.7324660947 0.4378665411  
H 1.0655654588 0.0719592747 -0.7771147731  
H -4.6738556675 -1.2865932301 -0.8519154263  
H -2.9349319884 -1.1375348509 -0.8604035452  
N -7.4428787998 1.6868998342 0.3711414909  
O -8.6356078565 1.7458042082 -0.3858364937  
C -9.837939124 1.6082705052 0.391067565  
C -7.0724233037 3.8215182533 -0.9610161458  
C -6.9011473589 3.8262461552 1.5449137565  
C -6.69026474 -0.6152043575 0.8506363094  
C -6.9586484783 0.1149721137 -1.5582708734  
H -10.59492281 1.639080644 -0.401973052  
C -9.9347314321 0.2683526815 1.0984696414  
H -6.9526826222 3.2446081782 -1.8814726056  
H -6.4139762419 4.6941630139 -1.0104203395  
H -8.1067740739 4.1644299952 -0.8949436541  
H -6.7232480774 3.2122488301 2.4318245433  
H -7.9116393485 4.2358631234 1.5945552405  
H -6.1986556286 4.6657943825 1.5513946397  
H -6.5527245054 -0.2451095761 1.8699082699  
H -5.9402151517 -1.3886321775 0.6705996151  
H -7.6731414064 -1.0836971482 0.7743305929  
H -6.9417344844 0.9607549723 -2.2488412083  
H -7.961491861 -0.3165983794 -1.5701938967  
H -6.25685177 -0.6366176053 -1.9313631698  
C -10.0733921067 2.8087771313 1.2874417004  
C -10.4458410389 4.0192291204 0.6930337866  
H -10.5873701762 4.0568541283 -0.3849668627  
C -10.6206595507 5.1684684656 1.4584752964

H -10.9032648539 6.1014588449 0.9807588719  
C -10.4363794589 5.1165142673 2.841057402  
H -10.5715269152 6.0097743805 3.4428326572  
C -10.0860118036 3.911480145 3.4453778877  
H -9.9441112531 3.8638580193 4.520620764  
C -9.9060245681 2.7644285343 2.6720110254  
H -9.6158150362 1.8373801454 3.1556764714  
H -9.8388525752 -0.5412513188 0.3700030453  
H -10.906684178 0.1776032229 1.5920440234  
H -9.1484571148 0.160139843 1.8479467441

1,5-DAAQ Aq-EIB

C -5.3653065436 2.6607838579 0.3313819712  
C -5.3428924092 1.2984669486 0.1315479226  
C -4.1154493712 0.6254482954 -0.1061819477  
C -2.9191127851 1.4027755652 -0.0847260785  
C -2.9906427506 2.7971077798 0.1488418542  
C -4.2018109276 3.4333952613 0.3489332312  
C -1.7628585308 3.6571612027 0.182966368  
C -0.4565434798 3.0276722285 -0.0325988021  
C -0.3803512416 1.6378500702 -0.2760507861  
C -1.6112866986 0.7795050746 -0.3205561814  
C 0.7396821056 3.7944229049 -0.0015854858  
C 0.8352415862 1.0084711491 -0.4838588393  
C 1.968952068 3.126859165 -0.2157166842  
C 2.0110144674 1.7688994868 -0.4504380759  
O -1.8854055728 4.864295215 0.3910027017  
O -1.479594245 -0.4224716595 -0.5551070004  
C -6.7741676811 3.1767305429 0.4703858631  
C -6.7456863036 0.7188457686 0.1877005276  
N -4.0794873955 -0.7119930698 -0.3386673491  
H -4.2161039121 4.505442939 0.5117867647  
N 0.7430398935 5.1324934495 0.2234129739  
H 2.8865491158 3.7085019291 -0.1923973259  
H 2.9702789367 1.2863643068 -0.6110795693  
H -0.1327338592 5.6109553933 0.3792245442  
H 1.6152419588 5.6325269504 0.2440552255  
H 0.8511966781 -0.0587533139 -0.6675223455  
H -4.9299480941 -1.2274738598 -0.4718194762  
H -3.1874175518 -1.1356835366 -0.5583399528  
N -7.5547658473 1.908459864 0.6550534443  
O -8.7703580145 1.9733188603 -0.0643283619  
C -9.9558862795 1.9250156508 0.738466993  
C -7.1558771062 3.9568364374 -0.7958561546  
C -6.9136437038 4.0541797019 1.7170133906  
C -6.8593854221 -0.3809586323 1.2530843571  
C -7.2022292748 0.2066011117 -1.1865671425  
C -11.0735439401 1.8219686924 -0.3000148924  
C -10.1507354821 3.2339845185 1.5203915892  
C -9.9872271573 0.7552555062 1.7057236611  
H -7.0370352806 3.3380108226 -1.6892571565

H -6.4928273102 4.8229802601 -0.8888728267  
H -8.1910491364 4.2961437303 -0.7401634213  
H -6.6366036323 3.4878163312 2.6095433444  
H -7.9400616495 4.4047120195 1.8340163712  
H -6.2651243925 4.932959919 1.639251389  
H -6.6319928582 0.0383821697 2.2364096994  
H -6.170168897 -1.2090273955 1.072539938  
H -7.8704911021 -0.7903784538 1.2721624407  
H -7.1952027963 1.0095015077 -1.9268322533  
H -8.2157146616 -0.1967742347 -1.1285581392  
H -6.5372700647 -0.5852630385 -1.5428136258  
O -10.0868587959 4.3097694563 0.7217097061  
C -10.3135914447 5.5816020859 1.3537015961  
C -9.9023572872 6.6539984593 0.3689909638  
O -10.3861203051 3.299064862 2.7031736815  
H -10.9763176772 0.8732968369 -0.8344736667  
H -11.0016579232 2.6445471818 -1.0138650729  
H -12.0510972118 1.8535605033 0.1892826588  
H -9.9273868681 -0.1785072114 1.1400345801  
H -10.923403501 0.7695251347 2.2675800809  
H -9.160222838 0.8163015968 2.4140519866  
H -9.7327192067 5.626730758 2.2794727348  
H -11.3728507189 5.6471404152 1.6221620038  
H -8.8352436789 6.577990756 0.1425702338  
H -10.0963031999 7.6419751035 0.7943827919  
H -10.4632827908 6.560308668 -0.5642009702

1,5-DAAQ Aq-EP

C -5.3483023146 2.6468071293 0.3613422094  
C -5.3249179849 1.2842432039 0.161364517  
C -4.0983061265 0.6124108457 -0.0818483984  
C -2.9025392998 1.3905942579 -0.063679449  
C -2.9744205021 2.7847860576 0.169867929  
C -4.1854604942 3.4203536911 0.3741218376  
C -1.7469406101 3.6456330515 0.199782493  
C -0.4409141417 3.0167914582 -0.0197067153  
C -0.3646715158 1.6269678704 -0.2630331298  
C -1.5951763328 0.7679639483 -0.3036916499  
C 0.7550169367 3.784222422 0.0070176025  
C 0.850551785 0.9981577205 -0.4745920642  
C 1.9839455674 3.117234486 -0.2110603953  
C 2.0259906622 1.7591920102 -0.4453387119  
O -1.8695987641 4.8527287235 0.4078768711  
O -1.4639363468 -0.433929027 -0.5387423295  
C -6.7580116918 3.160049739 0.5064220735  
C -6.7276512806 0.705046155 0.2128686808  
N -4.0632627189 -0.7242976209 -0.3174623291  
H -4.1996104383 4.492434075 0.5365148059  
N 0.758249865 5.1223213108 0.2315896892  
H 2.9012630701 3.6994306021 -0.1910871205  
H 2.9849626763 1.2771186753 -0.6090561676

H -0.1174206555 5.6003352132 0.3893006742  
H 1.6300289174 5.6232276451 0.2482388055  
H 0.8664024846 -0.0691197606 -0.6579629328  
H -4.9143529784 -1.239796955 -0.4459818547  
H -3.1717920865 -1.1485231756 -0.5383275322  
N -7.5280341371 1.8878702802 0.7063501751  
O -8.764699289 1.9439399043 0.0190443879  
C -9.9039942527 1.917225439 0.873163055  
C -7.155347833 3.9309571887 -0.7604721793  
C -6.891018607 4.0467168118 1.7470428832  
C -6.8517653826 -0.4139997905 1.2554500824  
C -7.1865302594 0.2205656 -1.1711829933  
C -10.1010630881 3.2354980249 1.625475401  
C -9.9713931419 0.740012 1.8236530258  
H -7.0331694988 3.3127498542 -1.6535998087  
H -6.5043629795 4.8056014901 -0.8588411204  
H -8.1946609427 4.2568984874 -0.6996653372  
H -6.6263537196 3.4824955921 2.644549502  
H -7.9119284967 4.4152655853 1.8570109093  
H -6.2298025907 4.9155294931 1.6659347204  
H -6.5871657822 -0.0276411439 2.242936659  
H -6.200655042 -1.2639204495 1.0386504225  
H -7.8769647136 -0.7858695253 1.2874059186  
H -7.1874692749 1.0391590759 -1.8938607759  
H -8.1962082276 -0.1922064908 -1.1190114459  
H -6.515081952 -0.5570817376 -1.5465135597  
O -10.0928713572 4.2842232918 0.7904543772  
C -10.3180728452 5.5720847775 1.3906107876  
C -9.987961455 6.6185376683 0.3492511191  
O -10.2918635331 3.3287887109 2.8139131553  
H -9.9520461068 -0.1924251537 1.2548588557  
H -10.900979304 0.7859584386 2.3947563401  
H -9.1364252461 0.7663621996 2.5254224351  
H -9.6894800411 5.6633115011 2.2812556879  
H -11.3625966356 5.6216527751 1.7142702411  
H -8.9331851952 6.5597642394 0.0671657025  
H -10.1835930182 7.6159754373 0.7510824505  
H -10.5961608311 6.4785845099 -0.5477088242  
H -10.7274209017 1.8654021621 0.1499003419

1,5-DAAQ Aq-Me

C -5.3624272872 2.6501966506 -0.000274783  
C -5.3162390225 1.2706909656 -0.0583388443  
C -4.0752941583 0.5898353763 -0.0912792615  
C -2.8872436848 1.3768525839 -0.0300002351  
C -2.9816309344 2.7874083858 0.0396576964  
C -4.2069526221 3.4313378794 0.0506372466  
C -1.7613562344 3.6562226583 0.104244492  
C -0.4412242551 3.0176570894 0.1077380019  
C -0.3429730314 1.6093616996 0.0437959031  
C -1.5647800465 0.7406231739 -0.0313925356

C 0.7472534793 3.7941907063 0.1751011818  
C 0.8856728749 0.9713851734 0.0460672251  
C 1.9903447067 3.1176440802 0.1766237549  
C 2.0533347575 1.7417770362 0.113767387  
O -1.900781893 4.8783331165 0.1542226627  
O -1.4163998912 -0.4803890606 -0.0899618049  
C -6.7871700214 3.1467486251 -0.045624611  
C -6.7179792551 0.6920822686 -0.1448594909  
N -4.0313689475 -0.7625209404 -0.2025344189  
H -4.2361713467 4.5144112137 0.0986612589  
N 0.7306623293 5.1495386348 0.2374569606  
H 2.9019115935 3.7068994782 0.2284265155  
H 3.0228162895 1.2529997364 0.1165759668  
H -0.1553331464 5.6346559103 0.2358915756  
H 1.5973206387 5.6572272427 0.2856338225  
H 0.9173855919 -0.1100422605 -0.0049592153  
H -4.8773424005 -1.2980797746 -0.1326968531  
H -3.1309090413 -1.2204897617 -0.1578486159  
N -7.5104938647 1.8861963447 0.2703522316  
O -8.7899544251 1.8543409041 -0.3136493314  
C -9.7878891363 1.9172791692 0.69293423  
C -7.1084008126 3.7414908573 -1.4254297531  
C -7.0819269402 4.1833225457 1.0408170001  
C -7.0404363082 -0.4151625573 0.8685782888  
C -7.0287091247 0.1956026184 -1.5673269325  
H -10.7426953997 1.8419018546 0.1680075265  
H -9.741269477 2.8640649338 1.2405298126  
H -9.6838947073 1.0905877171 1.4027935933  
H -6.857754452 3.0549827156 -2.2358053471  
H -6.5245760452 4.656413371 -1.5644663114  
H -8.1711180592 3.9860172257 -1.4912500347  
H -6.8846029498 3.7618564342 2.0292394959  
H -8.1301218272 4.4941486582 0.9891078222  
H -6.4632391353 5.0754302654 0.9020645421  
H -6.6629339527 -0.1566575504 1.8606763225  
H -6.6505722601 -1.3951831126 0.5758247948  
H -8.128034651 -0.5206750008 0.9228446634  
H -6.9133300852 0.9902939386 -2.3053704343  
H -8.0532010511 -0.1799011083 -1.6203456427  
H -6.3412903767 -0.6127381116 -1.8356675186

1,4-DAAQ Aq-STY

C -5.2134444077 2.5625617912 0.1327482804  
C -5.1128177705 1.1913807103 -0.0891307953  
C -3.875560795 0.584012279 -0.240447293  
C -2.7232157233 1.372510088 -0.1683244918  
C -2.8234214916 2.7518593958 0.0541722794  
C -4.0764073734 3.3532724408 0.2074054858  
C -1.6053173837 3.6038927304 0.1345040893  
C -0.291450049 2.9670597791 -0.0218776845  
C -0.1889640748 1.5485444439 -0.2494684814

C -1.396610652 0.7174942143 -0.3300020424  
C 0.8670405209 3.7600983828 0.0542798531  
C 1.0705660604 0.9414109319 -0.3972276594  
C 2.1278927876 3.1142779432 -0.0989649621  
C 2.2248157076 1.772626283 -0.313751875  
O -1.7375959464 4.8156572041 0.3298146956  
O -1.3535398428 -0.5008388289 -0.525682127  
C -6.6572253178 2.9906667787 0.2389973012  
C -6.4793343103 0.5563132975 -0.1631881444  
H -3.7635842546 -0.4821015394 -0.4152318771  
H -4.1193848924 4.424830109 0.3791143982  
N 0.8592423688 5.1045185995 0.2636144407  
N 1.2556636953 -0.3888763615 -0.6151999367  
H 3.030420769 3.7173729666 -0.0416991423  
H 3.2039821074 1.3142416175 -0.4261417373  
H -0.0246453179 5.5794784195 0.3797685783  
H 1.7291936578 5.6056422245 0.3143318898  
H 0.4493942505 -0.9944265406 -0.6762729847  
H 2.1879726396 -0.7534531888 -0.7067514979  
N -7.3618772218 1.660673365 0.3625660508  
O -8.5706407232 1.6790115123 -0.3711272329  
C -9.7493316434 1.5040390559 0.4328497946  
C -7.0636631402 3.787448506 -1.0083860428  
C -6.8741519841 3.8422871208 1.4930844966  
C -6.5543176492 -0.6741011124 0.7442189462  
C -6.7918458336 0.1531682685 -1.6118054697  
H -10.5265554888 1.5084941139 -0.3409030568  
C -9.7817377264 0.1622405401 1.1429094209  
H -6.9305636496 3.2039424522 -1.9222839072  
H -6.4358268744 4.6816063306 -1.0733226653  
H -8.1091172995 4.0953380953 -0.9402492473  
H -6.6780896137 3.2489423229 2.3899786191  
H -7.8932948113 4.2306088904 1.5404705659  
H -6.1896316343 4.6970501458 1.4796503835  
H -6.4116164873 -0.3830552196 1.7884326127  
H -5.7717366904 -1.3885158299 0.4692357877  
H -7.5156749896 -1.1811898714 0.6418684128  
H -6.7461426917 1.0110290068 -2.2863597198  
H -7.7878475067 -0.2890400632 -1.6832128116  
H -6.0516069963 -0.5836296956 -1.9390138084  
C -10.0007284104 2.6982608355 1.3329477741  
C -10.4349964704 3.8924320042 0.7476535497  
H -10.6107427855 3.9212495143 -0.3256053298  
C -10.6277346614 5.0371349881 1.5156994077  
H -10.9591068008 5.9576406276 1.0450568109  
C -10.3975195366 4.9967497764 2.8917449057  
H -10.5462396939 5.8864389401 3.4956425958  
C -9.9832914922 3.8074820257 3.4872254528  
H -9.8046798081 3.7692857819 4.5574034898  
C -9.7866930848 2.665012062 2.7113215632  
H -9.4471132329 1.7503720099 3.1866238044



H -9.694733192 -0.6437209259 0.4095639203  
H -10.7290065196 0.0451963023 1.6773116467  
H -8.9604686177 0.0746819521 1.8571207203

1,4-DAAQ Aq-EIB

C -5.3583981185 2.691172838 0.5007119759  
C -5.3294902702 1.3315783563 0.1983900362  
C -4.1285685435 0.6851216661 -0.0506867657  
C -2.9414221814 1.4221414324 0.0047316239  
C -2.9704971217 2.7887312495 0.3098534972  
C -4.1872045645 3.4305060476 0.5616008594  
C -1.7143293455 3.5853851337 0.3738618164  
C -0.4384913491 2.9073205877 0.1106880388  
C -0.4087164639 1.5017552107 -0.2022826915  
C -1.6535798677 0.7252967664 -0.2639919885  
C 0.7560376694 3.6452310243 0.180588426  
C 0.8152684689 0.8525957854 -0.4409867296  
C 1.9798422783 2.9560762432 -0.0577939655  
C 2.0080832847 1.6266213868 -0.353610863  
O -1.7850421636 4.786634724 0.6485451627  
O -1.6730903913 -0.4806574971 -0.5263047554  
C -6.7751148147 3.1698313028 0.7002936999  
C -6.7242486847 0.7553774018 0.1680347884  
H -4.0711427641 -0.3728889068 -0.2895051785  
H -4.1762968771 4.4911325299 0.7953513929  
N 0.8159149701 4.9808086373 0.441510391  
N 0.9315042626 -0.4640326575 -0.7696803566  
H 2.9097082542 3.5165380147 -0.0055170075  
H 2.9602896232 1.1348974706 -0.5353036517  
H -0.0348501179 5.4663911117 0.6889444326  
H 1.7122306797 5.4109370483 0.5935509612  
H 0.1031547227 -1.0424898344 -0.7626667091  
H 1.8458833685 -0.880848613 -0.8100186713  
N -7.5243745207 1.8667867256 0.7959229934  
O -8.7762708225 1.9671962697 0.1467769938  
C -9.9156400888 1.8168494239 1.0019438608  
C -7.2075840231 4.0453456605 -0.4840247182  
C -6.9053070645 3.9379647403 2.0179729026  
C -6.8057524241 -0.5126495604 1.0207703878  
C -7.1369018389 0.4407826655 -1.2771127485  
C -11.0839515452 1.747365846 0.017647223  
C -10.1122982028 3.0608748038 1.8829621716  
C -9.8558968539 0.5803858091 1.88106092  
H -7.0849357312 3.5183555238 -1.4334265415  
H -6.5780756379 4.9410148392 -0.5066909801  
H -8.2532241078 4.3390418804 -0.3795475432  
H -6.6222425633 3.2979369907 2.8570278675  
H -7.9292393985 4.2813512304 2.1719816039  
H -6.2545984598 4.8189035273 2.0078638922  
H -6.5730116993 -0.2840608886 2.064048454  
H -6.0884009332 -1.2542111385 0.6548459058

H -7.8008228864 -0.9583603783 0.9678698824  
H -7.0983586135 1.3306424237 -1.9093820181  
H -8.1520407854 0.0384311143 -1.308906475  
H -6.447321755 -0.3043528621 -1.6856302676  
O -10.1139889639 4.1912032057 1.1596669611  
C -10.3528430972 5.4072617869 1.8884332012  
C -10.0318022691 6.5585324397 0.9608415348  
O -10.2978859339 3.0378944991 3.0761899545  
H -10.982351595 0.8447387132 -0.5904884022  
H -11.079383821 2.6220157774 -0.6353454832  
H -12.0340973067 1.7052918379 0.5576641749  
H -9.8284682108 -0.3090046739 1.2464700787  
H -10.7446408896 0.5376438379 2.5138091314  
H -8.97468183 0.604690555 2.5233783052  
H -9.7264654167 5.4130136814 2.7853142101  
H -11.3981928459 5.4134634282 2.2134413873  
H -8.9764935052 6.537718208 0.6751069312  
H -10.2359311972 7.5077105369 1.4629170516  
H -10.6385271051 6.5067670592 0.0533994282

1,4-DAAQ Aq-EP

C -5.3444694262 2.6777888753 0.5024323545  
C -5.3109998185 1.3142191529 0.2180431825  
C -4.1092670302 0.6699621526 -0.0318212618  
C -2.9253454595 1.4132542421 0.0044452857  
C -2.9585876439 2.7837263615 0.2907309131  
C -4.1763511208 3.4233323513 0.5434850964  
C -1.7055127853 3.5867670257 0.3343892963  
C -0.4285624992 2.9105561868 0.0720524261  
C -0.3947344418 1.5009078577 -0.2217358271  
C -1.6364095075 0.7184778251 -0.2643844752  
C 0.7632318294 3.6543742942 0.1236292884  
C 0.8303266646 0.8536033282 -0.4598217384  
C 1.9884039032 2.9670556753 -0.1136618928  
C 2.0204031806 1.6338112389 -0.391301336  
O -1.7797300016 4.791514325 0.5923830379  
O -1.6526385868 -0.4909457619 -0.5105678971  
C -6.7622189658 3.1511937581 0.709955038  
C -6.7032469746 0.7318991816 0.2033815136  
H -4.0487732931 -0.3909061256 -0.2567573008  
H -4.1681466745 4.4870578503 0.7628004461  
N 0.8190201779 4.993379713 0.3665244328  
N 0.9496148074 -0.4670217798 -0.7703762162  
H 2.9161798894 3.532066215 -0.0752268876  
H 2.9734883066 1.1436257594 -0.5725005402  
H -0.0324424869 5.4794587611 0.6105582529  
H 1.7144041688 5.4307078499 0.5024926336  
H 0.1232858242 -1.0482240826 -0.7513737303  
H 1.8653332283 -0.8805106637 -0.8139317245  
N -7.4999133505 1.8437059237 0.8329422743  
O -8.7659395016 1.926235881 0.2049271193

C -9.8617474804 1.7875535463 1.1034392699  
C -7.2167790396 4.007355598 -0.4799918325  
C -6.8826171368 3.9385929695 2.0171215346  
C -6.7769396662 -0.5312992532 1.0630959185  
C -7.1263423595 0.4093812236 -1.2372103951  
C -10.0631527709 3.033716806 1.9685530817  
C -9.840496368 0.533674272 1.9528468218  
H -7.1003776784 3.471168673 -1.4248676749  
H -6.5972132368 4.9092442427 -0.520424766  
H -8.2642697986 4.2914215608 -0.3660369518  
H -6.6034502185 3.308410803 2.864804728  
H -7.9027030381 4.2949298374 2.1678387581  
H -6.2243645523 4.8134801048 1.9922636335  
H -6.5321534113 -0.2979834108 2.1025583894  
H -6.0658596961 -1.2766775693 0.692755625  
H -7.7739889407 -0.9742805009 1.0231245349  
H -7.0943819645 1.296054413 -1.8741694539  
H -8.1400421526 0.0036100751 -1.259866402  
H -6.437342397 -0.335414193 -1.6472855841  
O -10.1215696033 4.1453241498 1.2204479216  
C -10.3598484953 5.3730973779 1.9301847318  
C -10.1068839398 6.5083741274 0.9628178595  
O -10.2045638288 3.0274628808 3.1675010856  
H -9.83712562 -0.3464516645 1.3062654983  
H -10.7302971492 0.5054835393 2.5850889284  
H -8.9598542616 0.5236917536 2.5969017387  
H -9.6965150074 5.4155909395 2.7991338853  
H -11.390392249 5.3622214683 2.2992123382  
H -9.0647853848 6.5045484294 0.6316133176  
H -10.3115890457 7.4646368645 1.4510074124  
H -10.7508979076 6.4202171688 0.0844699238  
H -10.7180280131 1.7647403949 0.4177743601

1,4-DAAQ Aq-Me

C -5.2869219262 2.7211311169 -0.0276726587  
C -5.2390367237 1.323284584 -0.0657508089  
C -4.0265015252 0.6549498826 -0.0566484192  
C -2.844260883 1.4034074611 -0.0108500017  
C -2.8921698608 2.8020474669 0.0271981741  
C -4.1228998142 3.4693084212 0.0199601289  
C -1.6423464916 3.6092350086 0.0801841748  
C -0.3532511474 2.9073887335 0.0942475196  
C -0.3039547566 1.4684248298 0.0549517378  
C -1.5420794424 0.6818775349 0.0005983597  
C 0.8343280714 3.6580854668 0.1473447921  
C 0.932288282 0.7989317227 0.0691632515  
C 2.0706685134 2.9494256264 0.1610349261  
C 2.1172903389 1.5886856567 0.1237920285  
O -1.7299035304 4.8403781278 0.1110583151  
O -1.5452178895 -0.552228028 -0.0354772206  
C -6.7178924418 3.2038490078 -0.071431653

C -6.6337202259 0.7469736475 -0.1386021547  
H -3.9555184598 -0.4285752552 -0.0818775344  
H -4.1261755971 4.5549181932 0.0537954855  
N 0.8769870165 5.0172808697 0.1861521503  
N 1.0679153513 -0.5542313167 0.0331192374  
H 2.9952825495 3.5193943075 0.2022956664  
H 3.0788002861 1.0818918962 0.1354802135  
H 0.0111331567 5.5374135826 0.1784857196  
H 1.7649427878 5.48683547 0.2261945735  
H 0.2396049143 -1.1312251967 -0.0026684163  
H 1.9858930408 -0.9635045855 0.0522182733  
N -7.4254832366 1.9392513774 0.2778610566  
O -8.7207769888 1.9097584526 -0.2680737951  
C -9.6803509774 1.8487618897 0.7751116013  
C -7.0632975486 3.7661383563 -1.4594048877  
C -7.0247715064 4.2547450166 0.9965352706  
C -6.8662325336 -0.3792933646 0.8696142682  
C -6.9421840434 0.2391904303 -1.5560124638  
H -10.6547333487 1.828293716 0.2819033609  
H -9.6100613926 2.7262695645 1.4261426955  
H -9.5484885873 0.9447305368 1.3785468882  
H -6.8223833676 3.0631248562 -2.2583600828  
H -6.4858435537 4.6804847345 -1.6271906218  
H -8.1280978268 4.0038102736 -1.5141800238  
H -6.7897665798 3.8651928616 1.9897790842  
H -8.0862135551 4.5209022095 0.9607478556  
H -6.4446675235 5.1666008335 0.821984401  
H -6.6567265118 -0.0295577414 1.8831772955  
H -6.2254575942 -1.2384511176 0.6466249278  
H -7.9070587366 -0.7150216577 0.8171263353  
H -6.7510370562 0.9996756641 -2.3147797198  
H -7.9883807198 -0.0671683446 -1.6259621721  
H -6.3039804048 -0.6230927797 -1.7723271342

1,4,5-TAAQ Aq-STY

C -5.2116791431 2.5782700115 0.1665785838  
C -5.1579402621 1.2247409177 -0.0905762366  
C -3.9161031642 0.5776937765 -0.3144947616  
C -2.7285947381 1.3661375326 -0.2185477917  
C -2.8340500695 2.7446875148 0.0715223211  
C -4.0609713559 3.3595431708 0.2565924346  
C -1.6230591078 3.6100761508 0.1870455433  
C -0.3023238954 3.0109344855 -0.0113600459  
C -0.1916987889 1.6145566297 -0.327706289  
C -1.398823152 0.7736153902 -0.4429900489  
C 0.8447373676 3.8144549417 0.1223011021  
C 1.0764597548 1.0339651703 -0.5113272915  
C 2.1120405177 3.1935641478 -0.052675063  
C 2.2187040217 1.8691655818 -0.3556806037  
O -1.7713590717 4.806496472 0.4516848524  
O -1.2856231124 -0.4341905372 -0.7267657756

C -6.6334136692 3.0676303396 0.2820098687  
C -6.5539914675 0.6267756427 -0.1167792286  
N -3.867395521 -0.7565491694 -0.5909428153  
H -4.0896916107 4.4233906436 0.4637062423  
N 0.8153351863 5.1497308124 0.3896845629  
H 3.0088756785 3.7987874746 0.0510479204  
H 3.2023331986 1.427385849 -0.4937916928  
H -0.0743794634 5.5862087603 0.5865556194  
H 1.6770471152 5.6295991816 0.585879712  
N 1.299902473 -0.2691340316 -0.8608777358  
H -4.7070871591 -1.2325590562 -0.8670114679  
H -2.96880941 -1.1448095065 -0.8447649123  
H 0.5158548595 -0.9045673142 -0.8524340628  
H 2.2345954015 -0.630754353 -0.7693482351  
N -7.397913404 1.7772224082 0.3892967967  
O -8.5940649253 1.853332812 -0.3615076011  
C -9.7941376596 1.7430887208 0.4224113888  
C -6.9912847829 3.8933358727 -0.9620029102  
C -6.8164132604 3.9171709111 1.5428308453  
C -6.6920890439 -0.5388973461 0.8735411701  
C -6.9511529863 0.1917006087 -1.5363259671  
H -10.5549921473 1.7810030049 -0.3666936502  
C -9.9113595513 0.410844009 1.1412600868  
H -6.8830923718 3.3069062644 -1.8778420005  
H -6.3163836645 4.7527828568 -1.019373208  
H -8.0191085123 4.2560986232 -0.8979182191  
H -6.6508913321 3.3073691094 2.4350224865  
H -7.8179950507 4.348661401 1.5889458543  
H -6.0961389832 4.7414962676 1.541593799  
H -6.5509520208 -0.1672520134 1.8917983097  
H -5.953820908 -1.3241164355 0.6976757171  
H -7.6830222769 -0.9902129116 0.7963284318  
H -6.914713928 1.0346587031 -2.2295681403  
H -7.9643990874 -0.2150030229 -1.5446578569  
H -6.2704405944 -0.5786888411 -1.9100802127  
C -10.0042648974 2.9546791619 1.3102825864  
C -10.3579695644 4.1667432509 0.7077474637  
H -10.5026274029 4.1982832454 -0.3700285074  
C -10.5095910667 5.3248529807 1.4646641707  
H -10.7775257192 6.2589491077 0.9806455277  
C -10.3202214449 5.2806944471 2.8468293651  
H -10.4369769615 6.1809451762 3.4420253087  
C -9.9879919209 4.0745896277 3.4592551237  
H -9.8417093214 4.0331741306 4.5341854194  
C -9.8314874191 2.9184492366 2.6943895654  
H -9.5549203091 1.9903151555 3.1839979312  
H -9.8364981882 -0.4060122388 0.4184878918  
H -10.8811824897 0.3427831133 1.6427172283  
H -9.1211982159 0.2931159736 1.8852111007

1,4,5-TAAQ Aq-EIB

C -5.368858286 2.7474772983 -0.1377753882  
C -5.3714159791 1.3915312135 0.1213313442  
C -4.1559446057 0.6776320851 0.255757336  
C -2.9367896467 1.4137477318 0.144121641  
C -2.985814586 2.8016844699 -0.1141474846  
C -4.1875524451 3.4759229568 -0.2592629806  
C -1.7385943206 3.6110359541 -0.2484232721  
C -0.4430534015 2.9488991639 -0.0860123126  
C -0.3902546154 1.5444251821 0.209275431  
C -1.6313441283 0.7527394303 0.3118195116  
C 0.7365653471 3.7052407599 -0.2105289862  
C 0.8522291058 0.9098790197 0.3885363608  
C 1.9763650024 3.0332794989 -0.0277767841  
C 2.0278537923 1.7025021023 0.2613201626  
O -1.8374813538 4.8174467596 -0.4901254397  
O -1.5697203441 -0.4694160817 0.5431658464  
C -6.7703290101 3.2804466167 -0.2964766541  
C -6.7908463965 0.8528147386 0.1464420721  
N -4.1729187995 -0.6705104549 0.445823571  
H -4.1736849356 4.54077847 -0.463779604  
N 0.7652108961 5.0322857403 -0.519079529  
H 2.8975260324 3.602227649 -0.1232441482  
H 2.9918362561 1.2206682434 0.4037950367  
H -0.1088109948 5.5372074656 -0.5641730373  
H 1.6381035457 5.5282886372 -0.4581392796  
N 1.0200143256 -0.4079194399 0.7129899289  
H -5.0326286334 -1.1119750402 0.7182312223  
H -3.2922418261 -1.1251553598 0.6443735765  
H 0.2129512033 -1.0127537227 0.675755383  
H 1.9414912885 -0.80327404 0.6268546182  
N -7.5737710181 2.1368825603 0.2416631815  
O -8.7813882066 1.99594531 -0.4717298637  
C -9.9973834059 2.2112360418 0.276508573  
C -7.0584750154 3.6115382796 -1.7676005475  
C -6.9912237739 4.5242124685 0.5653598087  
C -7.1487511293 0.0139021905 1.3787638491  
C -7.0883190788 0.0497631631 -1.1308346903  
C -10.6807669891 3.4460093441 -0.3037785421  
C -9.688091508 2.3733659541 1.7756254208  
C -10.8485085876 0.9637769596 0.0721453109  
H -6.9142350685 2.7447752767 -2.41521831  
H -6.3723070132 4.3994062064 -2.0922814133  
H -8.0852077156 3.9659973988 -1.8861608874  
H -6.7705580248 4.2981354753 1.6125473865  
H -8.0274508363 4.8638090986 0.4954157783  
H -6.3357661902 5.3352878749 0.2325122845  
H -6.7537696496 0.4667631692 2.2921215148  
H -6.7954859194 -1.0193989116 1.3020145686  
H -8.2354267782 -0.033384326 1.4751105835  
H -6.981585177 0.6650439504 -2.0257163805  
H -8.1056854474 -0.3480962928 -1.1035181721

H -6.3832932196 -0.783601112 -1.2071111817  
O -9.48924494 3.6466894901 2.1255728299  
C -9.0799797474 3.8613895585 3.4861744823  
C -8.9705567063 5.3559186667 3.6947769477  
O -9.6712846057 1.4572190348 2.5627063207  
H -10.868358625 3.2731025398 -1.367130775  
H -10.0512817428 4.3302230205 -0.192729973  
H -11.6352295051 3.6351606535 0.1962340766  
H -10.9780154817 0.798754248 -1.0006971846  
H -11.8320678864 1.083596254 0.5350592461  
H -10.3614705447 0.0936762156 0.515931695  
H -8.123775111 3.348188814 3.6363072891  
H -9.8163596187 3.4026193413 4.1517622451  
H -8.2353273786 5.7913366488 3.0134608515  
H -8.6580318051 5.5641851053 4.721252383  
H -9.9348590357 5.8400332819 3.5210131524

1,4,5-TAAQ Aq-EP

C -5.3203163572 2.7066913352 -0.2144301046  
C -5.280047143 1.3651214837 0.1865369361  
C -4.0600592259 0.7152652416 0.3867898721  
C -2.8403281149 1.4575950746 0.1818523373  
C -2.9261971756 2.8205315948 -0.2083355008  
C -4.1764106614 3.4429114004 -0.4041699302  
C -1.7374657331 3.638178257 -0.440425558  
C -0.4342881067 3.0187454466 -0.2580588965  
C -0.3372940825 1.6496268118 0.1762809524  
C -1.5344391747 0.8301726305 0.3423998094  
C 0.7532776292 3.7788680507 -0.4883475609  
C 0.9545673806 1.0874299162 0.42521331  
C 1.9874097329 3.1846310289 -0.250705008  
C 2.083082898 1.872834294 0.2116076814  
O -1.8870808345 4.8489735503 -0.7793881771  
O -1.4414439 -0.4158651564 0.6073707827  
C -6.7466652781 3.1760742395 -0.3888693916  
C -6.683381129 0.8013408023 0.3009051267  
N -4.0187870527 -0.5957297899 0.8174127823  
H -4.1816038853 4.4851270978 -0.7056593556  
N 0.7159625945 5.077925766 -0.9982403747  
H 2.8915731818 3.7603651681 -0.4383493961  
H 3.0616405821 1.4441695895 0.4192167487  
H -0.2131967835 5.4912831227 -0.9426418055  
H 1.4784200291 5.6618695545 -0.6867283066  
N 1.1342920322 -0.1985377737 0.9420830044  
H -4.8087782396 -1.1759211331 0.5898938775  
H -3.086916294 -1.0063208032 0.7582476405  
H 0.3088952984 -0.7814289839 0.836780579  
H 2.0081496965 -0.6250784697 0.6702141629  
N -7.49922574 2.0631100188 0.274296586  
O -8.7329896862 1.7811721254 -0.3771908301  
C -9.7899799537 2.5168002935 0.2035937502

C -7.0992022973 3.3606901954 -1.8701445716  
C -6.983193921 4.4843485622 0.375070508  
C -6.9993409077 0.099761202 1.6258695303  
C -7.0006209768 -0.1381179605 -0.8774486339  
C -9.74448234 2.3678901545 1.7235824512  
C -11.0765207896 1.9420529695 -0.3604934969  
H -6.9289709548 2.444400003 -2.439029609  
H -6.4578700196 4.1438657821 -2.2849082411  
H -8.1460542051 3.6580675048 -1.9946657432  
H -6.7767917333 4.3290596539 1.4369795405  
H -8.0126669224 4.8409858971 0.2698925874  
H -6.3096771362 5.259643924 -0.003299568  
H -6.6697329177 0.7219740186 2.462492738  
H -6.5047799451 -0.8713048293 1.7076932743  
H -8.0799447781 -0.0518878411 1.7032053098  
H -6.9128825635 0.3827968703 -1.8330958413  
H -8.0098446867 -0.5492746813 -0.7907948765  
H -6.284261223 -0.9657522196 -0.8869814942  
O -9.4662991714 3.5271394004 2.3322800263  
C -9.2590730545 3.448932153 3.749523794  
C -8.9039996143 4.8399600028 4.2281711828  
O -9.9616779443 1.3349678671 2.3110775241  
H -11.0483616194 1.9916782638 -1.4514861733  
H -11.9405502072 2.5077570185 -0.0007771006  
H -11.1745150615 0.9003376984 -0.046620203  
H -8.4541410556 2.7310308931 3.9360260736  
H -10.1696762342 3.0665971155 4.2214955752  
H -8.0002669248 5.1968788233 3.728682839  
H -8.7241784675 4.8280370557 5.3065733332  
H -9.71679037 5.5401682054 4.0177859343  
H -9.6949184612 3.5825845129 -0.0403124127

1,4,5-TAAQ Aq-Me

C -5.3032664132 2.7380841728 -0.0258857556  
C -5.2826165125 1.3557822584 -0.0699113015  
C -4.0583445656 0.649020247 -0.1018489528  
C -2.850418572 1.4107072211 -0.0527310656  
C -2.9213252722 2.8203379988 0.0009599271  
C -4.1338696058 3.4928822326 0.0105789961  
C -1.685852976 3.6571360977 0.04958349  
C -0.3804534002 2.9945088205 0.0537519516  
C -0.3059030349 1.5609850478 0.0059905408  
C -1.5352776003 0.7481537106 -0.0468030375  
C 0.7874349116 3.7759843298 0.1195702437  
C 0.9466043664 0.9207437163 0.0232635807  
C 2.0374223692 3.0978949583 0.1477940907  
C 2.1099410525 1.737937395 0.1010523042  
O -1.8024888326 4.8853112549 0.0901176641  
O -1.4571775828 -0.4947762921 -0.0787585384  
C -6.7182794892 3.261636353 -0.0703829144  
C -6.6967658214 0.8051858785 -0.1481965751



N -4.056881389 -0.7077583322 -0.2099342023  
H -4.1366282522 4.576673032 0.0459569795  
N 0.7956584917 5.1378901838 0.1387420003  
H 2.9494890269 3.6866610878 0.201220152  
H 3.0818030841 1.2511177075 0.1156418022  
H -0.0860745522 5.6279642729 0.1947038366  
H 1.6621254624 5.6206162199 0.3047677326  
N 1.1363800444 -0.4298028806 -0.0597570437  
H -4.9153208375 -1.2122353859 -0.083205375  
H -3.1708114355 -1.1871947174 -0.1324333466  
H 0.3284870771 -1.0315577735 0.0008518206  
H 2.05270882 -0.7971369553 0.1342420151  
N -7.4641501056 2.0181266979 0.2602625644  
O -8.7469863689 2.0045316405 -0.3180135641  
C -9.7383851727 2.1033895431 0.6915554556  
C -7.0348149711 3.8501148347 -1.4538689542  
C -6.9880215372 4.3139101984 1.0075118062  
C -7.0443029846 -0.2872217983 0.8735722328  
C -7.0212069556 0.3044323972 -1.5661105037  
H -10.6971893803 2.0400433893 0.1721925355  
H -9.6698315578 3.0570742159 1.2247730064  
H -9.6482714933 1.2855812241 1.4136658849  
H -6.8001424102 3.1522472242 -2.2592605853  
H -6.4341903719 4.7524778545 -1.6030630297  
H -8.0930875169 4.113987973 -1.5177492866  
H -6.7977593929 3.8965306271 1.9990626911  
H -8.0289778255 4.6484056067 0.9553176993  
H -6.3489876514 5.1901067401 0.8596953222  
H -6.6494634407 -0.0372692599 1.8612002056  
H -6.6908751642 -1.2809537037 0.5804384335  
H -8.1342191081 -0.3569916018 0.9384079636  
H -6.8930959409 1.091732972 -2.3099218825  
H -8.0527047439 -0.0523819437 -1.6137914867  
H -6.3485244674 -0.5177166913 -1.8294375279

1,4,5,8-TAAQ Aq-STY

C -5.2194227585 2.5761791292 0.1897434409  
C -5.1216658045 1.2349864378 -0.0699941162  
C -3.8685358604 0.6058988566 -0.3258750888  
C -2.7102367324 1.4094554723 -0.2460472559  
C -2.8108393943 2.8129827879 0.0242990935  
C -4.0714922701 3.4215503843 0.2172992733  
C -1.5914699201 3.6380897555 0.0723114398  
C -0.2675140477 3.0112331623 -0.0599300021  
C -0.166861308 1.6096865062 -0.33024795  
C -1.3869386749 0.8020361107 -0.4744509819  
C 0.8929133223 3.8008383823 0.0638268417  
C 1.0943876647 0.9979428001 -0.4760411562  
C 2.1477681432 3.1554639984 -0.0844417456  
C 2.244016645 1.8186478841 -0.341980315  
O -1.6673964535 4.8732509582 0.2293849315

O -1.2872859529 -0.401307673 -0.7872962669  
C -6.6657352873 2.9990182782 0.3861597709  
C -6.4895453235 0.5728839989 -0.0747979722  
N -3.8241974608 -0.7390439232 -0.5929040161  
N -4.2190565429 4.7603131932 0.4589189082  
N 0.9043309177 5.1384125834 0.3566609977  
H 3.0517876438 3.7507340151 0.0161428102  
H 3.2238724075 1.3592636852 -0.4447008007  
H 0.0298008162 5.6393819962 0.3084585146  
H 1.7691673421 5.6384209473 0.2346422693  
N 1.29714858 -0.3371526895 -0.6992559832  
H -4.6612366643 -1.1880779974 -0.9177182893  
H -2.9323749558 -1.1029855712 -0.9012495222  
H 0.4991379291 -0.9024417732 -0.9475744373  
H 2.2208631358 -0.6359780955 -0.9639375519  
H -3.3957923104 5.3362340501 0.3477013217  
H -5.126007272 5.1762835428 0.3542118965  
N -7.3788555961 1.6718163501 0.4489856776  
O -8.5776723909 1.7220446435 -0.2988202742  
C -9.7732701319 1.5075365513 0.4721751795  
C -7.1457173184 3.8548807219 -0.7978790297  
C -6.8888743031 3.7165161871 1.7270933876  
C -6.5572277943 -0.6039217583 0.912166375  
C -6.8892069284 0.1389802108 -1.4950873128  
H -10.531194324 1.5522788271 -0.3193978993  
C -9.8276034318 0.1323671328 1.113048927  
H -7.0845975018 3.2940949819 -1.7334623213  
H -6.5322494843 4.7527856584 -0.9081902645  
H -8.181007823 4.1648272777 -0.6466199365  
H -6.7032810733 3.0140987639 2.5436673669  
H -7.9188655999 4.0703742611 1.8011719318  
H -6.2250671009 4.5715172934 1.8631280942  
H -6.4649927273 -0.2199672273 1.9315812983  
H -5.7585672879 -1.3298932289 0.7550161033  
H -7.5114992046 -1.1254431696 0.8178726291  
H -6.8987334157 0.9940017493 -2.1748501944  
H -7.8859628403 -0.3061437765 -1.4924289761  
H -6.1892436548 -0.5980129572 -1.8966686224  
H -9.6928356809 -0.6376867299 0.3488076166  
H -10.8015845562 -0.0166966321 1.5882558108  
H -9.0477407178 0.0161627747 1.8675637964  
C -10.0496878174 2.6528692276 1.4271793627  
C -10.4676342884 3.8771669807 0.8945884521  
H -10.6171979631 3.9622109955 -0.1797028994  
C -10.6782664926 4.9809041566 1.7160171509  
H -10.9962233442 5.9255332299 1.2856234849  
C -10.4858683592 4.8676080616 3.0937759516  
H -10.6489072141 5.724937644 3.7393069932  
C -10.0928307563 3.6466620431 3.637085317  
H -9.9454027449 3.5509573797 4.7083512749  
C -9.8769230086 2.5460067003 2.8077680096

H -9.5530166769 1.6071244826 3.2448894814

1,4,5,8-TAAQ Aq-EIB

C -5.3104845077 2.3964437182 0.308256056  
C -5.4136811364 1.0516663723 0.0740481966  
C -4.2648598145 0.2456501672 -0.1668697488  
C -3.00329492 0.8801827595 -0.110066519  
C -2.8994529036 2.2836160576 0.1600294421  
C -4.0578006765 3.0661611647 0.3525093742  
C -1.572600419 2.917906852 0.256214838  
C -0.3543991265 2.1141104288 0.0796113844  
C -0.4588885774 0.7271318842 -0.259319154  
C -1.782234985 0.0936756358 -0.3606930867  
C 0.9080935482 2.7231820545 0.2198801665  
C 0.7002617565 -0.0448034526 -0.473859044  
C 2.0565224462 1.9156132749 0.0127053991  
C 1.9572010136 0.5972303873 -0.3244385022  
O -1.4729117086 4.1381499416 0.491899199  
O -1.8583443511 -1.1161135783 -0.653674218  
C -6.674698039 3.0444634374 0.4362174776  
C -6.8667440348 0.6053122256 0.0829311515  
N -4.4162444974 -1.0973860615 -0.4018127618  
N -4.036303284 4.4271997282 0.5272484108  
N 1.1138474391 4.0278532874 0.5820570719  
H 3.0373139699 2.3701914418 0.1268940778  
H 2.8595649785 0.0136818922 -0.4883623953  
H 0.3174942852 4.6478976894 0.5732778272  
H 2.0353175656 4.4097526616 0.4460387253  
N 0.7093072384 -1.360794358 -0.8524354336  
H -5.3113384811 -1.4237421157 -0.7192841736  
H -3.5896998525 -1.5898490102 -0.7141094611  
H -0.1647183894 -1.8647798386 -0.8211818182  
H 1.5741642949 -1.8676228358 -0.7596572962  
H -3.1289449097 4.8375728403 0.7032356489  
H -4.8403922006 4.8592691625 0.9481415223  
N -7.5653929555 1.8446429368 0.5814662392  
O -8.7633178376 2.0469237916 -0.1450619753  
C -9.9597672449 2.0989455506 0.6395338693  
C -6.9696470524 3.8641242127 -0.8316707207  
C -6.8169962309 3.9038208316 1.7151337644  
C -7.1144041721 -0.5165012047 1.1016948882  
C -7.3453682089 0.1968955825 -1.3199536279  
C -11.0640207486 2.1476259558 -0.4178040244  
C -10.0353343696 3.3974272649 1.4575776218  
C -10.1303932242 0.9095705784 1.567818694  
H -6.9316379951 3.2264518047 -1.7180184551  
H -6.2099754629 4.6432948019 -0.9429297862  
H -7.9584525942 4.3194043149 -0.7722091891  
H -6.053034227 3.6451051418 2.4549814975  
H -7.781323372 3.7183211651 2.1872701325  
H -6.7581371039 4.977848245 1.4992723596

H -6.8711462777 -0.1559017582 2.1043854541  
H -6.5062507661 -1.4007069481 0.9044850551  
H -8.1635025529 -0.8163638926 1.0831132869  
H -7.2378863775 1.0206726787 -2.0284929922  
H -8.3974883428 -0.0947813456 -1.2913295511  
H -6.7690179039 -0.6493364293 -1.7022900172  
O -9.7641314661 4.4794108237 0.7160697535  
C -9.8271463807 5.7407504443 1.4027561331  
C -9.3665831198 6.8059666841 0.4321709642  
O -10.3439937861 3.4554541763 2.6247303486  
H -11.0514378341 1.2150750934 -0.988051573  
H -10.8972982191 2.9849799115 -1.0982215021  
H -12.041879294 2.2579809733 0.0590698575  
H -10.1646248736 -0.0068180522 0.9725353194  
H -11.0654510492 1.008569648 2.1225708885  
H -9.3090435295 0.8560456113 2.2837287257  
H -9.1896827511 5.6871401059 2.2909070496  
H -10.8555945729 5.9020118654 1.7399064594  
H -8.3322911841 6.6291186953 0.1243147875  
H -9.4233347421 7.7889211374 0.9067737903  
H -9.9958238981 6.8143957895 -0.4612658823

1,4,5,8-TAAQ Aq-EP

C -5.2926888075 2.3891022238 0.3228850663  
C -5.3931307082 1.0409648202 0.1069559065  
C -4.2445705018 0.2360000995 -0.1372599029  
C -2.9847823787 0.8753577357 -0.1007112861  
C -2.8831698697 2.2824143607 0.1504230731  
C -4.0421660519 3.0638763466 0.3439577441  
C -1.5574757604 2.9218644974 0.226940043  
C -0.3383467334 2.1188598354 0.053509866  
C -0.4412967345 0.7275617296 -0.2678526217  
C -1.7634981626 0.0897083292 -0.3534431262  
C 0.9234024278 2.7325249452 0.1795347692  
C 0.7184762745 -0.0441928662 -0.4795567744  
C 2.072663005 1.924930103 -0.0233296257  
C 1.9747249345 0.6023963247 -0.3440231445  
O -1.4597034069 4.1456846024 0.4441135368  
O -1.8388803223 -1.1230057955 -0.6341492996  
C -6.658035483 3.0330317271 0.4615169495  
C -6.8444738356 0.5905587031 0.1322001261  
N -4.3945271369 -1.1101560378 -0.3551749902  
N -4.0232576432 4.4272867428 0.4990421788  
N 1.1277663154 4.0421111684 0.5241765107  
H 3.0529560096 2.3830549796 0.0804912887  
H 2.8775934562 0.0189414411 -0.5054203018  
H 0.329887039 4.6601490381 0.5109551232  
H 2.0477744355 4.4244058034 0.3796659262  
N 0.7282918351 -1.3644136687 -0.8424659405  
H -5.2919867172 -1.4420598585 -0.6601123129  
H -3.5701735811 -1.6034088652 -0.6719121703

H -0.144862393 -1.8693489469 -0.8022804631  
H 1.5945399808 -1.868563921 -0.7483972365  
H -3.1153480691 4.8430060225 0.6595130095  
H -4.8243825635 4.863090625 0.9216630631  
N -7.5395315551 1.8298471045 0.633551586  
O -8.754435276 2.017187478 -0.0726381077  
C -9.9105424294 2.0769675403 0.7546760173  
C -6.977221967 3.8374517924 -0.8099106097  
C -6.7847574163 3.9065766314 1.7325710963  
C -7.0860803253 -0.5270350262 1.1563069967  
C -7.3326211769 0.1771608755 -1.2661043526  
C -10.0002833671 3.3835251961 1.5466946946  
C -10.1176399692 0.8816964312 1.6623087439  
H -6.9485561653 3.1919024875 -1.6907465553  
H -6.2246671896 4.6205057217 -0.9403453251  
H -7.9680668641 4.2866480529 -0.7394748831  
H -6.0072566285 3.6612876056 2.4627481636  
H -7.7397709695 3.7219878506 2.2234402092  
H -6.7355479073 4.9781547953 1.5027682113  
H -6.8235040956 -0.1680913169 2.1546972295  
H -6.4919490243 -1.4188085988 0.9508717196  
H -8.1388301842 -0.8147855779 1.1538045146  
H -7.2346238422 0.9999972314 -1.9770190254  
H -8.3823805517 -0.1209016838 -1.2293573585  
H -6.7531627888 -0.6658253772 -1.6510996763  
O -9.7579926671 4.4517583341 0.7776656751  
C -9.8229249206 5.7266465359 1.4396339731  
C -9.3970277275 6.7771930454 0.4378486671  
O -10.2930933487 3.4569899705 2.7166337736  
H -10.169157538 -0.0294056963 1.0619325656  
H -11.0541062083 0.9986323535 2.2111669171  
H -9.3035450706 0.8038198396 2.3847495846  
H -9.1659257524 5.6990406635 2.3147149339  
H -10.8459938881 5.8817128484 1.7953759658  
H -8.3668081501 6.60815657 0.1125928437  
H -9.4580132276 7.7690027168 0.8930792022  
H -10.0443637337 6.7578977021 -0.4422933974  
H -10.7172269269 2.1279036582 0.012091022

1,4,5,8-TAAQ Aq-Me

C -5.3182429969 2.7508258899 -0.0356133965  
C -5.2679399581 1.3790833506 -0.0853938063  
C -4.035702159 0.6741482955 -0.1306831323  
C -2.8493158249 1.4373377442 -0.062419042  
C -2.9017900956 2.8681336204 -0.0104823155  
C -4.1410003219 3.5454260943 -0.0264847372  
C -1.6508250942 3.6461073427 0.0283450142  
C -0.3541605112 2.9570670746 0.0996901593  
C -0.3017253731 1.5272833093 0.0476832241  
C -1.5446773141 0.752223676 -0.0767714034  
C 0.830408562 3.7125766745 0.2050505198

C 0.935245054 0.8548187723 0.1010418796  
C 2.0604247652 3.0061409436 0.259506657  
C 2.1104184798 1.6435423554 0.2098851365  
O -1.6823875838 4.8923503393 0.0039712867  
O -1.4850522733 -0.4879704637 -0.1913349085  
C -6.7569464521 3.2415215551 -0.0338223481  
C -6.6669008633 0.7856288169 -0.1228627614  
N -4.0542409272 -0.6961448944 -0.1910206038  
N -4.2598912639 4.9114391304 0.0123834026  
N 0.8837960189 5.0764316556 0.296385434  
H 2.982003271 3.5758278767 0.3480368561  
H 3.0714508216 1.1379018758 0.2591988057  
H 0.0394863554 5.5984968833 0.1162101912  
H 1.7794767771 5.523473793 0.1949338546  
N 1.088511523 -0.5044522375 0.0929335399  
H -4.8882478545 -1.1378485673 -0.5354095183  
H -3.1667649186 -1.1493393007 -0.3604624177  
H 0.2840744124 -1.0726720586 -0.1258736263  
H 2.0143143356 -0.8765019266 -0.0368002905  
H -3.4084348474 5.4394478663 -0.1215100211  
H -5.1249702511 5.3147210854 -0.3010953132  
N -7.4541194415 1.9723234776 0.3088502733  
O -8.7564000181 1.9438695987 -0.2223077349  
C -9.7168620674 1.8707238522 0.8207360079  
C -7.1599790373 3.8161861223 -1.4036170831  
C -7.1048414772 4.2413013568 1.0782914743  
C -6.9377150917 -0.3147019717 0.9131551642  
C -7.0305613342 0.2835955199 -1.5316645986  
H -10.6891602721 1.8536251941 0.3234217539  
H -9.6528848999 2.7401810982 1.481822816  
H -9.5883112955 0.9621681129 1.4166349733  
H -6.9541927673 3.114424135 -2.2131062317  
H -6.6051505047 4.7353361551 -1.6152343489  
H -8.2267722827 4.0503688663 -1.4091545496  
H -6.7426707765 3.8748565837 2.0413963708  
H -8.1935721182 4.3381952433 1.1244754044  
H -6.6970935369 5.2395062586 0.9081856012  
H -6.6007561867 0.006698692 1.9011742163  
H -6.4584395405 -1.2654605155 0.6724203661  
H -8.0163027344 -0.4941124367 0.9493688232  
H -6.8789856599 1.0552726883 -2.2877258164  
H -8.0773533609 -0.0270725853 -1.5568430254  
H -6.4105090884 -0.5747220182 -1.8078461758

AQ-NO radical

C 0.6230894508 1.2601415012 0.2232851445  
C 0.3225599994 -0.0913431029 0.4315199383  
C 1.3202545521 -1.0535092974 0.3889818999  
C 2.6345361622 -0.6535761839 0.1344185331  
C 2.9360332934 0.7022677951 -0.0744771869  
C 1.9248615157 1.665402736 -0.0299322272

C 4.3351186243 1.1487095611 -0.3479174959  
C 5.4013820122 0.1040486171 -0.3915294679  
C 5.1003615338 -1.2496545077 -0.1829662802  
C 3.7022281266 -1.6974405926 0.0905778802  
C 6.7174325674 0.4939165362 -0.6452523736  
C 7.726824327 -0.4616335797 -0.6905183039  
C 7.426838815 -1.8106712753 -0.4826723315  
C 6.1173651617 -2.2045891925 -0.22949469  
O 4.5956333784 2.3240195264 -0.5287966757  
O 3.4401556192 -2.8723501327 0.2718080531  
C -0.6093138402 2.1253766119 0.3143336776  
C -1.1490153356 -0.301667483 0.6883486643  
H 8.2173675815 -2.5533367368 -0.5188023941  
H 5.8584815198 -3.2453904183 -0.0648096781  
N -1.6352001844 1.094882016 0.5980799026  
O -2.8546978176 1.3902783933 0.7554325998  
C -0.9417191127 2.8300320074 -1.0036263275  
C -0.5521877423 3.1243455407 1.4731161785  
C -1.437059848 -0.8552352545 2.0864166783  
C -1.8270319409 -1.1509709295 -0.3900811426  
H -0.9666732073 2.1135707484 -1.8291636095  
H -0.1900589799 3.5939277457 -1.2228359229  
H -1.9216398211 3.3069608792 -0.9183372268  
H -0.3002507838 2.6171511061 2.4083923599  
H -1.5284163324 3.604071045 1.5817871557  
H 0.2026087828 3.8905311342 1.2735652871  
H -0.9383093736 -0.2530787278 2.8506910788  
H -1.0821546816 -1.8870372747 2.163902604  
H -2.515174647 -0.833664603 2.2657788715  
H -1.6055846982 -0.758983304 -1.3864542854  
H -2.9088367318 -1.1322752723 -0.2341068615  
H -1.4751795427 -2.1851065348 -0.3322324364  
H 1.1169582226 -2.109250475 0.5466927472  
H 2.1878843669 2.7066814561 -0.1953170981  
H 6.9242424125 1.5473308754 -0.8032212939  
H 8.7499665961 -0.1582409539 -0.8878139447

AQ-NO cation

C 0.6354781821 1.2564746111 0.2216477591  
C 0.33520831 -0.0935867407 0.4297086544  
C 1.3274237544 -1.0589967334 0.3885381812  
C 2.6390988245 -0.652017611 0.133670952  
C 2.9395193231 0.6987535373 -0.0745614345  
C 1.9337310555 1.6670712271 -0.0315894963  
C 4.3488470672 1.1467926348 -0.3499495198  
C 5.4067167525 0.1047701117 -0.3920219456  
C 5.1047742977 -1.2528510672 -0.1827297621  
C 3.715290662 -1.7020974514 0.0896438421  
C 6.7223842537 0.4946019109 -0.6454134259  
C7.731005479 -0.4630037874 -0.6900375727  
C 7.4310786208 -1.8115096014 -0.4822449506

C 6.121381671 -2.2075898179 -0.2290034219  
O 4.5800136662 2.3263028876 -0.5259764804  
O 3.4247715909 -2.8672410712 0.2732333953  
C -0.5810942935 2.1401094308 0.3078822261  
C -1.1299239552 -0.3276670442 0.6882305522  
H 8.2215304392 -2.553678099 -0.5181997637  
H 5.8671324222 -3.2495704467 -0.0648481034  
N -1.6421295621 1.0967343023 0.599337464  
O -2.7783820208 1.37204429 0.7458959835  
C -0.9680070826 2.8217299761 -1.0112710923  
C -0.5742561288 3.1198281878 1.4887888328  
C -1.4542982195 -0.8373990667 2.0987300887  
C -1.8479151705 -1.1349738323 -0.4013898862  
H -1.0198686994 2.1021795067 -1.8318029673  
H -0.1871278579 3.549715663 -1.2437529147  
H -1.9208096718 3.3461905673 -0.9086858783  
H -0.3488584058 2.6101461472 2.4285409097  
H -1.5316054948 3.6408470173 1.5624480854  
H 0.2134993899 3.8530322797 1.29998902  
H -0.9787202273 -0.2205506467 2.8649057073  
H -1.054758556 -1.8511434582 2.1792621622  
H -2.5346463711 -0.8697657205 2.2574774857  
H -1.6492434995 -0.7278245048 -1.3956029229  
H -2.9236861651 -1.1635800001 -0.213468074  
H -1.4555127762 -2.1540059124 -0.3644667381  
H 1.132521734 -2.1169711503 0.5452490959  
H 2.20529077 2.7064642933 -0.198238666  
H 6.9339226281 1.5469264072 -0.8040884736  
H 8.7539032636 -0.1600512258 -0.8870669073

AQ-NO anion

C 0.6212436645 1.2438626491 0.0990342705  
C 0.3196671483 -0.1121876544 0.3076375046  
C 1.3244717412 -1.069123645 0.2886691238  
C 2.6480750544 -0.6715067966 0.0582958363  
C 2.9509531291 0.690388684 -0.1511656654  
C 1.9288702606 1.6484770596 -0.1293220299  
C 4.3420643892 1.1389412533 -0.3962760029  
C 5.4193399455 0.0938506878 -0.4220671317  
C 5.1189038892 -1.2570180465 -0.2142912271  
C 3.7093911975 -1.7057805115 0.04123437  
C 6.73871514 0.4854644796 -0.6567505986  
C 7.7524934813 -0.4661423086 -0.6841352705  
C 7.4523910093 -1.8155253241 -0.4765802924  
C 6.1393806803 -2.2094034757 -0.2422456751  
O 4.6322559303 2.3117135574 -0.574999774  
O 3.4753617022 -2.8902544473 0.2251282272  
C -0.6343461993 2.0660768382 0.2175985171  
C -1.153447062 -0.2679095207 0.5766395025  
H 8.2451811557 -2.5573231893 -0.498281043  
H 5.8756571428 -3.2491647247 -0.0774684194



N -1.6693813429 1.015136457 0.0306735049  
O -2.9072869944 1.3643064359 0.5107628794  
C -0.8079535361 3.0937523952 -0.9017847255  
C -0.7193577493 2.7861279223 1.580392531  
C -1.4421273114 -0.463854941 2.0803679112  
C -1.8082292036 -1.4046146372 -0.2097776996  
H -0.712189398 2.6033988014 -1.874660057  
H -0.0782506472 3.9098754327 -0.8265987595  
H -1.8200895502 3.5020424883 -0.8176769417  
H -0.3254614173 2.174925993 2.3968503626  
H -1.7870411098 2.9610750644 1.7553792341  
H -0.1678159419 3.7332187629 1.5645476876  
H -0.7791913479 0.1349824341 2.7106353448  
H -1.3349014728 -1.514984891 2.372013679  
H -2.4727697449 -0.1223189679 2.2297331729  
H -1.5800759787 -1.2997247361 -1.2742266792  
H -2.8909569669 -1.3138627286 -0.076885656  
H -1.4791136375 -2.3903349173 0.142664616  
H 1.1147068483 -2.1232695451 0.4476815441  
H 2.1854773217 2.6915064543 -0.2928792943  
H 6.9407796538 1.5400799737 -0.8141079049  
H 8.7782861269 -0.1602588155 -0.8669889719

Me-Pyridine cation

C 6.7098238181 -0.4817046836 0.0784553169  
C 6.3348162693 -1.7858311281 -0.1784467915  
C 4.9778183492 -2.0962662506 -0.2707545992  
C 4.0336848064 -1.0867177338 -0.1022183506  
C 4.4639139816 0.2034480851 0.1533894106  
N 5.7796297331 0.4844401145 0.239090714  
H 7.7444691532 -0.1680256352 0.1634572599  
H 7.1011904152 -2.5413589018 -0.3031066723  
H 4.6614962615 -3.1143186065 -0.4718819128  
H 2.9705225974 -1.2848429077 -0.1659746872  
H 3.7822102645 1.0337095713 0.294323719  
C 6.2339967396 1.8665751236 0.5127580674  
H 5.3637588329 2.5113027026 0.6138273667  
H 6.8506619482 2.2071418077 -0.3193090508  
H 6.8074368301 1.8730084441 1.4399702013

Me-Pyridine radical

C 6.7876051964 -0.6738679376 -0.0787672576  
C 6.3042832512 -1.94803959 -0.152019179  
C 4.9115683757 -2.206469831 -0.1345566813  
C 4.0519715615 -1.0827105883 -0.064629642  
C 4.5510234046 0.185438673 0.0080035265  
N 5.9272521151 0.4176719627 0.0577692304  
H 7.8447584788 -0.4373142192 -0.0878515814  
H 7.0188711603 -2.7611672754 -0.2254274104

H 4.522192354 -3.2135033999 -0.1975676453  
H 2.9741582543 -1.207242343 -0.0684806013  
H 3.9258195112 1.0683707678 0.0642135361  
C 6.431939507 1.7543057788 -0.1696985204  
H 6.482626694 1.9953829613 -1.2409954287  
H 7.4325134271 1.8436825845 0.2593309541  
H 5.7801567089 2.4786524561 0.3240067003

Pyridine

C 6.6750398156 -0.4735834979 0.079142692  
C 6.3237493266 -1.7976694055 -0.1809671347  
C 4.9727070511 -2.1181849295 -0.2750436774  
C 4.0353973606 -1.1034893983 -0.1053619085  
C 4.4945480047 0.187858353 0.1511808604  
N 5.787080458 0.5099120037 0.244111609  
H 7.721333803 -0.1885511145 0.1589907815  
H 7.0930109649 -2.5521517824 -0.3053571732  
H 4.6569042693 -3.1372341515 -0.4763475008  
H 2.9709231146 -1.3017461392 -0.1691755282  
H 3.7895158315 1.0041400621 0.2888869795

AQ-Me-Pyridine Transition state (neutral)

C 0.3191256666 0.9835642651 0.4673311532  
C 0.2844490868 -0.3029101618 1.0230901161  
C 1.3798326794 -1.1467650727 0.9226388879  
C 2.5261959981 -0.6961052841 0.2584081968  
C 2.5609866447 0.594535304 -0.2990874248  
C 1.4495006235 1.4383349153 -0.1940756126  
C 3.7686592821 1.0921812918 -1.0148340705  
C 4.9480598163 0.1764788208 -1.1115112032  
C 4.9133708537 -1.1094582595 -0.5561692533  
C 3.6957661514 -1.6123462608 0.1533531707  
C 6.0968426393 0.6206441158 -1.7686285819  
C 7.2046964366 -0.2138348749 -1.8699726962  
C 7.1700724261 -1.4965972904 -1.3160724998  
C 6.027648994 -1.9438107195 -0.661216622  
O 3.8047875675 2.2056218183 -1.5093603508  
O 3.6716531411 -2.7359055445 0.6252016059  
C -0.9818889779 1.6984196868 0.7356276281  
C -1.0421517572 -0.537794502 1.7018076644  
H 8.0366687031 -2.1452929358 -1.3965063791  
H 5.9740851083 -2.9346723458 -0.2220663786  
N -1.8556654264 0.5512434137 1.0988247948  
O -2.9569193237 0.9016053856 1.8409656559  
C -4.5137189899 0.3891182843 0.5566742395  
C -1.5648554569 2.3766971475 -0.5051578492  
C -0.8298684105 2.7405874241 1.8562780599  
C -0.9155451857 -0.4422242728 3.2314982556  
C -1.6795865359 -1.8784908873 1.3335562773  
H -4.811129645 -0.2517045299 1.3786293283  
H -3.6068668253 0.1284604996 0.0117669742

H -4.7642973031 1.4396787333 0.6474176595  
H -1.6381161075 1.6590854464 -1.3280283581  
H -0.9540603772 3.2276249647 -0.8256116818  
H -2.5679152947 2.7443741757 -0.261503542  
H -0.291699866 2.3382416373 2.7165421949  
H -1.8295156116 3.0368747985 2.1837907091  
H -0.2812625348 3.6142286164 1.4888188186  
H -0.3433464492 0.4350472237 3.5389848044  
H -0.4139891429 -1.3321410315 3.6261360447  
H -1.9209787818 -0.3618042198 3.65217759  
H -1.7366181979 -1.9830512958 0.2457839853  
H -2.6932292807 -1.9072204868 1.748740688  
H -1.1143666955 -2.721724005 1.7450552213  
C -6.9691986512 0.0593670039 -0.3506152914  
C -7.9290264691 -0.3145519215 -1.2791607837  
C -7.5086570834 -0.8459095133 -2.4976883717  
C -6.1463958732 -0.9850525123 -2.7458544348  
C -5.2453220461 -0.5877414005 -1.765843124  
N -5.6644298978 -0.0809309999 -0.6046794435  
H -7.2182936289 0.4804086828 0.6195443372  
H -8.9802935538 -0.1902406836 -1.0479516551  
H -8.2360456044 -1.1474980291 -3.2440173496  
H -5.7790464943 -1.3934514093 -3.6798683807  
H -4.1673026431 -0.6648307725 -1.8848998824  
H 1.3798455951 -2.149194321 1.341992043  
H 1.5032469717 2.4295963006 -0.6359217724  
H 6.0969993222 1.620922598 -2.1893128829  
H 8.0981514151 0.1323969897 -2.3799952281

AQ-Me-Pyridine Transition state (radical)

C 0.6165326073 1.2511737919 0.1986082118  
C 0.32054352 -0.101740876 0.3749506237  
C 1.3184989191 -1.0621197195 0.3242196287  
C 2.6319337808 -0.6484994587 0.0924978789  
C 2.9290915424 0.7089882865 -0.0879837886  
C 1.9170665256 1.669892464 -0.0357047576  
C 4.3362619109 1.1657768085 -0.3399311407  
C 5.4021534037 0.1276807342 -0.3847393756  
C 5.1032547755 -1.2331909144 -0.2037118771  
C 3.7088472594 -1.6917081654 0.0404136404  
C 6.7199058139 0.5269917511 -0.6118683217  
C 7.7334552024 -0.4249745671 -0.657706284  
C 7.4362147924 -1.7782531138 -0.4777477554  
C 6.1246124535 -2.1830739785 -0.2514536607  
O 4.5752606238 2.3469326576 -0.4986691058  
O 3.4296323 -2.8650993159 0.1949441444  
C -0.6128197585 2.115748662 0.3108973689  
C -1.153682711 -0.3422750568 0.6202450884  
H 8.2304043875 -2.5165661066 -0.5141722129  
H 5.8708831846 -3.2283513328 -0.1089516546

N -1.6561975197 1.0607115131 0.4872713349  
O -2.8272128981 1.450059385 0.8346669924  
C -4.3194514119 0.5663656539 0.352681582  
C -0.9230207862 2.9040386511 -0.9635903909  
C -0.5866571562 3.0248383503 1.5435358079  
C -1.4254743425 -0.8495513038 2.0406107115  
C -1.7517905414 -1.2668198685 -0.4472503623  
H -4.20169799 -0.2650793498 1.030170899  
H -4.0205105627 0.4708841375 -0.6820818429  
H -4.9086153776 1.4185786469 0.656954991  
H -0.9441181078 2.2453710545 -1.8358327435  
H -0.1457705128 3.656549757 -1.1189833491  
H -1.8846782508 3.4143523837 -0.8646309179  
H -0.3971705456 2.4476982829 2.4521210119  
H -1.5348288824 3.5574319713 1.643340225  
H 0.218063976 3.7546130447 1.4247058481  
H -0.9798132904 -0.1845001161 2.7838327979  
H -0.9790525947 -1.8412502282 2.1511192807  
H -2.4974865979 -0.9321671907 2.2365185231  
H -1.6675960432 -0.819394422 -1.4414839399  
H -2.794688121 -1.5171905542 -0.2410415333  
H -1.1852071666 -2.201643758 -0.4498504039  
C -7.0506053232 -0.5454287925 0.7170395523  
C -8.2762780607 -1.128602433 0.4178045723  
C -8.5311579827 -1.5005782899 -0.9001630017  
C -7.5554993101 -1.2767228454 -1.8682331909  
C -6.3576942723 -0.6872766142 -1.4792304919  
N -6.1154224392 -0.3325485858 -0.2141987179  
H -6.8054474703 -0.2357510303 1.7305115023  
H -9.0088411119 -1.2836585876 1.2013072883  
H -9.4776916361 -1.9575479821 -1.1691141389  
H -7.7139747677 -1.5496800713 -2.905032481  
H -5.5682035394 -0.4906227937 -2.2009432537  
H 1.1267378644 -2.1236139194 0.4594250836  
H 2.1822265149 2.7142052496 -0.1785113103  
H 6.9277967734 1.5830919874 -0.7488240566  
H 8.7580199516 -0.1144098833 -0.8337335277

AQ-BF<sub>3</sub>-Me (radical)

C -7.1352472878 0.7769159552 -0.5559329065  
C -6.2921310143 1.6743407504 -1.2184319384  
C -4.9168948927 1.4758213269 -1.2037940184  
C -4.3844648055 0.3746706838 -0.5300440224  
C -2.9155609081 0.165512538 -0.5146843407  
C -2.3867703895 -1.059779755 0.1707620163  
C -1.0054776312 -1.240902345 0.117998982  
C -0.4455001732 -2.3549188518 0.7328718106  
C -1.2297951134 -3.3015657187 1.3696445707  
C -2.6566825204 -3.1866187771 1.3940430152  
C -3.2249396024 -1.9896293144 0.8113749256  
C -4.6869962048 -1.7087337401 0.8788645464

C -5.224165852 -0.5244245809 0.1329136333  
C -6.6052712644 -0.3161026653 0.1206458037  
C -0.3481399718 -4.4149739429 1.9199947903  
N 0.9854095864 -3.742055886 1.8399649502  
C 1.0133052942 -2.7350568593 0.7522156128  
O -5.4658032699 -2.3931195522 1.5245392249  
O -2.1584589301 0.953882865 -1.0517256034  
O 2.0197709203 -4.6835186064 1.7046325057  
C 2.9428174479 -4.5501173571 2.7750779611  
H -8.2091424601 0.9340645608 -0.5682813695  
H -6.7116316174 2.5266792163 -1.7431931831  
H -4.2362620818 2.1564505212 -1.7045948142  
H -0.4039428105 -0.49980078 -0.3991485377  
C -3.4381166067 -4.2446896702 1.8961031326  
H -7.2406922108 -1.0213946964 0.6451280671  
C -0.4446082736 -5.6937565365 1.068691578  
C -0.5642012161 -4.7495316603 3.4015518999  
C 1.4458230607 -3.2759980812 -0.6202057553  
C 1.9264996505 -1.5771440852 1.1588606312  
H 3.4179247101 -3.5640414032 2.7676257071  
H 3.695579438 -5.3247491049 2.613777401  
H 2.4506734116 -4.7012010293 3.7408544629  
B -3.3320643196 -4.6142463042 -1.1582027142  
H -4.5142933739 -4.2029988484 1.9095345976  
H -2.9548933372 -5.1357557447 2.266328873  
H -0.3249306645 -5.4857575885 0.0041150931  
H -1.4168893465 -6.1725834771 1.2078617757  
H 0.3359888999 -6.3931618802 1.3752449775  
H -0.5781029726 -3.8346304331 3.9985407082  
H 0.2719655427 -5.3718976694 3.7350233368  
H -1.4814678377 -5.3115553755 3.5852358042  
H 0.7729526076 -4.0533532712 -0.985585916  
H 2.4565070107 -3.6858775095 -0.5580977793  
H 1.4396148138 -2.4571054614 -1.3461903762  
H 1.6455449313 -1.2004960099 2.1452354914  
H 1.8665255552 -0.7608862554 0.4320927159  
H 2.9666654934 -1.9163526497 1.1902065479  
F -2.2213322592 -4.027366345 -1.5586105847  
F -4.4752902475 -3.9605453523 -1.1981507547  
F -3.3079669071 -5.8814232426 -0.7938625353

AQ-BF<sub>3</sub>-Me-Pyridine transition state (radical)

C -7.459087872 -0.1852848423 -0.8280663193  
C -6.8567281627 0.6872993837 -1.7407715872  
C -5.4758228362 0.8428969365 -1.7500470376  
C -4.6940045186 0.1101160538 -0.8538678382  
C -3.2143652052 0.2505145908 -0.8723536193  
C -2.4152158224 -0.7533567321 -0.0952014288  
C -1.0448422682 -0.7927714218 -0.3471654265  
C -0.3060604276 -1.7805463114 0.2765523498  
C -0.9022172293 -2.7324404429 1.1030864647

C -2.2846301752 -2.7328345035 1.3701414685  
C -3.0214607775 -1.6710341416 0.779103201  
C -4.4750319551 -1.4728488877 1.0867530599  
C -5.2973167067 -0.7536210262 0.064181889  
C -6.6845801292 -0.8939126548 0.083943639  
C 0.1298968589 -3.7114861221 1.6513093646  
N 1.3753952974 -3.126278646 1.054200892  
C 1.1730789112 -2.0022057155 0.1075117499  
O -4.9799596056 -1.7891959704 2.1453410214  
O -2.66227156 1.1085154066 -1.5400470987  
O 2.5293487905 -3.6887895149 1.0660837388  
C 3.1977068235 -4.5436144145 2.5678731855  
H -8.5375923707 -0.3088854989 -0.8307001178  
H -7.4693547437 1.2424318109 -2.4441692  
H -4.9819716558 1.5174376006 -2.4420041555  
H -0.6101808244 -0.0684132451 -1.0293570394  
C -2.9708771767 -3.8732733749 2.0208899227  
H -7.1275556685 -1.5679012343 0.8094779609  
C -0.0156478649 -5.1441069312 1.1231385991  
C 0.2076395452 -3.631718391 3.187261573  
C 1.5397471269 -2.4549732482 -1.3100742298  
C 2.0271817734 -0.8146298053 0.5552194811  
H 2.9785717799 -3.6925956837 3.1956449791  
H 4.1433931768 -4.6043110558 2.0490567425  
H 2.5007445413 -5.3629549886 2.4937428596  
B -3.6571593429 -4.7947781678 0.800304459  
H -3.7710143672 -3.5573792099 2.6858214503  
H -2.2889276462 -4.5197984743 2.573760325  
H -0.1518294082 -5.1413089431 0.0403993186  
H -0.9040591478 -5.6142155214 1.5434393536  
H 0.8663792114 -5.739992647 1.377950781  
H 0.6504000749 -2.680198306 3.4979157725  
H 0.7792291934 -4.4591314347 3.6172646015  
H -0.8017856974 -3.6772127691 3.5968586617  
H 0.9359082621 -3.3162619843 -1.6062704483  
H 2.600265125 -2.7137791055 -1.3653065758  
H 1.3340916996 -1.6363660859 -2.0044714091  
H 1.7624022748 -0.5099787584 1.5714548463  
H 1.8447516811 0.0300529394 -0.1140449565  
H 3.0889267258 -1.0738597271 0.5127391154  
F -2.6399816337 -5.1912758954 -0.1080458799  
F -4.6057800371 -4.0143276403 0.1088298945  
F -4.2503132926 -5.9286539408 1.3657550274  
N 4.005779845 -5.4548282731 4.1588712398  
C 5.1983905996 -5.0745884014 4.6242645466  
H 5.7027138763 -4.2846980781 4.0728592786  
C 5.7677423292 -5.653656196 5.752074928  
H 6.7383932967 -5.3209713694 6.1008377304  
C 5.0631794438 -6.6587288998 6.4110100019  
H 5.4783398786 -7.1312837512 7.2950087487  
C 3.8194742221 -7.0489819533 5.9218017237

H 3.2382469103 -7.8257602055 6.4046660499  
C 3.3250699758 -6.416935974 4.7862549853  
H 2.3590268788 -6.6841682046 4.3638373858

AQ-BF<sub>3</sub>-NO radical anion

C -7.0479733083 0.4162185825 -1.0595347312  
C -6.2231323601 1.3871272561 -1.6388365104  
C -4.8571270376 1.3836288224 -1.3831278253  
C -4.3117506757 0.396302826 -0.5587833664  
C -2.84313737 0.3639084261 -0.3011507582  
C -2.2849503874 -0.8691172054 0.3293526807  
C -0.9009829853 -1.0269974103 0.2981992306  
C -0.3707059652 -2.213796039 0.7744915895  
C -1.1864349002 -3.2506192949 1.2360239857  
C -2.5898358928 -3.1276073876 1.2782851996  
C -3.1149620593 -1.8786516462 0.8568410185  
C -4.5696755438 -1.5661025155 0.9887892973  
C -5.1375437591 -0.5641414095 0.0281689737  
C -6.5108060122 -0.5487742412 -0.2148435189  
C -0.3427172652 -4.4421478816 1.6663091592  
N 1.0262213676 -3.8953579403 1.450980796  
C 1.0936137037 -2.5652313706 0.8219328809  
O -5.2815673623 -2.0013532191 1.873112127  
O -2.1263108405 1.2882882256 -0.6533477097  
O 2.0700593312 -4.57793703 1.6738667834  
H -8.1132455771 0.4167423125 -1.2708645224  
H -6.6511301978 2.1420815734 -2.2916957614  
H -4.1925022221 2.1264444892 -1.8128037328  
H -0.2843677753 -0.2309421131 -0.1086312705  
C -3.486965054 -4.2789161244 1.5607027613  
H -7.1264756544 -1.3077378733 0.256459034  
C -0.5024802707 -5.6854823569 0.7842275843  
C -0.4631077735 -4.7871101581 3.1554137912  
C 1.7187024609 -2.6837311435 -0.5725894222  
C 1.9113397672 -1.6219582478 1.7073111665  
B -4.1437506541 -4.8201609188 0.1281770689  
H -4.3095768213 -4.0019667678 2.2181112335  
H -2.9448927263 -5.1089275222 2.0139372015  
H -0.4487095942 -5.4140918779 -0.2728201996  
H -1.471308184 -6.16044801 0.9407448135  
H 0.3036880962 -6.3845928522 1.027456313  
H -0.3607814689 -3.8834691066 3.7639181373  
H 0.3394722963 -5.4832455609 3.4165160206  
H -1.4259935977 -5.2502510586 3.3751335351  
H 1.1215869363 -3.3483703616 -1.2024611707  
H 2.731068145 -3.0884017513 -0.4827058799  
H 1.763690505 -1.6988156711 -1.0475892405  
H 1.4515039436 -1.5339527442 2.6955446381  
H 1.9593773575 -0.6277662805 1.2525839285  
H 2.925389902 -2.0164658705 1.8193728352  
F -3.1133565818 -5.2493385647 -0.7428029902

F -4.8569294162 -3.7669491053 -0.5029785752  
F -5.0140965179 -5.8935858814 0.3919734009

AQ-BF<sub>3</sub>-NO neutral

C -7.0705673232 0.5130600985 -0.9988480409  
C -6.2345797553 1.4803781838 -1.5663507403  
C -4.8652378677 1.4423879108 -1.3333448248  
C -4.3293801465 0.4231635053 -0.5425749676  
C -2.8659897578 0.3635499719 -0.3072656482  
C -2.3151972817 -0.8819912468 0.3288490402  
C -0.9289184313 -1.0326876551 0.2952193146  
C -0.407151634 -2.2140496435 0.7833736867  
C -1.2228599008 -3.2396121732 1.2625334261  
C -2.6241479806 -3.1285420591 1.295888892  
C -3.1479474793 -1.8815833009 0.8534245132  
C -4.6166211037 -1.5848675854 0.9479757441  
C -5.1662783785 -0.5388833708 0.0313732821  
C -6.542180454 -0.4869643583 -0.1896226029  
C -0.4072866059 -4.4281752089 1.7342933839  
N 0.9920675521 -3.9038650775 1.4870593371  
C 1.0520831265 -2.5702279592 0.7922153569  
O -5.3387917071 -2.0986628668 1.7773212065  
O -2.1175844264 1.2570738315 -0.6627043226  
O 1.9646129004 -4.4940190045 1.8040953295  
H -8.1386634044 0.5438384799 -1.1893666158  
H -6.6564178012 2.2614501245 -2.1906905385  
H -4.1941759725 2.183642438 -1.7549078335  
H -0.3197759317 -0.2363333664 -0.1214733262  
C -3.4840184793 -4.3048846776 1.518647155  
H -7.1714392691 -1.2406396451 0.2716182245  
C -0.4918365348 -5.7225343679 0.9026392607  
C -0.4876661008 -4.6994932207 3.245125846  
C 1.6190786249 -2.8390526522 -0.6125030125  
C 1.9510155193 -1.64635493 1.6147242018  
B -3.8865531194 -4.8469108565 -0.0258729446  
H -4.407003343 -4.0726016161 2.0416273171  
H -2.9720064033 -5.1142301488 2.0407698176  
H -0.3978282146 -5.5133585472 -0.1640137433  
H -1.4825831106 -6.1551466215 1.0391421579  
H 0.2758948648 -6.4227399141 1.2434375136  
H -0.2895748049 -3.7881817123 3.8155132421  
H 0.2160561524 -5.4846594447 3.5313314705  
H -1.5028544356 -5.0268421152 3.470791975  
H 0.9802220061 -3.5300709726 -1.1672784521  
H 2.6396204271 -3.2258901033 -0.5501045391  
H 1.6263980074 -1.8838138487 -1.1425561022  
H 1.5608958964 -1.5212125084 2.6276783406  
H 1.9502473086 -0.6691375409 1.1267177848  
H 2.9749303248 -2.0256878793 1.6496123239  
F -2.6842598401 -5.0449236412 -0.7626288524  
F -4.64971643 -3.8534736837 -0.6626714932



F -4.5795992816 -6.05000902 0.0781494566

## Solvent Phase Structure Cartesian Coordinates and Free Energies

AQ-NO singlet anion

G = -1052.802338 H

C 0.6098448143 1.2475474061 0.1061418982  
C 0.3080444666 -0.1054217491 0.3152183202  
C 1.3104260152 -1.0646231621 0.2942455422  
C 2.6327687223 -0.6660034777 0.061817631  
C 2.9352071109 0.6919769928 -0.1521474694  
C 1.9159048114 1.6521288862 -0.1302279888  
C 4.3324687475 1.1370772493 -0.4036595073  
C 5.4059201764 0.0964093998 -0.425008071  
C 5.1051978599 -1.2560839403 -0.2077403454  
C 3.7009846695 -1.7015395649 0.048481034  
C 6.7254048811 0.4853099949 -0.664111993  
C 7.7397533991 -0.4670651645 -0.6863170547  
C 7.4403472149 -1.8143357834 -0.468685625  
C 6.1269325574 -2.2073793145 -0.2302070886  
O 4.6048362979 2.3133844787 -0.5874221961  
O 3.4494327535 -2.8811615746 0.2404278998  
C -0.6455096581 2.0744526501 0.2219489213  
C -1.1687783622 -0.2659323344 0.5752475286  
H 8.2325901725 -2.5564281382 -0.4857720083  
H 5.8767742593 -3.2494386602 -0.0595261973  
N -1.6947249934 1.0279202763 0.0544973331  
O -2.9220241864 1.3830789552 0.595341511  
C -0.7948294995 3.0984280112 -0.9035704918  
C -0.6918086494 2.8127934394 1.57260953  
C -1.4385865578 -0.5086563204 2.0712853684  
C -1.7977707746 -1.4051000991 -0.2286145728  
H -0.7190098652 2.6078695458 -1.8790332638  
H -0.0349101861 3.886108968 -0.8400153342  
H -1.784039965 3.561556501 -0.8269361803  
H -0.4030320941 2.1706077061 2.4083822034  
H -1.7216609089 3.1439883942 1.7330719602  
H -0.0178658333 3.6770050892 1.5606192769  
H -0.9056463216 0.200012232 2.7097377661  
H -1.1302849976 -1.5214645571 2.3551821071  
H -2.5109924325 -0.3846007656 2.2435603546  
H -1.5634772404 -1.2969997392 -1.292064392  
H -2.8850036985 -1.3553919697 -0.107710591  
H -1.4512522743 -2.3866784405 0.1156716833  
H 1.0971839517 -2.1182819681 0.4535819511  
H 2.1699909626 2.69521462 -0.2984478396  
H 6.9401601785 1.5359720002 -0.8304473097  
H 8.7647154764 -0.1616180729 -0.8726343006

AQ-NO triplet anion

G = -1052.839037 H

C -6.1107577405 1.9926353538 -0.0359244503  
C -6.1057568344 0.5784904141 -0.014791921  
C -4.9081604896 -0.1050430092 0.0114734982  
C -3.6729639909 0.5840049515 0.0177936988  
C -3.6779901832 2.0052992042 -0.0034469776  
C -4.9180273593 2.6850994285 -0.0302218686  
C -2.4401970145 2.780418654 0.0016129758  
C -1.1950916845 2.0157003776 0.0297181383  
C -1.1900576192 0.5921559677 0.0509929058  
C -2.4297215708 -0.181845284 0.0458905536  
C 0.0350601033 2.7154846406 0.0357660137  
C 1.2208557798 2.01985638 0.0620106457  
C 1.2258554682 0.6060493161 0.0831394071  
C 0.0450108517 -0.0984194813 0.0778180206  
O -2.4431886708 4.0374612019 -0.0171608547  
O -2.4238218648 -1.4388779786 0.064641305  
C 2.6240120341 2.5781572101 0.0723615089  
N 3.41291867 1.3211274377 0.1014985918  
C 2.6329233041 0.0582422318 0.1100226503  
O 4.6809348438 1.32585482 0.1177924539  
H -7.0543738764 2.5307165766 -0.0566115829  
H -7.0455424144 0.0333724429 -0.019291727  
H -4.8815513207 -1.19052959 0.0279958982  
H -4.8990959935 3.7707559888 -0.0461467528  
H 0.0060117768 3.8020608521 0.0191358017  
H 0.0236479802 -1.1851855862 0.0936695817  
C 2.9292832715 3.4033955071 1.3244096886  
C 2.9628812008 3.3660584073 -1.1949751748  
C 2.9438873166 -0.727031382 1.3861424128  
C 2.9774920228 -0.7647649554 -1.1332363702  
H 2.6924453914 2.8360276135 2.2293614672  
H 2.3294836956 4.3185962922 1.3191943242  
H 3.9888052878 3.6761528481 1.3416034785  
H 2.7502773977 2.77189303 -2.0886819269  
H 4.0225429827 3.6387808965 -1.1918572824  
H 2.3633400251 4.2806438442 -1.2330465736  
H 2.7029424575 -0.1345624296 2.2737585524  
H 4.0053099226 -0.9916528145 1.4113734866  
H 2.3505758401 -1.6461983716 1.4083399519  
H 2.7607821398 -0.199094706 -2.0442789781  
H 2.3844419226 -1.6842992859 -1.1438922263  
H 4.0390569409 -1.0297670146 -1.1220823442

AQ-NO open-shell singlet anion

G = -1052.837980 H

C -6.1107577405 1.9926353538 -0.0359244503  
C -6.1057568344 0.5784904141 -0.014791921  
C -4.9081604896 -0.1050430092 0.0114734982  
C -3.6729639909 0.5840049515 0.0177936988  
C -3.6779901832 2.0052992042 -0.0034469776  
C -4.9180273593 2.6850994285 -0.0302218686

C -2.4401970145 2.780418654 0.0016129758  
C -1.1950916845 2.0157003776 0.0297181383  
C -1.1900576192 0.5921559677 0.0509929058  
C -2.4297215708 -0.181845284 0.0458905536  
C 0.0350601033 2.7154846406 0.0357660137  
C 1.2208557798 2.01985638 0.0620106457  
C 1.2258554682 0.6060493161 0.0831394071  
C 0.0450108517 -0.0984194813 0.0778180206  
O -2.4431886708 4.0374612019 -0.0171608547  
O -2.4238218648 -1.4388779786 0.064641305  
C 2.6240120341 2.5781572101 0.0723615089  
N 3.41291867 1.3211274377 0.1014985918  
C 2.6329233041 0.0582422318 0.1100226503  
O 4.6809348438 1.32585482 0.1177924539  
H -7.0543738764 2.5307165766 -0.0566115829  
H -7.0455424144 0.0333724429 -0.019291727  
H -4.8815513207 -1.19052959 0.0279958982  
H -4.8990959935 3.7707559888 -0.0461467528  
H 0.0060117768 3.8020608521 0.0191358017  
H 0.0236479802 -1.1851855862 0.0936695817  
C 2.9292832715 3.4033955071 1.3244096886  
C 2.9628812008 3.3660584073 -1.1949751748  
C 2.9438873166 -0.727031382 1.3861424128  
C 2.9774920228 -0.7647649554 -1.1332363702  
H 2.6924453914 2.8360276135 2.2293614672  
H 2.3294836956 4.3185962922 1.3191943242  
H 3.9888052878 3.6761528481 1.3416034785  
H 2.7502773977 2.77189303 -2.0886819269  
H 4.0225429827 3.6387808965 -1.1918572824  
H 2.3633400251 4.2806438442 -1.2330465736  
H 2.7029424575 -0.1345624296 2.2737585524  
H 4.0053099226 -0.9916528145 1.4113734866  
H 2.3505758401 -1.6461983716 1.4083399519  
H 2.7607821398 -0.199094706 -2.0442789781  
H 2.3844419226 -1.6842992859 -1.1438922263  
H 4.0390569409 -1.0297670146 -1.1220823442

AQ-NO radical

G = -1052.723378 H

C -6.130916885 1.9839633626 -0.036369304  
C -6.1259767569 0.5870009713 -0.0154892281  
C -4.919994146 -0.1066477876 0.0113391898  
C -3.7117442562 0.5928713247 0.0174102303  
C -3.7167066898 1.996150113 -0.0035650709  
C -4.9298720535 2.6866142559 -0.0304112368  
C -2.4418119856 2.7713602216 0.0023035891  
C -1.1601682738 2.0069056981 0.0307863183  
C -1.1551973462 0.6012246827 0.0517977045  
C -2.4314006496 -0.1727828868 0.0463144632  
C 0.0434211016 2.7166951351 0.0362246232  
C 1.2381636852 2.0122709164 0.0625645724

C 1.2431092709 0.6137701921 0.0834683406  
C 0.0533802727 -0.0995568756 0.078319484  
O -2.4455919573 3.990945004 -0.0156212495  
O -2.4265549503 -1.3923549971 0.0648345439  
C 2.6367500354 2.5771038141 0.0726155875  
N 3.425935413 1.3211859413 0.1022921931  
C 2.6456534904 0.0593933792 0.1102501604  
O 4.6922937087 1.3259114038 0.1188358893  
H -7.0724538213 2.5236182971 -0.0572829029  
H -7.0636720413 0.040317955 -0.020165272  
H -4.8993502868 -1.1914600378 0.0278071696  
H -4.9169011331 3.7715529077 -0.0463750204  
H 0.0207436781 3.8027311904 0.01975258  
H 0.0383844246 -1.185733245 0.0943165958  
C 2.9306361587 3.4043735359 1.3255955907  
C 2.9641668262 3.365827497 -1.196819365  
C 2.9452489648 -0.7279564917 1.3873665881  
C 2.9787751863 -0.7645853968 -1.1350773745  
H 2.6945633169 2.8375065538 2.2308769129  
H 2.3310246136 4.3194556141 1.3159022615  
H 3.9893768116 3.6779094743 1.3430191766  
H 2.7519348912 2.7715193544 -2.0903272615  
H 4.0231212025 3.6390853367 -1.1944799991  
H 2.3649202178 4.2805668342 -1.2309778689  
H 2.7050808745 -0.1359663799 2.2753248398  
H 4.0058948325 -0.9933591828 1.4128451702  
H 2.3521215678 -1.6471347352 1.4050939114  
H 2.7624473346 -0.1987629614 -2.0459276668  
H 2.3860114799 -1.6841488316 -1.1418199473  
H 4.0396338733 -1.0301611574 -1.1246789182

1,2,5,8-THAQ-NO singlet anion

G = -1353.6269 H

C -3.9193737818 2.7450037137 -0.0302420633  
C -3.9051664937 1.3695737405 0.0126539548  
C -2.6840687691 0.6516215042 0.0408281439  
C -1.4776772014 1.3621857519 0.0041989739  
C -1.4917668093 2.7951932771 -0.0371795815  
C -2.7147472264 3.4859673485 -0.0437869709  
C -0.2460548736 3.5371707889 -0.0623624403  
C 1.0261351567 2.8022586899 -0.0655211825  
C 1.0508719613 1.3895484178 -0.0285941886  
C -0.2151784669 0.6265865597 0.0191320945  
C 2.2333808313 3.5066079745 -0.1063031768  
C 3.4574975196 2.8052785397 -0.1133654975  
C 3.4676688633 1.4196569808 -0.0779223038  
C 2.26363933 0.7134474691 -0.0346479818  
O -0.2315952547 4.7953168953 -0.084161813  
O -0.1891629097 -0.615426067 0.0697925644  
C -5.3384540698 3.2586623462 0.0008708429  
C -5.3131438539 0.8310382636 0.0834245694

O -2.7301262569 -0.6842154932 0.1076432429  
O -2.7962988354 4.8225452863 -0.0546019874  
O 2.3321656945 4.8481508398 -0.1413874225  
O 4.615781856 3.4961875893 -0.1544736618  
H 4.4215844227 0.9022373134 -0.0843647644  
H 1.4129405084 5.2069084574 -0.1291187475  
H 4.4181132336 4.4461476317 -0.1752712684  
H 2.2637216066 -0.3704988156 -0.0058164776  
H -1.7905876515 -0.9986296391 0.1119794455  
H -1.8785912701 5.1759797433 -0.0659341801  
N -6.0919920333 2.0232001486 -0.3601666615  
O -7.4015226344 2.0265338619 0.0972687244  
C -5.6442994467 4.316313287 -1.0637877618  
C -5.6776538838 3.8306695478 1.3881870929  
C -5.6338601582 0.3501127713 1.5100679146  
C -5.601668492 -0.3047525739 -0.9020569957  
H -5.2754210184 3.9926534072 -2.0426159925  
H -5.2067117985 5.2880836128 -0.819613691  
H -6.7333989642 4.4142101277 -1.1239967075  
H -5.3940508184 3.151163632 2.195904111  
H -6.7606297713 3.9734633679 1.4310255164  
H -5.1650116101 4.7859186421 1.5426414797  
H -5.3400328374 1.0797921493 2.2688624086  
H -5.1173816876 -0.5924534057 1.7196663143  
H -6.7162245659 0.208825705 1.5746891762  
H -5.2472852323 -0.0422749899 -1.9041810954  
H -6.6885436883 -0.4320961257 -0.9450060684  
H -5.1386486191 -1.2462582731 -0.5948158867

1,2,5,8-THAQ-NO triplet anion

G = -1353.67933 H  
C -3.9058481954 2.7635972747 0.0879188656  
C -3.8950410671 1.3612764979 0.1325061313  
C -2.7032690785 0.6499417208 0.1226091725  
C -1.4771116861 1.3671710978 0.0660132708  
C -1.4888218984 2.7980793045 0.0205480065  
C -2.7299059877 3.4944222923 0.0323276068  
C -0.2569396034 3.5317741949 -0.0367830765  
C 0.9829272799 2.7979516063 -0.0473608115  
C 1.0081473721 1.3767951906 -0.002572525  
C -0.2337894816 0.6270164625 0.0555283545  
C 2.2082508695 3.502466374 -0.1035707245  
C 3.4158564395 2.8124211133 -0.1146716092  
C 3.433110233 1.4116455789 -0.0703096912  
C 2.2441025334 0.7051640735 -0.0150292594  
O -0.2462231528 4.8307356055 -0.0786285456  
O -0.2287189771 -0.6468154321 0.0961541776  
C -5.3117743558 3.3111111428 0.1088241258  
C -5.2901601953 0.7913078115 0.1889690706  
O -2.7133181047 -0.6961207677 0.16600871  
O -2.7783501644 4.8453643684 -0.009528036

O 2.2645319444 4.8528491821 -0.1483194561  
O 4.5868562984 3.503018445 -0.1689493691  
H 4.3922344307 0.9026907567 -0.080364422  
H 1.3033287166 5.1513567407 -0.1314264854  
H 4.3745272669 4.4490714802 -0.1934161429  
H 2.2448430143 -0.3788502723 0.0196479706  
H -1.7319147466 -0.9548016208 0.1473420385  
H -1.8280395725 5.1465320393 -0.0453231673  
N -6.0850644242 2.0449892345 0.1704833108  
O -7.3523519574 2.035938924 0.2052334443  
C -5.6792621383 4.0721573081 -1.1674564721  
C -5.6105557017 4.1528724876 1.3518880144  
C -5.5745098101 0.0241295811 1.4829006505  
C -5.643473255 -0.0567776727 -1.0356094079  
H -5.4718421282 3.4635014276 -2.0528450519  
H -5.0936544106 4.9930731418 -1.2267825182  
H -6.7440555875 4.3236370605 -1.1514281584  
H -5.3539651955 3.6018739853 2.2618113611  
H -6.6751353664 4.4044383714 1.3778807882  
H -5.0244040965 5.0748060112 1.3200978891  
H -5.3314926982 0.6368409346 2.3563180938  
H -4.9684401502 -0.8850566534 1.5099775355  
H -6.6335578619 -0.2481193478 1.5242235256  
H -5.449436499 0.4981527226 -1.9585008423  
H -6.7027700296 -0.3290326125 -1.0015303736  
H -5.0383488209 -0.9669871653 -1.0372659686

1,2,5,8-THAQ-NO open-shell singlet anion

G = -1353.678270 H  
C -3.9058481954 2.7635972747 0.0879188656  
C -3.8950410671 1.3612764979 0.1325061313  
C -2.7032690785 0.6499417208 0.1226091725  
C -1.4771116861 1.3671710978 0.0660132708  
C -1.4888218984 2.7980793045 0.0205480065  
C -2.7299059877 3.4944222923 0.0323276068  
C -0.2569396034 3.5317741949 -0.0367830765  
C 0.9829272799 2.7979516063 -0.0473608115  
C 1.0081473721 1.3767951906 -0.002572525  
C -0.2337894816 0.6270164625 0.0555283545  
C 2.2082508695 3.502466374 -0.1035707245  
C 3.4158564395 2.8124211133 -0.1146716092  
C 3.433110233 1.4116455789 -0.0703096912  
C 2.2441025334 0.7051640735 -0.0150292594  
O -0.2462231528 4.8307356055 -0.0786285456  
O -0.2287189771 -0.6468154321 0.0961541776  
C -5.3117743558 3.3111111428 0.1088241258  
C -5.2901601953 0.7913078115 0.1889690706  
O -2.7133181047 -0.6961207677 0.16600871  
O -2.7783501644 4.8453643684 -0.009528036  
O 2.2645319444 4.8528491821 -0.1483194561  
O 4.5868562984 3.503018445 -0.1689493691

H 4.3922344307 0.9026907567 -0.080364422  
H 1.3033287166 5.1513567407 -0.1314264854  
H 4.3745272669 4.4490714802 -0.1934161429  
H 2.2448430143 -0.3788502723 0.0196479706  
H -1.7319147466 -0.9548016208 0.1473420385  
H -1.8280395725 5.1465320393 -0.0453231673  
N -6.0850644242 2.0449892345 0.1704833108  
O -7.3523519574 2.035938924 0.2052334443  
C -5.6792621383 4.0721573081 -1.1674564721  
C -5.6105557017 4.1528724876 1.3518880144  
C -5.5745098101 0.0241295811 1.4829006505  
C -5.643473255 -0.0567776727 -1.0356094079  
H -5.4718421282 3.4635014276 -2.0528450519  
H -5.0936544106 4.9930731418 -1.2267825182  
H -6.7440555875 4.3236370605 -1.1514281584  
H -5.3539651955 3.6018739853 2.2618113611  
H -6.6751353664 4.4044383714 1.3778807882  
H -5.0244040965 5.0748060112 1.3200978891  
H -5.3314926982 0.6368409346 2.3563180938  
H -4.9684401502 -0.8850566534 1.5099775355  
H -6.6335578619 -0.2481193478 1.5242235256  
H -5.449436499 0.4981527226 -1.9585008423  
H -6.7027700296 -0.3290326125 -1.0015303736  
H -5.0383488209 -0.9669871653 -1.0372659686

1,2,5,8-THAQ-NO radical

G = -1353.547363 H

C -3.923652785 2.7499316139 0.0887912468  
C -3.9091362856 1.3750207317 0.1324579249  
C -2.6944890126 0.6539155381 0.1222445918  
C -1.4935715665 1.3685374397 0.0663992618  
C -1.5076039495 2.7962040785 0.0210196134  
C -2.7243081167 3.4919640785 0.032110455  
C -0.2530089066 3.5403115371 -0.0372722784  
C 1.015248518 2.8046341483 -0.0485196033  
C 1.038587369 1.3903624457 -0.0037900299  
C -0.22416 0.6292199425 0.0552790629  
C 2.2229972706 3.506381561 -0.1041986632  
C 3.4473686931 2.8013972109 -0.1151784846  
C 3.4545945797 1.4163797634 -0.0709291097  
C 2.2495017346 0.7124101859 -0.0152748475  
O -0.2502874571 4.793024336 -0.0774888818  
O -0.2102632281 -0.6101227092 0.0946354956  
C -5.3255361848 3.3078455406 0.1093436793  
C -5.2978573405 0.7898967395 0.1892795956  
O -2.7519345042 -0.6822721955 0.1666340798  
O -2.8188252226 4.8273070071 -0.0080572294  
O 2.3298718797 4.8452518283 -0.1501518445  
O 4.6050767383 3.4872079452 -0.1689721345  
H 4.4070873016 0.8966494523 -0.0803922508  
H 1.4211419131 5.220866346 -0.137316354

H 4.4155296712 4.4388836303 -0.1942865089  
H 2.2493874562 -0.3713941459 0.0195010458  
H -1.8156301891 -1.0063751331 0.1513045866  
H -1.9056289364 5.1905103487 -0.0447118828  
N -6.095603908 2.0407422696 0.1711455927  
O -7.3607536913 2.0280093533 0.2060339018  
C -5.6884697355 4.0671969111 -1.1692199568  
C -5.6192657612 4.1482014416 1.3545750059  
C -5.571731584 0.0233885955 1.4857616272  
C -5.6409716397 -0.0574270818 -1.0386061982  
H -5.4677536028 3.464600278 -2.0552339837  
H -5.1240073458 5.001041829 -1.2227528608  
H -6.7575734907 4.2972361833 -1.155447495  
H -5.3493393221 3.6031978353 2.2639564799  
H -6.687921445 4.3787760383 1.3846390241  
H -5.0543449935 5.0825534065 1.3172177051  
H -5.3160563861 0.631675023 2.3584213163  
H -4.9834492124 -0.8969257743 1.5071807151  
H -6.6343852266 -0.2311806863 1.531177871  
H -5.4344066883 0.4933067044 -1.9610690821  
H -6.70409166 -0.3124266121 -1.009462152  
H -5.0532037471 -0.9783049801 -1.0332380466

1,4,5-TAAQ-NO singlet anion

G = -1218.792343 H

C -5.3002078319 2.7445603644 -0.0399255825  
C -5.2748728799 1.3612305393 -0.072359345  
C -4.0479964504 0.6572036468 -0.0939385654  
C -2.8369252373 1.4152924992 -0.0491137479  
C -2.9080808394 2.8302937511 0.0026085515  
C -4.1244018096 3.497533217 0.0030134327  
C -1.6735076428 3.6617984847 0.055284845  
C -0.366470323 2.9988393386 0.0597915719  
C -0.2926074641 1.5638138213 -0.0080049254  
C -1.5266338973 0.7544255725 -0.0768805208  
C 0.8044393285 3.7754802578 0.1466794106  
C 0.9593707623 0.9230544687 0.0110650219  
C 2.0540580904 3.0950125469 0.1834434322  
C 2.1247567216 1.7357310739 0.1177747667  
O -1.7809282906 4.8937333881 0.1006712151  
O -1.4462652665 -0.4880974063 -0.153583559  
C -6.7225977506 3.242617915 -0.0914593724  
C -6.6900074347 0.8187748793 -0.1352884497  
N -4.0639346648 -0.7060445599 -0.1308215954  
H -4.1380999449 4.581908154 0.0373113357  
N 0.8286134165 5.1403754065 0.1671881637  
H 2.964164594 3.6848296323 0.2580841869  
H 3.0939673158 1.2434688031 0.139594698  
H -0.04506112 5.63398199 0.2825675871  
H 1.691295635 5.5965346208 0.4243216453  
N 1.1588044265 -0.4286037431 -0.103255502



H -4.9300383297 -1.1704492521 -0.3523381469  
H -3.1916814675 -1.190520233 -0.2831864372  
H 0.3544560387 -1.0310896142 -0.0053145757  
H 2.0621622995 -0.785784847 0.1722646764  
N -7.470753122 2.0205719325 0.2946707052  
O -8.7872357884 2.0087358911 -0.1437559906  
C -7.0559355703 3.7824265668 -1.4940874139  
C -7.0101563142 4.3373626719 0.9380559591  
C -7.0211625742 -0.2798044026 0.8854269111  
C -7.0446186402 0.318834024 -1.5486710463  
H -6.7754803326 3.0799963914 -2.283001542  
H -6.5291338681 4.7265650802 -1.6746220836  
H -8.1356855199 3.944064857 -1.5502057764  
H -6.7121654767 4.0070298395 1.9382713398  
H -8.087165463 4.5361269625 0.9460084108  
H -6.4847402429 5.2696429735 0.6995640867  
H -6.5740932852 -0.0538767198 1.8585552589  
H -6.7085905426 -1.2838030896 0.5765879012  
H -8.1107672593 -0.2842362104 0.9966452023  
H -6.6871349048 0.995487923 -2.3289690594  
H -8.136028753 0.2678375919 -1.6086546673  
H -6.6185523265 -0.6726869985 -1.7427824112

1,4,5-TAAQ-NO triplet anion

G = -1218.820115 H  
C -5.285844656 2.7599451957 -0.1417364474  
C -5.266219901 1.3560915972 -0.1702866884  
C -4.0566752433 0.656732372 -0.1311304136  
C -2.8242107245 1.4071438858 -0.0774372033  
C -2.8883109654 2.8274009767 -0.0365843313  
C -4.1287146665 3.4987959471 -0.0674568748  
C -1.6861113519 3.6532207069 0.0457372442  
C -0.3937070575 2.9904596952 0.031693722  
C -0.3167505717 1.5512777076 -0.0404992914  
C -1.528711052 0.7392158306 -0.0841013956  
C 0.8059018421 3.7635490499 0.1188384674  
C 0.9683229663 0.920529884 -0.0298630987  
C 2.0304080337 3.1022346021 0.1713361875  
C 2.1079830303 1.7138407675 0.0968615912  
O -1.8154465436 4.9119864274 0.1349865872  
O -1.4576775095 -0.5349775181 -0.1229923717  
C -6.694284167 3.3000169997 -0.189412951  
C -6.6706119428 0.7834595114 -0.2167480362  
N -4.0505370842 -0.7203818083 -0.0940885237  
H -4.1326660983 4.5829415928 -0.032572182  
N 0.7993791046 5.156410302 0.0997411658  
H 2.9415958398 3.6912752409 0.2483974781  
H 3.0805428789 1.227077682 0.1161318065  
H -0.1108043566 5.5600198131 0.3010770348  
H 1.5907365984 5.5873430348 0.5590278998  
N 1.146843815 -0.4525152176 -0.1930258943

H -4.8453208611 -1.2021023413 -0.4849721636  
H -3.1314498839 -1.1323355169 -0.2366261055  
H 0.307833491 -0.9963770806 -0.0240712005  
H 1.9983058351 -0.8128773701 0.2172589906  
N -7.466670513 2.0385463794 -0.1586128746  
O -8.7337794462 2.0270096553 -0.2035718389  
C -6.9931147172 4.0546153592 -1.4883490518  
C -7.0539722901 4.1511478857 1.0288150055  
C -7.0421200623 -0.0739774968 0.9981055588  
C -7.0214019593 0.0625963478 -1.5256656936  
H -6.7336255101 3.4448809378 -2.359060474  
H -6.4067914449 4.9777180997 -1.5229545836  
H -8.0565912298 4.3083900901 -1.5347707198  
H -6.8471309937 3.606519147 1.954875641  
H -8.1156578023 4.4143465815 0.99878581  
H -6.4629385163 5.0718109295 1.0253265633  
H -6.7980674539 0.4527707454 1.9254032899  
H -6.5040447108 -1.0249055987 0.9890548426  
H -8.1167400195 -0.2799832869 0.9794289727  
H -6.7336991923 0.6690401361 -2.3893428525  
H -8.1009736207 -0.1132421437 -1.5589363936  
H -6.5201093161 -0.9065057378 -1.6007842036

1,4,5-THAQ-NO open-shell singlet anion

G = -1218.819063 H

C -5.285844656 2.7599451957 -0.1417364474  
C -5.266219901 1.3560915972 -0.1702866884  
C -4.0566752433 0.656732372 -0.1311304136  
C -2.8242107245 1.4071438858 -0.0774372033  
C -2.8883109654 2.8274009767 -0.0365843313  
C -4.1287146665 3.4987959471 -0.0674568748  
C -1.6861113519 3.6532207069 0.0457372442  
C -0.3937070575 2.9904596952 0.031693722  
C -0.3167505717 1.5512777076 -0.0404992914  
C -1.528711052 0.7392158306 -0.0841013956  
C 0.8059018421 3.7635490499 0.1188384674  
C 0.9683229663 0.920529884 -0.0298630987  
C 2.0304080337 3.1022346021 0.1713361875  
C 2.1079830303 1.7138407675 0.0968615912  
O -1.8154465436 4.9119864274 0.1349865872  
O -1.4576775095 -0.5349775181 -0.1229923717  
C -6.694284167 3.3000169997 -0.189412951  
C -6.6706119428 0.7834595114 -0.2167480362  
N -4.0505370842 -0.7203818083 -0.0940885237  
H -4.1326660983 4.5829415928 -0.032572182  
N 0.7993791046 5.156410302 0.0997411658  
H 2.9415958398 3.6912752409 0.2483974781  
H 3.0805428789 1.227077682 0.1161318065  
H -0.1108043566 5.5600198131 0.3010770348  
H 1.5907365984 5.5873430348 0.5590278998  
N 1.146843815 -0.4525152176 -0.1930258943

H -4.8453208611 -1.2021023413 -0.4849721636  
H -3.1314498839 -1.1323355169 -0.2366261055  
H 0.307833491 -0.9963770806 -0.0240712005  
H 1.9983058351 -0.8128773701 0.2172589906  
N -7.466670513 2.0385463794 -0.1586128746  
O -8.7337794462 2.0270096553 -0.2035718389  
C -6.9931147172 4.0546153592 -1.4883490518  
C -7.0539722901 4.1511478857 1.0288150055  
C -7.0421200623 -0.0739774968 0.9981055588  
C -7.0214019593 0.0625963478 -1.5256656936  
H -6.7336255101 3.4448809378 -2.359060474  
H -6.4067914449 4.9777180997 -1.5229545836  
H -8.0565912298 4.3083900901 -1.5347707198  
H -6.8471309937 3.606519147 1.954875641  
H -8.1156578023 4.4143465815 0.99878581  
H -6.4629385163 5.0718109295 1.0253265633  
H -6.7980674539 0.4527707454 1.9254032899  
H -6.5040447108 -1.0249055987 0.9890548426  
H -8.1167400195 -0.2799832869 0.9794289727  
H -6.7336991923 0.6690401361 -2.3893428525  
H -8.1009736207 -0.1132421437 -1.5589363936  
H -6.5201093161 -0.9065057378 -1.6007842036

1,4,5-TAAQ-NO radical

G = -1218.716835 H

C -5.2998378855 2.7404221131 -0.1575389447  
C -5.2803581076 1.3556403032 -0.1949129183  
C -4.0560269226 0.6459905774 -0.1563205025  
C -2.8475308434 1.4083759005 -0.084590252  
C -2.9177350649 2.8193881476 -0.0458676242  
C -4.1306631951 3.4923479144 -0.0808922307  
C -1.6826787169 3.6563000536 0.0380034918  
C -0.3842506897 2.9966002226 0.0648415723  
C -0.3071396967 1.5579907955 0.0029735767  
C -1.5294492632 0.7466001076 -0.0673692706  
C 0.7851920007 3.7763225018 0.1493151823  
C 0.9474038372 0.9213644797 0.0216423206  
C 2.0413902369 3.0975146912 0.1713291813  
C 2.1152279529 1.7416254648 0.1084022787  
O -1.804316857 4.887734757 0.0829071662  
O -1.4520549203 -0.4980260017 -0.1145501184  
C -6.7020152437 3.2922658711 -0.1977635857  
C -6.6830996606 0.7783681279 -0.2578555388  
N -4.0592982146 -0.7144474191 -0.1555086045  
H -4.1453766627 4.5761249014 -0.0477183676  
N 0.8023642339 5.1311349038 0.2161609368  
H 2.949898308 3.6905146527 0.2380756285  
H 3.0857839006 1.2520852558 0.1218001747  
H -0.0663574579 5.6444875048 0.1863587304  
H 1.6860908871 5.6155410929 0.2559454926  
N 1.1488008948 -0.4231736749 -0.0630572804

H -4.9004145331 -1.2169570551 -0.3856519708  
H -3.1704031271 -1.1883082247 -0.2383139305  
H 0.3537911334 -1.0420890408 -0.0112058414  
H 2.0760584733 -0.783251916 0.1060382699  
N -7.474841553 2.0362124939 -0.2887377924  
O -8.7409652437 2.0261534763 -0.3180449162  
C -6.9652021041 4.1533499713 -1.4344963056  
C -7.0751248052 4.0419923277 1.0833868807  
C -7.0827957581 -0.0128920827 0.9933704918  
C -6.9987692888 -0.0062389973 -1.5371303703  
H -6.6937525381 3.6148376668 -2.3472607738  
H -6.3765408393 5.0738731823 -1.3803331739  
H -8.0259087244 4.4168353696 -1.4786034657  
H -6.8852008513 3.4231505578 1.9652818415  
H -8.1356748466 4.3080682288 1.0566750121  
H -6.4838754514 4.9589706467 1.1633356672  
H -6.8749253231 0.5670180952 1.897171416  
H -6.5403720416 -0.9597761875 1.0561016031  
H -8.154012196 -0.2298575303 0.9499492343  
H -6.6391118122 0.5297214731 -2.4201295674  
H -8.0837096454 -0.1244524309 -1.6120244481  
H -6.555841774 -1.0052732688 -1.5279583548